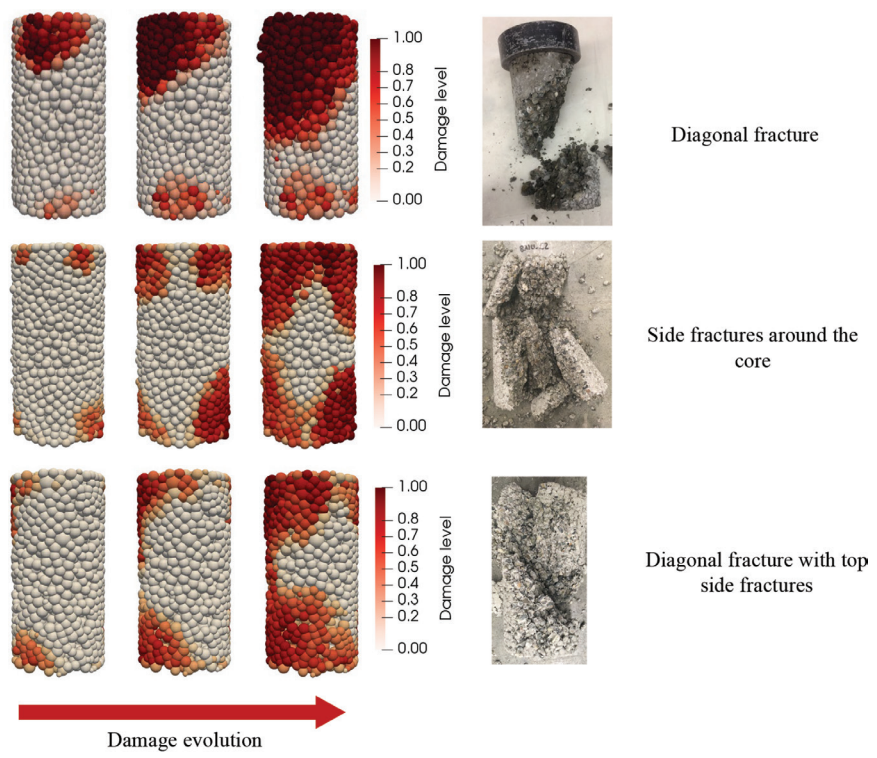


ACI MATERIALS JOURNAL

A JOURNAL OF THE AMERICAN CONCRETE INSTITUTE



Editorial Board

W. Jason Weiss, Editor-in-Chief,
Oregon State University
 Liberato Ferrara,
Polytechnic University of Milan
 Zachary C. Grasley,
Texas A&M University
 Shihoh Kawashima,
Columbia University
 Kamal H. Khayat,
Missouri University of Science & Technology

Board of Direction

President
 Antonio Nanni

Vice Presidents
 Michael J. Paul
 Maria Juenger

Directors
 Oscar R. Antommatei
 Peter Barlow
 Michael C. Brown
 Arturo Gaytan Covarrubias
 Anthony R. DeCarlo Jr.
 John W. Gajda
 Carol Hayek
 Kamal H. Khayat
 Robert C. Lewis
 Anton K. Schindler
 Matthew R. Sherman
 Lawrence L. Sutter

Past President Board Members
 Jeffrey W. Coleman
 Cary S. Kopczynski
 Charles K. Nmai

Executive Vice President
 Frederick H. Grubbe

Staff
Publisher
 John C. Glumb
Senior Managing Director of Technical Operations
 Michael L. Tholen

Engineers
 Will J. Gold
 Matthew R. Senecal
 Michael L. Tholen
 Gregory M. Zeisler

Managing Editor
 Lauren E. Mentz

Associate Editor
 Kimberly K. Olesky

Editors
 Erin N. Azzopardi
 Lauren C. Brown
 Kaitlyn J. Dobberteen
 Tiesha Elam
 Angela R. Noelker
 Kelli R. Slayden

ACI MATERIALS JOURNAL**NOVEMBER 2023, V. 120, No. 6**

A JOURNAL OF THE AMERICAN CONCRETE INSTITUTE
 AN INTERNATIONAL TECHNICAL SOCIETY

- 5 **Discrete Element Modeling of Pervious Concrete Compressive Strength to Optimize Mixture Composition**, by Othman AlShareedah and Somayeh Nassiri
- 19 **An Improved Prediction for Bond Strength of Deformed Bars in Concrete Externally Confined with Fiber-Reinforced Polymer**, by Zhenwen Xu and Dongming Yan
- 33 **Methodology for Predicting Concrete Strength after Short-Term Heat Exposure**, by Stephen Wright and Laura Redmond
- 47 **Examining Carbonation of Calcium Silicate-Based Cements in Real Time Using Neutron Radiography**, by Rita Maria Ghantous, Margaret N. Goodwin, Mehdi Khanzadeh Moradillo, Sean Quinn, Vahit Aktan, O. Burkan Isgor, Steven Reese, and W. Jason Weiss
- 61 **Numerical Compressive Toughness of Steel Fiber-Based Reinforced Concrete with Various Densities**, by Hak-Young Kim, Hye-Jin Lee, Keun-Hyeok Yang, and Seung-Jun Kwon
- 71 **Field Assessment of Biogenic Acid Attack in Concrete Structures**, by Ali Abu-Yosef, Stalin Armijos-Moya, and Randall Poston
- 81 **Family of Thermal Nomograms for Mass Concrete**, by J. Brown, L. E. Al-Hasani, J. Park, K. E. Kurtis, R. Gentry, and Y. K. Cho
- 95 **Automated Procedure to Identify Concrete Defects from Impact-Echo Data**, by Zachary W. Coleman and Anton K. Schindler
- 107 **Influence of Mixture Proportions and Permeability-Reducing Admixtures on Concrete Fluid Transport**, by R. M. Ghantous, V. Bui, S. Schaef, B. Fronczek, C. B. Jablonski, S. R. Reese, and W. J. Weiss
- 121 **Enhancing Factors of Stone Powder for Hardened Mortar**, by Hongbo Zhu, Yilu Zhang, Hongxiang Gou, Liang Ren, and Qing Chen
- 129 **Alkali-Silica Reaction Evaluation of Coarse Aggregates from Massachusetts Using Accelerated Tests**, by J. F. Muñoz, C. Balachandran, A. Shastry, R. Mulcahy, J. M. Robertson, and T. S. Arnold
- 141 **Corrosion Behavior of Conventional and Corrosion-Resistant Steel Reinforcements in High-Performance and Ultra-High-Performance Concrete**, by Ben Wang, Abdeldjelil Belarbi, Mina Dawood, and Bora Gencturk

Discussion is welcomed for all materials published in this issue and will appear ten months from this journal's date if the discussion is received within four months of the paper's print publication. Discussion of material received after specified dates will be considered individually for publication or private response. ACI Standards published in ACI Journals for public comment have discussion due dates printed with the Standard.

ACI Materials Journal
 Copyright © 2023 American Concrete Institute. Printed in the United States of America.

The *ACI Materials Journal* (ISSN 0889-325x) is published bimonthly by the American Concrete Institute. Publication office: 38800 Country Club Drive, Farmington Hills, MI 48331. Periodicals postage paid at Farmington, MI, and at additional mailing offices. Subscription rates: \$192 per year, payable in advance. POSTMASTER: Send address changes to: *ACI Materials Journal*, 38800 Country Club Drive, Farmington Hills, MI 48331.

Canadian GST: R 1226213149.

Direct correspondence to 38800 Country Club Drive, Farmington Hills, MI 48331. Telephone: +1.248.848.3700.
 Website: <http://www.concrete.org>.



MEETINGS

DECEMBER 2023

8—ATC at 50: Celebrating the Past, Engaging the Present, and Envisioning the Future, San Francisco, CA, www.atcouncil.org

18-19—ICCET 2023: International Conference on Concrete Engineering and Technology, Cairo, Egypt, <https://waset.org/concrete-engineering-and-technology-conference-in-december-2023-in-cairo>

JANUARY 2024

7-11—TRB 103rd Annual Meeting, Washington, DC, <https://www.trb.org/AnnualMeeting/AnnualMeeting.aspx>

16-18—AED Summit, Las Vegas, NV, https://aedsummit2024.mapyourshow.com/8_0/#/

22-25—World of Concrete, Las Vegas, NV, www.worldofconcrete.com

23-25—National Pavement Expo and Conference, Tampa, FL, <http://nationalpavementexpo.com>

FEBRUARY 2024

6-9—2024 PCI Convention at The Precast Show, Denver, CO, www pci.org/PCI/News-Events/Event-Category?type=conv

8-9—2024 Forensics Engineering Conference – Buildings & Infrastructure, Austin, TX, <https://executive.engr.utexas.edu/prof-dev/courses/44-forensics-engineering-conference>

8-10—The Precast Show, Denver, CO, <https://precast.org/theprecastshow>

11-13—Geo Week, Denver, CO, www.geo-week.com

24-25—Advanced Materials for Sustainable Infrastructure Development - Exploring Emerging Technologies for Reducing Carbon Emissions, Ventura, CA, www.grc.org/advanced-materials-for-sustainable-infrastructure-development-grs-conference/2024

FEBRUARY-MARCH 2024

25-1—Accelerating Sustainable Concrete Construction: A Holistic View, Ventura, CA, www.grc.org/advanced-materials-for-sustainable-infrastructure-development-conference/2024

MARCH 2024

3-5—ASA Shotcrete Convention and Technology Conference, Austin, TX, <https://shotcrete.org/2024-asa-shotcrete-convention-and-technology-conference-online>

Contributions to ACI Materials Journal

The *ACI Materials Journal* is an open forum on concrete technology and papers related to this field are always welcome. All material submitted for possible publication must meet the requirements of the "American Concrete Institute Publication Policy" and "Author Guidelines and Submission Procedures." Prospective authors should request a copy of the Policy and Guidelines from ACI or visit ACI's website at www.concrete.org prior to submitting contributions.

Papers reporting research must include a statement indicating the significance of the research.

The Institute reserves the right to return, without review, contributions not meeting the requirements of the Publication Policy.

All materials conforming to the Policy requirements will be reviewed for editorial quality and technical content, and every effort will be made to put all acceptable papers into the information channel. However, potentially good papers may be returned to authors when it is not possible to publish them in a reasonable time.

Discussion

All technical material appearing in the *ACI Materials Journal* may be discussed. If the deadline indicated on the contents page is observed, discussion can appear in the designated issue. Discussion should be complete and ready for publication, including finished, reproducible illustrations. Discussion must be confined to the scope of the paper and meet the ACI Publication Policy.

Follow the style of the current issue. Be brief—1800 words of double spaced, typewritten copy, including illustrations and tables, is maximum. Count illustrations and tables as 300 words each and submit them on individual sheets. As an approximation, 1 page of text is about 300 words. Submit one original typescript on 8-1/2 x 11 plain white paper, use 1 in. margins, and include two good quality copies of the entire discussion. References should be complete. Do not repeat references cited in original paper; cite them by original number. Closures responding to a single discussion should not exceed 1800-word equivalents in length, and to multiple discussions, approximately one half of the combined lengths of all discussions. Closures are published together with the discussions.

Discuss the paper, not some new or outside work on the same subject. Use references wherever possible instead of repeating available information.

Discussion offered for publication should offer some benefit to the general reader. Discussion which does not meet this requirement will be returned or referred to the author for private reply.

Send manuscripts to:
<http://mc.manuscriptcentral.com/aci>

Send discussions to:
Journals.manuscripts@concrete.org

ACI CONCRETE CONVENTION: FUTURE DATES

2024—March 24-28, Hyatt Regency New Orleans, New Orleans, LA

2024—November 3-7, Philadelphia Marriott Downtown, Philadelphia, PA

2025—Mar. 30-Apr. 3, Sheraton Centre Toronto Hotel, Toronto, ON, Canada

2025—October 26-30, Hilton Baltimore & Baltimore Marriott Inner Harbor, Baltimore, MD

For additional information, contact:

Event Services, ACI
38800 Country Club Drive
Farmington Hills, MI 48331
Telephone: +1.248.848.3795
email: conventions@concrete.org

ON FRONT COVER: 120-M59, p. 11, Fig. 5—Simulated compression testing by discrete element method (DEM) showing damage evolution of DEM packing. Simulated failure modes are compared to actual failure mode of pervious concrete cylinders. Model is able to predict different failure modes of actual pervious concrete.

Permission is granted by the American Concrete Institute for libraries and other users registered with the Copyright Clearance Center (CCC) to photocopy any article contained herein for a fee of \$3.00 per copy of the article. Payments should be sent directly to the Copyright Clearance Center, 21 Congress Street, Salem, MA 01970. ISSN 0889-3241/98 \$3.00. Copying done for other than personal or internal reference use without the express written permission of the American Concrete Institute is prohibited. Requests for special permission or bulk copying should be addressed to the Managing Editor, *ACI Materials Journal*, American Concrete Institute.

The Institute is not responsible for statements or opinions expressed in its publications. Institute publications are not able to, nor intend to, supplant individual training, responsibility, or judgment of the user, or the supplier, of the information presented.

Papers appearing in the *ACI Materials Journal* are reviewed according to the Institute's Publication Policy by individuals expert in the subject area of the papers.

STATEMENT OF OWNERSHIP



Statement of Ownership, Management, and Circulation

(All Periodicals Publications Except Requester Publications)

1. Publication Title ACI Materials Journal	2. Publication Number 0 8 8 9 _ 3 2 5 X	3. Filing Date Sept. 26, 2023
4. Issue Frequency bi-monthly	5. Number of Issues Published Annually 6	6. Annual Subscription Price \$192
7. Complete Mailing Address of Known Office of Publication (<i>Not printer</i>) (Street, city, county, state, and ZIP+4®) American Concrete Institute 38800 Country Club Drive Farmington Hills, MI 48331		Contact Person Kaitlyn Dobberteen Telephone (<i>Include area code</i>) 248-848-3819
8. Complete Mailing Address of Headquarters or General Business Office of Publisher (<i>Not printer</i>) American Concrete Institute, 38800 Country Club Drive, Farmington Hills, MI 48331		

9. Full Names and Complete Mailing Addresses of Publisher, Editor, and Managing Editor (*Do not leave blank*)
 Publisher (*Name and complete mailing address*)

John C. Glumb, 38800 Country Club Drive, Farmington Hills, MI 48331

Editor (*Name and complete mailing address*)

Kaitlyn Dobberteen, 38800 Country Club Drive, Farmington Hills, MI 48331

Managing Editor (*Name and complete mailing address*)

Lauren E. Mentz, 38800 Country Club Drive, Farmington Hills, MI 48331

10. Owner (*Do not leave blank. If the publication is owned by a corporation, give the name and address of the corporation immediately followed by the names and addresses of all stockholders owning or holding 1 percent or more of the total amount of stock. If not owned by a corporation, give the names and addresses of the individual owners. If owned by a partnership or other unincorporated firm, give its name and address as well as those of each individual owner. If the publication is published by a nonprofit organization, give its name and address.*)

Full Name	Complete Mailing Address
American Concrete Institute	38800 Country Club Drive Farmington Hills, MI 48331

11. Known Bondholders, Mortgagees, and Other Security Holders Owning or Holding 1 Percent or More of Total Amount of Bonds, Mortgages, or Other Securities. If none, check box ➤ None

Full Name	Complete Mailing Address

12. Tax Status (*For completion by nonprofit organizations authorized to mail at nonprofit rates*) (*Check one*)

The purpose, function, and nonprofit status of this organization and the exempt status for federal income tax purposes:

Has Not Changed During Preceding 12 Months

Has Changed During Preceding 12 Months (*Publisher must submit explanation of change with this statement*)

STATEMENT OF OWNERSHIP

13. Publication Title ACI Materials Journal		14. Issue Date for Circulation Data Below September 2023	
15. Extent and Nature of Circulation		Average No. Copies Each Issue During Preceding 12 Months	No. Copies of Single Issue Published Nearest to Filing Date
a. Total Number of Copies (<i>Net press run</i>)		1519	1489
b. Paid Circulation (<i>By Mail and Outside the Mail</i>)	(1) Mailed Outside-County Paid Subscriptions Stated on PS Form 3541 (<i>Include paid distribution above nominal rate, advertiser's proof copies, and exchange copies</i>)	940	946
	(2) Mailed In-County Paid Subscriptions Stated on PS Form 3541 (<i>Include paid distribution above nominal rate, advertiser's proof copies, and exchange copies</i>)		
	(3) Paid Distribution Outside the Mails Including Sales Through Dealers and Carriers, Street Vendors, Counter Sales, and Other Paid Distribution Outside USPS®	353	343
	(4) Paid Distribution by Other Classes of Mail Through the USPS (e.g., First-Class Mail®)		
c. Total Paid Distribution [<i>Sum of 15b (1), (2), (3), and (4)</i>] ►		1293	1289
d. Free or Nominal Rate Distribution (<i>By Mail and Outside the Mail</i>)	(1) Free or Nominal Rate Outside-County Copies included on PS Form 3541		
	(2) Free or Nominal Rate In-County Copies Included on PS Form 3541		
	(3) Free or Nominal Rate Copies Mailed at Other Classes Through the USPS (e.g., First-Class Mail)		
	(4) Free or Nominal Rate Distribution Outside the Mail (<i>Carriers or other means</i>)		
e. Total Free or Nominal Rate Distribution (<i>Sum of 15d (1), (2), (3) and (4)</i>)			
f. Total Distribution (<i>Sum of 15c and 15e</i>) ►		1293	1289
g. Copies not Distributed (<i>See Instructions to Publishers #4 (page #3)</i>) ►		226	200
h. Total (<i>Sum of 15f and g</i>)		1519	1489
i. Percent Paid (<i>15c divided by 15f times 100</i>) ►		100%	100%
16. Electronic Copy Circulation		Average No. Copies Each Issue During Preceding 12 Months	No. Copies of Single Issue Published Nearest to Filing Date
a. Paid Electronic Copies ►		141	141
b. Total Paid Print Copies (Line 15c) + Paid Electronic Copies (Line 16a) ►		1434	1430
c. Total Print Distribution (Line 15f) + Paid Electronic Copies (Line 16a) ►		1434	1430
d. Percent Paid (Both Print & Electronic Copies) (16b divided by 16c × 100) ►		100%	100%

I certify that 50% of all my distributed copies (electronic and print) are paid above a nominal price.

17. Publication of Statement of Ownership

If the publication is a general publication, publication of this statement is required. Will be printed

Publication not required.

in the November 2023 issue of this publication.

18. Signature and Title of Editor, Publisher, Business Manager, or Owner

Date
09/26/23

I certify that all information furnished on this form is true and complete. I understand that anyone who furnishes false or misleading information on this form or who omits material or information requested on the form may be subject to criminal sanctions (including fines and imprisonment) and/or civil sanctions (including civil penalties).

Title No. 120-M59

Discrete Element Modeling of Pervious Concrete Compressive Strength to Optimize Mixture Composition

by Othman AlShareedah and Somayeh Nassiri

Pervious concrete is a stormwater management practice used in the United States, Europe, China, Japan, and many other countries. Yet the design of pervious concrete mixtures to balance strength and permeability requires more research. Sphere packing models of pervious concrete were used in compressive strength testing simulations using the discrete element method with a cohesive contact law. First, three mixtures with varied water-cement ratios (w/c) and porosities were used for model development and validation. Next, an extensive database of simulated compressive strength and tested permeability was created, including 21 porosities at three w/c. Analysis of the database showed that for pavement applications where high permeability and strength are required, the advised porosity is 0.26 to 0.30, producing average strengths of 14.4, 11.1, and 7.7 MPa for w/c of 0.25, 0.30, and 0.35. The model can guide the mixture design to meet target performance metrics, save materials and maintenance costs, and extend the pavement life.

Keywords: compressive strength; discrete element method (DEM); mixture composition; pervious concrete; sustainable pavement.

INTRODUCTION

The increased urban development in the last century in the United States and other countries undergoing rapid urban development has led to the removal of vegetation and soil, grading of the land surface, and construction of roads and buildings. Consequently, the area of impermeable surfaces has increased, which leads to higher peak discharge and frequency of floods in urban areas.^{1,2} In addition to inundation and erosion damage to roads and buildings in flood-prone areas, the increased volume of runoff has been shown to carry more pollutants.³ One strategy to reduce flood hazards in urban areas uses infrastructures such as permeable pavements that increase infiltration and storage of water in the soil.^{2,4,5} One class of these pavements is pervious concrete pavement, which has been shown to reduce the risks of flooding, remove some pollutants, provide good acoustic absorption of traffic noise, and provide better skid resistance over traditional concrete surfaces.⁶⁻¹⁰

Researchers showed that pervious concrete could retain heavy metals such as dissolved phosphorus, copper, and zinc under different simulated rainfall intensities.⁹ Additionally, pervious concrete can be used as a drainage system in mine sites to filter the contaminated wastewater. Studies showed that pervious concrete could raise the low pH of the mine wastewater to 12, which precipitates heavy metals such as iron, aluminum, and magnesium. Sulfate ions in mine wastewater were also removed by the reaction with the dissolved portlandite from the cement paste in pervious concrete and the formation of gypsum.⁸

Pervious concrete has a granular skeleton of coarse aggregates bound by a cement paste coating at joint locations.¹¹ Pervious concrete is made by removing all or most of the fine aggregate from a standard concrete mixture, lowering the cement paste, and applying a certain level of compaction to create a solid, porous pavement material at the desired porosity for fast stormwater drainage.

Numerical modeling of pervious concrete—Pervious concrete pavement use has seen an increased interest in recent years.¹² In addition, there has been an uptick in research on various aspects of this technology, including mixture proportioning, testing, and characterization.¹¹ However, studies on modeling its mechanical properties (mainly compressive strength) as a function of porosity are scarce. Therefore, this model would have important implications for optimizing mixture composition and required compaction to achieve target mechanical properties. Furthermore, such a numerical model is a guiding tool to tailor the various properties with fewer lengthy and costly experimental trials.

The granular macrostructure of pervious concrete makes it the right candidate for models based on the discrete element method (DEM). The DEM accounts for discontinuities by modeling the material as an assembly of particles interacting based on a user-defined contact law. Two-dimensional (2-D) DEM models were developed by Lian et al.¹³ and Singh and Biligiri¹⁴ to predict the stress-strain behavior of pervious concrete using circular particles. Air voids were randomly distributed in the 2-D model to achieve the desired porosity in Lian et al.'s study. In another study by Singh and Biligiri, X-ray computed tomography (CT) scans of pervious concrete specimens were used to distribute the air voids for the model.^{13,14} These models were advanced to a three-dimensional (3-D) DEM model by Pieralisi et al.,¹⁵ who simulated compressive and tensile tests of pervious concrete consisting of spherical particles (aggregates) covered by a shell of cement paste. However, the experimental data set used to calibrate the model was produced using an unconventional compaction method (using a hydraulic press with a precise loading rate), which does not represent the standard practice of making pervious concrete cylinders. Thus, the input properties of their simulated specimens may require improvements. In another DEM study, Xie et al.¹⁶ recreated

fracture patterns of pervious concrete. In their study, contour shapes of aggregates were obtained using X-ray CT, then filled with clumped spheres and used in Particle Flow Code 3-D (PFC3D) DEM software. Cubical packings were generated in PFC3D, and a parallel-bond contact model was adopted to simulate the behavior of pervious concrete under compression. In this contact model, the particles were connected by imaginary discs that could resist axial forces and bending moments depending on the defined elastic properties of the bond.¹⁶ Compared to experimental results, their developed model captured the different stages of fracture in pervious concrete. The simulation revealed that the cracks in the cement paste bond between the aggregate are the main reason for failure in pervious concrete, while, unlike conventional concrete, cracks in the aggregate rarely occur. This model, however, relies on scanned aggregates and does not offer estimates of standard design parameters such as strength and porosity. Vaddy et al.¹⁷ used DEM with a spherical particle packing to model the behavior of pervious concrete under flexural strength. The calibrated model achieved 97% accuracy in predicting the flexural strength of pervious concrete at different porosity levels.¹⁷ The fracture behavior of pervious concrete made with steel slag was investigated by Xu et al.¹⁸ Spherical particles were employed to model pervious concrete notched beams under a three-point bending test using PFC3D with the parallel-bond contact model. The model correctly predicted the crack propagation path. In addition, the relationship of peak load with notch depth was accurately predicted by the calibrated model.¹⁸

In addition to DEM, other numerical methods were used to simulate the mechanical behavior of pervious concrete. Fascetti et al.¹⁹ modeled the fracture of pervious concrete under compression using the lattice discrete particle model (LDPM). In this approach, the concrete microstructure is discretized into polyhedral cells, where each polyhedral cell represents the aggregate covered by mortar in concrete. The microstructure of pervious concrete was reproduced to match the pervious concrete mixture with 24% porosity and specific aggregate gradation. The LDPM model was able to predict the failure modes of pervious concrete tested in the laboratory.¹⁹ The LDPM needs to be expanded to predict the compressive strength of pervious concrete with a wide range of porosity levels and aggregate gradations.

Research approach—The reviewed studies are successful examples of simulated mechanical testing of pervious concrete to predict its mechanical properties but have practical and technical limitations, as discussed previously. This study demonstrates the practical outcomes of simulating mechanical testing of pervious concrete for mixture optimization using an advanced 3-D model of the actual laboratory-cast cylinders. The model incorporates porosity and water-cement ratio (*w/c*) as inputs to predict the strength because past studies have shown porosity and the paste strength (controlled by the *w/c*) are the most critical parameters influencing the mechanical properties of pervious concrete.²⁰⁻²²

This modeling approach uses Yade DEM open-source code for sphere packing integrated with the constitutive

Table 1—Pervious concrete mixture compositions

Mixture ID	Coarse aggregate, kg/m ³	ASTM Type I/II cement, kg/m ³	<i>w/c</i>
M-0.34	1372	309	0.34
M-0.27	1630	285	0.27
M-0.25	1630	309	0.25

cohesive particle model (CPM) to govern the behavior of the interacting spheres.²³ In the last decade, Yade has emerged as a robust DEM platform widely used by researchers to estimate the mechanical and hydraulic properties of granular materials, rocks, and other porous solids.²⁴⁻²⁸ Furthermore, the CPM in Yade was explicitly developed and used by researchers to simulate the mechanical properties of conventional concrete.²⁹⁻³¹

In this study, spherical particles are used to create packings that represent pervious concrete porosity. The model parameters were defined based on the test results of cylinders from different mixture compositions with varied *w/c* and porosity. Experimental results of porosity and compressive strength of laboratory-cast pervious concrete cylinders were used to develop and calibrate the 3-D DEM-CPM model. The model was then used to create a large compressive strength data set of pervious concrete at 21 various porosity levels (0.15 to 0.35 range) and three *w/c*. In addition, permeability test results from the literature were gathered for the simulated porosity levels to include this performance parameter in the mixture optimization process. Finally, based on the model outputs and literature data, recommendations were provided to tailor the pervious concrete porosity and *w/c* to achieve the desired compressive strength and permeability with minimum laboratory trials for low and high mechanical stress applications.

RESEARCH SIGNIFICANCE

In this study, an advanced DEM model was used as a practical tool to determine the optimum *w/c* and porosity of pervious concrete that renders the desired performance parameters—that is, strength and permeability—for low and high mechanical stress applications (sidewalks versus street application). By identifying the suitable ranges of porosity and *w/c* that produce target levels of permeability and compressive strength, fewer laboratory trials are needed for mixture design—further customizing strength and permeability for the target application results in more economical and environmentally friendly mixtures using fewer virgin materials (cement and aggregate).

MATERIALS AND METHODS

Mixture design and preparation of specimens

Pervious concrete samples from three different mixture designs, as shown in Table 1, were used in the study. The mixtures had three distinct *w/c* of 0.25, 0.27, and 0.34. The mixtures were labeled with M for mixture, followed by their *w/c* value.

Regarding the aggregate particle-size distribution, 91% of the aggregate was sized between 9.5 and 4.76 mm, 6% was 2.38 mm, and 3% was 12.7 mm. In terms of admixtures,

1.451 and 1.409 kg/m³ of water-reducing and hydration-stabilizing admixtures, respectively, were used in all the mixtures.

A total of 55 cylinders were cast and tested for model development. The fresh pervious concrete was placed in cylindrical molds measuring 100 x 200 mm (diameter x height) in two equal lifts and compacted by striking the mold sides with a rubber mallet and drops of a Proctor hammer. Each mixture composition in Table 1 was used to cast cylinders with different porosity levels by changing the amount of pervious concrete placed in the molds and adjusting the compaction level. Higher porosity levels (>0.30) were achieved by reducing the mass of fresh pervious concrete in each cylinder mold and reducing the compaction effort, while lower porosity levels (<0.30) were achieved by increasing the fresh pervious concrete mass and compaction effort. At least two cylinders were made for each porosity level within a 0.22 to 0.37 porosity range. The cast cylinders were sealed to prevent moisture loss and kept in laboratory conditions to cure for 7 days before compression testing.

Test methods

Porosity of hardened pervious concrete—The porosity of pervious concrete cylinders was obtained following ASTM C1754/C1754M-12.³² First, the dry mass (M_d , in g) and the dimensions of the cylinder (in cm) are taken; then, the submerged mass (M_w , in g) is measured and used to estimate the porosity by Eq. (1)

$$\text{Porosity (fraction)} = 1 - \frac{(M_d - M_w)}{\rho_w V_s} \quad (1)$$

where V_s is the volume of the cylinder (cm³) based on measured dimensions; and ρ_w is the density of water, defined as 1 g/cm³.

Uniaxial compression test—The uniaxial compressive strength of pervious concrete cylinders at 7 days of age was obtained in a displacement-controlled loading regime at a 1 mm/min rate to allow for a no-shock steady loading. The vertical displacement of the cylinder under compression was measured using a linear variable differential transformer (LVDT). The stress-strain curve was obtained from the load-displacement measurements used for calibration and validation of the proposed model.

MODEL DESCRIPTION

DEM model description

Pervious concrete consists of coarse aggregates bonded by a thin layer of cement paste. When a pervious concrete specimen is loaded in compression to the maximum load capacity, cracks typically initiate in the cement paste that binds the aggregates.³³⁻³⁵ This behavior can be modeled using the DEM, where an assembly of spheres with a user-defined contact model describes the sphere skeleton's behavior under the applied stresses. In this study, Yade,²³ an open-source DEM platform, was used to model pervious concrete stress-strain behavior under uniaxial loading involving two major steps. First, Newton's second law is used to calculate the acceleration of the particles caused

by the applied load, which is then time-integrated using an explicit integration scheme to obtain the positions of the particles. Second, the contact forces generated by particle collision are calculated based on the constitutive law of the contact, which will be described in the following sections. For a given particle (i) at a one-time step, the translational and rotational motions are expressed using Eq. (2) and (3)

$$F_i = m_i \ddot{u}_i \quad (2)$$

$$M_i = I_i \ddot{\omega}_i \quad (3)$$

where F_i is the force (N); M_i is the moment (N·m); m_i is the mass (kg); I_i is the moment of inertia (kg·m²); \ddot{u}_i is the acceleration (m/s²); and $\ddot{\omega}_i$ is the angular acceleration (rad/s²). This process is repeated at every time step until the end of the simulation.^{23,36,37}

Polydispersed spherical particle packing spheres were packed in a cylindrical mold to form a 100 x 200 mm (diameter x height) cylinder similar to the actual pervious concrete cylinder. First, spheres were generated stochastically in the mold in different diameters (Fig. 1(a)) following the same particle-size distribution of the real aggregates used in this study. Then, compaction is applied by moving a rigid circular plate from the top opening of the mold down to compress the spheres while keeping the mold walls rigid to prevent mold expansion (Fig. 1(b)). The packing porosity is calculated as

$$P = \frac{V - V_s}{V} \quad (4)$$

where V_s is the total volume of all the spheres; and V is the volume of a cylinder occupied by the spheres. When the desired porosity (Eq. (4)) and the height of the packing (200 mm) are both achieved, the compaction is stopped. The compaction is allowed to continue to release the locked-in contact forces until the ratio of the applied forces to the contact forces is less than 1×10^{-4} . At this time, the simulation ends, and both the cylindrical mold and the loading plates are removed. The sphere packing (Fig. 1(c)) is then ready to be used in compression simulations. The number of spheres in each packing with a 0.22 to 0.37 porosity range (as seen in Table 2) was 2227 to 1781, respectively. The compacted cylinder is used in a new simulation where the CPM is assigned as the contact model, and two rigid plates are created at the top and bottom of the specimen for loading.

The contact model that governs the interaction between the spheres during compaction is a linear-elastic cohesionless model developed by Cundall and Strack.³⁸ In this contact model, forces are only transmitted in compression following a linear-elastic behavior as expressed in Eq. (5)

$$F_n = k_n \cdot u_n \quad (5)$$

where F_n is the compressive force in the normal direction; k_n is the contact stiffness; and u_n is the normal displacement. Furthermore, frictional forces are also transmitted according to Eq. (6)

$$F_T = k_T \cdot u_T \quad (6)$$

where F_T is the shear force; k_T is the contact shear stiffness; and u_T is the tangential displacement.

Effect of particle shape

While the use of spherical particle shape in the DEM provides computational simplicity, the use of spheres is not fully representative of the material response under external pressure at the microscopic level. For instance, researchers found that the use of spherical particles underestimates the friction angle, while using particles with an aspect ratio higher than 1 increases the friction angle of the packing and the shear force between particles due to the interlocking effect between particles.³⁹⁻⁴¹ As shown by Xie et al.¹⁶ and Fascetti et al.,¹⁹ modeling the actual particle shape in the DEM provides realistic failure modes and enables better analysis of the fracture patterns of concrete.

However, using irregular-shaped particles requires a more complex contact detection algorithm to calculate the resultant forces between the contact of corners and sides of the neighboring angular particles. These interactions result in a significant increase in required computational capacity. Liu et al.⁴² used actual aggregate shapes (obtained from

X-ray CT scans) to generate particle packings and model the response under the applied stress. A single simulation takes up to 8 hours using actual aggregate shapes, but it takes only 22 seconds to run the same simulation with spherical particles. In addition, a large database of scanned aggregates with a variety of shapes is required to generate DEM packings with irregular particle shapes that are representative of the actual pervious concrete.

Modeling particles as spheres enables predicting the response of packings with different particle sizes and porosity levels under compression at a significantly lower computational capacity and simulation time due to their lower complexity as opposed to the actual irregular shape of aggregates. While the use of the realistic aggregate shape provides insight into the microscopic behavior and fracture modes, the main objective of this study is to predict the global compressive strength of the packing as a function of particle size and porosity. Therefore, the spherical shape was adopted as the particle shape in the DEM modeling in this study due to the affordable computational cost and the lower complexity level compared to modeling the actual shape of the aggregates. Moreover, the error in estimating the exact interaction between particles due to spherical shapes can be somewhat offset by calibration of the contact model with actual experimental results.

Table 2—Calibration values of DEM model input parameters

Parameter	Description	Calibrated value
E	Contact bond Young's modulus, GPa	16.5
ν	Contact bond Poisson's ratio	0.15
ϕ	Contact bond friction angle	50 degrees
ϵ_t	Contact bond's maximum elastic strain in tension in normal direction	1.52×10^{-4}
C_{T0}	Bond's initial cohesion, MPa	1.45
γ_{int}	Interaction factor (Fig. 2)	For M-0.34: 1.50 For M-0.25: 1.63

Spheres contact model

In this study, the CPM contact model in Yade was used in which “fictitious” bonds are formed between spheres to represent the effect of cement paste in bonding the aggregates in pervious concrete. The bonds between spheres are created at the beginning of the simulation using an interaction factor (γ_{int}). By setting γ_{int} to 1, bonds are generated between spheres with a radius r_i only when they are directly in contact (Fig. 2(a)), while increasing the factor-generated bonds with the spheres that are overlapping in a circular zone with a radius equals to $\gamma_{int} \cdot r_i$, as illustrated in Fig. 2(b). Increasing γ_{int} results in higher strength due to a higher number of bonds

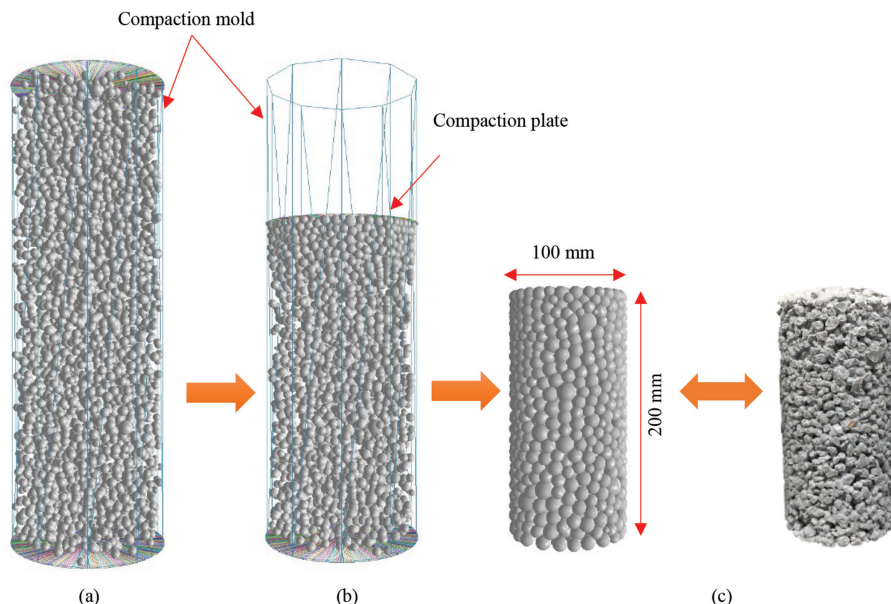


Fig. 1—Sphere packing process: (a) initial state; (b) compaction; and (c) final sample representing pervious concrete cylinder.

between spheres and vice versa. The user-defined properties of the bonds are uniform in all the packing.

Contact characteristics in normal direction—The CPM constitutive law of the local contact between spheres subjected to forces in the normal direction features damage-plastic behavior in tension and linear-hardening elastoplastic behavior in compression, as illustrated in Fig. 3.²⁹ The normal stress-strain equation that governs the contact between spheres is shown in Eq. (7)

$$\sigma_N = (1 - \omega H(\varepsilon_N))E\varepsilon_N \quad (7)$$

where σ_N is the normal stress (MPa); E is the bond elastic modulus in the normal direction (MPa); ε_N is the normal strain; ω is the damage variable, which is a ratio that reduces the stiffness of unloading or reloading of the tension portion of the model; and $H(\varepsilon_N)$ is the Heaviside function (0, 1), which turns on the damage variable only during tensile loading when the maximum elastic strain in tension (ε_t) is exceeded. The damage variable is identified based on Eq. (8)³⁷

$$\omega = 1 - \frac{\varepsilon_t}{\varepsilon_m} \exp\left(-\frac{\varepsilon_m - \varepsilon_t}{\varepsilon_f}\right) \quad (8)$$

where ε_m is the current maximum ε_N ; and ε_f represents the initial slope of the softening branch of the stress-strain curve

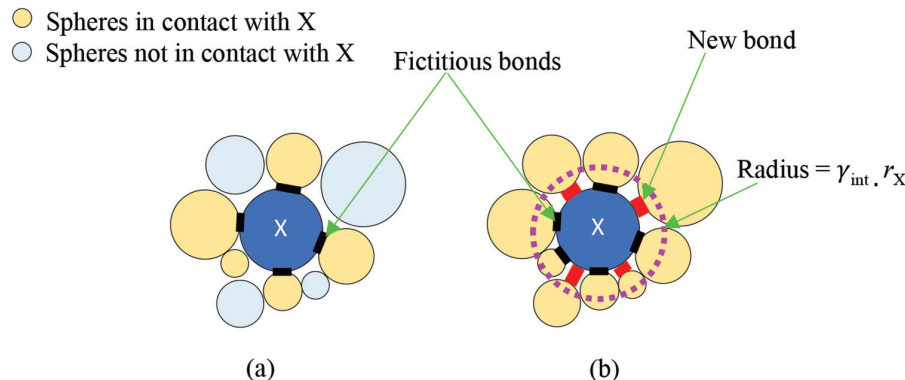


Fig. 2—Effect of interaction factor on bond creation between spheres: (a) $\gamma_{int} = 1$; and (b) $\gamma_{int} > 1$. Increasing γ_{int} factor increases number of bonds between neighboring spheres.

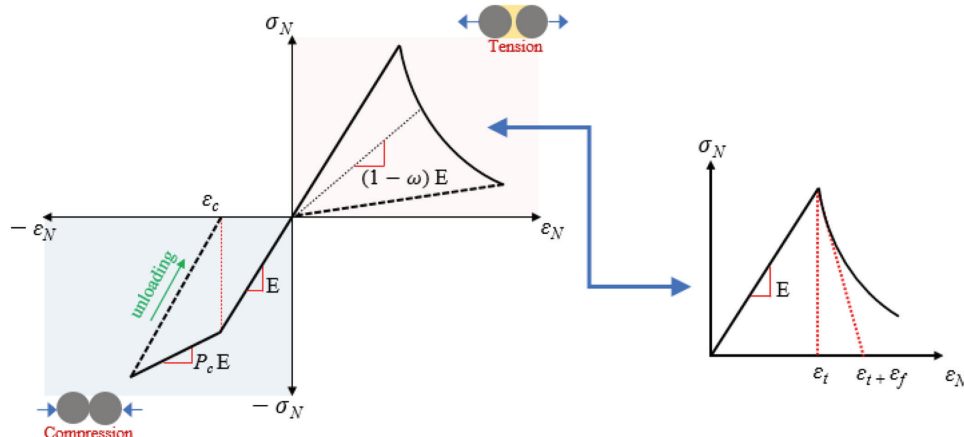


Fig. 3—Stress-strain curve of CPM model in normal direction with illustration of parameters of tensile portion of model.

(Fig. 3). Moreover, the tensile strength of the bond at each contact is calculated as the product of ε_t and E . In compressive loading, a linear-hardening elastoplastic model is adopted for the CPM, where ε_c is the maximum elastic strain in compression (which is calculated as 10 times ε_t), and P_c is a factor that determines the modulus of the hardening branch (taken as 0.3),²⁹ as seen in Fig. 3.

To obtain the forces generated from spheres interaction to be used in motions' equations (Eq. (2) and (3)), the stresses are multiplied by the contact area of the interacting spheres. The contact area (A_c) is calculated based on Eq. (9)

$$A_c = \pi r_{min}^2 \quad (9)$$

where r_{min} corresponds to the radius of the smaller sphere at the contact.²⁹ This will ensure that larger spheres in contact will have stronger bonds as compared to the bonds between smaller spheres.

Contact characteristics in shear direction—The contact shear stress (σ_T) of the CPM is defined as

$$\sigma_T = G(\varepsilon_T - \varepsilon_T^p) \quad (10)$$

where G is the shear modulus (calculated as 20% of E); ε_T is the shear strain; and ε_T^p is the plastic portion of the shear strain.²⁹ Unlike the normal stress formulation, here, the damage is imposed by limiting the shear stress instead of

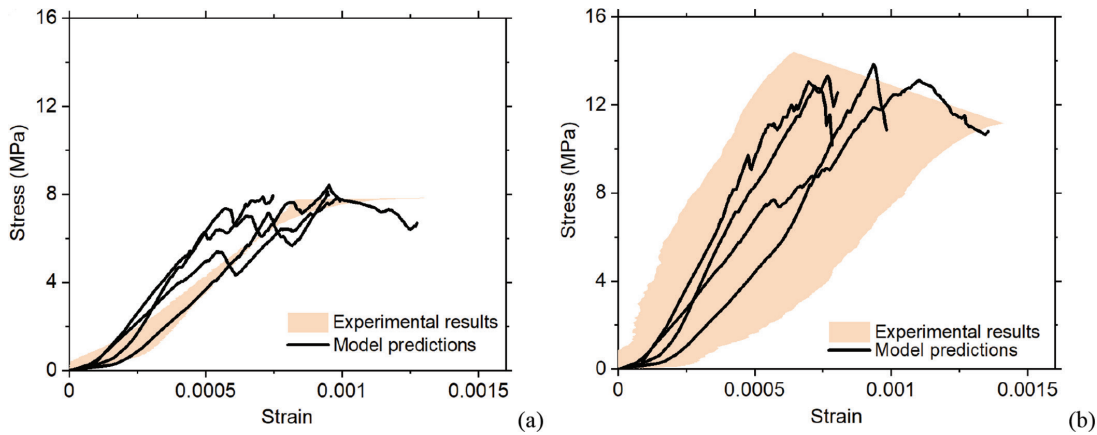


Fig. 4—Calibrated model predictions for stress-strain compared with experimental curves for: (a) M-0.34 (higher w/c); and (b) M-0.25 (lower w/c) (porosity = 0.24). Calibrated model is able to predict actual stress-strain curves of pervious concrete.

the shear strain. The yield shear stress σ_{Ty} is determined by a Mohr-Coulomb failure criterion, which is given as

$$\sigma_{Ty} = C_T - \sigma_N \tan \varphi \quad (11)$$

$$C_T = C_{T0}(1 - \omega) \quad (12)$$

where σ_N is the normal stress (Eq. (7)); and C_{T0} and φ are material input parameters that represent the initial cohesion and angle of friction, respectively.^{37,43} Based on the damage variable ω (Eq. (8)), C_{T0} is reduced to the current cohesion C_T during the simulation. Initially, the shear stress (σ_T) evaluated in Eq. (10) is compared with the yield shear stress (σ_{Ty}). If $\sigma_T < \sigma_{Ty}$, then σ_T is evaluated as $G \cdot \varepsilon_T$. However, if $\sigma_T > \sigma_{Ty}$, then the bond at the contact is damaged, and σ_T is considered as σ_{Ty} . The shear force is calculated similar to the normal force by multiplying σ_T with the contact area between the two interacting spheres.

Note that during DEM simulation, the bonds are formed between the spheres at the beginning of the simulation using γ_{int} , as shown in Fig. 2. Once the bonds that are connecting one sphere to other spheres are damaged, that particular sphere will be labeled so that no new bonds will be formed with other spheres, and the contact law will be cohesionless and fully elastic.²⁹

Simulation of uniaxial compression tests

For simulations, sphere packings were placed between two plates in which the bottom plate was fixed. In contrast, the top plate moves downward at a constant velocity equal to the loading rate in the actual test. Failure occurs when the packing collapses and cannot support more loading.

MODEL DEVELOPMENT

Parameters of DEM model

The measured stress-strain curves of the tested cylinders were used in defining the model parameter (γ_{int} , ε_t , E , v , φ , C_{T0}) to reproduce the behavior of pervious concrete under compression. Cylinders with the same porosity level but different w/c were used for calibration, including three cylinders from M-0.34 and three cylinders from M-0.25 mixtures, all with a porosity of 0.24. Four sphere packings with the

same dimensions and porosity (0.24) as the actual cylinders from each mixture design were created and used in the calibration. Using four sphere packings ensured that the calibrated parameters were representative of different random packing arrangements by the model for the same porosity level.

The sensitivity of the model parameters was tested by changing the values for one parameter at a time to study the sensitivity of compressive strength to that parameter for each sphere packing. Each parameter was changed at a time by doubling the benchmark value and then by reducing it to half. It was observed that the parameters could be listed in the order of sensitivity to the compressive strength as $\gamma_{int} > E > v > \varphi > C_{T0}$.

The last three parameters (the least influential parameters) of v , φ , and C_{T0} were fixed throughout the calibration process to simplify the model development process, while the values of the three most critical parameters— E , ε_t , and γ_{int} —were adjusted in an iterative process until the model error in estimating the peak stress (compressive strength) was less than 15%. The simulated stress-strain curves were also visually examined to ensure they were similar to the experimental relationships, as seen in Fig. 4. The model predictions for stress-strain followed the patterns of the measured stress-strain curves of pervious concrete cylinders. The jagged fluctuations in the simulated stress-strain curves result from the collapse of the voids and the bond breakage within the packing during the loading process (Fig. 4).

Finally, the peak stress from simulated stress-strain curves was compared to the laboratory-measured compressive strength of the cylinders, giving an error of less than 15%. Therefore, the values of the calibration parameters from these DEM models were deemed appropriate. These values are listed in Table 2. The v and φ values were selected based on testing results of concrete properties in other studies,⁴⁴⁻⁴⁶ while the C_{T0} value was fixed at 1.45 MPa based on initial calibration trials.

Next, the model was used to simulate the compressive strength testing of cylinders from all the other mixtures. The effect of the w/c is reflected in the value of the interaction factor, γ_{int} , which was calibrated for the two mixture designs, as shown in Table 2. Based on the calibration, the

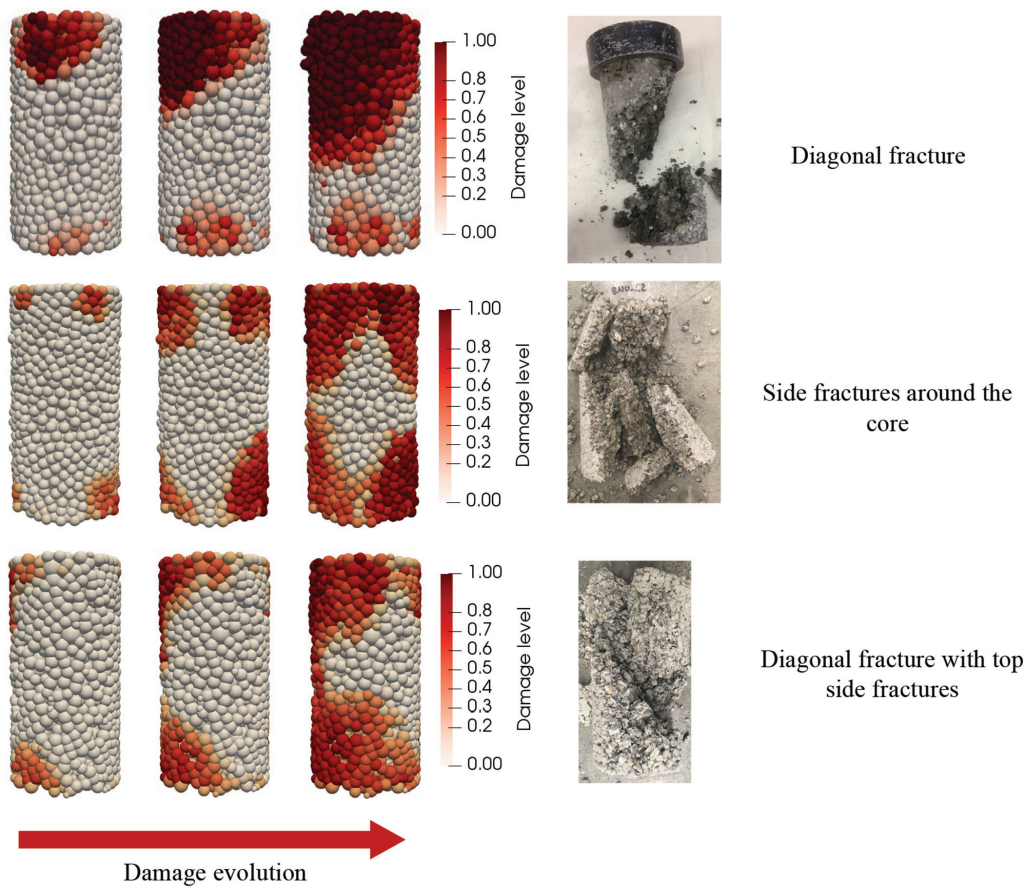


Fig. 5—Simulated compression testing by DEM showing damage evolution of DEM packing. Simulated failure modes are compared to actual failure mode of pervious concrete cylinders. Model is able to predict different failure modes of actual pervious concrete.

relationship between the w/c and the value of the γ_{int} in the DEM model is as follows.

$$\gamma_{int} = 1.9911 - 1.444 \times (w/c) \quad (13)$$

This linear relation was used to define the γ_{int} for mixtures with w/c different than the calibration mixtures. In future studies, more pervious concrete mixtures with the same porosity should be added to the data set to expand the application of this equation to a wider range of mixture formulations.

Figure 5 shows the damage progression in three cylinders that failed in different ways. A color-coding based on the average residual tensile strength of the bonds between neighboring spheres is used to show the damage level. When the bonds between one sphere and all neighboring spheres are entirely broken, the damage will be 1 (fully damaged), and the color turns dark red, as illustrated in Fig. 5. It can be seen that the model can capture some of the common failure modes of a concrete cylinder as depicted in ASTM C39/C39M-21,⁴⁷ such as diagonal fracture and side fractures. Previous studies also reported these failure modes when testing pervious concrete cylinders under compression.⁴⁸⁻⁵⁰

Comparison with experimental results

The model predictions of compressive strength were validated with the experimental results of the remaining

49 cylinders (after excluding the cylinders used for model calibration). Figure 6 illustrates the experimental results and the corresponding model predictions for the tested cylinders at different w/c .

It can be observed that the model predictions are reasonably accurate for w/c of 0.27 and 0.34 with an average error of 25% and 29% and a standard error of estimate (SEE) of 2.56 and 2.7 MPa, respectively. However, the model overestimates the compressive at a 0.25 w/c by an SEE of 5.09 MPa. This higher error is not resulting from an issue with the model calibration but rather an unsuitable mixture composition. At a 0.25 w/c and a porosity range of 0.27 to 0.32, the pervious concrete mixture was dry and non-workable, resulting in a poor distribution of cement paste and insufficient paste at some of the joints between the aggregates. Therefore, the compressive strength of the cylinders cast from this mixture declined sharply compared to specimens with 0.24 average porosity used for model calibration (Fig. 6). This effect cannot be captured in the model, resulting in overestimating the compressive strength. In practice, chemical admixtures can be used to enhance the workability of the mixture while keeping the w/c at 0.25 to achieve higher compressive strength.

Moreover, the differences between the model predictions and experimental results are strongly attributed to the difference in the particle shape. Using a uniform shape of spherical particles creates a different skeleton structure

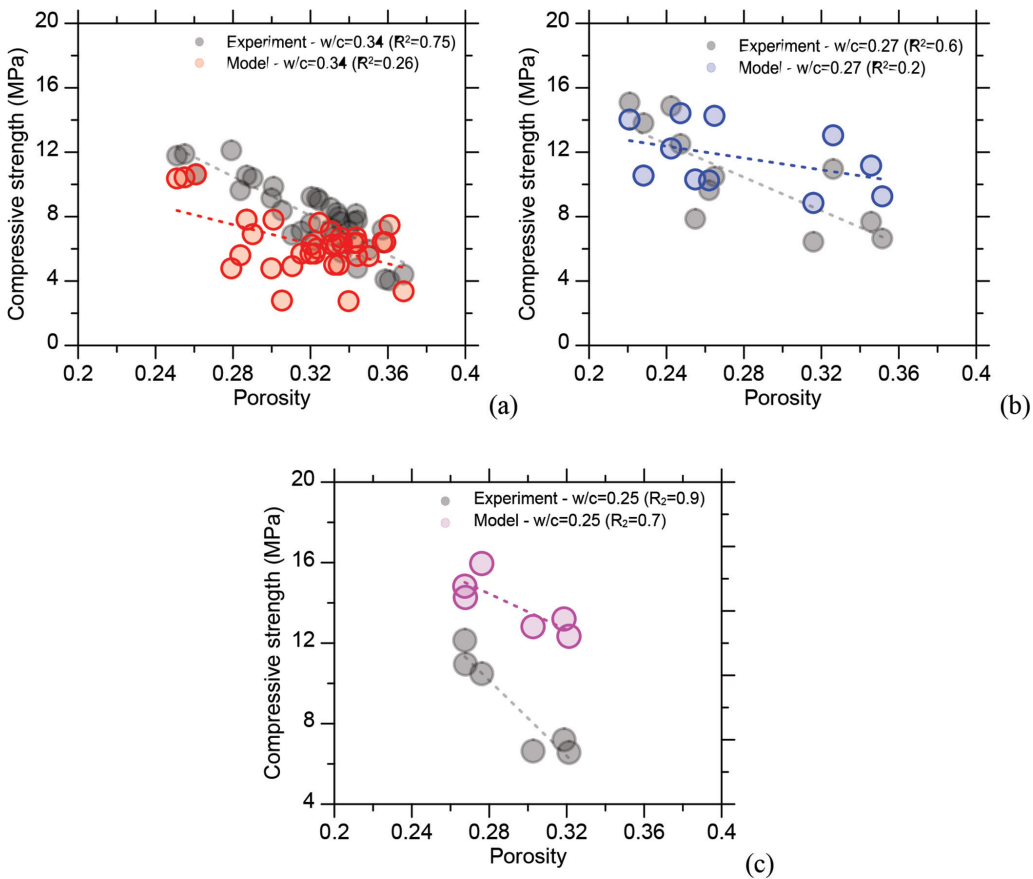


Fig. 6—Model predictions versus experimental results for compressive strength of pervious concrete cylinders from different w/c. Standard error of estimate for w/c of 0.25, 0.27, and 0.34 is 5.1, 2.56, and 2.7 MPa, respectively. Model predictions for pervious concrete with w/c of 0.27 and 0.34 are satisfactory; however, model overestimates compressive strength of pervious concrete with 0.25 w/c.

and pore distribution than the actual pervious concrete that consists of irregular-shaped aggregates. These differences in the particle shape affect the load-transfer paths and create different strength results at the same porosity level. Nevertheless, the model is useful in estimating the compressive strength of pervious concrete at a specific porosity level and w/c with reasonable accuracy.

This level of accuracy of the developed model in this study is similar to other numerical models developed for pervious concrete. For instance, the finite element model for fiber-reinforced pervious concrete developed by Akand and Yang⁵¹ reached a 23% error compared to experimental results. Other researchers have developed compressive strength prediction models for pervious concrete with higher accuracy. However, these models were either regression models based on specific mixture designs or did not include inputs such as aggregate gradation and w/c.^{13,52}

DEMONSTRATION OF MODEL'S PRACTICAL APPLICATIONS: EFFECT OF AGGREGATE SIZE ON COMPRESSIVE STRENGTH

The model was used to investigate the effect of aggregate size on the compressive strength of pervious concrete. Sphere packings with single-size spheres were generated at a 0.30 porosity and three sphere sizes: 2.38, 4.76, and 9.5 mm. Three packings were prepared for each sphere size

to account for the randomness of the sphere packing process and the associated variation in packing arrangements at the same porosity. The average compressive strength of the single-size sphere packings with the three sphere sizes is shown in Fig. 7.

As expected, increasing the sphere size creates larger pores in the packing, as illustrated in the horizontal cross-section view of the packings in Fig. 7. Increasing sphere sizes from 2.38 to 4.76 mm increased the compressive strength by 153%, while increasing the sphere sizes from 4.76 to 9.5 mm increased the compressive strength by 244%. Larger sphere sizes created more contact areas between the spheres (Eq. (13)), which increased the strength of the packing and vice versa. This phenomenon was confirmed by experiments in other studies.^{53–56} Furthermore, a larger aggregate size results in a thicker cement paste coating and a higher concentration of cement paste at the joints between aggregates, increasing strength. In contrast, reducing the aggregate size results in a larger number of aggregate particles and larger surface area for the same volumetric content, less cement paste at the joints between the aggregates, and thinner cement paste film on the aggregate surface, which results in lower strength.

From the stress-strain curve, the elastic modulus can be obtained as

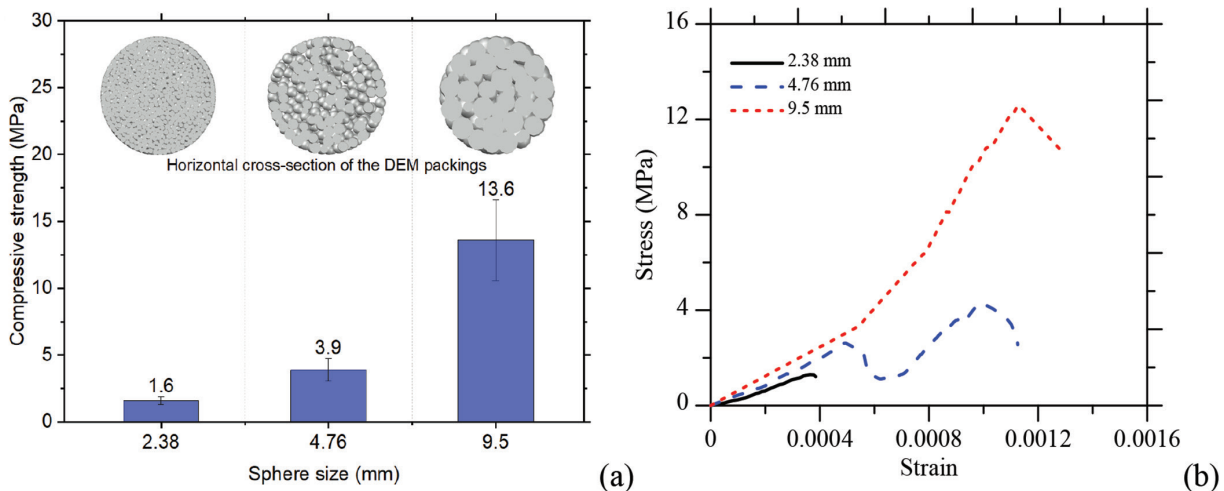


Fig. 7—Effect of sphere size on: (a) compressive strength; and (b) stress-strain curve of single-size sphere packings at 0.30 porosity level. Using larger aggregate size (2.38 to 9.5 mm) enhanced compressive strength and elastic modulus by up to 244 and 268%, respectively.

$$E = (S_2 - S_1)/(\varepsilon_2 - \varepsilon_1) \quad (14)$$

where E is the modulus of elasticity; S_1 and S_2 are the stress corresponding to 40 and 80% of the ultimate stress, respectively; and ε_1 and ε_2 are the strain at S_1 and S_2 . Using a larger single-size aggregate increases the elastic modulus of the packing. This behavior is captured by the model, as seen in Fig. 7(b). The E (Eq. (14)) of the 2.38, 4.76, and 9.5 mm single-size sphere packings is 4.7, 5.6, and 17.4 GPa, respectively. It can be observed that increasing the particle size from 2.38 to 4.76 and 9.5 mm increased E by 18.5 and 268%, respectively.

DEMONSTRATION OF MODEL'S PRACTICAL APPLICATIONS: EFFECT OF w/c ON COMPRESSIVE STRENGTH

The model was used to investigate the effect of the w/c (represented by the γ_{int} factor) on the compressive strength for the same porosity. Three sphere packings at 0.25 porosity were prepared. The sphere packings were assigned a γ_{int} factor of 1.63, 1.56, and 1.49 (based on Eq. (13)) to represent three w/c : 0.25, 0.3, and 0.35, respectively. Again, three randomly generated sphere packings for each w/c account for the variation in packing arrangements at the same porosity. Moreover, the sphere packings used in this section consisted of spheres with the same particle-size distribution as the actual aggregates described in the section "Mixture design and preparation of specimens."

The change in the average compressive strength for the w/c for sphere packings with the same porosity levels is shown in Fig. 8. In actual pervious concrete, the change in the w/c affects the strength of the cement paste that bonds the aggregates, and consequently, the strength of the packing is affected. For instance, at the same porosity, the increase in the w/c is associated with a reduction in the strength of the cement paste that transfers the load between the aggregates' skeleton, which adversely affects the strength of the pervious concrete.⁵⁷ Increasing the w/c from 0.25 to 0.3 and 0.35 resulted in a 21 and 47% reduction in the average

compressive strength (Fig. 8), showing the DEM model is sensitive to the changes in the w/c and captures its impact on the compressive strength correctly through the γ_{int} factor as defined by Eq. (13).

The stress-strain curves of the sphere packings tested with each w/c are shown in Fig. 8(b). In addition to reducing the compressive strength, increasing the w/c from 0.25 to 0.3 and 0.35 reduced the average E of the sphere packings by 19 and 31% (Fig. 8).

DEMONSTRATION OF MODEL'S PRACTICAL APPLICATIONS: MIXTURE DESIGN

The validated model was used to generate a large data set of 189 sphere packings in the porosity range of 0.15 to 0.35 (typically used in producing pervious concrete⁵⁸) to estimate the compressive strength. In addition, 53 data points of permeability results of pervious concrete with the 0.15 to 0.35 porosity range were collected from the literature.^{54,59-64} This section aims to develop recommendations for the design of pervious concrete pavement for different applications considering their required performance metrics (strength and permeability).

At each porosity level within the 0.15 to 0.35 range, three packings were generated to account for the variability in pervious concrete properties caused by the randomness of aggregate packing. In total, 63 cylindrical sphere packings were generated with the particle-size distribution described in the section "Mixture design and preparation of specimens." Three w/c were used in this analysis: 0.25, 0.3, and 0.34 (γ_{int} is 1.63, 1.56, and 1.5, respectively). This range was within the typical w/c used in producing pervious concrete as reported by ACI 522R-10.⁶⁵ The compressive strength results of the 63 packings at three w/c ($63 \times$ three w/c = 189 simulations) are shown in Fig. 9.

Based on the compressive strength data, a multi-linear regression model (Eq. (15)) was developed using Sigma-Plot statistical software. The coefficient of determination (R^2 value) of the developed model was 0.52, and its SEE was 2.7 MPa. The relationship between the simulated

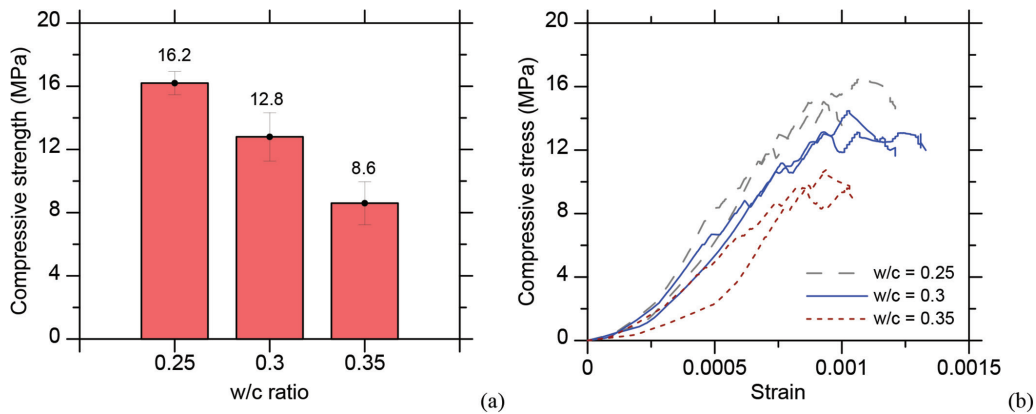


Fig. 8—(a) Effect of different w/c and γ_{int} parameter of model for sphere packings with 0.25 porosity on simulated compressive strength; and (b) stress-strain relationships of sphere packings with different modeled w/c.

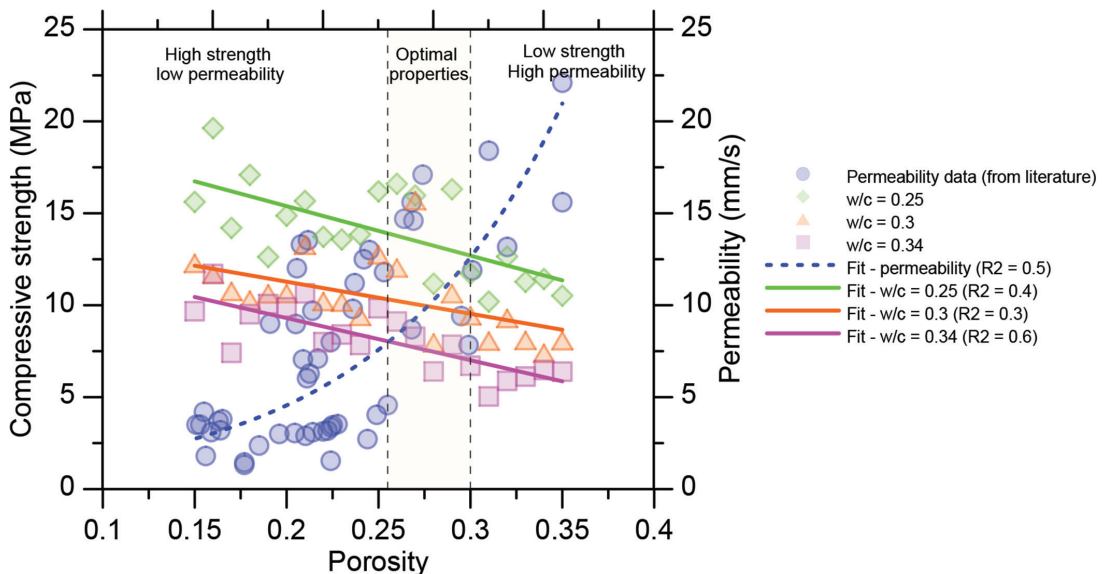


Fig. 9—Relationships between porosity, compressive strength, and permeability of pervious concrete for three w/c. Compressive strength data are generated by model, while permeability data are obtained from literature for same porosity levels.

compressive strength of pervious concrete and its porosity and w/c is as follows.

$$\text{Compressive strength (MPa)} = 35.976 - (65.736 \cdot w/c) - (0.224 \cdot \text{porosity (\%)}) \quad (15)$$

The scatteredness in the compressive strength results demonstrated in the low R^2 values is common in pervious concrete due to the large heterogeneity in the material caused by the random packing of aggregates (spheres in the model).^{22,48} Based on the model results, reducing the w/c from 0.34 to 0.3 enhanced the compressive strength by an average of 2.4 MPa at the same porosity range. In contrast, reducing the w/c from 0.34 to 0.25 enhanced the compressive strength by an average of 5.9 MPa. For pervious concrete pavement thickness design, the compressive strength in Eq. (15) can be used to estimate the flexural strength using Shah and Ahmad⁶⁶ as recommended by ACI 522R-10⁶⁵

$$f_r = 0.083 f_c^{2/3} \quad (16)$$

In addition, based on the 53 data points from the literature,^{54,59-64} the permeability of pervious concrete increases exponentially with increased porosity and can be estimated using the expression in Eq. (17) ($R^2 = 0.5$).

$$\text{Permeability (mm/s)} = 0.595 \cdot e^{10.177 \times \text{porosity}} \quad (17)$$

Based on Fig. 9, when relatively high strength and high permeability are desired, pervious concrete should be designed to have a porosity in the 0.26 to 0.3 range. Within this porosity range, pervious concrete can be produced with an average compressive strength of 7.7, 11.1, and 14.4 MPa when mixed with a w/c of 0.34, 0.3, and 0.25, respectively. In addition, pervious concrete with 0.26 to 0.3 porosity can attain a permeability ranging from 8.7 to 12.7 mm/s. It should be noted that reducing the w/c will affect the workability of the mixture; therefore, it is recommended to use dispersion admixtures to improve the workability and the compactibility of the mixture while maintaining a low w/c.

For pervious concrete in applications where mechanical stress is negligible but high permeability and a lower risk of

pore clogging is desired (for example, sidewalks or parking lots near heavy vegetation), a 0.30 to 0.35 porosity range can be used. In this range, permeability in the 12.7 to 21 mm/s range can be obtained with a lower risk of clogging and, therefore, maintenance. In a previous study by the authors, simulated pervious concrete with aggregate sizes in the 4.75 to 9.5 mm range and 0.3 porosity showed a lower risk of clogging than 0.2 porosity due to larger pore sizes, which can accommodate more sediment particles without fully blocking water flow.⁶⁷ In addition, pervious concrete with a 0.3 to 0.35 porosity level requires fewer virgin materials (aggregate and cement) and, thus, lower cost. The average compressive strength for a 0.30 to 0.35 porosity range is 6.1, 8.3, and 11.2 MPa for *w/c* of 0.34, 0.30, and 0.25.

In high-traffic applications where high strength is the top priority, the pervious concrete advised porosity is 0.15 to 0.26. The average compressive strength for a 0.15 to 0.26 porosity level is 9.3, 11, and 15 MPa. These porosities should be achieved by increasing compaction and maintaining the *w/c* at 0.34, 0.30, and 0.25 for each porosity level because, as shown in Fig. 9, higher compressive strength values can be achieved by reducing the porosity.

The foregoing discussion is an example of the practical use of numerical models to tailor the mixture design (that is, *w/c*, target porosity, and aggregate-size distribution) to achieve certain levels of mechanical properties. While this analysis is limited to a specific range of *w/c* and particle-size distributions, the model applications can extend to mixture designs with different *w/c* and aggregate sizes.

CONCLUSIONS

The discrete element method (DEM) was used in this study to simulate the mechanical behavior of pervious concrete under uniaxial compression using sphere packings and a cohesive contact model. The model incorporated the effect of porosity and mixture design by generating sphere packings with the same porosity of cast specimens and assigning cohesive bonds with a calibrated factor to represent the water-cement ratio (*w/c*) of pervious concrete.

The model was validated with the experimental results of 49 specimens with various mixture compositions. As a result, the model can estimate the compressive strength of pervious concrete with reasonable accuracy within the range of variation seen for the compressive strength of pervious concrete. Moreover, the model was found to be sensitive to the effect of aggregate size and *w/c* by testing sphere packings with different single-size spheres and *w/c* (bond interaction factor values) in uniaxial compressive strength testing. Model results indicated that increasing the sphere sizes from 2.38 to 4.76 and 9.5 mm enhanced the compressive strength by 153 and 244%. Furthermore, a higher *w/c* from 0.25 to 0.3 and 0.35 reduced the average simulated compressive strength by 21 and 47%.

The model was then used to simulate the compressive strength of pervious concrete at 21 varied porosity levels ranging from 0.15 to 0.35 at three *w/c*: 0.25, 0.3, and 0.34. The compressive strength results were combined with the permeability data set collected from the literature to recommend the optimum target porosity and *w/c* to meet specified

strength and permeability metrics. For the 4.75 to 9.5 mm aggregate gradation, it was concluded that a porosity range of 0.26 to 0.3 provides an optimum combination of strength and permeability. At a *w/c* of 0.25, the average estimated compressive strength is 14.4 MPa, and the average is 1.07 mm/s.

In future studies, the model calibration can be extended to include mixtures made with supplementary cementitious materials, recycled aggregates, and water-binder ratios (*w/b*) higher than 0.35 to expand the model applications. By identifying the best range of porosity and *w/c* to strike a balance between permeability and compressive strength, limited laboratory trials may be needed for mixture composition design. Furthermore, mixture composition optimization can produce more economical mixtures using fewer virgin materials, requiring less maintenance and vacuuming to remove clogging and extending the life cycle of the pavement.

AUTHOR BIOS

ACI member Othman AlShareedah was a PhD Candidate at Washington State University, Pullman, WA, at the time this work was done. He is currently a Research Scientist at James Hardie Building Products. He received his BS from Sohar University, Sohar, Oman, and his MSc from Sultan Qaboos University, Muscat, Oman. He is a member of ACI Committee 522, Pervious Concrete. His research interests include developing sustainable construction materials.

ACI member Somayeh Nassiri was an Assistant Professor at Washington State University at the time this work was done. She is currently an Associate Professor at the University of California, Davis, Davis, CA. She received her BS from the University of Tabriz, Tabriz, Iran, in 2004; her MS from the University of Tehran, Tehran, Iran, in 2007; and her PhD from the University of Pittsburgh, Pittsburgh, PA, in 2011, all in civil engineering. She is a member of ACI Committees 215, Fatigue of Concrete; 241, Nanotechnology of Concrete; 325, Concrete Pavements; and 522, Pervious Concrete; and ACI Subcommittee 325-A, Pavements-Design. Her research interests include concrete pavement design and materials.

REFERENCES

- Miller, J. D., and Hutchins, M., "The Impacts of Urbanisation and Climate Change on Urban Flooding and Urban Water Quality: A Review of the Evidence Concerning the United Kingdom," *Journal of Hydrology: Regional Studies*, V. 12, Aug. 2017, pp. 345-362. doi: 10.1016/j.ejrh.2017.06.006
- Konrad, C. P., "Effects of Urban Development on Floods," USGS Fact Sheet FS-076-03, U.S. Geological Survey, Reston, VA, Nov. 2003, 4 pp.
- Park, S.-B., and Tia, M., "An Experimental Study on the Water-Purification Properties of Porous Concrete," *Cement and Concrete Research*, V. 34, No. 2, Feb. 2004, pp. 177-184. doi: 10.1016/S0008-8846(03)00223-0
- Pickering, N., and Nassiri, S., "Stormwater Management and Roadways," *Oxford Research Encyclopedia of Environmental Science*, June 28, 2021.
- Kim, Y. J.; Al Wakeel, S.; Gaddafi, A.; and Cha, Y.-J., "In-Place Performance of Severely Deteriorated Pervious Concrete: A Case Study," *ACI Materials Journal*, V. 112, No. 2, Mar.-Apr. 2015, pp. 295-304. doi: 10.14359/51686993
- Rodin, H. III; Nassiri, S.; AlShareedah, O.; Yekkalar, M.; and Haselbach, L., "Evaluation of Skid Resistance of Pervious Concrete Slabs under Various Winter Conditions for Driver and Pedestrian Users," *Road Materials and Pavement Design*, V. 22, No. 6, 2021, pp. 1350-1368.
- Zhang, Y.; Li, H.; Abdelhady, A.; and Du, H., "Laboratorial Investigation on Sound Absorption Property of Porous Concrete with Different Mixtures," *Construction and Building Materials*, V. 259, Oct. 2020, Article No. 120414. doi: 10.1016/j.conbuildmat.2020.120414
- Shabalala, A. N.; Ekolu, S. O.; Diop, S.; and Solomon, F., "Pervious Concrete Reactive Barrier for Removal of Heavy Metals from Acid Mine Drainage – Column Study," *Journal of Hazardous Materials*, V. 323, Part B, Feb. 2017, pp. 641-653. doi: 10.1016/j.jhazmat.2016.10.027
- Ostrom, T. K., and Davis, A. P., "Evaluation of an Enhanced Treatment Media and Permeable Pavement Base to Remove Stormwater Nitrogen, Phosphorus, and Metals under Simulated Rainfall," *Water Research*, V. 166, Dec. 2019, Article No. 115071. doi: 10.1016/j.watres.2019.115071

10. Kevern, J. T.; Schaefer, V. R.; and Wang, K., "Mixture Proportion Development and Performance Evaluation of Pervious Concrete for Overlay Applications," *ACI Materials Journal*, V. 108, No. 4, July-Aug. 2011, pp. 439-448.
11. AlShareedah, O., and Nassiri, S., "Pervious Concrete Mixture Optimization, Physical, and Mechanical Properties and Pavement Design: A Review," *Journal of Cleaner Production*, V. 288, Mar. 2021, Article No. 125095. doi: 10.1016/j.jclepro.2020.125095
12. Weiss, P. T.; Kayhanian, M.; Gulliver, J. S.; and Khazanovich, L., "Permeable Pavement in Northern North American Urban Areas: Research Review and Knowledge Gaps," *International Journal of Pavement Engineering*, V. 20, No. 2, 2019, pp. 143-162. doi: 10.1080/10298436.2017.1279482
13. Lian, C.; Zhuge, Y.; and Beecham, S., "Numerical Simulation of the Mechanical Behaviour of Porous Concrete," *Engineering Computations*, V. 28, No. 8, 2011, pp. 984-1002. doi: 10.1108/02644401111178992
14. Singh, S. P., and Biligiri, K. P., "Numerical Simulation of Pervious Concrete Using Discrete Element Modeling Technique," *Journal of Testing and Evaluation*, V. 46, No. 6, 2018, 10 pp. doi: 10.1520/JTE20170141
15. Pieralisi, R.; Cavalaro, S. H. P.; and Aguado, A., "Discrete Element Modelling of Mechanical Behaviour of Pervious Concrete," *Cement and Concrete Composites*, V. 119, May 2021, Article No. 104005. doi: 10.1016/j.cemconcomp.2021.104005
16. Xie, C.; Yuan, L.; Zhao, M.; and Jia, Y., "Study on Failure Mechanism of Porous Concrete Based on Acoustic Emission and Discrete Element Method," *Construction and Building Materials*, V. 235, Feb. 2020, Article No. 117409. doi: 10.1016/j.conbuildmat.2019.117409
17. Vaddy, P.; Pandurangan, V.; and Biligiri, K. P., "Discrete Element Method to Investigate Flexural Strength of Pervious Concrete," *Construction and Building Materials*, V. 323, Mar. 2022, Article No. 126477. doi: 10.1016/j.conbuildmat.2022.126477
18. Xu, W.; Chen, B.; Chen, X.; and Chen, C., "Influence of Aggregate Size and Notch Depth Ratio on Fracture Performance of Steel Slag Pervious Concrete," *Construction and Building Materials*, V. 273, Mar. 2021, Article No. 122036. doi: 10.1016/j.conbuildmat.2020.122036
19. Fascatelli, A.; Ichimaru, S.; and Bolander, J. E., "Stochastic Lattice Discrete Particle Modeling of Fracture in Pervious Concrete," *Computer-Aided Civil and Infrastructure Engineering*, V. 37, No. 14, Nov. 2022, pp. 1788-1808.
20. Baxter, S. C.; Acton, K. A.; and Lederle, R. E., "Determination of Representative Volume Elements for Pervious Concrete," *ACI Materials Journal*, V. 117, No. 6, Nov. 2020, pp. 55-63.
21. AlShareedah, O.; Haider, M. M.; and Nassiri, S., "Correlating Laboratory and Field Compaction Levels to Achieve Optimum In Situ Mechanical Properties for Pervious Concrete Pavements," *Journal of Materials in Civil Engineering*, ASCE, V. 32, No. 10, Oct. 2020, p. 04020278. doi: 10.1061/(ASCE)MT.1943-5533.0003361
22. Nassiri, S., and AlShareedah, O., "Preliminary Procedure for Structural Design of Pervious Concrete Pavements," Report No. WA-RD 868.2, Washington State Department of Transportation, Olympia, WA, Nov. 2017, 46 pp.
23. Šmilauer, V.; Catalano, E.; Chareyre, B.; Dorofeenko, S.; Duriez, J.; Dyck, N.; Eliáš, J.; Er, B.; Eulitz, A.; Gladky, A.; Guo, N.; Jakob, C.; Kneib, F.; Kozicki, J.; Marzougui, D.; Maurin, R.; Modenese, C.; Scholtès, L.; Sibille, L.; Stránský, J.; Sweijen, T.; Thoeni, K.; and Yuan, C., "Yade Documentation," second edition, The Yade Project, 2015, 526 pp.
24. Chareyre, B.; Cortis, A.; Catalano, E.; and Barthélémy, E., "Pore-Scale Modeling of Viscous Flow and Induced Forces in Dense Sphere Packings," *Transport in Porous Media*, V. 92, No. 2, Mar. 2012, pp. 473-493. doi: 10.1007/s11242-011-9915-6
25. Tran, V. T.; Donzé, F.-V.; and Marin, P., "A Discrete Element Model of Concrete under High Triaxial Loading," *Cement and Concrete Composites*, V. 33, No. 9, Oct. 2011, pp. 936-948. doi: 10.1016/j.cemconcomp.2011.01.003
26. Harthong, B.; Jérier, J.-F.; Richefeu, V.; Chareyre, B.; Dorémus, P.; Imbault, D.; and Donzé, F.-V., "Contact Impingement in Packings of Elastic–Plastic Spheres, Application to Powder Compaction," *International Journal of Mechanical Sciences*, V. 61, No. 1, Aug. 2012, pp. 32-43. doi: 10.1016/j.ijmecsci.2012.04.013
27. Xie, L.; Jin, P.; Su, T.-C.; Li, X.; and Liang, Z., "Numerical Simulation of Uniaxial Compression Tests on Layered Rock Specimens Using the Discrete Element Method," *Computational Particle Mechanics*, V. 7, No. 4, July 2020, pp. 753-762.
28. Chen, J.; Huang, B.; and Shu, X., "Application of Discrete Element Method to Superpave Gyratory Compaction," *Road Materials and Pavement Design*, V. 13, No. 3, 2012, pp. 480-500.
29. Šmilauer, V., "Cohesive Particle Model Using the Discrete Element Method on the Yade Platform," PhD thesis, Czech Technical University in Prague, Prague, Czech Republic, 2010, 258 pp.
30. Nguyen, T. T.; Bui, H. H.; Ngo, T. D.; and Nguyen, G. D., "Experimental and Numerical Investigation of Influence of Air-Voids on the Compressive Behaviour of Foamed Concrete," *Materials & Design*, V. 130, Sept. 2017, pp. 103-119. doi: 10.1016/j.matdes.2017.05.054
31. Rios, A. J., "Simulation of Structural Behavior of Masonry Using Discrete Element Modeling," master's thesis, Polytechnic University of Catalonia, Barcelona, Catalonia, Spain, 2016, 115 pp.
32. ASTM C1754/C1754M-12, "Standard Test Method for Density and Void Content of Hardened Pervious Concrete (Withdrawn 2021)," ASTM International, West Conshohocken, PA, 2012.
33. Chen, Y.; Wang, K.; Wang, X.; and Zhou, W., "Strength, Fracture and Fatigue of Pervious Concrete," *Construction and Building Materials*, V. 42, May 2013, pp. 97-104. doi: 10.1016/j.conbuildmat.2013.01.006
34. Brake, N. A.; Allahdadi, H.; and Adam, F., "Flexural Strength and Fracture Size Effects of Pervious Concrete," *Construction and Building Materials*, V. 113, June 2016, pp. 536-543. doi: 10.1016/j.conbuildmat.2016.03.045
35. Vancura, M.; MacDonald, K.; and Khazanovich, L., "Microscopic Analysis of Paste and Aggregate Distresses in Pervious Concrete in a Wet, Hard Freeze Climate," *Cement and Concrete Composites*, V. 33, No. 10, Nov. 2011, pp. 1080-1085. doi: 10.1016/j.cemconcomp.2011.05.011
36. Nitka, M., and Tejchman, J., "Modelling of Concrete Behaviour in Uniaxial Compression and Tension with DEM," *Granular Matter*, V. 17, No. 1, Feb. 2015, pp. 145-164. doi: 10.1007/s10035-015-0546-4
37. Stránský, J., "Mesoscale Discrete Element Model for Concrete and Its Combination with FEM," PhD thesis, Czech Technical University in Prague, Prague, Czech Republic, 2018, 148 pp.
38. Cundall, P. A., and Strack, O. D. L., "A Discrete Numerical Model for Granular Assemblies," *Géotechnique*, V. 29, No. 1, Mar. 1979, pp. 47-65.
39. Gong, J.; Nie, Z.; Zhu, Y.; Liang, Z.; and Wang, X., "Exploring the Effects of Particle Shape and Content of Fines on the Shear Behavior of Sand-Fines Mixtures via the DEM," *Computers and Geotechnics*, V. 106, Feb. 2019, pp. 161-176. doi: 10.1016/j.compgeo.2018.10.021
40. Zhang, T.; Zhang, C.; Zou, J.; Wang, B.; Song, F.; and Yang, W., "DEM Exploration of the Effect of Particle Shape on Particle Breakage in Granular Assemblies," *Computers and Geotechnics*, V. 122, June 2020, Article No. 103542. doi: 10.1016/j.compgeo.2020.103542
41. Jensen, R. P.; Edil, T. B.; Bosscher, P. J.; Plesha, M. E.; and Kahla, N. B., "Effect of Particle Shape on Interface Behavior of DEM-Simulated Granular Materials," *International Journal of Geomechanics*, ASCE, V. 1, No. 1, 2001, pp. 1-19. doi: 10.1061/(ASCE)1532-3641(2001)1:1(1)
42. Liu, Y.; Zhou, X.; You, Z.; Yao, S.; Gong, F.; and Wang, H., "Discrete Element Modeling of Realistic Particle Shapes in Stone-Based Mixtures through MATLAB-Based Imaging Process," *Construction and Building Materials*, V. 143, July 2017, pp. 169-178. doi: 10.1016/j.conbuildmat.2017.03.037
43. Deb, D., *Finite Element Methods: Concepts and Applications in Geomechanics*, Prentice-Hall of India Private Limited, New Delhi, India, 2010.
44. Tejchman, J., and Bobiński, J., *Continuous and Discontinuous Modelling of Fracture in Concrete Using FEM*, Springer-Verlag GmbH, Berlin, Germany, 2012.
45. Jebli, M.; Jamin, F.; Malachanne, E.; Garcia-Diaz, E.; and El Yousoufi, M. S., "Experimental Characterization of Mechanical Properties of the Cement Paste–Aggregate Interface in Concrete," *EPJ Web of Conferences*, V. 140, 2017, Article No. 12014.
46. El Bitouri, Y.; Jamin, F.; Péliſsou, C.; and El Yousoufi, M. S., "Tensile and Shear Bond Strength between Cement Paste and Aggregate Subjected to High Temperature," *Materials and Structures*, V. 50, No. 6, Dec. 2017, Article No. 234. doi: 10.1617/s11527-017-1105-8
47. ASTM C39/C39M-21, "Standard Test Method for Compressive Strength of Cylindrical Concrete Specimens," ASTM International, West Conshohocken, PA, 2021, 8 pp.
48. Rangelov, M.; Nassiri, S.; and Chen, Z., "Preliminary Study to Develop Standard Acceptance Tests for Pervious Concrete," Report No. WA-RD 868.1, Washington State Department of Transportation, Olympia, WA, May 2017, 67 pp.
49. Rangelov, M.; Nassiri, S.; Haselbach, L.; and Englund, K., "Using Carbon Fiber Composites for Reinforcing Pervious Concrete," *Construction and Building Materials*, V. 126, Nov. 2016, pp. 875-885. doi: 10.1016/j.conbuildmat.2016.06.035
50. Jiao, K.; Chen, C.; Li, L.; Shi, X.; and Wang, Y., "Compression Fatigue Properties of Pervious Concrete," *ACI Materials Journal*, V. 117, No. 2, Mar. 2020, pp. 241-249.
51. Akand, L., and Yang, M., "Micromechanical Modelling of Pervious Concrete Reinforced with Treated Fibres," *Proceedings of the Institution of Civil Engineers - Construction Materials*, V. 176, No. 1, Jan. 2023, pp. 2-12.
52. Lian, C.; Zhuge, Y.; and Beecham, S., "The Relationship between Porosity and Strength for Porous Concrete," *Construction and Building*

- Materials*, V. 25, No. 11, Nov. 2011, pp. 4294-4298. doi: 10.1016/j.conbuildmat.2011.05.005
53. Deo, O., and Neithalath, N., “Compressive Behavior of Pervious Concretes and a Quantification of the Influence of Random Pore Structure Features,” *Materials Science and Engineering: A*, V. 528, No. 1, Nov. 2010, pp. 402-412. doi: 10.1016/j.msea.2010.09.024
54. Ibrahim, A.; Mahmoud, E.; Yamin, M.; and Patibandla, V. C., “Experimental Study on Portland Cement Pervious Concrete Mechanical and Hydrological Properties,” *Construction and Building Materials*, V. 50, Jan. 2014, pp. 524-529. doi: 10.1016/j.conbuildmat.2013.09.022
55. Yu, F.; Sun, D.; Wang, J.; and Hu, M., “Influence of Aggregate Size on Compressive Strength of Pervious Concrete,” *Construction and Building Materials*, V. 209, June 2019, pp. 463-475. doi: 10.1016/j.conbuildmat.2019.03.140
56. Sonebi, M., and Bassuoni, M. T., “Investigating the Effect of Mixture Design Parameters on Pervious Concrete by Statistical Modelling,” *Construction and Building Materials*, V. 38, Jan. 2013, pp. 147-154. doi: 10.1016/j.conbuildmat.2012.07.044
57. Ibrahim, H. A.; Goh, Y.; Ng, Z. A.; Yap, S. P.; Mo, K. H.; Yuen, C. W.; and Abutaha, F., “Hydraulic and Strength Characteristics of Pervious Concrete Containing a High Volume of Construction and Demolition Waste as Aggregates,” *Construction and Building Materials*, V. 253, Aug. 2020, Article No. 119251. doi: 10.1016/j.conbuildmat.2020.119251
58. Kia, A.; Wong, H. S.; and Cheeseman, C. R., “Clogging in Permeable Concrete: A Review,” *Journal of Environmental Management*, V. 193, May 2017, pp. 221-233. doi: 10.1016/j.jenvman.2017.02.018
59. Montes, F., and Haselbach, L., “Measuring Hydraulic Conductivity in Pervious Concrete,” *Environmental Engineering Science*, V. 23, No. 6, Nov./Dec. 2006, pp. 960-969. doi: 10.1089/ees.2006.23.960
60. Sata, V.; Wongsa, A.; and Chindaprasirt, P., “Properties of Pervious Geopolymer Concrete Using Recycled Aggregates,” *Construction and Building Materials*, V. 42, May 2013, pp. 33-39. doi: 10.1016/j.conbuildmat.2012.12.046
61. Zaetang, Y.; Wongsa, A.; Sata, V.; and Chindaprasirt, P., “Use of Lightweight Aggregates in Pervious Concrete,” *Construction and Building Materials*, V. 48, Nov. 2013, pp. 585-591. doi: 10.1016/j.conbuildmat.2013.07.077
62. Yu, F.; Sun, D.; Hu, M.; and Wang, J., “Study on the Pores Characteristics and Permeability Simulation of Pervious Concrete Based on 2D/3D CT Images,” *Construction and Building Materials*, V. 200, Mar. 2019, pp. 687-702. doi: 10.1016/j.conbuildmat.2018.12.135
63. Lori, A. R.; Hassani, A.; and Sedghi, R., “Investigating the Mechanical and Hydraulic Characteristics of Pervious Concrete Containing Copper Slag as Coarse Aggregate,” *Construction and Building Materials*, V. 197, Feb. 2019, pp. 130-142. doi: 10.1016/j.conbuildmat.2018.11.230
64. Zhang, Z.; Zhang, Y.; Yan, C.; and Liu, Y., “Influence of Crushing Index on Properties of Recycled Aggregates Pervious Concrete,” *Construction and Building Materials*, V. 135, Mar. 2017, pp. 112-118. doi: 10.1016/j.conbuildmat.2016.12.203
65. ACI Committee 522, “Report on Pervious Concrete (ACI 522R-10) (Reapproved 2011),” American Concrete Institute, Farmington Hills, MI, 2010, 40 pp.
66. Shah, S. P., and Ahmad, S. H., “Structural Properties of High Strength Concrete and its Implications for Precast Prestressed Concrete,” *PCI Journal*, V. 30, No. 6, Nov.-Dec. 1985, pp. 92-119. doi: 10.15554/pcij.11011985.92.119
67. AlShareedah, O., and Nassiri, S., “Spherical Discrete Element Model for Estimating the Hydraulic Conductivity and Pore Clogging of Pervious Concrete,” *Construction and Building Materials*, V. 305, Oct. 2021, Article No. 124749. doi: 10.1016/j.conbuildmat.2021.124749

ARE YOU A RESEARCHER?

SIGN UP FOR **ORCID** TODAY!

ORCID provides a persistent digital identifier that distinguishes you from every other researcher and, through integration in key research workflows such as manuscript and grant submission, supports automated linkages between you and your professional activities, ensuring that your work is recognized.

Individuals may use ORCID services freely and it's as easy as **1-2-3**:

1

REGISTER

2

USE YOUR ORCID ID

3

SHARE YOUR ORCID ID

For more information and to register, visit:

WWW.ORCID.ORG

Title No. 120-M60

An Improved Prediction for Bond Strength of Deformed Bars in Concrete Externally Confined with Fiber-Reinforced Polymer

by Zhenwen Xu and Dongming Yan

External bonding with fiber-reinforced polymer (FRP) offers a potential solution to mitigate the detrimental effects caused by load impact and corrosion, which can weaken the bond strength of reinforced concrete structures. However, existing models need to be improved in addressing the FRP confinement mechanism and failure modes. As a solution, the proposed model employs stress intensity factor (SIF)-based criteria to determine the internal pressure exerted on the steel-concrete interface during various stages of comprehensive concrete cracking. Critical parameters are evaluated using weight function theory and a finite element model. A bond-slip model is introduced for the FRP-concrete interface and reasonable assumptions on failure plane characteristics. The internal pressure model employed demonstrates that FRP confinement has the ability to generate dual peaks in stress distribution and modify their magnitude as the confinement level increases. The proposed predictive model demonstrates superior performance in failure modes, test methods, and wrap methods for assessing bond strength with FRP confinement. The accuracy of this model is indicated by an integral absolute error (IAE) of 9.6% based on 125 experimental data, surpassing the performance of the other three existing models. Moreover, a new confinement parameter is introduced and validated, showing an upper bound of 0.44 for enhancing FRP bond strength. Additionally, a general expression validating the bond strength model with FRP confinement is established, allowing for the prediction of bond length.

Keywords: analytical model; bond strength; fiber-reinforced polymer (FRP) confinement; stress intensity factor (SIF); weight function.

INTRODUCTION

In light of the challenges of inadequate anchorage design and corrosion-induced cracking in reinforced concrete (RC) elements, a viable solution lies in applying externally bonded fiber-reinforced polymer (FRP) reinforcement. This approach is recognized for its notable efficacy in repairing and reinforcing damaged RC structures: the reinforcement can be fortified through additional confinement, augmenting lap bond strength and reducing the risk of premature splitting failure.

To date, a wide range of research has been conducted on FRP effective confinement. In particular, single-layer FRP enhanced the ductility of bond failure, and the length of the reinforcement bond did not influence the bond strength enhancement $\Delta\tau_{spl}$.¹⁻³ Moreover, an increase in the level of FRP confinement led to a change in the failure mode. Separate investigations⁴ revealed that a higher rib height increased the bond strength and elastic stiffness, while FRP confinement increased the slip value. The bond strength enhancement

derived from FRP wrapping becomes more pronounced as the relative cover thickness ratio c/d decreases.⁵ Recent research has also examined the bond performance of reinforcement materials, engineered cementitious composites,^{6,7} and epoxy-coated reinforcement combined with seawater marine sand concrete,⁸ all subjected to FRP confinement under static loads. Furthermore, an improved method⁹ for testing FRP-confined specimens was compared by performing both static and cyclic load tests. While the critical slip increased with the number of cycles, the rate of increase was lower for carbon FRP (CFRP) confinement compared to unconfined beams.¹⁰ Moreover, a consistent trend was found in fatigue bond strength similar to that observed during static loading, regardless of variations in FRP type or cover thickness.^{11,12}

Furthermore, various authors evaluated FRP confinement's effectiveness in bond strength enhancement $\Delta\tau_{spl}$. Corrections to the expression for the stirrup confinement were applied to the bond strength enhancement $\Delta\tau_{spl}$ for the FRP confinement,^{1,2} where $\Delta\tau_{spl}$ was considered to be independent of the FRP strain. However, this model^{1,2} is limited to FRP reinforcement ratios ρ_f not exceeding 0.35%. Similarly, using the bond strength enhancement model $\Delta\tau_{spl}$ developed by stirrup confinement^{13,14} led to a linear increase in $\Delta\tau_{spl}$ with the number of FRP layers until reaching an upper limit of 0.25.¹³ Another study¹⁵ combined the elastic modulus ratios of the stirrups and FRP, along with the FRP equivalent area. An upper limit of $\Delta\tau_{spl}$ was eventually determined to be 0.40. Moreover, FRP strains with respect to concrete surface strain, reinforcement diameter, and FRP axial stiffness were also considered.⁵ However, the model is limited to specimens with short anchorage lengths and small relative concrete cover thicknesses. Based on the Mohr-Coulomb friction theory and the thick-walled cylindrical model, a study⁴ was conducted by considering the concrete cover, reinforcement diameter, and radial displacement of the concrete. However, it has not yet been validated for longer bond lengths. Recently, a practical strain control approach^{16,17} demonstrated improved accuracy in predicting the bond strength enhancement resulting from FRP confinement and the actual FRP strain experienced during bond

failure. However, these findings were based solely on beam-splitting tests, indicating the need for additional validation data. It is worth noting that different test methods, FRP types, and FRP layouts can yield varying upper bounds. Consequently, an urgent demand exists for a unified confinement model that effectively evaluates FRP confinement.

The previously mentioned models for partial bond strength enhancement can indirectly assess FRP confinement's effectiveness, but they cannot characterize bond strength directly. To address this limitation, some researchers have combined the unconfined model^{14,18-21} with the inclusion of the FRP confinement index K_{trf} to establish a confinement model that accurately reflects bond behavior. For instance, based on the unconfined model,¹⁴ a confinement index K_{trf} was introduced by considering the FRP effective stress.²² The FRP confinement index K_{trf} was also enhanced by incorporating aspects from the stirrup confinement index.¹⁵ Additionally, the confinement index K_{trf} built upon the unconfined model,^{23,24} which applies to both FRP strip types and FRP reinforcement. It is worth mentioning that the Gong et al.²⁵ model, inspired by the exponential form model,²⁶ solely considers the compressive strength and the contribution of FRP. Nevertheless, empirical models developed for specific databases need help when making reasonable predictions for other databases. In addition, parameter superposition contradicts the bond strength enhancement $\Delta\tau_{spl}$.

The aforementioned predictive model solely focuses on the ultimate bond strength. However, it fails to consider the multiple peaks observed on the bond-slip curves under FRP confinement.^{6,7} These peaks indicate that the efficacy of the FRP as a confining stress agent is determined not only by the distribution of tensile stress within the FRP,^{6,7} but also by the bond mechanism between the FRP and concrete at the surface cracks. Consequently, the exact mechanism for FRP confinement in each cracking scenario remains to be determined. Compared to conventional stirrup confinement, further research is required to refine different methods of FRP reinforcement (wrap technique, FRP type, and the number of FRP layers) to enhance the bond strength. Additionally, an appropriate prediction model must be developed to account for single and multiple confinement instances.

RESEARCH SIGNIFICANCE

The challenges related to FRP confining stress, bond strength augmentation, failure mechanism analysis, and theoretical bond models persist throughout each stage of concrete cracking. The study is significant for: 1) a better comprehension of the mechanisms through which externally applied FRP enhances the bond strength during different stages of concrete cracking; 2) the development of an improved model capable of accurately predicting the bond strength of deformed bars in FRP-confined concrete, accounting for various cases; 3) the proposal of a novel FRP confinement parameter to establish the upper limit of bond strength enhancement; and 4) the formulation of a comprehensive expression for bond length with FRP confinement in conjunction with a simplified model for bond strength. These findings have significant implications for future advancements in enhancing the design expressions of

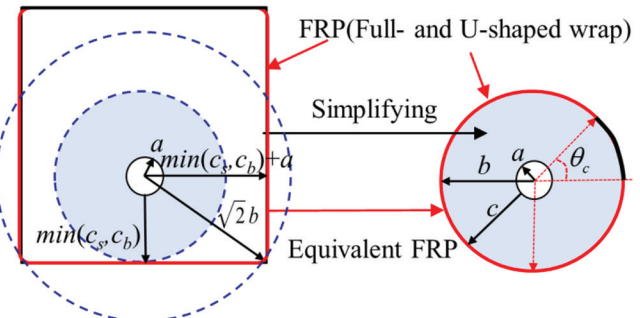


Fig. 1—Simplified approach for FRP confinement.

FRP and furthering the comprehension of confined bond performance.

ANALYSIS MODEL OF INTERNAL PRESSURE Simplification of concrete and FRP confinement

The rectangular concrete with FRP confinement depicted in Fig. 1 is simplified to a thick-walled cylindrical model, with the defect angle θ_c for the different wrapping methods indicated by the black line, where the defect angles θ_c are 0 and $\pi/2$ for full and U-shaped wraps, respectively. b and a represent the outer radius of the hollow cylinder and the deformed bar radius, and c represents the minimum thickness of the side and bottom concrete cover (c_s, c_b). However, using a minimum concrete cover thickness c suffered from an overestimation of the bond strength,^{4,5} so the recommended equivalent radius for the FRP in Fig. 1 is half of the inner and outer circles of the square.

Critical crack depth for failure mode

From the perspective of crack depth e , it is simply considered that pullout failure occurs in locally cracked concrete ($0 < e < c$) and vice versa for splitting failure ($e = c$), but FRP confinement causes a change in the critical crack depth e_{cr} when pullout failure occurs. The critical crack depth e_{cr} needs to be determined to evaluate the maximum pullout bond strength.

Assume that the concrete within the FRP is divided into the cracked part and uncracked part, where the cracked part is subjected to the internal pressure P_r exerted on the surface of the reinforcing rib, and the confining pressure P_e on the uncracked part can be determined by the force balance equation.

$$2\pi(e + a)P_e = 2\pi a P_r \quad (1)$$

The uncracked concrete can be regarded as a thick-walled cylinder subjected to uniform internal and external pressure, with the internal pressure being the reverse force P_e of the cracked concrete, and the external pressure being the radial confining force P_{fb} provided by the FRP. In addition, the FRP circumferential tensile stress is the maximum circumferential pressure stress $\sigma_{\theta max}$ to which this part of the concrete is subjected at $r = e + a$, equal to the concrete tensile strength f_t .

$$\sigma_{\theta max} = -\frac{b^2(P_{fb} - P_e)}{b^2 - (e + a)^2} + \frac{(e + a)^2 P_e - b^2 P_{fb}}{b^2 - (e + a)^2} \quad (2)$$

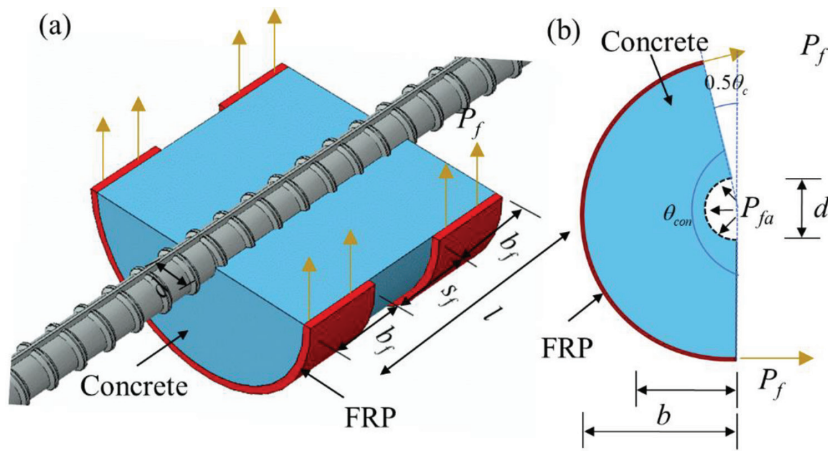


Fig. 2—FRP confinement model: (a) three-dimensional view; and (b) top view.

Given that the modulus of elasticity E_f of FRP is much greater than concrete E_c , it is further assumed that the concrete at FRP has zero radial displacement due to the effective confinement of FRP—that is, $U_{r=b}=0$. As per the theory of thick cylinders, the radial displacement U_r at any given radius r can be determined.

$$U_{r=b} = \frac{1}{E_c(r^2 - a^2)} \left[\frac{(a^2 P_e^2 - r^2 P_{fb}^2)r^2(1 - v_c)r -}{a^2 r^2(P_{fb} - P_e)(1 + v_c)\frac{1}{r}} \right] \quad (3)$$

Letting $U_{r=b}=0$ in the previous equation simplifies the calculation to give the FRP confining force expressed by Eq. (4),²⁷ where the concrete Poisson's ratio v_c is 0.2.

$$P_{fb} = \frac{2(e+a)^2}{(1+v_c)(e+a)^2 + (1-v_c)b^2} \quad (4)$$

Substituting Eq. (1) and (2) into Eq. (4) yields Eq. (5)

$$\frac{P_r}{f_i} = \frac{(1-v_c)b^2 + (1+v_c)(e+a)^2}{(1-v_c)b^2 - (1+v_c)(e+a)^2} \frac{(e+a)}{a} \quad (5)$$

Deriving e from the previous equation to find the critical crack depth e_{cr} of the concrete at which P_r reaches its maximum value

$$e_{cr} = 0.546 \times \frac{b + \sqrt{2}b}{2} - a \approx 0.659b - a \quad (6)$$

Therefore, $e_{cr} = (0.659b) - a$ can be considered the critical value for the occurrence of maximum pullout bond strength.

Theoretical model of internal pressure

The internal pressure P_r related to bond strength can be expressed by Eq. (7), where P_c and P_{fa} represent the internal pressure provided by the concrete and FRP confinement on the interface.

$$P_r = P_c + P_{fa} \quad (7)$$

As shown in Fig. 2, to account for the effect of FRP confinement in the development/splice region, according to the force

balance using Eq. (8), the FRP line load P_f over the bond length can be combined with the confining angle θ_{con} to determine the internal pressure P_{fa} acting on the reinforcing bar-concrete interface, where the FRP confining angle $\theta_{con} = \pi - 0.5\theta_c$. b_f and s_f are the width and spacing of the FRP, respectively.

$$\int_{-0.5\pi}^{0.5\pi} P_{fa} \times a \cos \theta d\theta = P_f + P_f \cos(0.5\theta_c) \quad (8)$$

Contribution of concrete

Case 1: Pullout failure—Despite some cracks observed around the reinforcement-concrete interface in specimens with a smaller concrete cover diameter-to-reinforcing bar diameter ratio c/d , bond failure due to pullout still occurred due to the FRP confinement. The internal pressure P_c by concrete contribution²⁸ is used for pullout failure in Eq. (9), where μ_1 is the steel-concrete friction coefficient.

$$P_c = \frac{\sqrt{f'_c}}{\mu_1} \left(\frac{2.88}{1 + 2.7e^{-0.75\frac{c}{d}}} \right) \quad (9)$$

Case 2: Splitting failure—The total internal pressure P_c at the interface can be considered to be provided by the inner cracked concrete P_{cr} and the outer uncracked concrete P_e in Eq. (10).

$$P_c = P_{cr} + P_e \quad (10)$$

Weight function theory

To investigate the issue of inner concrete cracks with specified geometric parameters, the weight function method²⁹ can effectively provide solutions for stress and displacement boundaries. When an arbitrarily distributed load σ_n is applied to a linear-elastic structure with a crack depth e , the weighted integral of the weight function $m(x, e)$ can be used to calculate the stress intensity factor (SIF) K_n value at the crack tip by Eq. (11) and (12).

$$K_n = \int_0^e \sigma_n(x, \theta) m(x, e) dx \quad (11)$$

$$m(x, e) = \frac{2}{\sqrt{2\pi(e-x)}} \left[\frac{1 + M_1 \left(1 - \frac{x}{e}\right)^{1/2} +}{M_2 \left(1 - \frac{x}{e}\right) + M_3 \left(1 - \frac{x}{e}\right)^{3/2}} \right] \quad (12)$$

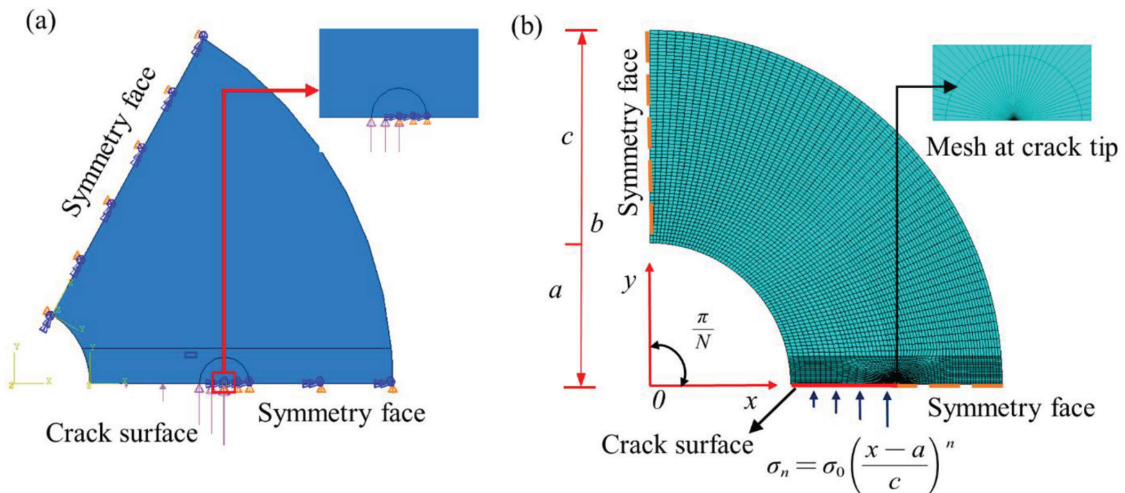


Fig. 3—Finite elements with in-plane cracks: (a) boundary confinement; and (b) load application.

where K_n represents the SIF for Mode I fracture; σ_n represents the stress distribution on the crack surface; and M_i ($i = 1, 2, 3$) represents the weight function coefficient.

Finite element model

To determine the weight function coefficient M_i ($i = 1, 2, 3$) in Eq. (12), it is necessary first to derive the SIF K_n at the crack tip using the finite element (FE) model. To increase the model's applicability and representativeness, as shown in Table A1 of Appendix A,* concrete compressive strength f'_c is varied from C20 to C60, along with the corresponding elastic modulus with a Poisson's ratio v_c of 0.2. Moreover, the concrete cover-to-reinforcing bar diameter ratio c/d is varied in the range of 1 to 4, incremented by intervals of 1, and the relative crack depth e/c is varied in the range of 0.1 to 0.9, incremented by intervals of 0.1. As shown in Fig. 3(a), the cracks in the inner concrete are assumed to be symmetrically distributed and modeled using the Abaqus FE code based on the crack numbers N , where the load application face includes a symmetry face and a crack surface. Local coordinates are set on the symmetry face to limit the radial displacement of the model. Near the cracked surface in Fig. 3(b), a segmentation surface is set and divided into smaller mesh sizes. At the crack front, the radius of the inner and outer contours surrounding the crack tip are specified as 0.1 and 1 mm, respectively. The convergence at the crack tip is achieved using a fine triangular mesh consisting of three-node linear plane strain triangular elements (CPE3). The integration beyond the crack front employs eight-node bilinear plane strain quadrilateral elements (CPE8R) to establish optimal load distribution.

Load distributions σ_n (where σ_0 is the magnitude of the applied load) are uniform, linear, and quadratic ($n = 0, 1, 2$) by Eq. (13) and are applied to the crack surface along the crack direction (x-direction) defined by the overall coordinates (x, y) . Finally, the SIF K_n for the three loading conditions can be derived from the Abaqus FE code.

*The Appendix is available at www.concrete.org/publications in PDF format, appended to the online version of the published paper. It is also available in hard copy from ACI headquarters for a fee equal to the cost of reproduction plus handling at the time of the request.

The SIF K_n ($n = 0, 1, 2$) is generally normalized to an influence coefficient without dimension F_n in Eq. (14), which is displayed in Table A1, provided in Appendix A.

$$F_n = \frac{K_n}{\sigma_0 \sqrt{\pi c}} \quad (14)$$

The influence coefficient F_n ($n = 0, 1, 2$) is a function of the cylinder radius ratio $y = b/a$ and the crack relative depth $x = e/c$. An algorithm (Appendix A) was developed to calculate the influence coefficient for crack number N ($N = 2, 3$) with an R^2 value of over 99.6% (refer to Fig. 4).

$$F_n(x, y) = \sum_{i=1}^4 \sum_{j=1}^4 A_{nij} x^{i-1} y^{j-1}, \quad n = 0, 1, 2 \quad (15)$$

Considering the crack relative depth $x = e/c$ and the influence coefficient F_n as variables, the weight function coefficient M_i ($i = 1, 2, 3$) can be determined by the following equations.

$$M_1 = \frac{\pi}{\sqrt{2}} \left(12F_0 - \frac{78\pi F_1}{x} + \frac{84F_2}{x^2} \right) - \frac{48}{5} \quad (16)$$

$$M_2 = \frac{\pi}{\sqrt{2}} \left(\frac{-105}{2F_0} + \frac{315F_1}{x} - \frac{315F_2}{x^2} \right) + 21 \quad (17)$$

$$M_3 = \frac{\pi}{\sqrt{2}} \left(48F_0 - \frac{264\pi F_1}{x} + \frac{252F_2}{x^2} \right) - \frac{64}{5} \quad (18)$$

SIF-based crack propagation criterion

The internal pressure P_{cr} exerted by cracked concrete on the interface is determined using the weight function, accomplished by introducing the SIF-based crack propagation criterion³⁰ into the thick-walled cylindrical model through Eq. (19), where $K_p(e)$ and $K_C(e)$ are the SIF caused by the stress distribution $\sigma_p(x)$ and cohesive stress $\sigma_c(x)$ acting on the crack surface, respectively.

$$K_p(e) - K_C(e) = 0 \quad (19)$$

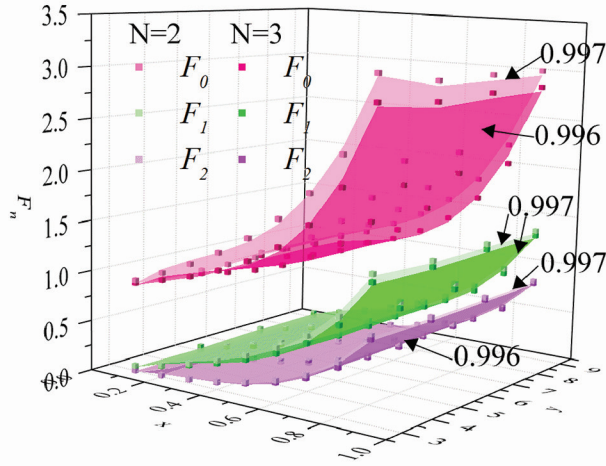


Fig. 4—Influence coefficient F_n through cylinder radius ratio y and relative crack depth x .

$K_p(e)$ represents the SIF caused by the stress distribution $\sigma_p(x)$ at the crack surface,³¹ and this can be modified in Eq. (20), where the inner pressure P_{cr} causes stress distribution $\sigma_p(x)$ at the crack surface in Eq. (21).

$$K_p(e) = \int_0^e (P_{cr} + \sigma_p(x)m(x, e))dx \quad (20)$$

$$\sigma_p(x) = \frac{P_{cr}a^2}{b^2 - a^2} \left(1 + \frac{b^2}{(a+x)^2} \right) \quad (21)$$

$K_C(e)$ represents the SIF caused by the cohesive stress $\sigma_c(x)$ distributed along the crack surface and can be expressed by Eq. (22).

$$K_C(e) = \int_0^e \sigma_c(x)m(x, e)dx \quad (22)$$

considering the relatively small concrete cover being examined, assuming that the crack width $w(x)$ follows an approximately linear pattern. The cohesive stress $\sigma_c(x)$ within the fictitious fracture zone, defined by Eq. (23),³² is dependent on the crack depth e ($0 \leq x \leq e$) and incorporates the exponential-softening traction-separation law³³ between the concrete cohesive stress $\sigma_w(x)$ and the fictitious crack width $w(x)$.³⁴

$$\sigma_c(x) = \sigma_w(x) + (f_t - \sigma_w(x))\frac{x}{e}, \quad 0 \leq x \leq e \quad (23)$$

Internal pressure P_{ec} at the crack tip is provided by the outer uncracked concrete in Eq. (24), where f_t represents the tensile strength of concrete.

$$P_{ec} = f_t \frac{b^2 - (a+e)^2}{b^2 + (a+e)^2} \quad (24)$$

In accordance with the equilibrium condition of forces, internal pressure P_{ei} at the interface can be expressed as

$$P_{ei} = P_{ec} \frac{a+e}{a} \quad (25)$$

The uncracked concrete provides more internal pressure on the interface than the crack tip. Due to the Lau et al.³⁵ model not considering the contribution of uncracked concrete, the critical crack depth e_{cr} is approximately equal to the radius a , consistent with the elastic-plastic analysis results. Equation (26) is suggested as the additional pressure P_e provided to the interface by uncracked concrete.

$$P_e = f_t \frac{e}{a} \frac{b^2 - (a+e)^2}{b^2 + (a+e)^2} \quad (26)$$

To derive the internal pressure-crack depth curve (P_c-e) at the interface, the relevant equations are substituted into Eq. (19) using an integral algorithm developed in Wolfram Mathematica 11.³⁶

$$\int_0^e \left\{ (P_c - P_e) + \left(\frac{(P_c - P_e)a^2}{b^2 - a^2} \left(1 + \frac{b^2}{(a+x)^2} \right) \right) m(x, e) \right\} dx - \int_0^e \sigma_c(x)m(x, e)dx = 0 \quad (27)$$

After cracks develop on the concrete surface ($e = c$), the residual confining pressure $P_{r,res}$ provided by the cracked concrete decreases as the surface crack width $w(c)$ increases. However, the whole concrete cover satisfies an anisotropic displacement field, with concrete boundary conditions where the inner strain equals the crack displacement, and the radial stress on the concrete surface equals the FRP confining stress. Therefore, assuming the residual confining pressure $P_{r,res}$ provided by the fully cracked concrete remains constant

$$P_{r,res} = P_{r,e=c} \quad (28)$$

The concrete parameters required for the analysis of internal pressure P_r are determined as follows³⁷: tensile strength $f_t = 0.3f'_c^{2/3}$; elastic modulus $E_c = 21,500((f'_c + 8)/10)^{1/3}$; and fracture energy $G_f = 0.032((f'_c + 8)/10)^{0.7}$. Based on experimental results,³⁸ most specimens exhibited cracking into one to three pieces. It is noted that the brittleness of concrete increases with compressive strength, increasing the singularity of the crack tip and then producing fewer cracks. Therefore, when concrete compressive strength $f'_c \geq 40$ MPa (5.8 ksi), the crack number is recommended to be $N = 2$; otherwise, $N = 3$.

Contribution of FRP confinement

The unified bond model combines the FRP confinement in Fig. 5 for both failure modes with respect to concrete crack depth e and surface crack width $w(c)$.

Case 1: Pullout failure—Figure 5(a) demonstrates the relationship between the variation in concrete crack depth e and the corresponding FRP circumferential concentrated force P_f . This force signifies the hoop effect exerted on the crack tip, which can be mathematically expressed by Eq. (29).

$$P_f = E_f \epsilon(c) A_f \quad (29)$$

To calculate the FRP section area A_f as mentioned in Eq. (30), Eq. (31) proposes a method to determine the equivalent number of layers n_{fe} of FRP over the bond length l , where m is the total number of FRP in the bond length l ; n_f is the number of FRP layers; E_f is the elastic modulus of the FRP; and b_f and t_f are the width and thickness of one FRP, respectively. When b_f is larger than bond length l , b_f is equal to l .

$$A_f = n_{fe}t_f \quad (30)$$

$$n_{fe} = \frac{mb_f}{l} \quad (31)$$

If the equivalent number of FRP layers $n_{fe} \leq 3$,^{1,5} it is advised to use double thickness ($2t_f$), whereas, using more layers, a similar effect to that of FRP sheets can be achieved,³⁹ so a single-layer thickness (t_f) is recommended.

Concrete strain $\varepsilon_c(e)$ at the crack tip is equal to cracking strain $\varepsilon_{ct} = f_t/E_c$, so the concrete strain $\varepsilon_c(c)$ at the FRP can be derived in Eq. (32), where E_c is the elastic modulus of concrete.

$$\varepsilon_c(c) = \varepsilon_c(e) \frac{2(e+a)^2}{b^2 + (e+a)^2}, 0 \leq e \leq c \quad (32)$$

Case 2: Splitting failure—Figure 5(b) shows that the core concrete is considered to be fully cracked when the crack depth exceeds the concrete cover ($e = c$). In this case, the circumferential concentrated force P_f exerted by the FRP provides a further confining stress to the interface, which is equal to the tensile force of FRP and the bond force between the FRP and surrounding concrete in Eq. (33). The concrete strain $\varepsilon_c(c)$ at the FRP in the first term is suggested to be equal to ε_{ct} . The bond force between the FRP and the cracked concrete in the second term is equal to the local bond stress $\tau_f(s)$ multiplied by the bond area A_{bf} as defined in Eq. (34). The determination of the concrete circumferential deformation Δ_0 , which is associated with the bond area A_{bf} in Eq. (35), involves deducing the analytical solution for both the total crack width $Nw(c)$ and cohesive stress $\sigma_w(c)$ within the internal crack. By doing so, the relative slip s between the FRP and concrete can be determined, and it is equivalent to the surface crack width $w(c)$ stated in Eq. (36). Ultimately, this enables the calculation of the circumferential concentrated force P_f exerted by the FRP.

$$P_f = E_f \varepsilon_{ct} A_f + \frac{\tau_f(s) A_{bf}}{l} \quad (33)$$

$$A_{bf} = mb_f \Delta_0 \quad (34)$$

$$\Delta_0 = Nw(c) + 2\pi b \frac{\sigma_w(c)}{E_c} \quad (35)$$

$$s = w(c) \quad (36)$$

An association is established between the local bond stress $\tau_f(s)$ and relative slip s occurring between the FRP and concrete. This relationship is expressed mathematically

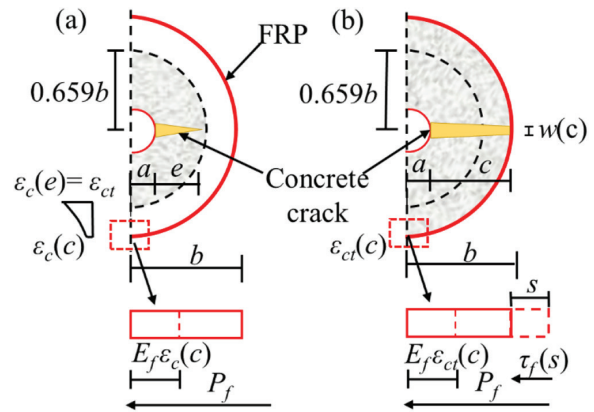


Fig. 5—Concrete strain and FRP tensile strength: (a) pullout failure; and (b) splitting failure.

through Eq. (37).⁴⁰ Following the existing literature, it is suggested that the peak bond stress should be set at a value of $3.5f_c^{0.19}$. Additionally, the corresponding slip s_0 is approximately 0.065 mm (0.00254 in.), which aligns closely with the findings presented by Dai et al.⁴¹ (0.064 mm [0.0025 in.])

$$\tau_f(s) = \tau_{fu} \frac{s}{s_0} \frac{3}{2 + \left(\frac{s}{s_0}\right)^3} s \leq w_0 \quad (37)$$

where w_0 is the crack width at which the cohesive stress reduces to zero; $w_0 = 5.2G_f/f_c$.

The flowchart in Fig. 6 analyzes the maximum internal pressure $P_{r,max}$ for both failure modes. The crack depth e and surface crack width $w(c)$ are the key parameters discussed within this context. Case (1) involves substituting the contributions of concrete cover (Eq. (9)) and FRP (Eq. (8)) into Eq. (7). On the other hand, Case (2) entails substituting the contributions of concrete cover specified by Eq. (10) to (23), (26) to (28), and (47) to (52) in the Appendix, and FRP specified by Eq. (29) to (37) into Eq. (7), enabling the derivation of the P_r - e curve. Next, further insights can be obtained by differentiating Eq. (7) concerning e and equating the resulting differential coefficient to zero.

ANALYTICAL FORMULATION OF BOND MODEL

Figure 7 illustrates the generation of internal pressure P_r resulting from bursting stress on the failure plane, denoted by the red line, which is balanced by the confining action of the surrounding concrete cover and FRP confinement, allowing the relationship between the maximum internal pressure $P_{r,max}$ and bond strength τ_u to be established over the rib spacing S_r . To consider the effect of bond length l on the experimental bond strength ($\tau_{u,exp}$), a reduction coefficient γ is introduced for modification.⁴²

Bond strength enhancement

The total bond strength can be attributed to the contribution of the concrete cover and the FRP confinement. This study introduces an alternative critical cracking method to assess the bond strength enhancement $\Delta\tau_{sp}/\sqrt{f_c}$ resulting from FRP confinement. In cases where the concrete cover undergoes complete cracking, the interfacial confining pressure P_{fa}

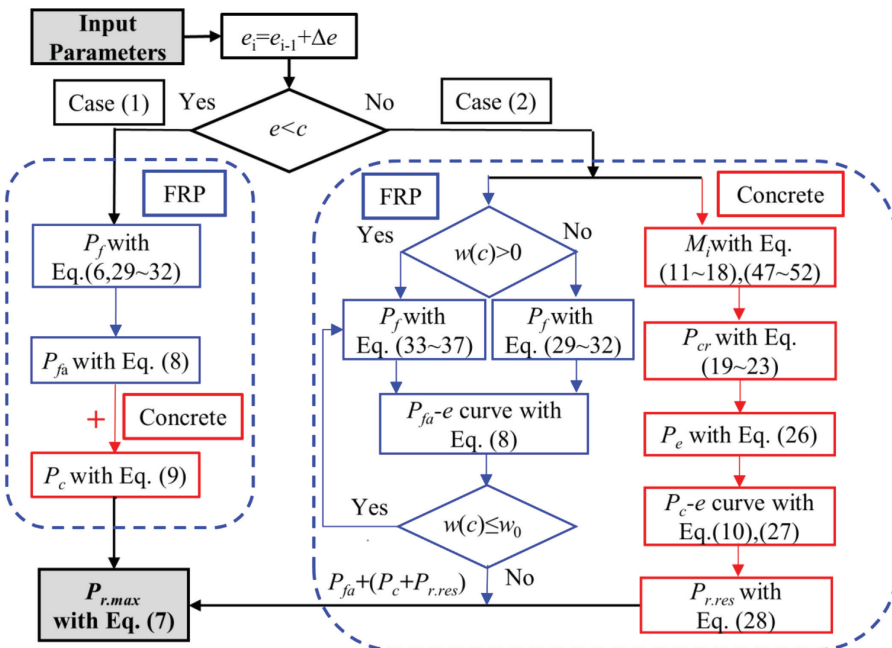


Fig. 6—Flowchart to determine internal pressure.

imparted by the FRP is determined by the maximum circumferential force $P_{f,max}$ experienced by the FRP, as indicated in Eq. (33). By simplifying the equations, a new proposed confinement parameter P_{f0} can be expressed by Eq. (38), where n_b is the number of split steel bars.

$$P_{f0} = \frac{2f_t(E_f n_f t_f + 3.5 f_c^{0.19}(0.13 + 2\pi b)) m b_f}{E_c n_b d(1 + \sin(0.5\theta_c))} l \quad (38)$$

Case 1: Pullout failure—Under the combined influence of the concrete cover and FRP confinement, the shear stress surpasses the shear strength of the concrete, which leads to the occurrence of a failure plane along the horizontal, as demonstrated in Fig. 7(a), due to the high cohesive strength at the interface between the reinforcement and concrete. In scenarios where the maximum bond strength is assumed, the concrete strain ε_c is considered equal to the cracking strain ε_{ct} ($\varepsilon_c([0.659b] - a) = \varepsilon_{ct}$) at a critical crack depth $e_{cr} = (0.659b) - a$, as stated in Eq. (32). By incorporating the internal pressures exerted by the concrete and FRP confinement, as described in Eq. (7) substituted into Eq. (39), the average bond strength τ_u over the rib spacing S_r is anticipated to consist of the interaction between the concrete-concrete interface among the ribs (S_{r0}) and the concrete-upper rib surface (S_{flat}). Regarding confined concrete, the coefficients of friction μ_1 and μ_2 for steel-concrete and concrete-concrete are 0.6²⁸ and 0.53,⁴³ respectively.

$$\tau_u = (P_c + P_{fa}) \frac{\pi(\mu_2 S_{r0} + \mu_1 S_{flat})(d + 2h_r)}{\pi d S_r} \gamma \quad (39)$$

Case 2: Splitting failure—In Fig. 7(b), the splitting failure mechanism for cracked concrete corresponds to the crushing of wedge-shaped concrete. The bond strength versus internal

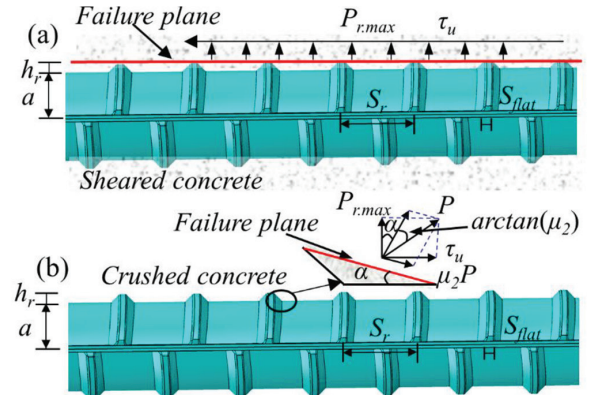


Fig. 7—Schematic for bond failure: (a) pullout failure; and (b) splitting failure.

pressure in the plane of splitting failure is represented by Eq. (40), and the relationship between recommended rib angle α and the rib height-rib spacing ratio (h_r/S_r) can be seen in the author's previous literature.⁴²

$$\tau_u = P_{r,max} \frac{\tan\left(\arctan\left(\alpha - \arctan\left(\frac{h_r}{S_r}\right)\right)\right) + \mu_2}{1 - \mu_2 \tan\left(\arctan\left(\alpha - \arctan\left(\frac{h_r}{S_r}\right)\right)\right)} \gamma \quad (40)$$

Darwin and Graham⁴⁴ suggested a plausible range of rib angles between 17 and 40 degrees, highlighting the need to consider this variation. In this study, for different confinement levels of FRP, the average rib angle $\alpha = 28.5$ degrees is used for the beam tests, and $\alpha = 40$ degrees for the better-confined pullout tests in the present study. If the rib geometry is not reported in the data sets,⁴⁵ the rib spacing S_r , rib height h_r , and rib surface width S_{flat} are taken according to the Chinese steel code.⁴⁶

MODEL VALIDATION AND COMPARISON

Validity of proposed bond model

One hundred twenty-five experimental data are used to validate the proposed model from pullout tests^{5,25,47,48} and beam tests^{11,16,22,49} with two main wrap modes: full wrap^{5,16,25,47,48} and U-shaped wrap.^{11,22,49} All data sets include splitting failure, while pullout failure is also accounted for in certain data sets.^{25,47,48} Moreover, rib spacing S_r and rib height h_r are taken as 12.37 and 1.73 mm (0.482 and 0.067 in.).^{22,45,49}

In Fig. 8, a comparative analysis explored the influence of two factors, namely the crack number N and the FRP thickness, on the relative internal pressure P_r/f_t . Two specimens, namely EC40D12-FC4-B⁵ and NC1S2,⁴⁹ were carefully chosen for this investigation. Generally, the relative internal pressure P_r/f_t increases and decreases during the local cracking stage ($w(c) = 0$). Furthermore, a detailed examination of the NC1S2⁴⁹ series demonstrates that an increase in cracking corresponds to an elevation in the relative internal pressure. Compared to the crack number N , in the EC40D12-FC4-B⁵ series, increasing the FRP thickness n_f positively affects both the relative internal pressure P_r/f_t and the critical crack depth e_{cr} . Unlike stirrup confinement, which had limited effects, superior FRP confinement not only led to a dual-peak internal pressure but also exhibited a substantial increase in internal pressure during the complete cracking stage ($w(c) > 0$) as well as a larger post-peak response, which aligns with the results obtained from bond-slip tests,^{6,7} emphasizing the importance of considering the bond performance between FRP and concrete.

The bond strength ratio ($R = \tau_{u,pre}/\tau_{u,exp}$) and the integral absolute error (IAE) are used to compare the predicted ($\tau_{u,pre}$) with the experimental bond strength ($\tau_{u,exp}$). The bond predictions from experimental data exhibit remarkable correlation, with errors between $\pm 15\%$. Figure 9(a) slightly underestimates pullout failure, while Fig. 9(b) demonstrates the most accurate prediction for the splitting failure mode. Furthermore, it should be mentioned that some specimens exhibit crack depths that do not exceed the critical crack depth e_{cr} . Employing the model described in Eq. (23) would lead to higher internal pressures. In contrast, Fig. 9(d) illustrates the bond strength ratio without FRP confinement, which displays the most significant deviation among the four cases examined. This could be attributed to the greater internal pressure exerted on the unconfined specimen when using the same crack width model.

Figure 10 illustrates a comparison of different wrap methods. The proposed model demonstrates an average ratio of 1.004 and an IAE of 9.6%. Notably, this model displays accurate predictions for full wrap applications (Fig. 10(a)). However, it underestimates the effectiveness of a U-shaped wrap (Fig. 10(b)). This discrepancy can be attributed to using a U-shaped wrap with glass FRP (GFRP) in the data provided by Hamad et al.,²² wherein the GFRP is thicker than CFRP. This difference in thickness results in stronger confinement performance on high-strength concrete than CFRP. Similar findings were observed by Ozden and Akpinar.⁵ Consequently, these factors contribute to the highest IAE observed in the U-wrap case (Fig. 10(b)). Furthermore, the overestimated FRP-confined beam-splitting test¹¹ can be attributed

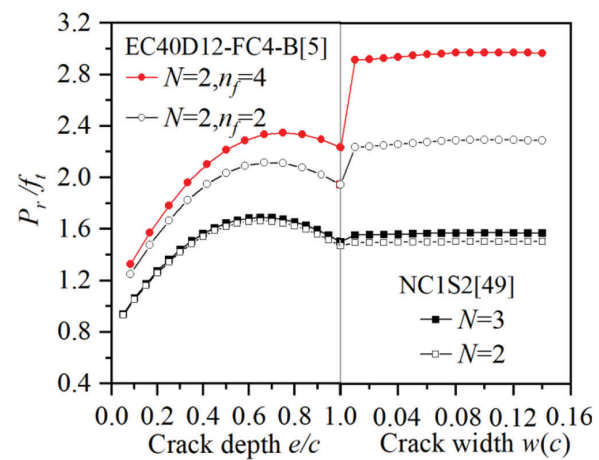


Fig. 8—Relative internal pressure P_r/f_t versus relative crack depth e/c and crack width $w(c)$.

to an average ratio of 1.21 for the unconfined series, which is consistent with the explanation of the crack width model in Fig. 9(d).

By combining the predicted and experimental ratios of bond strength from Fig. 9, the sensitivity of the influencing parameters (f'_c , c/d , and l/d) to the proposed model is further analyzed in Fig. 11. The mean bond strength ratios (R) in Fig. 11(a) verify the accuracy of the selection of $f'_c = 40$ MPa (5.8 ksi) to classify different crack numbers. This confirms that the FRP confinement of concrete yields a similar effect of enhancing equivalent compressive strength,⁵⁰ thereby reducing the occurrence of cracks. Figure 11(b) demonstrates that the mean ratios of 0.995 and 1.049 for small ($c/d < 1.5$) and large c/d ($c/d \geq 1.5$), respectively, indicate that the large c/d is more limited by the restrained end of the eccentric pullout test.⁴⁸ For the bond length ratio l/d in Fig. 11(c), assuming a reduction factor $\gamma = 8.5$ satisfactorily ensures accurate bond strength prediction. Additionally, as the confinement level increases, the bond length's impact on bond strength diminishes compared to stirrup confinement ($\gamma = 8$).⁴² To summarize, the bond strength ratio determined by the proposed model is slightly affected by c/d and can be further simplified by integrating FRP confinement parameters to predict bond strength accurately.

Comparison with available models

When considering the determination of bond strength in current methodologies, empirical models incorporating FRP confinement^{1,15,25} are commonly employed for comparison in Fig. 12 and 13. These models are expressed by Eq. (41) to (43), where b_w is the width of the specimen.

$$\tau_u = \left(0.0996 + 0.249 \frac{c}{d} + 4.15 \frac{d}{l} + \frac{1}{60} \left(\frac{E_f}{230} + 0.5 \right) \left(\frac{b_w}{d} \right) \left(1 - \left(\frac{2n_f b_f}{0.0035 b_w s_f} - 1 \right)^2 \right) \right) \sqrt{f'_c} \quad (41)$$

$$\tau_u = \frac{\sqrt{f'_c}}{\pi} \left(1.44 \left(\frac{c}{d} + 0.5 \right) + \frac{56.3 \pi d}{4l} \right) \left(0.1 \frac{c_{max}}{c} + 0.9 \right) + \sqrt{f'_c} \frac{50 E_f n_f b_f}{E_s n_b d s_f} \quad (42)$$

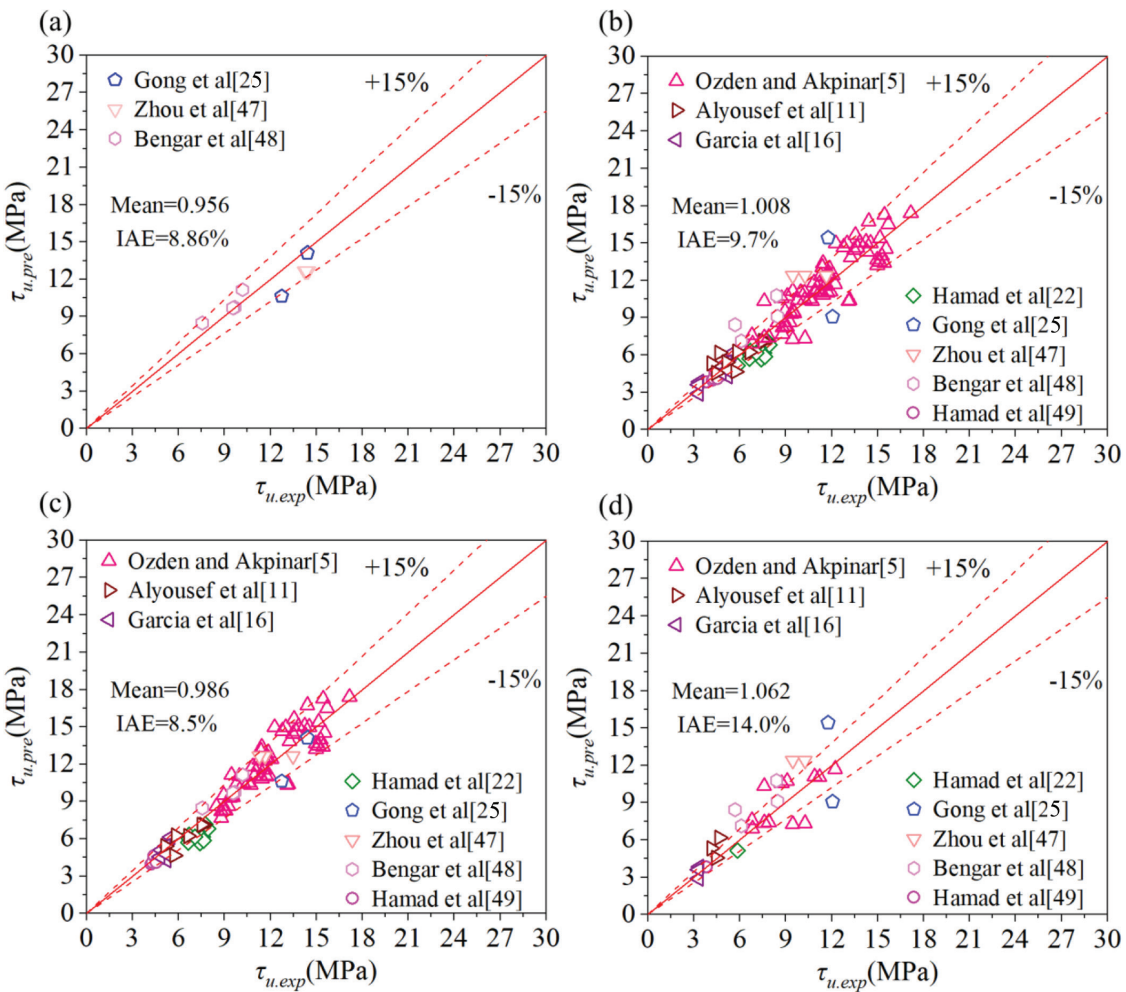


Fig. 9—Comparison of predicted and experimental bond strength: (a) pullout failure; (b) splitting failure; (c) with FRP; and (d) without FRP. (Note: 1 MPa = 0.145 ksi.)

$$\tau_u = \sqrt{f'_c} \frac{0.07}{1 - 0.97e^{-0.127 \frac{E_f n_f t_f b_f}{E_{sp} b_{dl}}}} \quad (43)$$

All the experimental data sets in this study have been validated, confirming the mean ratio of 1.004 for the proposed model. This value is closest to 1, indicating that the model provides the most accurate predictions with the smallest IAE (IAE = 9.6%). In comparison, other available models exhibit different ratios and higher IAE values. The Harajli et al. model¹⁵ yields a ratio of 1.146 with an IAE value of 31.2%, while the Kono et al. model¹ demonstrates a ratio of 0.768 with an IAE value of 26.4%. The Gong et al. model²⁵ produces a ratio of 1.527 with an IAE value of 40.2%. It is worth noting that the Gong et al. model²⁵ tends to overestimate the results of beam tests,^{11,16,22,49} likely because it was specifically tailored to fit the experimental pullout data. Additionally, the FRP confinement capacity of the beam test with a U-shaped wrap proves to be significantly inadequate, particularly after the cracks propagate to the concrete surface. On the other hand, the underestimation observed in all the data sets by the Kono et al. model¹ can be attributed to the original data set being fitted with transverse reinforcement confinement, leading to limited participation of the FRP in the confinement process.

The comparison of the specimens used in beam tests presented in Fig. 12 and 13 reveals that, apart from the Gong et al. model,²⁵ three other models—Kono et al.,¹ Harajli et al.,¹⁵ and the current proposed model—exhibit higher accuracy in predicting bond strength. Specifically, in Fig. 12(a), the bond strength of GFRP is underestimated by all three models (Kono et al.,¹ Harajli et al.,¹⁵ and the current proposed model) when compared to Hamad et al.^{22,49} Concerning pullout tests, the current proposed model tends to overestimate the data from Bengar et al.⁴⁸ in both Fig. 12(a) and 13(d), particularly without FRP confinement. This discrepancy can be attributed to lower bond data for compressive strength C40 (C40-U-20-25 and C40-U-20-35) compared to corresponding C30 values (C30-U-20-25 and C30-U-20-35). Additionally, Harajli et al.'s model¹⁵ underestimates the pullout failure^{25,47,48} depicted in Fig. 13(b) and yields the highest IAEs (26.7 and 32.0%) for both test methods. This outcome may be due to the reliance of their model on beam tests,^{22,49} which lack sufficient FRP confinement. The comparison shows that the proposed model for the bond strength of deformed bars embedded in concrete with FRP provides reasonable estimates and a wide range of applications.

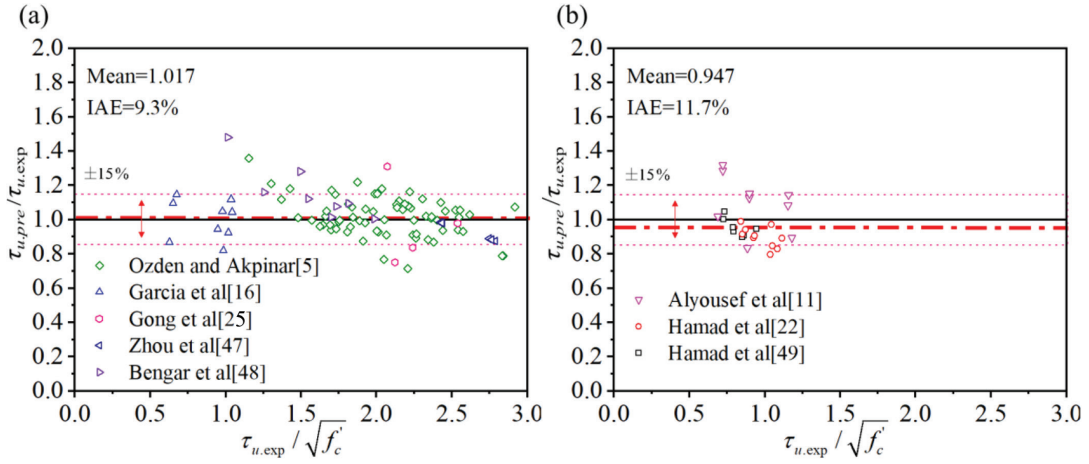


Fig. 10—Comparison of wrap methods: (a) full wrap; and (b) U-shaped wrap.

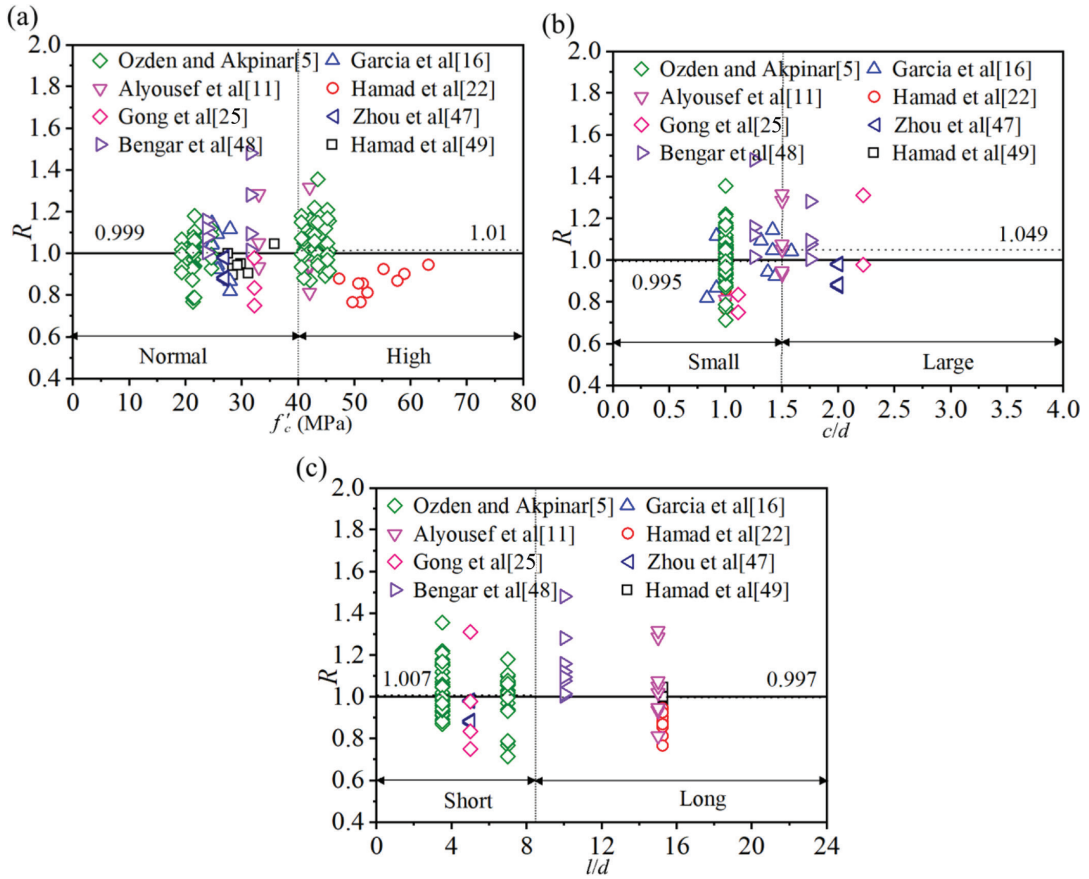


Fig. 11—Influence parameters of prediction-to-experiment ratio: (a) f'_c ; (b) c/d ; and (c) l/d .

Confinement effect of FRP

The occurrence of either the former peak or the latter peak relies on the confinement in the low-peak critical state ($e = c$, $w(c) = 0$). Comparative analysis with beam tests^{11,16,22,49} reveals that the pullout test⁵ offers improved confinement and demonstrates a stronger confinement effect on the bond between FRP and concrete. This effect leads to a larger latter peak after the concrete surface cracks, as validated in Fig. 8. Consequently, this paper exclusively employs the beam test for precise prediction in the first term from Eq. (33). Figure 14 presents the bond strength enhancement $\Delta\tau_{spl}/\sqrt{f'_c}$ as a function of the FRP confinement pressure P_{f0} . Notably, the splitting

bond capacity increases up to an upper bound $\Delta\tau_{spl}/\sqrt{f'_c} \leq 0.44$ in Eq. (44), which is consistent with the findings of Kono et al.² ($\Delta\tau_{spl}/\sqrt{f'_c} \leq 0.44$), slightly surpassing the values obtained by Harajli et al.¹⁵ and Garcia et al.^{16,17} ($\Delta\tau_{spl}/\sqrt{f'_c} \leq 0.4$). This distinction can be attributed to the insufficient confinement capacity of FRP in the beam test and the small residual internal pressure $P_{r,res}$ in Eq. (28) provided by the concrete compared to the maximum internal pressure $P_{r,max}$. Consequently, the former peak remains larger even after reaching the peak bond stress τ_{fu} of FRP-concrete in Eq. (33). In addition, compared to the Garcia et al.^{16,17} model, more data are used to validate Eq. (44) and involved different long bond

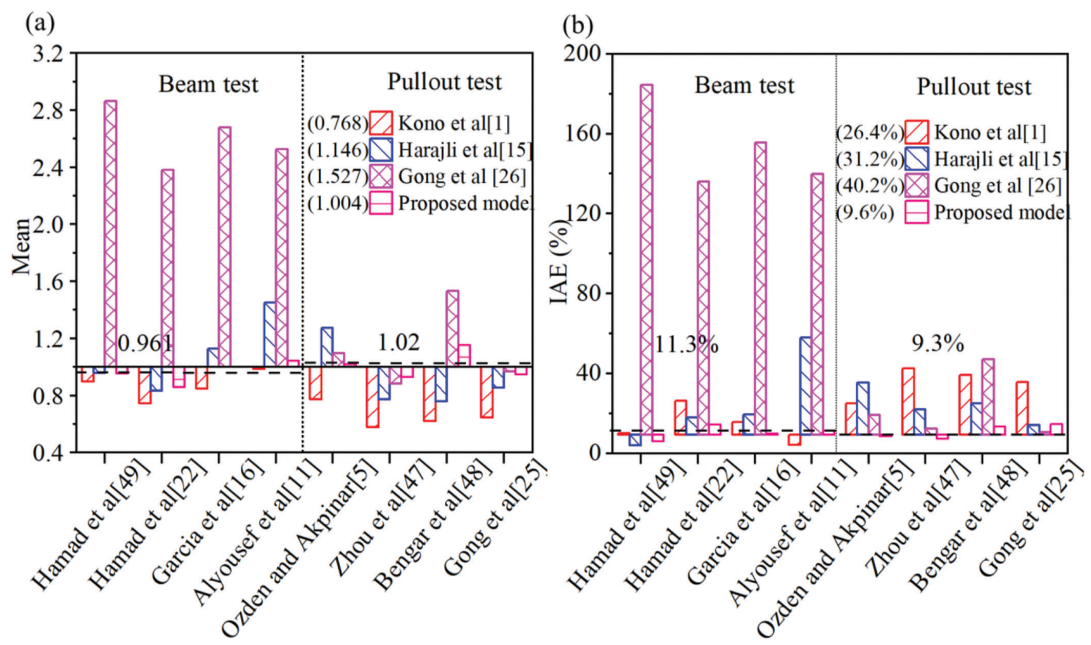


Fig. 12—Comparison of bond strength ratios by various models: (a) mean; and (b) IAE.

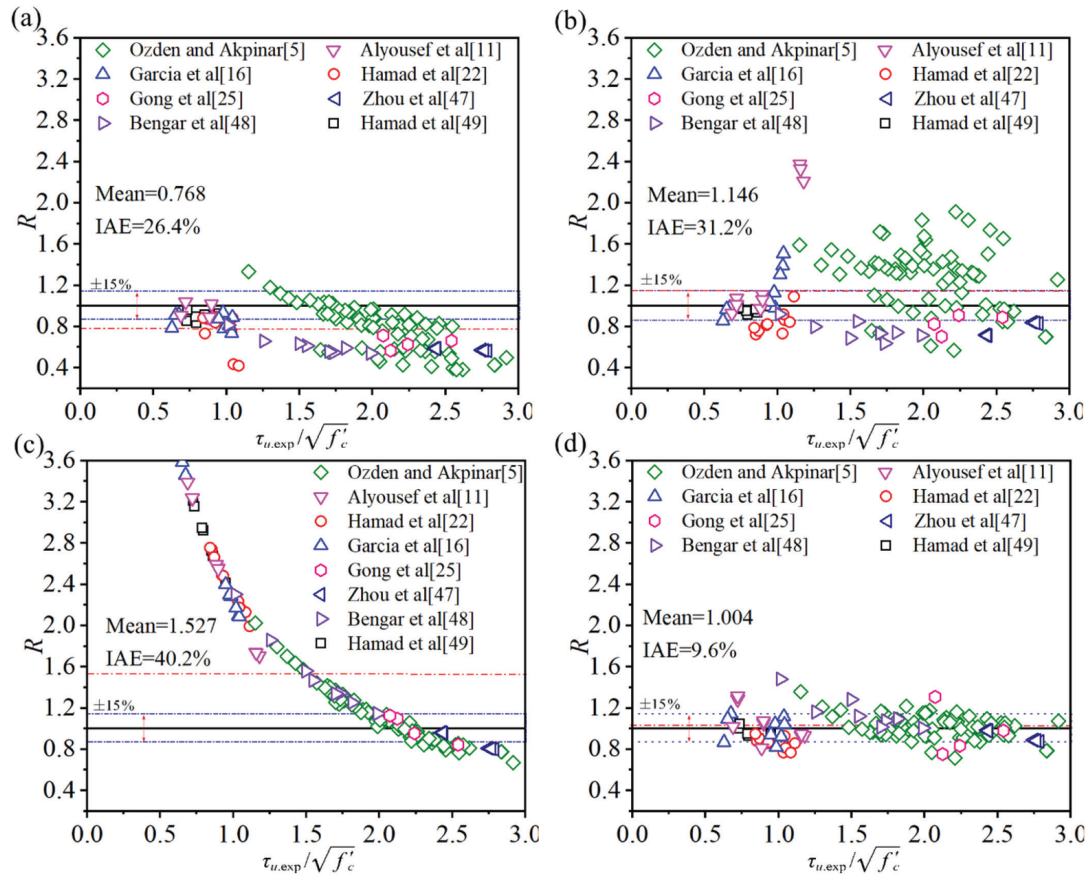


Fig. 13—Prediction-to-experiment ratios for different models: (a) Kono et al.¹; (b) Harajli et al.¹⁵; (c) Gong et al.²⁵; and (d) proposed model.

lengths,¹⁶ full wrap,¹⁶ U-shaped wrap,^{11,22,49} FRP types⁴⁹ and FRP strips,²² indicating the applicability of the model.

$$\Delta\tau_{sp}/\sqrt{f'_c} = 0.44 + 0.1\ln(P_f) \quad (44)$$

Combined with the analysis results of Fig. 14, this indicates that successive increases in the number of FRP layers lead to a corresponding increase in the confining stress. However, it is observed that the enhancement effect on bond strength diminishes beyond a certain limit of FRP layering due to the presence of the adhesive layer, an observation

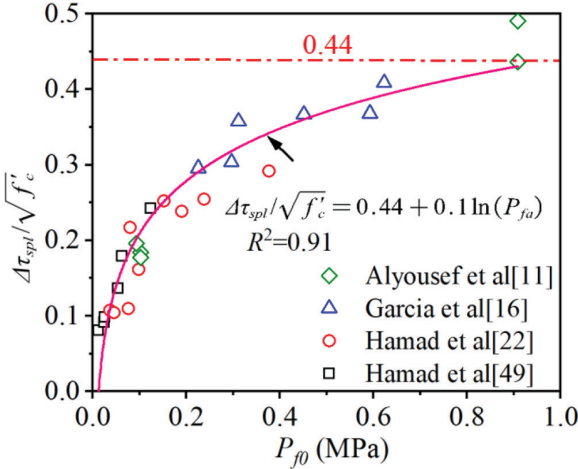


Fig. 14—Bond strength enhancement $\Delta\tau_{spl}/\sqrt{f'_c}$ versus confinement pressure P_{f0} .

similar to that made by Ozden and Akpinar.⁵ To investigate the effect of the equivalent number of layers n_{fe} on the bond strength ratio R , in combination with the bond strength ratio from Fig. 9(c), Fig. 15 shows the mean bond strength ratios (0.965 and 1.027) to verify the accuracy of $n_{fe} = 3$ to classify the FRP thickness for Eq. (31). Similarly, the mean ratios of 1.011 and 0.954 for CFRP and GFRP show a slight underestimation of GFRP confinement, probably because the increase in the confining effect of GFRP on high-strength concrete²⁰ is weaker than CFRP.⁵¹ To further investigate the impact of the equivalent number of layers n_{fe} on the bond strength ratio R , the mean bond strength ratios (0.965 and 1.027) are shown in Fig. 15 alongside the bond strength ratio obtained from Fig. 9(c). These values confirm the accuracy of using $n_{fe} = 3$ as a classification criterion for FRP thickness in Eq. (31). Similarly, the mean ratios of 1.011 and 0.954 for CFRP and GFRP, respectively, indicate a slight underestimation of GFRP confinement. This discrepancy may be attributed to the comparatively stronger confining effect of GFRP on high-strength concrete²⁰ as opposed to CFRP.⁵¹ In conclusion, an equivalent number of FRP layers $n_{fe} = 3$ can serve as an appropriate boundary for offering practical design recommendations when evaluating the necessary FRP thickness for bonded reinforcement.

Compared to the failure of pullout under confinement by FRP, the mechanism of bond failure through splitting is more intricate and necessitates the consideration of additional parameters in the theoretical model. To simplify the prediction model for the splitting bond strength, integration can be used to determine the maximum internal pressure $P_{r,max}$. This integration is performed using 114 sets of experimental data on splitting,^{5,11,16,22,25,47-49} as depicted in Fig. 16. Subsequently, the fitted bond strength $\tau_{u,f}$ is derived from the combined influence of concrete compressive strength, concrete cover c , and FRP confinement. This relationship is represented by Eq. (45), with an R -squared value of 82.5%. Remarkably, Fig. 16 displays a strong positive correlation between the fitted bond strength $\tau_{u,f}$ and the corresponding experimental values $\tau_{u,exp}$, exhibiting a mean ratio of 1.018, a standard deviation (SD) of 0.141, a coefficient of variation (COV) of 0.138, and an IAE of 10.9%, which closely aligns

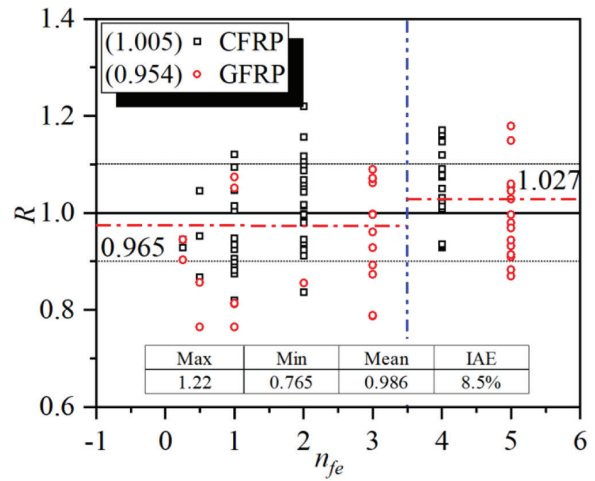


Fig. 15—Bond strength ratio R versus equivalent number of FRP layers n_{fe} .

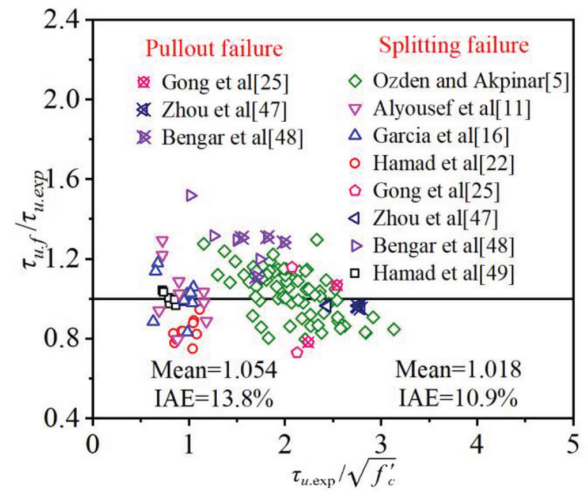


Fig. 16—Ratio of fitted to experimental bond strength $\tau_{u,f}/\tau_{u,exp}$.

with the results shown in Fig. 9(b). Moreover, the accuracy of the model is further confirmed through validation experiments involving pullout failure under FRP confinement, consisting of 11 additional test results from validation data sets.^{25,47,48} In these data sets, the parameters $\alpha = 40$ degrees and $\mu_2 = 0.6$ are employed, resulting in a mean value of 1.054. Overall, Fig. 16 demonstrates a substantial correlation with the experimental bond strength $\tau_{u,exp}$, thereby endorsing using Eq. (45) to identify critical points for bond-slip curves associated with various failure modes.

$$\tau_{u,f} = \frac{3.865\sqrt{f'_c}}{1 + 4.531e^{-1.646\frac{c}{d} - 1.188\frac{E_f f_r n_f t_f}{d E_c (1 + \sin(0.5\theta_c))} - \frac{m b_f}{l}}} \quad (45)$$

$$\frac{\tan\left(\alpha - \arctan\left(\frac{h_r}{S_r}\right)\right) + \mu_2}{1 - \mu_2 \tan\left(\alpha - \arctan\left(\frac{h_r}{S_r}\right)\right)}^\gamma$$

Bond length

In conjunction with the findings presented in Fig. 16, an effort has been made to provide practical engineering guidelines for bond strength. Equation (45) incorporates $h/S_r = 0.117$, $l = mb_f$, and $\alpha = 28.5$ degrees. Additionally, it is commonly observed that the bond length l of deformed reinforcing bars falls within the range of 30 to 50d. Accordingly, assuming $l = 40d$, the reduction coefficient γ can be approximated as 0.461. Consequently, for the practical design applications, Eq. (45) can be simplified to Eq. (46), where f_y is the yield strength of steel bars.

$$\frac{l}{d} = f_y \frac{1 + 4.531e^{-1.646\frac{c}{d} - 1.188\frac{E_f n_f t_f}{d E_c (1 + \sin(0.50c))}} \frac{mb_f}{l}}{18.425 \sqrt{f'_c}} \quad (46)$$

CONCLUSIONS

To understand the local bond behavior of deformed reinforcement in fiber-reinforced polymer (FRP)-confined concrete, a unified bond theory is used to predict the bond strength under various practical cases. Combining the available experimental data with extensive analysis, comparison, and validation, the following conclusions can be drawn:

1. Two critical failure mechanisms are analyzed by combining concrete cover and FRP confinement in terms of crack depth and crack width. Stress intensity factors (SIFs) are determined for thick-walled cylinders with varying crack numbers using finite element (FE) models. The SIF-based crack propagation criterion is introduced to derive analytical expressions for internal pressure using weight function theory.

2. The internal pressure model employed in this research demonstrates that FRP confinement has the ability to generate dual peaks in stress distribution and modify their magnitude as the level of confinement increases. Furthermore, a parameter sensitivity analysis demonstrates that the influence of compressive strength and bond length on bond strength diminishes progressively with higher levels of confinement.

3. The proposed model can accurately predict the wrap methods, FRP confinement, and failure modes, with splitting failures being the most accurately predicted. Compared to the chosen bond models with FRP confinement, the proposed model outperforms them by providing the most precise estimation of the bond strength for deformed bars. The integral absolute error (IAE) associated with the proposed model is determined to be 9.6%, which is relatively lower than that observed in alternative models.

4. With consideration of FRP strips, reinforcement methods, and FRP types, a new parameter P_{fa} for FRP confinement is proposed and validated, revealing an upper limit of 0.44 for bond strength enhancement—a critical determinant to ascertain the adequacy of confinement in preventing splitting failure. Additionally, a design recommendation is put forward, advocating the adoption of an equivalent number of FRP layers ($n_{fe} = 3$) as a threshold to determine the appropriate thickness of a single layer of FRP.

5. A simplified expression is suggested for the splitting bond strength, which is highly correlated with the experimental bond strength, with a mean ratio of 1.018 and an IAE

of 10.9%. Furthermore, its applicability extends to pullout failure, making it suitable for assessing the bond length of FRP confinement.

AUTHOR BIOS

Zhenwen Xu received his PhD from the College of Civil Engineering and Architecture at Zhejiang University, Hangzhou, Zhejiang, China. His research interests include the mechanical properties and interfacial corrosion of steel bars and damaged concrete.

Dongming Yan is a Professor in the College of Civil Engineering and Architecture at Zhejiang University. He received his PhD from Dalian University of Technology, Dalian, Liaoning, China. His research interests include new materials in civil engineering, mechanical properties of concrete, and anticorrosion technology for steel structures.

ACKNOWLEDGMENTS

The authors appreciate the financial support from the National Key Research and Development Program of China (No. 2022YFE0109200).

REFERENCES

1. Kono, S.; Matsuno, K.; and Kaku, T., "Bond-Slip Behavior of Longitudinal Reinforcing Bars Confined with FRP Sheets," *Proceedings of the 12th World Conference on Earthquake Engineering (12WCEE 2000)*, Auckland, New Zealand, 2000, Paper No. 0642.
2. Kono, S.; Matsuno, K.; and Kaku, T., "Experimental Study on Bond-Slip Behavior of Longitudinal Bars in Reinforced Concrete Beams Confined with Fiber Reinforced Polymer Sheets," *Fourth International Symposium: Fiber Reinforced Polymer Reinforcement for Reinforced Concrete Structures*, SP-188, C. W. Dolan, S. H. Rizkalla, and A. Nanni, eds., American Concrete Institute, Farmington Hills, MI, 1999, pp. 333-346.
3. Kono, S.; Inazumi, M.; and Kaku, T., "Bond Splitting Behavior of Reinforced Concrete Members Confined with CFRP Sheets," *Proceedings of the Third International Symposium on Non-Metallic (FRP) Reinforcement for Concrete Structures (FRPRCS-3)*, Sapporo, Japan, 1997, pp. 14-16.
4. Tastani, S. P., and Pantazopoulou, S. J., "Direct Tension Pullout Bond Test: Experimental Results," *Journal of Structural Engineering*, ASCE, V. 136, No. 6, June 2010, pp. 731-743. doi: 10.1061/(ASCE)ST.1943-541X.0000159
5. Ozden, S., and Akpinar, E., "Effect of Confining FRP Overlays on Bond Strength Enhancement," *Construction and Building Materials*, V. 21, No. 7, July 2007, pp. 1377-1389. doi: 10.1016/j.conbuildmat.2006.08.003
6. Zhao, D.; Zhou, Y.; Xing, F.; Sui, L.; Ye, Z.; and Fu, H., "Bond Behavior and Failure Mechanism of Fiber-Reinforced Polymer Bar-Engineered Cementitious Composites Interface," *Engineering Structures*, V. 243, Sept. 2021, Article No. 112520. doi: 10.1016/j.engstruct.2021.112520
7. Zhou, Y.; Fu, H.; Li, P.; Zhao, D.; Sui, L.; and Li, L., "Bond Behavior between Steel Bar and Engineered Cementitious Composite (ECC) Considering Lateral FRP Confinement: Test and Modeling," *Composite Structures*, V. 226, Oct. 2019, Article No. 111206. doi: 10.1016/j.comstruct.2019.111206
8. Wang, J.; Xiao, F.; and Yang, J., "Experimental Study on Bond Behavior between Epoxy-Coated Reinforcement (ECR) and Seawater Sea-Sand Concrete (SSC) under FRP-Steel Confinement," *Construction and Building Materials*, V. 385, July 2023, Article No. 131426. doi: 10.1016/j.conbuildmat.2023.131426
9. Harajli, M. H., "Effect of Confinement Using Steel, FRC, or FRP on the Bond Stress-Slip Response of Steel Bars under Cyclic Loading," *Materials and Structures*, V. 39, No. 6, July 2006, pp. 621-634. doi: 10.1007/s11527-005-9054-z
10. Rteil, A. A.; Soudki, K. A.; and Topper, T. H., "Preliminary Experimental Investigation of the Fatigue Bond Behavior of CFRP Confined RC Beams," *Construction and Building Materials*, V. 21, No. 4, Apr. 2007, pp. 746-755. doi: 10.1016/j.conbuildmat.2006.06.022
11. Alyousef, R.; Topper, T.; and Al-Mayah, A., "Fatigue Bond Stress-Slip Behavior of Lap Splices in the Reinforcement of Unwrapped and FRP-Wrapped Concrete Beams," *Journal of Composites for Construction*, ASCE, V. 20, No. 6, Dec. 2016, p. 04016039. doi: 10.1061/(ASCE)CC.1943-5614.0000699
12. Alyousef, R.; Topper, T.; and Al-Mayah, A., "Effect of FRP Wrapping on Fatigue Bond Behavior of Spliced Concrete Beams," *Journal of Composites for Construction*, ASCE, V. 20, No. 1, Feb. 2016, p. 04015030. doi: 10.1061/(ASCE)CC.1943-5614.0000588
13. Hamad, B. S.; Rteil, A. A.; and Soudki, K. A., "Bond Strength of Tension Lap Splices in High-Strength Concrete Beams Strengthened

- with Glass Fiber Reinforced Polymer Wraps," *Journal of Composites for Construction*, ASCE, V. 8, No. 1, Feb. 2004, pp. 14-21. doi: 10.1061/(ASCE)1090-0268(2004)8:1(14)
14. Orangun, C. O.; Jirska, J. O.; and Breen, J. E., "A Reevaluation of Test Data on Development Length and Splices," *ACI Journal Proceedings*, V. 74, No. 3, Mar. 1977, pp. 114-122.
 15. Harajli, M. H.; Hamad, B. S.; and Rteil, A. A., "Effect of Confinement on Bond Strength between Steel Bars and Concrete," *ACI Structural Journal*, V. 101, No. 5, Sept.-Oct. 2004, pp. 595-603.
 16. Garcia, R.; Helal, Y.; Pilakoutas, K.; and Guadagnini, M., "Bond Behavior of Substandard Splices in RC Beams Externally Confined with CFRP," *Construction and Building Materials*, V. 50, Jan. 2014, pp. 340-351. doi: 10.1016/j.conbuildmat.2013.09.021
 17. Garcia, R.; Helal, Y.; Pilakoutas, K.; and Guadagnini, M., "Bond Strength of Short Lap Splices in RC Beams Confined with Steel Stirrups or External CFRP," *Materials and Structures*, V. 48, No. 1-2, Jan. 2015, pp. 277-293. doi: 10.1617/s11527-013-0183-5
 18. Cai, J.; Pan, J.; Tan, J.; and Li, X., "Bond Behaviours of Deformed Steel Rebars in Engineered Cementitious Composites (ECC) and Concrete," *Construction and Building Materials*, V. 252, Aug. 2020, Article No. 119082. doi: 10.1016/j.conbuildmat.2020.119082
 19. Santos, J., and Henriques, A. A., "New Finite Element to Model Bond-Slip with Steel Strain Effect for the Analysis of Reinforced Concrete Structures," *Engineering Structures*, V. 86, Mar. 2015, pp. 72-83. doi: 10.1016/j.engstruct.2014.12.036
 20. Malek, A.; Scott, A.; Pampanin, S.; and Hoult, N. A., "Postyield Bond Deterioration and Damage Assessment of RC Beams Using Distributed Fiber-Optic Strain Sensing System," *Journal of Structural Engineering*, ASCE, V. 145, No. 4, Apr. 2019, p. 04019007. doi: 10.1061/(ASCE)ST.1943-541X.0002286
 21. Zhou, B.; Wu, R.; and Feng, J., "Two Models for Evaluating the Bond Behavior in Pre- and Post-Yield Phases of Reinforced Concrete," *Construction and Building Materials*, V. 147, Aug. 2017, pp. 847-857. doi: 10.1016/j.conbuildmat.2017.04.067
 22. Hamad, B. S.; Soudki, K. A.; Harajli, M. H.; and Rteil, A. A., "Experimental and Analytical Evaluation of Bond Strength of Reinforcement in Fiber-Reinforced Polymer-Wrapped High-Strength Concrete Beams," *ACI Structural Journal*, V. 101, No. 6, Nov.-Dec. 2004, pp. 747-754.
 23. Harajli, M. H., "Bond Strengthening of Steel Bars Using External FRP Confinement: Implications on the Static and Cyclic Response of R/C Members," *7th International Symposium on Fiber-Reinforced Polymer (FRP) Reinforcement for Concrete Structures*, SP-230, C. K. Shield, J. P. Busel, S. L. Walkup, and D. D. Gremel, eds., American Concrete Institute, Farmington Hills, MI, 2005, pp. 579-596.
 24. Zuo, J., and Darwin, D., "Splice Strength of Conventional and High-Relative Rib Area Bars in Normal and High-Strength Concrete," *ACI Structural Journal*, V. 97, No. 4, July-Aug. 2000, pp. 630-641.
 25. Gong, Y.; Shan, Y.; Liu, X.; Ding, F.; and Wu, Y., "Static Bond Behavior between Corroded Corner Steel Bar and Concrete under the Hoop Confinement of CFRP Sheets," *Composite Structures*, V. 276, Nov. 2021, Article No. 114589. doi: 10.1016/j.compstruct.2021.114589
 26. Wu, Y.-F., and Zhao, X.-M., "Unified Bond Stress-Slip Model for Reinforced Concrete," *Journal of Structural Engineering*, ASCE, V. 139, No. 11, Nov. 2013, pp. 1951-1962. doi: 10.1061/(ASCE)ST.1943-541X.0000747
 27. Huang, L.; Xu, L.; Chi, Y.; Deng, F.; and Zhang, A., "Bond Strength of Deformed Bar Embedded in Steel-Polypropylene Hybrid Fiber Reinforced Concrete," *Construction and Building Materials*, V. 218, Sept. 2019, pp. 176-192. doi: 10.1016/j.conbuildmat.2019.05.096
 28. Dehestani, M.; Asadi, A.; and Mousavi, S. S., "On Discrete Element Method for Rebar-Concrete Interaction," *Construction and Building Materials*, V. 151, Oct. 2017, pp. 220-227. doi: 10.1016/j.conbuildmat.2017.06.086
 29. Glinka, G., and Shen, G., "Universal Features of Weight Functions for Cracks in Mode I," *Engineering Fracture Mechanics*, V. 40, No. 6, 1991, pp. 1135-1146. doi: 10.1016/0013-7944(91)90177-3
 30. Dugdale, D. S., "Yielding of Steel Sheets Containing Slits," *Journal of the Mechanics and Physics of Solids*, V. 8, No. 2, May 1960, pp. 100-104. doi: 10.1016/0022-5096(60)90013-2
 31. Yang, S. T.; Ni, Y. L.; and Li, C. Q., "Weight Function Method to Determine Stress Intensity Factor for Semi-Elliptical Crack with High Aspect Ratio in Cylindrical Vessels," *Engineering Fracture Mechanics*, V. 109, Sept. 2013, pp. 138-149. doi: 10.1016/j.engfracmech.2013.05.014
 32. Xu, S., and Reinhardt, H. W., "Crack Extension Resistance and Fracture Properties of Quasi-Brittle Softening Materials like Concrete Based on the Complete Process of Fracture," *International Journal of Fracture*, V. 92, No. 1, July 1998, pp. 71-99. doi: 10.1023/A:1007553012684
 33. Reinhardt, H. W.; Cornelissen, H. A. W.; and Hordijk, D. A., "Tensile Tests and Failure Analysis of Concrete," *Journal of Structural Engineering*, ASCE, V. 112, No. 11, Nov. 1986, pp. 2462-2477. doi: 10.1061/(ASCE)0733-9445(1986)112:11(2462)
 34. Xu, F.; Wu, Z.; Li, W.; Liu, W.; Wang, S.; and Du, D., "Analytical Bond Strength of Deformed Bars in Concrete Due to Splitting Failure," *Materials and Structures*, V. 51, No. 6, Dec. 2018, Article No. 139. doi: 10.1617/s11527-018-1266-0
 35. Lau, I.; Fu, G.; Li, C.-Q.; De Silva, S.; and Guo, Y., "Critical Crack Depth in Corrosion-Induced Concrete Cracking," *ACI Structural Journal*, V. 115, No. 4, July 2018, pp. 1175-1184. doi: 10.14359/51702261
 36. Wolfram Research, Inc., "Wolfram Mathematica 11," Wolfram Research, Inc., Champaign, IL, 2018.
 37. fib, "CEB-FIP Model Code 1990," CEB Bulletin No. 213/214, International Federation for Structural Concrete, Lausanne, Switzerland, 1993, 460 pp.
 38. Wu, C.; Chen, G.; Volz, J. S.; Brow, R. K.; and Koenigstein, M. L., "Local Bond Strength of Vitreous Enamel Coated Rebar to Concrete," *Construction and Building Materials*, V. 35, Oct. 2012, pp. 428-439. doi: 10.1016/j.conbuildmat.2012.04.067
 39. Harajli, M. H., and Dagher, F., "Seismic Strengthening of Bond-Critical Regions in Rectangular Reinforced Concrete Columns Using Fiber-Reinforced Polymer Wraps," *ACI Structural Journal*, V. 105, No. 1, Jan.-Feb. 2008, pp. 68-77.
 40. Nakaba, K.; Kanakubo, T.; Furuta, T.; and Yoshizawa, H., "Bond Behavior between Fiber-Reinforced Polymer Laminates and Concrete," *ACI Structural Journal*, V. 98, No. 3, May-June 2001, pp. 359-367.
 41. Dai, J.; Ueda, T.; and Sato, Y., "Development of the Nonlinear Bond Stress-Slip Model of Fiber Reinforced Plastics Sheet-Concrete Interfaces with a Simple Method," *Journal of Composites for Construction*, ASCE, V. 9, No. 1, Feb. 2005, pp. 52-62. doi: 10.1061/(ASCE)1090-0268(2005)9:1(52)
 42. Xu, Z.; Liu, Y.; Zeng, Q.; and Yan, D., "An Improved Model for Predicting Bond Strength of Deformed Rebars in Concrete with Stirrups," *Engineering Fracture Mechanics*, V. 276, Part B, Dec. 2022, Article No. 108893. doi: 10.1016/j.engfracmech.2022.108893
 43. Mousavi, S. S.; Guizani, L.; and Ouellet-Plamondon, C. M., "Simplified Analytical Model for Interfacial Bond Strength of Deformed Steel Rebars Embedded in Pre-cracked Concrete," *Journal of Structural Engineering*, ASCE, V. 146, No. 8, Aug. 2020, p. 04020142. doi: 10.1061/(ASCE)ST.1943-541X.0002687
 44. Darwin, D., and Graham, E. K., "Effect of Deformation Height and Spacing on Bond Strength of Reinforcing Bars," *ACI Structural Journal*, V. 90, No. 6, Nov.-Dec. 1993, pp. 646-657.
 45. Zhang, X.; Dong, W.; Lv, C.; Yang, M.; and Ou, J., "Analytical Approach to Modeling the Effect of Transverse Reinforcements on the Bond Strength of Deformed Bars," *Journal of Structural Engineering*, ASCE, V. 145, No. 6, June 2019, p. 04019046. doi: 10.1061/(ASCE)ST.1943-541X.0002293
 46. GB/T 1499.2-2018, "Steel for the Reinforcement of Concrete—Part 2: Hot Rolled Ribbed Bars," Standardization Administration of the People's Republic of China, Beijing, China, 2018.
 47. Zhou, Y.; Dang, L.; Sui, L.; Li, D.; Zhao, X.; Xing, F.; and Wu, Y., "Experimental Study on the Bond Behavior between Corroded Rebar and Concrete under Dual Action of FRP Confinement and Sustained Loading," *Construction and Building Materials*, V. 155, Nov. 2017, pp. 605-616. doi: 10.1016/j.conbuildmat.2017.08.049
 48. Bengar, H. A.; Hosseinpour, M.; and Celikag, M., "Influence of CFRP Confinement on Bond Behavior of Steel Deformed Bar Embedded in Concrete Exposed to High Temperature," *Structures*, V. 24, Apr. 2020, pp. 240-252. doi: 10.1016/j.istruc.2020.01.017
 49. Hamad, B. S.; Rteil, A. A.; Salwan, B. R.; and Soudki, K. A., "Behavior of Bond-Critical Regions Wrapped with Fiber-Reinforced Polymer Sheets in Normal and High-Strength Concrete," *Journal of Composites for Construction*, ASCE, V. 8, No. 3, June 2004, pp. 248-257. doi: 10.1061/(ASCE)1090-0268(2004)8:3(248)
 50. Shehata, I. A. E. M.; Carneiro, L. A. V.; and Shehata, L. C. D., "Strength of Short Concrete Columns Confined with CFRP Sheets," *Materials and Structures*, V. 35, No. 1, Jan. 2002, pp. 50-58. doi: 10.1007/BF02482090
 51. Spoelstra, M. R., and Monti, G., "FRP-Confined Concrete Model," *Journal of Composites for Construction*, ASCE, V. 3, No. 3, Aug. 1999, pp. 143-150. doi: 10.1061/(ASCE)1090-0268(1999)3:3(143)

Title No. 120-M61

Methodology for Predicting Concrete Strength after Short-Term Heat Exposure

by Stephen Wright and Laura Redmond

Exposure to high temperature is well known to cause concrete degradation and lead to compressive strength loss. However, most research focuses on concrete exposed to high temperatures for more than 1 hour; and the available predictive equations for concrete strength loss due to heat exposure do not consider the effects of concrete thermal mass or account for variation in concrete thermal properties. This work proposes a methodology to create a predictive equation for the compressive strength loss in concrete exposed to heat. The proposed method leverages concrete temperature data from transient thermal analyses of concrete specimens correlated to results from experimental testing. The resulting equation from the analyzed data set predicted compressive strength loss with a root-mean-square error (RMSE) of 1.35% absolute error of the measured strength loss, and the maximum absolute underprediction in strength loss was 12.4% across all 26 cases examined.

Keywords: concrete strength; heat exposure; predictive model; residual strength; short duration.

INTRODUCTION

Many researchers^{1–11} have examined the effects of heat exposure on the mechanical properties of concrete including compressive strength, elastic modulus, durability, and explosive spalling. Exposure of concrete to high temperatures results in a loss of compressive strength that becomes more severe with higher temperatures. Most research^{2,3,5,6,11} focuses on fire-like scenarios with temperatures ranging from 392 to 1472°F (200 to 800°C) and exposure times greater than 1 hour. The authors hypothesize that temperatures as low as approximately 212°F (100°C) and exposure times of less than an hour could prove detrimental to concrete compressive strength.

At temperatures above 392°F (200°C), the cement matrix dehydrates and in combination with thermal expansion will lead to microcracks. At temperatures above 752°F (400°C), decomposition of calcium hydroxide crystals in the matrix occurs, which reduces the strength of the concrete. Upon cooling, moisture will be reabsorbed to reform calcium hydroxide crystals, causing an expansion that further spreads the cracks and reduces the concrete strength.^{1,2,6} Some research^{4,7,8} has been conducted regarding the effects of both temperature and exposure duration on strength loss of heat-exposed concrete. At high temperatures, an increase in exposure time leads to a greater decrease in compressive strength, especially for durations of less than 3 hours. Change in exposure times has a lesser effect on strength loss for both lower temperatures and longer exposure times. Concrete exposed to heat can also undergo an unusual phenomenon known as explosive spalling.^{12–19} Although spalling effects

are not explicitly considered in this paper or existing equations for compressive strength loss due to heat exposure, spalling effects should be considered for concrete with low permeability or in rapid heating scenarios.

Only a few models have been made to predict the strength loss of concrete based on the temperature and exposure time using techniques like statistical fitting⁸ and advanced neural networking (ANN).⁷ These models are a function of ambient temperature (the temperature of the environment to which the concrete is exposed) and exposure time and do not consider the influence of geometry, concrete density, or thermal properties on the true duration of heating in the concrete. Thus, the models are not generalizable to different thermal properties of concrete or specimen geometries not tested in each study.

The objective of this paper is to present a framework for the development of a model for predicting strength reduction of concrete due to short-duration, high-heat exposure. To accomplish this, concrete cylinders with and without thermocouples were exposed to different short-term heating scenarios, and the noninstrumented cylinders were tested for compressive strength. The temperature data from a series of finite element models (FEMs) correlated to test data from this study and studies in the literature were used to formulate an equation to predict the strength loss of the concrete based on the temperature and duration of the heat exposure across the cylinder cross section. The final equation resulted in a coefficient of determination of 0.85, a root-mean-square error (RMSE) of 1.35%, and a maximum underprediction in strength loss of 12.4% across all 26 cases examined.

RESEARCH SIGNIFICANCE

The proposed methodology can be used for a variety of applications and heat sources, as it is directly informed by temperature predictions from a transient thermal analysis of the specific application. To the authors' knowledge, no other existing methodology for predicting strength loss of concrete exposed to high temperatures considers the effects of thermal mass or accounts for variation in concrete thermal properties in a fashion that could be applied to any thermal loading scenario. In addition, the experimental data of

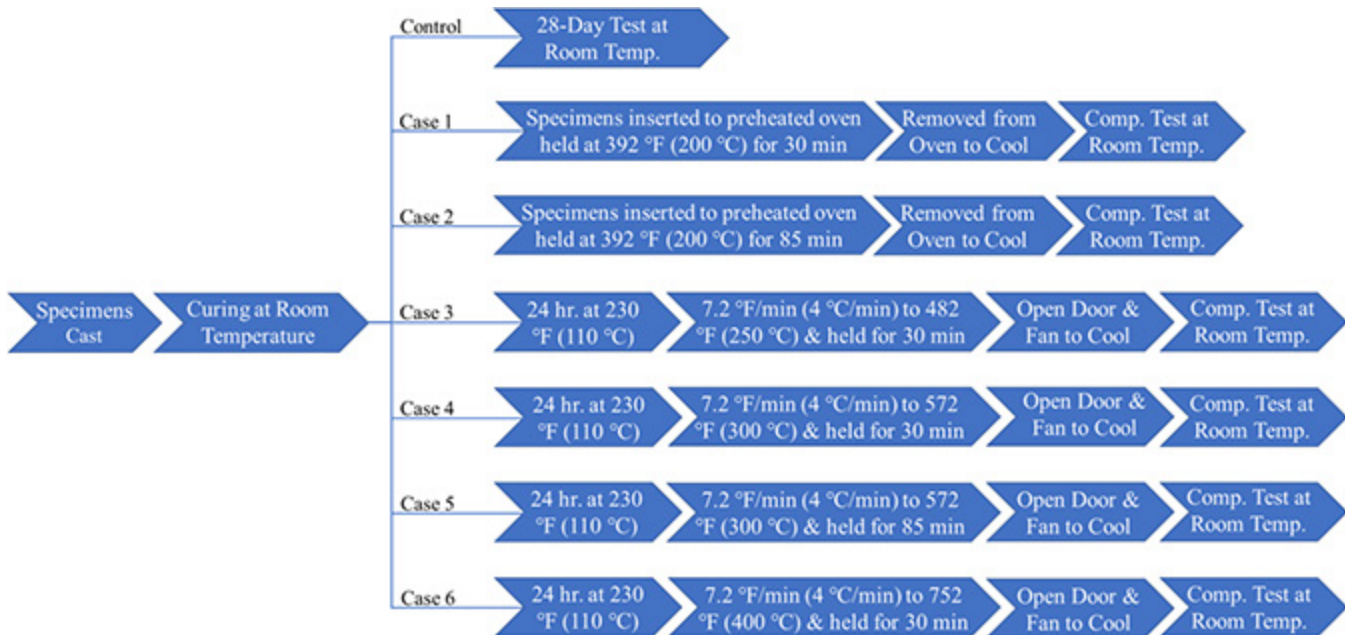


Fig. 1—Timeline for curing and testing of specimens.

this work contributes to the limited literature on concrete exposed to high temperatures for less than 1 hour.

EXPERIMENTAL INVESTIGATION

To investigate the effect of short-duration, high-temperature heat exposure on the compressive strength of concrete, concrete cylinders without steel reinforcement having a diameter of 4 in. (102 mm) and a length of 8 in. (203 mm) were exposed to various heating conditions, and their compressive strength was compared to a set of control specimens. All cylinders were made from the same batch of normal-strength concrete to best match thermal properties across all specimens. All cylinders were fully cured in a humidity-controlled chamber at 70°F (21°C), 100% humidity for 28 days in accordance with ASTM C31/C31M. The control specimens used to characterize the baseline strength of the concrete were tested in compression at room temperature at 28 days following ASTM C39/C39M. The timeline of the curing, heat exposure, and compression testing for each of the cylinders is shown in Fig. 1. The experimental specimens were tested for compressive strength after having been exposed to heat in an oven for either 30 or 85 minutes at temperatures ranging from 392 to 752°F (200 to 400°C), as can be seen in Fig. 1. The heating regimen was selected to fill a gap in the literature for short-duration heat exposure of concrete that would be useful in evaluating structural retrofit options that may include welding or heat-curing operations. In these retrofit applications, the concrete is exposed to low-temperature heating for short durations (relative to a fire or nuclear reactor scenario). For Cases 1 and 2, the oven was preheated to the peak temperature prior to inserting the concrete specimens, subjecting the specimens to an instantaneous change in environmental temperature. For Cases 3 to 6, the cylinders were dried in an oven at 230°F (110°C) for a duration of 24 hours prior to reduce the risk of explosive spalling, then the specimens were placed in the oven at 70°F (21°C) and the oven was ramped at the rates shown in Fig. 1.

Table 1—Concrete mixture design

Cement	400 lb (181.4 kg)
Fly ash	130 lb (59.0 kg)
Fine aggregate	1500 lb (680.4 kg)
Coarse aggregate	1725 lb (782.4 kg)
Water	31 gal. (117.3 L)
Water reducer	20 oz. (591.5 mL)

Cooling procedures varied by case. For Cases 1 and 2, the cylinders were removed and cooled at room temperature. For Cases 3 to 6, the oven was turned off after the cylinder heating was complete, the oven doors were opened, and fans were used to help cool the specimens. The timeline for preparation and testing the specimens can be seen in Fig. 1.

Materials

The concrete mixture used had a mean 28-day compressive strength of 4460 psi (30.75 MPa). The mixture design for the concrete used to create the specimens can be seen in Table 1. Calcium silicate insulation boards with a density of 40 lb/ft³ (640.74 kg/m³) were used on the top and the bottom of the cylinders. Type K thermocouples with different electrical insulation jacketing were used, depending on the maximum oven temperature. Polyvinyl chloride (PVC) jacketing was used in Cases 1 and 2, fiberglass jacketing was used in Cases 4 and 5, and ceramic braid jacketing was used in Cases 3 and 6.

Specimen preparation

The 4 in. (102 mm) diameter, 8 in. (203 mm) tall concrete cylinders were simultaneously cast. After the 28-day curing period, one bore hole was drilled in several of the cylinders on one of the flat faces with a diameter of 0.5 in. (12.7 mm) to a depth of 4 in. (102 mm). The radial location of the hole was either at the center of the cylinder or 1 in. (25.4 mm) from the center. Once the holes were drilled, compressed air was

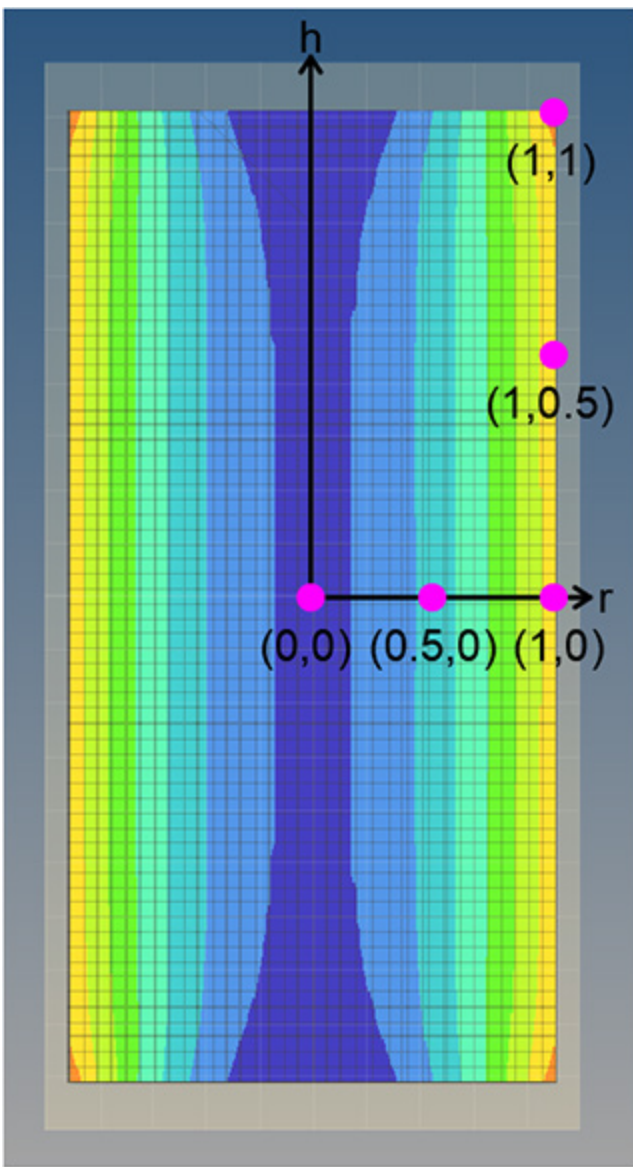


Fig. 2—Diagram of thermocouple locations with representative temperature contour lines. (Note: Full-color PDF can be accessed at www.concrete.org.)

used to blow out any concrete dust remaining on the surface or in the hole. The thermocouples were then placed inside the drilled holes in the concrete cylinders. Sanded grout was used to fill the drilled holes. A vibration table was used to make sure the grout filled the holes, removing as much of the air voids as possible. Thermocouples were also placed along the length of the cylinders on the exterior surface and secured using a small amount of high-temperature epoxy. The positions of the thermocouples in each cylinder are referred to using normalized (radial, height) coordinates as in Fig. 2. Each instrumented cylinder contained one internal thermocouple and between one and three external thermocouples. Duplicate measurement points across multiple cylinders were used where possible.

To simulate real-world heating scenarios of a concrete column exposed to heat where it would be predominately

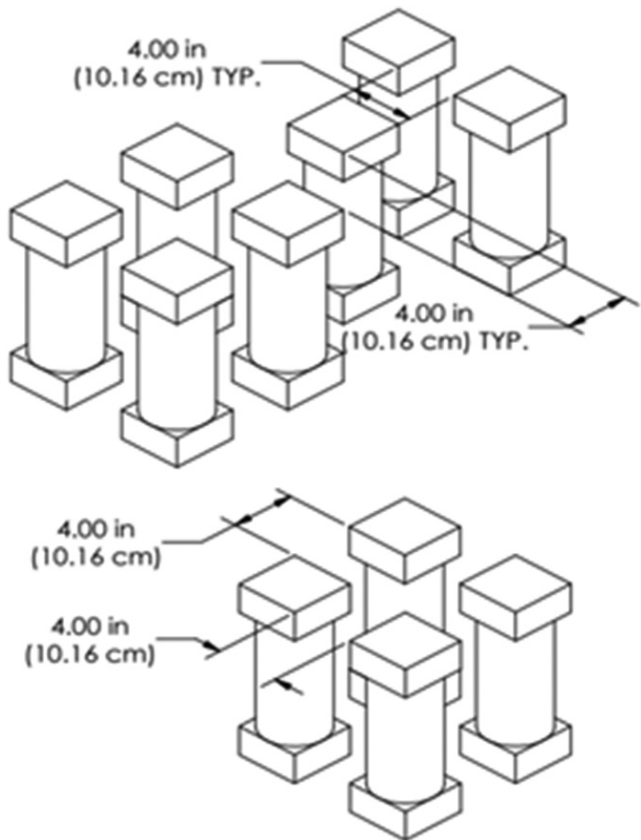


Fig. 3—Schematic for specimen layout: furnace (top); and oven (bottom).

exposed to heat on all sides along its length, and to simplify model correlation, calcium silicate insulation boards were placed on the top and bottom of cylinders to minimize heat transfer through these faces. The boards were cut into 4 x 4 in. (102 x 102 mm) sections and stacked to be 2 in. (51 mm) in thickness. Finite element analysis (FEA) was conducted to verify the effectiveness of this insulation. Analysis cases were conducted with no insulation, perfectly adiabatic insulation, and realistic insulation (with the 2 in. [51 mm] thick calcium silicate insulation). The analysis showed that the calcium silicate boards provided prevented large thermal gradients from developing along the length of the cylinder so that the primary direction of the thermal gradient was radial.

Oven arrangement

The specimens were laid out in specific patterns during heating to allow sufficient fluid (air) movement between them and a similar view factor to the oven walls for consistent heating. The first two cases were heated in a large conventional oven. Due to size constraints, only four specimens could fit in the oven at once with 4 in. (102 mm) spacing between cylinders and between the cylinders and the walls of the oven, as shown in Fig. 3. Cases 3 to 6 were heated in a muffle furnace with similar spacing conventions, also shown in Fig. 3. In the conventional oven, two specimens were instrumented at a time, and in the muffle furnace, four were instrumented at a time due to increased space.

Data collected

In addition to the instrumented test specimens discussed previously, thermocouples were placed inside the oven (Cases 1 to 2) and furnace (Cases 3 to 6) to measure the internal air temperature. Thermocouples were also used to measure the ambient air temperature outside of the oven and furnace. In totality, for each case, there was a minimum of seven thermocouple locations on the concrete cylinders: two thermocouples located at ($r = 0, h = 0$), two at ($r = 0.5, h = 0$), at least one at ($r = 1, h = 0$), at least one at ($r = 1, h = 0.5$) and at least one at ($r = 1, h = 1$), with duplicates added where possible. Thermocouple data were recorded over the entirety of the heating phase of the specimens and several hours of data in the cooling phase such that there was sufficient data in the cooling phase to correlate the FEMs.

In addition to the thermocouple data recorded during the heating, the specimens without thermocouples were also tested in compression. Specimens with thermocouples were not compression tested due to the error that would have been introduced by the holes drilled for the thermocouples. For each heating case except Case 6, three specimens were tested in compression in accordance with ASTM C39/C39M. In Case 6, only two specimens were tested because one non-instrumented specimen was damaged during heating due to explosive spalling.

EXPERIMENTAL RESULTS

Thermal results

Temperature data collected from thermocouples within the cylinder were taken for each case to validate the results of the heat-transfer FEM. Temperature measurements were taken along the length and radius of the cylinder to better understand the heat-transfer effects caused by the material properties and boundary conditions.

Compression results

The results for the compressive strength of the concrete specimens tested can be seen in Fig. 4. As the duration and the temperature of the heat exposure increases, the compressive strength decreases. There was an outlier compressive strength recorded for Case 4, which is shown in Fig. 4. This outlier was not considered when analyzing the compressive results to develop a predictive equation because it is higher than any of the control (unheated) specimens.

FINITE ELEMENT MODELS

Geometry

Heat-transfer FEA was conducted to predict the temperature history for the specimens across the entire cross section. The model geometry consists of a 4 x 8 in. (102 x 203 mm) diameter length cylinder to represent the concrete specimen with a 4 x 4 x 2 in. (102 x 102 x 51 mm) thick section on each flat face of the cylinder to represent the calcium silicate insulation. Three-dimensional heat-transfer elements were used with a typical element side length of 0.118 in. (3 mm) for the concrete and 0.2 in. (5 mm) for the insulation.

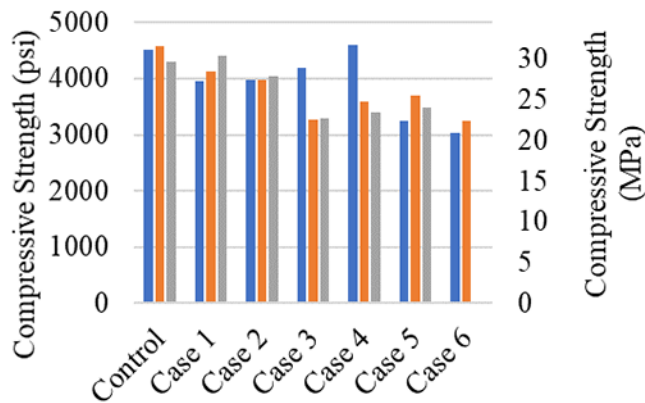


Fig. 4—Compressive strength results.

Boundary conditions

The flat faces of the cylinder were conductively coupled with the insulation. The remaining faces of insulation and the outer diameter of the cylinder had convection and radiation heat-transfer boundary conditions applied using a heat-transfer coefficient to the measured internal oven temperature or measured ambient air temperature, depending on the environment that the specimens were exposed to. An initial temperature of 70°F (21°C) was prescribed to all nodes for the start of the transient thermal model.

Material properties for thermal model

Thermal conductivity, specific heat, and density must be defined for each material. The values used for the thermal conductivity, specific heat, and density of the calcium silicate insulation were 0.069 BTU/ft·h·°F, 0.25 BTU/lb·°F, and 40 lb/ft³ (0.12 W/m·K, 1030 J/kg·K, and 640.7 kg/m³), as specified by the manufacturer. The measured concrete density was 145 lb/ft³ (2323 kg/m³). Concrete thermal conductivity was measured using a heat flow meter apparatus in accordance with ASTM C518-17 and was found to be 0.376 BTU/ft·h·°F (0.65 W/m·K) at room temperature. In the model, thermal conductivity varied from this value at room temperature to 0.330 BTU/ft·h·°F (0.57 W/m·K) at 793°F (423°C) based on published trends for concrete thermal properties.¹⁸⁻²¹ Concrete specific heat was initially assumed to be 0.20 BTU/lb·°F (850 J/kg·K). This is consistent with published values for the specific heat of concrete at room temperature, which can range from 0.12 to 0.29 BTU/lb·°F (500 to 1200 J/kg·K).¹⁹⁻²³

Initial heat-transfer analysis

Initial calculations were made to determine approximate values for the heat-transfer coefficients for the FEM. The convection heat-transfer coefficient h_{conv} is defined within Eq. (1), where q''_{conv} is heat flux and $(T_1 - T_2)$ is the temperature difference between the environment and the material surface. To account for radiation effects, the radiation heat transfer was linearized into an effective convection heat-transfer coefficient and added to the convective heat-transfer coefficient to create a total effective heat-transfer coefficient. Radiative heat flux q''_{rad} is defined in Eq. (2). In this equation, ϵ is emissivity; σ is the Stefan-Boltzmann constant; and F is the view factor. By setting the heat flux of Eq. (2) equal to

the heat flux of Eq. (1), an effective heat-transfer coefficient h_{rad} can be found for the radiative heat transfer, as shown in Eq. (3). The total heat-transfer coefficient can be calculated as shown in Eq. (4), which can be used for total heat flux as shown in Eq. (5).

In Cases 1 and 2, the emissivity was estimated as 0.4 for the heating phase due to the low-emissivity metallic interior of the oven, and increased to 0.85 for the concrete emissivity in the cooling phase. A value of 0.9 was used for emissivity of the furnace interior due to the ceramic interior. Once again, an emissivity of 0.85 was used for the concrete during the cooling phase of the analysis for Cases 3 to 6. The view factor was estimated as 0.8 for all test configurations due to the close proximity of the specimens in the oven and furnace.

$$q''_{conv} = h_{conv}(T_1 - T_2) \quad (1)$$

$$q''_{rad} = \varepsilon\sigma F(T_1^4 - T_2^4) \quad (2)$$

$$h_{rad} = \varepsilon\sigma F(T_1^2 + T_2^2)(T_1 + T_2) \quad (3)$$

$$h_{total} = h_{conv} + h_{rad} \quad (4)$$

$$q''_{total} = h_{total}(T_1 - T_2) \quad (5)$$

A correlation for the Nusselt number for a vertical plate²⁴ was used for free convection, as seen in Eq. (6), because the cylinder axes were aligned with the gravity vector. This means that buoyancy-driven flow was also aligned axially with the cylinder, making the flow of the air most similar to that of a vertical plate. For the cooling phase of Cases 3 to 6, which used a fan, a correlation for the Nusselt number for flow across a cylinder²⁵ was used for forced convection, as seen in Eq. (7), because the flow direction was perpendicular to the cylinder axes. Both of these correlations for the Nusselt number can be related to the heat-transfer coefficient through Eq. (8) and (9), respectively.

$$\overline{Nu_L} = \left[0.825 + \frac{0.387 Ra_L^{1/6}}{(1 + (0.492/Pr)^{9/16})^{8/37}} \right] \quad (6)$$

$$Nu_D = (0.4Re^{0.5} + 0.06Re^{2/3})Pr^{0.4} \left(\frac{\mu_\infty}{\mu_w} \right)^{0.25} \quad (7)$$

$$\overline{Nu_L} = \frac{h_{free}L}{k} \quad (8)$$

$$Nu_D = h_{forced}D/k \quad (9)$$

In these equations, Ra is the Rayleigh number; Pr is the Prandtl number; Re is the Reynolds number; μ is the fluid viscosity; h is the convection heat-transfer coefficient; k is the thermal conductivity of the fluid; L is the cylinder length; and D is the cylinder diameter. Properties of air were calculated using the film temperature of air, which is defined as the average of the surface temperature and free stream gas temperature. To calculate the Reynolds number in Eq. (7), the forced-convection air velocity was taken as the air velocity of the fan used in Cases 3 to 6 as specified by

the manufacturer (19.7 ft/s [6 m/s]). It should be noted that Eq. (7) is intended for use on a single cylinder in cross flow, but the experimental setup consists of two rows of cylinders inside an oven, with only one of the six faces of the oven open to a fan. As the flow would be greatly impeded, the true heat-transfer coefficient for the cooling phases of Cases 3 to 6 will be overestimated by Eq. (7). Thus, the approach was to assume the true heat-transfer coefficient was somewhere between the values assuming free convection (Eq. (6)) and forced convection (Eq. (7)). The models for Cases 3 to 6 were initially built using a value for the convection heat-transfer coefficient that was equal to h_{free} plus 50% of ($h_{forced} - h_{free}$).

The convection heat-transfer coefficient and the linearized radiation heat-transfer coefficient vary as a function of cylinder surface temperature and air temperature. In all cases, the cylinder surface temperature was obtained from the thermocouples fixed to the cylinder surfaces for the calculations of the heat-transfer coefficients. The air temperature was similarly taken from thermocouples used to measure the air temperature inside the oven and furnace for each case, with the exception of Case 5. In this case, the thermocouple data was unusable, and the oven temperature during the heating phase was estimated to be identical to Case 4, which had the same peak temperature and oven ramp rate.

Plots showing the initial (uncalibrated) finite element (FE) results compared to the thermocouple data can be seen as follows. Figure 5 shows the comparison for Case 1 at the following locations: ($r = 0, h = 0$) (top left), ($r = 0.5, h = 0$) (top right), ($r = 1, h = 0$) (bottom left), and ($r = 1, h = 0.5$) (bottom right). This plot shows that the initial model tends to reach a lower peak temperature and cool off slower than the experimental specimens. The results of the initial models of Cases 2 to 6 can be found in the Appendix.

MODEL CALIBRATION WITH TEST DATA

Calibration process

Although the initial analysis was in reasonable agreement with test data, a model calibration effort was undertaken to calibrate the model and improve the accuracy prior to developing the predictive equation for concrete strength loss. The goal of model calibration was to minimize the RMSE between the model and thermocouple data. The parameters adjusted during the model calibration process were limited to concrete specific heat, convection coefficients, and the product of emissivity and view factor. These parameters were selected as they had the most potential for error in the original estimations. Concrete conductivity and density were based on physical measurements of the sample. In comparison, the parameters selected for the calibration were based on literature values and empirical correlations. Care was taken to only adjust these parameters in a way that was consistent across the various test cases.

The specific heat of the concrete was correlated to a value of 0.17 BTU/lb·°F (700 J/kg·K), which lies within the expected range from the literature.¹⁹⁻²³ Table 2 summarizes the percent change in convection coefficients and change in the product of emissivity and view factor over their initial values required to calibrate each of the models. For Cases 1 and 2, the convection heat-transfer coefficient was required

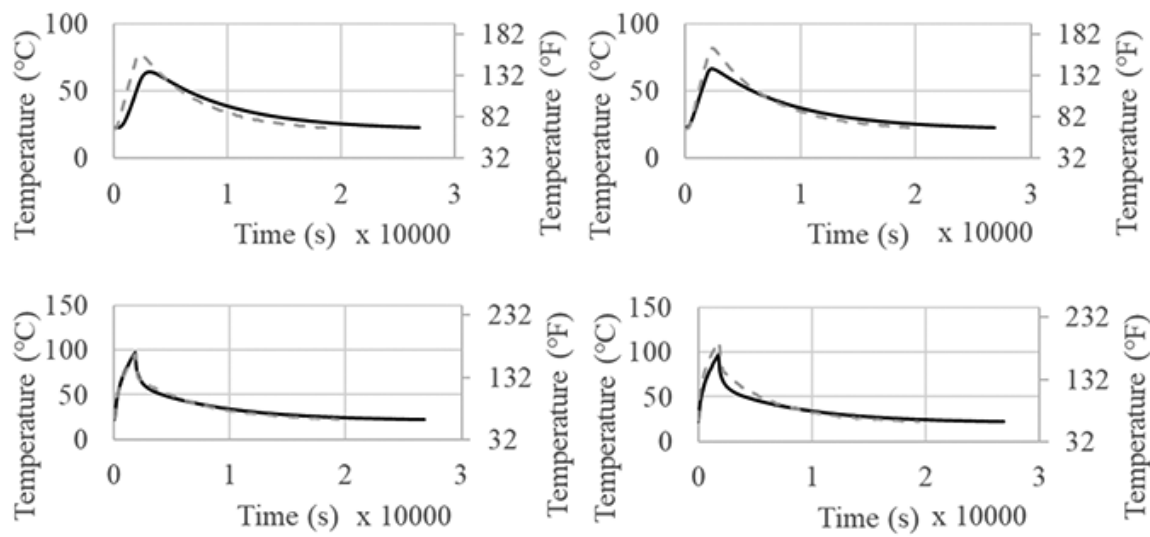


Fig. 5—Case 1 (392°F [200°C] for 30 minutes) initial model fit (FE results in black; thermocouple data in gray dashed line).

Table 2—Characteristics of different heating cases for model correlation

	Cases 1 and 2	Case 3	Cases 4 and 5	Case 6
Oven temperature, °F (°C)	392 (200)	482 (250)	572 (300)	752 (400)
Warm-up convection (free/forced)	Free	Free	Free	Free
Cooldown convection (free/forced)	Free	Mixed	Mixed	Mixed
Oven interior surface	Bare metal	Ceramic insulation	Ceramic insulation	Ceramic insulation
Change in h_{conv} during warm-up	+25%	+30%	+30%	+30%
Change in h_{conv} during cooldown	-25%	Refer to Eq. (10)	Refer to Eq. (10)	Refer to Eq. (10)
Change in ϵF during warm-up	-1.25%	-1.25%	-1.25%	-1.25%
Change in ϵF during cooldown	-1.25%	-1.25%	-1.25%	-1.25%

to change by 25% during warm-up and cooldown, which is within the uncertainty for Nusselt number correlations. For Cases 1 to 6, ϵF was reduced by 1.25%. For Cases 3 to 6, the convection heat-transfer coefficient had to be increased by 30% during the heating phase. Due to the assumptions used in Nusselt number correlations (laminar versus turbulent flow, isothermal versus uniform heat flux) not perfectly matching the testing scenario,²⁴ this was deemed an acceptable level of tolerance to allow the FEM to match the experimental data. In the cooling phase, the convection model had to be adjusted and resulted in a calibrated heat-transfer coefficient shown in Eq. (10). This decrease is reasonable considering the uncertainty in the empirical correlations and the optimistic values for the forced-convection heat-transfer coefficient that did not account for impeded flow from the presence of two rows of cylinders.

$$h_{conv} = 0.75h_{free} + 0.1875(h_{forced} - h_{free}) \quad (10)$$

Plots showing the calibrated FE results compared to the thermocouple data can be seen as follows. Figure 6 shows the comparison for Case 1 at the following locations: ($r = 0, h = 0$) (top left), ($r = 0.5, h = 0$) (top right), ($r = 1, h = 0$) (bottom left), and ($r = 1, h = 0.5$) (bottom right). This plot shows the calibrated model has a much better fit with the experimental peak temperature and cooling rate and is

consistent with observations from the other five cases (refer to the Appendix).

ADDITIONAL CASES FROM LITERATURE TO INFORM CONCRETE STRENGTH LOSS MODEL FOR SHORT-TERM HEAT EXPOSURE

Three additional studies from the literature^{2,4,11} that had clearly defined test procedures and heating durations were used to provide additional data points to calibrate the proposed strength loss model. Using the same thermal modeling methods that were used in this work, models were built to simulate the conditions and temperature profiles of heat-exposed concrete specimens described in previous literature. This was done to increase the data available for the strength loss model.

In the three studies considered,^{2,4,11} the concrete had a similar compressive strength to the concrete used in this work and also had roughly similar strength loss data to that in this work. In the research conducted by Liu et al.,² concrete cylinders (using limestone and river sand aggregates) of 6 x 12 in. (152 x 305 mm) were heated one at a time in a custom-made furnace for 6-hour durations with a ramp rate of 18°F/min (10°C/min) up to 1472°F (800°C). In the research conducted by Mohamedbhai,⁴ 4 in. (102 mm) concrete cubes (using basalt aggregates) were heated in a muffle furnace for durations between 1 and 4 hours at up to 1472°F (800°C) and with nonlinear ramp rates designed to

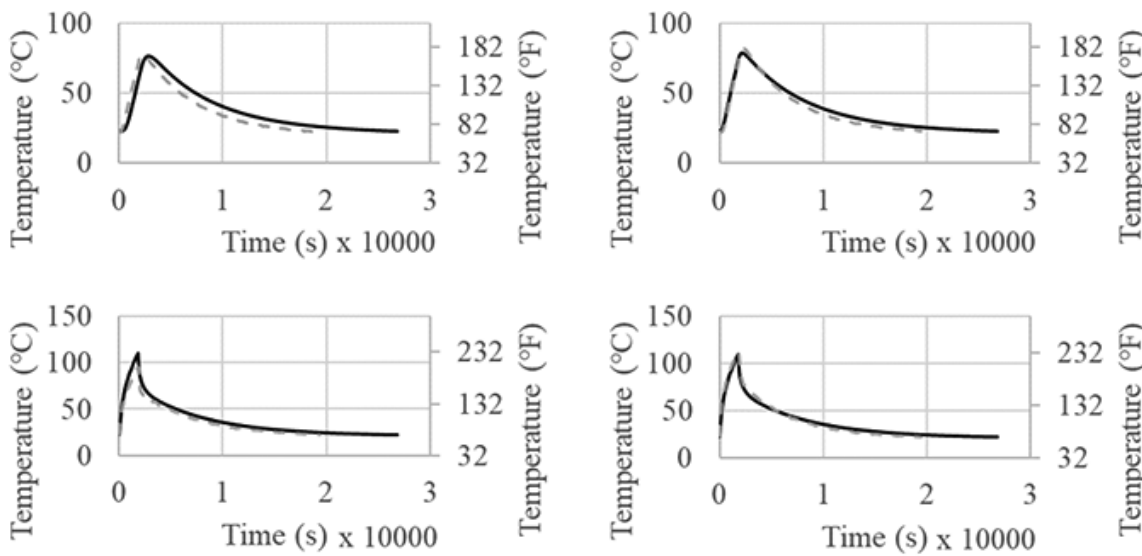


Fig. 6—Case 1 (392°F [200°C] for 30 minutes) calibrated model fit (FE results in black; thermocouple data in gray dashed line).

model a standard fire. In the study conducted by Abrams,¹¹ 3 x 6 in. (76 x 152 mm) concrete cylinders (using varying aggregate types) were heated in an electric furnace using a steel ring to conduct heat to the concrete. The ramp rate of the furnace was adjusted to ensure the temperature gradient did not exceed 150°F (83°C), and the specimens were removed from the furnace after the specified internal equilibrium temperature was achieved, up to 1472°F (800°C).

DESCRIPTION OF MODEL FOR CONCRETE STRENGTH LOSS AFTER SHORT-TERM HEAT EXPOSURE

The proposed model for predicting the compressive strength loss of concrete accounting for the transient effects of short-term heating uses temperature data from transient thermal analysis of the subject concrete specimen. The proposed model assumes the temperature gradient is primarily through the cross section and does not account for significant variation in temperature along a member's length, which is consistent with temperature measurements and FEM predictions. The proposed model is calibrated with data having peak exposure temperatures up to 1472°F (800°C) based on the data set and cases from the literature with sufficient information to generate thermal FEMs.

Several steps are necessary to post-process the data from the transient thermal analysis to use in the proposed model. First, all of the nodal temperature data for a cross section of the concrete member at midheight is extracted from the FE results and compiled into a data table arranged based on the physical location of each node in the model. Then, for each time step, the temperature data is classified into temperature bins, as shown in Table 3. The bin definitions were selected based on anticipated transitions in concrete damage phenomena from the literature. Below 302°F (150°C), the temperatures are not sufficient to release chemically bound water; between 302 and 572°F (150 and 300°C), chemically bound water can be released, but temperatures are below the threshold for microcracking.¹ Between 572 and 752°F

(300 and 400°C), microcracking begins but temperatures are not sufficient to cause calcium hydroxide decomposition.¹ Between 752 and 1472°F (400 and 800°C), calcium hydroxide decomposition will occur.¹

After nodal temperature data through time is sorted into temperature bins, geometric data is used to calculate what percentage of the cross section falls within each bin at each timestamp. This data is then sorted into the following geometric percentile bins: 0% of the cross section within the given temperature bin, 100% of the cross section within the given temperature bin, and 10 different bins in between 0 and 10%, 10 and 20%, and so on. Then, a summation is performed to determine the total time throughout the analysis that a given geometric percentile bin is within a given temperature range; for example, 40 to 50% of the cross section was between 347 and 482°F (175 and 250°C) for 9000 seconds of the analysis. A weighting factor is assigned to each geometric percentile bin that is equal to the mean of each geometric percentile bin (for example, 40 and 50%) and has a weighting factor of 45%. The time value for a given geometric percentile bin within each temperature bin is multiplied by its weighting factor to convert the time values for each geometric percentile to an effective unified time value (t_i) (for example, 40 and 50% of the cross section between 347 and 482°F [175 and 250°C] with a weighting of 45% for 9000 seconds becomes 4050 seconds between 347 and 482°F [175 and 250°C] for the unified time value). All time values are summed for each temperature bin, so the cross section has a single value of exposure time for a given temperature, bin as shown in Eq. (11).

$$t_i = \sum_j t_{ij} \times A_j \quad (11)$$

Herein, t_i is the unified time value within a given temperature bin i ; t_{ij} is the total time that a given area of the cross section (within geometric percentile bin j) spends within a given temperature bin i ; and A_j is the weighting factor in percent for geometric percentile bin j . The unified time

Table 3—Temperature bins for concrete strength loss model

Temperature bin number	Lower-bound temperature	Upper-bound temperature
1	203°F (95°C)	302°F (150°C)
2	302°F (150°C)	572°F (300°C)
3	572°F (300°C)	752°F (400°C)
4	752°F (400°C)	1472°F (800°C)

value can be interpreted as the effective amount of time the entire cross section spends within a temperature bin, where the times are weighted by the percentage of the cross-sectional area within that temperature bin. Note that it should be ensured that the mesh size of the model is sufficiently fine that further mesh refinement does not cause a significant change in the area percentage calculations or the temperature results of the analysis.

Once the temperature data from a transient thermal analysis is post-processed, it can be used within the strength loss model. The strength loss model that was found to have a good fit was a linear regression model. The input and response variables in the model were transformed, however, to improve the fit of the data. The response variable, the ratio of strength loss, was transformed using the logit function. This allows the strength loss to be defined over the entire real number line instead of being limited to 0 to 1. This transformation was necessary for linear regression due to the statistical assumptions involved in linear regression models. The input variables were also transformed by taking the inputs equal to the square root of the unified time value of each temperature bin. This gives the curves in the model a shape which approximates the asymptotic behavior observed in the data set. After performing these transformations, the regression model was constructed using least-square estimation in R.²⁶⁻²⁹

The model shows a strong fit with a coefficient of determination of 0.85. The RMSE was also calculated in both the transformed and original space for the response variable. In the transformed space, it was found to be 0.0768, and in the original space, it was found to be a 1.35% strength loss. The final regression equation can be seen in Eq. (12). This accounts for transforming the input variables into their appropriate form and transforming the response back into a ratio of strength loss on a scale of 0 to 1 (for example, 0.8 corresponds to an 80% strength loss).

$$\delta = \frac{e^{(-2.065+0.001013\sqrt{t_1}+0.00503\sqrt{t_2}+0.01106\sqrt{t_3}+0.00997\sqrt{t_4}+0.01068\sqrt{t_5})}}{1 + e^{(-2.065+0.001013\sqrt{t_1}+0.00503\sqrt{t_2}+0.01106\sqrt{t_3}+0.00997\sqrt{t_4}+0.01068\sqrt{t_5})}} \quad (12)$$

The regression line as well as confidence and prediction intervals for the regression model can be seen in Fig. 7. These plots show the shape of the regression curves for a heating condition that would result in concrete temperatures in the single-temperature bin, denoted in the x-axis of each plot. This was done to permit visualization of the multidimensional function.

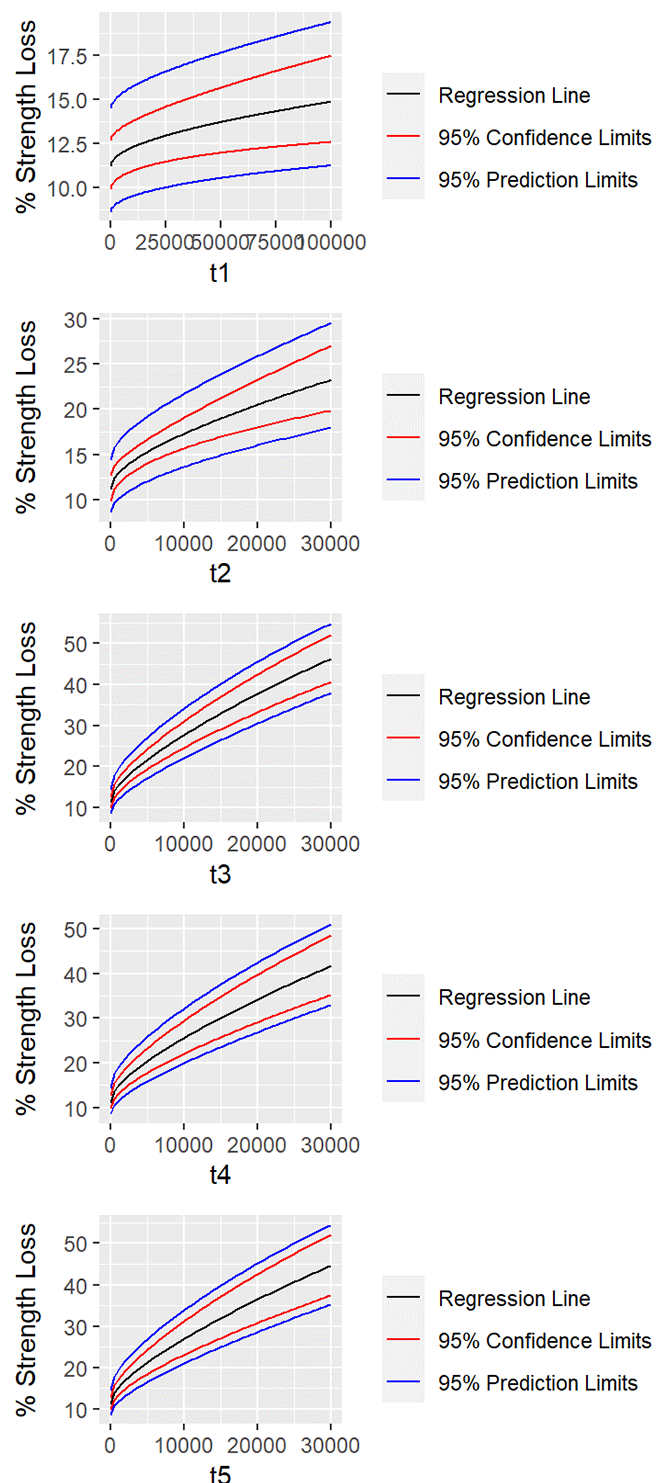


Fig. 7—Regression function for each temperature bin.

CONCRETE STRENGTH LOSS MODEL RESULTS AND DISCUSSION

Results summary

The results of the proposed model are compared to the experimental results from this study and literature results. Table 4 summarizes the results of the predictions of the proposed model. The predictions made by the proposed model generally give a low error, and the maximum over-prediction of compressive strength loss is 13.7% and the maximum underprediction of compressive loss is 12.4%.

Table 4—Comparison between experimental data and current predictions

Reference	Max temperature, °F (°C)	Exposure duration, min	Experimental strength loss, %	Predicted strength loss, %	Absolute error, %
Case 1	329 (200)	30	6.7	11.4	4.7
Case 2	329 (200)	85	10.4	15	4.6
Case 3	482 (250)	30	19.6	19.2	-0.4
Case 4	572 (300)	30	22	20.5	-1.5
Case 5	572 (300)	85	21.6	22.3	0.7
Case 6	752 (400)	30	29.7	30.2	0.5
Liu et al. ² Case 1	212 (100)	360	12.4	12.1	-0.3
Liu et al. ² Case 2	329 (200)	360	23.8	22.1	-1.7
Liu et al. ² Case 3	572 (300)	360	20.8	23.8	3
Liu et al. ² Case 4	752 (400)	360	40.5	54.2	13.7
Liu et al. ² Case 5	1112 (600)	360	64	72.1	8.1
Liu et al. ² Case 6	1472 (800)	360	79.3	86.6	7.3
Mohamedbhai ⁴ Case 1	329 (200)	60	18	14.2	-3.8
Mohamedbhai ⁴ Case 2	329 (200)	120	15	16.1	1.1
Mohamedbhai ⁴ Case 3	329 (200)	180	12	17.3	5.3
Mohamedbhai ⁴ Case 4	329 (200)	240	25	18.4	-6.6
Mohamedbhai ⁴ Case 5	752 (400)	60	30	26.5	-3.5
Mohamedbhai ⁴ Case 6	752 (400)	120	28	31.1	3.1
Mohamedbhai ⁴ Case 7	752 (400)	180	40	34.9	-5.1
Mohamedbhai ⁴ Case 8	752 (400)	240	42	38.4	-3.6
Mohamedbhai ⁴ Case 9	1112 (600)	240	54	52.9	-1.1
Mohamedbhai ⁴ Case 10	1472 (800)	240	76	68.2	-7.8
Abrams ¹¹ Case 1	400 (204)	142	17.1	17.3	0.2
Abrams ¹¹ Case 2	700 (371)	175	40.9	28.5	-12.4
Abrams ¹¹ Case 3	1000 (538)	278	54.65	45.8	-8.85
Abrams ¹¹ Case 4	1300 (704)	352	76.35	64.4	-11.95

Comparison to other models

The proposed model can be compared to the model by Tsai et al.⁸ as it is one of the few in the literature to predict concrete strength loss as a function of exposure time and temperature. However, Tsai et al.⁸ only considers the ambient temperature and does not account for the thermal mass of the concrete, nor does it explicitly account for different thermal properties of concrete—though the tuned parameter D loosely represents these material properties.⁸ The parameters from the strength degradation equations proposed by Tsai et al. are specific to the data set selected for calibration. This proves true as using the parameters for the equation by Tsai et al. calibrated to their concrete specimens to predict the strength loss for the cases listed in Table 4 led to large errors (over 100% error in many cases).

The proposed equation can also be compared to the results of Mohamedbhai,⁴ who derived a relationship for concrete strength degradation as a function of temperature and exposure duration in 1-hour intervals. For an 85-minute exposure at 392°F (200°C), linear interpolation between the 1- and 2-hour durations presented by Mohamedbhai⁴ results in a concrete strength loss of 21.58%⁴ compared to the current

model's prediction of 16.1% strength loss and the actual measured reduction of 10.4%. Results of this data set by Mohamedbhai⁴ are in family with the results of the present testing, keeping in mind variation between the two data sets will exist due to changes in concrete thermal properties.

The key advantage to the presented methodology for developing a strength loss model compared to others in the literature is that it may be generalized to other geometries, concrete thermal properties, and heating conditions by using heat-transfer FEA to determine temperature data needed for the model input. The rigor of the required inputs for this method of determining strength loss allows for a more physically based and therefore more generally applicable model. Most of the literature regarding degradation of concrete compressive strength due to heat exposure does not consider the effects of heating and cooling time, section geometry, or concrete thermal properties,¹⁻⁶ which can be captured by the proposed methodology.

Although the proposed methodology shows a lot of promise, until more data is gathered, the authors note the limitations of the presented model for predicting strength loss of concrete under short-duration heating. The model

was constructed using a limited data set that comprised data from this study as well as experiments conducted by others. To further improve this model, which is focused on short-duration, radially symmetric heating conditions, a larger data set would be required with a greater diversity in heating durations and geometry (varying specimen size). The model could also be improved by including the properties of the concrete mixture as inputs for the model.

CONCLUSIONS

This work aimed to form a framework for creating a model to predict the reduction in concrete compressive strength due to the temperature and duration of heat exposure, which can be generalized for a variety of heating conditions and specimen geometries. A predictive model was successfully created to empirically correlate temperature data from finite element analyses (FEAs) of heated concrete specimens to the experimentally measured strength reduction of the specimens. The predictive model was shown to predict strength loss with a root-mean-square error (RMSE) of 1.35%. Compared to existing models in the literature, the proposed methodology has the advantages of considering the influence of concrete thermal mass, specimen geometry, and thermal properties on the predicted strength loss. The modeling approach could be leveraged to make models specific to a variety of geometries and thermal boundaries as it is based on transient analysis of the specific heating conditions for the structure in question.

AUTHOR BIOS

Stephen Wright is a PhD Student at Clemson University, Clemson, SC, where he received his BS and MS in civil engineering. His research interests include forensic investigation and retrofit and model validation.

ACI member Laura Redmond is an Assistant Professor in the Glenn Department of Civil Engineering at Clemson University. Her research interests include advanced simulation for structural design and health monitoring, model verification, and validation by test.

REFERENCES

1. Hertz, K. D., "Concrete Strength for Fire Safety Design," *Magazine of Concrete Research*, V. 57, No. 8, 1991, pp. 445-453. doi: 10.1680/macr.2005.57.8.445
2. Liu, Y.; Huo, J.; Jin, B.; and Li, Z., "Effect of Microstructural Evolution on Mechanical Behavior of Concrete After High Temperatures," *Magazine of Concrete Research*, V. 70, No. 15, 2018, pp. 770-784. doi: 10.1680/jmacr.17.00197
3. Sabeur, H.; Colina, H.; and Bejjani, M., "Elastic Strain, Young's Modulus Variation During Uniform Heating of Concrete," *Magazine of Concrete Research*, V. 59, No. 8, 2007, pp. 559-566. doi: 10.1680/macr.2007.59.8.559
4. Mohamedbhui, G. T. G., "Effect of Exposure Time and Rates of Heating and Cooling on Residual Strength of Heated Concrete," *Magazine of Concrete Research*, V. 38, No. 136, 1986, pp. 151-158. doi: 10.1680/jmacr.1986.38.136.151
5. Cheng, F.; Kodur, V. K. R.; and Wang, T., "Stress-Strain Curves for High Strength Concrete at Elevated Temperatures," *Journal of Materials in Civil Engineering*, ASCE, V. 16, No. 1, 2004, pp. 84-90. doi: 10.1061/(ASCE)0899-1561(2004)16:1(84)
6. Hossain, K. M. A., "Macro- and Microstructural Investigations on Strength and Durability of Pumice Concrete at High Temperature," *Journal of Materials in Civil Engineering*, ASCE, V. 18, No. 4, 2006, pp. 527-536. doi: 10.1061/(ASCE)0899-1561(2006)18:4(527)
7. Chiang, C., and Yang, C., "Artificial Neural Networks in Prediction of Concrete Strength Reduction Due to High Temperature," *ACI Materials Journal*, V. 102, No. 2, Mar.-Apr. 2005, pp. 93-102.
8. Tsai, C.; Chiang, C.; Yang, C.; and Chen, C., "Tracking Concrete Strength under Variable High Temperature," *ACI Materials Journal*, V. 102, No. 5, Sept.-Oct. 2005, pp. 322-329.
9. Knaack, A. M.; Kurama, Y. C.; and Kirkner, D. J., "Compressive Strength Relationships for Concrete under Elevated Temperatures," *ACI Materials Journal*, V. 107, No. 2, Mar. 2010, pp. 164-175.
10. Kodur, V. K. R.; Raut, N. K.; Mao, X. Y.; and Khalil, W., "Simplified Approach for Evaluating Residual Strength of Fire-Exposed Reinforced Concrete Columns," *Materials and Structures*, V. 46, No. 12, 2013, pp. 2059-2075. doi: 10.1617/s11527-013-0036-2
11. Abrams, M. S., "Compressive Strength of Concrete at Temperatures to 1600F," *Temperature and Concrete*, SP-25, American Concrete Institute, Farmington Hills, MI, 1971, pp. 33-58.
12. Bažant, Z. P., and Thongthai, W., "Pore Pressure in Heated Concrete Walls: Theoretical Prediction," *Magazine of Concrete Research*, V. 31, No. 107, 1979, pp. 67-76. doi: 10.1680/macr.1979.31.107.67
13. Zhao, J.; Zheng, J.; Peng, G.; and Sun, P., "Spalling and Cracking Modelling of High-Performance Concrete Exposed to Elevated Temperatures," *Magazine of Concrete Research*, V. 69, No. 24, 2017, pp. 1276-1287. doi: 10.1680/jmacr.16.00139
14. Debicki, G.; Haniche, R.; and Delhomme, F., "An Experimental Method for Assessing the Spalling Sensitivity of Concrete Mixture Submitted to High Temperature," *Cement and Concrete Composites*, V. 34, No. 8, 2012, pp. 958-963. doi: 10.1016/j.cemconcomp.2012.04.002
15. Dwaikat, M. B., and Kodur, V. K. R., "Hydrothermal Model for Predicting Fire-Induced Spalling in Concrete Structural Systems," *Fire Safety Journal*, V. 44, No. 3, 2009, pp. 425-434. doi: 10.1016/j.firesaf.2008.09.001
16. Zhang, H. L., and Davie, C. T., "A Numerical Investigation of the Influence of Pore Pressures and Thermally Induced Stresses for Spalling of Concrete Exposed to Elevated Temperatures," *Fire Safety Journal*, V. 59, 2013, pp. 102-110. doi: 10.1016/j.firesaf.2013.03.019
17. Fu, Y., and Li, L., "Study on Mechanism of Thermal Spalling in Concrete Exposed to Elevated Temperatures," *Materials and Structures*, V. 44, No. 1, 2011, pp. 361-376. doi: 10.1617/s11527-010-9632-6
18. Hertz, K. D., "Limits of Spalling of Fire-Exposed Concrete," *Fire Safety Journal*, V. 38, No. 2, 2003, pp. 103-116. doi: 10.1016/S0379-7112(02)00051-6
19. Kodur, V. K. R., and Sultan, M. A., "Effects of Temperature on Thermal Properties of High-Strength Concrete," *Journal of Materials in Civil Engineering*, ASCE, V. 15, No. 2, 2003, pp. 101-107. doi: 10.1061/(ASCE)0899-1561(2003)15:2(101)
20. Kodur, V. K. R.; Yu, B.; and Dwaikat, M. M. S., "A Simplified Approach for Predicting Temperature in Reinforced Concrete Members Exposed to Standard Fire," *Fire Safety Journal*, V. 56, 2013, pp. 39-51. doi: 10.1016/j.firesaf.2012.12.004
21. Naser, M. Z., "Properties and Material Models for Modern Construction Materials at Elevated Temperatures," *Computational Materials Science*, V. 160, 2019, pp. 16-29. doi: 10.1016/j.commatsci.2018.12.055
22. Kodur, V. K. R., and Khalil, W., "Effect of Temperature on Thermal Properties of Different Types of High-Strength Concrete," *Journal of Materials in Civil Engineering*, ASCE, V. 23, No. 6, 2011, pp. 793-801. doi: 10.1061/(ASCE)MT.1943-5533.0000225
23. Jin, L.; Du, X.; and Zhang, R., "Characterization of Temperature-Dependent Heat Conduction in Heterogeneous Concrete," *Magazine of Concrete Research*, V. 70, No. 7, 2018, pp. 325-339. doi: 10.1680/jmacr.17.00174
24. Bergman, T. L.; Lavine, A. S.; Incropera, F. P.; and Dewitt, D. P., *Fundamentals of Heat and Mass Transfer*, seventh edition, John Wiley & Sons, New York, 2011.
25. Necati, Ö. M., *Heat Transfer*, first edition, Scientific International, New Delhi, India, 2018.
26. R Core Team, "R: A Language and Environment for Statistical Computing," Version 4.2.1 (2022-06-23 ucrt), R Foundation for Statistical Computing, Vienna, Austria, 2023, <https://www.R-project.org/>. (last accessed Oct. 24, 2023)
27. Wickham, H.; Averick, M.; Bryan, J.; Chang, W.; McGowan, L.; François, R.; Grolemund, G.; Hayes, A.; Henry, L.; Hester, J.; Kuhn, M.; Pedersen, T.; Miller, E.; Bache, S.; Müller, K.; Ooms, J.; Robinson, D.; Seidel, D.; Spinu, V.; Takahashi, K.; Vaughan, D.; Wilke, C.; Woo, K.; and Yutani, H., "Welcome to the Tidyverse," *Journal of Open Source Software*, V. 4, No. 43, 1686, 2019. doi: 10.21105/joss.01686
28. Pedersen, T., "Patchwork: The Composer of Plots," R package version 1.1.3, 2022, <https://CRAN.R-project.org/package=patchwork>. (last accessed Oct. 24, 2023)
29. Schloerke, B.; Cook, D.; Larmarange, J.; Briatte, F.; Marbach, M.; Thoen, E.; Elberg, A.; and Crowley, J., "GGally: Extension to 'ggplot2,'" R package version 2.1.2, 2021, <https://CRAN.R-project.org/package=GGally>. (last accessed Oct. 24, 2023)

APPENDIX

The following figures are presented herein to show the goodness of fit between the FEA results and the thermocouple data taken from experiments. Figures A1 to A5 show the initial model fit for Cases 2 to 6. Figures A6 to A10 show the calibrated model fit. Each follows the same location convention of $(r = 0, h = 0)$ (top left), $(r = 0.5, h = 0)$ (top right), $(r = 1, h = 0)$ (bottom left), and $(r = 1, h = 0.5)$ (bottom right).

right). For instances where a location is missing, this is due to unusable thermocouple data. For Case 5 (Fig. A4 and A9), the $(r = 1, h = 0)$ location data is partially usable (through the heating phase, but not including the cooling phase) and has still been included to show the goodness of fit during the heating phase.

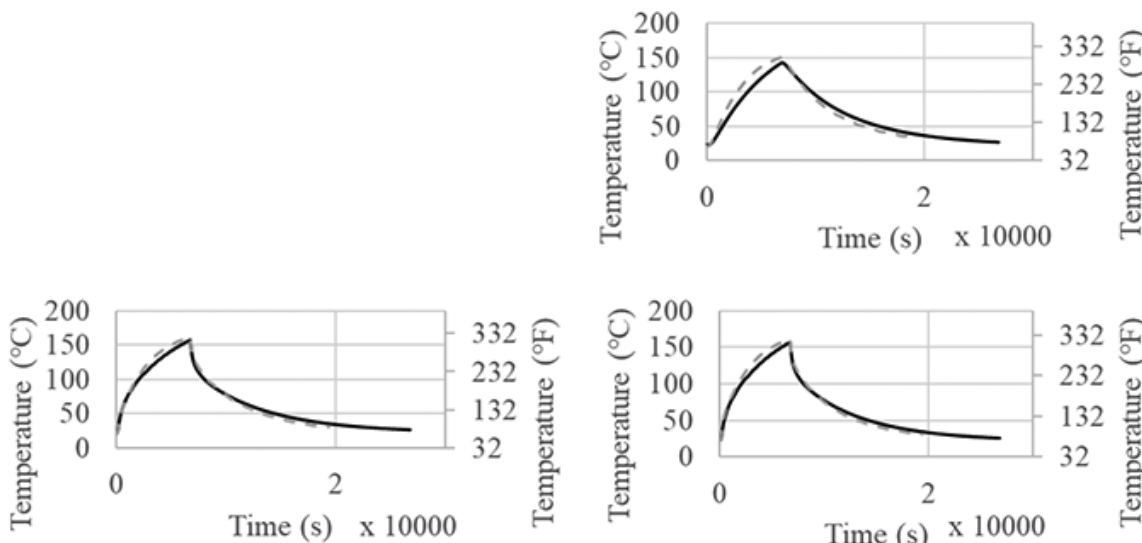


Fig. A1—Case 2 (392°F [200°C] for 85 minutes) initial model fit (FE results in black; thermocouple data in gray dashed line).

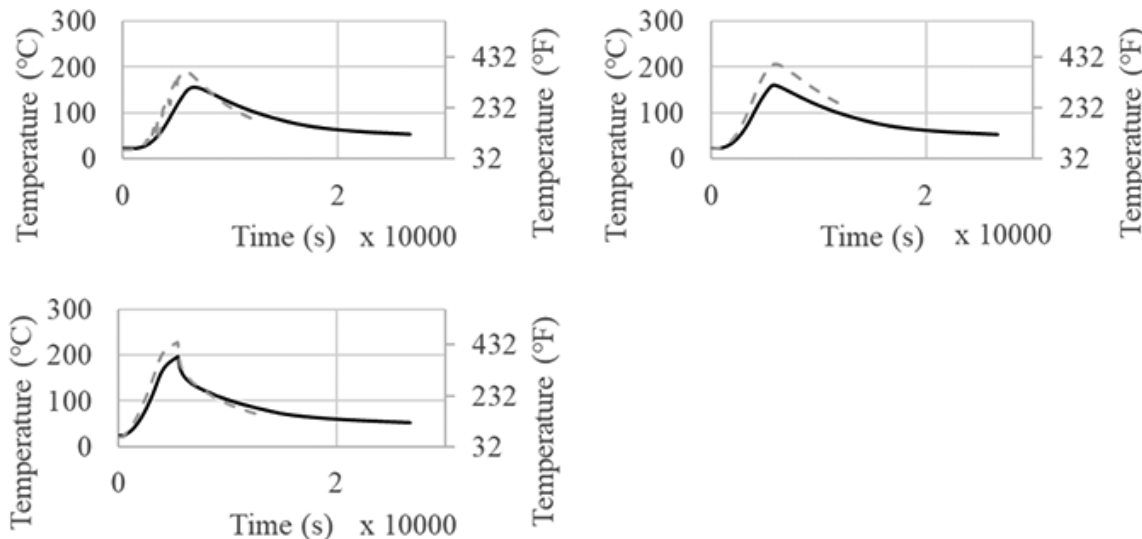


Fig. A2—Case 3 (482°F [250°C] for 30 minutes) initial model fit (FE results in black; thermocouple data in gray dashed line).

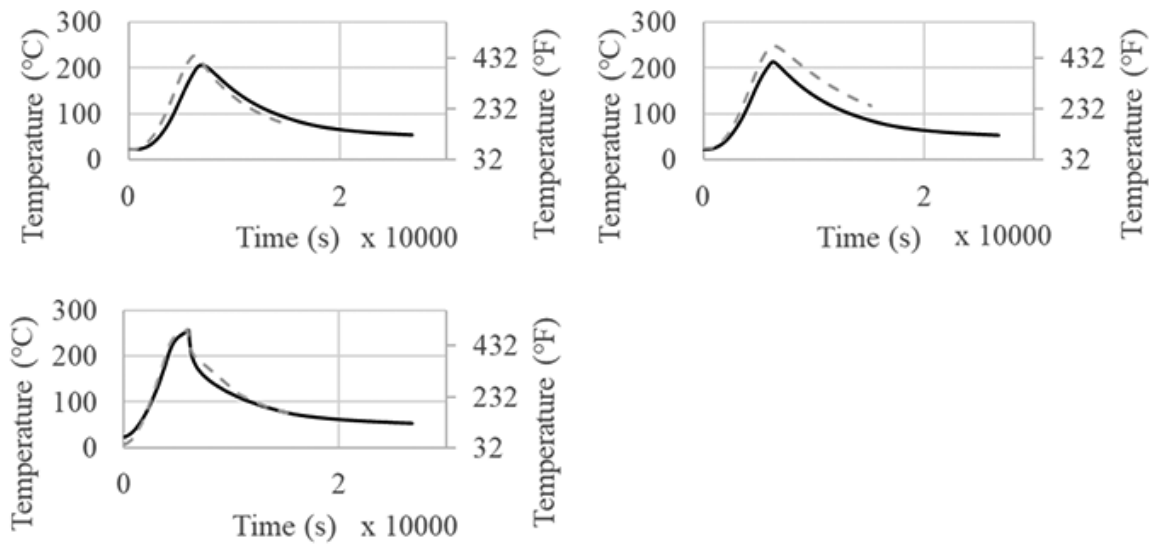


Fig. A3—Case 4 (572°F [300°C] for 30 minutes) initial model fit (FE results in black; thermocouple data in gray dashed line).

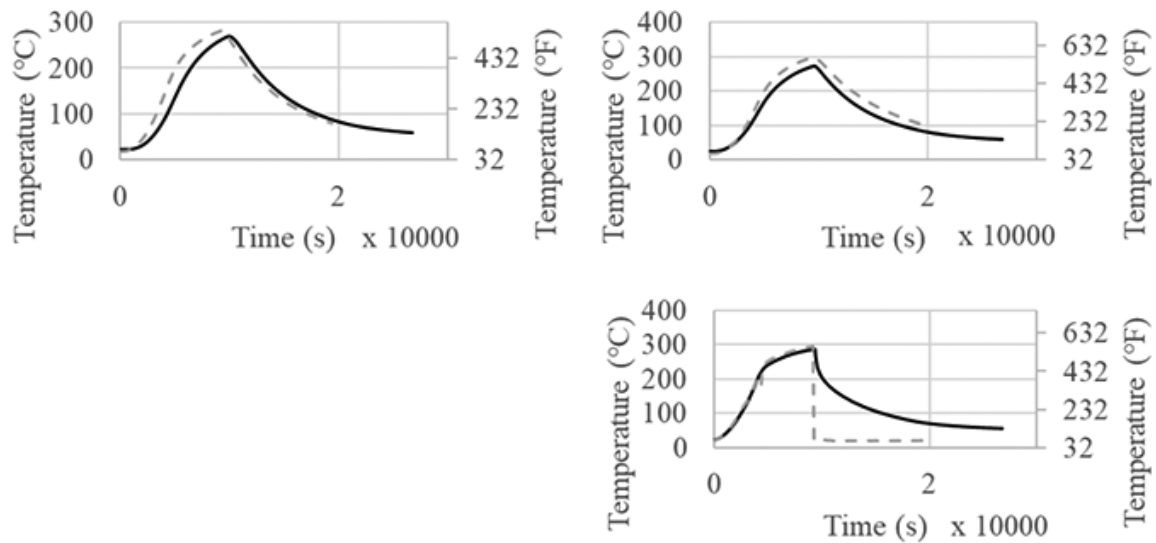


Fig. A4—Case 5 (572°F [300°C] for 85 minutes) initial model fit (FE results in black; thermocouple data in gray dashed line).

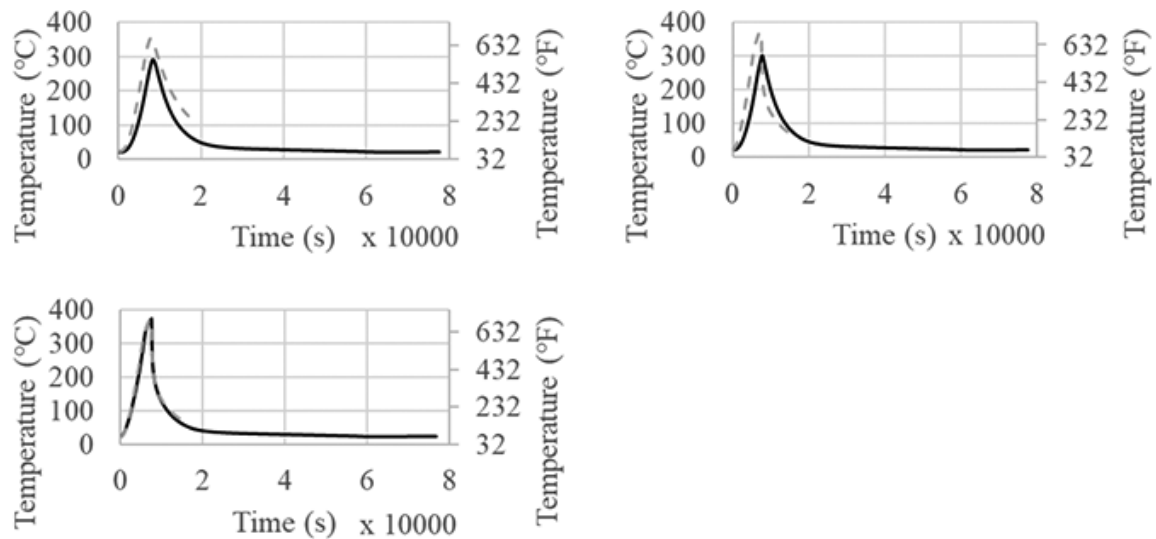


Fig. A5—Case 6 (752°F [400°C] for 30 minutes) initial model fit (FE results in black; thermocouple data in gray dashed line).

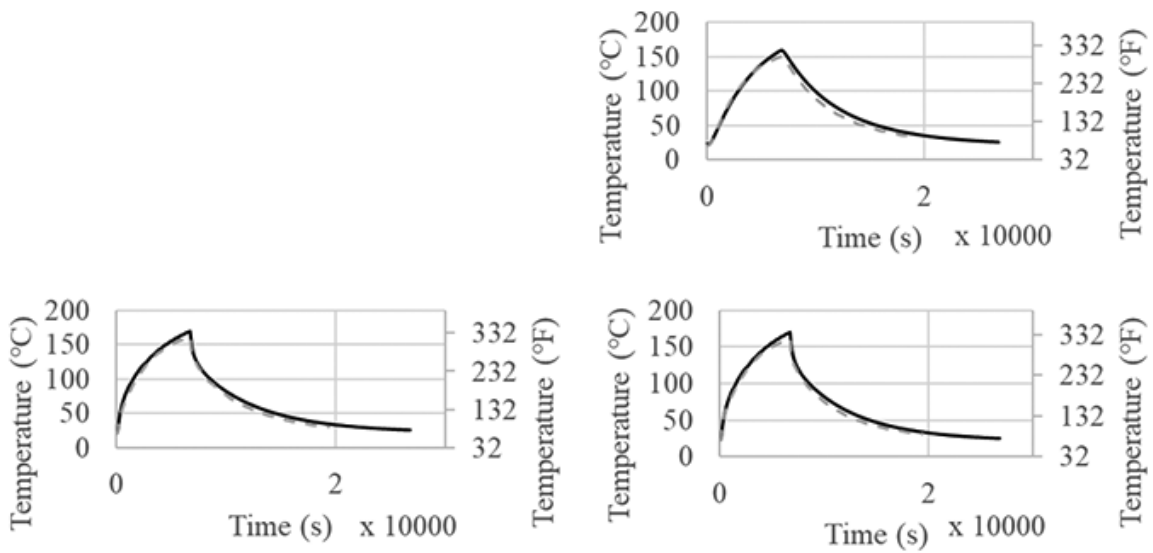


Fig. A6—Case 2 (392°F [200°C] for 85 minutes) calibrated model fit (FE results in black; thermocouple data in gray dashed line).

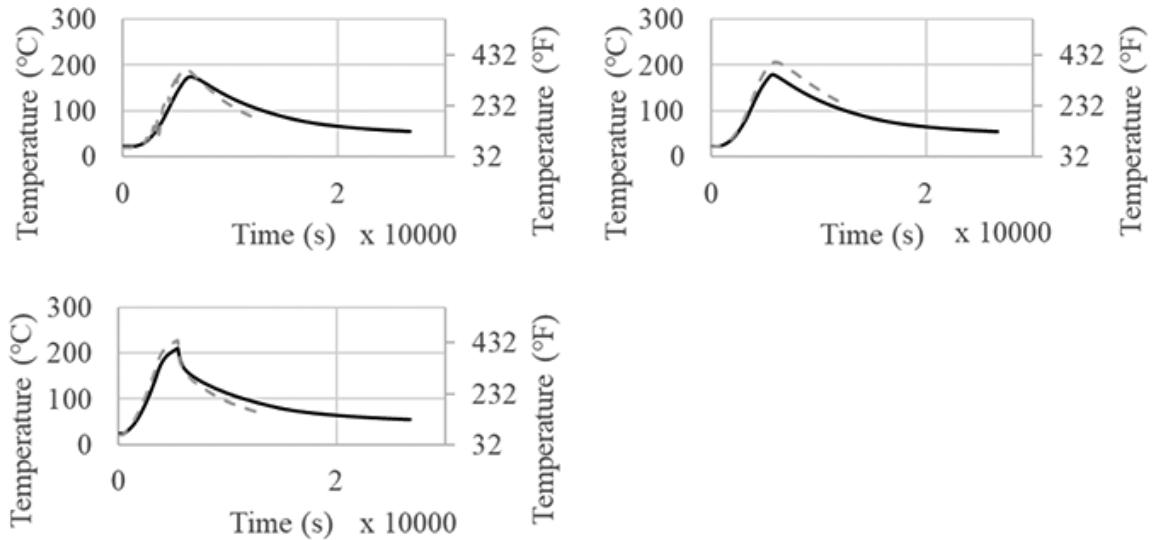


Fig. A7—Case 3 (482°F [250°C] for 30 minutes) calibrated model fit (FE results in black; thermocouple data in gray dashed line).

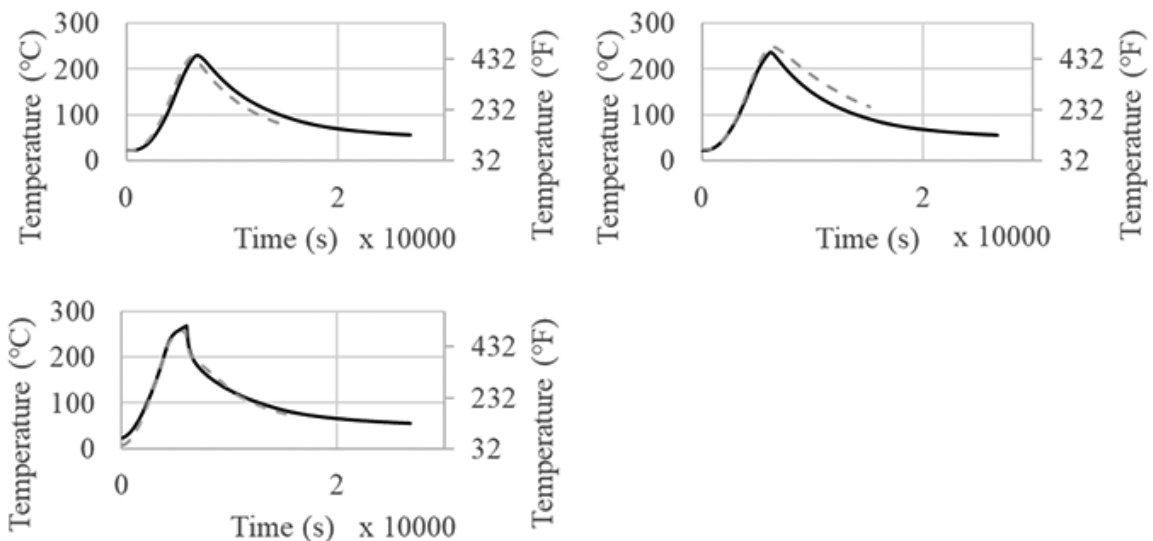


Fig. A8—Case 4 (572°F [300°C] for 30 minutes) calibrated model fit (FE results in black; thermocouple data in gray dashed line).

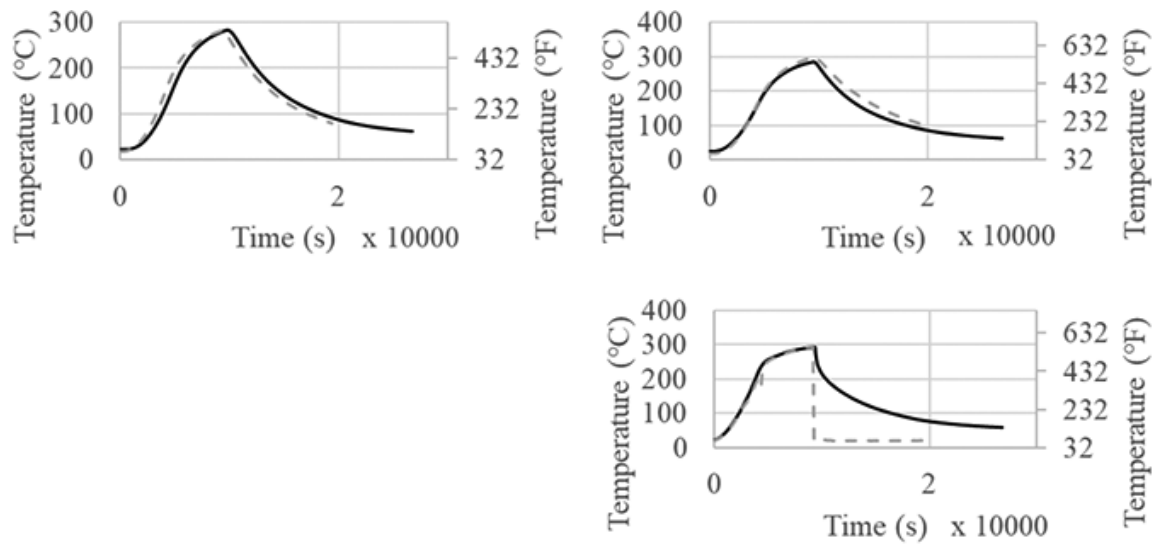


Fig. A9—Case 5 (572°F [300°C] for 85 minutes) calibrated model fit (FE results in black; thermocouple data in gray dashed line).

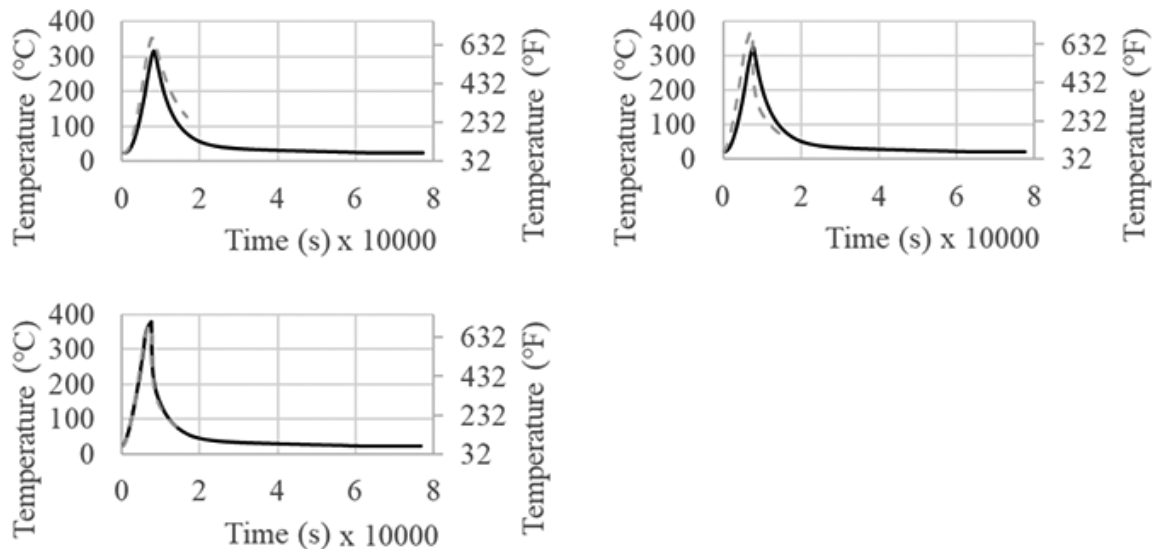


Fig. A10—Case 6 (752°F [400°C] for 30 minutes) calibrated model fit (FE results in black; thermocouple data in gray dashed line).

Title No. 120-M62

Examining Carbonation of Calcium Silicate-Based Cements in Real Time Using Neutron Radiography

by Rita Maria Ghantous, Margaret N. Goodwin, Mehdi Khanzadeh Moradllo, Sean Quinn, Vahit Aktan, O. Burkan Isgor, Steven Reese, and W. Jason Weiss

Carbonatable calcium silicate cement (CSC) is a promising approach to reducing the carbon footprint associated with concrete production. Carbonatable CSC gains strength by reacting with carbon dioxide (CO_2). While the concept of carbonation is well known, more information on the curing process is needed. This study focuses on studying the impact of drying time, carbonation duration, and degree of saturation (DOS) on the carbonation reaction of CSC mortar. Samples were exposed to different drying durations at controlled environmental conditions to reach various DOSs ranging from 100 to 0%. The samples were then exposed to carbonation under the same environmental conditions for different durations. Neutron radiography (NR) was performed on the samples during drying to determine the DOS corresponding to various drying durations. NR was also used during the carbonation period to determine the degree of carbonation (DOC) in real time. The impact of carbonation on the diffusivity of water vapor (D_h) and pore size distribution of CSC-based samples was examined using dynamic vapor sorption (DVS). It was concluded that the carbonation reaction increased as the DOS decreased from 100 to 40%. The carbonation reaction ceased for samples with DOS values less than 6% DOS. It was also concluded that as the DOC increased, the pore structure was refined, which led to a decrease in the D_h of the CSC mortar samples.

Keywords: calcium silicate cements; carbonation; diffusion coefficients; drying; neutron radiography.

INTRODUCTION

Several approaches are being investigated to reduce the carbon footprint of concrete.¹⁻⁵ One of the approaches substitutes part of the ordinary portland cement (OPC) with supplementary cementitious materials (SCMs),⁶⁻⁹ or by ground limestone.^{4,10} Another approach is using geopolymers such as alkali-activated fly ash.¹¹⁻²¹ These approaches rely on hydraulic, pozzolanic reactions. An alternative approach has been introduced and suggests a non-hydraulic cement that reacts with carbon dioxide (CO_2) to harden. This carbonation reaction uses calcium silica cements (CSCs) such as pseudowollastonite, wollastonite ($\text{CaO}\cdot\text{SiO}_2$), and rankinite ($3\text{CaO}\cdot 2\text{SiO}_2$).²²⁻²⁷ These CSCs react with CO_2 to form stable calcium carbonate (CaCO_3) and silica (SiO_2) gel that provide mechanical strength for the microstructure.^{24,26,28} These CSCs require less limestone and can be prepared using existing cement kilns at a lower temperature than OPC, which reduces the CO_2 emissions by 30% as compared to OPC.²⁹ In addition, the carbonation reaction of CSC captures 300 kg of CO_2 per ton of cement used.²⁹ As a result, CSC has proven to be efficient in reducing the energy

requirement and carbon footprint of cement manufacturing by 70% as compared to OPC.^{22,23,25-27}

To understand the properties of these CSC-based materials and to be able to better incorporate them as an alternative to OPC, their durability³⁰⁻³³ as well as their microstructure and strength development³¹⁻³⁶ have been studied. The freezing-and-thawing performance of CSC concrete was found to be equal to or better than OPC concrete samples.^{30,37} This is partially because CSC-based samples have a bimodal pore structure³¹: large pores (>10 nm) corresponding to the space between unreacted CSC particles, and small pores (<10 nm) found inside the reacted silica gel. The fluid inside the small pores (that is, pore solution) freezes at approximately -30°C , while the fluid in larger pores of CSC cement freezes at approximately -5°C . The temperature of standard freezing-and-thawing performance testing such as ASTM C666 stays above the freezing temperature of small pores. In addition, the larger pores are often not saturated, which reduces the in-place degree of saturation (DOS) and improves their freezing-and-thawing performance.³⁸

CSC systems also showed a higher resistance to salt degradation than OPC.^{38,39} This increased resistance of CSC samples to salt damage is due to their chemical composition that does not contain calcium monosulfoaluminate and calcium hydroxide, which are primarily responsible for salt damage development.³⁹⁻⁴¹ This chemical composition of CSC samples also increased their resistance to sulfate attack³⁷ and acid resistance, as well as their resistance to high temperatures⁴² when compared to OPC samples. Based on the prior studies, CSC-based materials have superior durability characteristics under aggressive environments as compared to OPC samples.^{30-32,38,39}

The mechanical strength of CSC-based cementitious materials has been studied by various researchers and was found comparable to OPC-based materials.^{30,33-35} The compressive strength of CSC mortar samples or CSC paste samples averaged between 35 and 48 MPa after 3 days of carbonation curing.^{33,35} The compressive strength of CSC concrete was able to reach 70 MPa.³⁰ The strength development in CSC materials is dependent on the carbonation reaction evolution. Ashraf et al.³⁵ concluded that the carbonation rate of

CSC-based cement paste and mortar are dependent on their water-binder ratio (*w/b*), temperature, and CO₂ concentrations. These carbonation rates were found to be the highest for mortar samples with a water-cement ratio of 0.40. In addition, it was concluded that the carbonation reaction could not occur without the presence of free water in the pores.³⁵

Khanzadeh Moradlo et al.³⁶ introduced a procedure to quantify the degree of carbonation (DOC) throughout the depth of the CSC mortar samples using neutron radiography (NR). This enabled discussions to begin on the influence of the moisture content throughout the sample depth on the carbonation evolution.

Based on the aforementioned studies, CSC-based materials seemed to be a very promising approach to improve concrete sustainability. Previous studies have begun to assess the curing of CSC-based materials. This study expands upon information in the literature to describe the drying and carbonation processes. The influence of the DOS of CSC mixtures on the evolution of the carbonation of CSC-based materials has not been fully investigated under a controlled environment—that is, controlled relative humidity (RH) and temperature. The first objective of this study is to introduce an experimental procedure to evaluate the drying and carbonation of fresh CSC mortar under controlled environmental conditions using NR. The second objective of this study is to determine the impact of the DOS of the CSC-based mortar on the rate of the carbonation reaction at a controlled RH and temperature. The third objective of this paper is to determine the impact of carbonation on the pore structure and diffusivity of water vapor (D_h) of CSC mortar samples. The behavior of carbonated CSC mortar samples will be compared with the nonlinear water diffusivity model of Bažant and Najjar⁴³ in non-saturated concrete.

RESEARCH SIGNIFICANCE

This paper describes the development of a drying and carbonation chamber that can be placed in a neutron beam line. This enables the drying and carbonation of fresh CSC materials to be studied under a controlled environment. The drying of CSC systems was studied to determine the DOS when CO₂ is introduced to the system. The optimal DOS that results in a higher rate of carbonation reaction was identified. In addition, the influence of the DOS on the uniformity of the carbonation profile was investigated. This paper also determines how carbonation changes the pore structure and diffusivity of water vapor of CSC samples. The findings of this paper can be used to improve the drying and carbonation of CSC materials.

EXPERIMENTAL PROCEDURE

Materials and mixture design

The chemical composition of the CSC used in this study was determined using X-ray fluorescence spectroscopy analyses, the results of which are shown in Table 1. The specific gravity of CSC was measured to be equal to 2.84 using the Le Chatelier flask procedure (ASTM C188-17⁴⁴). A standard graded sand (ASTM C778-17⁴⁵) with a specific gravity of 2.65 was used to prepare the mortar samples. A

Table 1—Chemical composition of CSC

Components	Mass, %
CaO	45.00
SiO ₂	47.20
Al ₂ O ₃	2.76
Fe ₂ O ₃	1.07
MgO	0.78
SO ₃	0.22
K ₂ O	0.80
Na ₂ O	0.27
TiO ₂	0.08
SrO	0.09
P ₂ O ₅	0.03
MnO	0.04
Cl	0.03
ZnO	0.01
LOI	1.60

set-retarding admixture (conforming to ASTM C494-19⁴⁶ for Type B retarder) was added to the cementitious matrix. The mixture proportions of the mortar prepared in this study are shown in Table 2. A 0.43 water-CSC ratio (*w/c*) was used in this study for the mortar sample preparation to ensure the highest reaction rate for CSC.^{35,36} The set retarder was added to the mortar mixture design to delay any minor hydration reactions which may interfere with drying.³⁶

Sample preparation

The mortar was mixed following a modified procedure of ASTM C305-14.⁴⁷ First, the set-retarding admixture was mixed with the deionized water. Second, the CSC and sand were mixed with the liquid using a vacuum mixer at 400 revolutions per minute (rpm) for 2 minutes at 80% vacuum level. The mixer was then stopped for 15 seconds and any materials that may have collected on the side of the mixing bowl were scraped down into the bulk of the mixing bowl. The materials were then mixed for an additional minute at 350 rpm at a vacuum level of 80%.

The CSC mortar was cast into a prismatic Polytetrafluoroethylene (PTFE) mold with inner dimensions of 60 mm wide, 50 mm tall, and 20 mm deep. PTFE was used for the molds due to its low neutron attenuation coefficient⁴⁸ and its lack of reaction with cement. The materials inside the mold were consolidated. The surface of the sample was finished and exposed to the environmental conditions investigated in this study.

Environmental conditions tested in this study

The rate of carbonation of CSC mortar was studied for four DOSs: 100, 65, 40, and 13% (average DOS over the depth of the sample). The RH and temperature were fixed at 40% and 60°C respectively during both the drying and the carbonation durations.

To determine the drying durations to reach the targeted DOSs, fresh mortar samples were exposed to drying

immediately after casting for durations of 0, 0.25, 0.5, 0.75, 1, 2, 3, 4, 5, 16, 18, 20, 23, 25, 27, 29, and 42 hours. The DOSs were calculated for each of these drying durations. The drying durations leading to the targeted DOSs were selected to be used to study the dependency of carbonation evolution of CSC materials on their DOS.

For each targeted DOS, four different carbonation durations were tested: 1.5, 3, 5, and 20 hours. The different carbonation durations tested in this study for the various DOSs are summarized in Table 3. All these carbonation conditions were performed in a $99 \pm 1\%$ CO₂ environment.

Drying and carbonation chamber

A chamber was designed to study the drying and carbonation of CSC mortar at controlled RH and temperature. The chamber was designed to be placed in a neutron beamline to enable in-place neutron radiography of CSC mortar samples during drying and carbonation. Figure 1(a) shows the major components of the chamber. The chamber walls (labeled No. 5 in Fig. 1(a)) are constructed of aluminum due to its low-neutron macroscopic cross section.⁴⁹ As illustrated in

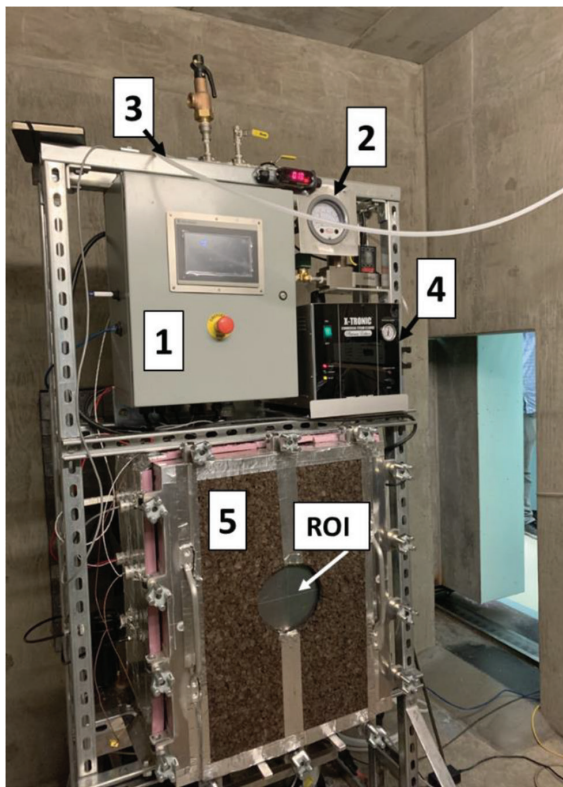
Fig. 1(a), insulation panels are mounted on the outside walls of the chamber to aid in providing a stable temperature inside the chamber. The middle section of the chamber, corresponding to the sample location (illustrated by No. 8 in Fig. 1(b)) and to the region of interest (ROI), is not covered by insulating materials to enable NR measurements to quantify the drying and carbonation of CSC mortar sample (Fig. 1(a)). The control cabinet (labeled No. 1 in Fig. 1(a)) runs the system. The human-machine interface (HMI) located on the outside of the cabinet is the primary means to control and program the different environmental cycles needed for a run such as temperature, RH, CO₂ injection, and duration for each cycle. Various sensors and gas circulation ports are installed through the left and right walls of the chamber as shown in Fig. 1(b). The heater (No. 5 in Fig. 1(b)) along with the temperature sensor (No. 4 in Fig. 1(b)) allows the chamber to be maintained at the set point temperature value.

Table 3—Carbonation durations tested in this study for each targeted DOS

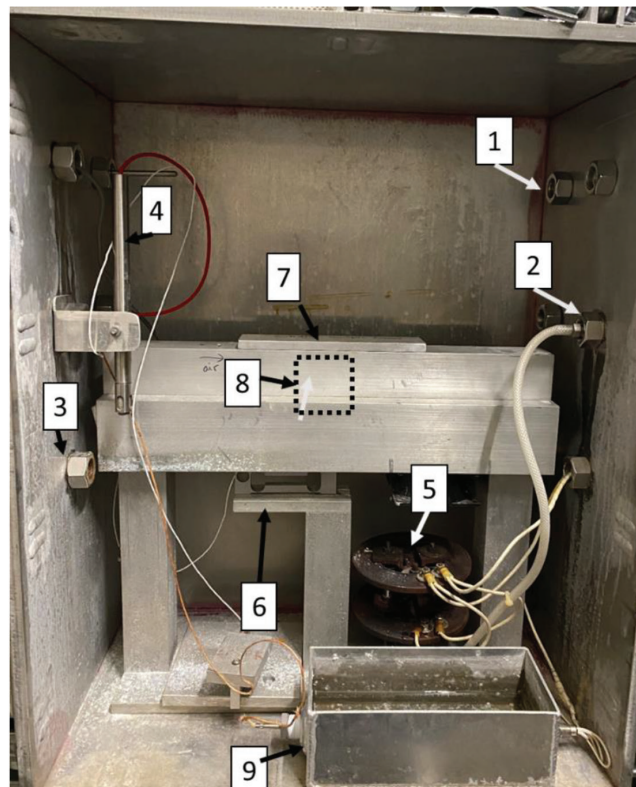
DOS, %	Carbonation durations, hours
13	1.5, 3, 5, 20
40	1.5, 3, 5, 20
65	1.5, 3, 5, 20
100	1.5, 3, 5, 20

Table 2—Mixture proportions of mortar prepared in this study

Materials	CSC	Deionized water	Sand	Retarder
Mass, g	100	43.0	275	0.50



(a)



(b)

Fig. 1—Experimental setup to study drying and carbonation of CSC mortar samples using NR: (a) exterior view of chamber: (1) control cabinet, (2) pressure gauge, (3) CO₂ injection, (4) steam generator, and (5) chamber; and (b) interior view of chamber showing major components: (1) CO₂ injection/exhaust points; (2) steam injection point; (3) CO₂ sampling point; (4) temperature and relative humidity measurement point; (5) gas heater; (6) load cell (400 g capacity), (7) sample housing, (8) sample location, and (9) immersion heater.

The heater will increase the temperature to the set point value and once the sensor detects the set point temperature, the heater will remain at the set temperature. The temperature sensor is continuously controlling the temperature to keep the temperature at the set point value. The RH can be controlled using the immersion heater (No. 9 in Fig. 1(b)), the steamer (No. 4 in Fig. 1(a)), and the RH sensor (No. 4 in Fig. 1(b)). The chamber is connected to a CO₂ tank. CO₂ gas enters the system through the mass flow controller, resulting in an increase in the system pressure measured using the pressure gauge (No. 2 in Fig. 1(a)). An exhaust valve opens when the pressure in the chamber exceeds 0.74 kPa. When the pressure in the system is below 0.1 kPa the mass flow controller injects CO₂ gas. Controlling the injection and exhaust of the chamber maintains a 100% CO₂ concentration. A CO₂ analyzer connected to the chamber is continuously measuring the CO₂ concentration inside the chamber. The CO₂ flow was programmed to be equal to 5 L per minute until the CO₂ content reaches 100% after which the CO₂ flow drops to 1.5 L per minute.

This chamber is in the NR facility (NRF) of the Oregon State TRIGA® Reactor (OSTR). This facility is a 1.1 MW TRIGA water-cooled research reactor that uses uranium/zirconium hydride fuel elements in a circular grid array. The tangential beam port used by the NRF allows thermal neutrons to pass through the collimator. A shutter is located between the end of the collimator and the NRF facility. Once the shutter is open, the thermal neutrons enter the imaging chamber. The carbonation and drying chamber are located perpendicular to the thermal neutron beam in front of the cesium iodide scintillation detector (CsI with 5 μm diameter doped with Gd) and the digital camera (50 mm f/1.2 lens⁵⁰⁻⁵³) as schematized in Fig. 2(a). A radiograph of the CSC mortar sample is given in Fig. 2(b). The spatial resolution of the radiographs was measured to be approximately equal to 90 μm.⁵⁰⁻⁵³

Degree-of-saturation calculations

Fresh mortar samples were exposed to drying at 60°C temperature and 40% RH directly after preparation. To track the DOS evolution during the drying period, several radiographs of the mortar sample were captured at the following drying durations: 0, 0.25, 0.5, 0.75, 1, 2, 3, 4, 5, 16, 18, 20, 23, 25, 27, 29, and 42 hours. For each time, three radiographs were captured with an exposure time of 2 seconds, and they were combined using a median filter that served in eliminating the artifacts caused by gamma rays and reducing the variability in the measured intensities.^{54,55} A background correction was performed by capturing multiple images from the background with open beam (flat field) as well as with closed beam (dark-field). ImageJ™ software was used to process the NR images.⁵⁶ First, for each time, the background noise was corrected using Eq. (1)⁵⁷

$$I_t = \frac{I_{image} - I_{DF}}{I_{FF} - I_{DF}} \quad (1)$$

where I_t is the corrected neutron transmitted intensity through the sample; I_{image} is the average transmitted intensity

through the sample; I_{DF} is the average transmitted intensity through the background with a closed beam (dark field); and I_{FF} is this intensity with an open beam (flat-field).

After the drying experiment, the samples were fully dried at 105°C to capture oven-dry radiographs and thus calculate the time-dependent DOS throughout the depth of the sample according to Eq. (2)

$$DOS = \frac{\ln\left(\frac{I_{OD}}{I_t}\right)}{\ln\left(\frac{I_{OD}}{I_{0min}}\right)} \quad (2)$$

where I_t is the corrected neutron-transmitted intensity through the sample at the various drying durations; I_{0min} is the corrected neutron transmitted intensity through the sample immediately after casting and before exposure to the drying environment (that is, saturation state); and I_{OD} is the neutron transmitted intensity through the oven dried mortar sample.

Degree of carbonation calculations

In this study, the procedure defined by Khanzadeh Moradlo et al.³⁶ has been used to determine the DOC over the depth of the CSC mortar. This procedure consists of oven drying the CSC mortar samples at the end of the carbonation period and thereafter collecting a neutron radiograph on these samples. The effective macroscopic cross section (attenuation coefficient) of the oven dried carbonated CSC mortar sample can be determined using the Beer-Lambert law (Eq. (3))

$$\frac{\ln\left(\frac{I_{OD-carb}}{I_0}\right)}{X_s} = -(\Sigma_{uc} V_{uc} + \Sigma_{rc} V_{rc} + \Sigma_{bp} V_{bp} + \Sigma_{ag} V_{ag} + \Sigma_a V_a) \quad (3)$$

where Σ_{uc} , Σ_{rc} , and Σ_{bp} are the macroscopic cross sections of uncarbonated CSC, carbonated CSC, and additional bound products (that is, bound water in silica gel and bound CO₂ in calcium carbonate), respectively; Σ_{ag} and Σ_a are the macroscopic cross sections of sand (0.0133 mm⁻¹), and air (0 mm⁻¹), respectively; V_{uc} , V_{rc} , and V_{bp} are the volume fractions of uncarbonated CSC, carbonated CSC, and additional bound products, respectively; V_{ag} and V_a are the volume fractions of sand and air, respectively; X_s is the thickness of the carbonated CSC mortar sample; and $I_{OD-carb}$ and I_0 are the transmitted neutron intensity through the oven-dried (OD) carbonated CSC mortar and open beam, respectively. Σ_{uc} was measured to be equal to 0.0175 mm⁻¹ and was assumed to be equal to Σ_{rc} . The sum of V_{uc} and V_{rc} is equal to the volume fraction of the original cement (V_{oc}) in the mortar sample which is 0.194 in this study. Consequently, Eq. (3) can be simplified into Eq. (4)

$$\frac{\ln\left(\frac{I_{OD-carb}}{I_0}\right)}{X_s} = -(\Sigma_{uc} V_{oc} + \Sigma_{bp} V_{bp} + \Sigma_{ag} V_{ag} + \Sigma_a V_a) \quad (4)$$

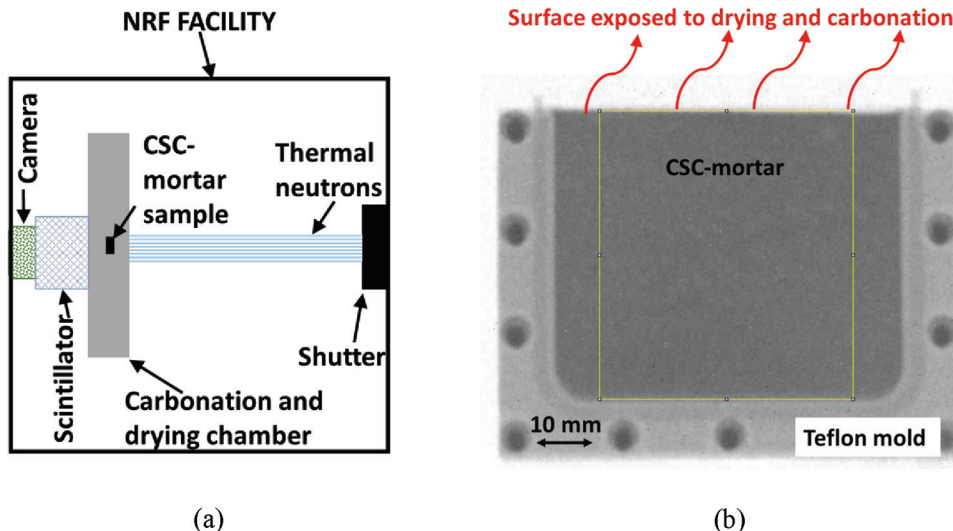


Fig. 2—(a) Location of drying and carbonation chamber inside NRF; and (b) neutron radiograph for CSC mortar sample exposed to one-dimensional (1-D) drying and carbonation inside PTFE mold.

In addition, extra CSC mortar samples were oven-dried immediately after the drying period at 105°C temperature without any exposure to CO₂, and then neutron radiographs were taken of these OD noncarbonated CSC samples. The effective macroscopic cross section of these noncarbonated CSC mortar samples can be expressed as shown in Eq. (5) according to Beer-Lambert law

$$\frac{\ln\left(\frac{I_{OD-no-carb}}{I_0}\right)}{X_s} = -\left(\sum_{uc} V_{oc} + \sum_{ag} V_{ag} + \sum_a V_a\right) \quad (5)$$

where $I_{OD-no-carb}$ is the transmitted neutron intensity through the OD noncarbonated CSC mortar.

By combining Eq. (4) and (5), the attenuation coefficient of the additional bound products can be determined using Eq. (6)

$$\frac{\ln\left(\frac{I_{OD-no-carb}}{I_{OD-carb}}\right)}{X_s} = \sum_{bp} V_{bp} \quad (6)$$

Khanzadeh Moradllo et al.³⁶ defined a correlation between the attenuation coefficient of bound products ($\sum_{bp} V_{bp}$) and the mass gains using CSC powders that were carbonated for different durations. Because this current study and Khanzadeh Moradllo et al.³⁶ used the same CSC (Table 1), the same correlation defined in Khanzadeh Moradllo et al.³⁶ has been used here to determine the percent mass gain induced by the carbonation reaction spatially in the CSC mortar sample. The profile of the DOC in the CSC mortar sample was determined by dividing the percent mass gain determined at each depth by the maximum percent mass gain due to carbonation reaction, found to be equal to 31.65% for the CSC tested in this study.³⁶

Pore structure characterization and diffusivity coefficient measurements

Three slab-shaped specimens of 60 ± 0.5 mg were extracted from the oven-dried (OD) carbonated CSC mortar at different depths that correspond to different degrees of carbonation. The sample that was used for this test was carbonated for 20 hours after 4 hours of drying at 60°C and 40% RH. One of the specimens had a 50% DOC that was extracted from the top part (1 mm deep from the sample surface) of the OD carbonated CSC mortar. The second specimen had a DOC of 30% that was extracted at 10 mm depth, while the third one was extracted at a depth of 48 mm and had a 9% DOC. These slab-shaped specimens were saturated in 0.25 mL of water in a microcentrifuge tube for 48 hours. They were then used to determine the impact of the carbonation of CSC mortar on the pore size distribution and diffusivity coefficient of the mortar samples.

After saturation, the specimens were placed in a tared quartz pan in the environmental chamber of the dynamic vapor desorption (DVS) analyzer to obtain the water vapor desorption isotherm. The mass of the sample was continuously monitored while varying the RH inside the chamber at controlled steps and at a constant temperature of 23°C. At the beginning of the experiment, the RH was reduced to 97.5% and was maintained at this value for either 48 hours or until the mass change between successive measurements was smaller than 0.001% over a duration of 15 minutes. The RH was then decreased by 2.5% RH steps from 97.5 to 80% RH, 4% RH steps from 80 to 76% RH, 6% RH steps from 76 to 70% RH, 10% RH steps from 70 to 30% RH, then decreased to 11% and 0% RH.

At each humidity value, the sample was allowed to equilibrate for 48 hours or until the mass change between successive measurements was smaller than 0.001% over a duration of 15 minutes.

Based on the Barret-Joyner-Halenda theory,⁵⁸ the pore radius r_p (m) is assumed to be the sum of r_k (m) (Kelvin radius) and t -curve (m) (thickness of water absorbed film). By assuming that the angle of liquid-solid contact is 0, the

Kelvin Laplace equation can be used in order to determine r_k as shown in Eq. (7), while the t -curve can be determined using Eq. (8)^{59,60}

$$r_k = \frac{-2\gamma V_m}{RT} \cdot \frac{1}{\ln RH} \quad (7)$$

$$t = \left(\frac{AV_m}{6\pi RT \ln RH} \right)^{1/3} \quad (8)$$

where γ is the surface tension of the pore solution (72×10^{-3} N/m); V_m is its molar volume (assumed to be equal to the water molar volume 18.02×10^{-6} m³/mol); R is the ideal gas constant (8.314 J/(mol.K)); T is the temperature (296.15K); and A is the Hamaker constant for the interaction of solid-liquid-gas (-6×10^{-20} J).⁶¹

For each RH step in the DVS, the diffusivity of water D_m (m²/s) was calculated using Eq. (9)^{62,63}

$$D_m = (a_{\sqrt{t}})^2 \frac{\pi d^2}{16(\Delta m_{max})^2} \quad (9)$$

where d is the thickness of the slab-shaped specimen (3.3 mm in average in this study); and $a_{\sqrt{t}}$ is determined for each RH step using Eq. (10)

$$\Delta m_t = a_{\sqrt{t}} \times \sqrt{t} \quad (10)$$

where Δm_t denotes the change in mass of the sample during the desorption process at each RH step; and Δm_{max} is the total change in mass of the sample after achieving equilibrium at each RH step. $a_{\sqrt{t}}$ and Δm_{max} are illustrated in Fig. 3.

For each RH step, the diffusivity of water vapor D_h (m²/s) was calculated by multiplying the slope of the desorption isotherm by the corresponding diffusivity of water (D_m), according to Eq. (11)⁶³

$$D_h = D_m \frac{dM}{dH} \quad (11)$$

where dM/dH corresponds to the slope of the desorption isotherm at each RH step.

EXPERIMENTAL RESULTS AND DISCUSSION

Degree-of-saturation evolution during drying period

Figure 4 illustrates the DOS profiles as a function of the depth of the CSC mortar, exposed to drying at 40% RH and 60°C immediately after casting, for different drying durations. The measured DOS decreased as drying duration increased. Four different DOSs, listed in Table 3, were targeted to study the dependency of carbonation evolution on the pore saturation. The values of these four different DOSs were 100, 65, 40, and 13% on average. Based on Fig. 4, exposing a fresh CSC mortar sample to one-dimensional (1-D) drying at 60°C and 40% RH for 2, 4, and 20 hours will lead to an average DOS of 65%, 40%, and 13%, respectively, over the sample depth. Samples with 13% average DOS value showed a gradient that is more advanced as compared

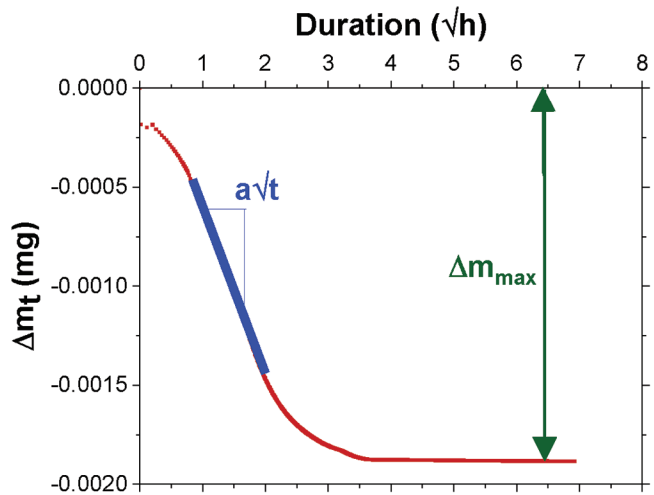


Fig. 3—Example of change in mass of sample with respect to square root of time during desorption process at one RH step.

to other higher targeted DOS values. The 100% DOS corresponds to a fresh mortar sample that is not exposed to any drying. Consequently, CSC mortar samples were exposed to the following four different drying durations before exposure to CO₂: 0, 2, 4, and 24 hours at 60°C and 40% RH. Therefore, the impact of four different initial DOSs on the carbonation of CSC mortar will be studied.

It should be noted that the rate at which CSC mortar samples dry is faster and more linear compared to OPC due to their non-hydraulic characteristics. According to Fig. 4, samples exposed to drying durations less than 4 hours had a uniform moisture content over the sample depth. However, samples exposed to drying for a duration longer than 5 hours showed a gradient in their moisture content. The gradient in the moisture content for samples exposed to longer than 16 hours is greater than the gradient noted for samples dried for 5 hours. Sixty-two percent of the original water evaporated from the CSC mortar samples after 4 hours of drying at 40% RH and 60°C temperature. Figure 5 illustrates the average DOS of CSC mortar samples with respect to the square root of the drying duration. It can be noted from Fig. 5 that the rate of drying after 16 hours is smaller than the rate of drying measured at the beginning of the drying period.

Influence of degree of saturation on evolution of carbonation reaction

Figure 6 illustrates the evolution of the DOC profiles obtained from neutron radiography on CSC mortar carbonated for four different durations. Figure 6(a) illustrates the carbonation evolution in CSC mortar samples that were carbonated immediately after casting in a 100% CO₂ environment, 60°C temperature, and 40% RH without any pre-drying. The DOS of these samples was 100% at the beginning of the carbonation reaction. For these samples, CO₂ should first dissolve in the pore solution, then travel by diffusion through the saturated pores to the reaction sites. Figures 6(b), (c), and (d) show the DOC for CSC mortar samples with initial DOS at the beginning of the carbonation phase of $65\% \pm 1.7\%$, $40\% \pm 2.7\%$, and $13 \pm 5\%$ on average,

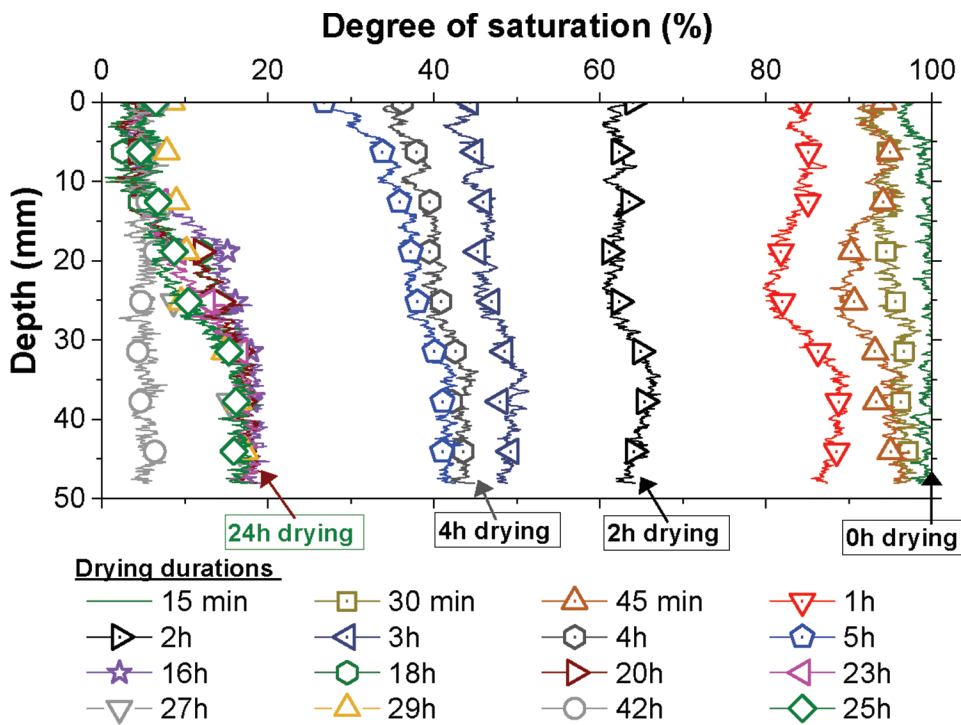


Fig. 4—Degree-of-saturation profile for mortar samples exposed to 1-D drying at 40% RH and 60°C temperature.

respectively. For these samples, the pores of the CSC mortar are partially saturated, that is, a thin layer of pore solution will be present at the pore surface. In this case, CO₂ transports through the pores in a gas form, dissolves within this layer of pore solution and diffuses through this pore solution layer to react with CSC cement. Higher DOC values were measured in samples with a DOS lower than 100%. For instance, after 20 hours of carbonation, the highest DOC measured in 100% DOS sample was approximately 18% (Fig. 6(a)). Samples with 65% ± 1.7% DOS had a DOC of up to 42% after 20 hours of carbonation (Fig. 6(b)). The samples with 40% ± 2.7% DOS had a DOC for up to 50% (Fig. 6(c)) after 20 hours of carbonation.

This is explained by the fact that the diffusion coefficient of CO₂ in aqueous solution is 10⁴ times lower than in the gas phase.⁶⁴ For instance, at 35°C and atmospheric pressure, the diffusion coefficient of CO₂ in water is equal to 2.47 × 10⁻⁵ cm²/s.⁶⁵ The diffusion coefficient of CO₂ in air at atmospheric pressure and 20°C was reported to be equal to 1.6 × 10⁻¹ cm²/s.⁶⁶ For this reason, the carbonation reaction will occur at a faster rate in samples with partially saturated pores. Figure 7 aims to illustrate this dependency of the rate of carbonation on the initial DOS of the CSC mortar sample. In Fig. 7, for each DOS, the average rate of the carbonation reaction was determined from the top 10 mm of the sample surface according to Eq. (12)

$$\bar{R}_c = \frac{1}{n} \sum_{x=1}^n \bar{R}_x \quad (12)$$

where n is the number of the carbonation durations tested for each DOS; and \bar{R}_x is the average rate of carbonation calculated on the top 10 mm of the sample surface for each carbonation duration, according to Eq. (13)

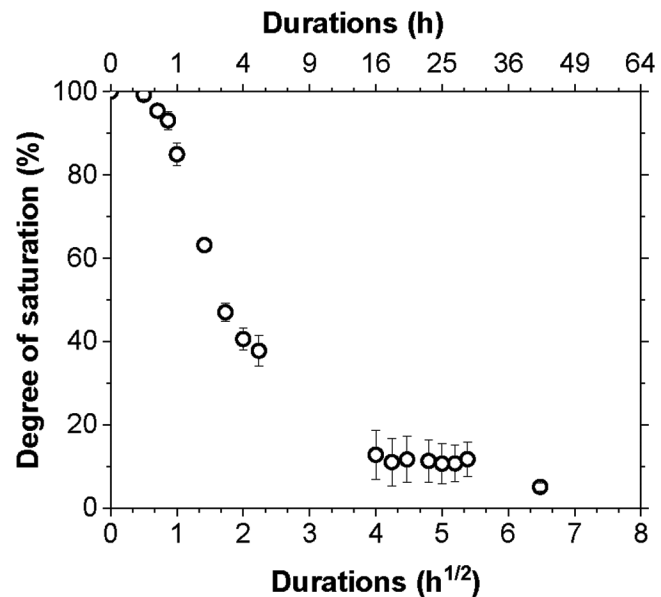


Fig. 5—Decrease in degree of saturation of samples based on CSC mortar with respect to square root of drying duration.

$$\bar{R}_x = \frac{1}{p} \sum_{x=1}^p \frac{DOC}{\sqrt{t}} \quad (13)$$

where p is the number of pixels for the first 10 mm on the sample surface; DOC is the degree of carbonation measured for each pixel; and t is the carbonation duration (hours).

It can be noted from Fig. 7 that the rate of carbonation increases with a decrease in the initial DOS from 100 to 60%. The rate of carbonation was the lowest for samples with an average DOS of 6.5% because a minimum amount of water is needed for the carbonation reaction to occur, that is, for the CO₂ dissolution before reaction with CSC. This is

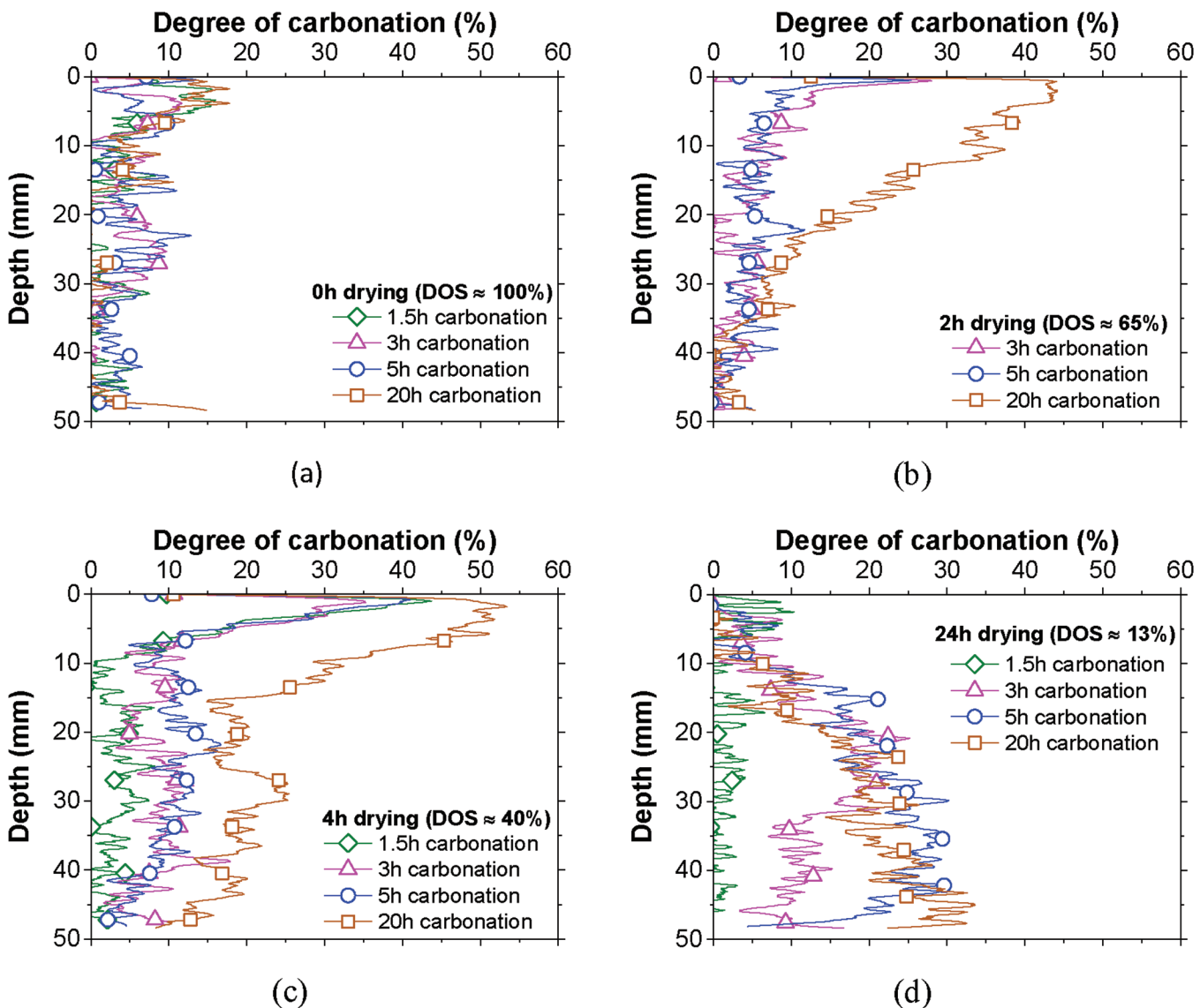


Fig. 6—DOC profiles of CSC mortar samples for varying carbonation duration for different initial DOS: (a) 100% DOS; (b) 65% DOS; (c) 40% DOS; and (d) 13% DOS.

in accordance with the study of Ashraf et al.³⁵ showing that a lack of water will limit the carbonation reaction. This dependency of the carbonation reaction on the internal moisture content of CSC mortar samples is in accordance with what is established in the literature for conventional OPC cementitious materials.⁶⁷⁻⁷⁶

For all carbonation durations, a gradient in the DOC profiles is present for all the CSC mortar samples illustrated in Fig. 6. For samples with an average initial DOS of 60 and 40% (Fig. 6(b) and (c), respectively) the DOC is greater in the upper section of the sample (0 to 20 mm). The DOS profiles for these samples at the end of the drying period (Fig. 4) are uniform throughout the sample depth and no significant gradient in the DOS can be noted for these two samples. These samples are exposed to 1-D carbonation; consequently, the CO_2 will start first dissolving within the thin layer of water located inside the pores near the sample surface, that is, in contact with CO_2 . Dissolved CO_2 will then diffuse to the closest reaction site to react with CSC and form carbonation products that have a higher volume compared to

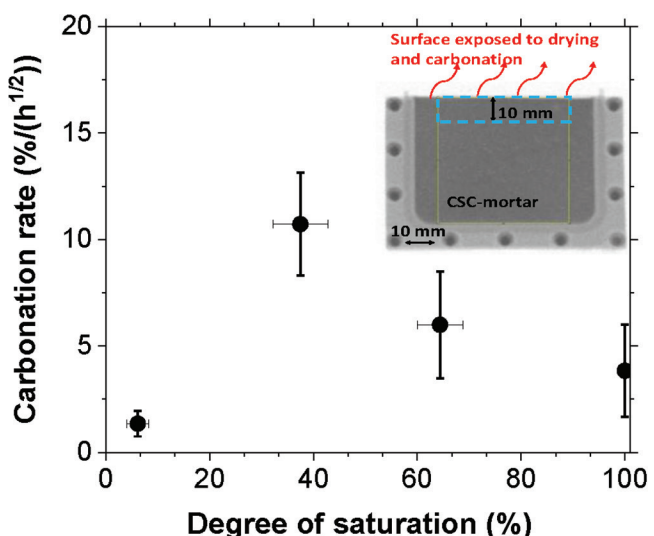


Fig. 7—Rate of carbonation reaction in first 10 mm of sample surface with respect to initial degree of saturation of CSC mortar sample.

original CSC.³¹ The matrix porosity is then refined near the surface, which would limit CO₂ diffusion to deeper sections of the sample (deeper than 30 mm).

A gradient was also visible in the samples that were dried for 24 hours (Fig. 6(d)). The DOC was higher in the lower part of the sample (>15 mm) as compared to the values measured on the sample surface. A significant gradient exists in the initial DOS of the samples dried for 24 hours as noted in Fig. 4. The average initial DOS in the first 15 mm of CSC mortar after 24 hours of drying is approximately 6.5 ± 1.3%, while a higher average value of 16.1 ± 3.3% was measured in deeper sections in the sample (Fig. 4). The amount of water remaining in the pores of the first 15 mm of the CSC mortar sample after 24 hours of drying was insufficient for the carbonation reaction to occur. The CO_{2(g)} was able to diffuse through these relatively dry pores located in the upper section of the CSC mortar sample to deeper sections in the CSC mortar sample (>30 mm), where the average DOS was 18.4 ± 1.2%, and was able to dissolve in this water and react with CSC to form carbonation products.

Figure 8(a) shows on the same graph the DOS profile after 24 hours of drying and the DOC profiles for different carbonation durations. Figure 8(b) represents the DOC with respect to the DOS for a sample exposed to 24 hours of drying followed by 20 hours of carbonation. It can be seen from both Fig. 8(a) and (b) that a DOS higher than 6% is needed for the carbonation reaction to occur. The carbonation reaction will be limited in a medium with a DOS below 6% due to the lack of water. In summary, carbonation does not occur in either a dry cementitious matrix (DOS < 6%) nor in a fully saturated one. At a low moisture content, chemical reactions are inhibited because of the lack of water. At high moisture content, CO₂ diffusion is limited by insufficient air due to the matrix pores saturation.

Influence of carbonation reaction on diffusivity coefficients of CSC mortar

Figures 9(a) and (b) illustrate the impact of the DOC of CSC mortar samples on their pore structure. Figure 9(a)

illustrates that 90% of the pores in a sample with a low DOC (~9%) are larger than 40 nm in pore radius. In partially carbonated samples (~30% DOC), 43% of the pores have a pore radius smaller than 40 nm (Fig. 9(a)). The development of carbonation products resulted in pore filling and refinement (that is, smaller pores) (Fig. 9(a) and (b)). These measurements are in accordance with the theory explained in the study of Villani et al.³¹ and Ashraf et al.³⁴

The refined pore structure of samples with a greater DOC resulted in a decrease in D_h (Fig. 9(c)). It can be observed that D_h measured on CSC mortar samples is higher than the values reported for conventional mortar samples made using OPC.^{62,63} Bažant and Najjar⁷⁷ studied the dependency of D_h on the pore humidity of conventional cementitious materials and developed Eq. (14)

$$D_h = D_1 \left(\alpha_l + \frac{1 - \alpha_l}{1 + \left(\frac{1 - RH}{1 - RH_c} \right)^n} \right) \quad (14)$$

where D_1 corresponds to D_h at high RH; α_l corresponds to D_h at low RH; RH is the pore RH; RH_c is a constant representative of the pore RH corresponding to the inflection point in the curve of D_h with respect to RH; and n is a constant that was defined in Bažant and Najjar⁷⁷ to vary between 6 and 16 depending on the mixture design and describes the sharpness of the curve correlating D_h to RH.

The fitted lines in Fig. 9(c) were obtained using Eq. (14). It can be observed that D_h of CSC mortar samples can be described using Eq. (14), which can be a powerful tool in describing the changes of the microstructure with carbonation. For these fitted lines, RH_c was set to be equal to 0.84, n was fixed to 6 in this study for the best-fit, which is within the range (that is, 6 to 16) that is typically used for OPC.⁷⁷ The D_1 values were related to the DOC. D_1 was equal to 2.8×10^{-11} , 1.8×10^{-11} , and 1.1×10^{-10} m²/s for samples with 50%, 30%, and 9% DOC, respectively.

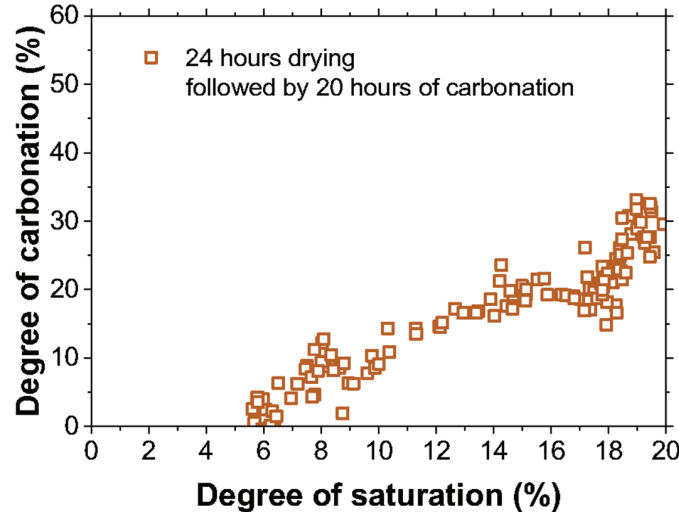
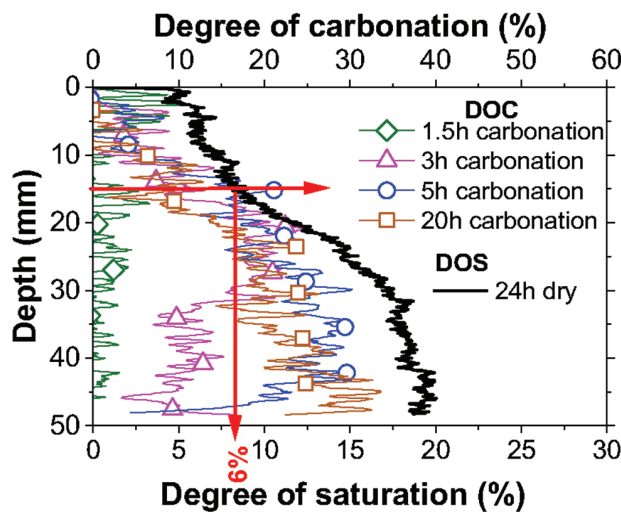


Fig. 8—Minimum pore saturation needed for carbonation reaction to occur: (a) DOC and DOS profiles after 24 hours of drying and various carbonation durations; and (b) DOC with respect to DOS for sample exposed to 24 hours drying and 20 hours carbonation.

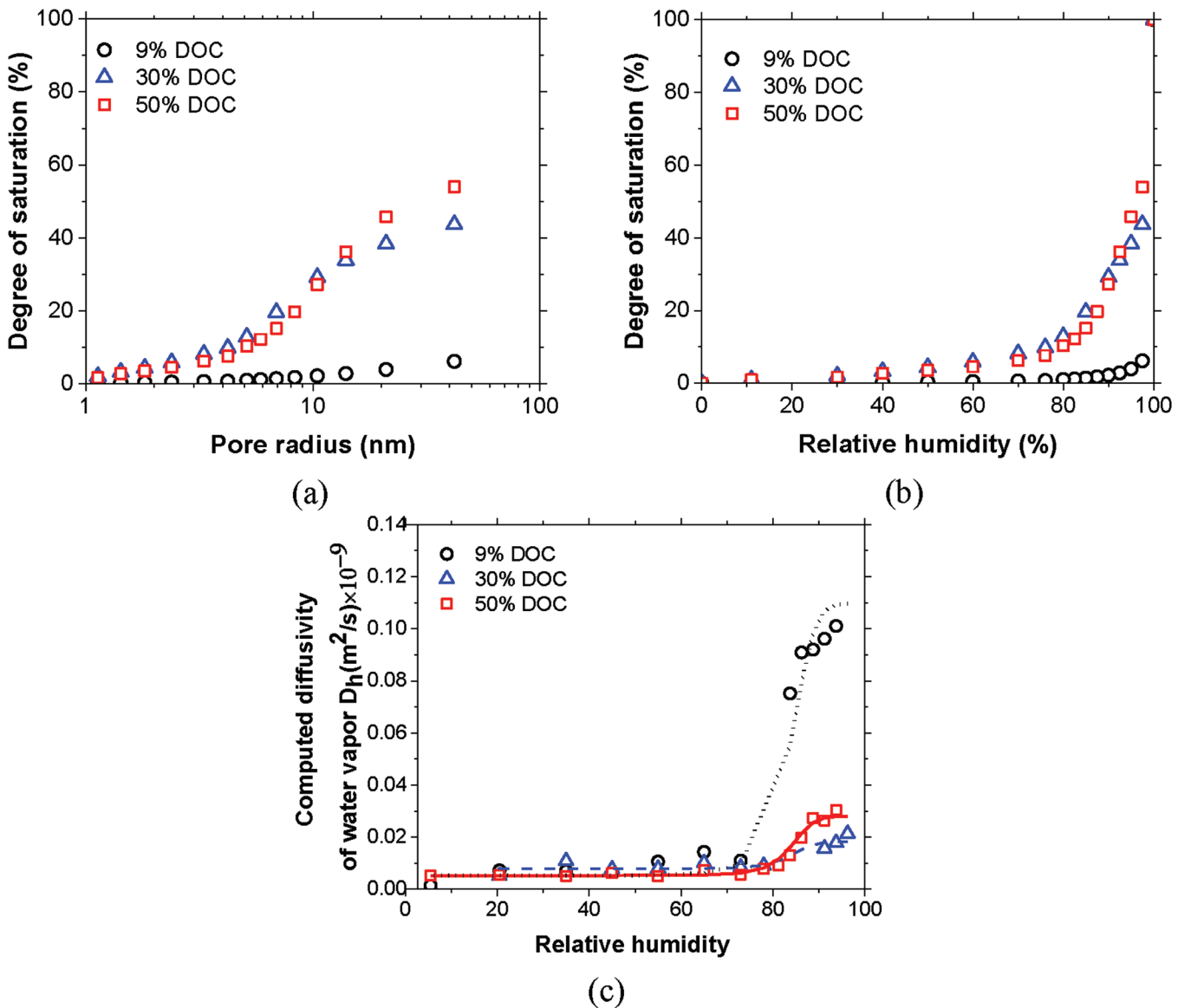


Fig. 9—Impact of DOC on: (a) pore structure of CSC mortar; (b) desorption isotherm of CSC mortar; and (c) D_h in CSC mortar.

CONCLUSIONS

Calcium silicate cement (CSC)-based mortar samples were prepared for this study using CSC, aggregate, and water. The interaction between drying, degree of saturation (DOS), and carbonation of CSC mortar samples was examined using neutron radiography. For the purpose of this study, a drying and carbonation chamber was developed that can be placed in a neutron beam line and that enables radiographs to evaluate the in-place drying and carbonation of CSC samples under a controlled environment (that is, relative humidity, temperature, and CO_2 concentration). The dependency of pore structure of CSC samples on their degree of carbonation (DOC) was investigated using dynamic vapor sorption. In addition, the nonlinear diffusivity of water vapor (D_h) was determined for CSC mortar samples with different DOC.

It was first observed that the ingress of CO_2 and rate carbonation of CSC mortar samples depend on their saturation level. Samples with a high DOS (~100%) impeded CO_2 ingress as the diffusion of CO_2 in vapor is much faster than its diffusion through an aqueous medium. Therefore,

vapor-filled pore space is needed for the carbonation reaction to occur. It was also observed that in a matrix with a DOS below 6%, the carbonation reaction does not occur due to the lack of water. Information is therefore needed on the optimum pre-drying conditions of CSC mortar samples to permit CO_2 ingress without limiting the carbonation reaction.

For this reason, the carbonation of CSC mortar samples with various initial DOS ranging from 65 to 13% in average was examined. For samples with an intermediate DOS (that is, between ~65 and 40%), as the carbonation duration increased, carbonation products developed in the upper section of the samples and filled the pores of the CSC mortar samples leading to pore refinement in this section. The pore refinement, localized in the upper section of the sample, induced a decrease in the D_h of the matrix in this upper section of the sample limiting the ability of CO_2 to reach the lower section of the sample. Consequently, a gradient in the DOC profile and crusting was observed in the CSC mortar samples with intermediate DOS. The DOC was not uniform

along the sample depth with higher values in the upper sections of the sample as compared to the lower sections.

AUTHOR BIOS

ACI member Rita Maria Ghantous is a Research Associate in the School of Civil and Construction Engineering at Oregon State University, Corvallis, OR. She received her MS from École Centrale de Nantes, Nantes, France, and her PhD in civil engineering from Institut National des Sciences Appliquées de Toulouse, Toulouse, France. She is a member of ACI Committee 130, Sustainability of Concrete. Her research interests include durability and sustainability of cementitious materials.

Margaret N. Goodwin was a Graduate Research Assistant at Oregon State University, where she also received her MS. She is a Reactor Operator at Idaho National Laboratory. Her research interests include applications of neutron radiography in concrete materials.

ACI member Mehdi Khanzadeh Moradlo is an Assistant Professor at Temple University, Philadelphia, PA. He received his MS from the University of Tehran, Tehran, Iran, and his PhD from Oklahoma State University, Stillwater, OK. He is a member of ACI Committees 130, Sustainability of Concrete; 242, Alternative Cements; and 564, 3-D Printing with Cementitious Materials. His research interests include durability and sustainability of concrete and cementitious materials, analytical imaging and microscopy techniques, internal curing, and alternative cementitious materials.

Sean Quinn is the Senior Technical Operations Manager at Solidia Technologies Inc., Piscataway, NJ. He received his BSc in materials science and engineering from Rutgers University, The State University of New Jersey, New Brunswick, NJ, in 2011. His research interests include the development and implementation of processing strategies for carbonatable calcium silicate cement-based concretes.

Vahit Aktan is the Chief Scientist at Solidia Technologies Inc. He received his PhD in materials science from Rutgers University. His research interests include carbonatable calcium silicate cement-based concrete.

O. Burkan Isgor, FACI, is a Professor in the School of Civil and Construction Engineering at Oregon State University. He is Chair of ACI Committee 222, Corrosion of Metals in Concrete. His research interests include concrete durability, reinforcement corrosion, service life, and thermodynamic modeling of cementitious systems.

Steven Reese is the Radiation Center Director and Associate Professor in the School of Nuclear Science and Engineering at Oregon State University. He received his BS in science from Oregon State University and his PhD in radiological health sciences from Colorado State University, Fort Collins, CO. He is a certified health physicist, holds a senior reactor operators license, and serves on the executive committee of the National Organization of Test, Research, and Training Reactors.

W. Jason Weiss, FACI, is the Edwards Distinguished Professor of Engineering at Oregon State University. He received his BAE in architectural engineering from Pennsylvania State University, University Park, PA, and his MS and PhD in civil engineering from Northwestern University, Evanston, IL. He is Editor in Chief of the ACI Materials Journal and a member of the ACI Technical Activities Committee.

ACKNOWLEDGMENTS

The authors gratefully acknowledge the support of Solidia Technologies Inc. The authors also acknowledge receipt of the cement materials from Solidia Technologies Inc. The contents of this paper reflect the views of the authors, who are responsible for the facts and the accuracy of the data presented herein.

REFERENCES

1. Danish, A.; Salim, M. U.; and Ahmed, T., "Trends and Developments in Green Cement 'A Sustainable Approach,'" *Sustainable Structures and Materials, an International Journal*, V. 2, No. 1, 2019, pp. 45-60.
2. Habert, G., and Roussel, N., "Study of Two Concrete Mix-Design Strategies to Reach Carbon Mitigation Objectives," *Cement and Concrete Composites*, V. 31, No. 6, 2009, pp. 397-402. doi: 10.1016/j.cemconcomp.2009.04.001
3. Venkatarama Reddy, B. V., "Sustainable Materials for Low Carbon Buildings," *The International Journal of Low Carbon Technologies*, V. 4, No. 3, 2009, pp. 175-181. doi: 10.1093/ijlct/ctp025
4. Bharawadj, K.; Chopperla, K. S. T.; Choudhary, A.; Glosser, D.; Ghanous, R. M.; Vasedevan, G.; Ideker, J. H.; Isgor, B.; Trejo, D.; and Weiss, J. W., "CALTRANS: Impact of the Use of Portland-Limestone Cement on Concrete Performance as Plain or Reinforced Material," Oregon State University, Corvallis, OR, 2021, 320 pp.
5. Kline, J., and Kline, C., "Cement Plants of the Future," *International Cement Review*, 2019.
6. Lothenbach, B.; Scrivener, K.; and Hooton, R. D., "Supplementary Cementitious Materials," *Cement and Concrete Research*, V. 41, No. 12, 2011, pp. 1244-1256. doi: 10.1016/j.cemconres.2010.12.001
7. Thomas, M., *Supplementary Cementing Materials in Concrete*, CRC Press, Boca Raton, FL, 2013.
8. Gartner, E., "Industrially Interesting Approaches to 'Low-CO₂' Cements," *Cement and Concrete Research*, V. 34, No. 9, 2004, pp. 1489-1498. doi: 10.1016/j.cemconres.2004.01.021
9. Flower, D. J. M., and Sanjayan, J. G., "Greenhouse Gas Emissions Due to Concrete Manufacture," *The International Journal of Life Cycle Assessment*, V. 12, No. 5, 2007, pp. 282-288. doi: 10.1065/lca2007.05.327
10. Jayapalan, A. R.; Lee, B. Y.; and Kurtis, K. E., "Can Nanotechnology Be 'Green'? Comparing Efficacy of Nano And Microparticles in Cementitious Materials," *Cement and Concrete Composites*, V. 36, 2013, pp. 16-24. doi: 10.1016/j.cemconcomp.2012.11.002
11. Davidovits, J., "Geopolymers: Inorganic Polymeric New Materials," *Journal of Thermal Analysis and Calorimetry*, V. 37, No. 8, 1991, pp. 1633-1656. doi: 10.1007/BF01912193
12. Duxson, P.; Fernández-Jiménez, A.; Provis, J. L.; Lukey, G. C.; Palomo, A.; and van Deventer, J. S., "Geopolymer Technology: The Current State of the Art," *Journal of Materials Science*, V. 42, No. 9, 2007, pp. 2917-2933. doi: 10.1007/s10853-006-0637-z
13. Duxson, P.; Provis, J. L.; Lukey, G. C.; and van Deventer, J. S., "The Role of Inorganic Polymer Technology in the Development of 'Green Concrete,'" *Cement and Concrete Research*, V. 37, No. 12, 2007, pp. 1590-1597.
14. van Deventer, J. S.; Provis, J. L.; Duxson, P.; and Brice, D. G., "Chemical Research and Climate Change as Drivers in the Commercial Adoption of Alkali Activated Materials," *Waste and Biomass Valorization*, V. 1, No. 1, 2010, pp. 145-155. doi: 10.1007/s12649-010-9015-9
15. Xu, H., and Van Deventer, J. S. J., "The Geopolymerisation of Aluminosilicate Minerals," *International Journal of Mineral Processing*, V. 59, No. 3, 2000, pp. 247-266. doi: 10.1016/S0301-7516(99)00074-5
16. Palomo, A.; Grutzeck, M. W.; and Blanco, M. T., "Alkali-Activated Fly Ashes: A Cement for the Future," *Cement and Concrete Research*, V. 29, No. 8, 1999, pp. 1323-1329. doi: 10.1016/S0008-8846(98)00243-9
17. Hardjito, D.; Wallah, S. E.; Sumajouw, D. M.; and Rangan, B. V., "On the Development of Fly Ash-Based Geopolymer Concrete," *ACI Materials Journal*, V. 101, No. 6, Nov.-Dec. 2004, pp. 467-472.
18. Stengel, T.; Heinz, D.; and Reger, J., "Life Cycle Assessment of Geopolymer Concrete—What is the Environmental Benefit," *Proceedings of the 24th Biennial Conference of the Concrete Institute of Australia*, Sydney, Australia, 2009.
19. Witherspoon, R.; Wang, H.; Aravindan, T.; and Omar, T., "Energy and Emissions Analysis of Fly Ash Based Geopolymers," *Proceedings, SSEE International Conference: Solutions for a Sustainable Planet*, Melbourne, Australia, 2009.
20. McLellan, B. C.; Williams, R. P.; Lay, J.; Van Riessen, A.; and Corder, G. D., "Costs and Carbon Emissions for Geopolymer Pastes in Comparison to Ordinary Portland Cement," *Journal of Cleaner Production*, V. 19, No. 9-10, 2011, pp. 1080-1090. doi: 10.1016/j.jclepro.2011.02.010
21. Habert, G.; d'Espinose de La Caillierie, J. B.; and Roussel, N., "An Environmental Evaluation of Geopolymer Based Concrete Production: Reviewing Current Research Trends," *Journal of Cleaner Production*, V. 19, No. 11, 2011, pp. 1229-1238. doi: 10.1016/j.jclepro.2011.03.012
22. Meyer, V.; Sahu, S.; and Dunster, A., "Properties of Solidia Cement and Concrete," *Proceedings of the 1st International Conference on Innovation in Low-Carbon Cement and Concrete Technology*, London, UK, June 2019, pp. 24-26.
23. Klemm, W. A., and Berger, R. L., "Calcination and Cementing Properties of CaCO₃-SiO₂ Mixtures," *Journal of the American Ceramic Society*, V. 55, No. 10, 1972, pp. 485-488. doi: 10.1111/j.1151-2916.1972.tb13411.x
24. Bukowski, J. M., and Berger, R. L., "Reactivity and Strength Development of CO₂ Activated Non-Hydraulic Calcium Silicates," *Cement and Concrete Research*, V. 9, No. 1, 1979, pp. 57-68. doi: 10.1016/0008-8846(79)90095-4
25. DeCristofaro, N.; Meyer, V.; Sahu, S.; Bryant, J.; and Moro, F., "Environmental Impact of Carbonated Calcium Silicate Cement-Based Concrete," *Proceedings of the 1st International Conference on Construction Materials for Sustainable Future*, CoMS, Zadar, Croatia, 2017.

26. Riman, R. E.; Atakan, V.; Vakifahmetoglu, C.; Li, Q.; and Tang, L., "Synthetic Formulations and Methods of Manufacturing and Using Thereof," U.S. Patent No. 9,216,926, Washington, DC, 2015.
27. Svensson, K.; Neumann, A.; Feitosa Menezes, F.; Lempp, C.; and Pöllmann, H., "Carbonation of Natural Pure and Impure Wollastonite," *SN Applied Sciences*, V. 1, No. 4, 2019, pp. 1-12. doi: 10.1007/s42452-019-0328-4
28. Sahu, S., and DeCristofaro, N., "Part One of a Two-Part Series Exploring the Chemical Properties and Performance Results of Sustainable Solidia Cement TM and Solidia Concrete TM," Solidia Technologies, 2013, pp. 1-12.
29. Meyer, V.; DeCristofaro, N.; Bryant, J.; and Sahu, S., "Solidia Cement an Example of Carbon Capture and Utilization," *Key Engineering Materials*, V. 761, 2018, pp. 197-203. doi: 10.4028/www.scientific.net/KEM.761.197
30. Jain, J.; Atakan, V.; DeCristofaro, N.; Jeong, H.; and Olek, J., "Performance of Calcium Silicate Based Carbonated Concretes Vs. Hydrated Concretes Under Freeze-Thaw Environments," Solidia Technologies, 2015.
31. Villani, C.; Spragg, R.; Tokpatayeva, R.; Olek, J.; and Weiss, W. J., "Characterizing the Pore Structure of Carbonated Natural Wollastonite," 4th International Conference on the Durability of Concrete Structures, West Lafayette, IN, 2014.
32. Ashraf, W., and Olek, J., "Carbonation Behavior of Hydraulic and Non-Hydraulic Calcium Silicates: Potential of Utilizing Low-Lime Calcium Silicates in Cement-Based Materials," *Journal of Materials Science*, V. 51, No. 13, 2016, pp. 6173-6191. doi: 10.1007/s10853-016-9909-4
33. Ashraf, W.; Olek, J.; and Jain, J., "Microscopic Features of Non-Hydraulic Calcium Silicate Cement Paste and Mortar," *Cement and Concrete Research*, V. 100, 2017, pp. 361-372. doi: 10.1016/j.cemconres.2017.07.001
34. Ashraf, W.; Olek, J.; and Tian, N., "Multiscale Characterization of Carbonated Wollastonite Paste and Application of Homogenization Schemes to Predict Its Effective Elastic Modulus," *Cement and Concrete Composites*, V. 72, 2016, pp. 284-298. doi: 10.1016/j.cemconcomp.2016.05.023
35. Ashraf, W.; Olek, J.; and Sahu, S., "Phase Evolution and Strength Development During Carbonation of Low-Lime Calcium Silicate Cement (CSC)," *Construction and Building Materials*, V. 210, 2019, pp. 473-482. doi: 10.1016/j.conbuildmat.2019.03.038
36. Moradillo, M. K.; Ghantous, R. M.; Quinn, S.; Aktan, V.; Reese, S.; and Weiss, W. J., "Quantifying Drying and Carbonation in Calcium Silicate-Cement Systems Using Neutron Radiography," *ACI Materials Journal*, V. 119, No. 2, Mar. 2022, pp. 231-242.
37. Jain, J. A.; Seth, A.; and DeCristofaro, N., "Environmental Impact and Durability of Carbonated Calcium Silicate Concrete," *Proceedings of the Institution of Civil Engineers-Construction Materials*, V. 172, No. 4, 2019, pp. 179-191. doi: 10.1680/jcoma.17.00004
38. Farnam, Y.; Villani, C.; Washington, T.; Spence, M.; Jain, J.; and Weiss, J., "Performance of Carbonated Calcium Silicate Based Cement Pastes and Mortars Exposed to NaCl and MgCl₂ Deicing Salt," *Construction and Building Materials*, V. 111, 2016, pp. 63-71. doi: 10.1016/j.conbuildmat.2016.02.098
39. Villani, C.; Farnam, Y.; Washington, T.; Jain, J.; and Weiss, J., "Performance of Conventional Portland Cement and Calcium Silicate Based Carbonated Cementitious Systems During Freezing and Thawing in the Presence of Calcium Chloride Deicing Salts," *Transportation Research Record: Journal of the Transportation Research Board*, V. 2508, 2015, pp. 48-54.
40. Monical, J.; Villani, C.; Farnam, Y.; Unal, E.; and Weiss, W. J., "Using Low Temperature Differential Scanning Calorimetry to Quantify Calcium Oxychloride Formation for Cementitious Materials in the Presence of Calcium Chloride," *Advances in Civil Engineering Materials*, V. 5, No. 2, 2016, pp. 142-156. doi: 10.1520/ACEM20150024
41. Suraneni, P.; Azad, V. J.; Isgor, O. B.; and Weiss, W. J., "Deicing Salts and Durability of Concrete Pavements And Joints," *Concrete International*, V. 38, No. 4, Apr. 2016, pp. 48-54.
42. Ashraf, W. B.; Olek, J.; Jeong, H.; and Atakan, V., "Effects of High Temperature on Carbonated Calcium Silicate Cement (CSC) and Ordinary Portland Cement (OPC) Paste," *Proceedings of the 5th International Conference on Durability of Concrete Structures*, China, 2016.
43. Bažant, Z. P., and Najjar, L. J., "Nonlinear Water Diffusion in Nonsaturated Concrete," *Materiales de Construcción*, V. 5, No. 1, 1972, pp. 3-20.
44. ASTM C188-17, "Standard Test Method for Density of Hydraulic Cement," ASTM International, West Conshohocken, PA, 2017.
45. ASTM C778-17, "Standard Specification for Standard Sand," ASTM International, West Conshohocken, PA, 2017.
46. ASTM C494/C494M-19, "Standard Specification for Chemical Admixtures for Concrete," ASTM International, West Conshohocken, PA, 2019.
47. ASTM C305-14, "Standard Practice for Mechanical Mixing of Hydraulic Cement Pastes and Mortars of Plastic Consistency," ASTM International, West Conshohocken, PA, 2014.
48. Kaçal, M. R.; Akman, F.; Sayyed, M. I.; and Akman, F., "Evaluation of Gamma-Ray and Neutron Attenuation Properties of Some Polymers," *Nuclear Engineering and Technology*, V. 51, No. 3, 2019, pp. 818-824. doi: 10.1016/j.net.2018.11.011
49. Nuclear Data Services, "Evaluated Nuclear Data File (ENDF)," International Atomic Energy Agency, Vienna, Austria, <https://www-nds.iaea.org/exfor/endf.htm>. (last accessed Nov. 9, 2023)
50. Moradillo, M. K.; Montanari, L.; Suraneni, P.; Reese, S. R.; and Weiss, J., "Examining Curing Efficiency using Neutron Radiography," *Transportation Research Record: Journal of the Transportation Research Board*, V. 2672, No. 27, 2018, pp. 13-23. doi: 10.1177/0361198118773571
51. Moradillo, M. K.; Qiao, C.; Keys, M.; Hall, H.; Ley, M. T.; Reese, S.; and Weiss, W. J., "Quantifying Fluid Absorption in Air-Entrained Concrete Using Neutron Radiography," *ACI Materials Journal*, V. 116, No. 6, Nov. 2019, pp. 213-226. doi: 10.14359/51716980
52. Moradillo, M. K.; Qiao, C.; Isgor, B.; Reese, S.; and Weiss, W. J., "Relating the Formation Factor of Concrete to Water Absorption," *ACI Materials Journal*, V. 115, No. 6, Nov. 2018, pp. 887-898. doi: 10.14359/51706844
53. Moradillo, M. K.; Reese, S. R.; and Weiss, W. J., "Using Neutron Radiography to Quantify the Settlement of Fresh Concrete," *Advances in Civil Engineering Materials*, V. 8, No. 1, 2019, pp. 71-87. doi: 10.1520/ACEM20180086
54. Hussey, D. S.; Spernjak, D.; Weber, A. Z.; Mukundan, R.; Fairweather, J.; Brosha, E. L.; Davey, J.; Spendelow, J. S.; Jacobson, D. L.; and Borup, R. L., "Accurate Measurement of the Through-Plane Water Content of Proton-Exchange Membranes Using Neutron Radiography," *Journal of Applied Physics*, V. 112, No. 10, 2012, p. 13. doi: 10.1063/1.4767118
55. Weiss, W.; Geiker, M. R.; and Hansen, K. K., "Using X-ray Transmission/Attenuation to Quantify Fluid Absorption in Cracked Concrete," *International Journal of Materials and Structural Integrity*, V. 9, 1/2/3, 2015, pp. 3-20. doi: 10.1504/IJMSI.2015.071107
56. Schneider, C. A.; Rasband, W. S.; and Eliceiri, K. W., "NIH Image to ImageJ: 25 Years of Image Analysis," *Nature Methods*, V. 9, No. 7, 2012, pp. 671-675. doi: 10.1038/nmeth.2089
57. Kang, M.; Bilheux, H. Z.; Voisin, S.; Cheng, C. L.; Perfect, E.; Horita, J.; and Warren, J. M., "Water Calibration Measurements for Neutron Radiography: Application to Water Content Quantification in Porous Media," *Nuclear Instruments & Methods in Physics Research. Section A, Accelerators, Spectrometers, Detectors and Associated Equipment*, V. 708, 2013, pp. 24-31. doi: 10.1016/j.nima.2012.12.112
58. Barrett, E. P.; Joyner, L. G.; and Halenda, P. P., "The Determination of Pore Volume and Area Distributions in Porous Substances. I. Computations from Nitrogen Isotherms," *Journal of the American Chemical Society*, V. 73, No. 1, 1951, pp. 373-380. doi: 10.1021/ja01145a126
59. Leão, T. P., and Tuller, M., "Relating Soil Specific Surface Area, Water Film Thickness, and Water Vapor Adsorption," *Water Resources Research*, V. 50, No. 10, 2014, pp. 7873-7885. doi: 10.1002/2013WR014941
60. Rajabipour, F., and Weiss, J., "Electrical Conductivity of Drying Cement Paste," *Materials and Structures*, V. 40, No. 10, 2007, pp. 1143-1160. doi: 10.1617/s11527-006-9211-z
61. Tuller, M., and Or, D., "Water Films and Scaling of Soil Characteristic Curves at Low Water Contents," *Water Resources Research*, V. 41, No. 9, 2005, doi: 10.1029/2005WR004142
62. Garbalinska, H., "Application of \sqrt{t} -type, Logarithmic and Half-Time Methods in Desorptive Measurements of Diffusivity in Narrow Humidity Ranges," *Cement and Concrete Research*, V. 36, No. 7, 2006, pp. 1294-1303. doi: 10.1016/j.cemconres.2006.01.007
63. Villani, C.; Spragg, R.; Pour-Ghaz, M.; and Weiss, W. J., "The Role of Deicing Salts on the Non-Linear Moisture Diffusion Coefficient of Cementitious Materials During Drying," The 10th International Symposium on Brittle Matrix Composites, Warsaw, Poland, 2012, pp. 101-114.
64. Burg, S. P., *Postharvest Physiology and Hypobaric Storage of Fresh Produce*, CABI, Miami, FL, 2004.
65. "Gases Solved in Water - Diffusion Coefficients," The Engineering Toolbox, https://www.engineeringtoolbox.com/diffusion-coefficients-d_1404.html. (last accessed Nov. 9, 2023)
66. "Air - Diffusion Coefficients of Gases in Excess of Air," The Engineering Toolbox, https://www.engineeringtoolbox.com/air-diffusion-coefficient-gas-mixture-temperature-d_2010.html. (last accessed Nov. 9, 2023)
67. Crank, J., *The Mathematics of Diffusion*, Oxford University Press, Oxford, UK, 1979.
68. Mehdipour, I.; Falzone, G.; La Plante, E. C.; Simonetti, D.; Neithalath, N.; and Sant, G., "How Microstructure and Pore Moisture Affect Strength Gain in Portlandite-Enriched Composites That Mineralize CO₂,"

- ACS Sustainable Chemistry & Engineering*, V. 7, No. 15, 2019, pp. 13053-13061. doi: 10.1021/acssuschemeng.9b02163
69. Tuuti, K., "Corrosion of Steel in Concrete," doctoral thesis, Swedish Cement and Concrete Research Institute, Stockholm, Sweden, 1982, 145 pp.
70. Verbeck, G. J., "Carbonation of Hydrated Portland Cement," Cement and Concrete special Technical Publication, V. 205, 1958, pp. 17-36.
71. Galan, I.; Andrade, C.; and Castellote, M., "Natural and Accelerated CO₂ Binding Kinetics in Cement Paste at Different Relative Humidities," *Cement and Concrete Research*, V. 49, 2013, pp. 21-28. doi: 10.1016/j.cemconres.2013.03.009
72. Papadakis, V. G.; Vayenas, C. G.; and Fardis, M. N., "Experimental Investigation and Mathematical Modeling of the Concrete Carbonation Problem," *Chemical Engineering Science*, V. 46, No. 5-6, 1991, pp. 1333-1338. doi: 10.1016/0009-2509(91)85060-B
73. jae-dong, J.; Hirai, K.; and Mihashi, H., "Influence of Environmental Moisture and Temperature on Carbonation of Mortar," *Concrete Research and Technology*, V. 1, No. 1, 1990, pp. 85-94. doi: 10.3151/crt1990.1.1_85
74. Houst, Y. F., and Wittmann, F. H., "Depth Profiles of Carbonates Formed During Natural Carbonation," *Cement and Concrete Research*, V. 32, No. 12, 2002, pp. 1923-1930. doi: 10.1016/S0008-8846(02)00908-0
75. Thiery, M., "Modélisation de la carbonatation atmosphérique des matériaux cimentaires. Prise en compte des effets cinétiques et des modifications microstructurales et hydriques," PhD thesis, Études et recherches des laboratoires des ponts et chaussées-série ouvrages d'art, 2006, 331 pp.
76. Papadakis, V. G.; Fardis, M. N.; and Vayenas, C. G., "Hydration and Carbonation of Pozzolanic Cements," *ACI Materials Journal*, V. 89, No. 2, Mar.-Apr. 1992, pp. 119-130.
77. Bažant, Z. P., and Najjar, L. J., "Drying of Concrete as a Nonlinear Diffusion Problem," *Cement and Concrete Research*, V. 1, No. 5, 1971, pp. 461-473. doi: 10.1016/0008-8846(71)90054-8

We're Building the Future

Mission: We make strategic investments in ideas, research, and people to create the future of the concrete industry

Through its councils and programs, the ACI Foundation helps to keep the concrete industry at the forefront of advances in material composition, design, and construction. Our focus:



Our Concrete Innovation Council identifies technologies and innovation that are aligned with ACI and industry strategies and helps facilitate their use when appropriate



Our Concrete Research Council advances the knowledge and sustainable aspects of concrete materials, construction, and structures by soliciting, selecting, financing, and publishing research



Our Scholarship Council supports our future concrete innovators and leaders by administering fellowships and scholarships to help bridge the financial gap for students



Our Veterans Rebate for ACI Certification program helps honorably discharged veterans and increases skills in the industry's workforce. ACICertification.org/veteranrebate



Title No. 120-M63

Numerical Compressive Toughness of Steel Fiber-Based Reinforced Concrete with Various Densities

by Hak-Young Kim, Hye-Jin Lee, Keun-Hyeok Yang, and Seung-Jun Kwon

A reliable compressive stress-strain model was established for concrete with varying densities reinforced with either steel fibers alone, or a combination of steel fibers and micro-synthetic fibers. Moreover, a simple equation was presented to determine the compressive toughness index of fiber-reinforced concrete in a straightforward manner. The fiber reinforcing index was introduced to explain the effect of various parameter conditions of fibers on the enhancement of the concrete properties under compression. Numerical and regression analyses were performed to derive equations to determine the key parameter associated with the slope at the pre- and post-peak branches and compressive toughness index through extensive parametric studies. The proposed models are promising tools to accurately predict the stress-strain relationships of fiber-reinforced concrete with different densities, resulting in less-scattered values between experiments and predictions, and reasonably assess the efficiency of fiber reinforcements in enhancing the compressive response of concrete.

Keywords: compressive toughness; concrete density; fiber reinforcing index; stress-strain relationship.

INTRODUCTION

The use of fiber reinforcement in concrete structures has attracted increasing attention since the 1970s to enhance the unsatisfactory properties of concrete, such as low tensile and crack resistances, non-negligible shrinkage deformation, and low-ductility post-peak failure.^{1,2} Compared with synthetic and inorganic mineral fibers, steel fibers are more commonly used owing to their advantages in terms of economics, manufacturing facilities, reinforcement effects, and resistance to environmental factors.³⁻⁵ Moreover, the use of steel fibers in combination with microfibers such as polypropylene (PP), nylon, polyvinyl alcohol (PVA), and polyethylene (PE) fibers can help enhance the synergistic effect for controlling crack propagations at different loading levels and the hardening or plastic flow performance at the post-peak branch of the load-displacement relationship of concrete elements.⁶⁻¹⁰ However, the practical application of fiber-reinforced concrete for building structures is limited due to the lack of design approaches in code provisions and analytical models to reasonably explain the effect of the fibers on the post-peak responses of structural concrete elements, even for steel fiber-reinforced concrete.

The design and analysis of structural elements necessitates reliable constitutive models of concrete. In particular, the compressive stress-strain relationship of unconfined concrete is required to predict the ultimate strength and post-peak performance of reinforced concrete structures. Additionally, the compressive toughness index of fiber-reinforced

concrete is commonly calculated from the stress-strain relationship.¹¹ Notably, the characteristics of the stress-strain relationship are significantly affected by the compressive strength and density of concrete.¹² For example, concrete designed to have a higher strength and lower density exhibits a steeper slope at the descending branch of the stress-strain curve, indicating a more brittle post-peak failure. Thus, at the same compressive strength, structural lightweight aggregate concrete (LWAC) exhibits a lower modulus of elasticity and toughness index compared to those of normalweight concrete (NWC).^{13,14} The use of fibers can help enhance the slopes at the pre-peak and post-peak branches of the stress-strain relationship of concrete.¹³⁻¹⁶ The effectiveness of fibers in improving the post-peak performance is more prominent for LWAC than NWC.¹⁴ This aspect can be attributed to the fact that the bridging action of fibers can restrict the cracks from opening up instead of the aggregate interlock action, which is not likely to develop for LWAC due to the fracture of lightweight aggregate particles along the crack plane.¹⁷ Overall, the existing models developed for fiberless concrete cannot be used to evaluate the compressive stress-strain relationship of fiber-reinforced concrete.

Most of the recent models¹⁸⁻²¹ for the compressive stress-strain relationship have focused on fiberless NWC, and extremely few analytical studies^{22,23} have been performed for fiber-reinforced concrete, especially fiber-reinforced LWAC.¹⁴ The stress-strain characteristics of fiber-reinforced concrete are affected by various parameters, including the length, deformed shape, aspect ratio, tensile and bond strengths, and surface treatment of fibers, as well as the mixture proportions, including the fiber content, water-cementitious materials ratio (w/cm), and content and type of aggregate particles. Liu et al.¹⁴ empirically proposed a stress-strain model by statistically fitting a damage parameter into test results obtained from nine LWAC specimens reinforced with steel and/or carbon fibers with volumetric fractions ranging between 0 and 0.9%. Nataraja et al.²² modified Carreira and Chu's model²⁴ certifying the parabola curve for fiberless NWC by performing a regression analysis using data sets experimentally obtained for 14 steel fiber-reinforced NWC specimens to consider the effect of the fiber content on the slopes of the pre- and post-peak branches.

Mansur et al.²³ tested the stress-strain behavior of high-strength (70 to 120 MPa [10.2 to 17.4 ksi]) NWC reinforced with conventional hooked-end steel fibers to examine the effect of the aspect ratio and volumetric fraction of the fibers on the improvement of the post-peak branches. However, these existing models were developed based on limited test data. Hence, it is necessary to establish a more comprehensive model that can enhance the scope of application and improve the accuracy of predictions, considering the diverse design conditions of fibers in concrete with different densities.

One of the primary objectives of using fibers in concrete is to enhance its toughness and ductility. Compressive toughness is a key parameter that represents the material's ability to withstand compressive forces without exhibiting rapid failure characteristics. Enhancing the compressive toughness of concrete allows it to absorb more energy before failure, resulting in better performance and increased ductility.²⁵ Therefore, understanding the compressive toughness of fiber-reinforced concrete is crucial for designing structures that can withstand high compressive loads without experiencing premature failure.

This study aimed to establish two reliable design models: 1) the compressive stress-strain relationship of concrete with different densities reinforced either using steel fibers alone or using a combination of steel fibers and micro-synthetic fibers; and 2) a simple equation to determine the compressive toughness index of fiber-reinforced concrete in a straightforward manner. To consider the effect of fibers on the improvement of the compressive response, a reinforcing index of fiber was introduced in the stress-strain model generalized by Yang et al.¹² for fiberless concrete. To this end, a regression analysis was performed based on test data sets compiled from a wide variety of fiber-reinforced concrete specimens. Furthermore, an extensive parametric study was conducted using the proposed stress-strain relationship to formulate the compressive toughness index of the fiber-reinforced concrete in accordance with ASTM C1018-97.¹¹ The reliability of the proposed models was confirmed through a comparative analysis with the experimental data and existing equations.

RESEARCH SIGNIFICANCE

While design models rationally realizing the compressive stress-strain relationship of fiber-reinforced concrete are still limited, this study proposed a general model to explain the effectiveness of fibers on the stress-strain response of concrete with different densities. This study also proved that the addition of fibers exceeding a specific limit is insignificant in enhancing the toughness of concrete, although the upper limit for the fiber addition depends on the density and compressive strength of concrete. The formulated equation for the compressive toughness index is promising for fiber design to achieve the targeted compressive ductility of concretes with different densities.

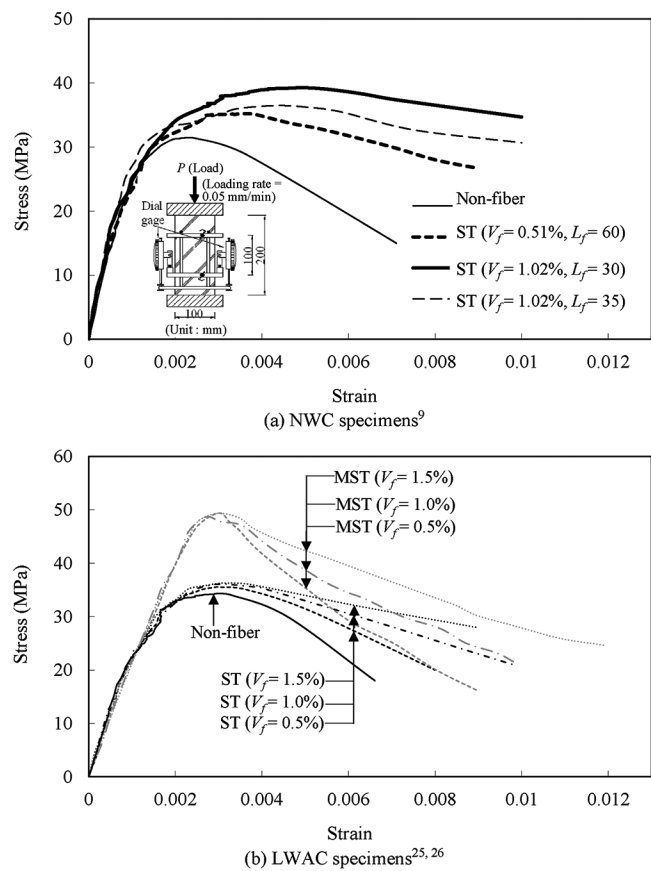


Fig. 1—Typical stress-strain curves of steel fiber-reinforced concrete.

MATHEMATICAL GENERALIZATION FOR STRESS-STRAIN RELATIONSHIP

Basic equation

Figure 1 shows the typical stress-strain curves of steel fiber-reinforced concrete specimens tested by Kim et al.²⁵ and Yang.^{9,26} The stress-strain relationship can be characterized as follows: 1) the initial slope at the pre-peak branch corresponds to a nearly linear response, regardless of the fiber content; 2) the effect of fiber on the slope at the pre-peak branch is insignificant; 3) the pre-peak branch begins to display a distinct nonlinear response at 60 to 75% peak stress due to the initiation of microcracks; 4) the strain at the peak stress increases with the increase in the compressive strength of concrete and fiber content and decrease in the concrete density (ρ_c); 5) the stress rapidly decreases beyond the strain corresponding to the peak stress, exhibiting a softening response; and 6) the slope at the post-peak branch is steeper for concrete with a lower density and higher compressive strength, whereas the slope is improved with the increase in the content and aspect ratio of fibers. Thus, the stress-strain curve of fiber-reinforced concrete resembles a parabola with its vertex at the peak stress. This finding indicates that the tangential modulus of elasticity gradually decreases from a maximum value at the origin to zero at the peak stress, beyond which the modulus becomes negative at the post-peak branch. Yang et al.¹² considered this physical meaning when deriving a complete curve to represent the typical stress-strain relationship and proposed the following general

Table 1—Frequency distribution of main parameters in separate databases for fiber-reinforced concrete

Parameters		Details for LWAC (total of 45 specimens)					Details for NWC (total of 35 specimens)				
f'_c	MPa	≤30.0	30.1 to 40.0	40.1 to 50.0	50.1 to 60.0	>60.1	≤30.0	30.1 to 40.0	40.1 to 50.0	50.1 to 60.0	>60.1
	Number	3	6	20	8	8	14	3	4	8	6
ρ_c	kg/m ³	≤1700	1701 to 1750	1751 to 1800	1801 to 1850	1851 to 1900	Approximately 2300				
	Number	5	11	8	16	5					
Fiber properties	Type	Straight steel	Deformed steel	Carbon	PP	Hybrid	Steel	PP	Hybrid		
	Number	6	19	5	2	13	9	2	16	4	4
	$\sum V_f, \%$	≤0.49	0.50 to 0.60	0.61 to 0.80	0.81 to 1.00	1.01 to 1.50	≤0.49	0.50 to 0.60	0.61 to 0.80	0.81 to 1.50	1.51 to 2.00
	Number	10	10	3	15	7	9	10	4	3	9
	β_f	<0.3	0.3 to 0.5	0.5 to 1.0	1.0 to 2.0	>2.0	<0.3	0.3 to 0.5	0.5 to 1.0	1.0 to 2.0	>2.0
	Number	7	7	9	16	6	1	2	10	15	7

Note: 1 kg/m³ = 0.0624 lb/ft³; 1 MPa = 145 psi.

form with the key parameter β_1 , which is associated with the slopes of the pre-peak and post-peak branches

$$y = \frac{(\beta_1 + 1)x}{x^{\beta_1+1} + \beta_1} \quad (1)$$

where $y (= f'_c/f_c')$ is the normalized stress; $x (= \varepsilon_c/\varepsilon_{0f})$ is the normalized strain; f'_c is the compressive strength of concrete; ε_{0f} is the strain at f'_c of fiber-reinforced concrete; and f_c is the concrete stress corresponding to strain ε_c .

In general, the modulus of elasticity of concrete is defined as the slope of the form joining the origin and point of $0.4f'_c$ at the pre-peak response.¹² It has been reported²⁷ that the uncertainty of measurement at the softening response increases when the strain exceeds the point corresponding to $0.5f'_c$. Thus, Yang et al. selected the secant moduli of $0.4f'_c$ at the pre-peak response and $0.5f'_c$ at the post-peak softening response as reference points to determine the value of β_1 . Applying the reference points to Eq. (1), β_1 for fiber-reinforced concrete can be formulated as follows

$$0.4(X_a)^{\beta_1+1} + (0.4 - X_a)\beta_1 - X_a = 0 \text{ for } \varepsilon_c \leq \varepsilon_{0f} \quad (2a)$$

$$(X_d)^{\beta_1+1} + (1 - 2X_d)\beta_1 - 2X_d = 0 \text{ for } \varepsilon_c > \varepsilon_{0f} \quad (2b)$$

where $X_a = 0.4f'_c/(E_{cf}\varepsilon_{0f})$; $X_d = \varepsilon_{0.5f}/\varepsilon_{0f}$; E_{cf} is the modulus of elasticity of the fiber-reinforced concrete; and $\varepsilon_{0.5f}$ is the strain corresponding to $0.5f'_c$ at the post-peak branch of fiber-reinforced concrete. Once the material properties of E_{cf} , ε_{0f} , and $\varepsilon_{0.5f}$ are known, β_1 can be determined from the numerical analysis solution of Eq. (2).

The modulus of elasticity (E_c), strain (ε_0) at the peak stress, and strain ($\varepsilon_{0.5}$) corresponding to $0.5f'_c$ for conventional fiberless concrete are commonly expressed as a function of f'_c and ρ_c . For fiber-reinforced concrete, these properties are affected by the type, content, aspect ratio, and interfacial

bond strength of fibers. For example, the values of E_{cf} , ε_{0f} , and $\varepsilon_{0.5f}$ tend to increase with the increase in the aspect ratio and volume fraction of steel fibers, as shown in Fig. 1. This phenomenon implies that numerous parameters must be considered to determine the values of E_{cf} , ε_{0f} , and $\varepsilon_{0.5f}$ for fiber-reinforced concrete. However, the available experimental data for such mechanical properties of concrete reinforced with various fibers are scarce compared with the database for fiberless concrete, as indicated in Table 1. Hence, in this study, the increment in E_c , ε_0 , and $\varepsilon_{0.5}$ owing to the addition of fibers relative to the values determined from the equations for fiberless concrete proposed by Yang et al. were considered through a regression analysis based on experimental data sets. Furthermore, a fiber reinforcing index (β_f) was introduced as a dimensionless parameter to explain the effect of various parameter conditions of fiber on the enhancement in the concrete properties under compression

$$\beta_f = \sum_{i=1}^n g_i V_{fi} S_{fi}^{0.1} \sqrt{\tau_i/f'_c} \quad (3)$$

where i is the type of fiber in each concrete specimen; g is the snubbing factor of discontinuous fibers; τ is the interfacial bond strength of the fiber against the cement matrix; and V_f and S_f are the volumetric fraction and aspect ratio of fiber, respectively. Notably, this index is a modified form of that defined by Yang⁹ to reflect the reduced efficiency of fibers in concrete with a higher compressive strength and consider the overestimation of the reinforcement effectiveness of micro-synthetic or inorganic mineral fibers with an extremely high aspect ratio, in terms of restricting the opening of macroracks. Moreover, it is challenging to reasonably measure the values of g and τ of fibers because the bridging action of discontinuous fibers depends on numerous parameters, such as the orientation, dispersion, and length of fibers, workability of concrete, and interlocking friction between the fibers and aggregates or cement matrix. In this

Table 2—Typical mechanical properties of different fibers

Type	ρ_f , MPa	F_f , MPa	E_f , GPa	τ , MPa
PP ²	0.91 (0.90 to 0.95)	>400 (60 to 700)	4.2 (1.5 to 10.0)	
PVA ²	1.3 (approximately 1.3)	>1200 (850 to 1600)	27.6 (25 to 41)	1.02
Carbon ²	1.8 (1.60 to 1.90)	>4000 (1500 to 7000)	240 (30 to 500)	4.5
Steel fiber ²⁵	Straight	7.85 (approximately 7.8)	2600 (2100 to 2800)	8.6
	Crimped			11.2
	Hooked-end			16.2 ($d_f > 0.2$ mm) 18.7 ($d_f \leq 0.2$ mm)

Note: ρ_f , F_f , E_f , and τ denote density, modulus of fiber elasticity, tensile strength, and interfacial bond strength between fiber and cement matrix, respectively. Values in parentheses refer to common ranges considered in previous studies. 1 MPa = 145 psi; 1 GPa = 145 ksi; 1 mm = 0.039 in.

study, g was set as 2.9 and 2.0 for steel and micro-synthetic fibers, respectively, considering the typical snubbing effect observed in the fiber pullout tests conducted by Li et al.²⁸ For the bond strength of fibers, the experimental values available in the literature were considered; if the value was unavailable, average values^{2,25} were selected from the commonly occurring ranges summarized in Table 2.

Modulus of elasticity (E_{cf})

The modulus of elasticity (E_c) of fiberless concrete depends on the compressive strength of the cement matrix and the stiffness, strength, and content of the aggregates.^{29,30} Yang et al. empirically formulated E_c as a function of f'_c and ρ_c from a regression analysis based on 2680 data sets for NWC, 370 data sets for LWAC with ρ_c ranging from 1200 to 2000 kg/m³ (74.9 to 124.9 lb/ft³), and 245 data sets for heavyweight concrete with ρ_c ranging from 2500 to 4450 kg/m³ (156.1 to 277.8 lb/ft³). In general, the addition of steel fibers can lead to a slight increase in the modulus of elasticity of concrete⁹ because of the higher stiffness of steel compared to that of concrete. To examine the rate of increase of the modulus of elasticity, E_{cf} of fiber-reinforced concrete was normalized by E_c predicted from the equation proposed by Yang et al. for fiberless concrete and then plotted as a function of β_f (Fig. 2). For the database to examine E_{cf} ,^{9,14,31-36} the ranges of the main parameters were as follows: f'_c ranged from 24.8 to 67.3 MPa (3.6 to 9.76 ksi) for NWC and from 11.9 to 78.5 MPa (1.72 to 11.39 ksi) for LWAC; ρ_c ranged from 1498 to 1846 kg/m³ (93.5 to 115.2 lb/ft³) for LWAC, V_f ranged from 0.32 to 2.0% for NWC and from 0.2 to 1.5% for LWAC, S_f ranged from 37.5 to 541 for NWC and from 58 to 1285 for LWAC, and β_f ranged from 0.027 to 1.73 for NWC and from 0.009 to 1.84 for LWAC, as summarized in Table 1. All the concrete specimens were reinforced with single steel fibers or hybrid steel fibers with synthetic fibers. The normalized E_{cf}/E_c slightly increased in proportion to β_f . This trend was consistent across concrete types. Through a linear regression analysis of the data sets plotted in Fig. 2, E_{cf} could be expressed as follows

$$E_{cf} = (0.098\beta_f + 1)E_c = (0.098\beta_f + 1)\left[8470(f'_c)^{1/3}\left(\frac{\rho_c}{\rho_0}\right)^{1.17}\right] \text{ (MPa)} \quad (4)$$

where ρ_0 (= 2300 kg/m³ [143.58 lb/ft³]) is a reference value for the concrete density. Equation (4) indicates that the

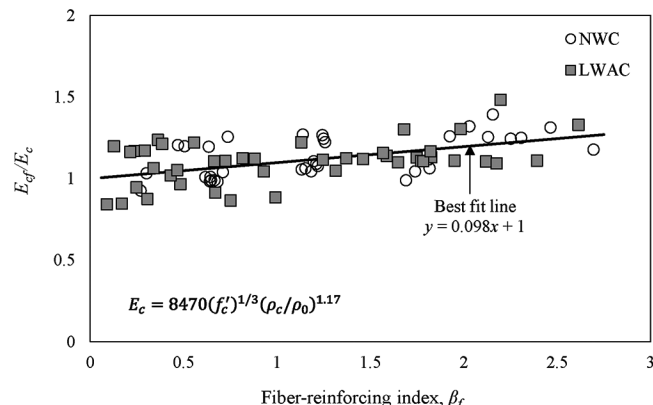


Fig. 2—Modulus of elasticity of fiber-reinforced concrete.

efficiency of fibers in enhancing the modulus of elasticity of concrete is marginally affected by f'_c and ρ_c .

Strain at peak stress (ϵ_{0f})

Most of the existing stress-strain models^{14,18-20} for fiberless concrete formulate ϵ_0 as a function of f'_c through a regression analysis based on NWC test data, and extremely few studies have been conducted to examine the effect of fiber reinforcement on the increase in the strain at the peak stress. Liu et al.¹⁴ presented ϵ_{0f} of fiber-reinforced LWAC as a function of f'_c from a regression analysis based on limited test data, as summarized in Table 3. Specifically, this equation did not consider the effect of the fiber on the strain, although the regression analysis included fiber-reinforced LWAC specimens. Nataraja et al.²² presented ϵ_{0f} of steel fiber-reinforced concrete as $(\epsilon_0 + 0.0006w_f S_f)$, where w_f is the weight fraction of steel fibers. Mansur et al.²³ expressed ϵ_{0f} for high-strength concrete reinforced with hooked-end steel fibers, considering the test parameters of f'_c , V_f , and S_f . The existing models indicate that the strain at the peak stress increases with the increase in f'_c . Moreover, the low stiffness of lightweight aggregate particles results in a lower modulus of elasticity of concrete, which leads to a greater strain at the peak stress. This phenomenon implies that the concrete density affects the value of ϵ_{0f} , although this observation has not been considered in the existing models. To formulate a reliable model for ϵ_{0f} , test data sets were compiled from the literature^{9,14,31-36} and a regression analysis was conducted, similar to the approach for E_{cf} . To account for the lack of data sets, the measured values of ϵ_{0f} were normalized by the

Table 3—Existing stress-strain models for fiber-reinforced concrete

Researcher	Equations
Liu et al. ¹⁴	$f_c = a\epsilon_c + (3 - 2a)\epsilon_c^2 + (a - 2)\epsilon_c^3 \text{ for } \epsilon_c \leq \epsilon_{0f};$ $f_c = \frac{k_1 \beta \epsilon_c}{k_1 \beta - 1 + \epsilon_c^{k_1 \beta}} \text{ for } \epsilon_c > \epsilon_{0f};$ $a = 1.797 E_{cf}/E_f - 1.264; \beta = 1/[1 - (f'_c/\epsilon_c E_{cf})];$ $E_{cf} = 5681.6 f'_c^{0.403} (\rho_c/2250)^{1.146};$ $\epsilon_{0f} = 3.496 \times 10^{-5} \times f'_c + 0.001.$ <p>For carbon fiber, $k_1 = 1.343 V_f + 0.108 f'_c - 6.811;$ $k_2 = 0.715 V_f + 0.048 f'_c - 2.538;$</p> <p>For steel fiber, $k_1 = -0.22 V_f - 0.017 f'_c + 1.758;$ $k_2 = 0.299 V_f + 0.014 f'_c - 0.505.$</p> <p>This model was based on LWAC specimens reinforced with either carbon or steel fibers.</p>
Nataraja et al. ²²	$f_c = \frac{\beta(\epsilon_c/\epsilon_{0f})}{\beta - 1 + (\epsilon_c/\epsilon_{0f})^\beta} \cdot f'_c;$ $\epsilon_{0f} = \epsilon_0 + 0.0006 R I; \beta = 0.5811 + 1.93 R I^{-0.7406}, R I = w_f S_f;$ <p>w_f is the weight fraction of the fiber.</p> <p>This model was based on NWC specimens reinforced with conventional crimped macro-steel fibers.</p>
Mansur et al. ²³	$f_c = f'_c \left[\frac{\beta(\epsilon_c/\epsilon_{0f})}{\beta - 1 + (\epsilon_c/\epsilon_{0f})^\beta} \right] \text{ for } \epsilon_c \leq \epsilon_{0f};$ $f_c = f'_c \left[\frac{k_1 \beta (\epsilon_c/\epsilon_{0f})}{k_1 \beta - 1 + (\epsilon_c/\epsilon_{0f})^{k_1 \beta}} \right] \text{ for } \epsilon_c > \epsilon_{0f};$ $E_{cf} = (10,300 - 400 V_f) f_c^{1/3};$ $\epsilon_{0f} = [0.0005 + 0.00000072 (V_f S_f)] f_c^{0.35};$ $\beta = \frac{1}{1 - \frac{f'_c}{\epsilon_{0f} E_{cf}}};$ $k_1 = (50/f'_c)^{3.0} [1 + 2.5 (V_f S_f)^{2.5}];$ $k_2 = (50/f'_c)^{1.3} [1 - 0.11 (V_f S_f)^{-1.1}].$ <p>This model was based on NWC specimens reinforced with conventional hooked-end macro-steel fibers.</p>

ϵ_0 values calculated from the equation proposed by Yang et al. for fiberless concrete, as presented in Fig. 3. Although a certain degree of scatter of data points occurred inevitably because of different sources for data collection, ϵ_{0f} could be expressed as follows (Fig. 3)

$$\epsilon_{0f} = (0.93 \beta_f + 1)[0.0016 \exp\{240(f'_c/E_c)\}] \quad (5)$$

Strain ($\epsilon_{0.5f}$) at 50% of peak stress at post-peak branch

In general, the slope at the post-peak branch of the stress-strain curve significantly depends on the brittleness of concrete. Thus, Yang et al. considered f'_c and ρ_c in formulating $\epsilon_{0.5f}$. Moreover, the addition of fibers improves the post-peak response of concrete with less brittle failure characteristics, as shown in Fig. 1. However, it is challenging to determine the slope at the post-peak branch for fiber-reinforced concrete. None of the existing studies have clarified the slope at the post-peak branch for fiber-reinforced concrete. In this study, the measured values of $\epsilon_{0.5f}$ were normalized by $\epsilon_{0.5}$ calculated using Yang et al.'s equation for fiberless concrete to derive a simple closed-form equation for $\epsilon_{0.5f}$, as presented in Fig. 4. According to the regression

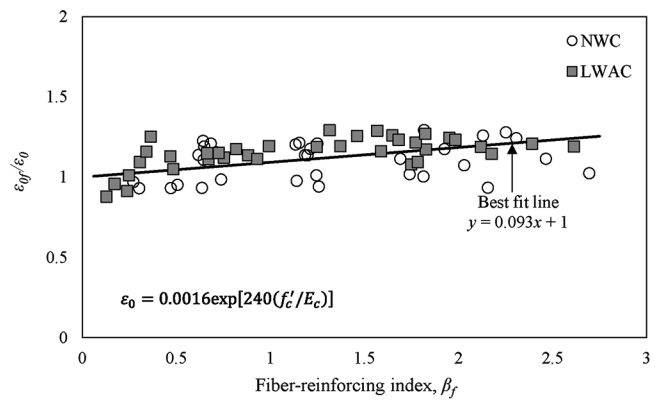


Fig. 3—Strains at peak stress of fiber-reinforced concrete.

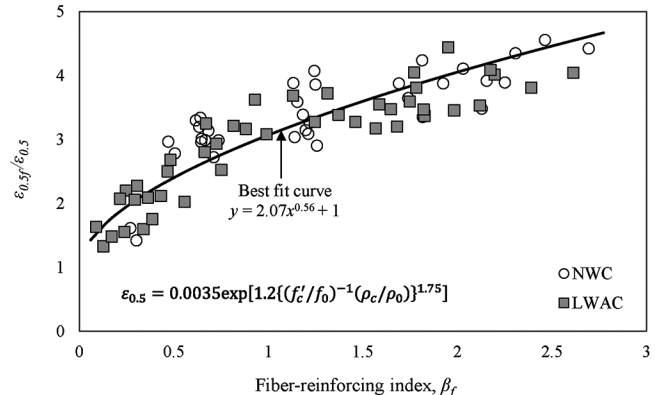


Fig. 4—Strains at 50% peak stress at descending branch of fiber-reinforced concrete.

analysis based on data sets^{9,14,31-36} compiled from 35 NWC and 41 LWAC specimens, $\epsilon_{0.5f}$ could be formulated as follows

$$\epsilon_{0.5f} = (2.07 \beta_f^{0.56} + 1) 0.0035 \exp\left[1.2 \left\{ (f'_c/f_0)^{-1} (\rho_c/\rho_0) \right\}^{1.75}\right] \quad (6)$$

where f_0 (= 10 MPa [1.45 ksi]) is a reference value for the concrete compressive strength.

Parameter β_1

To set β_1 in Eq. (1), an analytical parametric study was performed with the following ranges of main variables: f'_c (10 to 80 MPa [1.45 to 11.6 ksi]); ρ_c (1500 to 2300 kg/m³ [93.6 to 143.6 lb/ft³]); and β_f (0.1 to 2.7). For the selected variables, E_{cf} , ϵ_{0f} , and $\epsilon_{0.5f}$ were calculated using the equations presented in the preceding subsections and substituted into Eq. (2). The solution of Eq. (2) was numerically obtained using the Newton-Raphson method. Thus, the analytically obtained results were optimized through a nonlinear regression analysis to derive the following best-fit equations for β_1 (Fig. 5)

$$\beta_1 = 0.15 \exp(0.86 \xi) \text{ for } \epsilon_c \leq \epsilon_{0f} \quad (7a)$$

$$\beta_1 = 0.34 \exp(0.35 \xi) \text{ for } \epsilon_c > \epsilon_{0f} \quad (7b)$$

where ξ is defined as $(f'_c/f_0)^{0.47} (\rho_c/\rho_0)^{-0.8} (\beta_f)^{-0.18}$ to simplify β_1 .

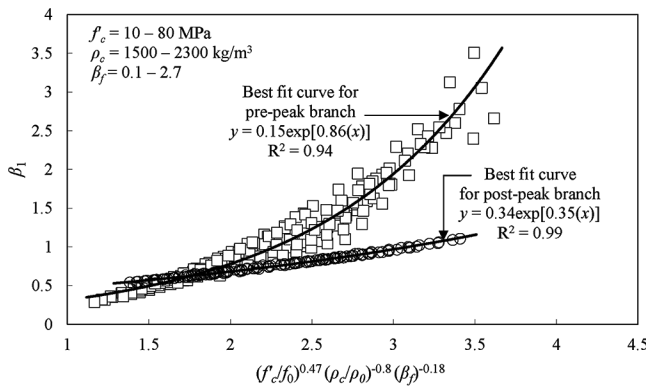


Fig. 5—Regression analysis for parameter β_1 . (Note: $1 \text{ kg/m}^3 = 0.0624 \text{ lb/ft}^3$; $1 \text{ MPa} = 145 \text{ psi}$.)

Verification of proposed model

Experimental stress-strain curves were compiled from the literature^{9,14,31-36} and compared with the analytical models proposed by Liu et al.,¹⁴ Nataraja et al.,²² Mansur et al.,²³ and the proposed model. The data sets containing fiber-reinforced concrete included data of 35 LWAC and 45 NWC specimens. In general, experimental stress-strain research for fiber-reinforced concrete is limited compared to that for fiberless concrete. For the fiber-reinforced LWAC data sets, f'_c , ρ_c , and β_f varied from 24.8 to 67.3 MPa (3.6 to 9.76 ksi), from 1498 to 1886 kg/m³ (93.5 to 117.7 lb/ft³), and from 0.1 to 2.65, respectively. The corresponding ranges for fiber-reinforced NWC data sets were from 11.9 to 78.5 MPa (1.72 to 11.39 ksi), from 2300 and 2420 kg/m³ (143.6 to 151.1 lb/ft³), and from 0.12 to 2.7. Figure 6 shows the comparisons of the analytically and experimentally obtained curves. The curves selected for the comparisons covered different strength categories and fiber-reinforcement effectiveness for each type of concrete. The reliability of the proposed model was examined considering the normalized root-mean-square error (NRMSE) calculated for each stress-strain curve, as summarized in Table 4. Note that the use of hybrid fibers, specifically steel and synthetic fibers, in concrete has been shown to offer a better post-peak response of the stress-strain curve over using either fiber type individually. Steel fibers with a relatively longer length are effective for controlling macrocrack propagation and enhancing the post-cracking behavior of concrete. Synthetic fibers with a relatively shorter length and smaller diameter can be well dispersed in concrete, which can contribute to improving the resistance to the propagation of internal splitting cracking due to transverse tensile stresses. Thus, the use of a combination of these two types of fibers can offer superior mechanical properties and better stress-strain performance than using either fiber type individually.

Liu et al.'s¹⁴ model does not consider the effect of fiber reinforcement on the increase in E_c and ϵ_0 , whereas the slope of the stress-strain curve is expressed as a linear function of V_f and f'_c , as summarized in Table 3. Thus, the accuracy of this model fluctuates considerably depending on ρ_c and the steel fiber content (Fig. 6(a)). For concrete with $\beta_f \approx 0.2$, this model tends to overestimate the slopes at the pre-peak and yields a steeper slope at the post-peak branches of the stress-strain curve. Furthermore, this model underestimates the slopes at

the pre-peak for concrete with $\beta_f \geq 1.0$ and yields smaller predictions at the post-peak branch than the values obtained experimentally for this type of concrete. The inconsistency of this model becomes more notable for LWAC with a smaller V_f . The mean ($\gamma_{e,m}$) and standard deviation ($\gamma_{e,s}$) of the NRMSEs determined from this model are 0.401 and 0.124, respectively, for fiber-reinforced LWAC. The corresponding values for fiber-reinforced NWC are 0.355 and 0.178.

Nataraja et al.²² used 14 test specimens to formulate ϵ_0f and the slope at the post-peak branch of the stress-strain relationship of steel fiber-reinforced NWC with a compressive strength not exceeding 50 MPa (7.25 ksi). Because of the limited test data sets, this model (Fig. 6(b)) frequently yields smaller predictions at the post-peak branch than the values obtained experimentally, regardless of the value of β_f . Additionally, the inconsistency of this model becomes more notable for LWAC with f'_c exceeding approximately 30 MPa (4.35 ksi). This model provides slightly lower values of $\gamma_{e,m}$ and $\gamma_{e,s}$ than those obtained using Liu et al.'s model.

Mansur et al.²³ modified the Carreira and Chu²⁴ model to describe the effect of hooked-end steel fibers in enhancing the slopes of pre-peak and post-peak branches by performing a regression analysis using 18 high-strength NWC data sets. Notably, this model does not reasonably represent the shape of the stress-strain curves for LWAC reinforced with different types of fibers. Similar to the predictions obtained using Liu et al.'s model, this model (Fig. 6(c)) overestimates the slope at the pre-peak branch for concrete with $\beta_f \approx 0.2$ and yields steeper slopes at the post-peak branch for concrete with $\beta_f \geq 1.0$. The values of $\gamma_{e,m}$ and $\gamma_{e,s}$ of the NRMSEs obtained from this model are 0.430 and 0.123, respectively, for fiber-reinforced LWAC, and 0.292 and 0.125, respectively, for fiber-reinforced NWC, indicating an unsatisfactory agreement for the former concrete type. Overall, the existing models cannot reliably estimate the stress-strain relationship of LWAC reinforced with different types of fibers.

In contrast, the proposed model (Fig. 6(d)) can accurately predict the slopes at the pre-peak and post-peak branches, regardless of the variations in ρ_c and type and content of fibers. Thus, the calculated stress-strain relationships correspond well with the measured curves, and the values of E_{cf} , ϵ_0f , and $\epsilon_{0,5f}$ increase with the increase in the content and aspect ratio of fibers, resulting in greater slopes at the pre-peak branch and smaller rates of decrease of the stress at the post-peak branch for concrete with greater β_f . The values of $\gamma_{e,m}$ and $\gamma_{e,s}$ of the NRMSEs associated with the proposed model for fiber-reinforced LWAC and NWC are 0.234, 0.077, 0.127, and 0.045, respectively, indicating the higher reliability of this model compared to the existing models. Overall, the proposed model outperforms the existing models in terms of the accuracy in predicting the stress-strain relationships of concrete with different densities and reinforced with various types and contents of fibers.

COMPRESSIVE TOUGHNESS INDEX Parametric analysis

ASTM C1018 specifies the compressive toughness index (I_c) as a ratio of the area of the stress-strain curve up to $3\epsilon_0f$ to that calculated at the pre-peak branch up to ϵ_0f . This index

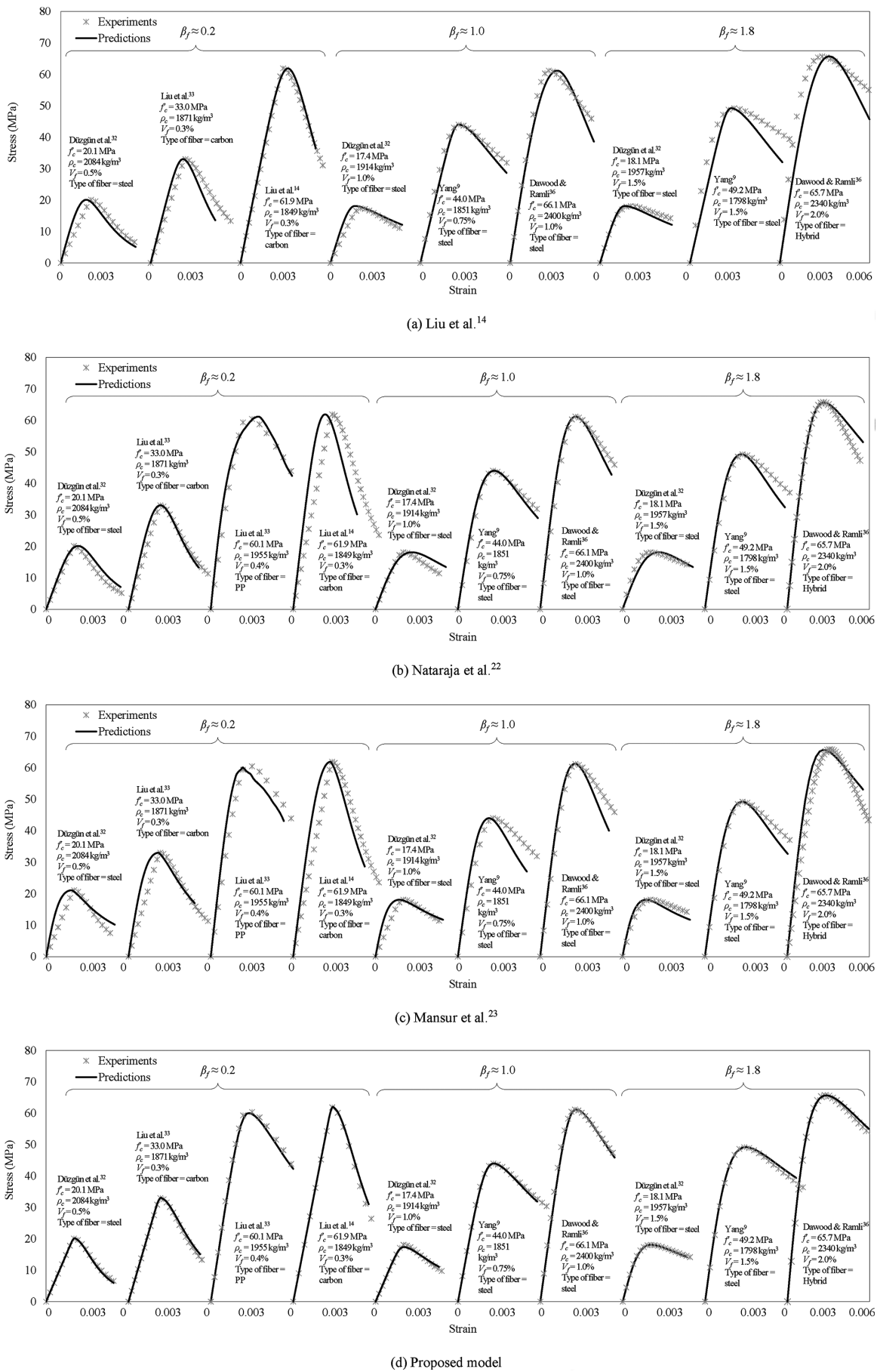


Fig. 6—Comparison of predicted stress-strain curves with experimental results. (Note: $1 \text{ kg/m}^3 = 0.0624 \text{ lb/ft}^3$; $1 \text{ MPa} = 145 \text{ psi}$.)

Table 4—Comparison of NRMSE obtained from each stress-strain curve

Type	Level of β_f	Statistical value	Study			
			Liu et al. ¹⁴	Nataraja et al. ²²	Mansur et al. ²³	Proposed model
LWAC	$\beta_f \approx 0.2$	$\gamma_{e,m}$	0.422	0.449	0.306	0.273
		$\gamma_{e,s}$	0.108	0.150	0.021	0.008
	$\beta_f \approx 1.0$	$\gamma_{e,m}$	0.393	0.238	0.652	0.204
		$\gamma_{e,s}$	0.105	0.112	0.203	0.079
	$\beta_f \approx 1.8$	$\gamma_{e,m}$	0.339	0.413	0.388	0.212
		$\gamma_{e,s}$	0.190	0.125	0.185	0.139
NWC	Subtotal	$\gamma_{e,m}$	0.401	0.382	0.430	0.234
		$\gamma_{e,s}$	0.124	0.117	0.123	0.077
	$\beta_f \approx 0.2$	$\gamma_{e,m}$	0.627	0.468	0.399	0.199
		$\gamma_{e,s}$	0.446	0.279	0.348	0.111
	$\beta_f \approx 1.0$	$\gamma_{e,m}$	0.198	0.290	0.243	0.098
		$\gamma_{e,s}$	0.061	0.078	0.148	0.045
	$\beta_f \approx 1.8$	$\gamma_{e,m}$	0.275	0.212	0.201	0.089
		$\gamma_{e,s}$	0.081	0.136	0.083	0.041
Total	Subtotal	$\gamma_{e,m}$	0.355	0.333	0.292	0.127
		$\gamma_{e,s}$	0.178	0.122	0.125	0.045
	$\beta_f \approx 0.2$	$\gamma_{e,m}$	0.387	0.335	0.376	0.172
		$\gamma_{e,s}$	0.149	0.136	0.147	0.071

Note: NRMSE = $(1/(f_c)_m) \sum [(f_c)_{Exp} - (f_c)_{Pre}]^2/n]^{1/2}$, where $(f_c)_m$ is mean stress in obtained stress-strain curve; $(f_c)_{Exp}$ and $(f_c)_{Pre}$ are experimental and predicted stresses, respectively; and n is number of points in experimental stress-strain curve. $\gamma_{e,m}$ and $\gamma_{e,s}$ are mean and standard deviation, respectively, of NRMSEs calculated for each specimen.

can be used to quantitatively assess the ductility enhancement of fiber-reinforced concrete. This aspect indicates that a reliable compressive stress-strain model must be used to evaluate I_c in a straightforward manner. Therefore, an extensive analytical parametric study was conducted using the stress-strain relationship derived in this study to formulate I_c . The area of the stress-strain curve up to a certain boundary was calculated from the composite trapezoidal rule approximated through the Lagrange interpolation. The parametric study adopted the same ranges of variables as considered in the parametric analysis to derive β_1 . For the analytically calculated results for each parameter, a statistical optimization was performed to formulate the following best-fit equation for I_c (Fig. 7)

$$I_c = 7.9 [(f'_c/f_0)^{-1.7} (\rho_c/\rho_0)^2 (\beta_f)^{0.8}]^{0.23} \quad (8)$$

Comparison with test results

A set of 35 data points for I_c of fiber-reinforced concrete was compiled from the literature.^{14,37-39} Because no reliable previous equation for I_c was available, the measured I_c and predictions obtained using Eq. (8) were directly compared, as shown in Fig. 8. The predictions obtained from the proposed equation are in agreement with the test results, regardless of the variations in ρ_c and the type and β_f of fibers. The mean (γ_m) and standard deviation (γ_s) of the ratios of the

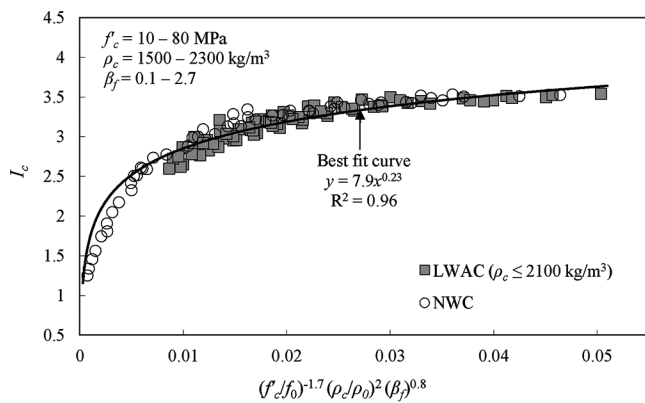


Fig. 7—Regression analysis for compressive toughness index I_c . (Note: $1 \text{ kg/m}^3 = 0.0624 \text{ lb/ft}^3$; $1 \text{ MPa} = 145 \text{ psi}$.)

experimentally obtained values and predictions are 0.95 and 0.13, respectively, for fiber-reinforced LWAC. The corresponding values are 0.95 and 0.09 for fiber-reinforced NWC. Furthermore, the proposed equation can reasonably consider the effect of fiber reinforcement in enhancing I_c . Overall, the proposed equation is a promising tool to assess, in a straightforward manner, the enhancement in the compressive ductility of concrete through the addition of different fibers and promote the design of the fiber reinforcement to achieve the targeted ductility of concrete with different densities.

CONCLUSIONS

A reliable compressive stress-strain relationship of fiber-reinforced concrete with different densities was established to determine the compressive toughness index of such concrete. The quality and quantity of data available for modeling is limited, which could affect the accuracy of the model. Moreover, the properties of concrete may vary depending on the source of ingredients, production method, and curing condition. This variability could impact the accuracy of the model if it is not adequately accounted for. Hence, future work can be aimed at verifying the reliability of the proposed models under expanded parametric conditions, including different types and contents of nonmetallic fibers and different densities of concrete. The following conclusions were derived from the analytical modeling and comparative analysis with test results:

- The existing models cannot reliably estimate the stress-strain response of lightweight aggregate concrete (LWAC) reinforced with different types of fibers, and their accuracy significantly depends on the concrete density (ρ_c) and fiber reinforcing index (β_f). Thus, the existing models result in relatively large scatter values of the normalized root-mean-square errors (NRMSEs) calculated for each stress-strain curve; specifically, the mean NRMSEs exceed 0.382 and 0.299 for fiber-reinforced LWAC and normalweight concrete (NWC), respectively.

- The effect of fiber reinforcements in enhancing the modulus of elasticity, strain at the peak stress, and strain at 50% peak stress at the post-peak branch can be evaluated using the fiber reinforcing index identified in the present study. The key parameter (β_1) introduced to explain the different slopes at the pre- and post-peak branches can be

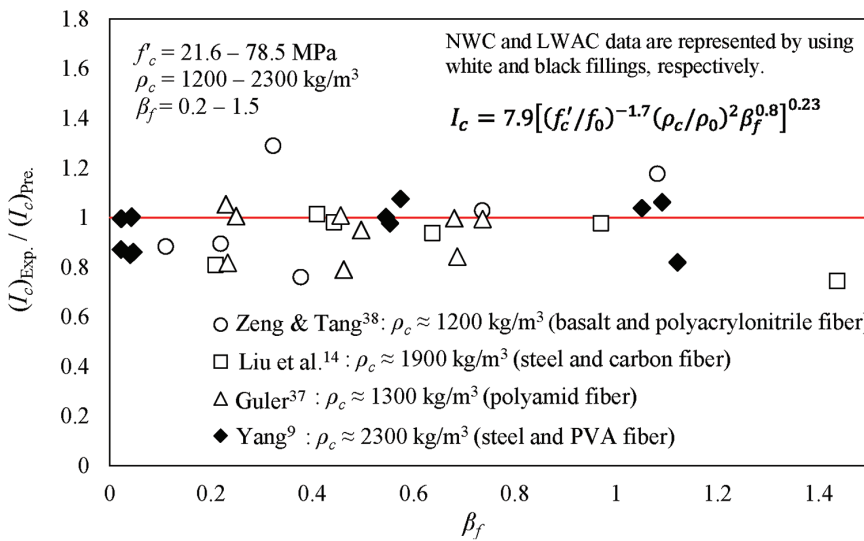


Fig. 8—Comparison of I_c associated with experiments and predictions. (Note: $1 \text{ kg/m}^3 = 0.0624 \text{ lb/ft}^3$; $1 \text{ MPa} = 145 \text{ psi}$.)

formulated as a function of the compressive strength (f'_c) and density (ρ_c) of concrete and β_f .

3. The proposed model outperforms the existing models in terms of the accuracy of predicting the stress-strain relationships of concrete with different densities and reinforced with various types and contents of fibers. The mean and standard deviation of NRMSEs associated with the proposed model for fiber-reinforced LWAC and NWC are 0.234 and 0.077, and 0.127 and 0.045, respectively.

4. The compressive toughness indexes predicted from the proposed equation are in agreement with the test results, regardless of the variations in ρ_c and the type and β_f of fibers. The mean and standard deviation of the ratios of the experimentally obtained values and predictions for fiber-reinforced LWAC and NWC are 0.95 and 0.13, and 0.95 and 0.09, respectively.

AUTHOR BIOS

Hak-Young Kim is a Research Professor at Kyonggi University, Suwon, South Korea. He received his BS, MS, and PhD in architectural engineering from Dankook University, Seoul, South Korea, in 2004, 2009, and 2015, respectively. His research interests include the development of design models of sustainable concrete using various recycling materials.

Hye-Jin Lee is a Doctoral Student at Kyonggi University, where she received her MS in architectural engineering in 2018. Her research interests include examining the mechanical properties of lightweight aggregate concrete.

ACI member Keun-Hyeok Yang is a Professor at Kyonggi University. He received his BS, MS, and PhD in architectural engineering from Chung-Ang University, Seoul, South Korea, in 1995, 1999, and 2002, respectively. His research interests include the development of sustainable concrete materials and structural technology.

ACI member Seung-Jun Kwon is a Professor at Hannam University, Daejeon, South Korea. His research interests include modeling microstructure and deterioration analysis in cement composites using neural network algorithms and strengthening techniques for concrete structures.

ACKNOWLEDGMENTS

This work was supported by a grant from the Korea Agency for Infrastructure Technology Advancement (KAIA) funded by the Ministry of Land, Infrastructure and Transport (Grant 22NANO-C156177-03).

NOTATION

E_c = modulus of elasticity of concrete

E_{cf}	= modulus of elasticity of fiber-reinforced concrete
f_0	= reference value for compressive strength of concrete (= 10 MPa [1.45 ksi])
f_c	= concrete stress corresponding to strain ϵ_c
f'_c	= 28-day compressive strength of fiber-reinforced concrete
g	= snubbing factor of discontinuous fiber
I_c	= compressive toughness index of concrete
R^2	= determination coefficient
S_f	= aspect ratio of fiber
V_f	= volumetric fraction of fiber
w_f	= weight fraction of fiber
β_1	= parameter for determining slopes of pre- and post-peak branches of stress-strain curve
β_f	= reinforcing index of fiber
ϵ_0	= strain at peak stress
ϵ_{0f}	= strain at peak stress of fiber-reinforced concrete
$\epsilon_{0.5}$	= strain corresponding to 50% peak stress at descending branch
$\epsilon_{0.5f}$	= strain corresponding to 50% peak stress at descending branch of stress-strain curve of fiber-reinforced concrete
$\gamma_{e,m}$	= mean of NRMSEs
$\gamma_{e,s}$	= standard deviation of NRMSEs
γ_m	= mean of ratios between experimentally obtained and predicted values
γ_s	= standard deviation of ratios between experimentally obtained and predicted values
ρ_0	= reference value for oven-dry density of concrete (= 2300 kg/m ³ [143.58 lb/ft ³])
ρ_c	= density of concrete
τ	= interfacial bond strength between fiber and cement matrix

REFERENCES

1. ACI Committee 544, "Guide to Design with Fiber-Reinforced Concrete (ACI 544.4R-18)," American Concrete Institute, Farmington Hills, MI, 2018, 44 pp.
2. Shafei, B.; Kazemian, M.; Dopko, M.; and Najimi, M., "State-of-the-Art Review of Capabilities and Limitations of Polymer and Glass Fibers Used for Fiber-Reinforced Concrete," *Materials (Basel)*, V. 14, No. 2, 2021, Article No. 409. doi: 10.3390/ma14020409
3. Hassanpour, M.; Shafigh, P.; and Mahmud, H. B., "Lightweight Aggregate Concrete Fiber Reinforcement - A Review," *Construction and Building Materials*, V. 37, 2012, pp. 452-461. doi: 10.1016/j.conbuildmat.2012.07.071
4. Barros, J. A. O., and Cruz, J. S., "Fracture Energy of Steel Fiber-Reinforced Concrete," *Mechanics of Composite Materials and Structures*, V. 8, No. 1, 2001, pp. 29-45.
5. Islam, M. M. U., "Investigation of Long-Term Tension Stiffening Mechanism for Ultra-High-Performance Fiber Reinforced Concrete (UHPFRC)," *Construction and Building Materials*, V. 321, 2022, Article No. 126310. doi: 10.1016/j.conbuildmat.2022.126310
6. Xie, C.; Cao, M.; Khan, M.; Yin, H.; and Guan, J., "Review on Different Testing Methods and Factors Affecting Fracture

- Properties of Fiber Reinforced Cementitious Composites," *Construction and Building Materials*, V. 273, 2021, Article No. 121766. doi: 10.1016/j.conbuildmat.2020.121766
7. Chen, B., and Liu, J., "Contribution of Hybrid Fibers on the Properties of the High-Strength Lightweight Concrete Having Good Workability," *Cement and Concrete Research*, V. 35, No. 5, 2005, pp. 913-917. doi: 10.1016/j.cemconres.2004.07.035
 8. Wight, J. K., and MacGregor, J. G., *Reinforced Concrete: Mechanics and Design*, Prentice Hall, Upper Saddle River, NJ, 2011.
 9. Yang, K.-H., "Tests on Concrete Reinforced with Hybrid or Monolithic Steel and Polyvinyl Alcohol Fibers," *ACI Materials Journal*, V. 108, No. 6, Nov.-Dec. 2011, pp. 664-672.
 10. Kamjou, A. S.; Khaloo, A.; and Hassanpour, S., "Experimental and Numerical Investigation of Minimum Required Fiber Content in Bending Characteristics of 100 MPa UHPC-Formulated Concrete," *Case Studies in Construction Materials*, V. 16, 2022, Article No. e01066. doi: 10.1016/j.cscm.2022.e01066
 11. ASTM C1018-97, "Standard Test Method for Flexural Toughness and First-Crack Strength of Fiber-Reinforced Concrete (Using Beam With Third-Point Loading) (Withdrawn 2006)," ASTM International, West Conshohocken, PA, 1997.
 12. Yang, K.-H.; Mun, J.-H.; Cho, M.-S.; and Kang, T. H.-K., "Stress-Strain Model for Various Unconfined Concretes in Compression," *ACI Structural Journal*, V. 111, No. 4, July-Aug. 2014, pp. 819-826.
 13. Gao, J.; Sun, W.; and Morino, K., "Mechanical Properties of Steel Fiber-Reinforced, High-Strength, Lightweight Concrete," *Cement and Concrete Composites*, V. 19, No. 4, 1997, pp. 307-313. doi: 10.1016/S0958-9465(97)00023-1
 14. Liu, X.; Wu, T.; and Liu, Y., "Stress-Strain Relationship for Plain and Fibre-Reinforced Lightweight Aggregate Concrete," *Construction and Building Materials*, V. 225, 2019, pp. 256-272. doi: 10.1016/j.conbuildmat.2019.07.135
 15. Islam, M. M. U., "Investigation of Tensile Creep for Ultra-High-Performance Fiber Reinforced Concrete (UHPFRC) for the Long-Term," *Construction and Building Materials*, V. 305, 2021, Article No. 124752. doi: 10.1016/j.conbuildmat.2021.124752
 16. Islam, M. M. U.; Li, J.; Roychand, R.; Saberian, M.; and Chen, F., "A Comprehensive Review on the Application of Renewable Waste Tire Rubbers and Fibers in Sustainable Concrete," *Journal of Cleaner Production*, V. 374, 2022, Article No. 133998. doi: 10.1016/j.jclepro.2022.133998
 17. Islam, M. M. U.; Li, J.; Wu, Y.-F.; Roychand, R.; and Saberian, M., "Design and Strength Optimization Method for the Production of Structural Lightweight Concrete: An Experimental Investigation for the Complete Replacement of Conventional Coarse Aggregates by Waste Rubber Particles," *Resources, Conservation and Recycling*, V. 184, 2022, Article No. 106390. doi: 10.1016/j.resconrec.2022.106390
 18. Almusallam, T. H., and Alsayed, S. H., "Stress-Strain Relationship of Normal, High-Strength and Lightweight Concrete," *Magazine of Concrete Research*, V. 47, No. 170, 1995, pp. 39-44. doi: 10.1680/macr.1995.47.170.139
 19. Lu, Z.-H., and Zhao, Y.-G., "Empirical Stress-Strain Model for Unconfined High-Strength Concrete under Uniaxial Compression," *Journal of Materials in Civil Engineering*, ASCE, V. 22, No. 11, 2010, pp. 1181-1186. doi: 10.1061/(ASCE)MT.1943-5533.0000095
 20. Mansur, M. A.; Wee, T. H.; and Chin, M. S., "Derivation of the Complete Stress-Strain Curves for Concrete in Compression," *Magazine of Concrete Research*, V. 47, No. 173, 1995, pp. 285-290. doi: 10.1680/macr.1995.47.173.285
 21. Wee, T. H.; Chin, M. S.; and Mansur, M. A., "Stress-Strain Relationship of High-Strength Concrete in Compression," *Journal of Materials in Civil Engineering*, ASCE, V. 8, No. 2, 1996, pp. 70-76. doi: 10.1061/(ASCE)0899-1561(1996)8:2(70)
 22. Nataraja, M. C.; Dhang, N.; and Gupta, A. P., "Stress-Strain Curves for Steel-Fiber Reinforced Concrete under Compression," *Cement and Concrete Composites*, V. 21, No. 5-6, 1999, pp. 383-390. doi: 10.1016/S0958-9465(99)00021-9
 23. Mansur, M. A.; Chin, M. S.; and Wee, T. H., "Stress-Strain Relationship of High-Strength Fiber Concrete in Compression," *Journal of Materials in Civil Engineering*, ASCE, V. 11, No. 1, 1999, pp. 21-29. doi: 10.1061/(ASCE)0899-1561(1999)11:1(21)
 24. Carreira, D. J., and Chu, K.-H., "Stress-Strain Relationship for Plain Concrete in Compression," *ACI Journal Proceedings*, V. 82, No. 6, Nov.-Dec. 1985, pp. 797-804.
 25. Kim, H.-Y.; Yang, K.-H.; and Lee, H.-J., "Toughness Performance of Lightweight Aggregate Concrete Reinforced with Steel Fibers," *ACI Materials Journal*, V. 120, No. 5, Sept. 2023, pp. 3-13.
 26. Yang, K.-H., "Slump and Mechanical Properties of Hybrid Steel-PVA Fiber Reinforced Concrete," *Journal of the Korea Concrete Institute*, V. 22, No. 5, 2010, pp. 651-658. doi: 10.4334/JKCI.2010.22.5.651
 27. fib, *Structural Concrete: Textbook on Behaviour, Design and Performance*, International Federation for Structural Concrete, Lausanne, Switzerland, 1999, 244 pp.
 28. Li, V. C.; Mihashi, H.; Wu, H. C.; Alwan, J.; Brincker, R.; Horii, H.; Leung, C.; Maalej, M.; and Stang, H., "Micromechanical Models of Mechanical Response of HPFRCC," *High Performance Fiber Reinforced Cement Composites 2 (HPFRCC 2): Proceedings of the Second International RILEM Workshop*, A. E. Naaman and H. W. Reinhardt, eds., E & FN Spon, London, UK, 1996, pp. 43-100.
 29. Islam, M. M. U.; Mo, K. H.; Alengaram, U. J.; and Jumaat, M. Z., "Mechanical and Fresh Properties of Sustainable Oil Palm Shell Lightweight Concrete Incorporating Palm Oil Fuel Ash," *Journal of Cleaner Production*, V. 115, 2016, pp. 307-314. doi: 10.1016/j.jclepro.2015.12.051
 30. Islam, M. M. U.; Mo, K. H.; Alengaram, U. J.; and Jumaat, M. Z., "Durability Properties of Sustainable Concrete Containing High Volume Palm Oil Waste Materials," *Journal of Cleaner Production*, V. 137, 2016, pp. 167-177. doi: 10.1016/j.jclepro.2016.07.061
 31. Sahoo, S.; Selvaraju, A. K.; and Suriya Prakash, S., "Mechanical Characterization of Structural Lightweight Aggregate Concrete Made with Sintered Fly Ash Aggregates and Synthetic Fibres," *Cement and Concrete Composites*, V. 113, 2020, Article No. 103712. doi: 10.1016/j.cemconcomp.2020.103712
 32. Düzgün, O. A.; Gül, R.; and Aydin, A. C., "Effect of Steel Fibers on the Mechanical Properties of Natural Lightweight Aggregate Concrete," *Materials Letters*, V. 59, No. 27, 2005, pp. 3357-3363. doi: 10.1016/j.matlet.2005.05.071
 33. Liu, X.; Wu, T.; Chen, H.; and Liu, Y., "Compressive Stress-Strain Behavior of CFRP-Confining Lightweight Aggregate Concrete Reinforced with Hybrid Fibers," *Composite Structures*, V. 244, 2020, Article No. 112288. doi: 10.1016/j.compstruct.2020.112288
 34. Wang, S.; Zhang, M.-H.; and Quek, S. T., "Mechanical Behavior of Fiber-Reinforced High-Strength Concrete Subjected to High Strain-Rate Compressive Loading," *Construction and Building Materials*, V. 31, 2012, p. 1-11. doi: 10.1016/j.conbuildmat.2011.12.083
 35. Tayebi, M., and Nematzadeh, M., "Effect of Hot-Compacted Waste Nylon Fine Aggregate on Compressive Stress-Strain Behavior of Steel Fiber-Reinforced Concrete after Exposure to Fire: Experiments and Optimization," *Construction and Building Materials*, V. 284, 2021, Article No. 122742. doi: 10.1016/j.conbuildmat.2021.122742
 36. Dawood, E. T., and Ramli, M., "Mechanical Properties of High Strength Flowing Concrete with Hybrid Fibers," *Construction and Building Materials*, V. 28, No. 1, 2012, pp. 193-200. doi: 10.1016/j.conbuildmat.2011.08.057
 37. Guler, S., "The Effect of Polyamide Fibers on the Strength and Toughness Properties of Structural Lightweight Aggregate Concrete," *Construction and Building Materials*, V. 173, 2018, pp. 394-402. doi: 10.1016/j.conbuildmat.2018.03.212
 38. Zeng, Y., and Tang, A., "Comparison of Effects of Basalt and Polyacrylonitrile Fibers on Toughness Behaviors of Lightweight Aggregate Concrete," *Construction and Building Materials*, V. 282, 2021, Article No. 122572. doi: 10.1016/j.conbuildmat.2021.122572
 39. Marar, K.; Eren, Ö.; and Yitmen, İ., "Compression Specific Toughness of Normal Strength Steel Fiber Reinforced Concrete (NSSFRC) and High Strength Steel Fiber Reinforced Concrete (HSSFRC)," *Materials Research*, V. 14, No. 2, 2011, pp. 239-247. doi: 10.1590/S1516-14392011005000042

Title No. 120-M64

Field Assessment of Biogenic Acid Attack in Concrete Structures

by Ali Abu-Yosef, Stalin Armijos-Moya, and Randall Poston

Biogenic sulfuric acid attack (BSA) is a biodegradation mechanism that causes accelerated deterioration of concrete sewer systems and wastewater treatment structures. BSA is a multi-stage biological process that deposits sulfuric acid over concrete surfaces. Due to its complex nature, there are no current standards to evaluate the presence, extent, and severity of BSA in concrete structures during service.

The authors evaluated the chemical and biological conditions in an operational digester where BSA activity was suspected. The evaluation included microbial culture testing, quantitative polymerase chain reaction (qPCR) analysis of biofilm samples, pH measurements, and petrographic assessment of extracted samples. To evaluate the effect of oxygen on BSA activity, evaluations were performed in strictly anaerobic and oxygen-rich environments inside the same digester.

The investigation determined that oxygen injection caused significant changes in the biological and chemical conditions inside the digester. The addition of oxygen promoted BSA activity and the associated production of sulfuric acid, and therefore accelerated concrete deterioration.

Keywords: anaerobic digester; biogenic sulfuric acid attack (BSA); culture testing; microbiologically induced concrete corrosion (MICC); petrography; pH; quantitative polymerase chain reaction (qPCR).

INTRODUCTION

Concrete structures used for wastewater storage, treatment, and transportation can experience severe degradation due to acid-producing biological activity. This deterioration mechanism is called biogenic sulfuric acid attack (BSA) or microbiologically induced concrete corrosion (MICC). Concrete disintegration due to BSA compromises the structural integrity and reduces the service life of these structures. Under extreme conditions, the rate of material loss due to microbial activity can exceed 0.5 in. (12 mm) per year.^{1,2} A 1991 Environmental Protection Agency report documented BSA-induced damage in sewer networks and environmental structures throughout the United States.³ Several failures of concrete and steel structures have been attributed to cross-sectional losses due to severe BSA activity.³⁻⁵

BSA is a multi-phase biochemical mechanism that typically occurs near the top surfaces of enclosed, wastewater-containing structures. Figure 1 schematically describes the BSA mechanism in a concrete digester. The acid formation due to biological activity occurs in four sequence-critical phases^{2,6-8}:

1. Naturally occurring, anaerobic sulfate-reducing bacteria (SRB) consume the sulfate-rich waste material and produce hydrogen sulfide solution ($H_2S_{(aq)}$). This process

occurs below the waterline, where anaerobic conditions are maintained.

2. The flow of the wastewater, and associated turbulence, inside the structure releases the $H_2S_{(aq)}$ into the headspace as hydrogen sulfide gas ($H_2S_{(g)}$). Due to its inert nature, the released $H_2S_{(g)}$ does not affect the surrounding concrete surfaces.

3. If oxygen is available in the headspace, sulfur-oxidizing microorganisms (SOMs) cultivate in the thin moisture film, which typically forms over the concrete surfaces located above the waterline due to condensation. The SOMs consume $H_2S_{(g)}$ and produce sulfuric acid (H_2SO_4). The biologically produced (biogenic) acid is deposited directly on the concrete surface.

4. The deposited sulfuric acid surface dissolves the cement paste, forming weak and friable gypsum and ettringite deposits.⁹

Once the cement paste is dissolved, coarse aggregates are dislodged and the cross-sectional thickness of the concrete member is progressively reduced. The severity of BSA deterioration is dependent on: 1) the nutrient (sulfate) concentrations in the wastewater; 2) the oxygen concentration in the headspace; and 3) the permeability of the concrete material.⁹

The amount of nutrients available in the organic matter is highly variable and depends on the source and local conditions. Sulfate-rich waste promotes rapid growth of SRB, increasing the hydrogen sulfide (H_2S) concentration in the system.⁹

The presence of oxygen in the system is necessary for the microbial acid attack mechanism.^{7,10,11} The air within the headspace of a sewer pipe creates ideal conditions that promote the growth of SOM populations and the production of sulfuric acid. Without oxygen, the SOM cultures become dormant, restricting the sulfuric acid production and thus reducing the severity of the ensuing concrete damage.

Field evaluation of BSA activity

Field evaluation of BSA activity in existing concrete structures is limited to visual assessments and petrographic evaluation of concrete samples.^{4,11} The petrographic evaluations aim to identify the by-products of BSA—namely, gypsum and ettringite. The severity of the attack is typically

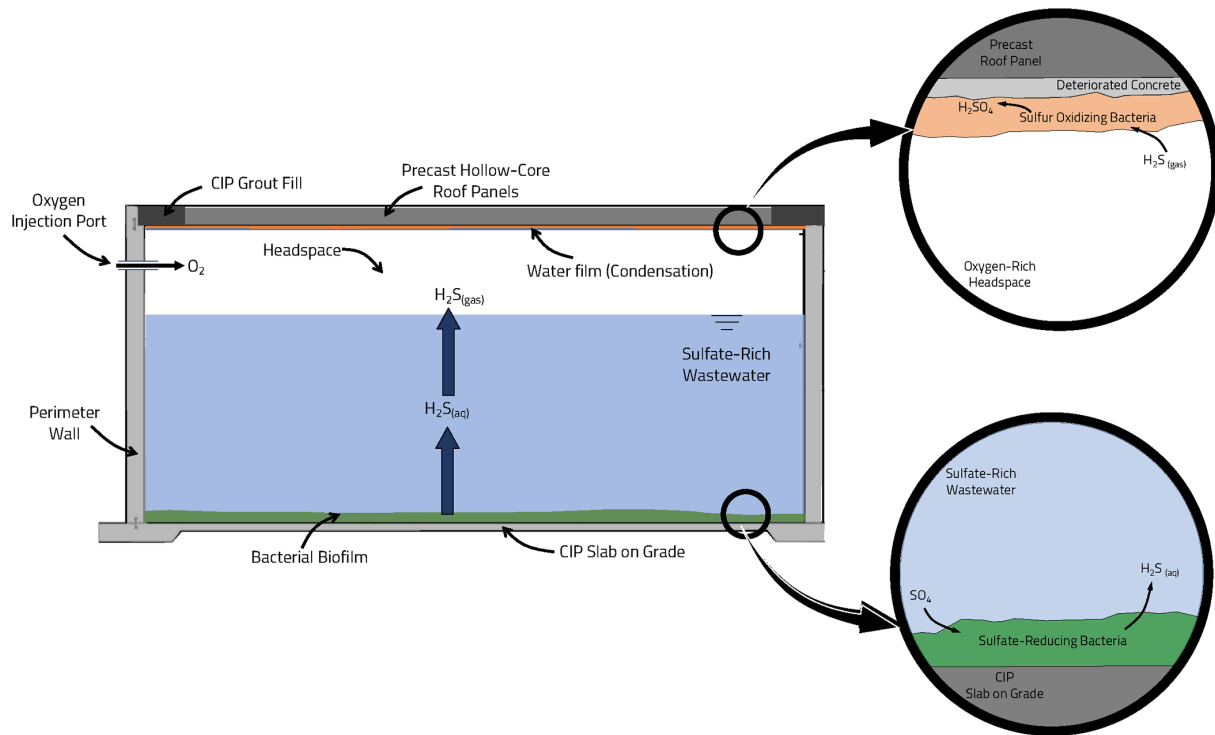


Fig. 1—Schematic showing cross section of typical digester and various elements of BSA mechanism.

estimated by measuring the loss of concrete thickness over the time that the structure was in service. Because direct access to operational wastewater facilities is not feasible, field assessments typically take place after significant BSA damage has already occurred.

The state-of-practice in field evaluation of BSA-related damage does not normally lend itself to early detection of microbial activity. If detected early, measures to control and limit additional BSA damage can be implemented. This proactive approach can mitigate the need for costly repairs or replacements for the severely deteriorated wastewater systems.

In the oil and gas industry, microbiologically induced corrosion (MIC) of steel pipelines is a costly problem. MIC affects steel elements embedded in nutrient-rich environments.¹² Corrosion of steel due to MIC also affects steel infrastructure and can lead to sudden failures. In the oil and gas industry, the risk of MIC damage is often evaluated by monitoring the growth of specific microbial cultures over the steel surface. For example, the presence of high concentrations of SRB and acid-producing bacteria (APB) over the exposed steel surfaces can provide an early indication of potential MIC issues.^{12,13} The growth and composition of the microbial cultures can be evaluated by taking small biofilm samples from the steel surface. The samples can then be examined using growth mediums or deoxyribonucleic acid (DNA) analysis.

This study examines the reliability of using testing methods commonly used to assess MIC in steel pipelines for the detection of BSA in concrete structures. To this end, biofilm samples collected from an operating reinforced concrete digester were examined using artificial growth media and quantitative polymerase chain reaction (qPCR).

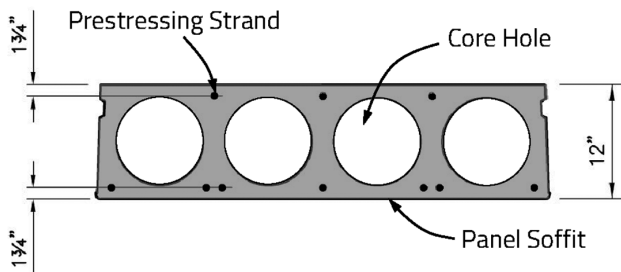
The authors verified the BSA activity inside the digester through petrographic assessment of a concrete sample. Employing techniques that are widely used in the oil and gas industry to evaluate the potential for aggressive BSA activity in environmental structures can facilitate early detection and allow for timely remediation.

RESEARCH SIGNIFICANCE

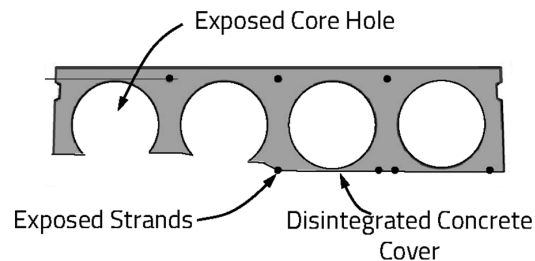
In the last few decades, research efforts have focused on the prevention and protection of concrete structures against BSA activity.^{2,8} Limited research efforts, however, examined the reliability of field assessment methods for detecting BSA activity in existing structures. Early detection of BSA activity allows for the timely and inexpensive implementation of remediation measures. Field evaluation methods can also be used to validate the reliability of new BSA prevention methods when applied into existing structures under typical operating conditions. This study evaluates the reliability of biological assessment methods in detecting active BSA deterioration in an operational concrete structure.

STRUCTURE DESCRIPTION

This study includes the evaluation of the roof structure in an anaerobic digester that uses animal manure to produce methane gas, which is later consumed to produce electricity. The digester is comprised of cast-in-place reinforced concrete foundation slab and walls. The roof of the digester was constructed using 12 in. (300 mm) thick, 36 ft (11 m) long, prestressed, precast hollow-core panels. The ends of the roof precast panels were partially filled on site using a structural grout. Figure 1 shows a simplified cross section of the digester, and Fig. 2 shows a typical cross section of the hollow-core precast roof panels.



a) As-Built Condition



b) Distressed Panel

Fig. 2—Illustration comparing (a) as-built cross section of precast panels to (b) panel condition after exposure to BSA activity.



Fig. 3—Soffit of precast roof panels with hollow cores exposed due to BSA activity.

Environmental conditions inside digester

The anaerobic digester is partially filled with diluted animal waste (Fig. 1). The animal waste flows at a slow rate through the digester chamber. Naturally occurring microbial cultures inside the digester break down the organic nutrients in the animal waste. To promote microbial activity, the chamber is kept at 100°F (38°C) and under anaerobic (oxygen-free) conditions. Anaerobic conditions are conducive to greater microbial activity and more efficient breakdown of the organic waste below the waterline.³

The decomposition of the animal waste produces methane and hydrogen sulfide (H_2S) gases. These gases are primarily generated below the waterline and move gradually into the headspace due to the flow of animal waste inside the digester. The digesters are intended to remain airtight to capture the methane gas inside the headspace.

Because H_2S is a toxic gas, the Environmental Protection Agency and Occupational Safety and Health Administration have strict regulations for controlling its concentration.¹⁴ To comply with federal regulations, facility operators employ different measures to control and stabilize the H_2S levels inside the digesters. Sometimes, oxygen is injected

into the headspace of the digesters to reduce elevated H_2S concentrations. While oxygen injection into an anaerobic digester reduces the production efficiency, this mitigation approach is both economical and effective in controlling H_2S concentrations.

Structural collapse

Less than 10 years after construction, the roof of an anaerobic digester partially collapsed. The collapse occurred during regular operations with no externally applied loading. Figure 3 shows the condition of the roof structure near the collapsed area. The hollow-core precast elements exhibited severe concrete disintegration and significant cross-sectional losses. The loss of the bottom concrete cover exposed the previously embedded prestressing strands, resulting in a complete loss of flexural capacity.

During service, the operator of the collapsed digester injected oxygen for an extended period before the collapse. Hence, the operator was interested in evaluating the structural condition of other similar digester facilities. The authors understand that oxygen injection was used intermittently at the other similar facilities.

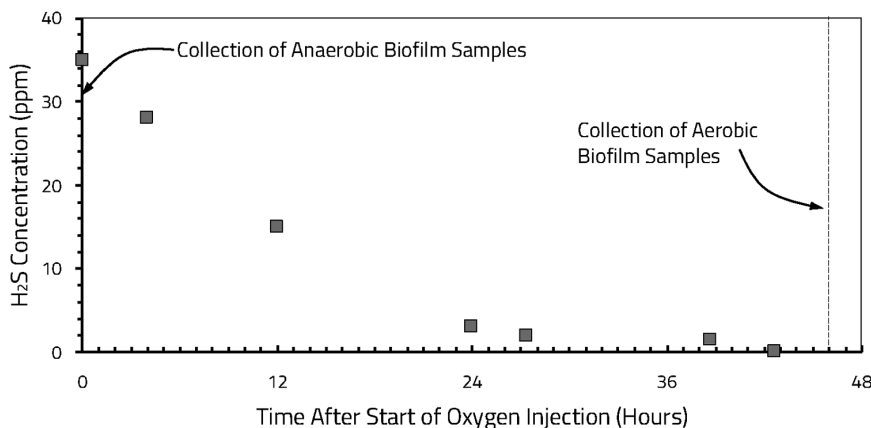


Fig. 4—Change in hydrogen sulfide concentration inside operating digester after start of oxygen injections.

EXPERIMENTAL STUDY

To evaluate the effect of oxygen injection on the microbial activity and concrete surface conditions, the authors collected biofilm samples at an operating digester before and after oxygen injection. The collected biofilm samples were evaluated using growth culture techniques and qPCR testing. In addition, the authors measured the chemical properties of the concrete surface inside the digester before and after oxygen injection. Finally, concrete samples collected from the roof of the digester were evaluated petrographically and using X-ray diffraction (XRD) spectroscopy.

Biofilm sample collection

Biofilm samples were collected from the roof of an operating digester. The digester remained strictly anaerobic for 60 days before the first group of samples was collected (anaerobic samples). This first set of samples represents the baseline condition where the microbial activity is anaerobic.

After collecting the anaerobic biofilm sample, the operator injected oxygen into the headspace of the digester while monitoring the change in the H₂S concentrations. After 36 hours of oxygen injection, the H₂S concentrations decreased from 35 ppm to a concentration of less than 2 ppm. Figure 4 plots the change in H₂S concentrations after the start of oxygen injection. After the H₂S concentrations stabilized below the detection threshold of the H₂S monitor, the authors collected the second set of biofilm samples (aerobic samples).

All biofilm samples were collected from an existing pipe penetration in the digester's roof. The penetration was located approximately 20 ft (6 m) from the oxygen injection port. To prevent cross contamination, the anaerobic biofilm samples were collected from the western half of the pipe penetration and the aerobic samples were collected from the eastern half of the pipe penetration. After each sample collection, the operators reinstalled the pipe and hermetically sealed the pipe penetration.

The collected biofilm samples were used for microbial culture growth testing and preparation of the qPCR analysis samples. The collected biofilm samples were inoculated within 5 minutes of collection into the growth culture solutions or placed into specifically designed preservation kits for subsequent qPCR testing.

Culture testing

Microbial culture growth testing is a common technique used to estimate the populations of specific bacterial cultures in a particular environment. This standardized test method is widely used in the oil and gas industry to monitor microbial activity in steel pipelines.¹³

The test is performed by placing (inoculating) a sample of the biofilm in a growth medium. The growth medium is specifically formulated to promote the growth of a single bacterial species and inhibit other forms of growth. Numerous growth media have been commercially developed to evaluate different types of bacterial cultures that contribute to corrosion in steel and concrete elements. If the biofilm sample contains living cultures of the bacterial species being examined, rapid growth occurs in the medium. The microbial growth triggers a change in the color or consistency of the growth medium.

To estimate the bacterial population in a sample, multiple duplicate vials containing the same growth medium are inoculated with different concentrations of the original biofilm sample. The biofilm sample is diluted in a serial manner. At each dilution step, the concentration of the original bacterial sample is reduced. The authors performed culture growth testing for six bacterial populations. The discussion in this paper, however, is limited to SRB and SOMs.

The inoculated samples are monitored for 14 days to detect any changes in the color or consistency of the test media.¹³ The concentration of a given bacterial culture is estimated based on the vial with the lowest concentration that has changed color after 14 days.

For each exposure condition (before and after oxygen injection), one of the collected biofilm samples was inoculated in the SRB growth media. For the SRB growth cultures, four vials were used; hence, the dilution of the samples in the anaerobic media ranged from 1:10 to 1:100,000. The formulation of the SRB media used in this study complies with the Modified Postgate's B formula described in NACE Standard TM 194.¹³

Because SOM populations are critical for BSA attacks in concrete, six SOM growth media vials were used in this study (that is, sample dilution ranging between 1:10 and 1:1,000,000). The growth media used to evaluate the SOM

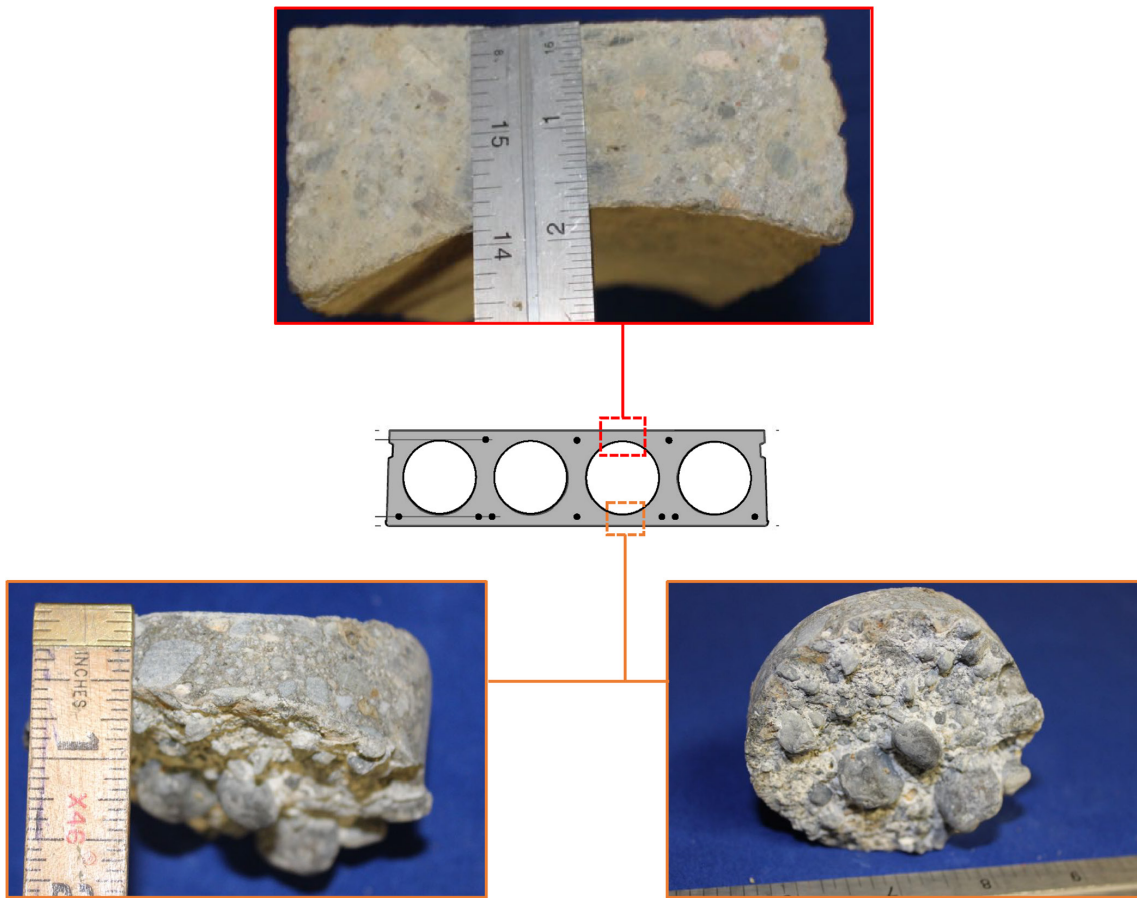


Fig. 5—Condition of top and bottom flanges of precast roof panel from operating digester. Note that soffit core is significantly smaller than top flange core, even though both areas originally had same thickness.

populations is a proprietary formula developed by an independent company.

qPCR testing

The use of molecular microbiological evaluation techniques to study biological cultures has gained popularity in forensic assessments of MIC activity in oil pipelines^{15–17} and BSA-induced damage in concrete structures.¹⁸ qPCR testing detects and enumerates the DNA or ribonucleic acid (RNA) sequences of specific bacterial cultures in a biofilm sample.¹⁹ qPCR targets and amplifies specific gene sequences within a sample. Based on the quantity of the amplified gene after qPCR processing, the population of the examined bacterial species in the sample can be estimated. The specific genetic sequence associated with SOM and SRB populations can be reliably targeted using qPCR technology.^{16,19}

Compared to traditional microbial culture growth testing, gene counting technology (for example, qPCR) provides rapid and accurate quantification of specific bacterial populations within a sample.¹⁸ Because it relies on the amplification of existing gene signatures and not growth over time, qPCR can detect active and dormant microorganisms within the evaluated samples. Furthermore, qPCR allows the detection of bacterial species that may not grow in a standard growth medium or under normal inoculation conditions (for example, room temperature).

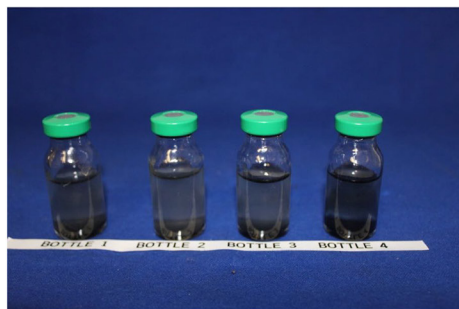
In this study, the qPCR method is used to study the change in SOM and SRB bacterial populations before and after oxygen injection into the anaerobic digester. The authors collected three replicate samples for qPCR testing before oxygen injection. Similarly, three samples were collected after oxygen injection. After collection, the six samples were immediately placed in DNA preservation kits. The qPCR analysis was performed by an independent laboratory.¹⁹

Assessment of surface conditions

A flat-surface pH meter was used to document the change in concrete surface conditions along the precast panel soffit. The pH measurements were performed immediately after biofilm sample collection during the two stages of the investigation (that is, before and after oxygen injection). The pH meter was placed at multiple points directly over the concrete surface. During each collection stage, the recorded pH values were generally consistent with limited variability.

Petrographic assessment

The investigation included petrographic assessment of a concrete sample collected from the soffit of the digester's roof. The authors collected a 3 in. (75 mm) diameter concrete core sample from a precast roof segment. Figure 5 shows the sample collected and the condition of the top and bottom flanges of the hollow-core precast panel. The bottom-flange concrete sample (that is, roof soffit) contained



a) Anaerobic Samples at 14 Days



b) Aerobic Samples at 14 Days

Fig. 6—Condition of SRB media vials for samples collected before (left) and after (right) oxygen injection. Note that change of vial solution color to black indicates positive reaction.



a) Anaerobic Samples at 14 Days



b) Aerobic Samples at 14 Days

Fig. 7—Condition of SOM media vials for samples collected before (left) and after (right) oxygen injection. Note that change of vial solution color from purple to light yellow indicates positive reaction. (Full-color PDF can be accessed at www.concrete.org.)

white friable product that was loosely adhered to sound concrete substrate. When compared to the top flange sample, the bottom flange sample, where SBA activity is expected, experienced a significant loss in thickness.

After extraction, the collected concrete sample was stored in an airtight package. An independent materials laboratory performed a petrographic assessment of the soffit sample in accordance with ASTM C856.²⁰

The authors also collected samples of the friable deposit observed over the precast panel soffit. The collected deposit samples were evaluated using XRD. XRD technology is commonly used for material identification and analysis of chemical compositions. In this study, XRD is used to verify the presence of gypsum, a by-product of SBA, in the collected samples.

EXPERIMENTAL RESULTS

The results of the microbial activity evaluation, material testing, and petrographic assessments are provided in this section.

Microbial culture growth results

Figure 6 shows the final condition of the SRB growth media vials for the samples collected before and after oxygen injection. All vials of the anaerobic sample indicated a positive response by changing their color from transparent to black. In contrast, only three of the four vials inoculated with the aerobic sample indicated a positive response.

Figure 7 shows the final condition of the SOM growth media vials for the samples collected before and after oxygen injection. Color change of the vial solution from

Table 1—Estimated SRB and SOM populations based on growth culture testing results

	Anaerobic biofilm samples, viable cells/mL	Aerobic biofilm samples, viable cells/mL
SRB	>4,000,000	400,000
SOM	No growth detected	66,000

purple to light yellow indicates a positive reaction. None of the vials containing the anaerobic sample indicated a positive response. This suggests that prior to oxygen injection, the viable SOM population was below the detectable limit of the culture growth testing method. In contrast, for the sample collected after oxygen injection, four of the six SOM vials indicated a positive reaction.

The concentration of the bacterial populations was estimated based on the guidelines provided by NACE Standard TM 194.¹³ Table 1 summarizes the estimates for the SRB and SOM populations in the biofilm samples collected before and after oxygen injection. It should be noted that growth culture testing can only detect viable bacterial cells, which can consume the specific nutrients included in the growth media.

The results of the culture testing show oxygen injection caused a significant change in the SRB and SOM populations (Table 1). Before oxygen injection, when the digester was strictly anaerobic, the SRB population count was greater than 4 million viable cells/mL, which is the maximum detectable concentration using the test media. After oxygen was injected into the digester, the population of viable SRB cultures dropped by at least 10 times. Because SRB

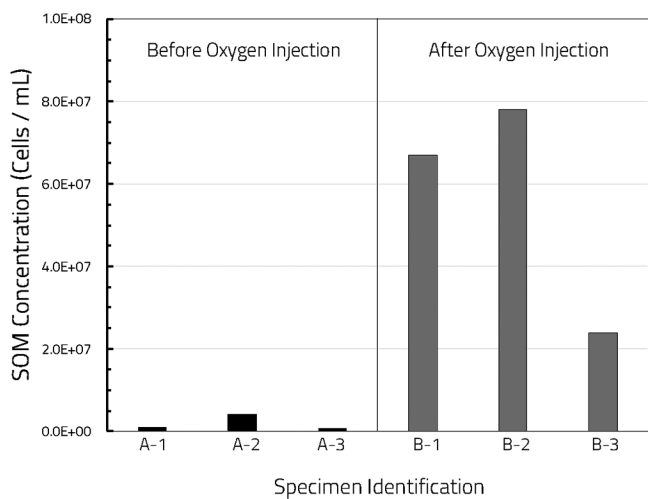


Fig. 8—SOM concentrations measured using qPCR for two sets of samples collected before and after oxygen injection.

are anaerobic species that thrive in oxygen-free conditions, the reduction in SRB population after oxygen exposure is expected.¹¹

It should be noted that SRB results are only representative of the conditions in the soffit of the digester's roof (that is, within the headspace). The SRB populations at the bottom of the digester, however, are marginally affected by oxygen injection into the headspace. This is because the concentration of oxygen that can diffuse through multiple feet (meters) of wastewater is limited. Hence, during oxygen injection, the SRB populations attached to the concrete in the digester's headspace are expected to decrease, while the SRB populations located below the waterline are not affected by the oxygen addition to the headspace.

As shown in Table 1, oxygen injection promoted the growth of SOM cultures. For the anaerobic samples, none of the vials had a positive reaction. This suggests that the concentration of viable SOM before oxygen injection was below the detection threshold. Because SOMs are aerobic microorganisms, the presence of oxygen is critical for their viability.⁷ Hence, the lack of growth in the media samples collected when the digester was under anaerobic conditions is a reasonable result. The samples collected after limited oxygen exposure (that is, aerobic samples) showed positive reactions in four of the six SOM media vials. Based on the culture testing results, injecting oxygen for 48 hours resulted in conditions that promoted the growth of SOM populations.

qPCR analysis results

An independent laboratory performed the qPCR DNA analysis for the six biofilm samples that were collected from the digester. Samples A-1, A-2, and A-3 are three identical samples that were collected before oxygen injection (anaerobic samples). Samples B-1, B-2, and B-3 were all collected after oxygen injection (aerobic samples). qPCR analyses that target SOM populations were performed on all collected samples. SRB populations were only analyzed in one of the samples collected before oxygen injection (A-1) and one of

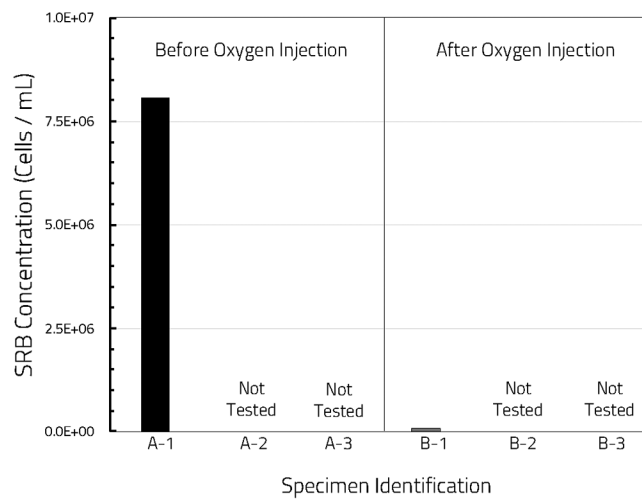


Fig. 9—SRB concentrations measured using qPCR for two samples. One sample was collected before (A-1) and second sample was collected after (B-1) oxygen injection.

the samples collected after oxygen injection (B-1). Figures 8 and 9 show the qPCR analysis results for the SOM and SRB populations, respectively.

Like the culture growth testing results, the qPCR analysis demonstrates a change in bacterial culture composition due to oxygen injection. The SRB populations decreased after oxygen injection. In contrast, the SOM concentrations increased after oxygen injection. The increase in SOM populations was evident in all three duplicate samples. While the measured SOM concentrations in each of the samples varied, the overall trend appears to confirm the increase in SOM populations after oxygen injection.

Culture testing using growth media only accounts for active bacteria that consume a specific nutrient combination. In contrast, the population measured using qPCR technology include all viable species in the evaluated sample. Because qPCR traces the DNA signatures, the activity level in the biofilm sample does not affect the results. Hence, direct comparison between the numeric values of the qPCR concentrations and those estimated using culture testing is not meaningful. However, the results from both test methods can be used to evaluate the overall trends and changes in sample composition after oxygen injection.

Surface conditions testing results

Multiple surface pH measurements were performed on the soffit of the digester's roof before and after oxygen injection. Before oxygen injection, the surface pH was approximately 6.4. The surface pH decreased to 4.3 after 48 hours of oxygen injection, indicating that the surface became more acidic.

The authors also measured the pH of biofilm samples using pH test strips. The pH values obtained from the swab samples were similar to those measured at the surface using a pH meter. The samples collected before oxygen injection exhibited a pH of 6.5 and those collected after oxygen injection had a pH of 4.0.

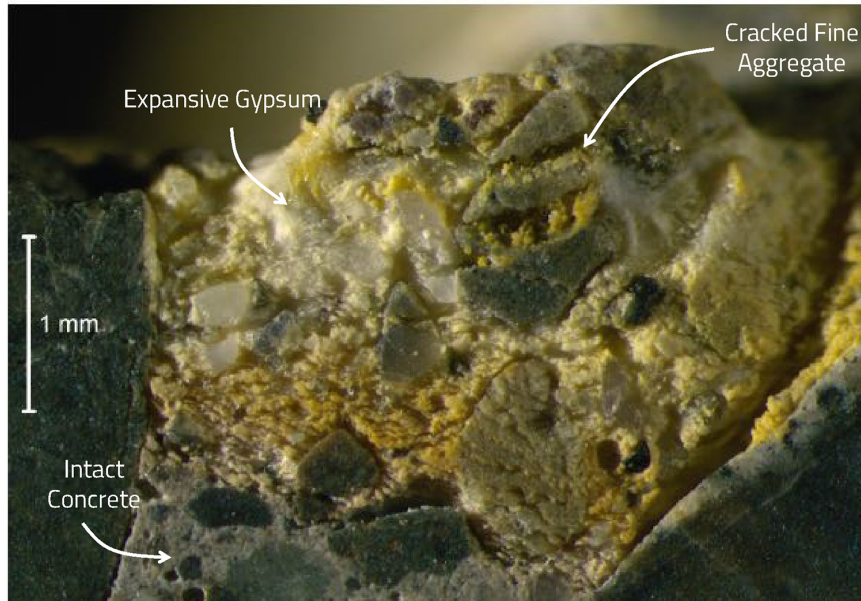


Fig. 10—Photograph of outer layer of concrete sample showing gypsum deposits over original concrete.

Petrographic evaluation findings

The petrographic assessment determined that the precast panels were cast using good-quality concrete material. The original concrete exhibited a moderately low water-cement ratio ranging between 0.37 and 0.42. The concrete was a portland cement mixture and did not contain supplementary cementitious materials. The coarse aggregates were well-graded and comprised naturally occurring gravel. The fine aggregates were primarily natural sand.

The petrographic analysis confirmed that the observed disintegration in the outer layer of the sample was the result of acid attack. The paste and aggregate material located within the outer 5/8 in. (16 mm) of the concrete sample was in poor condition and appeared to be compromised by acid exposure (Fig. 10).

XRD testing confirmed that the friable white yellowish product observed in the sample was gypsum and ettringite (Fig. 11). The expansive gypsum material caused microcracking at the interface between the disintegrated concrete material and the original concrete substrate. The microcracking extended through some of the fine aggregates located either within the disintegrated layer or near the interface zone. Figure 10 is a photograph of the outer layer of the concrete sample showing the gypsum deposits over the original concrete substrate. Fine parallel microcracks were also observed within the gypsum layer (white yellowish deposit). Distress of aggregates in the disintegrated layer can also be seen.

The gypsum layer was fully carbonated and exhibited a pH of less than 9.0 (the threshold pH value for phenolphthalein). In contrast, the maximum carbonation depth in the original concrete substrate was less than 0.1 in. (2 mm). The rapid rate of carbonation at the outer layer is likely the result of exposure to sulfuric acid produced by the BSA activity.

DISCUSSION

The microbial and material testing performed in this study demonstrated that oxygen injection caused significant changes in the environment surrounding the interior surfaces of the digester roof. After oxygen injection, the composition of the biofilm populations substantially changed, leading to a change in the chemical characteristics of the concrete surface. Based on the testing performed, oxygen injection for only 48 hours produced the following changes in the soffit of the elevated roof panels:

- Reduced the population and activity of the anaerobic SRB populations, as confirmed by growth culture testing and qPCR gene analysis;
- Promoted the growth of the acid-producing and aerobic SOM populations, as confirmed by growth culture testing and qPCR gene analysis; and
- Reduced the surface pH of the roof soffit, creating a highly acidic exposure condition.

Before oxygen injection, the environment inside the digester was virtually anaerobic. Under anaerobic conditions, SRB cultures were active and present at high concentrations. SRB cultures consume sulfate and produce hydrogen sulfide gas, a weak acid. Concrete exposed to hydrogen sulfide gas does not experience acid-induced disintegration. The limited effect of the weak hydrogen sulfide acid on the environment within the headspace was confirmed by the surface pH measurements performed before oxygen injection. Before oxygen injection, the roof soffit exhibited a relatively neutral pH that was greater than 6.4. At this pH level, concrete remains intact and does not disintegrate.⁸

Based on the microbial testing results, conditions inside the digester before oxygen injection were not suitable for the growth and activity of the acid-producing SOM cultures. Viable SOM populations were virtually nonexistent before oxygen was injected into the digester. SOM concentrations were only detected after aerobic conditions were established through oxygen injection. The substantial increase in SOM

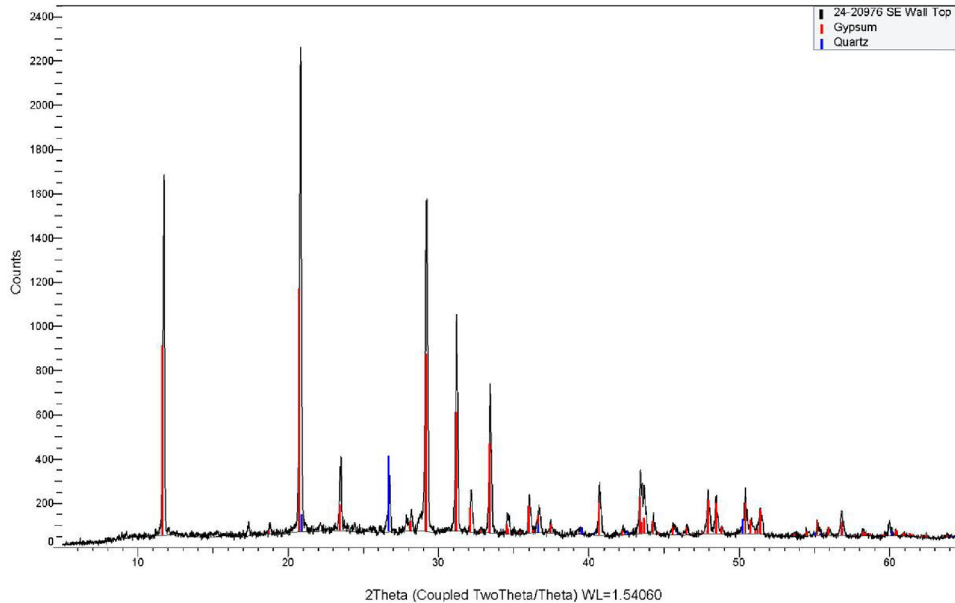


Fig. 11—XRD pattern of soft, friable product observed in disintegrated concrete samples. Peaks coincide with signature gypsum and quartz signals. Quartz likely present in fine aggregate material.

populations after oxygen injection was confirmed by the results of growth culture testing and genetic qPCR analysis. Because SOMs oxidize hydrogen sulfide to produce sulfuric acid, the growth of SOM cultures corresponded with a reduction in the hydrogen sulfide concentrations in the digester's headspace (Fig. 1). Production of highly acidic sulfuric acid was confirmed by the reduction of the pH levels in the roof soffit and the biofilm samples. After oxygen injection, the pH of the elevated roof soffits decreased from a relatively neutral pH of 6.4 to an acidic pH of 4.0.

The biologically produced acid caused substantial damage to the exposed concrete in the digester headspace. The acid exposure disintegrated the cementitious paste, producing gypsum and ettringite. The petrographic assessment and XRD testing results confirmed the presence of friable, expansive gypsum deposits. The expansive gypsum progressively diffused into the concrete, causing microcracking in the cement paste and the fine aggregates.

CONCLUSIONS

The study examined the change in bacteria populations and surface characteristics before and after oxygen was injected into an operating concrete digester. The testing program included the evaluation of biofilm samples using: 1) the microbial growth culture technique described in NACE Standard TM 194; and 2) gene counting using quantitative polymerase chain reaction (qPCR) technology. The assessment also evaluated the changes in the pH of the concrete surface due to oxygen injection.

The testing indicated that oxygen injection caused significant changes in the biological and chemical conditions inside the digester. The investigation results indicate that oxygen injection created conditions that were conducive to biogenic sulfuric acid attacks. The study also demonstrated that microbial growth cultures and qPCR technology can

be used to detect and identify biogenic sulfuric acid attack (BSA) in concrete structures.

AUTHOR BIOS

ACI member Ali Abu-Yosef is a Senior Associate at Pivot Engineers in Austin, TX. He is a member of ACI Committees 222, Corrosion of Metals in Concrete; 342, Evaluation of Concrete Bridges and Bridge Elements; and 364, Rehabilitation. He received his BS from the University of Jordan, Amman, Jordan, and his MS and doctoral degrees from The University of Texas at Austin, Austin, TX.

Stalin Armijos-Moya is a Project Engineer with Pivot Engineers, working on evaluation, repair, and strengthening of structures. He received his BS from Armed Forces University – ESPE, Sangolqui, Ecuador, and his MS and PhD from The University of Texas at Austin.

Randall Poston, FACI, is a Structural Engineer and the Founding Senior Principal of Pivot Engineers in Austin, TX. He is a member of ACI Committee 318, Structural Concrete Building Code, and chaired the committee for the 2014 code cycle. Poston received his bachelor's, master's, and doctoral degrees in civil engineering from The University of Texas at Austin in 1978, 1980, and 1984, respectively. Poston was elected to the National Academy of Engineering in 2017.

ACKNOWLEDGMENTS

The authors would like to thank G. Moulzolf of American Engineering Testing, Inc. for providing the results of the petrographic and X-ray diffraction assessments.

REFERENCES

1. St. John, D.; Poole, A.; and Sims, I., *Concrete Petrography - A Handbook of Investigative Techniques*, Arnold, London, UK, 1998.
2. Lines, S.; Rothstein, D.; Rollins, B.; and Alt, C., "Microbially Induced Corrosion of Concrete," *Concrete International*, V. 43, No. 5, May 2021, pp. 28-32.
3. U.S. EPA, "Hydrogen Sulfide Corrosion in Wastewater Collection and Treatment Systems - Report to Congress," United States Environmental Protection Agency, Washington, DC, 1991.
4. Abu Yosef, A.; Ahern, M.; and Poston, R., "Concealed Threat," *Civil Engineering Magazine*, V. 86, No. 1, Jan. 2016.
5. Hou, H.; Steiner, K.; Fraczek, J.; and Mahaney, J., "Biogenic Sulfuric Acid Attack and Case Studies," *Concrete International*, V. 42, No. 5, May 2020, pp. 33-38.
6. George, R. P.; Vishwakarma, V.; Samal, S. S.; and Mudali, K., "Current Understanding and Future Approaches for Controlling Microbially

- Influenced Concrete Corrosion: A Review," *Concrete Research Letters*, V. 3, 2012, pp. 491-506.
7. Okabe, S.; Odagiri, M.; Ito, T.; and Satoh, H., "Succession of Sulfur-Oxidizing Bacteria in the Microbial Community on Corroding Concrete in Sewer Systems," *Applied and Environmental Microbiology*, V. 73, No. 3, 2007, pp. 971-980. doi: 10.1128/AEM.02054-06
 8. ACI Committee 201, "Guide to Durable Concrete (ACI 201.2R-08)," American Concrete Institute, Farmington Hills, MI, 2008, 49 pp.
 9. Mori, T.; Nonaka, T.; Tazaki, K.; Koga, M.; Hikosaka, Y.; and Noda, S., "Interactions of Nutrients, Moisture and pH on Microbial Corrosion of Concrete Sewer Pipes," *Water Research*, V. 26, No. 1, 1992, pp. 29-37. doi: 10.1016/0043-1354(92)90107-F
 10. Islander, R. L.; Devinny, J. S.; Mansfeld, F.; Postyn, A.; and Shih, H., "Microbial Ecology of Crown Corrosion in Sewers," *Journal of Environmental Engineering*, ASCE, V. 117, No. 6, 1991, pp. 751-770. doi: 10.1061/(ASCE)0733-9372(1991)117:6(751)
 11. House, M. W., and Weiss, W. J., "Review of Microbially Induced Corrosion and Comments on Needs Related to Testing Procedures," *4th International Conference on the Durability of Concrete Structures*, West Lafayette, IN, 2014.
 12. Little, B., and Lee, J., *Microbiologically Influenced Corrosion*, John Wiley & Sons, New York, 2007, 279 pp.
 13. NACE TM 194-2014-SG, "Field Monitoring of Bacterial Growth in Oil and Gas Systems," NACE International, Houston, TX, 2014.
 14. U.S. EPA, "Report to Congress on Hydrogen Sulfide Air Emissions Associated with Extraction of Oil and Natural Gas," United States Environmental Protection Agency, Washington, DC, 2014.
 15. Lee, C.; Brown, B.; Jones, D.; Duet, S.; Cornell, J.; Sharma, N.; and Lin, X., "Field Applications for On-Site DNA Extraction and qPCR," *Corrosion 2015 Conference and Expo*, Houston, TX.
 16. Leleika, S.; Harmon, A.; and Eisenlord, S., "Quantifying Sulfur Oxidizing Bacteria Using qPCR," *Corrosion Conference and Expo*, Houston, TX, 2018.
 17. Zhu, X.; Kilbane, J.; Ayala, A.; and Modi, H., "Application of Quantitative, Real-Time PCR in Monitoring Microbiologically Influenced Corrosion (MIC) in Gas Pipelines," *Corrosion 2005*, Houston, TX, 2005.
 18. Huber, B.; Herzog, B.; Drewes, J.; Koch, K.; and Muller, E., "Characterization of Sulfur Oxidizing Bacteria Related to Biogenic Sulfuric Acid Corrosion in Sludge Digesters," *BMC Microbiology*, V. 153, No. 16, 2016, pp. 1-11. doi: 10.1186/s12866-016-0767-7
 19. LuminUltra, "Microbiologically Influenced Corrosion Monitoring Techniques," LuminUltra Technologies Ltd., Fredericton, NB, Canada, 2020.
 20. ASTM C856-17, "Standard Practice for Petrographic Examination of Hardened Concrete," ASTM International, West Conshohocken, PA, 2017.

Title No. 120-M65

Family of Thermal Nomograms for Mass Concrete

by J. Brown, L. E. Al-Hasani, J. Park, K. E. Kurtis, R. Gentry, and Y. K. Cho

Thermal management of mass concrete can adversely impact a project's cost and schedule, both during planning and in execution. Nomograms are presented as aids to quickly identifying and making tradeoffs among promising thermal management options. First, the temperature of fresh concrete and a worst-case adiabatic temperature estimate is provided by a nomogram based on simple physical models. A subsequent nomogram accounts for the impact of size, shape, and environment and is based on a surrogate model generated from many three-dimensional (3-D) finite element simulations without postcooling. Finally, nomograms for postcooling are given, similarly founded on finite element-derived surrogate models, for two classes of cooling pipe layouts. The use of these nomograms, with an awareness of their estimated error, is discussed for the initial development of mass concrete thermal management plans.

Keywords: mass concrete; nomograms; thermal management.

INTRODUCTION

The exothermic cement hydration reaction necessarily results in a temperature increase in concrete. With typical cements and initial conditions in large volumes, temperatures can rise to the point that, along with accompanying temperature gradients, thermally induced volume changes and stresses can cause cracking. High temperatures can also lead to delayed ettringite formation, resulting in cracking.¹⁻³ Volumes of sufficient size—in conjunction with concrete properties, boundary conditions, and initial conditions to make thermal behavior a concern—are termed mass concrete.⁴

Mass concrete temperatures may be mitigated by cooling prior to emplacement (precooling) and fluid circulation through pipes embedded in the concrete after emplacement (postcooling). Thermal gradients can be mitigated directly with insulation⁵ or indirectly by precooling and/or postcooling. Precooling slows the exothermic hydration reaction, granting time for heat transfer within the concrete to weaken temperature gradients. The judicious placement of pipes and choice of piping material allows postcooling to lower temperatures in core regions, decreasing spatial differences.

The methods chosen to control temperatures in mass concrete can have significant project cost and schedule implications. The many parameters that bear on thermal management decision-making—for example, precooling and/or postcooling, cooling water temperatures, pipe spacing, cost factors, and so on—lead to a large tradeoff space. Traversing this space to find acceptable solutions can be time-consuming and repetitive. Herein, simple models are developed that encapsulate many mass concrete situations, permit rapid initial exploration of mass concrete thermal management plans, and can be represented in the enduring and easy-to-use form of nomograms.

As expedient, visual, purpose-built computers embodying closed-form mathematical equations, nomograms have a long history, dating back centuries to when computations were laborious. Nomograms have a deep legacy in civil engineering, including as aids in the design and construction of the French rail network.⁶⁻⁸ With the advent of rapid and powerful electronic computers, their use has waned, although they are still used today in clinical medical settings⁹ as well as in engineering. Nevertheless, one may ask: Why use nomograms when rapid computation is cheap and abundant with today's general-purpose digital computers? The present response is that nomograms do more than compute point solutions; they represent all solutions simultaneously and visually depict the nature of the relations between variables. In conjunction with the human visual system, this allows rapid exploration of the parameter space and assessment of tradeoffs, so that promising (and unpromising) options can be identified. Furthermore, nomograms resist obsolescence because they are not tied to a programming language or particular computing technology.

ACI 207.2R-07² contains many charts that can be considered basic nomograms, as well as three sophisticated, bona fide nomograms depicting quantitative relationships between variables in postcooling. The 13th edition of the Portland Cement Association's (PCA's) *Design and Control of Concrete Mixtures*¹⁰ also contains basic nomograms for the temperature of freshly mixed concrete and surface moisture evaporation rate, among others. Silva and Šmilauer¹¹ presented a nomogram for the maximum temperature of concrete as a function of binder content, percentage of supplementary cementitious materials (SCMs), concrete thickness, and initial and ambient temperatures. Their method was to run many one-dimensional (1-D) finite element analysis (FEA) simulations and regress linear models on the resulting data, thereby encapsulating the salient results of the simulations and creating a closed-form surrogate model of their simulations that can be represented in nomographic form. Nguyen et al.¹² also use this surrogate model approach to create a nomogram for maximum temperatures in cubes as a function of cement content and initial temperature.

RESEARCH SIGNIFICANCE

Surrogate models, represented as nomograms, for predicting maximum concrete temperature with and without postcooling are developed from detailed simulations of

“primary” physics models. The surrogate models and nomograms herein account for three-dimensional (3-D) geometry in contrast to Silva and Šmilauer,¹¹ are not limited to cubes in contrast to Nguyen et al.,¹² and apply to postcooling in contrast to both. These nomograms are packaged with (in-sample) error estimates, and their predictive value and applicability are assessed. Additionally, the applicability of a simplified primary model and its surrogate for postcooling are analyzed. These nomograms facilitate assessment of thermal management plans.

METHODS

This paper presents a set of nomograms for concrete temperature to aid in developing mass concrete thermal management plans. The particular cases cover:

1. Maximum temperature of concrete without postcooling during hydration for nonadiabatic conditions given initial temperature, size of the emplacement as parameterized by volume and surface area, and ambient conditions; and

2. Maximum temperature of postcooled concrete during hydration given initial temperature, cooling water temperature, and pipe size.

Both cases use numerical simulations and regression to derive closed-form surrogate models representable as nomograms, similar to Silva and Šmilauer¹¹ and Nguyen et al.¹² However, the nomograms presented herein are limited to a particular concrete mixture. These two cases also inform decisions regarding precooling in addition to aiding in the decision whether or not to postcool; if the decision is made to postcool, the nomograms help choose pipe size, piping layout, and cooling water temperature. For the second (postcooling) case, each nomogram is limited to pipes of one material (for example, cross-linked polyethylene [PEX] pipe) and one concrete mixture. However, the method presented can easily be applied to other mixtures and pipes.

Two concrete mixtures were used in this work and are described, along with notation and other parameter values, in Appendix A; for brevity, the admixtures are not detailed herein. The reason for the two concretes is that isothermal calorimetry was conducted for the cement in Concrete B to improve the hydration reaction’s modeling. Further details on this point are given in the relevant sections that follow.

All nomograms were made using the open-source Python package PyNomo.¹³

Temperature data from two real-world concrete emplacements located outside of Atlanta, GA, were used for comparison purposes as described in the following sections. Briefly, these emplacements were:

1. A 5.6 m wide x 3.7 m deep x 1.4 m high footing for an abutment wall. This was not postcooled. This emplacement is referred to as “the footing.”

2. A 1.83 m wide x 18.3 m deep x 6.1 m high abutment wall. This was postcooled using PEX piping arranged in a 0.31 x 0.610 m pipe array with chilled water. This is referred to as “the wall” or “the abutment wall.”

Both emplacements used Concrete B, although with different admixtures.

General considerations

Cases 2 and 3 involve transient, multidimensional heat transfer with a nonlinear term modeling hydration. As such, closed-form exact solutions of the governing (partial differential) equations do not exist. Herein, as with Silva and Šmilauer¹¹ and Nguyen et al.,¹² a surrogate modeling approach is used in which results from many numerical simulations are regressed to define a closed-form equation that encapsulates those simulation results. This regressed equation is then converted into nomogram form.

The heat diffusion equation gives the governing equation for the temperature of the concrete with a source term for cement hydration

$$\rho_c c_c \frac{\partial T_c}{\partial t} = \kappa_c \nabla^2 T_c + \dot{e}_{gen} \quad (1)$$

Herein, ρ_c is the density of the concrete; c_c is the specific heat of the concrete; T_c is concrete temperature as a function of space and time t ; κ_c is the thermal conductivity of the concrete; and \dot{e}_{gen} is a source term for the thermal power generated by hydration in, for example, W/m³. For Concrete A, \dot{e}_{gen} is modeled using the Arrhenius-based three-parameter maturity model

$$\dot{e}_{gen} = H_u m_{cm} \frac{da}{dt} = H_u m_{cm} \left\{ \left(\frac{\tau}{t_e} \right)^{\beta} \left(\frac{\beta}{t_e} \right) \alpha_u \exp \left(- \left[\frac{\tau}{t_e} \right]^{\beta} \right) \right\} \left\{ \exp \left(\frac{E_a}{R} \left[\frac{1}{T_r} - \frac{1}{T_c} \right] \right) \right\} \quad (2)$$

where all temperatures are absolute thermodynamic temperatures; H_u is the ultimate energy released by hydration of cementitious materials at 100% hydration; m_{cm} is the mass of cementitious material per unit volume of concrete (sometimes also denoted C_c); $a = a(t_e)$ is the time-varying degree of hydration; E_a is the apparent activation energy; R is the universal gas constant; T_r is a reference temperature (herein taken to be 294.25 K = 21.1°C); τ is a time parameter encoding a delay in onset of hydration after mixing; β is a shape parameter encoding rate of hydration; and t_e is the equivalent age given by

$$t_e = \int_{t=0}^t \exp \left(\frac{E_a}{R} \left[\frac{1}{T_r} - \frac{1}{T_c} \right] \right) dt \approx \sum_{i=0}^t \exp \left(\frac{E_a}{R} \left[\frac{1}{T_r} - \frac{1}{T_c} \right] \right) \Delta t \quad (3)$$

where Δt is the simulation timestep. Empirical relations for the parameters H_u , E_a , α_u , τ , and β can be found in Riding et al.^{14,15}

For Concrete B, \dot{e}_{gen} is modeled from calorimetry. Specifically, the work of Xu et al.¹⁶ is drawn upon and isothermal cement calorimetry data is used to simulate the adiabatic temperature history $T_{c,a}$ of hydrating concrete.¹⁷ Such simulated adiabatic temperature rise is then used to find the parameters of the \dot{e}_{gen} model of Cervera et al.¹⁸ by regression. This model for \dot{e}_{gen} is derived by thermodynamic reasoning, starting with the assumption that diffusion is the primary physical mechanism in cement hydration. Despite

recent research casting doubt on this underlying assumption,¹⁹ the current study nevertheless uses Cervera's model as it permits an easily constructed model of hydration from isothermal calorimetry that represents hydration more accurately than the three-parameter model using the relations of Riding et al.^{14,15} for this cement. In doing this, this model is not considered to be a true representation of the underlying physics and chemistry, but employs it as a curve fit to data that yields a computationally convenient calculation recipe.

The Cervera model begins similar to other models, relating the rate of energy generation to the rate of change of the degree of hydration, but rather than use the equivalent age t_e , an Arrhenius-type relation models rate of change of α with real-time t

$$\dot{e}_{gen} = H_u m_{cm} \frac{d\alpha}{dt} = H_u m_{cm} A(\alpha, t) \cdot \exp\left(-\frac{E_a}{RT_c}\right) \quad (4)$$

where $A(\alpha, t)$ is a normalized affinity, which can be expressed in terms of the adiabatic concrete temperature history $T_{c,a}$ as

$$A(\alpha) = \frac{\alpha_u}{\Delta T_a} \frac{\partial T_{c,a}}{\partial t} \cdot \exp\left(-\frac{E_a}{RT_{c,a}}\right) \quad (5)$$

The affinity A can also be modeled with polynomials of varying degree.^{18,20,21} Herein, the polynomial used by Cervera et al. is used

$$A(\alpha) = \psi_1(\psi_2 + \alpha)(\alpha_u - \alpha) \cdot \exp\left(-\psi_3 \frac{\alpha}{\alpha_u}\right) \quad (6)$$

where ψ_* are material properties experimentally determinable by regressing Eq. (5) and (6) together on adiabatic temperature histories and initial concrete temperatures $T_{i,c}$. Herein, ψ_* of the form is taken

$$\begin{aligned} \psi_1 &= \gamma_{1,0} T_{i,c}^2 + \gamma_{1,1} T_{i,c} + \gamma_{1,2} \\ \psi_2 &= \gamma_{2,0} \cos\left[\gamma_{2,1} \cdot \left(\frac{T_{i,c} - T_{i,c,min}}{T_{i,c,max} - T_{i,c,min}}\right) + \gamma_{2,2}\right] + \gamma_{2,3} \quad (7) \\ \psi_3 &= \gamma_{3,0} T_{i,c}^2 + \gamma_{3,1} T_{i,c} + \gamma_{3,2} \end{aligned}$$

where $T_{i,c}$ is the initial concrete temperature upon placement; and $T_{i,c,min}$ and $T_{i,c,max}$ are the minimum and maximum initial temperatures used in the set of adiabatic temperature rise simulations ($T_{c,a}$ as simulated from isothermal calorimetry) used for regression. The ultimate product of these regressions is values for the parameters ψ_* . Equations (4) through (7) thus constitute a complete experimentally derived model for \dot{e}_{gen} as a function of initial concrete temperature.

Appendix B provides validation of these two \dot{e}_{gen} models.

Case 1: no postcooling

For emplacements that are not postcooled, a series of 3-D finite element simulations were run on cuboids of varying sizes and shapes, initial temperatures, and ambient temperatures. The governing equation is Eq. (1) in Cartesian coordinates where, for this case, the hydration term \dot{e}_{gen} is modeled using the three-parameter model of Eq. (2) and (3) with the

parameters computed with the relations of Riding et al.^{14,15} for Concrete A.

The boundary condition on the bottom surface ($x,y,z = 0$) is conservatively taken to be adiabatic, while the boundary conditions on all other surfaces were modeled with a convection-type condition, where the convection coefficient incorporates the influence of formwork as necessary and under the assumption that formwork thermal mass is negligible compared to concrete thermal mass. Solar radiation was not modeled.

Simulations were conducted using the open-source finite-element platform FEniCS,^{22,23} version 2019.1.0. Thirty cuboids between 0.2 and 15.3 m³ (0.3 and 20 yd³) were simulated at each of the 17 combinations of initial and ambient conditions spanning 4.4 to 32.2°C for a total of 510 simulations, each run to model 96 hours = 4 days of curing. To save computational time, symmetry was used to limit the domain of each simulation and was one-quarter of a cuboid with symmetry conditions applied at each subdividing plane. In all cases, the convection coefficient was taken to be 2.8 W/(m²K) for the sides (incorporating formwork) and 23 W/(m²K) for the top surface (no formwork).

For each simulation, the maximum concrete temperature at any time and any location $T_{max,c}$ in the simulated domain was found. To relate this maximum temperature to the parameters and ensure dimensional consistency, scaling arguments^{24,25} were used to postulate the following relation

$$\frac{T_{max,c}}{T_{i,c}} = G\left(\frac{qA^3}{V^2}, \frac{T_\infty}{T_{i,c}}, \frac{T_{i,c}}{\Delta T_a}, \frac{qA\Delta T_a c_c^3 \rho_c^2}{\kappa_c^2}\right) \quad (8)$$

in which V is the cuboid volume; and qA is the area of the sides and top of the cuboid, from which heat transfer q may occur between concrete surfaces and the surroundings. The function G is an unknown but assumed, somewhat arbitrarily, to be of the multiplicative form, the log-transformed version of which

$$\begin{aligned} \log\left(\frac{T_{max,c}}{T_{i,c}}\right) &= \log(a) + b \cdot \log\left(\frac{qA^3}{V^2}\right) + c \cdot \log\left(\frac{T_\infty}{T_{i,c}}\right) \\ &\quad + d \cdot \log\left(\frac{T_{i,c}}{\Delta T_a}\right) + f \cdot \log\left(\frac{qA\Delta T_a c_c^3 \rho_c^2}{\kappa_c^2}\right) \quad (9) \end{aligned}$$

was regressed on simulation data using the Python package statsmodels²⁶ to determine the constants $\{a,b,c,d,f\}$. In dimensional form, Eq. (9) can be rewritten

$$T_{max,c} = C_1 \cdot T_{i,c}^g \cdot q A^h \cdot V^j \cdot T_\infty^k \quad (10)$$

in which $C_1 = a c_c^m \cdot \kappa_c^n \cdot \rho_c^p \cdot \Delta T_a^q$ is a constant for a given concrete and the exponents $\{a,g,h,j,k,m,n,p,q\}$ are simple functions of the exponents and coefficients in Eq. (8) and (9). Equation (10) is a surrogate model: an encapsulation of the simulations on which it is regressed and may be converted into nomogram form.

Case 2: postcooling

Two different postcooling situations were modeled: a single cylinder of concrete with a cooling pipe along its axis, and a 3-D array of pipes of varying arrangements. In both situations, the hydration term \dot{e}_{gen} is modeled following Cervera et al.¹⁸ through Eq. (4) through (7) for Concrete B. Flow rates were all taken to be such that flows are fully turbulent.

The single-cylinder simulations used a dimensional form of the model of Myers et al.²⁷ that describes concrete temperatures in the radial direction and water temperatures along the axial pipe. In this model, the heat transfer in the axial direction of the concrete is shown to be negligible, so the governing Eq. (1) in cylindrical coordinates becomes 1-D. The outer surfaces of the concrete—that is, the cylindrical surface at the maximum radius and the capping doughnut surfaces at the top and bottom of the cylinder—are adiabatic.

Similar to the modeling of the formwork in Case 1, the pipe wall is not modeled explicitly (that is, temperatures within the pipe wall are not simulated), and the impact of pipe geometry and material is incorporated into the boundary condition for the concrete at $r = r_p$, the outer radius of the pipe/inner radius of the (hollow) concrete cylinder

$$\kappa_c \frac{\partial T_c}{\partial r} |_{r=r_p} = H(T_c|_{r=r_p} - T_w) \quad (11)$$

where T_w is the water temperature; and H is a heat transfer coefficient that encapsulates conduction through the pipe wall and fully developed turbulent convection between the inner pipe surface and the flowing water

$$H = \frac{1}{r_p} \left(\frac{\ln(r_p/r_{pi})}{\kappa_p} + \frac{1}{h_p r_{pi}} \right)^{-1} \quad (12)$$

where r_{pi} is the inner radius of the pipe; κ_p is the thermal conductivity of the pipe material; and h_p is the convection coefficient within the pipe as computed using the Darcy friction factor and the Gnielinski correlation.²⁸⁻³⁰

The temperature of the water is modeled by

$$\frac{\dot{V}}{\pi r_p^2} \frac{\partial T_w}{\partial z} = \frac{2H}{\rho_w c_w r_p} (T_c|_{r=r_p} - T_w) \quad (13)$$

where \dot{V} is the water volume flow rate; and ρ_w and c_w are the density and specific heat of water, respectively. The boundary condition is $T_{e,w} = T_w(z = 0, t)$, where $T_{e,w}$ is the water temperature at the entrance of the pipe. Note that the governing equations for this case are both 1-D but in different directions; this model is referred to as being quasi-one-dimensional.

This model was implemented in the open-source spectral method solution package Dedalus³¹ due to the ease with which the equation for the concrete can be solved with spectral methods nearly simultaneously with Eq. (13) for the water, which is solved using an explicit Euler scheme at each time step.

Despite the limitations of this model (no connection to the surrounding environment, only one pipe) its relatively simple nature and computational efficiency compared to a full 3-D simulation with an array of pipes facilitates the exploration of the parameter space, which is larger for postcooling that for the case without postcooling (additional parameters include, for example, pipe sizes and lengths, concrete cylinder radii, water flow rates, and inlet temperatures in addition to initial concrete temperature). To enable efficient coverage of this parameter space, the Python package scikit-optimize was used to select samples by Latin hypercube sampling (LHS)^{32,33} given the static choice of Concrete B and PEX tubing. In total, 2700 distinct simulations were run, and as with the no-postcooling case, the maximum concrete temperature at any place and time $T_{max,c}$ was found and stored for each simulation.

An additional caveat with this quasi-one-dimensional model is that it likely informs only situations in which pipes are tightly packed so that the adiabatic boundary condition on the outer surface of the cylinder can be approximated. It is postulated that hexagonal packing—refer to Fig. 1(a) for an example—may be informed by this model, something that will be discussed in the “Results” section. Note that the red circle in this figure, and the similar figures to follow, depicts an “effective thermal spacing” hypothesized to indicate the locus of maximum temperature and to serve as the appropriate spacing metric to use in these nomograms (please refer to www.concrete.org for full-color version of figures).

For square and rectangular packing, 3-D simulations were run varying nominal pipe sizes, spacing between pipes, flow rates, water inlet temperatures, and initial temperatures for cuboids of sufficient size that the surroundings do

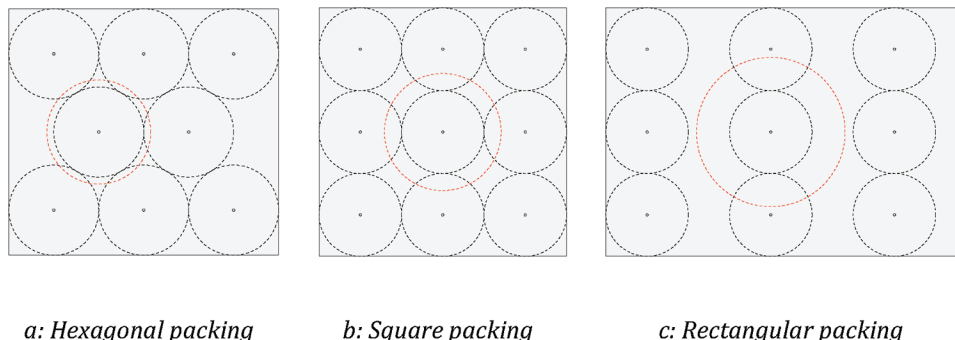


Fig. 1—Three types of pipe packing. Small solid circles represent pipes. Gray circles centered on pipes represent minimum physical spacing, whereas red circle is postulated “effective thermal spacing.”

not influence maximum temperatures $T_{max,c}$. Symmetry was used to limit the computational domain to the square or rectangular volume around the pipe with symmetry boundary conditions applied. In total, 328 distinct 3-D simulations were run—a smaller number than previously due to the smaller effective parameter space revealed by the quasi-one-dimensional simulations. The maximum concrete temperature at any place and time $T_{max,c}$, as well as the maximum temperature at the deepest point of the cuboid (chosen because it was guaranteed to be far from piping, which for some cases with smaller pipes led to isolated elements of low quality; in practice, the difference between these temperatures was negligible), was found and stored for each simulation.

Appendix B also provides comparisions between simulations using the quasi-one-dimensional Myers model and 3-D postcooling models against an exact solution.

As with the no-postcooling case, dimensional analysis was used to find dimensionless groupings of the important parameters. In this case

$$\frac{T_{max}}{\Delta T_a} = K \left(\frac{T_{i,c}}{\Delta T_a}, \frac{T_{e,w}}{\Delta T_a}, \frac{r_p^2 c_c \Delta T_a}{v_c^2}, \frac{r_c^2 c_c \Delta T_a}{v_c^2} \right) \quad (14)$$

where $v_c = \kappa_c / (\rho_c c_c)$ is the thermal diffusivity of the concrete. As before, the function K was assumed to be multiplicative in its inputs $T_{i,c}/\Delta T_a$ and so on. This function K was log-transformed to allow multi-linear regression on the simulation results, thus yielding the parameters for a surrogate model. In dimensional form, this surrogate model is

$$T_{max,c} = C_2 T_i^0 r_c^0 T_w^0 r_p^0 \quad (15)$$

where $C_2 = \beta c_c^\phi v_c^\zeta \Delta T_a^\delta$ is a constant for a given concrete; β serves the same role as a in Eq. (9); and all Greek letters are determined by the regression.

RESULTS

No postcooling

Regressions were carried out on simulation data for the cuboids shown in Fig. 2, each of which has a volume to heat transfer area ratio $V/qA \geq 0.305$ m (smaller V/qA ratios, which may not qualify as mass concrete, led to poor-quality regressions). For this condition, Fig. 3 depicts the error between the surrogate model maximum temperature predictions given by the surrogate model—Eq. (10)—and the finite element simulations corresponding to each surrogate model prediction. The median error is 0.311°C and the first and third quartiles are -1.35 and 1.14°C ; thus, roughly 50% of the errors are under $4/3^\circ\text{C}$.

Equation (10) after regression is depicted nomographically in Fig. 4. Users are thus aware of the approximate nature of this nomogram and can use it to account for the risk due to inaccuracy; the errors depicted in the histogram of Fig. 3 are represented as a quartile box-plot-type feature in the space between the maximum temperature axis and the gridded field under it: the outer dots depict the minimum and maximum errors and the whiskers depict the range

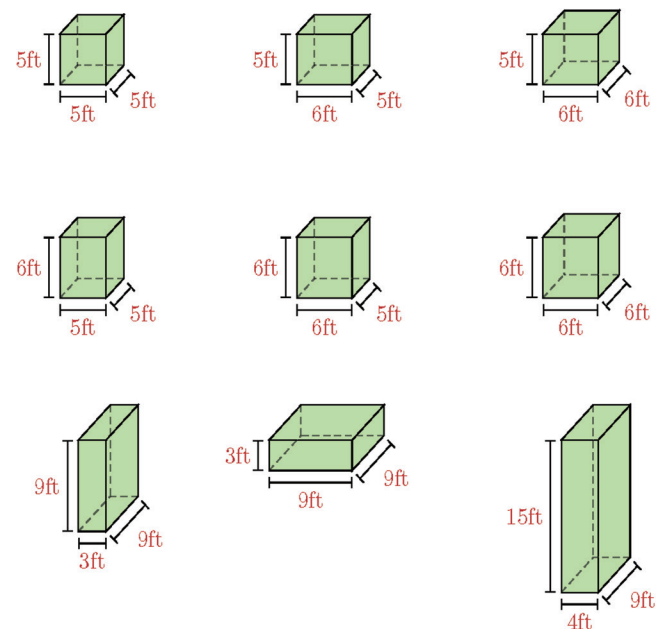


Fig. 2—Case 1 cuboids used for regressions.

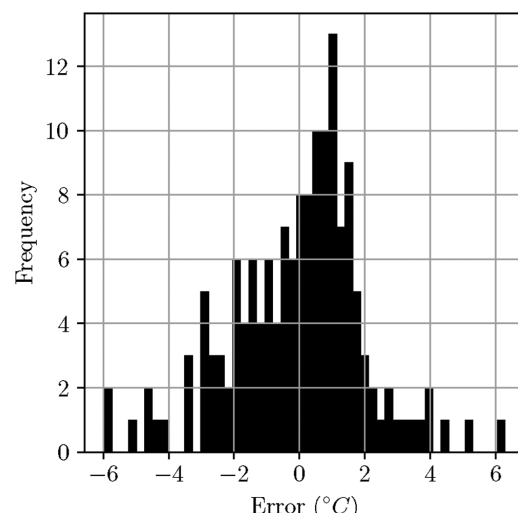


Fig. 3—Histogram of error between no-postcooling surrogate model and simulation results used to generate surrogate model (that is, this is an in-sample comparison).

between the 25th and 75th percentiles. Here, the solid cyan isopleth depicts an out-of-sample use of the nomogram: the previously described real-world abutment wall, herein using Concrete A instead of Concrete B and simulated as if it were not postcooled; the upward-pointing arrow in the quartile plot shows the maximum temperature of this wall from such a simulation. The nomogram gives a maximum temperature of 83°C , whereas the finite-element simulation gives 82°C —an overestimation of 1°C or a percent error of 1%.

Postcooling

Given that the surrogate model for postcooling, Eq. (5), is of the same form as the surrogate model for the no-postcooling case, the nomograms for postcooling are likewise of the same form. Here, nomograms for the hex packing and rectangular packing configurations are given along with the examination of the use of the “physical

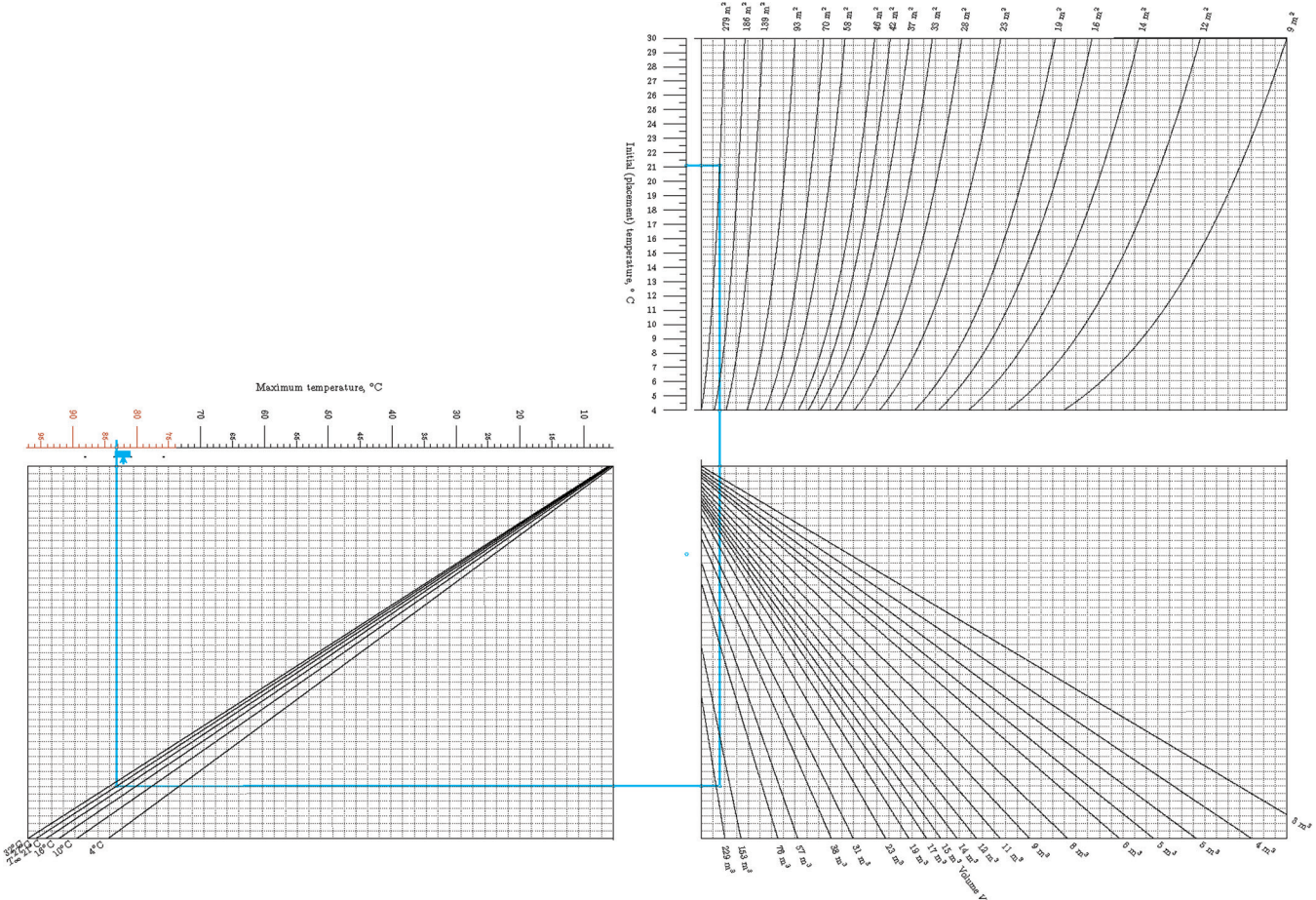


Fig. 4—No postcooling nomogram. Isopleth is out-of-sample calculation representing real-world mass concrete wall (1.83 m wide x 18.3 m deep x 6.1 m high).

spacing” and “effective thermal spacing” as depicted by the black and red circles, respectively, in Fig. 1(a) through (c). The effective thermal spacing is postulated to best represent the adiabatic conditions in the model used for hexagonal packing as it intersects the point equidistant from three neighboring cooling pipes. Similar considerations suggest this is the case for square or rectangular packing as well.

For brevity, figures showing errors analogous to Fig. 4 are omitted and refer readers to the quartile plots in the nomograms.

Figure 5 shows a nomogram founded on the quasi-one-dimensional model of Myers et al.²⁷ postulated to be appropriate for hexagonal packing. The dashed and solid green isopleths depict the physical and effective thermal spacing; the green arrow is the solution of a 3-D finite-element simulation of hexagonal packing corresponding to this example. Differences between the nomogram computation and finite-element simulation are 2°C in both cases; rounding to the nearest place, the error is 4% for both.

Hex packing is the most efficient space-filling arrangement, but it may be difficult to implement in practice. The authors postulate that only the effective pipe-to-pipe spacing should be used for square or rectangular packing. This effective spacing is simply the diagonal distance between pipes for such packing arrangements. Figure 6 shows a nomogram based on the Myers model with isopleths for square and rectangular piping arrangements. The green isopleth is

for square packing with 0.31 m pipe-to-pipe spacing; the green arrow is the 3-D finite-element simulation result for this arrangement, which is considered the true result. The red isopleth is for a 0.31 x 0.610 m pipe array, with the red arrow depicting the corresponding 3-D finite-element simulation “true” result. In both cases, the nomogram substantially overestimates the maximum temperature. With square packing, the nomogram (green isopleth) gives a maximum temperature of just under 47°C, whereas the 3-D simulation (green arrow) yielded approximately 38°C—a difference of approximately 9°C. For rectangular spacing, the difference between red isopleth (nomogram calculation) and red arrow (3-D simulation) is roughly 5°C. This motivates the need for a separate set of nomograms for such piping arrangements.

Figure 7 depicts a nomogram for square or rectangular packing, trained using 3-D simulations of such arrangements, with an out-of-sample comparison between a nomogram calculation and the real-world abutment wall as post-cooled. In this case:

- Initial temperature of 21°C;
- Effective spacing for a 0.31 x 0.610 m pipe array being 0.68 m;
- Chilled water temperature of 7.2°C; and
- 19 mm PEX tubing.

The maximum monitored temperature was 54.2°C. Figure 7 depicts this comparison.

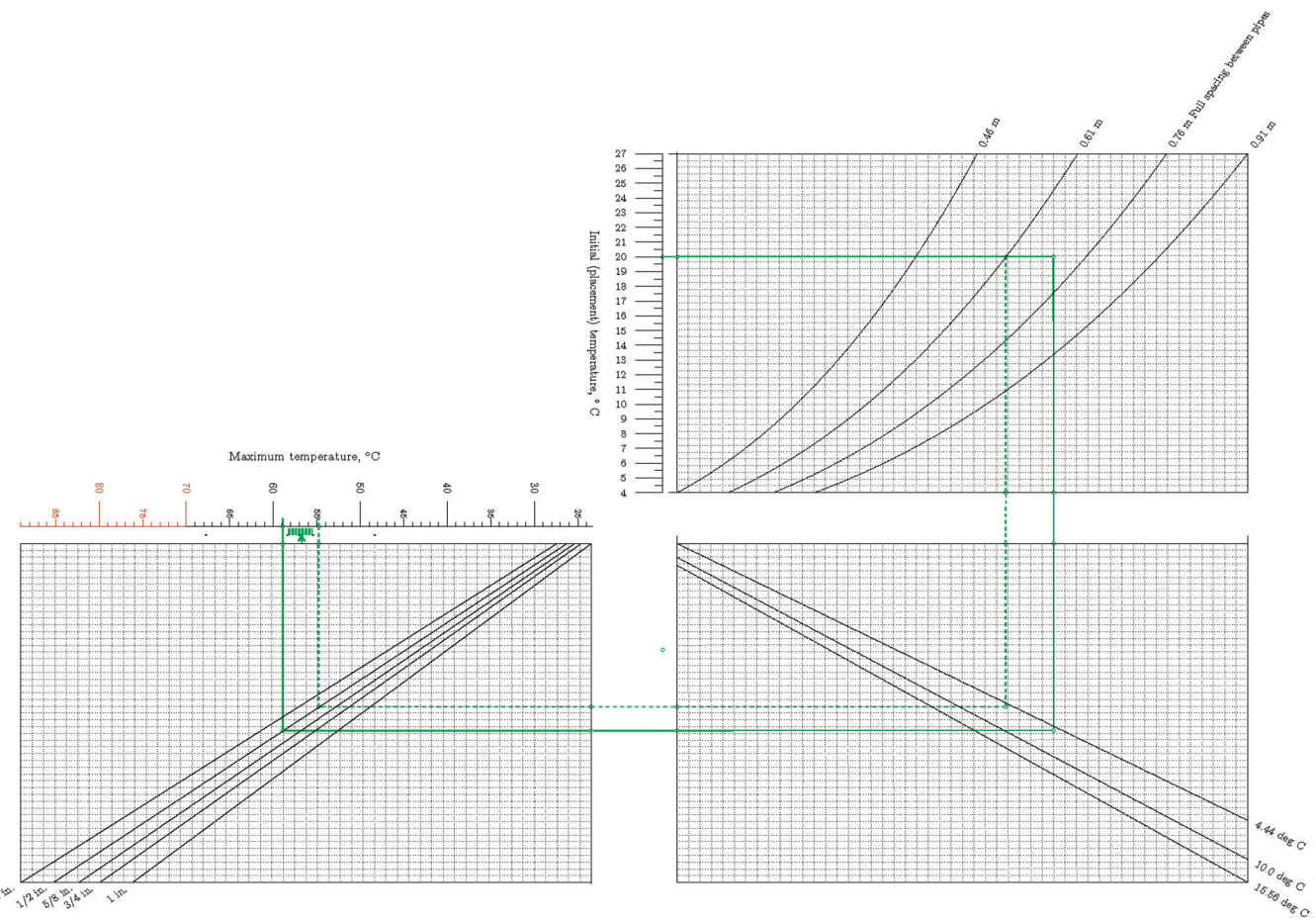


Fig. 5—Postcooling nomogram from Myers model, postulated for hex packing, using physical spacing with out-of-sample hex packing comparison. Green arrow indicates 3-D finite-element simulation result corresponding to isopleth. (Note: Full-color PDF can be accessed at www.concrete.org.)

Here, the nomogram gives a peak temperature of approximately 50°C—an underestimate of 4.2°C and an error of just under 8%.

Summary

Table 1 summarizes the data depicted in Fig. 4 through 7 using more precise values calculated from the underlying surrogate models. For Fig. 4 through 6, the “true” values of $T_{max,c}$ are taken to be out-of-sample 3-D finite-element simulations. In the no-postcooling case of Fig. 4, this simulation is of the abutment wall (but not postcooled), an emplacement one order of magnitude larger than the largest in the training set shown in Fig. 2 (204 versus 15.3 m³). The 1.3% error in this case suggests that a relatively small training set of the sizes used (Fig. 2) may provide sufficient information for a surrogate model to handle such large extrapolations; testing this conjecture this is a topic of ongoing work.

Figures 5 and 6 were trained on the quasi-one-dimensional Myers model, while the “true” values of $T_{max,c}$ were taken from 3-D finite-element simulations. The percent errors of -3.5 and 3.7% for using physical (pipe-to-pipe) or effective spacing (Fig. 5) indicates the Myers model works well for hexagonal packing, whereas the 48.0, 23.2, and 10.8% errors (Fig. 6) suggest distrust or at best caution for square or rectangular spacing.

Figure 7 was trained on 3-D finite-element simulations, and the true value of $T_{max,c}$ is from real-world monitored data of the actual, postcooled abutment wall during hydration. The error in this case is 7.4%, approaching the conventional sufficient engineering accuracy value of 5%.

DISCUSSION AND CONCLUSIONS

The nomograms presented herein are intended to support a variety of decisions on the thermal aspects of mass concrete. When considered with the maximum possible (adiabatic) temperature of a given emplacement calculated, say, using

$$T_{c,max,a} = T_{i,c} + \Delta T_a \quad (16)$$

where

$$\Delta T_a = \frac{H_u m_{cm} \alpha_u}{\rho_c c_c} \quad (17)$$

and α_u is the ultimate degree of hydration; a no-postcooling nomogram such as Fig. 4 can reveal how “non-adiabatic” a situation is—that is, it indicates how the size and shape of the emplacement cause deviation from the “worst case” and may be useful in deciding if postcooling is necessary.

Figure 7 and Table 1 show that the real-world wall is comfortably below the maximum allowable temperature

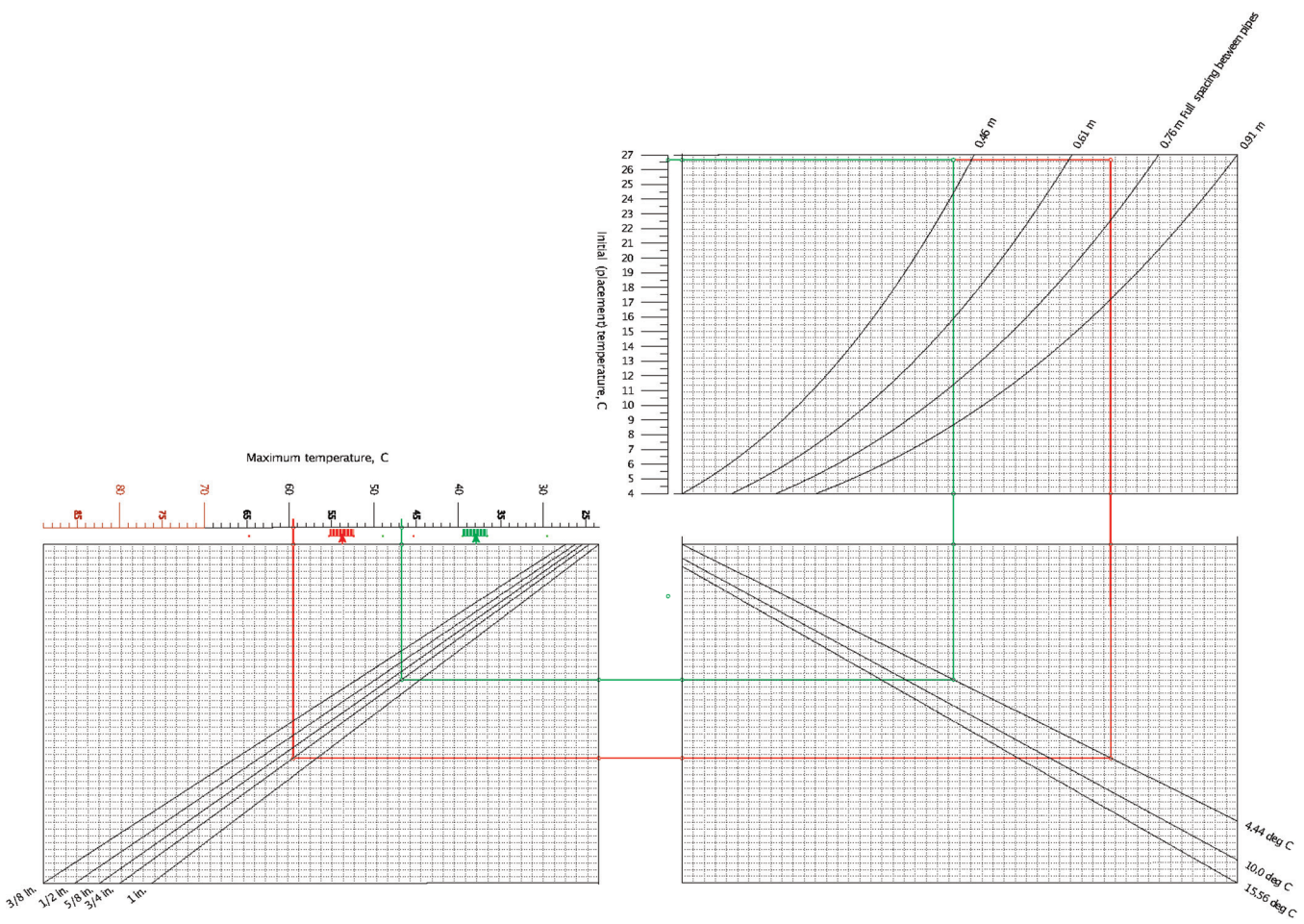


Fig. 6—Postcooling nomogram from Myers model, compared to out-of-sample comparisons using effective thermal spacing for square packing situation (green isopleth) and rectangular packing situation (red isopleth). Green and red arrows point out results of 3-D finite-element simulations corresponding to green and red isopleths, respectively. (Note: Full-color PDF can be accessed at www.concrete.org.)

Table 1—Summary of results in Fig. 5 through 7

Figure	Computational geometry	No postcooling				
		True T_{max} , °C	Nomogram T_{max} , °C	Error %		
4	Abutment wall	82.1	83.2	1.3%		
Postcooling						
		True T_{max} , °C	Physical spacing		Effective spacing	
			Nomogram T_{max} , °C	Error %	Nomogram T_{max} , °C	Error %
5	0.31 m hex packing	56.7	54.7	-3.5%	58.8	3.7%
6	0.31 x 0.31 m pipe spacing	37.9	56.1	48.0%	46.7	23.2%
6	0.31 x 0.61 m pipe spacing	53.7	—	—	59.5	10.8%
7	0.31 x 0.61 m pipe spacing	54.2	—	—	50.2	-7.4%

of 73.9°C. This project employed both precooling of fresh concrete to 21°C by liquid nitrogen as well as postcooling, and using the nomograms presented herein, one could ask if this project could be conducted with only one thermal management technique. Equation (16) with $\Delta T_a = 52^\circ\text{C}$ (Appendix A) shows that with precooling to 21°C, the maximum possible temperature would be 73°C, just below the allowable maximum temperature, although not

comfortably. Working “backwards” using Fig. 7, starting with a maximum allowable temperature of 73.9°C and incorporating, as a rough accounting for uncertainty, the minimum to maximum ends of the boxplot below the maximum temperature axis—a roughly 12°C span—can give a conservative estimate of the allowable initial temperature given the postcooling system used for this project. Starting with a maximum temperature of 73.9°C – 12°C = 61.9°C, the

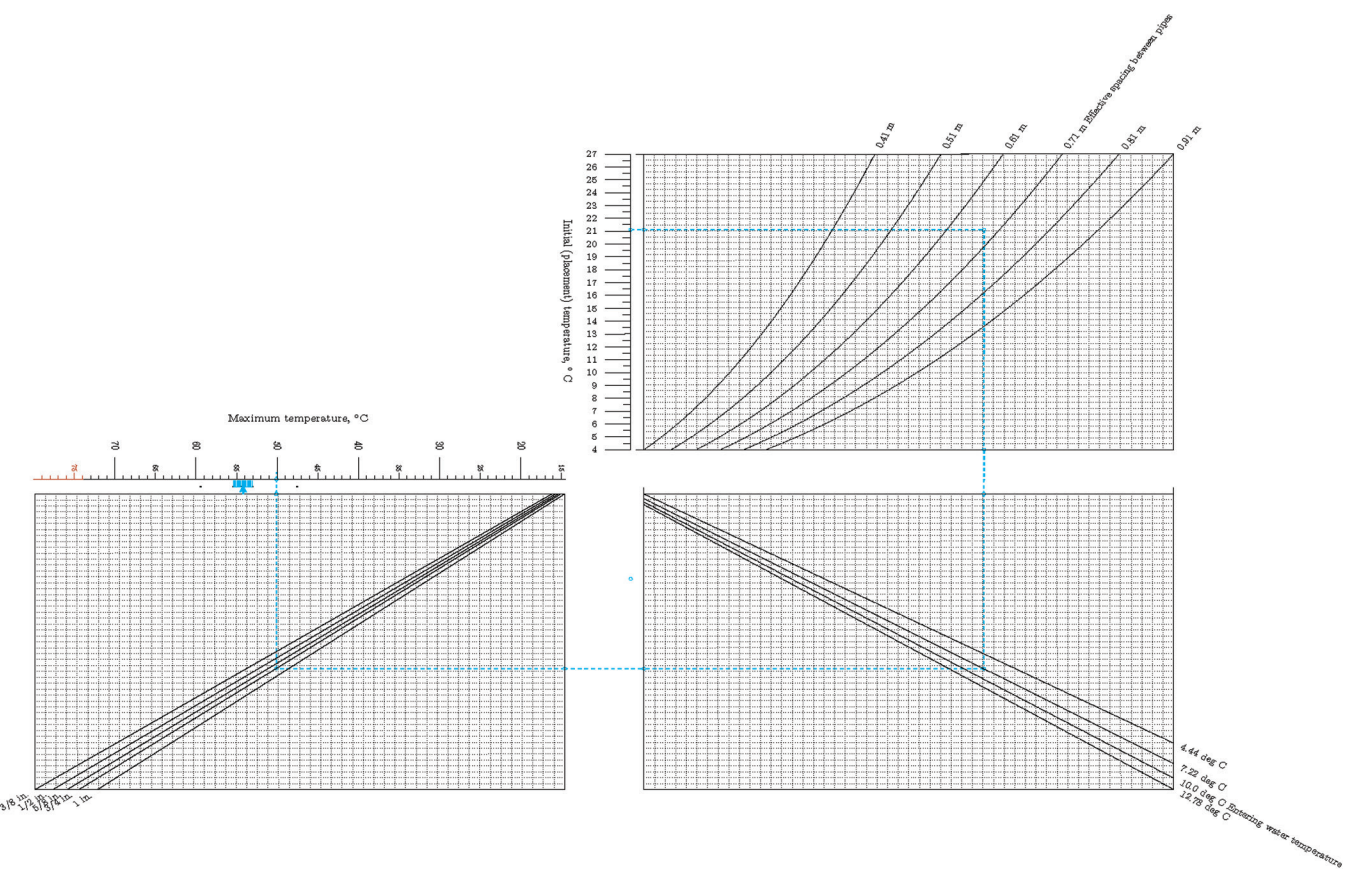


Fig. 7—Postcooling nomogram from 3-D finite-element simulations of rectangular or square packing. Dashed cyan isopleth is out-of-sample case—abutment wall—and cyan arrow gives maximum monitored temperature. (Note: Full-color PDF can be accessed at www.concrete.org)

nomogram suggests the initial concrete temperature can be as high as 32.5°C and that precooling may not be necessary.

The boxplots in the nomograms depict the spread in the simulations underlying the surrogate models that the nomograms visually depict. However, this spread is likely an imperfect estimate of the true uncertainty. Their use in the aforementioned discussions carries the additional risk that their use to quantify the uncertainty is itself uncertain.

Future work includes a more rigorous assessment of uncertainty and making the nomograms applicable to a variety of concrete designs (one of the limitations of the present work). Here, the nomograms are tied to a particular concrete mixture, parameterized in the surrogate models by the constants C_1 and C_2 . However, these terms are not required to be taken as constants and can be decomposed into free parameters such as ΔT_a and depicted as nomogram axes. With more calorimetry data, simulation runs with a variety of concrete designs and a wider array of shapes, sizes, and boundary conditions will increase the generality of these nomograms. This additional work, coupled with Bayesian techniques and alternative forms of surrogate models, will also give more confident uncertainty estimates. Furthermore, the techniques used herein will be applied to temperature differences and thermal gradients.

The uncertainty to underscore that these nomograms and their use are intended to be used as preliminary analyses is emphasized in support of crafting thermal management plans for mass concrete: they rapidly identify promising designs as

well as illuminate designs to avoid. This, together with the limitations embedded in the nomograms due to assumptions such as ignoring the impact of solar gains, motivates not their disuse but use to find only a small number of plans to be finalized with more detailed analyses.

AUTHOR BIOS

Jason Brown is a Senior Research Engineer in the School of Civil and Environmental Engineering at Georgia Institute of Technology, Atlanta, GA. He received his BS in engineering from Baylor University, Waco, TX, and his MS in mechanical engineering and PhD in architecture from Georgia Institute of Technology. His research interests include heat transfer and building energy modeling.

Luna E. Al-Hasani is a graduate of the School of Civil and Environmental Engineering at Georgia Institute of Technology and a Researcher in civil engineering. She received her BSc from the University of Jordan, Amman, Jordan; her MSc from the University of Sheffield, Sheffield, UK; and her PhD from Georgia Institute of Technology in 2012, 2014, and 2022, respectively. Her research interests include the durability of concrete and the properties of concrete at early ages.

Jisoo Park is an Assistant Professor in the Department of Built Environment at Indiana State University, Terre Haute, IN. He received his BS and MS in civil engineering from Hanyang University, Seoul, South Korea, and his PhD in civil engineering from Georgia Institute of Technology in 2008, 2010, and 2020, respectively. His research interests include building construction materials and construction automation.

Kimberly E. Kurtis, FACI, is the Raymond Allen Jones Chair and Professor in the School of Civil and Environmental Engineering at Georgia Institute of Technology. She is a Director on the ACI Board of Direction and is a member of ACI Committees 201, Durability of Concrete; 225, Hydraulic Cements; and 236, Material Science of Concrete. Her research interests

include composition and processing linkages to multi-scale structure and performance for a range of applications.

Russell Gentry is a Professor of architecture and civil engineering at Georgia Institute of Technology. He received his BSCE and MSCE from Georgia Institute of Technology and his PhD in civil engineering from the University of Michigan, Ann Arbor, MI. He is a member of ACI Committee 440, Fiber-Reinforced Polymer Reinforcement.

Yong Kwon Cho is a Professor at Georgia Institute of Technology. He received his BS, MS, and PhD in civil engineering from Inha University, Tashkent, Uzbekistan, in 1996; Georgia Institute of Technology in 1997, and the University of Texas at Austin, Austin, TX, in 2000, respectively. He received the Tucker-Hasegawa Award from the International Association for Automation and Robotics in Construction (IAARC) in 2022. His research interests include infrastructure maintenance, construction automation, and robotics.

ACKNOWLEDGMENTS

This work was funded by the Georgia Department of Transportation under RP 16-25 and RP 19-04, for which the authors wish to express their gratitude.

REFERENCES

1. ACI Committee 207, "Guide to Mass Concrete (ACI 207.1R-05)," American Concrete Institute, Farmington Hills, MI, 2006, 30 pp.
2. ACI Committee 207, "Report on Thermal and Volume Change Effects on Cracking of Mass Concrete (ACI 207.2R-07)," American Concrete Institute, Farmington Hills, MI, 2007, 28 pp.
3. Collepardi, M., "A State-of-the-Art Review on Delayed Ettringite Attack on Concrete," *Concrete Durability*, V. 25, No. 4, 2003, pp. 401-407. doi: 10.1016/S0958-9465(02)00080-X
4. American Concrete Institute, "ACI Concrete Terminology (ACI CT-21)," ACI, Farmington Hills, MI, 2021, 80 pp.
5. ACI Committee 207, "Cooling and Insulating Systems for Mass Concrete (ACI 207.4R-20)," American Concrete Institute, Farmington Hills, MI, 2020, 20 pp.
6. Evesham, H. A., *The History and Development of Nomography*, Docent Press, LLC, Boston, MA, 1982.
7. Hankins, T. L., "Blood, Dirt, and Nomograms: A Particular History of Graphs," *Isis*, V. 90, No. 1, 1999, pp. 50-80. doi: 10.1086/384241
8. Brodetsky, S., *A First Course in Nomography*, George Bell & Sons, London, UK, 1920.
9. Balachandran, V. P.; Gonen, M.; Smith, J. J.; and DeMatteo, R. P., "Nomograms in Oncology: More Than Meets the Eye," *The Lancet. Oncology*, V. 16, No. 4, 2015, pp. e173-e180. doi: 10.1016/S1470-2045(14)71116-7
10. Kosmatka, S. H., *Design and Control of Concrete Mixtures*, 13th edition, Portland Cement Association, Skokie, IL, 1992.
11. Silva, W. R. L., and Šmilauer, V., "Nomogram for Maximum Temperature of Mass Concrete," *Concrete International*, V. 37, No. 5, May 2015, pp. 30-36.
12. Nguyen, T.-C.; Nguyen, V.-Q.; Aniskin, N.; Phung, B.-T.; and Hoang, Q.-L., "Building a Nomogram to Predict Maximum Temperature in Mass Concrete at an Early Age," *E3S Web Conference*, V. 263, 2021, 10 pp.
13. Roschier, L., and Boulet, D., "pyNomo," 2020.
14. Riding, K. A.; Poole, J. L.; and Folliard, K. J.; Juenger, M. C. G.; and Schindler, A. K., "New Model for Estimating Apparent Activation Energy of Cementitious Systems," *ACI Materials Journal*, V. 108, No. 5, Sept.-Oct. 2011, pp. 550-557.
15. Riding, K. A.; Poole, J. L.; and Folliard, K. J.; Juenger, M. C. G.; and Schindler, A. K., "Modeling Hydration of Cementitious Systems," *ACI Materials Journal*, V. 109, No. 2, Mar.-Apr. 2012, pp. 225-234.
16. Xu, Q.; Wang, K.; Medina, C.; and Engquist, B., "A Mathematical Model to Predict Adiabatic Temperatures from Isothermal Heat Evolutions with Validation for Cementitious Materials," *International Journal of Heat and Mass Transfer*, V. 89, 2015, pp. 333-338. doi: 10.1016/j.ijheatmasstransfer.2015.05.035
17. Al-Hasani, L. E.; Park, J.; Perez, G.; Herndon, H. N.; Brown, J. B.; Cho, Y. K.; Gentry, T. R.; and Kurtis, K. E., "Quantifying Concrete Adiabatic Temperature Rise Based on Temperature-Dependent Isothermal Calorimetry; Modeling and Validation," *Materials and Structures*, V. 55, No. 7, 2022, p. 191. doi: 10.1617/s11527-022-02023-6
18. Cervera, M.; Oliver, J.; and Prato, T., "Thermo-Chemo-Mechanical Model for Concrete. I: Hydration and Aging," *Journal of Engineering Mechanics*, ASCE, V. 125, No. 9, 1999, pp. 1018-1027. doi: 10.1061/(ASCE)0733-9399(1999)125:9(1018)
19. Scrivener, K.; Ouzia, A.; Julland, P.; and Kunhi Mohamed, A., "Advances in Understanding Cement Hydration Mechanisms," *Cement and Concrete Research*, V. 124, 2019, p. 105823. doi: 10.1016/j.cemconres.2019.105823
20. Zhou, W.; Feng, C.; Liu, X.; Liu, S.; and Zhang, C., "A Macro-Meso Chemo-Physical Analysis of Early-Age Concrete Based on a Fixed Hydration Model," *Magazine of Concrete Research*, V. 68, No. 19, 2016, pp. 981-994. doi: 10.1680/jmacr.15.00321
21. Zhou, W.; Tian, W.; Qi, T.; Liu, S.; Feng, C.; Ma, G.; and Chang, X., "Investigation on Hydration and Mechanical Properties of Mortar Containing Limestone Powder and Fly Ash Based on the Coupled Chemical-Thermal-Mechanical Method," *Materials (Basel)*, V. 13, No. 19, 2020, p. 4387. doi: 10.3390/ma13194387
22. Logg, A.; Kent-Andre, M.; and Wells, G. N., *Automated Solution of Differential Equations by the Finite Element Method*, Springer, New York, 2012.
23. Alnæs, M. S.; Blechta, J.; Hake, J.; Johansson, A.; Kehlet, B.; Logg, A.; Richardson, C.; Ring, J.; Rognes, M. E.; and Wells, G. N., "The FEniCS Project version 1.5," *Archive of Numerical Software*, V. 3, 2015.
24. Buckingham, E., "On Physically Similar Systems; Illustrations of the Use of Dimensional Equations," *Physical Review*, V. 4, No. 4, 1914, pp. 345-376. doi: 10.1103/PhysRev.4.345
25. Sonin, A., "A Generalization of the Pi-Theorem and Dimensional Analysis," *Proceedings of the National Academy of Sciences of the United States of America*, V. 101, No. 23, 2004, pp. 8525-8526. doi: 10.1073/pnas.0402931101
26. Seabold, S., and Perktold, J., "Statsmodels: Econometric and Statistical Modeling with Python," 9th Python in Science Conference, Austin, TX, 2010.
27. Myers, T. G.; Fowkes, N. D.; and Ballim, Y., "Modeling the Cooling of Concrete by Piped Water," *Journal of Engineering Mechanics*, ASCE, V. 135, No. 12, 2009, pp. 1375-1383. doi: 10.1061/(ASCE)EM.1943-7889.0000046
28. Incropera, F. P., and DeWitt, D. P., *Introduction to Heat Transfer*, John Wiley & Sons, Inc., New York, 1990.
29. Saleh, J. M., "Heat Transfer in Pipe Flow," *Fluid Flow Handbook*, first edition, McGraw-Hill Education, New York, 2002.
30. Silcox, G. D.; Noble, J. J.; Sarofim, A. F.; Wankat, P. C.; and Knaebel, K. S., "Heat Transfer by Convection," D. W. Green and M. Z. Southard, eds., *Perry's Chemical Engineers' Handbook*, ninth edition, McGraw-Hill Education, New York, 2019.
31. Burns, K. J.; Vasil, G. M.; Oishi, J. S.; Lecoanet, D.; and Brown, B. P., "Dedalus: A Flexible Framework for Numerical Simulations with Spectral Methods," *Physical Review Research*, V. 2, No. 2, 2020, p. 023068. doi: 10.1103/PhysRevResearch.2.023068
32. Giunta, A.; Wojtkiewicz, S.; and Eldred, M., "Overview of Modern Design of Experiments Methods for Computational Simulations (Invited)," 41st Aerospace Sciences Meeting and Exhibit, American Institute of Aeronautics and Astronautics, Reston, VA, 2003.
33. Viana, F. A. C., "A Tutorial on Latin Hypercube Design of Experiments," *Quality and Reliability Engineering International*, V. 32, No. 5, 2016, pp. 1975-1985. doi: 10.1002/qre.1924
34. Haji-Sheikh, A., "Temperature and Heat Flux Solutions in Two-Layer Concentric Hollow Cylinders with Prescribed Surface Conditions and Volumetric Heat Sources," *Technical Report*, University of Nebraska-Lincoln, Lincoln, NE, Sept. 2014, <https://mme-exact.unl.edu/>. (last accessed Oct. 19, 2023)

APPENDIX A

Table A1—Notation and parameter values

Symbol	Description	Unit	Case 1: Concrete A	Case 2: Concrete B
A	Normalized affinity	1/h	NA	Varies
c_c	Specific heat of concrete	J/kgK	1062	1062
c_w	Specific heat of water	J/kgK	4184	
E_a	Apparent activation energy	J/mol	40,955	37,433
\dot{e}_{gen}	Rate of energy released by hydration	W/m ³		Varies
H	Heat-transfer coefficient	W/m ² K	NA	Varies
H_u	Ultimate energy released by hydration	J/g	472	NA
h_p	Convection coefficient inside cooling pipe	W/m ² K	NA	Varies
m_a	Mass of all aggregate per unit volume of concrete	kg/m ³	1744	1706
m_{cm}	Mass of cementitious material per unit volume of concrete (Type I/II); denoted C_c in some references	kg/m ³	413	397
m_w	Mass of water per unit volume of concrete	kg/m ³	202	182
q_A	Heat-transfer area	m ²		Varies
R	Universal gas constant	J/mol K	8.314	
r_p	Outer radius of cooling pipe	m	NA	Varies
r_{pi}	Inner radius of cooling pipe	m	NA	Varies
T_c	Concrete temperature	K		Varies
$T_{c,a}$	Adiabatic temperature history of concrete	K	NA	Varies
$T_{c,max,a}$	Maximum temperature under adiabatic conditions	K		Varies
$T_{e,w}$	Cooling water entrance temperature	K	NA	Varies
$T_{i,c}$	Initial concrete temperature at placement	K		Varies
T_r	Reference temperature	K	294.25	NA
T_w	Temperature of water in cooling pipe	K		Varies
t	Time	h		Varies
t_e	Equivalent age	h	Varies	NA
V	Volume	m ³		Varies
\dot{V}	Volume flow rate of cooling water	m ³ /s	NA	Varies
w/c	Water-cement ratio	—	0.488	0.458
α	Degree of hydration	Unitless		Varies
α_u	Ultimate degree of hydration	Unitless	0.837	0.78
β	Shape parameter	Unitless	0.84	NA
ΔT_a	Adiabatic temperature rise of concrete	K	65.1	52.0
Δt	Simulation time step	h	0.25, typically	
$\gamma_{1,0}$	Regression parameter	1/sK ²	NA	1.060
$\gamma_{1,1}$	Regression parameter	1/sK	NA	-621.1
$\gamma_{1,2}$	Regression parameter	1/h	NA	91,720
$\gamma_{2,0}$	Regression parameter	Unitless	NA	-0.005103
$\gamma_{2,1}$	Regression parameter	Unitless	NA	-2.899
$\gamma_{2,2}$	Regression parameter	Unitless	NA	3.608
$\gamma_{2,3}$	Regression parameter	Unitless	NA	0.005836
$\gamma_{3,0}$	Regression parameter	1/K ²	NA	0.003416
$\gamma_{3,1}$	Regression parameter	1/K	NA	-2.036
$\gamma_{3,2}$	Regression parameter	Unitless	NA	307.1

Table A1, cont.—Notation and parameter values

Symbol	Description	Unit	Case 1: Concrete A	Case 2: Concrete B
κ_c	Thermal conductivity of concrete	W/mK	1.7	1.7
κ_p	Thermal conductivity of cooling pipe	W/mK	NA	0.41
v_c	Thermal diffusivity of concrete	m ² /s	6.786×10^{-7}	7.002×10^{-7}
ρ_c	Density of concrete	kg/m ³	2359	2286
ρ_w	Density of (cooling) water	kg/m ³	NA	~1000
τ	Time parameter	h	14.6	NA

Note: NA is not available.

APPENDIX B

Figures B1 and B2 compare adiabatic temperatures for Concrete B derived from isothermal cement calorimetry and simulated adiabatic temperatures using the three-parameter maturity model (Eq. (5) and (6) in the text) and the Cervera \dot{e}_{gen} model fitted to isothermal cement calorimetry (Eq. (7) through (10) in the text).

As a check on the 3-D finite-element simulations (done with FEniCS), a simulation was conducted using the Cervera \dot{e}_{gen} model and compared to the real-world footing as described in the “Methods” section. Figure B3 shows a comparison between temperatures recorded at a location 0.41 m below the top surface and temperatures at that same location from the finite-element simulation. Here, the simulation overpredicts the maximum temperature by 1.7°C, an error of 2.5%.

To validate the implementation of the postcooling models, the quasi-one-dimensional model and the full 3-D finite-element models were tested against an exact analytical solution for the temperature field of a two-layer hollow cylinder with constant \dot{e}_{gen} in one or both layers. Specifically, this exact solution is 1-D so that the “cylinder” it models is in fact a disk with convective boundary conditions around the inner and outer circumferences of the domain; this situation is labeled R3C13B00T00G11, and details of the solution can be found in the Exact Analytical Conduction Toolbox.³⁴ In this case, the exact solution was configured to mimic PEX tubing encased in a concrete cylinder with an adiabatic condition at the outside of the outer cylinder and convection derived from water flow rates in the inner hollow of the disk. A constant $\dot{e}_{gen} = 974 \text{ W/m}^3$, equal to the total energy of hydration of Concrete B released at a constant rate over 36 hours, was applied to the concrete, with $\dot{e}_{gen} = 0$ for the pipe layer. Initial and water entrance temperatures were taken to be 0°C, a choice which makes for convenient computation of the exact solution. Further details are given in Table B1. Results from quasi-one-dimensional (Myers, implemented in Dedalus) and 3-D (implemented in FEniCS) simulations were taken at the entrance plane of the respective cylinders. Figures B4 and B5 show both simulations match well to the exact solution and indicate that the treatment of heat transfer through the pipe wall is adequately handled in the model of Myers et al.²⁷

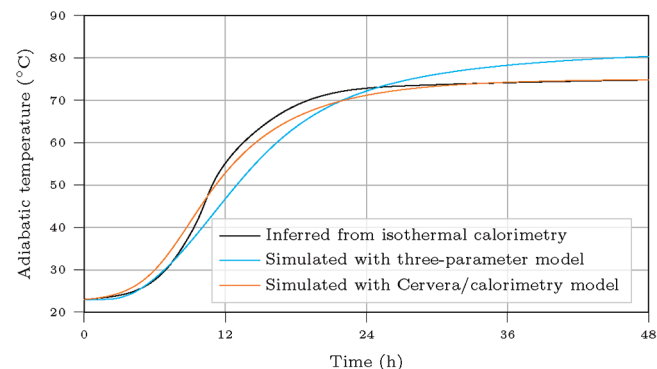


Fig. B1—Comparison of adiabatic temperature histories: Concrete B, initial temperature 23°C.

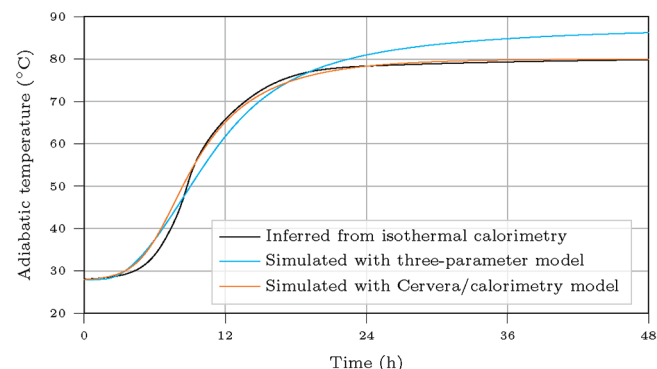


Fig. B2—Comparison of adiabatic temperature histories: Concrete B, initial temperature 28°C.

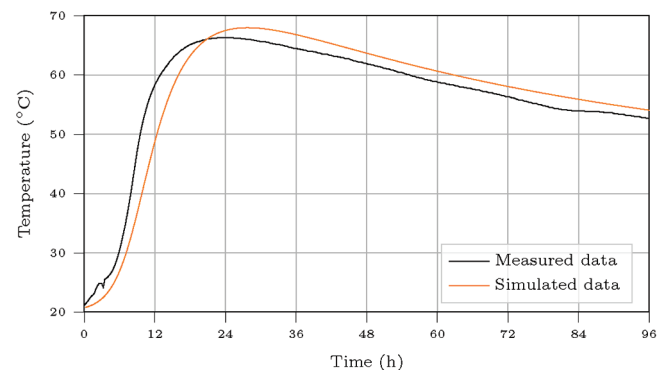


Fig. B3—Comparison of 3-D finite-element simulation model to real-world emplacement.

Table B1—Parameters used in postcooling validations

Test	PEX pipe size	Cylinder radius, m	\dot{V} , L/m
1	13 mm	0.2	9.5
2	19 mm	0.52	21

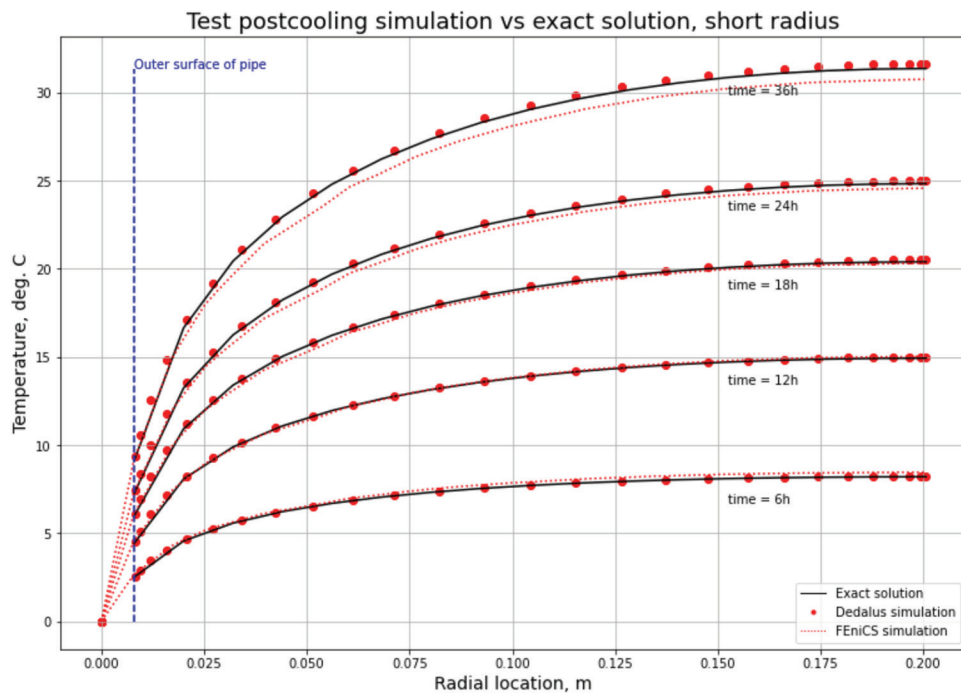


Fig. B4—Postcooling simulation validation test 1.

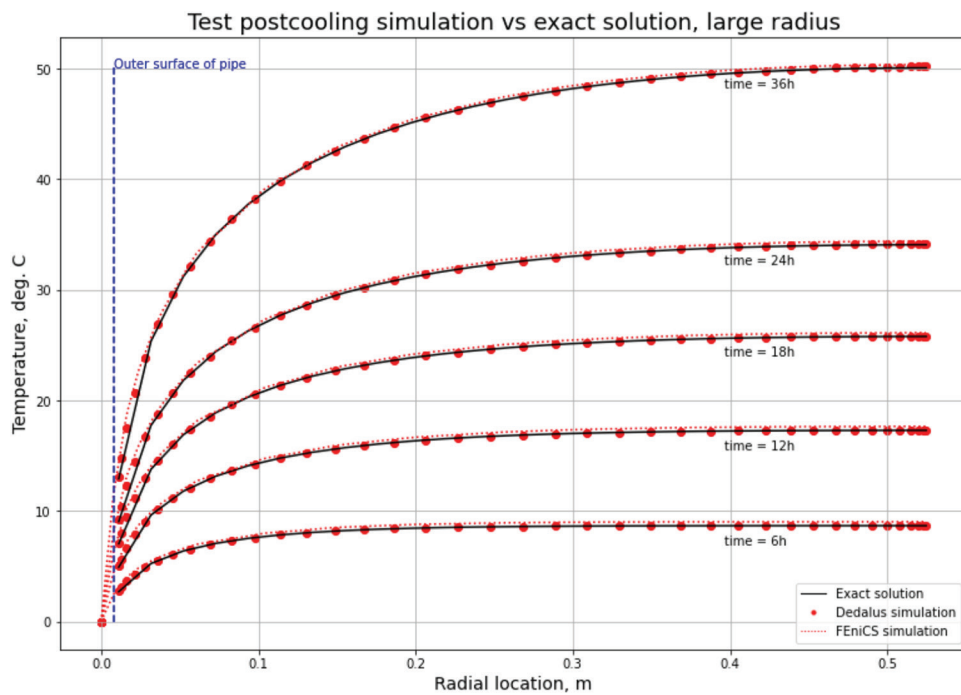


Fig. B5—Postcooling simulation validation test 2.

JOIN AN ACI Chapter!

The American Concrete Institute has Chapters and Student Chapters located throughout the world. Participation in a local chapter can be extremely rewarding in terms of gaining greater technical knowledge and networking with leaders in the concrete community.

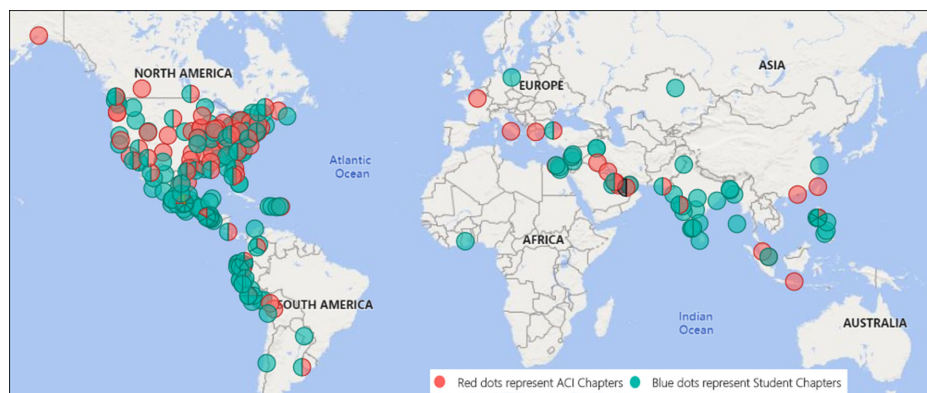
Because chapters are distinct and independent legal entities, membership includes both ACI members and non-ACI members and is made up of a diverse blend of architects, engineers, consultants, contractors, educators, material suppliers, equipment suppliers, owners, and students—basically anyone interested in concrete. Many active ACI members initially became involved in ACI through their local chapter. In addition to technical programs and publications, many chapters sponsor ACI Certification programs, ACI educational seminars, project award recognition programs, and social events with the goal of advancing concrete knowledge.

Check out the Chapters Special Section from the November 2020 *Concrete International*: www.concrete.org/publications/concreteinternational.aspx

Student Chapters

Join or form an ACI Student Chapter to maximize your influence, knowledge sharing, and camaraderie! ACI has 240+ student chapters located throughout the world, each providing opportunities for students to:

- Connect with their peers and participate in concrete-related activities such as: student competitions, ACI Conventions, ACI Certification Programs, ACI Educational Seminars, local chapter meetings, social events, and community service projects;
- Network with members of local chapters, many of whom have been in the industry for decades and can help to develop professional relationships and offer career advice;
- Win recognition for their universities through the University Award; and
- Learn about the many scholarships and fellowships offered by the ACI Foundation and by ACI's local chapters.



American Concrete Institute
www.concrete.org/chapters



Title No. 120-M66

Automated Procedure to Identify Concrete Defects from Impact-Echo Data

by Zachary W. Coleman and Anton K. Schindler

In this study, a procedure for interpreting impact-echo data in an automated, simple manner for detecting defects in concrete bridge decks is presented. Such a procedure is needed because it can be challenging for inexperienced impact-echo users to correctly distinguish between sound and defective concrete. This data interpretation procedure was developed considering the statistical nature of impact-echo data in a manner to allow impact-echo users of all skill levels to understand and implement the procedure. The developed method predominantly relies on conducting segmented linear regression analysis of the cumulative probabilities of an impact-echo data set to identify frequency thresholds distinguishing sound concrete from defective concrete. The accuracy of this method was validated using two case studies of five slab specimens and a full-scale bridge deck, each containing various typical defects. The developed procedure was found to be able to predict the condition of the slab specimens containing shallow delaminations without human assistance within 3.1 percentage points of the maximum attainable accuracy. It was also able to correctly predict the condition of the full-scale bridge deck containing delaminations, voids, corrosion damage, concrete deterioration, and poorly constructed concrete within 3.5 percentage points of the maximum attainable accuracy.

Keywords: bridge decks; condition assessment; corrosion; delamination; nondestructive testing; voids.

INTRODUCTION

Since its development in the 1980s, the impact-echo method has proven to be a versatile tool in nondestructive evaluations of concrete elements. Previous work has validated the utility of the impact-echo method to detect defects in a variety of structural elements, including bridge decks (Azari and Lin 2019; Coleman et al. 2021; Coleman and Schindler 2022; Gucunski et al. 2013; Lin et al. 2018; Olson et al. 2011; Tawhed and Gassman 2002) and post-tensioned ducts (Tinkey and Olson 2007; Zou et al. 2016). In particular, ground-coupled impact echo has been successfully used to locate delaminations (Cheng and Sansalone 1993; Lin and Sansalone 1996; Sansalone and Carino 1989), voids (Coleman et al. 2021; Tinkey and Olson 2007), and honeycombing (Azari and Lin 2019; Coleman et al. 2021). Each of the foregoing defects may produce frequency spectra distinctly different from those resulting from waves reflecting off the edges of the element, allowing the defects to be discerned from sound concrete. Nonetheless, Sansalone (1997) acknowledged that successful interpretation of impact-echo frequency spectra to assess the condition of a tested element often relies on pattern recognition skills developed from vast experience and training. Due to the

complex nature of impact-echo data interpretation, novice users of the method may struggle to meaningfully implement the method. The need to manually interpret each waveform measured from impact-echo testing has been a barrier to the impact-echo test method becoming more widely implemented (Sengupta et al. 2021).

Background on impact-echo testing

The impact-echo method is a stress-wave method in which a mechanical impact force is used to generate stress waves (P- and S-waves) that propagate into a medium (ACI 228.2R-13 [ACI Committee 228 2013]). The stress waves are reflected after encountering an internal or external boundary of two materials of divergent acoustic impedance. The large contrast in acoustic impedance between air and concrete allows for almost complete reflection at the interface of air and concrete (Carino 2001), such as at a delamination or the bottom of a suspended slab. The arrival of the reflected waves at the location of the impact force results in surface displacements that are recorded in the time domain by an adjacent transducer. The arrival time of the reflected wave can be used to determine the depth from which the reflection occurred, which can facilitate flaw detection, estimating the thickness of the tested element. For relatively thin elements, the surface displacement due to the impact force and the reflected stress wave occur within a short time of one another, making it difficult to determine the correct arrival time of the reflected wave. Given that the arriving wave will continue to reflect between the impact location and reflection surface, a transient resonance condition is established (Sansalone 1997), which can allow one to identify where a wave was reflected from in the frequency domain. The peak frequency associated with the reflected wave (f_p) is related to reflection depth in accordance with Eq. (1), as proposed by Sansalone and Street (1997)

$$f_p = \beta C_p / 2d \quad (1)$$

where β is a correctional factor depending on the geometry of the tested element; C_p is the compression wave (P-wave) speed of concrete; and d is the distance from the surface to the reflection location. Sansalone (1997) reported that the

value of β depends on the geometry of the tested element and that a value of 0.96 is appropriate for plate-like elements. Gibson and Popovics (2005) further noted that the value of β for plate-like elements ranges from 0.94 to 0.96 and is a function of the Poisson's ratio of the element. Using the appropriate value of β , the compression wave velocity (C_p), and the peak frequency excited during impact-echo testing (f_p), the depth to the reflection (d) can thus be determined from Eq. (1). Shifts in the calculated depth (d) or the peak frequency (f_p) can be used as indicators of the presence of a flaw or change in section geometry. The peak frequency can be extracted from the frequency spectra produced by applying a fast Fourier transform to the data measured in the time domain (Carino 2001).

Approaches to post-processing impact-echo data

Various post-processing algorithms have been proposed by researchers to address the weaknesses of the impact-echo method. As early as 1992 (Pratt and Sansalone 1992), machine-learning methods have been proposed to interpret impact-echo data points as corresponding to locations of sound or defective concrete. Some machine-learning methods are automatic, requiring no human assistance (Dorafshan and Azari 2020; Sengupta et al. 2021). However, many of these methods rely on large quantities of training data to accurately interpret the condition of a structural element using impact-echo data. Thus, these methods may lack versatility in impact-echo evaluations of structural elements with geometric configurations or defect characteristics dissimilar to those from which the training data were extracted. Additionally, the statistically complex nature of these methods introduces difficulties to novice impact-echo users seeking to develop pattern-recognition skills for interpreting impact-echo data. Other methods such as two-dimensional (2-D) and three-dimensional (3-D) stack imaging of spectral amplitudes have been developed (Hashimoto et al. 2020; Ohtsu et al. 2013; Ohtsu and Watanabe 2002; Yamada et al. 2017) to facilitate visual identification of defects and structural features. Gucunski et al. (2008) further demonstrated that visualization of the relative intensities of wave reflections within 3-D and 2-D slices can facilitate identifying bridge deck locations in need of repair. However, these methods require manual interpretation of data, which may: 1) result in novice impact-echo users making incorrect conclusions regarding the condition of an element; and 2) significantly increase the time required for analyses of impact-echo data sets. Procedures fusing the spectra obtained from multiple impact sources have also been used to automate the detection of delaminations (Xie et al. 2012; Zhang et al. 2012); however, these procedures cannot be used for impact-echo configurations having only one impact source and transducer.

This paper introduces an automated, user-based impact-echo (AUBIE) data interpretation procedure tailored to allow impact-echo users of varying experience levels to accurately predict the condition of a structural element while learning pattern-recognition skills to develop testing expertise. The procedure is predicated on observations regarding the statistical nature of impact-echo data and simple, readily

implementable statistical evaluation methods. It may be executed in an automatic fashion or may be interrupted at each step to allow the user to make key decisions to improve the ability of the method to distinguish between sound and defective concrete.

RESEARCH SIGNIFICANCE

This paper discusses the development and validation of an automated, novice-tailored procedure for executing impact-echo data analysis for condition assessments of structural elements. Automated implementation of the method may reduce the time required to interpret impact-echo data and allow novice operators to achieve meaningful condition assessments. It is also expected that the key observations discussed herein regarding the statistical nature of impact-echo data will allow novice users to develop expertise to use outputs from the impact-echo test method to distinguish between sound and defective concrete.

PRINCIPLES OF AUTOMATED IMPACT-ECHO DATA INTERPRETATION PROCEDURE

To develop the framework for an automated, user-based data interpretation procedure, the statistical distribution of impact-echo data corresponding to sound concrete was first considered. A large sample ($N = 769$) of frequencies measured at locations of sound concrete was extracted from an impact-echo evaluation of a 7.25 in. x 18 ft x 31 ft (184 mm x 5.5 m x 9.4 m) reinforced concrete bridge deck conducted by Coleman and Schindler (2022). The statistical distribution of the data is presented in two ways in Fig. 1. In Fig. 1(a), the measured frequencies, f , are plotted against their cumulative probabilities, while in Fig. 1(b), they are plotted against their corresponding standard normal variables, z_i , approximately equivalent to the inverse of the cumulative distribution function of the standard normal distribution. The latter way of plotting data, described in greater depth by Nowak and Collins (2013), is approximately equivalent to plotting the data on normal probability paper, in which data that plot along straight lines can be considered normally distributed. When the vertical axis is transformed as previously described, the mean of a normally distributed random variable exists where $z_i = 0$; furthermore, the slope of the best-fit straight line is equal to the reciprocal of the standard deviation of the random variable.

Through inspection of Fig. 1, it is clearly observed that peak impact-echo frequencies corresponding with sound concrete are normally distributed. From Fig. 1(a), the distribution of cumulative probabilities mimics the S-shape characteristic of normally distributed random variables. Furthermore, the frequencies from Fig. 1(b) (graphed with the transformed vertical axis) plot along a straight line, indicating that the frequencies are normally distributed. In the remainder of this paper, frequency distributions will be considered using the transformed vertical axis to facilitate visual assessment of the data and follow-up analyses and discussions.

Of additional importance is that the mean frequency (f_p) from Fig. 1 can be reasonably estimated using Eq. (1) (Sansalone and Street 1997). For the data plotted in Fig. 1, β and d values equal to 0.96 and 7.25 in. (24 and 184 mm),

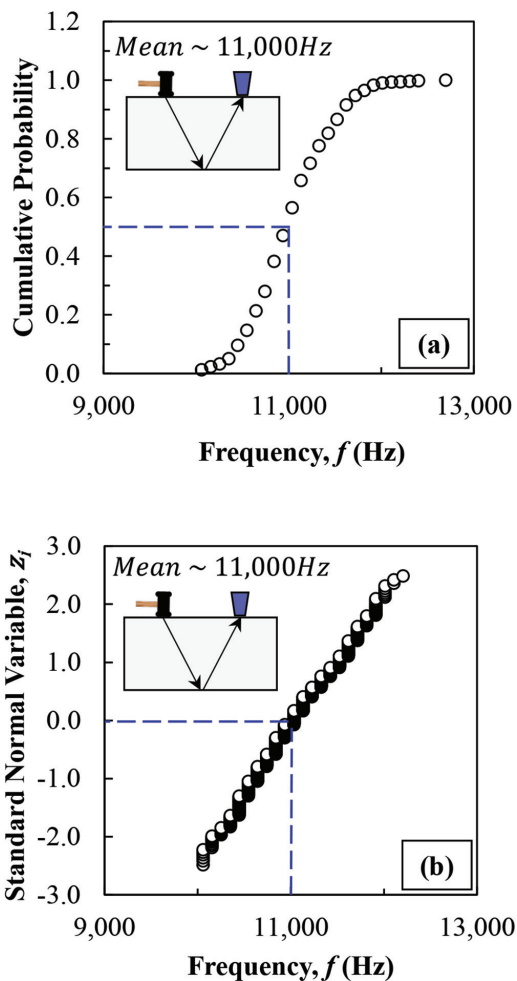


Fig. 1—Measured impact-echo frequency data of sound concrete in bridge deck plotted using: (a) cumulative probabilities; and (b) standard normal variables corresponding to plotting data on normal probability paper.

respectively, were used with the measured P-wave speed (C_p) of the bridge deck to predict that the mean peak frequency at sound deck locations should be 11,250 Hz. From Fig. 1, the mean frequency corresponding with a cumulative probability of 0.50 and a standard normal variable of 0.0 is approximately 11,000 Hz, which is only 250 Hz less than the predicted frequency, f_μ . Therefore, Eq. (1) can be used to reasonably estimate the mean peak frequency of sound concrete if the P-wave speed and characteristic cross-sectional dimensions are accurately known. The P-wave speed and cross-sectional dimensions can be determined using ASTM C1383 (2015) and ground truthing (for example, measurement of an extracted core or drill hole), respectively.

To understand the effects of defects on the statistical distribution of impact-echo data, the remaining ($N = 157$) peak frequencies corresponding to locations of shallow/deep delaminations, shallow/deep voids, concrete deterioration, and poorly constructed concrete of the bridge deck constructed by Coleman and Schindler (2022) were added to the frequencies previously presented in Fig. 1. The complete data set is plotted against recomputed standard normal variables, reflecting the increased size of the data set in Fig. 2. Notably, the data set no longer plots along one straight line but three approximately linear segments, indicating that the defective low frequencies, sound frequencies, and defective high frequencies each plot along a unique statistical distribution. From Fig. 2, the slopes of the segments are significantly different from one another, with that of the sound deck being the steepest. Given that the slope of a linear segment is equal to the reciprocal of the standard deviation, it can be concluded that the distributions of defective frequencies have high variances relative to that of the distribution of sound frequencies. Within Fig. 2, the low frequencies were caused by the excitation of the flexural vibration mode of shallow delamination, shallow voids, and simulated

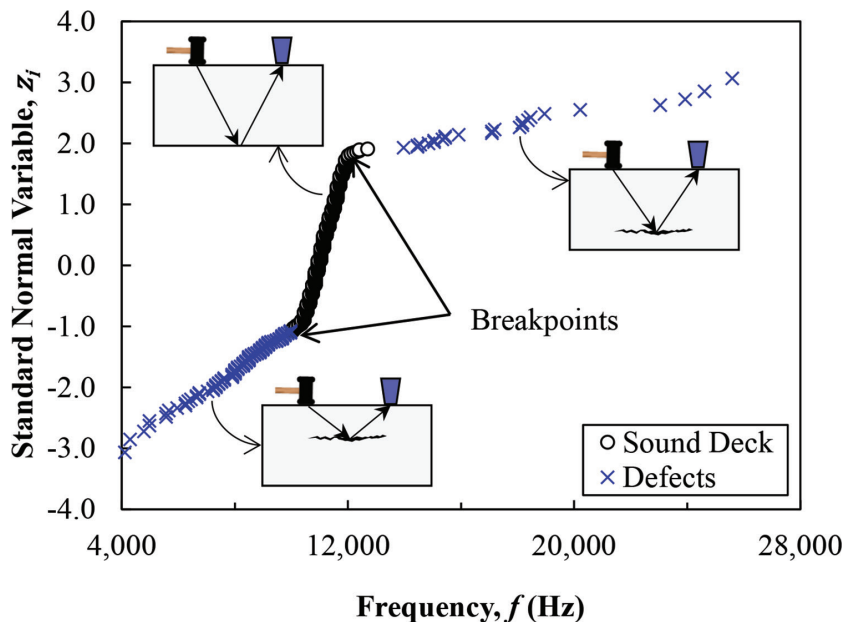


Fig. 2—Measured impact-echo frequency data of sound and defective locations in concrete bridge deck.

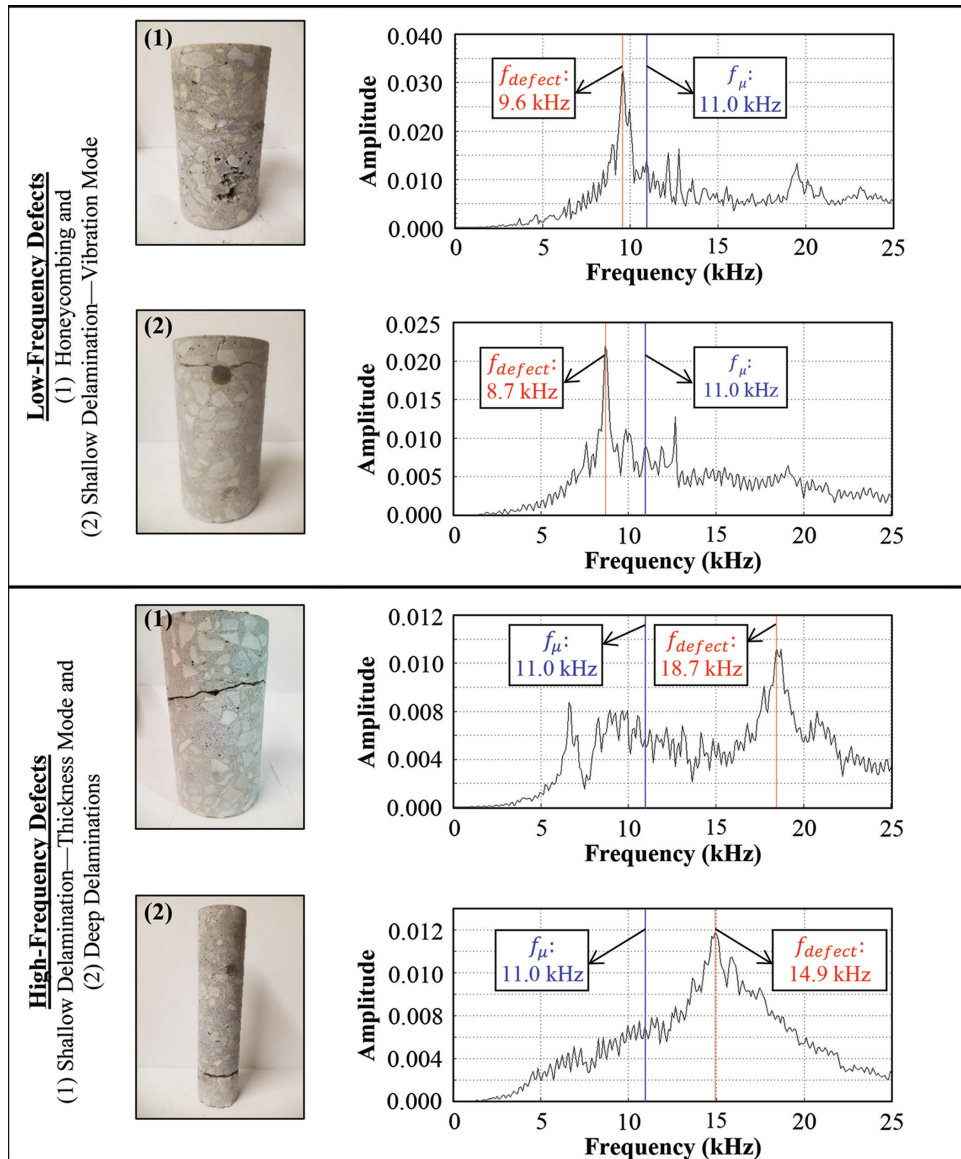


Fig. 3—Typical measured impact-echo frequency spectra with defects causing low and high frequencies (core images from Coleman [2021]).

deteriorated/honeycombed concrete. The high frequencies were caused by the excitation of the thickness mode of the shallow and deep delaminations. As noted by Sansalone and Carino (1989), the frequency spectrum obtained over a delamination would be expected to contain both the thickness mode (caused by multiple P-wave reflections between the surface and delamination) and the flexural vibration mode (due to vibrations of the delaminated slab). To assist in understanding the effect of each type of defect on the frequency distribution, cores containing various defects and the typical frequency spectra corresponding to each defect are shown in Fig. 3 (core images from Coleman 2021).

Knowing that a distribution of sound impact-echo data will have a lower variance (steeper slope) than that of a distribution of defective data, a novice impact-echo operator may easily be able to identify the frequencies corresponding to sound concrete through visual inspection of Fig. 2. In doing so, the breakpoints, defined as the points of apparent intersection of adjacent linear segments, need to be determined.

In Fig. 2, the two breakpoints represent the minimum and maximum bounds of the sound distribution, assuming no overlap with the adjacent defective segments. Thus, if the breakpoints can be identified, all frequencies outside of the range bounded by the breakpoints can be classified as corresponding to defects in the concrete. While a novice can likely visually estimate the breakpoints when the data is plotted as in Fig. 2, an automated method for selecting the breakpoints was pursued to assist operators in cases where the breakpoints may not be as obvious and to allow for quicker data post-processing.

To develop this automated method, the software package *segmented* (Muggeo 2022), for the free statistical analysis software *R*, was implemented to locate any breakpoints. To locate the breakpoint(s), the package uses segmented linear regression in which the independent variables (peak frequencies in this case) are first partitioned into groups separated by an initial guess of the breakpoint(s). Linear segments are fit to each group, and the guess is iteratively updated using

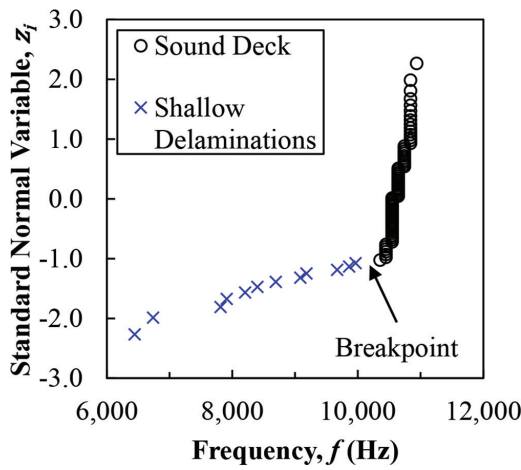


Fig. 4—Measured impact-echo frequency observations of sound and delaminated locations in concrete bridge deck.

maximum likelihood estimation until possible convergence to the breakpoint(s) (Muggeo 2003). For a novice impact-echo operator, two difficulties may arise when using the *segmented* package: 1) the number of expected breakpoints must be specified; and 2) an initial guess of the breakpoint(s) must be provided.

When deciding how many breakpoints to specify in impact-echo data analysis, two situations might arise. The first is that in which two breakpoints exist (such as in Fig. 2), where there is some distribution of frequencies from sound concrete along with low and high frequencies (relative to the frequencies of sound concrete) associated with defects. The second situation of when only one breakpoint exists is presented in Fig. 4 using data from a bridge-deck specimen containing shallow delaminations, reported by Coleman et al. (2021). The distribution of sound frequencies can easily be identified by its characteristic high slope, while the low frequencies of the shallow delaminations comprise a segment with a relatively low slope. Because the shallow delaminations only resulted in low frequencies (that is, there is only one segment of defective frequencies), only one breakpoint exists. As a part of the novice-tailored impact-echo data interpretation procedure, an automated method for determining whether one or two breakpoints exist within a given data set was developed and will be presented later in this paper.

The last step to automate the location of the breakpoint(s) was to develop a procedure for determining an initial guess of the breakpoint(s) for the segmented linear regression analysis. Knowing that peak frequencies corresponding to sound concrete are normally distributed, it was anticipated that an empirical coefficient of variation and expected mean frequency of sound concrete could be used to estimate the true distribution of sound frequencies. For a given structural element, the expected mean frequency, f_{μ} , could be determined using Eq. (1); the empirical coefficient of variation could be determined by surveying the coefficient of variation of sound frequencies extracted from locations of specimens known to be free of defects. Applying this approach to 12 bridge-deck specimens of either 7.25 or 12.00 in. (184 or 305 mm) thickness and tested by Coleman et al. (2022),

an approximate coefficient of variation of 2% was selected. Because the observed breakpoints of Fig. 2 and 4 occur near the extreme values of the distribution of sound frequencies, an initial guess of the breakpoint(s) could be computed using Eq. (2)

$$f_B = f_{\mu} \pm 2(0.02f_{\mu}) \quad (2)$$

where f_B is the initial guess of the breakpoint(s); and $0.02f_{\mu}$ is the sample standard deviation, assuming a 2% coefficient of variation. Two sample standard deviations away from the expected mean (f_{μ}) were hypothesized to provide a reasonable initial estimate of the breakpoint locations, because some overlap may exist between the distributions of defective concrete and sound concrete at the tails of the normal distribution of sound frequencies.

NOVICE-TAILORED INTERPRETATION PROCEDURE STEPS

The sequential steps required to execute the AUBIE data interpretation procedure are provided hereafter based on the framework previously discussed. For some steps, commentary is provided to provide additional guidance for a potential user. A flowchart containing each step is provided in Fig. 5 to illustrate the main ideas of the procedure.

Step 1—Determine the P-wave speed (C_p) of the concrete element using ASTM C1383-15 or another appropriate method (for example, ground truthing with coring).

Step 2—Calculate the expected mean peak frequency corresponding to sound concrete (f_{μ}) using the P-wave speed and expected characteristic dimension (d) using Eq. (1).

Step 3—Plot the measured peak frequencies in increasing order against the accompanying standard normal variables, z_i , using the following approximate solution reported by Nowak and Collins (2013)

$$z_i \approx -t_i + \frac{c_0 + c_1 t_i + c_2 t_i^2}{1 + d_1 t_i + d_2 t_i^2 + d_3 t_i^3} \text{ for } p_i \leq 0.5 \quad (3)$$

where $c_0 = 2.515517$; $c_1 = 0.802853$; $c_2 = 0.010328$; $d_1 = 1.432788$; $d_2 = 0.189269$; $d_3 = 0.001308$; $p_i = i/(N + 1)$ (Gumbel 1954); and $t_i \approx \sqrt{-\ln(p_i^2)}$. If $p_i > 0.5$, calculate t_i using $p_i^* = (1 - p_i)$ in Eq. (3).

Step 4—Create a copy of the data plotted in Step 3 that contains no duplicate frequencies, preserving the median data point within a given group of duplicates. Execute the *segmented* package (Muggeo 2022) on the reduced data set, initially assuming two breakpoints exist. Input an initial guess for the two breakpoints, f_B , using Eq. (2), with one guess less than the expected mean, f_{μ} , and the other greater than it. In some cases, either guess may be rejected by the *segmented* package, generally when the guess is outside the range of measured frequencies in the data set. When this occurs, the guess is iteratively changed until it is within the range of measured frequencies and accepted (for example, an initial guess greater than the maximum measured frequency would be decreased until it is within the range of the data and accepted by the package).

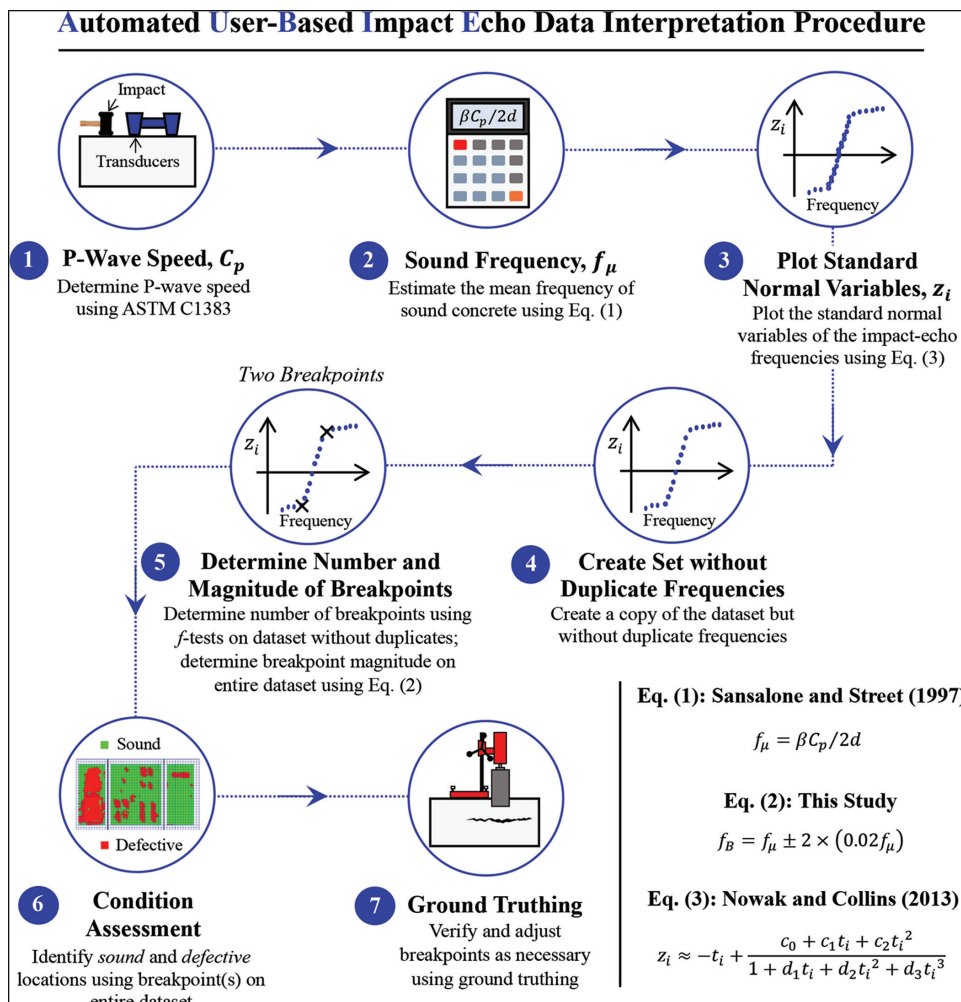


Fig. 5—Flowchart of AUBIE data interpretation procedure.

Step 4 is conducted to determine how many breakpoints exist. To fully automate the interpretation procedure, it is necessary to establish whether one or two breakpoints exist in the impact-echo data. To determine this, a reduced data set is analyzed using segmented linear regression. As shown in Fig. 4, when impact-echo frequencies are plotted against standard normal variables, repeated measurements (likely the result of instrumentation precision) plot as vertical lines having infinite slopes. When the *segmented* package is executed assuming two breakpoints exist, the algorithm may converge to one of these vertical lines as a breakpoint, given the contrast in slopes between repeated measurements and an adjacent segment within the distribution of sound frequencies. These breakpoints do not represent real breakpoints, which delineate frequencies of sound concrete from defective concrete, but rather bifurcations in the sound distribution of frequencies. To mitigate the risk of the algorithm converging to a repeated measurement as a breakpoint, duplicate frequencies are excluded just for the purpose of identifying whether one or two breakpoints exist in the full data set, while the median data point within a group of duplicates is preserved. Thus, the data within the sound distribution of frequencies is effectively “smoothed” to preclude the algorithm from converging upon false breakpoints within the sound data.

If a guess of the breakpoint is too close to the extreme values of the data set, the *segmented* package may reject the guess. In such cases, the rejected guess needs to be distanced from the extreme values. It is worth noting that, due to the high variance (small slope) of segments of defective frequencies, if an initial guess is rejected, there likely only exists one true breakpoint. Per Fig. 2, for cases in which two breakpoints exist, the distribution of sound data is much different from the extreme values of the data set, and the guess should therefore not be rejected.

Step 5(a)—Separate the reduced data set into three subsets using the two breakpoints computed from Step 4. Subset 1 contains all frequencies less than the lesser of the two breakpoints. Subset 2 contains all frequencies between the two breakpoints, inclusive. Subset 3 contains all frequencies greater than the larger of the two breakpoints. Conduct two two-way f -tests, comparing the variances between the following pairs of subsets, assuming a significance level of 0.01: Subsets 1 and 2, and Subsets 2 and 3. If the analysis fails to reject the null hypothesis for either test (that there is no statistically significant difference in sample variance), only one breakpoint exists in the data set; Step 5(b) should then be implemented. Otherwise, two breakpoints exist, which should now be determined using the entire (non-reduced) data set; Step 5(b) should be skipped.

It is initially assumed that two breakpoints exist (therefore, there exist defects causing both high and low frequencies relative to the sound frequencies). This assumption is subsequently evaluated using hypothesis testing. If: a) the null hypothesis that presumes that two breakpoints do not exist cannot be rejected with statistical significance; or b) the *segmented* package cannot identify two breakpoints, the interpretation procedure proceeds assuming that only one breakpoint exists.

As can be observed in Fig. 2 and 4, a characteristic feature of segments separated by true breakpoints is the stark contrast in slopes of adjacent segments, with the segment of sound frequencies having the largest slope. Given that the slope of a linear segment is equal to the reciprocal of the standard deviation, the slopes of the segments are related to the variances of the respective data sets. Thus, *f*-tests may be implemented to test whether the slopes of adjacent segments are significantly different from one another. True breakpoints are expected to result in statistically different slopes between adjacent segments. Due to the stark difference in slopes observed between defective and sound segments from Fig. 2 and 4, a low significance level of 0.01 is justified.

Step 5(b)—Compute the mean measured frequency of the entire (non-reduced) data set. If the mean is greater than the expected mean, f_{μ} , add two sample standard deviations to the mean frequency using Eq. (2). Otherwise, subtract two sample standard deviations from the mean using Eq. (2). Use the resulting frequency as an initial guess of the single breakpoint in the *segmented* package. If the analysis does not accept this guess, iteratively change it such that it is closer to the mean frequency of the data set until a breakpoint can be statistically identified by the *segmented* algorithm.

At this point, it is known that only one breakpoint exists, and thus the most accurate breakpoint can be determined by analyzing the entire data set. If only one breakpoint exists, it is necessary to determine whether that breakpoint exists at a frequency greater or less than the mean frequency of the sound data. In other words, do the defects present in the structural element result in low or high frequencies relative to the sound frequencies? It is thus assumed that the distribution of defective frequencies will skew the mean of the entire data set in the direction of the breakpoint, away from the expected mean frequency.

Step 6—Categorize each measurement location as defective or sound depending on how its measured frequency relates to the computed breakpoint(s).

If it was determined that only one breakpoint existed: Compute the variances of: 1) all measured frequencies greater than or equal to the breakpoint; and 2) all frequencies less than the breakpoint. If the variance of the first group is less than that of the latter, any location with a frequency less than the breakpoint frequency is characterized as defective concrete. Otherwise, if the variance of the second group is greater than that of the second, any location with a frequency greater than the breakpoint's frequency is characterized as defective concrete.

If it was determined that two breakpoints existed: The subset from Step 5(a) of frequencies with the least variance corresponds to all observations of sound concrete. It

is expected that this should correspond with Subset 2. The remaining measured frequencies correspond to locations with defective concrete.

The condition of an element at a given location is determined based on which subset the measured frequency corresponding to that location falls into. Given that the distribution of frequencies from sound concrete was observed to have the lowest variance, a frequency belonging to the subset of least variance is associated with a location of sound concrete. The remaining measured frequencies correspond to locations where defects are present in the concrete.

Step 7—Conduct ground truthing to verify the validity of the determined breakpoint(s). Adjust the breakpoint(s) as necessary depending on the results of the ground truthing.

Ground truthing is essential to validate the results of nondestructive evaluations (Gucunski et al. 2013). Accordingly, the authors highly recommend that ground truthing is performed in concert with the developed interpretation procedure such that the method is not used as a “black box.”

EXPERIMENTAL VALIDATION

To evaluate the effectiveness of the AUBIE data interpretation procedure to correctly predict the condition (sound or defective) of a concrete element, two case studies were selected from the literature. The first study comprised five 7.25 in. or 12 in. x 3 ft x 7 ft (184 mm or 305 mm x 0.9 m x 2.1 m) bridge deck specimens containing shallow and deep voids or delaminations that were tested by Coleman et al. (2021). The second study consisted of the 7.25 in. x 18 ft x 31 ft (184 mm x 5.5 m x 9.4 m) full-scale bridge deck containing shallow and deep voids/delaminations, reinforcement corrosion, concrete deterioration, and poorly constructed concrete tested by Coleman and Schindler (2022). Where appropriate, the prediction accuracy of the interpretation procedure was quantitatively compared against the maximum attainable accuracy (as determined by ground truthing consisting of coring and *a priori* knowledge of the deck condition at each location of testing) reported by the authors. As noted by Coleman et al. (2021), the frequency response indicative of the voids and deep delaminations in the bridge deck specimens did not always coincide with the known location of those defects; therefore, in such situations, a visual comparison of the spatial contour plot of the measured frequencies and the deck condition predicted by the AUBIE procedure was used to evaluate the capabilities of the procedure.

Case Study 1: Five slab specimens with voids and delaminations

The AUBIE data interpretation procedure was implemented to predict the condition of Specimens DL1, DL3, DL5, DL6, and V2 reported by Coleman et al. (2021). Specimen characteristics and reported/procedure accuracy rates (as applicable) are presented in Table 1. The reported maximum attainable accuracy rate is provided to indicate the maximum potential of the impact-echo method to correctly predict the condition of an element. Furthermore, the procedure accuracy rate indicates how closely the AUBIE procedure matches the maximum attainable accuracy, assuming

an operator can perfectly interpret all impact-echo data. For Specimens DL6 and V2, the frequency response indicative of defects did not coincide with the defect locations; therefore, no maximum or procedure accuracy is available based on ground truthing. The effectiveness of the AUBIE procedure to predict the condition of these specimens is assessed visually later.

From Table 1, it is observed that the AUBIE data interpretation procedure exhibited accuracy rates nearly the same as the maximum attainable accuracy for Specimens DL1, DL3, and DL5, each containing shallow delaminations. The average difference in the maximum attainable accuracy and the procedure accuracy for these three specimens was 3.1 percentage points, with Specimen DL5 having the largest difference of 5.8 percentage points. It is possible that Specimen DL5 exhibited the largest discrepancy in accuracy because that specimen contained partially bonded shallow delaminations, whereas the delaminations from Specimens DL1 and DL3 were completely unbonded. Overall, these results indicate that the AUBIE data interpretation procedure has an excellent ability to automatically and accurately predict the condition of bridge decks containing shallow delaminations.

Spatial contour plots of the peak frequencies measured and the accompanying condition prediction for Specimens DL6 and V2 are presented in Fig. 6. From Fig. 6(a), high frequencies (shown in cyan to red hues) indicative of deep, partially bonded delaminations (with “U” indicating the percentage of unbonded area) can be observed at or near the defect locations. The predicted deck condition when the AUBIE data interpretation procedure was implemented is shown in Fig. 6(b) beneath the previous plot, with the green and red areas representing predictions of sound concrete and defects, respectively. Through visual comparison of the two contour plots, it is observed that the automated procedure correctly classified all high frequencies as indicative of defects. Furthermore, the low frequencies (shown in blue and purple hues) indicative of sound concrete were all classified as sound by the automated procedure. Thus, the AUBIE data interpretation procedure exhibited an excellent ability to correctly classify the condition of Specimen DL6, which contained deep, partially bonded delaminations.

Similarly, the frequency contour plot of Specimen V2, shown in Fig. 6(c), was compared to the accompanying condition contour plot, presented in Fig. 6(d), to assess the accuracy of the AUBIE data interpretation procedure. From the frequency contour plot, high frequencies (shown in cyan to red hues) indicative of voids in the concrete can be observed at or near the location of most voids. Within the accompanying condition contour plot, all these high frequencies were correctly associated with a defect. Furthermore, the automated procedure correctly classified all low frequencies (shown in a magenta hue) as frequencies associated with sound concrete. However, there exist some potentially sound locations that the AUBIE data interpretation procedure classified as corresponding to a defect—for example, Location X = 28 in. (711 mm) and Y = 4 in. (102 mm). Overall, the AUBIE data interpretation procedure exhibited a good ability to correctly classify the condition of

Table 1—Characteristics and accuracy rates of five slab validation specimens

Specimen ID	Defect(s)	Defect depth, in.	Maximum accuracy, %	Procedure accuracy, %
DL1*	Delaminations	2.63	98.8	98.8
DL3*	Delaminations	2.63	97.6	94.1
DL5*	Delaminations	2.63	92.9	87.1
DL6†	Delaminations	10.38	N/A	N/A
V2†	Clay-filled voids	2.63 and 10.38	N/A	N/A

*Depth of specimen is 7.25 in.

†Depth of specimen is 12.00 in.

Note: N/A is not available because defect locations did not align with characteristic frequencies; 1 in. = 25.4 mm.

Specimen V2, which contained shallow and deep clay-filled voids of varying sizes.

Case Study 2: Full-scale bridge deck with various defects

While the AUBIE data interpretation procedure accurately predicted the condition of the previous small-scale specimens containing only one type of defect in one specimen at a time, it was of interest to investigate if the method was similarly accurate for full-scale elements that simultaneously contained various types of defects. Thus, the AUBIE data interpretation procedure was implemented to predict the condition of the 7.25 in. x 18 ft x 31 ft (184 mm x 5.5 m x 9.4 m) full-scale bridge deck containing shallow and deep voids/delaminations, reinforcement corrosion, concrete deterioration, and poorly constructed concrete as documented by Coleman and Schindler (2022). It is worth noting that impact-echo testing was conducted to identify mechanical damage (for example, delaminations) of the concrete due to reinforcement corrosion, not the corrosion itself.

The distribution of peak frequencies measured during impact-echo testing of the bridge deck is presented in Fig. 2. It can clearly be observed that the distribution of frequencies corresponding to locations of sound deck concrete plotted as a linear segment with a high slope (that is, low variance), while the frequencies corresponding to locations of defective deck concrete plotted as two linear segments with low slopes (that is, high variance). When implemented, the automated procedure was correctly able to identify that two breakpoints existed, resulting in a prediction accuracy of 88.1%, as compared to the maximum attainable accuracy of 91.6%. Without any human assistance, the AUBIE data interpretation procedure was able to accurately predict the condition of the bridge deck within 3.5 percentage points of the maximum attainable accuracy. The effectiveness of the AUBIE data interpretation procedure in predicting the deck condition was also considered through visual comparison of the spatial contour plot of peak frequencies and associated condition contour plot shown in Fig. 7. Of the defects that are detectable using impact echo (that is, in which there exists a visual contrast in frequencies between sound and defective locations), all were identified as defects (shown in a red hue) by the AUBIE data interpretation procedure.

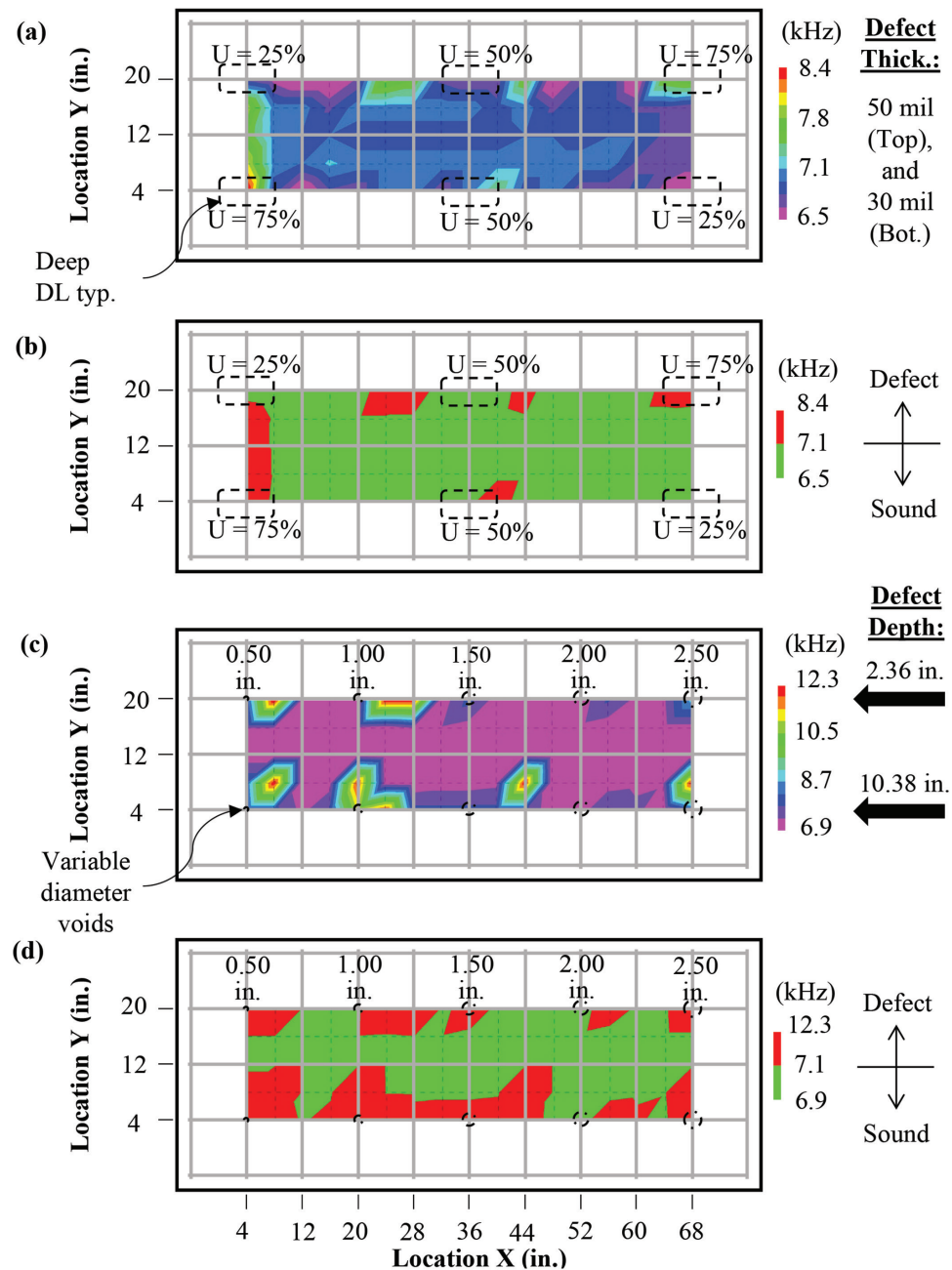


Fig. 6—Frequency and automated interpretation procedure condition contour plots of: (a) and (b) Specimen DL6; and (c) and (d) Specimen V2. (Note: 1 in. = 25.4 mm.)

Furthermore, the vast majority of the locations predicted to be sound (shown in a green hue) were truly sound. In concert with the 88.1% accuracy rate achieved, these observations indicate that the AUBIE data interpretation procedure was able to effectively characterize the condition of the bridge deck.

Discussion of results

Using the AUBIE data interpretation procedure, condition prediction accuracies of 3.1 and 3.5 percentage points lower, respectively, than the maximum attainable accuracies from the bridge-deck specimens and full-scale bridge deck were achieved. These prediction accuracies were achieved through the automatic execution of the proposed AUBIE data interpretation procedure without user intervention.

While these results are encouraging and suggest that novice impact-echo users can use the automated procedure to meaningfully interpret impact-echo data, a word of caution should be made regarding “blindly” relying on the method without oversight. Such implementation of the method: 1) does not assist the impact-echo operator in learning about the effect of defects on the statistical distribution of impact-echo data; and 2) may potentially result in less-than-optimal predictions of the condition of a structural element. While the interpretation procedure was developed to automatically determine the number and locations of breakpoints, human oversight in verifying that those breakpoints seem reasonable through visual analysis of plots such as Fig. 2 is recommended. Due to the high variance of frequencies corresponding to many defects, a strong visual contrast exists in the slopes of linear

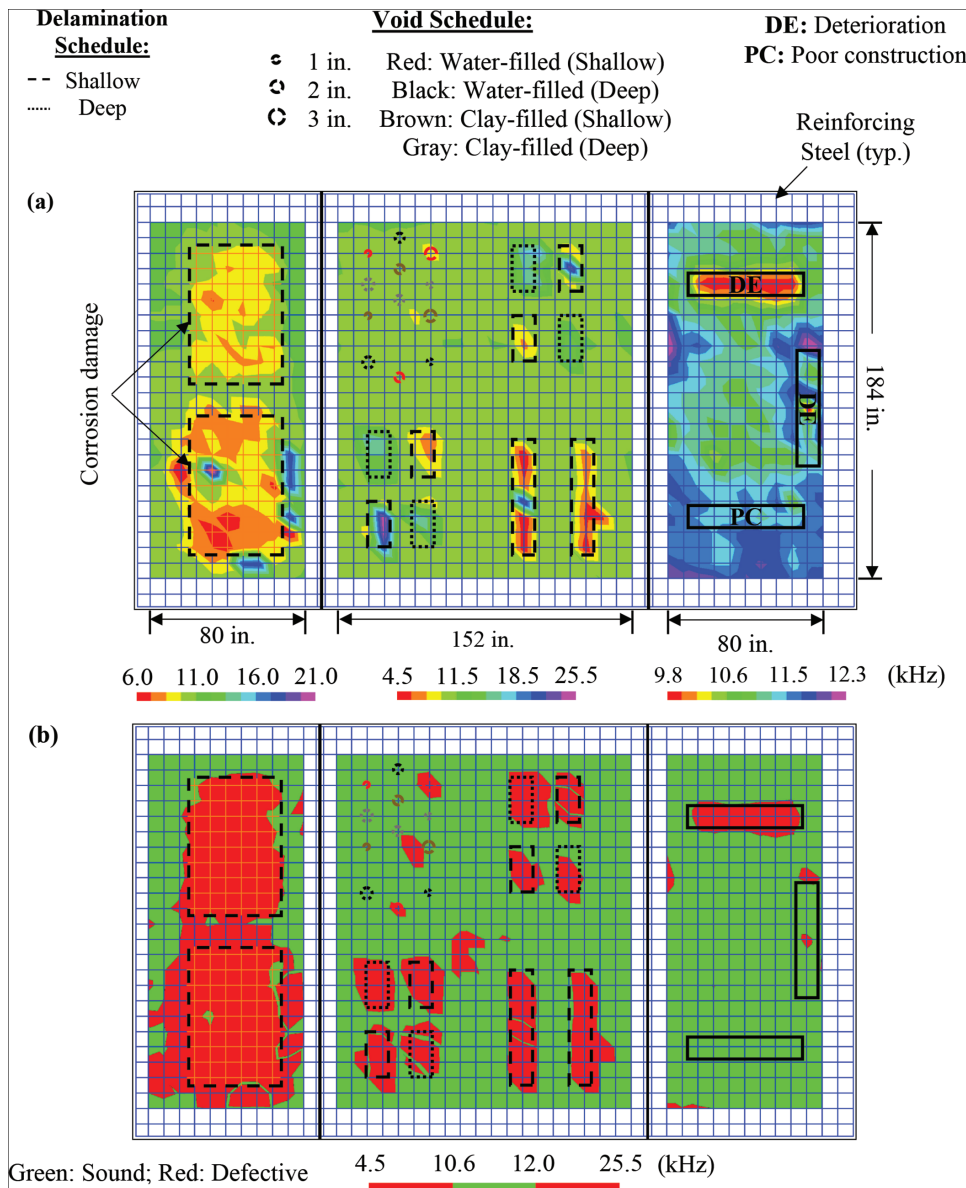


Fig. 7—Contour plots of: (a) measured frequencies; and (b) AUBIE data interpretation procedure condition of full-scale bridge deck containing various defects. (Note: 1 in. = 25.4 mm; full-color PDF can be accessed at www.concrete.org.)

segments of impact-echo data from sound and defective locations. Therefore, while not strictly necessary to use the AUBIE interpretation procedure, human oversight during each step of the procedure is recommended and generally straightforward.

CONCLUSIONS

In this study, a simple approach was developed for determining the condition of a structural element using impact-echo data. This approach was termed the automated, user-based impact-echo (AUBIE) data interpretation procedure. Through the development of this method, several key observations regarding the statistical nature of impact-echo data were noted. Through recognition of these observations, it is expected that the developed procedure will allow novice impact-echo users to identify sample-level differences between peak frequencies from sound and defective locations in a structural element. Thus, novices may use the developed

procedure to make meaningful predictions of sound versus defective concrete within an element while developing pattern-recognition skills and expertise in interpreting impact-echo data. To validate the accuracy of the developed procedure to make such predictions, the method was implemented without human assistance on two case studies from the literature comprising tests of five bridge deck specimens and one full-scale bridge deck containing various types of known defects. Based on the work conducted in this study, it was concluded that:

1. Measured peak frequencies from impact-echo testing of locations with sound bridge deck concrete are normally distributed.
2. In many cases, a distribution of measured peak frequencies from locations with defective concrete may also be normally distributed and has a significantly higher variance than a distribution of peak frequencies from sound locations, allowing the defective locations to be clearly distinguished.

3. Defects in concrete can result in frequency distributions that are either lower or higher than the frequencies characteristic of sound concrete. Whether the frequencies are lower or higher is influenced by the type of defect and the mode excited during testing.

4. Using the AUBIE data interpretation method, the condition of bridge deck specimens containing shallow delaminations could be accurately predicted within 3.1 percentage points of the maximum attainable accuracy. Frequencies associated with deep, partially bonded delaminations and shallow/deep voids could also be discerned from frequencies corresponding with sound concrete.

5. Using the interpretation procedure, the condition of a full-scale bridge deck containing shallow and deep voids/delaminations, reinforcement corrosion, concrete deterioration, and poorly constructed concrete could be predicted within 3.5 percentage points of the maximum attainable accuracy.

Future work in developing and further validating the developed interpretation procedure might focus on structural elements currently or previously in service where the locations of defects are accurately known. Given the general framework of the developed procedure, it is also expected that the method may be applicable for a broader range of structural elements (for example, grouted post-tensioned ducts) with appropriate modification (for example, changing the shape factor from Eq. (1) to reflect the geometry of the tested element). Without similar validation experiments, it is unclear if the AUBIE data interpretation procedure is either accurate or applicable to other elements.

AUTHOR BIOS

ACI member Zachary W. Coleman is a PhD Candidate at Virginia Polytechnic Institute and State University, Blacksburg, VA. He received his BS and MS in civil engineering from Lafayette College, Easton, PA, and Auburn University, Auburn, AL, respectively. He received the ACI Foundation Daniel W. Falconer Memorial Fellowship in 2020 and the ACI-James Instruments Student Award for Research on NDT of Concrete in 2022. He is a member of ACI Committee 228, Nondestructive Testing of Concrete, and Joint ACI-ASCE Committee 408, Bond and Development of Steel Reinforcement.

Anton K. Schindler, FACI, is Director of the Highway Research Center and a Professor at Auburn University. He received his MSE and PhD from The University of Texas at Austin, Austin, TX. He is on the ACI Board of Direction and is Chair of the ACI Foundation's Scholarship Council; past Chair of ACI Committees 231, Properties of Concrete at Early Ages, and 237, Self-Consolidating Concrete; and a member of the ACI Technical Activities Committee. He received the ACI Wason Medal for Materials Research in 2006 and 2011.

ACKNOWLEDGMENTS

This work was supported by the Alabama Department of Transportation (ALDOT) (Award No.: ALDOT Project 930-956). The funding, cooperation, and assistance of ALDOT are gratefully acknowledged. The contents of this paper reflect the views of the authors, who are responsible for the facts and accuracy of the data presented. The contents do not necessarily reflect the official views or policies of ALDOT.

REFERENCES

- ACI Committee 228, 2013, "Report on Nondestructive Test Methods for Evaluation of Concrete in Structures (ACI 228.2R-13)," American Concrete Institute, Farmington Hills, MI, 82 pp.
- ASTM C1383-15, 2015, "Standard Test Method for Measuring the P-Wave Speed and the Thickness of Concrete Plates Using the Impact-Echo Method," ASTM International, West Conshohocken, PA, 11 pp.
- Azari, H., and Lin, S., 2019, "Evaluation of the Impact Echo Method for Concrete Bridge Decks with Asphalt Overlays," *Transportation Research Record: Journal of the Transportation Research Board*, V. 2673, No. 2, Feb., pp. 436-444. doi: 10.1177/0361198119828676
- Carino, N. J., 2001, "The Impact-Echo Method: An Overview," *Structures 2001: Proceedings of the 2001 Structures Congress and Exposition*, P. C. Chang, ed., Washington, DC, 18 pp.
- Cheng, C., and Sansalone, M., 1993, "The Impact-Echo Response of Concrete Plates Containing Delaminations: Numerical, Experimental and Field Studies," *Materials and Structures*, V. 26, No. 5, June, pp. 274-285. doi: 10.1007/BF02472949
- Coleman, Z. W., 2021, "Evaluation of Nondestructive Test Methods for Concrete Bridge Deck Condition Assessment," master's thesis, Auburn University, Auburn, AL, 389 pp.
- Coleman, Z. W., and Schindler, A. K., 2022, "Investigation of Ground-Penetrating Radar, Impact Echo, and Infrared Thermography Methods to Detect Defects in Concrete Bridge Decks," *Transportation Research Record: Journal of the Transportation Research Board*, pre-print, 14 pp. doi: 10.1177/03611981221101027
- Coleman, Z. W.; Jetzel, C. M.; and Schindler, A. K., 2022, "Evaluation of Nondestructive Test Methods to Assess the In-Place Condition of Concrete Structures," ALDOT Research Report ALDOT 930-951, Highway Research Center, Auburn University, Auburn, AL, 244 pp.
- Coleman, Z. W.; Schindler, A. K.; and Jetzel, C. M., 2021, "Impact-Echo Defect Detection in Reinforced Concrete Bridge Decks without Overlays," *Journal of Performance of Constructed Facilities*, ASCE, V. 35, No. 5, Oct., p. 04021058. doi: 10.1061/(ASCE)CF.1943-5509.0001638
- Dorafshan, S., and Azari, H., 2020, "Deep Learning Models for Bridge Deck Evaluation Using Impact Echo," *Construction and Building Materials*, V. 263, Dec., Article No. 120109. doi: 10.1016/j.conbuildmat.2020.120109
- Gibson, A., and Popovics, J. S., 2005, "Lamb Wave Basis for Impact-Echo Method Analysis," *Journal of Engineering Mechanics*, ASCE, V. 131, No. 4, Apr., pp. 438-443. doi: 10.1061/(ASCE)0733-9399(2005)131:4(438)
- Gucunski, N.; Imani, A.; Romero, F.; Nazarian, S.; Yuan, D.; Wiggenhauser, H.; Shokouhi, P.; Taffe, A.; and Kutrubis, D., 2013, "Nondestructive Testing to Identify Concrete Bridge Deck Deterioration," Strategic Highway Research Program 2 (SHRP 2) Report S2-R06A-RR-1, Transportation Research Board, Washington, DC, 96 pp.
- Gucunski, N.; Slabaugh, G.; Wang, Z.; Fang, T.; and Maher, A., 2008, "Impact Echo Data from Bridge Deck Testing: Visualization and Interpretation," *Transportation Research Record: Journal of the Transportation Research Board*, V. 2050, No. 1, Jan., pp. 111-121. doi: 10.3141/2050-11
- Gumbel, E. J., 1954, "Statistical Theory of Extreme Values and Some Practical Applications: A Series of Lectures," *Applied Mathematics Series*, V. 33, National Bureau of Standards, Washington, DC, 60 pp.
- Hashimoto, K.; Shiotani, T.; and Ohtsu, M., 2020, "Application of Impact-Echo Method to 3D SIBIE Procedure for Damage Detection in Concrete," *Applied Sciences*, V. 10, No. 8, Article No. 2729.
- Lin, J.-M., and Sansalone, M., 1996, "Impact-Echo Studies of Interfacial Bond Quality in Concrete: Part 1—Effects of Unbonded Fraction of Area," *ACI Materials Journal*, V. 93, No. 3, May-June, pp. 223-231.
- Lin, S.; Meng, D.; Choi, H.; Shams, S.; and Azari, H., 2018, "Laboratory Assessment of Nine Methods for Nondestructive Evaluation of Concrete Bridge Decks with Overlays," *Construction and Building Materials*, V. 188, Nov., pp. 966-982. doi: 10.1016/j.conbuildmat.2018.08.127
- Muggeo, V. M. R., 2003, "Estimating Regression Models with Unknown Break-Points," *Statistics in Medicine*, V. 22, No. 19, pp. 3055-3071. doi: 10.1002/sim.1545
- Muggeo, V. M. R., 2022, "Package 'Segmented': Regression Models with Break-Points/Change-Points (with Possibly Random Effects) Estimation," The Comprehensive R Archive Network (CRAN), <https://cran.r-project.org/web/packages/segmented/index.html>. (last accessed Sept. 21, 2023)
- Nowak, A. S., and Collins, K. R., 2013, *Reliability of Structures*, CRC Press, Boca Raton, FL, 407 pp.
- Ohtsu, M., and Watanabe, T., 2002, "Stack Imaging of Spectral Amplitudes Based on Impact-Echo for Flaw Detection," *NDT & E International*, V. 35, No. 3, Apr., pp. 189-196. doi: 10.1016/S0963-8695(01)00045-7
- Ohtsu, M.; Yamada, M.; and Sonoda, T., 2013, "Quantitative Evaluation of SIBIE Procedure and Case Studies," *Construction and Building Materials*, V. 48, Nov., pp. 1248-1254. doi: 10.1016/j.conbuildmat.2012.12.003
- Olson, L. D.; Tinkey, Y.; and Miller, P., 2011, "Concrete Bridge Condition Assessment with Impact Echo Scanning," *Emerging Technologies for Material, Design, Rehabilitation, and Inspection of Roadway Pavements: Proceedings of GeoHunan 2011 International Conference*, D.-H. Chen, J.-R. Chang, M. Zaman, C. Zhao, and Z. Yao, eds., Hunan, China, pp. 59-66.
- Pratt, D., and Sansalone, M., 1992, "Impact-Echo Signal Interpretation Using Artificial Intelligence," *ACI Materials Journal*, V. 89, No. 2, Mar.-Apr., pp. 178-187.

- Sansalone, M., 1997, "Impact-Echo: The Complete Story," *ACI Structural Journal*, V. 94, No. 6, Nov.-Dec., pp. 777-785.
- Sansalone, M., and Carino, N. J., 1989, "Detecting Delaminations in Concrete Slabs with and without Overlays Using the Impact-Echo Method," *ACI Materials Journal*, V. 86, No. 2, Mar.-Apr., pp. 175-184.
- Sansalone, M., and Street, W. B., 1997, *Impact-Echo: Nondestructive Evaluation of Concrete and Masonry*, Bullbrier Press, Jersey Shore, PA, 339 pp.
- Sengupta, A.; Guler, S. I.; and Shokouhi, P., 2021, "Interpreting Impact Echo Data to Predict Condition Rating of Concrete Bridge Decks: A Machine-Learning Approach," *Journal of Bridge Engineering*, ASCE, V.26, No.8, Aug., p.04021044.doi:10.1061/(ASCE)BE.1943-5592.0001744
- Tawhed, W. F., and Gassman, S. L., 2002, "Damage Assessment of Concrete Bridge Decks Using Impact-Echo Method," *ACI Materials Journal*, V. 99, No. 3, May-June, pp. 273-281.
- Tinkey, Y., and Olson, L. D., 2007, "Impact-Echo Scanning for Grout Void Detection in Post-Tensioned Bridge Ducts — Findings from a Research Project and a Case History," *New Horizons and Better Practices: Proceedings of the 2007 Structures Congress*, R. Lyons, ed., Long Beach, CA, 13 pp.
- Xie, Z.; Zhang, Y.; and Wu, H. F., 2012, "Automated Data Fusion and Visualization for Impact-Echo Testing of Concrete Structures," *IEEE Sensors Journal*, V. 12, No. 12, Dec., pp. 3446-3453. doi: 10.1109/JSEN.2012.2210705
- Yamada, M.; Yagi, Y.; and Ohtsu, M., 2017, "Identification of Delamination in Concrete Slabs by SIBIE Procedure," *Proceedings*, 12th International Conference on Damage Assessment of Structures, Kitakyushu, Japan, 6 pp.
- Zhang, Y.; Wei, X.; Tsai, Y.-T.; Zhu, J.; Fetrat, F. A.; and Gucunski, N., 2012, "Multisensor Data Fusion for Impact-Echo Testing of Concrete Structures," *Smart Materials and Structures*, V. 21, No. 7, July, Article No. 075021. doi: 10.1088/0964-1726/21/7/075021
- Zou, C.; Chen, Z.; Dong, P.; Chen, C.; and Cheng, Y., 2016, "Experimental and Numerical Studies on Nondestructive Evaluation of Grout Quality in Tendon Ducts Using Impact-Echo Method," *Journal of Bridge Engineering*, ASCE, V. 21, No. 2, Feb., p. 04015040. doi: 10.1061/(ASCE)BE.1943-5592.0000759

Title No. 120-M67

Influence of Mixture Proportions and Permeability-Reducing Admixtures on Concrete Fluid Transport

by R. M. Ghantous, V. Bui, S. Schaeaf, B. Fronczeck, C. B. Jablonski, S. R. Reese, and W. J. Weiss

This study uses neutron radiography (NR) and visual inspection to quantify water penetration in concrete samples exposed to water pressure on one face. It provides experimental data regarding the impact of mixture proportions on the hydraulic permeability of concrete. Specifically, it illustrates the influence of water-cement ratio (w/c), curing duration, entrained air content, and coarse aggregate (CA) size and volume on water transport. In addition, this paper quantifies the impact of permeability-reducing admixtures (PRAs) on water transport in concrete. It was observed that decreasing the w/c and/or increasing the curing duration reduced the fluid transport. Liquid and powder PRAs efficiently reduced fluid transport in concrete without impacting the compressive strength. The liquid PRA showed more consistent results, likely due to better dispersion than the powder PRA. Fluid ingress in concrete samples appears to increase with entrained air content due to a lower degree of saturation (DOS) at the start of the test. Increasing the CA volume fraction or decreasing the CA size will increase the fluid transport in concrete due to an increase in the connectivity of the interfacial transition zone. The influence of entrained air content, curing duration, CA volume fraction, and CA size was less noticeable on mixtures with PRAs due to the higher density and low permeability of these samples compared to control samples.

Keywords: concrete mixture design; degree of saturation (DOS); interfacial transition zone (ITZ); neutron radiography (NR); permeability; permeability-reducing admixtures (PRAs); visual inspection.

INTRODUCTION

Research is being performed to increase the service life of concrete exposed to aggressive environments.¹⁻⁴ Reducing the fluid transport properties of concrete is one approach to improve durability.⁵⁻⁷ Hydraulic permeability occurs when the concrete is exposed to a pressure gradient.^{8,9} Reductions in the permeability of concrete occur by decreasing the water-cement ratio (*w/c*) of the concrete mixture, increasing the curing duration, or replacing the ordinary portland cement with supplementary cementitious materials (SCMs), which can lead to a decrease in the concrete porosity and pores connectivity.¹⁰⁻¹² Permeability-reducing admixtures (PRAs) can also be used to reduce fluid ingress.¹³

PRAs have been widely used in the concrete industry.¹⁴⁻¹⁷ PRAs are classified into five categories according to ACI 212.3R-16¹⁸ and labeled as hydrophobic water repellents, polymer products, finely divided solids, hydrophobic pore blockers, and crystalline products. Hydrophobic water repellents and polymer products describe materials primarily applied on hardened concrete surfaces.¹⁹⁻²¹ The finely divided solids are added as a mixture constituent to densify the microstructure and include common SCMs such as

silica fume, slag, or fly ash.¹⁴ Hydrophobic pore blockers and crystalline products are typically integrally mixed with concrete.¹⁸ Hydrophobic pore blockers can be effective against some forms of fluid ingress; however, they are generally not as effective in cases where the concrete is exposed to pressure (that is, hydraulic permeability). Crystalline products reduce concrete permeability by absorbing water and reacting with the hydration products of concrete, leading to crystalline products that fill the concrete pores.¹⁸ As a result, crystalline products are typically more efficient in concrete exposed to water pressure (that is, hydraulic permeability).

There is a lack of standardized procedures to test the benefit of using PRAs in concrete.²² This includes a lack of standardized methods for sample preconditioning before permeability assessment, which may increase the variability in measurements.²³ The water permeability of concrete samples containing crystalline PRAs is reported to reduce by 15 to 90% compared to untreated samples.^{13,24-30} This wide range of efficiency (15 to 90%) is due to a combination of factors, including the wide range of PRA chemistries, dosages, *w/c*, testing age, and mixture designs of the reference samples used for comparison in the literature. Second, it is due to the variability in the permeability measurements themselves, which was found to be between 30 and 50% for identical concrete samples.²³

This paper aims to quantify the variability observed in the data recorded in the literature by providing experimental data regarding the impact of mixture proportions and curing conditions on the hydraulic permeability of concrete samples. This paper illustrates the influence of *w/c*, curing duration, entrained air content, coarse aggregate (CA) size, and CA volume on the water transport in concrete. The impact of these various parameters was studied on concrete samples without PRAs, with crystalline product PRA in a liquid form, and with crystalline product PRA in a powder form. Two experimental procedures have been used to assess fluid transport in the concrete samples and are both based on quantifying water penetration in the concrete. The first assesses the depth of water penetration using visual inspection according to a modified version of the DIN 1048-5:1991 procedure.³¹ The second uses neutron radiography (NR) to determine the amount of water penetrating through the

depth of the concrete. For both procedures, the samples were exposed to water pressure applied to one face of the sample for the same testing duration. Previous work³² concluded that the depth of water penetration values obtained from visual inspection may underestimate the actual depth of water penetration.

RESEARCH SIGNIFICANCE

Challenges exist in accurately measuring hydraulic permeability in concrete²³ and assessing the benefit of PRAs in reducing water transport in concrete.²² This paper quantifies the variability associated with hydraulic permeability measurements by evaluating the influence of the mixture

Table 1—Chemical and physical properties of cement used in this study

Cement oxides	Percent by mass of OPC I/II
Silicon dioxide (SiO_2)	19.90
Aluminum oxide (Al_2O_3)	4.50
Ferric oxide (Fe_2O_3)	3.10
Calcium oxide (CaO)	64.00
Magnesium oxide (MgO)	2.30
Sulfur trioxide (SO_3)	3.30
Equivalent alkali ($\text{Na}_2\text{O}_{\text{eq}}$)	0.55
Loss on ignition (LOI)	3.10
Bogue phase composition	Percent by mass of OPC I/II
Tricalcium silicate (C_3S)	67.00
Dicalcium silicate (C_2S)	3.00
Tricalcium aluminate (C_3A)	6.00
Tetracalcium aluminoferrite (C_4AF)	9.00
Specific gravity	3.15

Table 2—Mixture proportions and fresh properties of concrete mixtures without PRAs

Mixture ID	1-U	2-U	3-U	4-U	5-U	6-U	7-U
CA, kg/m ³	979	984	977	984	982	1119	956
Sand, kg/m ³	887	891	887	891	891	762	891
Cement, kg/m ³	427	386	349	338	386	386	386
Water, kg/m ³	149	162	174	142	162	162	162
HRWRA, L/m ³	2.06	0.97	0.53	0.97	1.30	0.75	0.99
Powder PRA, %bwcm	0	0	0	0	0	0	0
Liquid PRA, L/m ³	0	0	0	0	0	0	0
w/c	0.35	0.42	0.50	0.42	0.42	0.42	0.42
Designed air content, %	2.5	2.5	2.5	6.0	2.5	2.5	2.5
Measured air content, %	2.9	2.5	3.0	6.6	2.8	2.1	2.5
Paste V_{fr} , %	28.5	28.4	28.5	24.9	28.4	28.4	28.4
CA V_{fr} , %	35.0	35.0	34.9	35.0	35.0	40.0	35.0
Sand V_{fr} , %	33.9	33.9	33.9	33.9	33.9	29.0	33.9
Slump, mm	210	191	171	197	184	172	178
Unit weight, kg/m ³	2436	2425	2393	2329	2421	2433	2399
Curing duration, days	28	28	28	56	56	56	56

Note: U is untreated; V_{fr} is volume fraction; the paste V_{fr} displayed in this table does not include the V_{fr} of entrained air content; %bwcm is percent by weight of cement.

proportions and the curing duration. Understanding the impact of various parameters on concrete hydraulic permeability is key in developing a plan to reduce variability for tests conducted between laboratories, thereby improving permeation measurements for use in concrete durability specifications.

EXPERIMENTAL PROGRAM

Experimental design

The chemical and physical properties of the Type I/II ordinary portland cement (OPC; ASTM C150/C150M-19a) used in this study are given in Table 1. The Blaine fineness of the cement was 379 m²/kg. The fine aggregate was natural river sand with a specific gravity of 2.61 and an absorption of 1.79%. The CA (American Association of State Highway and Transportation Officials [AASHTO] No. 8 and 57) had a specific gravity of 2.80 and absorption values of 1% and 0.7%, respectively. The AASHTO standard used for the aggregate size is AASHTO M 43. Various admixtures have been added to the concrete mixture design, including a high-range water-reducing admixture (HRWRA), PRA in a powder form, and a PRA in a liquid form. Both PRAs used in this study fall within the category of crystalline products as per the classification of ACI 212.3R-16¹⁸ and have similar active ingredients.

Seventeen concrete mixtures were prepared in this study with varying w/c, entrained air content, CA size, CA volume fraction, and PRA type to study the impact of these various parameters on the fluid transport in concrete under pressure. The mixture characteristics of concrete samples without any PRAs are shown in Table 2. Table 3 illustrates the mixture characteristics of concrete samples containing PRA in either liquid or powder form.

Table 3—Mixture proportions and fresh properties of concrete mixtures with PRAs

Mixture ID	1-P	1-L	2-P	2-L	3-P	3-L	4-L	5-L	6-L	7-L
CA, kg/m ³	979	979	984	984	977	977	984	982	1119	956
Sand, kg/m ³	887	887	891	891	887	887	891	891	762	891
Cement, kg/m ³	427	427	386	386	349	349	338	386	386	386
Water, kg/m ³	149	149	162	162	174	174	142	162	162	162
HRWRA, L/m ³	2.55	2.26	1.45	1.09	0.97	0.88	1.09	1.61	0.8	0.99
Powder PRA, %bwcm	1	0	1	0	1	0	0	0	0	0
Liquid PRA, L/m ³	0	6.2	0	6.2	0	6.2	6.2	6.2	6.2	6.2
w/c	0.35	0.35	0.42	0.42	0.50	0.50	0.42	0.42	0.42	0.42
Designed air content, %	2.5	2.5	2.5	2.5	2.5	2.5	6.0	2.5	2.5	2.5
Measured air content, %	2.8	2.9	2.7	2.6	3.0	3.0	5.5	2.4	2.2	2.8
Paste V _{fr} , %	28.5	28.5	28.4	28.4	28.5	28.5	24.9	28.4	28.4	28.4
CA V _{fr} , %	35.0	35.0	35.0	35.0	34.9	34.9	35.0	35.0	39.9	35.0
Sand V _{fr} , %	33.9	33.9	33.9	33.9	33.9	33.9	33.9	33.9	29.0	33.9
Slump, mm	210	203	178	197	171	185	197	184	178	191
Unit weight, kg/m ³	2450	2443	2415	2425	2388	2393	2355	2437	2434	2377
Curing duration, days	28	28	28	28	28	28	56	56	56	56

Note: V_{fr} is volume fraction; P is powder PRA; L is liquid PRA; the paste V_{fr} displayed in this table does not include the V_{fr} of entrained air content.

The mixing procedure consists first of adding water into the mixer, then adding HRWRA and liquid PRA (when applicable). The CA, cement with powder PRA (when applicable), and sand were then consecutively loaded into the mixing drum. The powder PRA was added to the dry cement when applicable. The materials were then mixed at high speed for 7 minutes.

The slump (ASTM C143/C143M), unit weight (ASTM C138/C138M), and air content (ASTM C231/C231M) were measured immediately at the end of the mixing duration by an ACI Level I certified technician. The HRWRA was adjusted to achieve a slump of 178 ± 13 mm (7 ± 0.5 in., which is the original unit in which the slump was measured in this study) for all concrete mixtures prepared in this study.

For each concrete mixture, samples with various geometries were prepared as follows:

- Six cylindrical concrete samples of 152 mm in diameter and 305 mm in height were used for depth of water penetration following the modified procedure of DIN 1048-5.³¹ A description of how the samples were cut for this test is given later in this paper.
- Two concrete prisms of 76.2 mm in width, 76.2 mm in height, and 254 mm in length were used to measure fluid transport in concrete samples under pressure using NR measurements.³² A description of how the samples were cut for this test is given later in this paper.
- Two cylindrical concrete samples of 102 mm in diameter and 203 mm in height were used for compressive strength testing following ASTM C39/C39M.

For all three geometries, the fresh concrete was placed in two layers, and each layer was vibrated until the surface was flattened without segregation to achieve good consolidation. The surface of the concrete was finished. Samples were sealed cured for 24 hours, after which they were demolded

Table 4—Comparing influence of various parameters on hydraulic permeability of concrete

Influence of following parameters on fluid movement in concrete	Mixture IDs to compare
PRAs	1-U, 1-P, and 1-L 2-U, 2-P, and 2-L 3-U, 3-P, and 3-L
w/c	1-U, 2-U, and 3-U 1-P, 2-P, and 3-P 1-L, 2-L, and 3-L
Entrained air content	4-U and 7-U 4-L and 7-L
CA size	5-U and 7-U 5-L and 7-L
CA volume fraction	6-U and 7-U 6-L and 7-L

and moist cured at 23 ± 2°C for either 28 or 56 days, as listed in Tables 2 and 3.

Table 4 illustrates the mixture IDs prepared to examine the influence of various parameters on the fluid transport in concrete under pressure.

Experimental procedures for fluid ingress measurements and results illustration

Two procedures were used to determine the fluid transport in concrete samples under pressure: 1) a modified DIN 1048-5 standard; and 2) NR measurements.

The first procedure, based on DIN 1048-5,³¹ consists of visually determining the depth of water penetration at the end of the exposure period of concrete samples to water pressure. At the end of the designated curing period, a cylindrical sample of 102 mm in height and 152 mm in diameter was cut from the middle section of each of the cast concrete samples

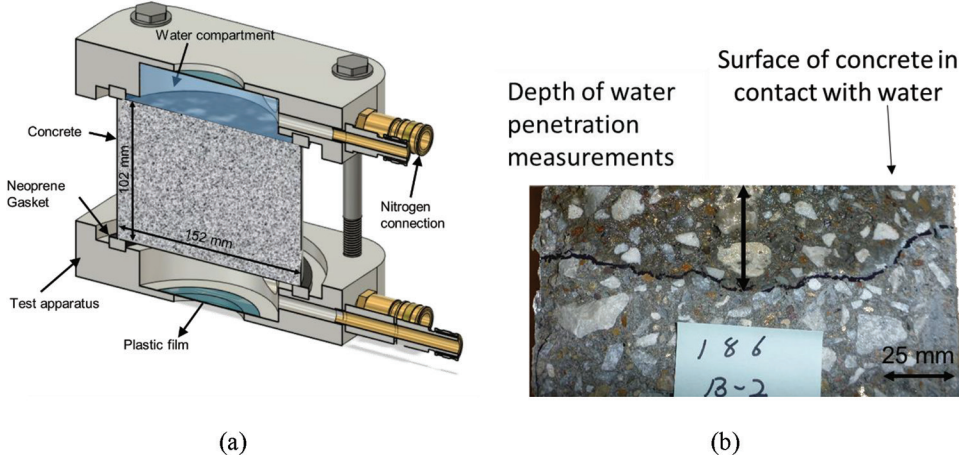


Fig. 1—(a) Isometric drawing of pressure cell used for depth of water penetration measurements following DIN 1048-5; and (b) depth of water penetration measurements. Note that water ingress is identified using black permanent marker, as illustrated in this figure.

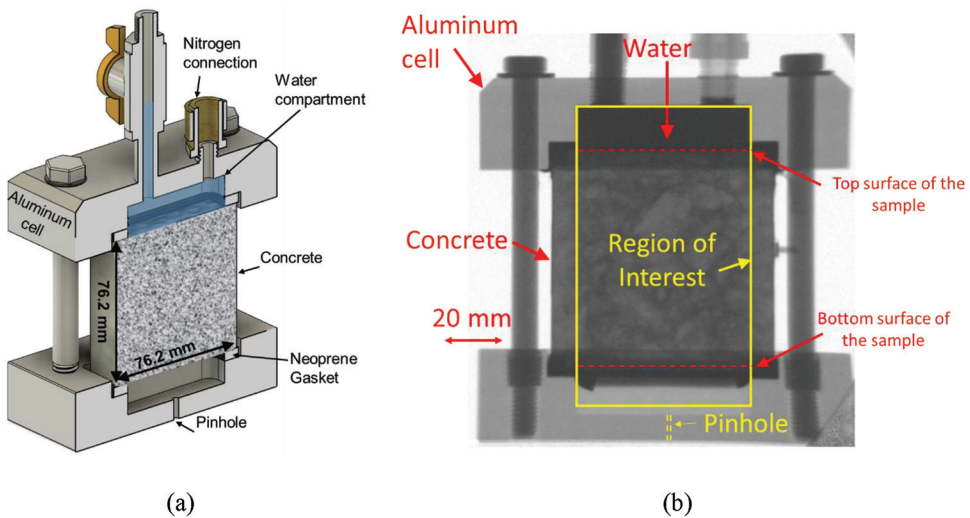


Fig. 2—(a) Isometric drawing of pressure cell used for fluid transport measurements using NR; and (b) neutron radiograph for concrete sample inside pressure cell.

(diameter of 152 mm and height of 305 mm) using a water-cooled, diamond-tipped saw blade. The vertical sides of the cut sample were sealed with aluminum tape. The sample was then submerged in water for 24 hours before placing it in the test apparatus illustrated in Fig. 1(a). The sample was then exposed to a water pressure of 0.5 MPa for 7 days, after which the sample was split in half using ASTM C496-96. The depth of water ingress was immediately marked, and the maximum depth of water penetration was recorded for each sample (Fig. 1(b)). Six samples were tested for each mixture to obtain the average value and standard deviation of the maximum depth of water penetration.

The second procedure used NR to quantify the amount of water penetrating the concrete sample exposed to water pressure with a high spatial and temporal resolution. This procedure has been defined and compared with the procedure based on DIN 1048-5,^{31,32} where it was shown that visual inspection underestimates the depth of water penetration.

The NR measurements use a different sample geometry (prisms) than that used for visual inspection (cylinders). At the end of the curing period, three prismatic concrete

samples of 76.2 mm in height, 76.2 mm in width, and 38.1 mm in depth were cut from the middle section of the cast beam using a water-cooled, diamond-tipped saw blade. This geometry has been chosen for NR measurements as it allows the volumetric water content per pixel area to remain in the measurable range.³³ Similar to the visual inspection procedure, the vertical sides of the sample were sealed with aluminum tape before submerging the sample in water for a 24-hour duration. The sample was placed inside the permeability apparatus and exposed to 0.5 MPa water pressure for 7 days, as illustrated in Fig. 2(a).

The permeability apparatus was placed in the NR facility at the Oregon State TRIGA® Reactor (OSTR). This facility is a 1.1 MW water-cooled research reactor that uses uranium/zirconium hybrid fuel elements in a circular grid array. The tangential beam port used by the NR facility allows thermal neutrons, $0.091 \text{ eV} \pm 0.015 \text{ eV}$; $4.41 \times 10^6 \pm 2.9 \times 10^{53} \text{ neutrons cm}^{-2} \text{ s}^{-1}$, to pass through the collimator.³⁴ The permeability apparatus is located in the neutron beam line in front of the imaging system that consists of a cesium iodide scintillation detector (CsI, with 5 μm diameter doped with

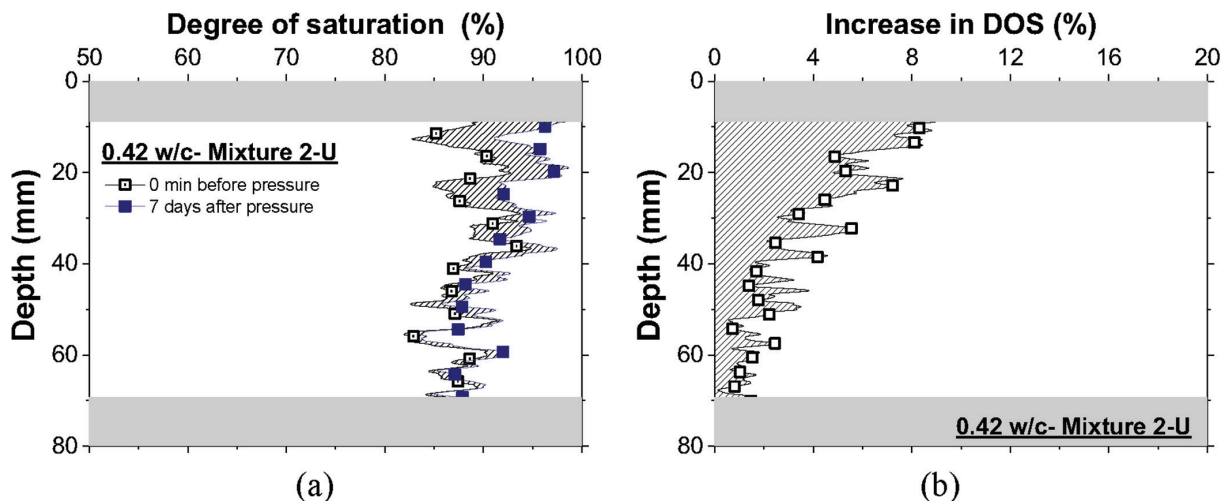


Fig. 3—(a) Initial and final DOS during permeability test; and (b) increase in DOS of concrete sample at end of permeability test.

gadolinium) and a digital camera (50 mm f/1.2 lens). More information on the NR facility and its layout at the OSTR can be found in Moradlo et al.³³ and Ghantous et al.³⁵ The spatial resolution of the radiographs is approximately equal to 90 μm .³³

Figure 2(b) illustrates an NR of a concrete sample inside the permeability apparatus. The water penetration cannot be accurately quantified in the top section of the sample (that is, 8 ± 1.2 mm from the surface) and the bottom section of the samples (that is, 70 to 76.2 mm depth) (Fig. 2(b)). This is because these two sections are located inside the upper and lower compartment of the permeability cell, where the neutron beam interacts with the fixture, gasket, water, and the sample and gets attenuated significantly. As illustrated in Fig. 2(b), a pinhole is present in the lower compartment of the permeability cell to allow pressure dissipation.³²

Radiographs of the concrete sample inside the permeability apparatus were captured throughout each test to quantify the water ingress through the sample depth. Five radiographs were collected for each sample with an exposure time of 2 seconds. In addition, five radiographs were also collected from the background with an open beam (flat field) and a closed beam (dark field). ImageJ software combined the five radiographs collected for each element (sample, flat field, dark field) using a median filter to reduce measurement variability. Flat-field and dark-field radiographs were used to eliminate the background noise and artifacts caused by gamma rays, as illustrated in Eq. (1)^{36,37}

$$I_t = \frac{I_{sample} - I_{DF}}{I_{FF} - I_{DF}} \quad (1)$$

where I_t is the neutron transmitted intensity through the concrete sample after background correction; I_{sample} is the neutron transmitted intensity through the concrete sample before background correction; and I_{FF} and I_{DF} are the neutron transmitted intensities through the flat-field and dark-field radiographs, respectively. I_{sample} , I_{FF} , and I_{DF} were measured in the region of interest illustrated by the rectangle drawn in Fig. 2(b).

At the end of the permeability test (7 days), the samples were removed from the permeability cells, and the aluminum tape was removed before exposing the concrete samples to drying at 105°C. Drying continued until reaching a constant mass (that is, less than 0.01% variation within 24 hours). Five radiographs were collected for the oven-dried samples, open beam, and closed beam. A median filter was used to combine the radiographs of each element. The samples were then vacuum saturated using saturated lime solution following the procedure described in AASHTO TP 135-20.^{38,39} At the end of the vacuum-saturation procedure, the samples were kept immersed in the solution for 48 ± 4 hours at atmospheric pressure. After that, radiographs were collected on the vacuum-saturated samples (that is, with all pores filled with solution) and on the background with an open and closed beam.

The degree of saturation (DOS) along the depth of the concrete samples was then calculated using Eq. (2)

$$DOS_t = \frac{\ln\left(\frac{I_{OD}}{I_t}\right)}{\ln\left(\frac{I_{OD}}{I_{sat}}\right)} \quad (2)$$

where DOS_t is the DOS along the depth of the concrete sample at a given duration of exposure to water pressure; I_t is the corrected neutron transmitted intensity through the concrete sample at a given duration of exposure to water pressure; I_{OD} is the corrected neutron transmitted intensity through the oven-dried concrete sample; and I_{sat} is the corrected neutron transmitted intensity through the vacuum-saturated concrete sample.

Figure 3(a) illustrates the DOS profile along the sample depth before exposure to water pressure (0 minutes) and 7 days after exposure to water pressure. The increase in the DOS is visible in the dashed surface, calculated according to Eq. (3), and illustrated in Fig. 3(b)

$$DOS_{inc} = DOS_{7d} - DOS_{ini} \quad (3)$$

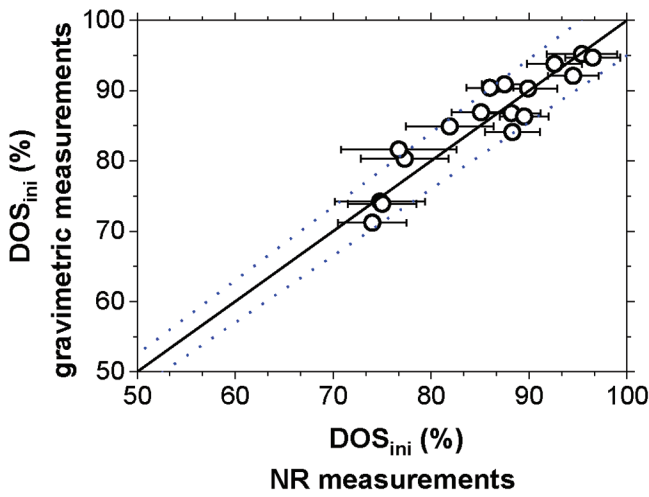


Fig. 4—Comparison of average initial degree of saturation obtained from NR measurements with that obtained from gravimetric measurements.

where DOS_{inc} is the increase in DOS; DOS_{7d} is the DOS profile measured after 7 days of exposure of the concrete sample to water pressure; and DOS_{ini} is the initial DOS of the saturation profile measured on the concrete sample before exposure to water pressure.

The initial DOS of the concrete before exposure to water pressure is important and influences the fluid ingress measurements. The average initial DOS obtained from NR measurements for each mixture was calculated according to Eq. (4) and compared to the gravimetric values calculated according to Eq. (5). As illustrated in Fig. 4, the average initial DOS obtained from NR measurements is within $\pm 5\%$ of the gravimetric measurements. Table 5 illustrates the average initial DOS values obtained from NR measurements for each mixture tested in this study

$$DOS_{ini-NR} = \frac{\sum_{i=1}^n DOS_i}{n} \quad (4)$$

where DOS_{ini-NR} is the average initial DOS along the sample depth obtained from NR; n is the number of pixels between 9 and 65 mm depth—that is, areas that are not interfering with the testing fixture as stated earlier; and DOS_i is the value of the DOS at each pixel along the sample depth

$$DOS_{ini-G} = \frac{m_0 - m_{Al} - m_{OD}}{m_{sat} - m_{OD}} \quad (5)$$

where DOS_{ini-G} is the initial DOS obtained from gravimetric measurements before the exposure of the sample to water pressure; m_0 is the mass of the sample before exposure to water pressure (g); m_{Al} is the mass of aluminum tape (g); m_{OD} is the mass of the oven-dried sample (g); and m_{sat} is the mass of the vacuum-saturated sample (g).

Equation (6) can be used to calculate the increase in the mass of the concrete sample due to water ingress after 7 days of exposure to water pressure³³

$$\Delta m = \left(\sum_{i=0}^n \frac{\ln\left(\frac{I_{ini}}{I_{7d}}\right)}{\sum_w} \times S_{pixel} \times \rho_w \right) \times w \quad (6)$$

Table 5—Initial degree of saturation for all mixtures at beginning of permeability test

Mixture ID	Average initial degree of saturation (0 minutes)—NR measurements, %
1-U	81.9 ± 4.5
1-P	77.3 ± 4.5
1-L	76.7 ± 5.9
2-U	88.2 ± 3.0
2-P	85.1 ± 3.0
2-L	87.5 ± 2.3
3-U	74.8 ± 4.6
3-P	75.0 ± 3.5
3-L	74.0 ± 3.5
4-U	88.3 ± 2.8
4-L	89.5 ± 2.5
5-U	86.0 ± 2.4
5-L	89.9 ± 3.0
6-U	92.6 ± 2.8
6-L	95.4 ± 3.6
7-U	94.5 ± 2.6
7-L	96.5 ± 2.8

where Δm is the total change in the mass of the sample at the end of 7 days of exposure to water pressure due to water ingress between 9 and 64 mm depth; I_{7d} and I_{ini} are the corrected neutron transmitted intensities through the concrete sample after 7 days of exposure to water pressure and before exposure to water pressure, respectively; S_{pixel} is equal to 0.0081 mm^2 ; ρ_w is the water density (1 g/cm^3); Σ_w is the macroscopic cross section of water, measured to be equal to 0.1304 mm^{-1} according to the procedure detailed in Moradlo et al.³³ and Goodwin et al.⁴⁰; n is the number of pixels along the sample depth (between 9 and 65 mm); and w is the number of pixels in the width of the sample.

RESULTS AND DISCUSSION

Influence of PRAs and w/c on fluid transport in concrete

Figure 5 illustrates the increase in DOS along the depth of the concrete samples after 7 days of exposure to water pressure for mixtures with various w/c and with and without PRAs. Figure 6(a) illustrates the increase in the mass of the samples, calculated from NR measurements according to Eq. (6), for different PRA forms as well as w/c . The depths of water penetrations obtained using visual inspection on mixtures with various w/c and various PRA forms are illustrated in Fig. 6(b). It can be first noted from both Fig. 5 and 6 that the amount and depth of water penetrating the concrete samples increased with the increase in the w/c , irrespectively of the PRA form. Samples with a low w/c (that is, 0.35 in this study) have less capillary porosity and lower pore connectivity, which explains their low hydraulic permeability.⁴¹ An increase in the w/c of the concrete mixture from 0.35 to 0.50 leads to an increase in the concrete capillary porosity and porosity at the interfacial

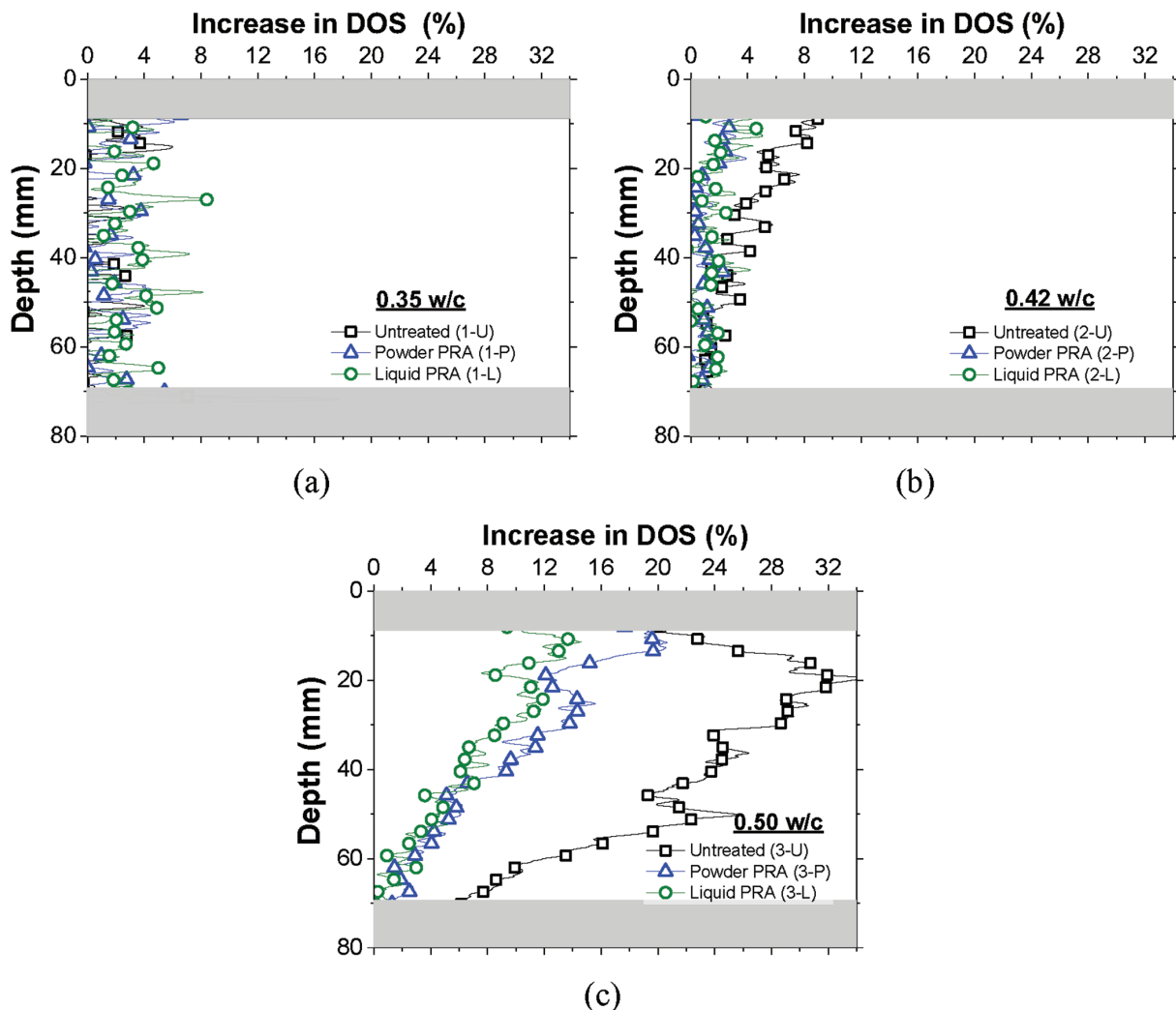


Fig. 5—Influence of liquid and powder PRAs on fluid ingress in concrete with w/c of: (a) 0.35; (b) 0.42; and (c) 0.50.

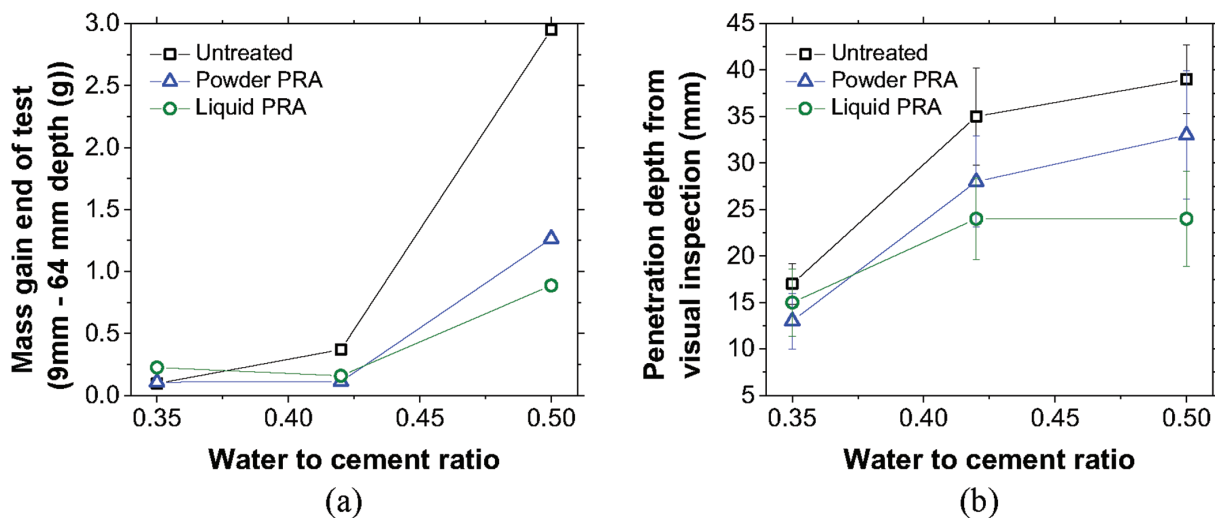


Fig. 6—Influence of PRAs on fluid ingress in concrete samples with various w/c, as illustrated using: (a) mass gain obtained from NR measurements; and (b) visual depth of water penetration.

transition zone (ITZ) between the aggregate and cement paste.^{41,42} The increased capillary porosity and connected ITZ porosity would be expected to increase the hydraulic permeability and decrease the compressive strength of concrete samples, as illustrated in Fig. 7(a).

Second, for both mixtures with a w/c of 0.42 and 0.50, samples with both liquid and powder PRAs outperformed plain concrete samples and showed a lower amount of water penetrating the concrete samples. For samples with a w/c of 0.35, the amount of water penetrating untreated samples (that

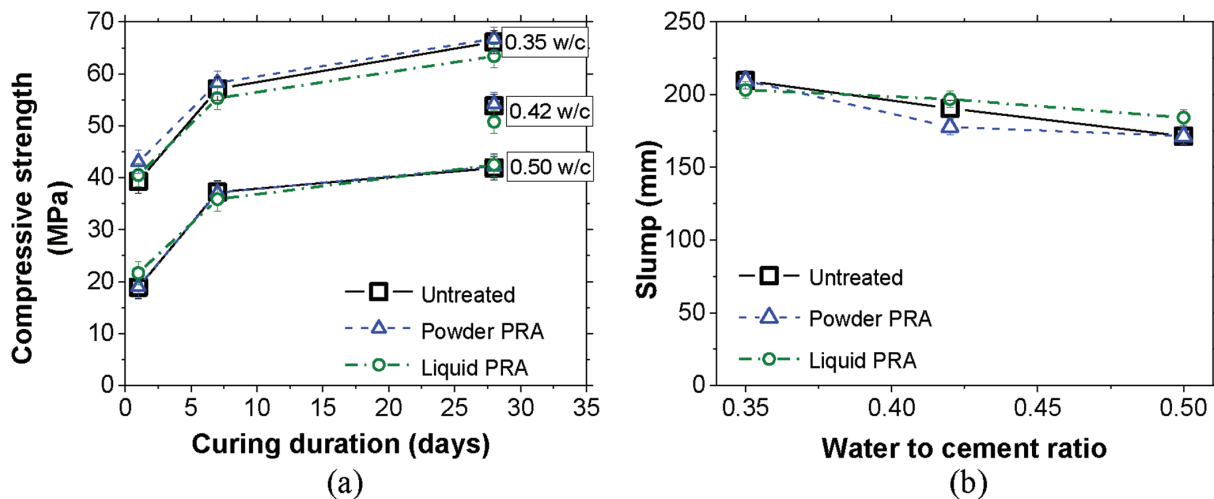


Fig. 7—Influence of PRAs on: (a) compressive strength of concrete; and (b) slump of concrete with various mixture designs.

is, without PRAs) was hard to distinguish from samples with liquid or powder PRAs due to the low hydraulic permeability of these samples due to their dense matrix. Consequently, the benefit of PRAs in reducing the hydraulic permeability of concrete is immediately visible for mixtures with a *w/c* higher than 0.35 (that is, with high hydraulic permeability). This is consistent with the findings of Hassani et al.,²⁵ where it was shown that the efficiency of PRAs is highly dependent on the *w/c* and type of cementitious materials used (various SCM types).²⁵

Third, it can be noted that liquid PRA outperforms powder PRA in decreasing fluid ingress in concrete (that is, reducing the amount of water penetrating the concrete sample and the depth of water penetration), as illustrated in Fig. 5 and 6.

Figure 7(a) illustrates the compressive strength evolution with respect to time, PRA form, and *w/c*. Based on Fig. 7(a), it can be noted that the addition of PRA does not influence the compressive strength of the concrete samples, which is consistent with the literature.^{13,26}

Furthermore, the targeted slump of 178 ± 13 mm was achievable for all mixtures irrespective of the PRA form (liquid or powder) (Fig. 7(b)). Liquid and powder PRAs are chemically similar; however, liquid PRA is distributed more uniformly during mixing. In contrast, powder PRA requires more mixing time and a greater amount of HRWRA to achieve the same targeted slump (Table 3). Consequently, liquid PRA is slightly more efficient than powder PRA. Based on the results of this study, liquid PRA can be beneficial in decreasing fluid ingress in concrete samples.

Influence of curing duration on fluid transport in concrete

Figure 8(a) illustrates the increase in DOS for untreated samples at 28 and 56 days (that is, without PRAs). In contrast, Fig. 8(b) shows the increase in DOS for samples made with liquid PRA at 28 and 56 days. The influence of curing duration on the depth of water penetration obtained by visual inspection is illustrated in Fig. 9(a) for both mixtures with and without liquid PRA.

The increase in the moist-curing duration from 28 to 56 days significantly decreased the amount of water

penetrating the untreated concrete sample (Fig. 8(a)). This is consistent with a decrease in the depth of water penetration (Fig. 9(a)). The increased curing duration resulted in a larger volume of hydration products and a decrease in the capillary porosities⁴³ (Fig. 8(d)). This increase in matrix density decreased pore connectivity,⁴⁴ resulting in less fluid ingress. Figure 8(c) shows a higher initial DOS in samples that were moist-cured for 56 days compared to those moist-cured for 28 days (due to water curing). The volume of empty pores in the 56-day cured samples is smaller than in the 28-day cured samples. That could also explain the visible decrease in the fluid ingress with the increase in the curing duration of untreated concrete samples.

The increase in DOS measured in the samples cured for 28 days (empty symbols) and those cured for 56 days (filled symbols) is more significant for untreated samples (Fig. 8(a)) than in the samples with liquid additives (Fig. 8(b)). Consequently, when liquid PRA is added to the concrete mixture design, the influence of the curing duration on the fluid ingress in the concrete samples exists but is less noticeable than that of the untreated samples (Fig. 8(b) and 9(a)). This agrees with the results in Pazderka and Hájková.²⁶ Crystalline PRAs absorb water that reacts with the hydration products, leading to crystalline products that densify the matrix and reduce permeability. Thus, the densification of the matrix induced by the increase in the curing duration from 28 to 56 days will have less of an impact on the fluid ingress in samples containing liquid PRA. It should also be noted from Fig. 8(c) and Table 5 that the initial DOSs of all mixtures cured for 56 days and containing liquid PRA are slightly higher than the untreated mixture. This could be linked to their hydrophilic characteristic.

Influence of entrained air content on fluid transport in concrete

For untreated concrete, the amount of water and the depth of water penetration increased with the increase in the entrained air content, as illustrated in Fig. 10(a) and 9(b), respectively. Figure 11(a) illustrates that the initial DOS measured along the depth of the concrete samples with 2.5% air is greater than the DOS measured on samples with

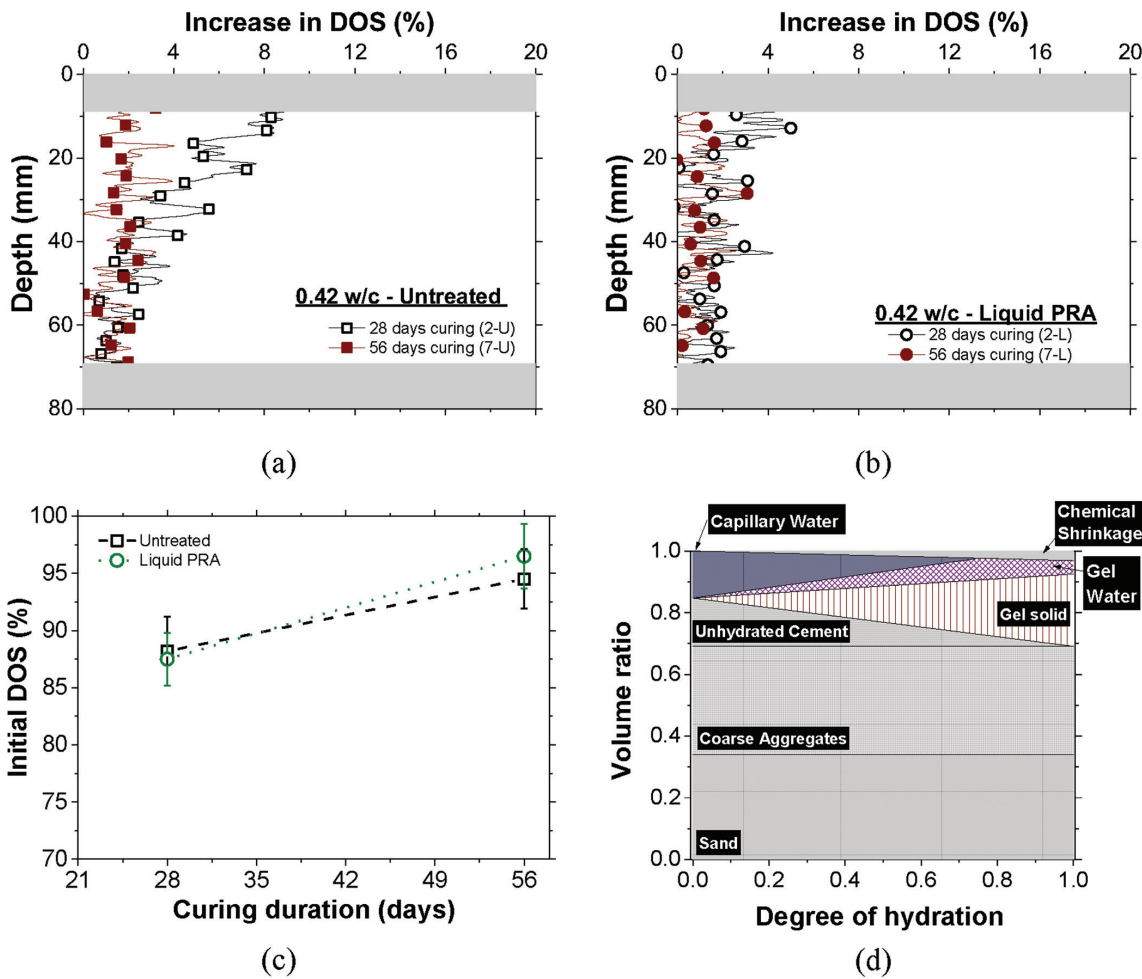


Fig. 8—Influence of curing duration on fluid transport in concrete samples: (a) without PRAs; and (b) with liquid PRA; (c) initial DOS at start of test with respect to curing duration; and (d) Powers' model for hydration evolution.

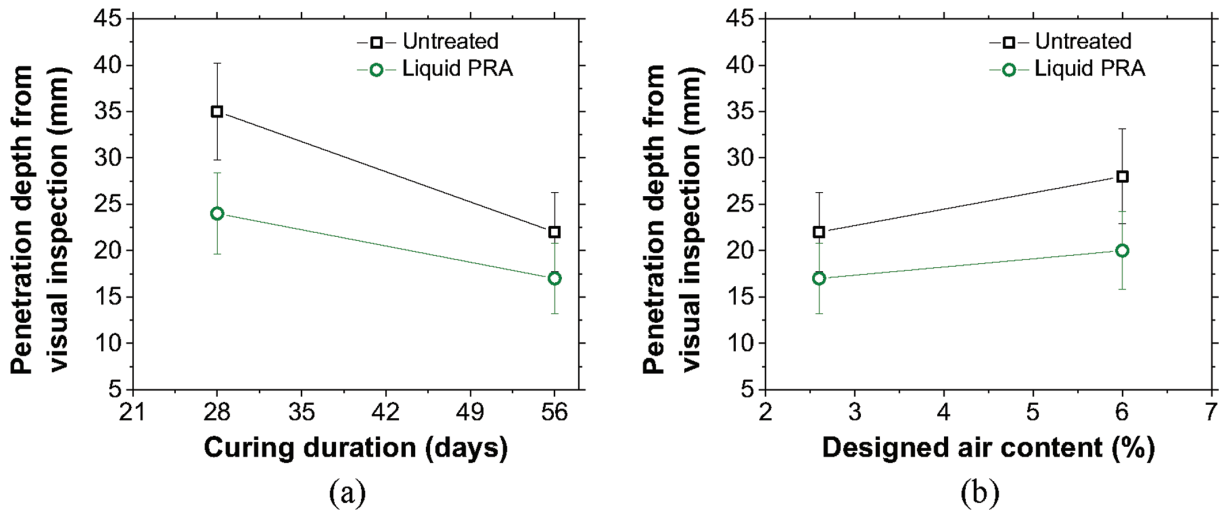


Fig. 9—Influence of PRAs on fluid ingress in concrete samples with respect to: (a) curing duration; and (b) air content, as illustrated using visual depth of water penetration.

6.0% air. This is due to the entrained air voids being vapor-filled (that is, empty) at the beginning of the pressure test (Fig. 11(b)) and filling during testing.³⁹

These results illustrate the importance of the initial DOS at the start of the permeability test on the fluid ingress results. Consequently, close attention is needed for the sample

preconditioning before the permeability test. The same DOS should be ensured in two different samples at the start of the permeability test to be able to compare their resistance to fluid ingress.

The influence of the entrained air content on the amount of water and depth of water penetrating concrete samples

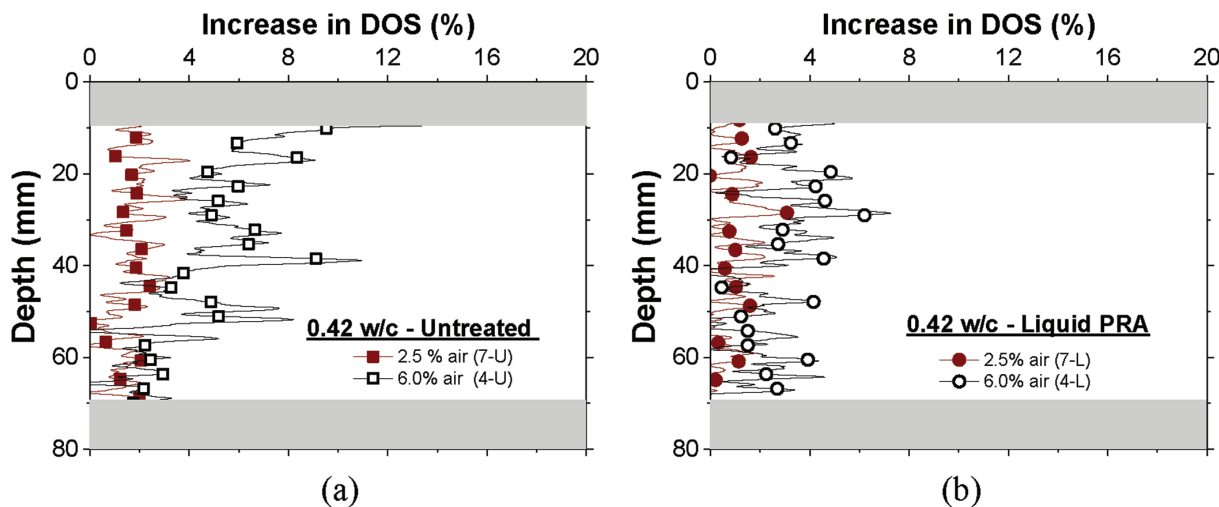


Fig. 10—Influence of entrained air content on fluid transport in concrete samples: (a) without PRAs; and (b) with liquid PRA.

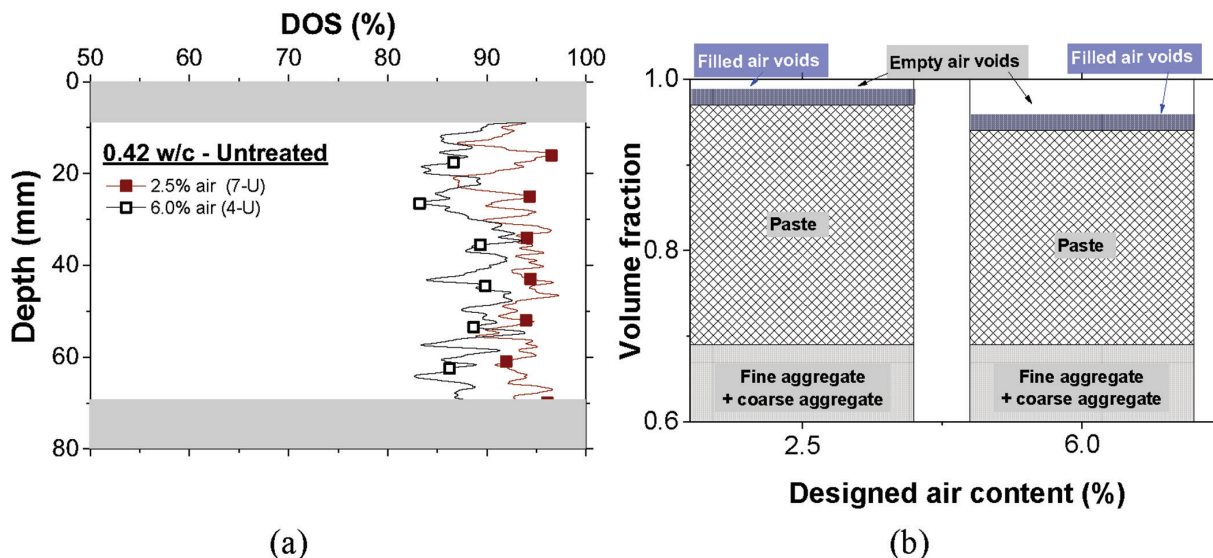


Fig. 11—(a) Initial DOS with respect to entrained air content of concrete; and (b) illustration of volume fraction of entrained air filled at start of permeability test.

with liquid PRAs is less visible than in the mixtures without PRAs, as shown in both Fig. 10(b) (empty symbols and filled symbols close to each other) and Fig. 9(b). This is due to the reduced permeability of samples with liquid PRA, as previously explained.

Influence of CA volume and size on fluid transport in concrete

The fluid ingress measured on untreated concrete samples increased with an increase in the CA volume fraction from 35 to 40%. This was visible from both the NR measurements (Fig. 12(a)) and visual inspection (Table 6). The volume fraction of paste was constant for both Mixture 7 (with 35% CA volume fraction) and Mixture 6 (40% CA volume fraction), while the volume fraction of sand was changed between these two mixtures (Tables 2 and 3).

To explain this difference in measurements, the literature describes that an ITZ can exist between the cement paste and the aggregates as a result of poor packing of the cement grains around the aggregate surfaces and the preference for

calcium hydroxide to precipitate on the aggregate surfaces.⁴⁵ The ITZ is more porous (less dense) than the bulk paste matrix,⁴⁶ and therefore the ITZ influences the transport properties of the concrete. Shane et al.⁴⁷ showed that the permeability of the ITZ is up to 500 times greater than the permeability of the paste. An increase in the permeability of mortar samples was noted by increasing the volume fraction of fine aggregates from 35 to 45%,^{47,48} which is ascribed to ITZ percolation. Similarly, by increasing the CA volume from 35 to 40%, ITZ percolation increased as well as ITZ connection to the concrete surface in contact with water (as illustrated later). This leads to an increase in the fluid ingress in concrete exposed to water pressure.

Based on NR measurements, the amount of water penetrating the concrete samples with liquid PRA appears comparable for both concrete mixtures with different CA volume fractions (Fig. 12(b)). In addition to the fact that crystalline liquid PRA works by densifying the matrix and decreasing its permeability,¹⁸ the ITZ in the literature is dependent on parameters including admixture dosage,

Table 6—Influence of CA volume fraction and size on depth of water penetration in concrete samples

	Depth of water penetration by visual inspection at 56 days, mm		
	40% CA volume fraction (AASHTO No. 57 and 8; Mixtures 6-U and 6-L)	35% CA volume fraction (AASHTO No. 57 and 8; Mixtures 7-U and 7-L)	35% CA volume fraction (AASHTO No. 8; Mixtures 5-U and 5-L)
Untreated	24 ± 4.3	22 ± 4.3	25 ± 2.4
Liquid PRA	22 ± 5.6	17 ± 3.8	19 ± 5.0

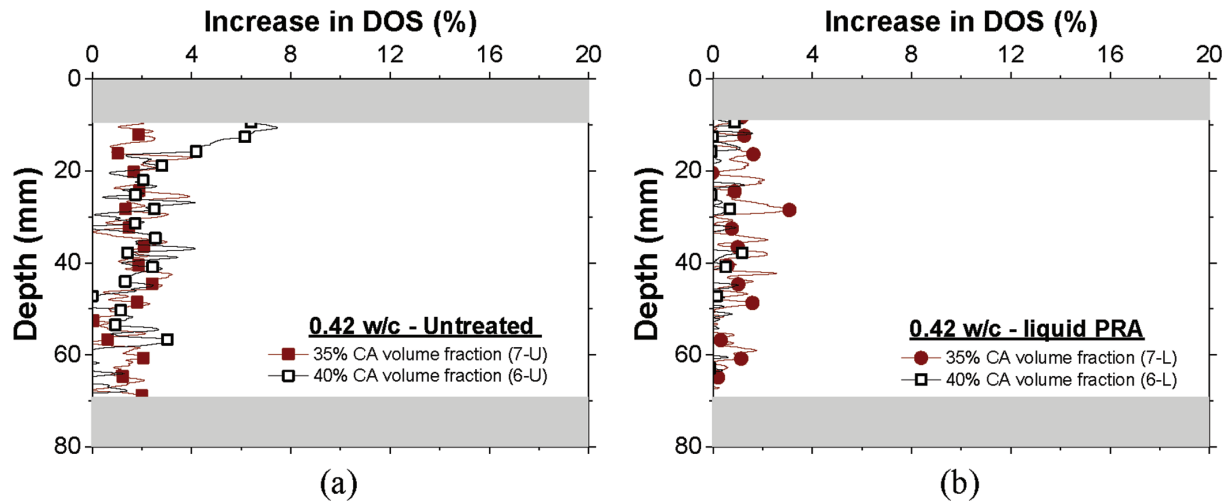


Fig. 12—Influence of volume fraction of CA on fluid transport in concrete samples: (a) without PRAs; and (b) with liquid PRA.

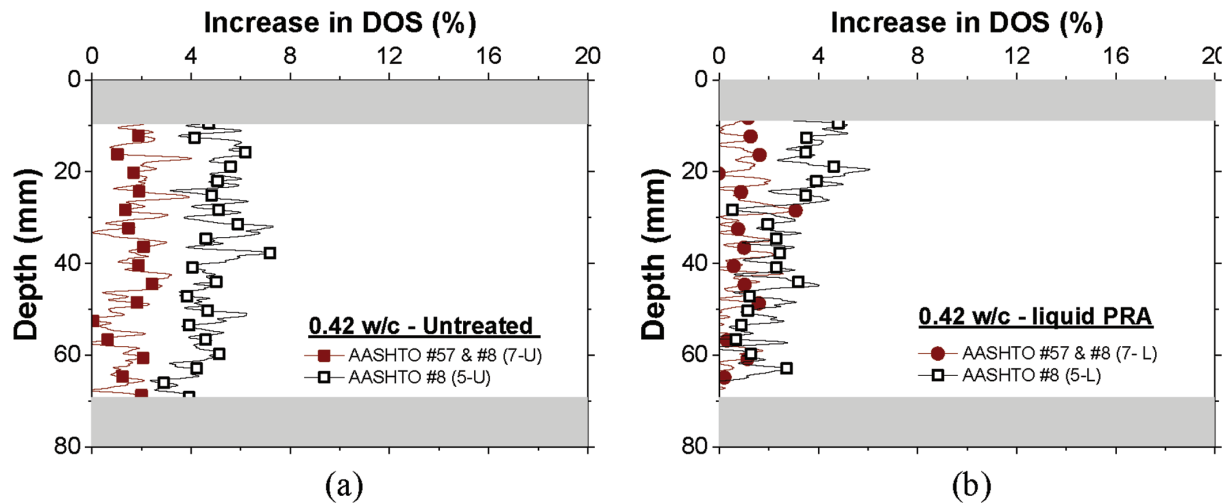


Fig. 13—Influence of size of CA on fluid transport in concrete samples: (a) without PRAs; and (b) with liquid PRA.

mixing procedure, and *w/c*.^{49,50} For instance, the ITZ was absent or hard to identify in mixtures with a low *w/c* or in mixtures containing silica fume.⁵⁰ It could be hypothesized herein that liquid PRA may be beneficial in decreasing the porosity of the ITZ. The depth of water penetration obtained by visual inspection did show a slight increase with the increase in the CA volume fraction of samples with liquid PRA (Table 6). Differences between the NR and visual observations may be due to the higher variability in optical inspection measurements and the dependency of the visibility of water by the naked eye on the size of pores being filled with water.³²

The amount of water, illustrated in Fig. 13(a), as well as the depth of water penetration, noted in Table 6, in untreated concrete samples prepared with small CA size (AASHTO

No. 8), are higher than those reported on untreated concrete samples with a better CA size distribution (AASHTO No. 8 and 57). Similarly, the CA size also impacted concrete with liquid PRA. Still, the influence of CA size on fluid ingress in concrete samples with liquid PRA was less advanced than in concrete without liquid PRA (Fig. 13(b) and Table 6). By decreasing the CA size and keeping their volume fraction constant, the surface area of the ITZ increases in addition to a possible increase in ITZ percolation, as schematized in Fig. 14. This will lead to a higher porosity and conductivity pathway, allowing for water ingress in the concrete samples.

In addition, the initial DOS for untreated mixtures with AASHTO No. 8 CA was $86.0 \pm 2.4\%$, which is lower than the mixture containing AASHTO No. 8 and 57 CA ($94.5 \pm 2.6\%$), as noted in Table 5. Similarly, the initial DOS of

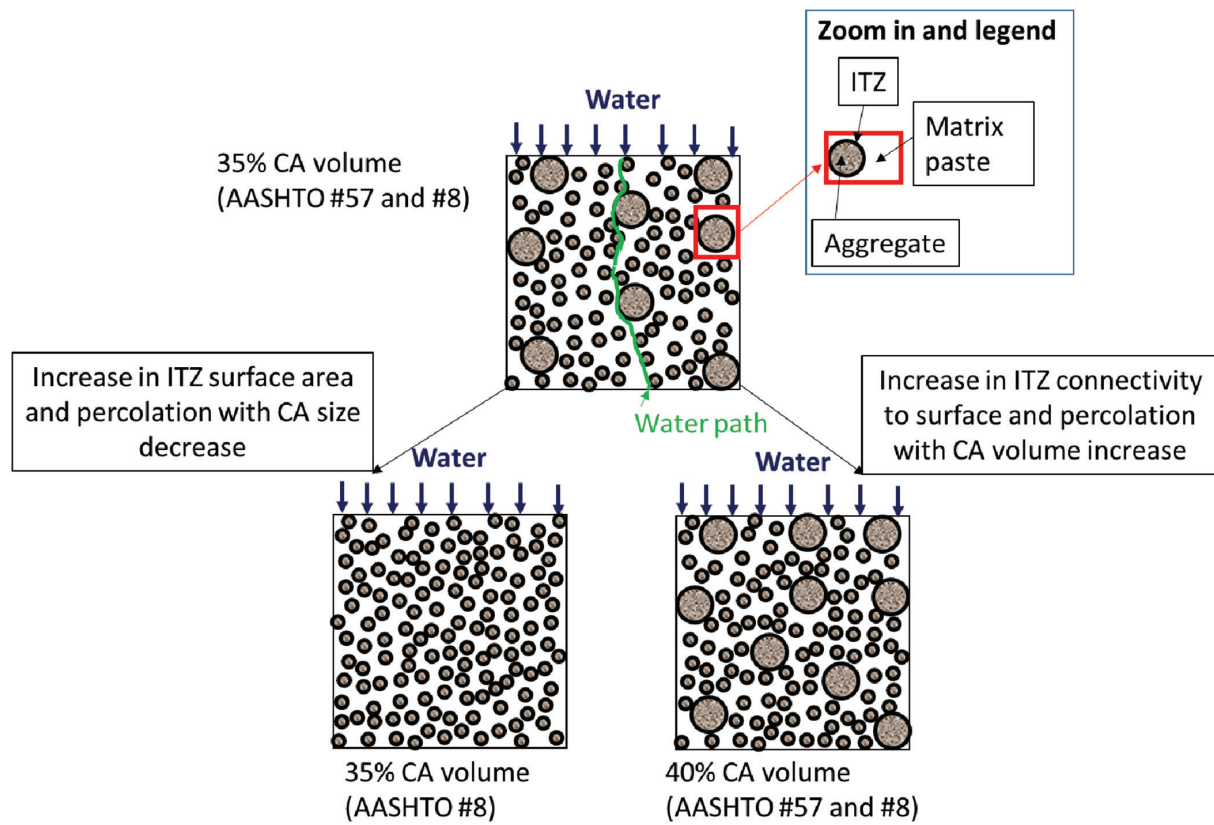


Fig. 14—Illustration of influence of CA volume fraction and size on ITZ percolation and connectivity to concrete surface. Note that only CAs are illustrated in this schematic presentation, and sand is not illustrated herein.

samples with liquid PRA and small CA size (Mixture 5-L) was 7% higher than the average initial DOS measured on samples with liquid PRA and better CA size distribution (Mixture 7-L). The surface area of the ITZ increased when the size of CA decreased, and these larger pore sizes will take longer to fill at atmospheric pressure. For this reason, at the start of the uniaxial water pressure test, more pores will be empty in samples with smaller CA sizes (Mixtures 5-U and 5-L) compared to mixtures with coarser aggregates (AASHTO No. 8 and 57). This will then lead to more fluid ingress in the sample with smaller CA size.

CONCLUSIONS

This paper provided experimental data regarding the influence of water-cement ratio (w/c), entrained air content, coarse aggregate (CA) size, CA volume, curing duration, and permeability-reducing admixtures (PRAs) on the water transport in the concrete samples under water pressure applied to one face. At the end of the pressure test, the depth of water penetration was assessed by visual inspection, while neutron radiography (NR) was used to determine the amount of water ingress in the sample depth.

As expected, reducing the w/c or increasing the curing duration decreased the fluid transport in concrete due to a reduction in porosity and connected flow paths through pores.

Liquid and powder PRAs, with a crystalline products classification, were proven beneficial for decreasing the water transport in concrete mixtures without impacting the compressive strength. However, for samples with a low w/c

(that is, 0.35 in this study) or long curing duration (56 days in this study), the benefit of admixtures is less than in mixtures with a higher w/c or shorter curing durations.

The liquid and powder PRAs used in this study were chemically similar; however, the performance of the liquid PRA was more consistent than the powder PRA, likely due to better dispersion. It was also noted that the mixtures with powder PRAs required additional high-range water-reducing admixture (HRWRA) to achieve the targeted slump.

Fluid ingress increased with entrained air content due to the lower initial degree of saturation (DOS) in concrete with a higher air content. This is because larger air voids (that is, entrained and entrapped air voids) take longer to fill than matrix pores (gel and capillary pores) at atmospheric pressure.

An increase in the volume of CA (from 35 to 40%) or a decrease in the size of the CA (from AASHTO No. 57 and 8 to only AASHTO No. 8) increased the fluid ingress in the concrete samples due to the increase in the interfacial transition zone (ITZ) percolation and connectivity.

The impact of the curing duration, entrained air content, CA volume fraction, and CA size on the fluid ingress in concrete samples was less noticeable in mixtures with PRA than in untreated mixtures. The liquid PRA reduced concrete permeability by absorbing water, reacting with the hydration products, and forming crystalline products that densify the matrix. As a result of the reduced porosity (high matrix density) of samples with liquid PRA and the corresponding low permeability, the influence of mixture proportions and curing duration was less noticeable on fluid ingress.

in samples with PRAs than on untreated concrete (that is, samples without PRAs).

The initial DOS before the start of the permeability test has a significant influence on the fluid ingress measurements. Care should be taken during sample preconditioning, and the same DOS should be ensured at the start of the test for an accurate comparison between two separate concrete samples.

AUTHOR BIOS

Rita Maria Ghantous is a Research Associate in the School of Civil and Construction Engineering at Oregon State University, Corvallis, OR. She received her MS from École Centrale de Nantes, Nantes, France, and her PhD in civil engineering from the National Institute of Applied Sciences of Toulouse, Toulouse, France. Her research interests include the durability and sustainability of concrete.

Van Bui, FACI, is a Senior Scientist responsible for the development of specialty admixtures and technical services for Master Builders Solutions Admixtures US, LLC (MBS), Beachwood, OH. He received his MEng from Slovak University of Technology in Bratislava, Bratislava, Slovakia, and the Asian Institute of Technology, Bangkok, Thailand, and his PhD from the University of Wollongong, Wollongong, NSW, Australia, in 1983, 1994, and 1999, respectively. He is a member of several ACI technical committees. He has approximately 40 years of experience in concrete and other cementitious material technologies and admixture development.

Steve Schaeff is the Manager of the Engineering Group responsible for the development of specialty admixtures and technical services for MBS, where he has been part of the research and development community for over 17 years. He received his MS in civil engineering from Purdue University, West Lafayette, IN.

Brett Fronczeck is a Concrete Technician at MBS, supporting North America's product development and technical service activities. He leads concrete mixture evaluations, conducts durability testing, field evaluations, and technology demonstrations.

Clay B. Jablonski is an Undergraduate Research Assistant in the School of Nuclear Science and Engineering at Oregon State University.

Steve R. Reese is the Radiation Center Director and Associate Professor in the School of Nuclear Science and Engineering at Oregon State University. He received his BS in science from Oregon State University and his PhD in radiological health sciences from Colorado State University, Fort Collins, CO. He is a Certified Health Physicist and holds a senior reactor operator license.

W. Jason Weiss, FACI, is the Edwards Distinguished Chair in Engineering at Oregon State University. He received his BAE from The Pennsylvania State University, State College, PA, in 1995, and his MS and PhD from Northwestern University, Evanston, IL, in 1997 and 1999, respectively. He is the Editor-in-Chief of the ACI Materials Journal and a member of the ACI Technical Activities Committee and the ACI Board of Direction.

ACKNOWLEDGMENTS

The authors gratefully acknowledge the support of Master Builders Solutions Admixtures US, LLC. The active chemicals in this study's permeability-reducing admixtures (PRA) are trade secrets and cannot be provided in this paper. The contents of this paper reflect the views of the authors, who are responsible for the facts and the accuracy of the data presented herein.

REFERENCES

- Graveen, C.; Falker, E. M.; Beaver, M.; Neithalath, N.; Weiss, W. J.; Olek, J.; Nantung, T. E.; and Gallivan, V. L., "Performance Related Specifications (PRS) for Concrete Pavements in Indiana, Volume 1: Executive Summary," Report No. FHWA/IN/JTRP-2004/13-1, Joint Transportation Research Program, Indiana Department of Transportation and Purdue University, West Lafayette, IN, 2009. doi: 10.5703/1288284314213
- Graveen, C.; Falker, E. M.; Beaver, M.; Neithalath, N.; Weiss, W. J.; Olek, J.; Nantung, T. E.; and Gallivan, V. L., "Performance Related Specifications (PRS) for Concrete Pavements in Indiana, Volume 2: Technical Report," Report No. FHWA/IN/JTRP-2004/13-2, Joint Transportation Research Program, Indiana Department of Transportation and Purdue University, West Lafayette, IN, 2009. doi: 10.5703/1288284314214
- Weiss, W. J., "Concrete Pavement Joint Durability: A Sorption-Based Model for Saturation, the Role of Distributed Cracking, and Calcium Oxychloride Formation," *Concreep 10: Proceedings of the 10th International Conference on Mechanics and Physics of Creep, Shrinkage, and Durability of Concrete and Concrete Structures*, C. Hellmich, B. Pichler, and J. Kollegger, eds., Vienna, Austria, 2015, pp. 211-218.
- Mackenzie, J. R., and Alexander, M. G., "Using Durability to Enhance Concrete Sustainability," *Journal of Green Building*, V. 4, No. 3, 2009, pp. 52-60. doi: 10.3992/jgb.4.3.52
- Weiss, J., and Shields-Cook, S., "Relating Transport Properties to Performance in Concrete Pavements," *CP Road Map MAP Brief*, National Concrete Pavement Technology Center, Iowa State University of Science and Technology, Ames, IA, 2014, 6 pp.
- Chini, A. R.; Muszynski, L. C.; and Hicks, J. K., "Determination of Acceptance Permeability Characteristics for Performance-Related Specifications for Portland Cement Concrete," final report, Florida Department of Transportation, Tallahassee, FL, 2003, 162 pp.
- Bentz, D. P.; Clifton, J. R.; Ferraris, C. F.; Garboczi, E. J.; and Torrents, J. M., "Transport Properties and Durability of Concrete: Literature Review and Research Plan," NISTIR 6395, National Institute of Standards and Technology, Gaithersburg, MD, 1999.
- Garboczi, E. J., "Permeability, Diffusivity, and Microstructural Parameters: A Critical Review," *Cement and Concrete Research*, V. 20, No. 4, 1990, pp. 591-601. doi: 10.1016/0008-8846(90)90101-3
- Meletiou, C. A.; Tia, M.; and Bloomquist, D., "Development of a Field Permeability Test Apparatus and Method for Concrete," *ACI Materials Journal*, V. 89, No. 1, Jan.-Feb. 1992, pp. 83-89.
- Saricimen, H.; Maslehdin, M.; Al-Tayyib, A. J.; and Al-Mana, A. I., "Permeability and Durability of Plain and Blended Cement Concretes Cured in Field and Laboratory Conditions," *ACI Materials Journal*, V. 92, No. 2, Mar.-Apr. 1995, pp. 111-116.
- Shattaf, N. R.; Alshamsi, A. M.; and Swamy, R. N., "Curing/Environment Effect on Pore Structure of Blended Cement Concrete," *Journal of Materials in Civil Engineering*, ASCE, V. 13, No. 5, 2001, pp. 380-388. doi: 10.1061/(ASCE)0899-1561(2001)13:5(380)
- Philipose, K. E.; Feldman, R. F.; and Beaudoin, J. J., "Durability Predictions from Rate of Diffusion Testing of Normal Portland Cement, Fly Ash, and Slag Concrete," AECL-10489, Atomic Energy of Canada Limited, Chalk River, ON, Canada, 1991, 24 pp.
- Munn, R. L.; Chang, Z. T.; and Kao, G., "Performance of Australian Commercial Concretes Modified with a Permeability Reducing Admixture," *Proceedings of the 22nd Biennial Conference of the Concrete Institute of Australia*, Melbourne, VIC, Australia, 2005, pp. 17-19.
- Riding, K. A.; Tibbetts, C. M.; and Ferraro, C. C., "Testing Methods to Assess the Durability of Concrete Permeability Reducing Admixtures," final report, Florida Department of Transportation, Tallahassee, FL, 2020, 69 pp.
- Biparva, A., and Gupta, R., "Smart Waterproofing System: A Review," *Proceedings*, International Conference on Future Concrete, Doha, Qatar, 2010, 10 pp.
- Muhammad, N. Z.; Keyvanfar, A.; Majid, M. Z. A.; Shafagh, A.; and Mirza, J., "Waterproof Performance of Concrete: A Critical Review on Implemented Approaches," *Construction and Building Materials*, V. 101, Part 1, 2015, pp. 80-90. doi: 10.1016/j.conbuildmat.2015.10.048
- Giannini, E. R.; Lindly, J. K.; and Dunn, J. R., "Comparative Evaluation of Concrete Bridge Deck Sealers," ALDOT Report No. 930-861, Alabama Department of Transportation, Montgomery, AL, 2015, 103 pp.
- ACI Committee 212, "Report on Chemical Admixtures for Concrete (ACI 212.3R-16)," American Concrete Institute, Farmington Hills, MI, 2016, 76 pp.
- Pfeifer, D. W., and Scali, M. J., "Concrete Sealers for Protection of Bridge Structures," NCHRP Report No. 244, Transportation Research Board, Washington, DC, 1981, 148 pp.
- Pincheira, J. A., and Dorshorst, M. A., "Evaluation of Concrete Deck and Crack Sealers," Report No. WHRP 06-09, Wisconsin Highway Research Program, Madison, WI, 2005, 164 pp.
- Almusallam, A. A.; Khan, F. M.; Dulaijan, S. U.; and Al-Amoudi, O. S. B., "Effectiveness of Surface Coatings in Improving Concrete Durability," *Cement and Concrete Composites*, V. 25, No. 4-5, 2003, pp. 473-481. doi: 10.1016/S0958-9465(02)00087-2
- Tibbetts, C. M.; Riding, K. A.; and Ferraro, C. C., "A Critical Review of the Testing and Benefits of Permeability-Reducing Admixtures for Use in Concrete," *Cement*, V. 6, 2021, Article No. 100016. doi: 10.1016/j.cement.2021.100016
- Hooton, R. D., "What is Needed in a Permeability Test for Evaluation of Concrete Quality," *MRS Online Proceedings Library*, V. 137, 1988, pp. 141-149. doi: 10.1557/PROC-137-141

24. Hassani Esgandani, M.; Vessalas, K.; Baweja, D.; and Schmidt, Z., "Effect of Chemical Admixtures on Water Penetration of Concrete," *RILEM International Workshop on Performance-Based Specification and Control of Concrete Durability*, Paris, France, 2014.
25. Hassani, M.; Vessalas, K.; Sirivivatnanon, V.; and Baweja, D., "Influence of Permeability-Reducing Admixtures on Water Penetration in Concrete," *ACI Materials Journal*, V. 114, No. 6, Nov.-Dec. 2017, pp. 911-922.
26. Pazderka, J., and Hájková, E., "Crystalline Admixtures and Their Effect on Selected Properties of Concrete," *Acta Polytechnica*, V. 56, No. 4, 2016, pp. 306-311. doi: 10.14311/AP.2016.56.0306
27. Silva, E. F.; Moreira, M.; Manzano, M. A. R.; and Blanco, R., "Case Study of Permeability-Reducing Admixture Use in Anti-Flotation Slabs: Building in Brasilia, Brazil," *Journal of Building Pathology and Rehabilitation*, V. 2, No. 1, 2017, Article No. 1. doi: 10.1007/s41024-016-0014-5
28. Kapustin, F. L., and Pomazkin, E. P., "Effect of Waterproofing Penetrating Capillary Mixture on Concrete Waterproofness and Cement Stone Microstructure," *Power Technology and Engineering*, V. 52, No. 2, 2018, pp. 168-171. doi: 10.1007/s10749-018-0927-z
29. Mačanovskis, A.; Krasnikovs, A.; Sprūge, I.; Šahmenko, G.; and Lukašenoks, A., "Mechanical Properties and Self-Healing Effect of Concrete Containing Capillary Hydro Insulation Admixture," *Rīgas Tehniskās Universitātes Zinātniskie Raksti*, V. 18, No. 1, 2016, pp. 17-21. doi: 10.1515/cons-2016-0003
30. Teng, L.-W.; Huang, R.; Chen, J.; Cheng, A.; and Hsu, H.-M., "A Study of Crystallizing Mechanism of Penetration Sealer Materials," *Materials (Basel)*, V. 7, No. 1, 2014, pp. 399-412. doi: 10.3390/ma7010399
31. DIN 1048-5:1991, "Testing of Hardened Concrete," Deutsches Institut für Normung, Berlin, Germany, 1991.
32. Ghantous, R. M.; Fronczeck, B.; Jablonski, C. B.; Bui, V.; Schaeff, S.; Reese, S. R.; and Weiss, W. J., "Using Neutron Radiography to Assess Parameters Associated with Water Permeability Testing," *Advances in Civil Engineering Materials*, V. 12, No. 1, 2023, 21 pp. doi: 10.1520/ACEM20220061
33. Moradillo, M. K.; Montanari, L.; Suraneni, P.; Reese, S. R.; and Weiss, J., "Examining Curing Efficiency Using Neutron Radiography," *Transportation Research Record: Journal of the Transportation Research Board*, V. 2672, No. 27, 2018, pp. 13-23. doi: 10.1177/0361198118773571
34. Gadd, M. S., "Characterization of the Oregon State University Neutron Radiography Facility," LA-UR-07-5375, Los Alamos National Laboratory, Los Alamos, NM, 2007.
35. Ghantous, R. M.; Valadez-Carranza, Y.; Reese, S. R.; and Weiss, W. J., "Drying Behavior of 3D Printed Cementitious Pastes Containing Cellulose Nanocrystals," *Cement*, V. 9, 2022, Article No. 100035. doi: 10.1016/j.cement.2022.100035
36. Hussey, D. S.; Spernjak, D.; Weber, A. Z.; Mukundan, R.; Fairweather, J.; Brosha, E. L.; Davey, J.; Spendelow, J. S.; Jacobson, D. L.; and Borup, R. L., "Accurate Measurement of the Through-Plane Water Content of Proton-Exchange Membranes Using Neutron Radiography," *Journal of Applied Physics*, V. 112, No. 10, 2012, Article No. 104906. doi: 10.1063/1.4767118
37. Schneider, C. A.; Rasband, W. S.; and Eliceiri, K. W., "NIH Image to ImageJ: 25 Years of Image Analysis," *Nature Methods*, V. 9, No. 7, 2012, pp. 671-675. doi: 10.1038/nmeth.2089
38. AASHTO TP 135-20, "Standard Method of Test for Determining the Total Pore Volume in Hardened Concrete Using Vacuum Saturation," American Association of State Highway and Transportation Officials, Washington, DC, 2020, 7 pp.
39. Bu, Y.; Spragg, R.; and Weiss, W. J., "Comparison of the Pore Volume in Concrete as Determined Using ASTM C642 and Vacuum Saturation," *Advances in Civil Engineering Materials*, V. 3, No. 1, 2014, pp. 308-315. doi: 10.1520/ACEM20130090
40. Goodwin, M. N.; Ghantous, R. M.; Weiss, W. J.; and Reese, S. R., "Neutron Radiography of Cement Paste Made with Light and Heavy Water," *Journal of Radioanalytical and Nuclear Chemistry*, V. 331, No. 12, 2022, pp. 5113-5121. doi: 10.1007/s10967-022-08493-w
41. Rangaraju, P. R., "Development of Some Performance-Based Material Specifications for High-Performance Concrete Pavement," *Transportation Research Record: Journal of the Transportation Research Board*, V. 1834, No. 1, 2003, pp. 69-76. doi: 10.3141/1834-09
42. Neville, A. M., *Properties of Concrete*, fourth edition, Addison Wesley Longman Limited, Boston, MA, 1995.
43. Powers, T. C., "A Discussion of Cement Hydration in Relation to the Curing of Concrete," *Proceedings of the 27th Annual Meeting of the Highway Research Board*, V. 27, 1948, pp. 178-188.
44. Bharadwaj, K.; Glosser, D.; Moradillo, M. K.; Isgor, O. B.; and Weiss, W. J., "Toward the Prediction of Pore Volumes and Freeze-Thaw Performance of Concrete Using Thermodynamic Modelling," *Cement and Concrete Research*, V. 124, 2019, Article No. 105820. doi: 10.1016/j.cemconres.2019.105820
45. Breton, D.; Carles-Gibergues, A.; Ballivy, G.; and Grandet, J., "Contribution to the Formation Mechanism of the Transition Zone between Rock-Cement Paste," *Cement and Concrete Research*, V. 23, No. 2, 1993, pp. 335-346. doi: 10.1016/0008-8846(93)90099-U
46. Scrivener, K. L., and Nemati, K. M., "The Percolation of Pore Space in the Cement Paste/Aggregate Interfacial Zone of Concrete," *Cement and Concrete Research*, V. 26, No. 1, 1996, pp. 35-40. doi: 10.1016/0008-8846(95)00185-9
47. Shane, J. D.; Mason, T. O.; Jennings, H. M.; Garboczi, E. J.; and Bentz, D. P., "Effect of the Interfacial Transition Zone on the Conductivity of Portland Cement Mortars," *Journal of the American Ceramic Society*, V. 83, No. 5, 2000, pp. 1137-1144. doi: 10.1111/j.1151-2916.2000.tb01344.x
48. Halamicova, P.; Detwiler, R. J.; Bentz, D. P.; and Garboczi, E. J., "Water Permeability and Chloride Ion Diffusion in Portland Cement Mortars: Relationship to Sand Content and Critical Pore Diameter," *Cement and Concrete Research*, V. 25, No. 4, 1995, pp. 790-802. doi: 10.1016/0008-8846(95)00069-O
49. Pope, A. W., and Jennings, H. M., "The Influence of Mixing on the Microstructure of the Cement Paste/Aggregate Interfacial Zone and on the Strength of Mortar," *Journal of Materials Science*, V. 27, No. 23, 1992, pp. 6452-6462. doi: 10.1007/BF00576298
50. Alexander, M. G.; Mindess, S.; Diamond, S.; and Qu, L., "Properties of Paste-Rock Interfaces and Their Influence on Composite Behaviour," *Materials and Structures*, V. 28, No. 9, 1995, pp. 497-506. doi: 10.1007/BF02473154

Title No. 120-M68

Enhancing Factors of Stone Powder for Hardened Mortar

by Hongbo Zhu, Yilu Zhang, Hongxiang Gou, Liang Ren, and Qing Chen

To improve the added application value of an industrial waste stone powder (SP), the optimizing mechanism of SP for the structure and composition of hydrothermal synthetic hardened cement stone was investigated in this paper. Cement was partially replaced by SP, silica fume (SF), or ground-granulated blast-furnace slag (GGBS), and then the microstructure with different SP content was tested through X-ray diffraction, thermogravimetric analysis (TG-DTG), mercury intrusion porosimetry (MIP), and scanning electronic microscopy. The findings indicate that the incorporation of SP in autoclaved products significantly enhanced compressive and flexural strengths. As the proportion of SP in cement was increased, a corresponding increase in the content of tobermorite within autoclaved cement mortar was observed. This increase in tobermorite concentration results in an initial rise followed by a subsequent decline in both compressive and flexural strengths. The maximum compressive and flexural strengths were achieved at an SP content of 15%. In addition, the mechanical strength was further improved by adding SP+GGBS or SP+SF. The strengthening mechanism of SP reveals that the change in the ratio of calcium and silicon ions (C/S) caused by SP in the sample was conducive to the formation of tobermorite and strength increase. Meanwhile, an increase in the quantity and a decrease in the crystal size of tobermorite were observed with an increase in the content of stone powder; resulting in a more compact microstructure of the sample. Moreover, the mechanical strength of cement composites doping SP+GGBS or SP+SF was further improved through superposition effects of SP and GGBS or SF with high activity. Currently, it is mainly applied to pipe pile products, and the strengthening effect of SP increases its use value. Meanwhile, the study of SP strengthening mechanism has laid a theoretical foundation for its application in high-strength autoclave and improved the relevant theory.

Keywords: hydrothermal synthesis; microstructure; stone powder; tobermorite.

INTRODUCTION

Natural sand is a non-renewable resource. In recent years, due to the shortage of natural sand resources and its rising price, manufactured sand has been widely used because of its stable quality, low cost, and environmental friendliness. The widespread employment of manufactured sand has resulted in the generation of substantial quantities of stone powder (SP) by-products, thereby creating a pressing need for their increased use.^{1,2}

According to the upstream raw material—the composition of stone—SP can be divided into siliceous and calcareous. Calcareous powder is the traditional raw material resource of concrete admixture. Currently, concrete admixtures mainly consist of iron tailings,^{3,4} fly ash,^{5,6} and blast-furnace slag.⁷ SP lacks pozzolanic activity; however, adding a small amount of SP to cement or concrete can enhance the microstructure of cement stone by exploiting its micro-filling

effect.⁸ Simultaneously, during high-temperature and high-pressure autoclave curing of concrete incorporating SP, the activated calcium component within SP undergoes a hydrothermal reaction with siliceous materials in the material system, thereby compensating for the inertness of SP.^{9,10}

At present, the research has been extensive on the influence of the SP content of manufactured sand on the performance of cement-based materials. Many scholars have reported the influence of SP on the macroperformance of concrete.^{11,12} Wang et al.¹³ reported that there are obvious differences in the influence of SP content on the elastic modulus, compressive and flexural strengths of concrete. Aliabdo et al.,¹⁴ Rodrigues et al.,¹⁵ and Hyun et al.¹⁶ found that the compressive strength, tensile strength, and elastic modulus of concrete generally decreased with the increase of SP content. Generally, the content of SP replacing cement is usually less than 30%, without sacrificing too much hardening performance.¹⁷⁻¹⁹ The use of no more than 5% SP instead of cement can improve the early compressive strength of concrete.^{20,21} Wu et al.²² developed a statistical analysis method to verify the impact of SP content between 3 and 15% on the mechanical properties of medium sand C80 concrete. Similarly, Çelik and Marar²³ revealed that adding SP not more than 10% to replace cement can improve the compressive strength of concrete. Besides, Li et al.²⁴ demonstrated that a sample has the best performance when the SP content is 10%. Aruntaş et al.²⁵ and Binici et al.²⁶ found that overall replacement of cement by granite SP is low, generally between 5 and 15%. At the same time, some authors have found that the optimum content of SP can improve the performance of mortar.^{27,28} Alyousef et al.²⁹ concluded that when SP replaced 20% of cement-based materials, the compressive strength increased from 30 to 41 MPa. Abbasi et al.³⁰ pointed out that the compressive strength and tensile strength of samples added with 5% SP increased 18.8% and 10.46%, respectively. Some researchers have explored the feasibility of using SP to produce ultra-high-performance concrete.^{31,32} However, the study of the application of SP in high-strength pipe piles is relatively scarce. Additionally, further investigation is required to fully understand the impact of SP on the microstructural level of cement-based materials.

Therefore, this study aims to investigate the performance and micro-mechanisms of SP in the production of

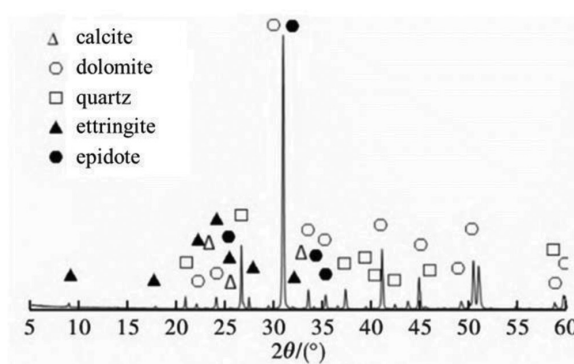


Fig. 1—XRD patterns of SP.

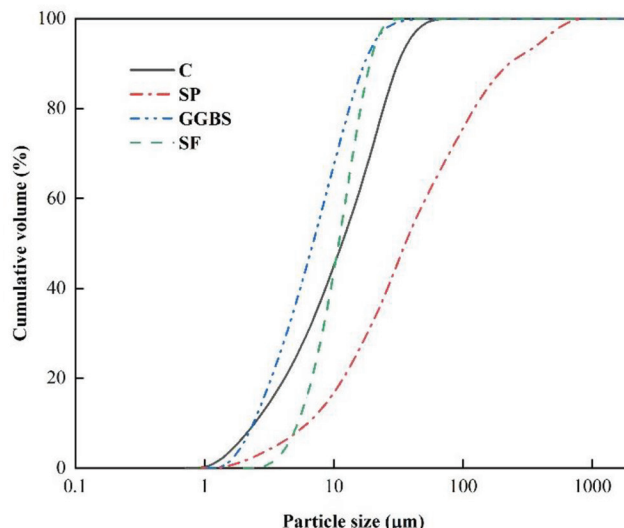


Fig. 2—Particle size distribution curve of cementitious materials.

autoclaved pipe pile products by partially replacing cement with SP, silica fume (SF), and ground-granulated blast-furnace slag (GGBS). The structural analysis of the cement mortar will be carried out using X-ray diffraction (XRD) analysis, thermogravimetric (TG) analysis, pore structure analysis, and scanning electronic microscopy (SEM). This research aims to explore the impact of SP on the properties of high-strength autoclaved concrete and its micro-mechanisms, develop effective technical solutions, and enhance its practical application value.

RESEARCH SIGNIFICANCE

The research results of this paper possess technical value, theoretical value, and environmental protection significance. First, the use of SP in high-strength autoclaved products can significantly improve the compressive and flexural strengths, which enhances its application value. Second, research on the strengthening mechanism of SP lays a theoretical foundation for its application in high-strength autoclave and improves the relevant theories. Finally, solid waste SP is turned into treasure for high-strength autoclaved products, which alleviates the harm of solid waste to the environment and harmonizes economic construction with resources and environment.

Table 1—Chemical composition of cementitious materials, wt %

Materials	CaO	SiO ₂	Al ₂ O ₃	Fe ₂ O ₃	SO ₃	MgO	K ₂ O
C	65.00	20.90	4.56	3.23	2.65	0.87	0.71
SP	58.90	8.85	2.90	0.92	0.15	26.26	0.65
SF	0.46	97.77	0.22	0.07	0.16	0.44	0.42
GGBS	42.16	32.74	16.12	0.40	1.31	5.77	0.23

Table 2—Mixture proportions, g

Code	Cement	SP	GGBS	SF	Sand	Water	PC
1	450	0	—	—	1350	110	18
2	405	45	—	—	1350	110	18
3	382	68	—	—	1350	110	18
4	360	90	—	—	1350	110	18
5	360	45	45	—	1350	110	18
6	360	63	—	27	1350	110	18

MATERIALS AND METHODS

Raw materials

SP, P-II 52.5 portland cement (C), GGBS, and SF were used as cementitious materials, the components of which are listed in Table 1. The XRD of SP is shown in Fig. 1 and the particle size distribution curves of four types of cementitious materials are shown in Fig. 2.

Table 1 reveals that SP is predominantly composed of CaO, constituting almost 60% of the total content, followed by MgO, which comprises over 26% of the content. Furthermore, SP is comprised of approximately 10% SiO₂ and a negligible amount of Al₂O₃. These findings suggest that the primary mineral composition of SP is limestone and dolomite. Figure 1 shows that the mineral composition of SP is mainly calcite, dolomite, quartz, ettringite, and so on, which is relatively complex.

Polycarboxylate high-range water-reducing admixture (PC), sand (S), and running water (W) were also used in this study.

Preparation methods

The design of C80 steam-cured pipe pile products was conducted based on the mixing proportions outlined in Table 2 and three specimens were prepared for each group. The specimens were prepared by placing cement mortar into a 40 x 40 x 160 mm cement mortar standard mold and vibrating on a vibration table, as per GB/T 17671-2021. The molded specimens were placed in a curing box at a temperature of 20 ± 1°C and a relative humidity not less than 90% for 24 hours; the mold was then removed to obtain the cement mortar specimens. After being steam-cured at 1.6 MPa and 200°C for 10 hours, the specimens were tested. The fluidity of each mixing ratio was tested using the jump table test, as per GB/T 2419-2005. At the same time, the 20 x 20 x 20 mm cement paste specimens were prepared for microscopic analysis after removing the sand from the specimen.

Test methods

The X-ray diffractometer used for semi-quantitative analysis of the amount of hydration products using the

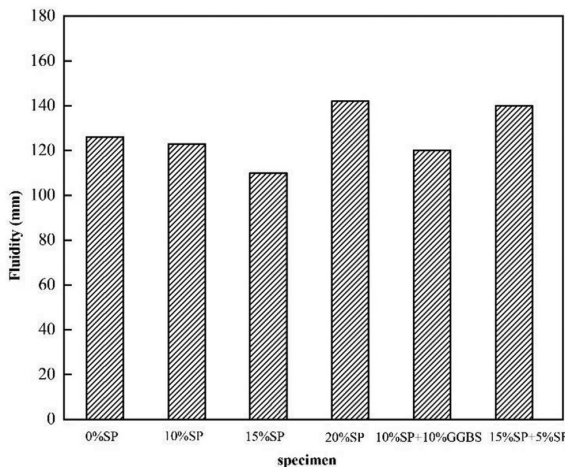


Fig. 3—Jumping table fluidity of sample.

R-value method had a scanning range of 5 to 90 degrees and a scanning rate of 5 deg/min. A field emission high-resolution SEM was used. TG analysis was conducted at a heating rate of 10°C/min⁻¹ in a nitrogen atmosphere. Testing compressive and flexural strengths by cement compression and bending resistance were performed with an integrated test machine with a 50 N/s loading rate. The total porosity and pore size distribution of specimens were tested using an automatic mercury porosimeter with a measurable pore size range of 5 nm to 800 µm.

RESULTS AND DISCUSSION

Fluidity

The influence of different amounts of SP on the fluidity of the sample is presented in Fig. 3. The results indicate that the fluidity of the sample initially decreases and then increases with an increase in SP content. The reduction in fluidity is evident when compared to the sample without SP, with decreases of 2.4% and 12.7% observed when the SP content is 10% and 15%, respectively. However, when the SP content is increased to 20%, the fluidity of the sample increases by 12.7%. Furthermore, when combined with mineral powder or silica fume, an increase in fluidity of 4.8% and 11.1%, respectively, is observed.

Compressive and flexural strengths

Autoclaved mortar was prepared by replacing 0, 10, 15, and 20% cement with SP and SP mixed with SF or GGBS, respectively. The results are shown in Fig. 4.

Based on the data presented in Fig. 4, it is evident that the addition of SP in quantities of 10, 15, and 20% results in corresponding improvements in flexural and compressive strengths when compared to the control sample, which contains no SP. The improvements in flexural strength are 2%, 13.3%, and 8.1%, respectively, while the improvements in compressive strength are 0.6%, 2.6%, and 0.9%, respectively.

With the increase of SP content, the compressive and flexural strengths increase initially and then decrease. And the strength increases with the enhancement of SP content when SP content does not exceed 15%. The reasons may

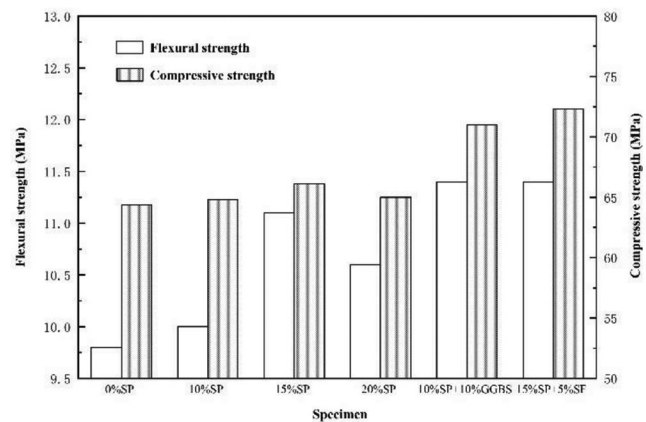


Fig. 4—Influence of SP, SF, and GGBS on strength of hardened cement mortars.

be: 1) SP optimizes the gradation of the mortar system as fine aggregate fills the voids between the cement particles, which makes the pore structure of the cement mortar more compact^{33,34}; 2) at the fresh mixing stage of cement mortar, SP will absorb part of water, thus reducing the water-cement ratio of cement paste³⁵; and 3) SP has nucleation in cement-based materials that promotes the growth of early hydration products of cement and optimizes the pore structure of cement mortar.³⁶⁻³⁸ The incorporation of SF or GGBS with SP leads to a considerable improvement in both flexural and compressive strengths. This enhancement can be attributed to the higher reactivity of SF and GGBS compared to SP, which can be effectively stimulated by high-temperature steam curing, as reported in previous studies.^{39,40} When the dosage of SP exceeds 15%, the decrease in compressive and flexural strengths may be due to a lack of sufficient cement content to activate the SP, resulting in a decrease in the degree of reaction between the SP and cement.

XRD analysis

Figure 5 shows the XRD curve of each sample. In 20, the diffraction peaks near the angles of 27 and 31 degrees are characteristic peaks of tobermorite, which is a typical product of autoclaved cement products. The diffraction peaks near 18, 34, 47, and 50 degrees are calcium hydroxide crystal (CH). The formation process of tobermorite is: CH+SiO₂—C-S-H (II)+α-C₂SH—C-S-H (I)—tobermorite.⁴¹ A semi-quantitative analysis of tobermorite and CH with RIR value is⁴²

$$RIR_i = \frac{I_i}{I_{col}} \quad (1)$$

where I_i and I_{col} are phase i and reference substance, respectively, of the integral strength of the strongest peak of α-Al₂O₃.

If there are N phases in a system, the mass fraction of the i -th phase can be given by the RIR value of each phase, as shown in Eq. (2)

$$W_i = \frac{I_i/RIR_i}{\sum_{i=1}^N I_i/RIR_i} \quad (2)$$

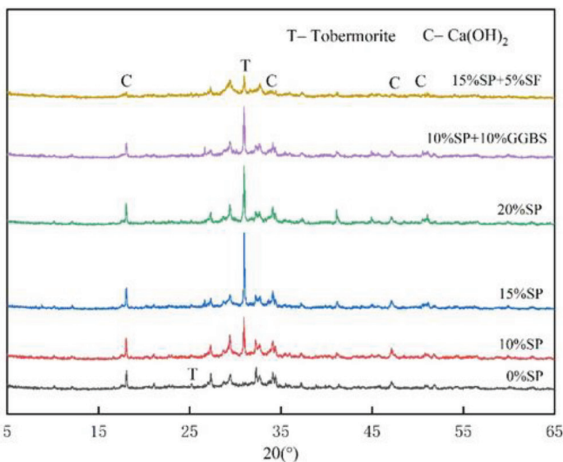


Fig. 5—XRD patterns of samples with different stone powder content.

Table 3 presents the findings which demonstrate distinct variations in CH and tobermorite content between the control sample and SP-containing samples. Specifically, the control sample exhibits a markedly higher CH content and lower tobermorite content. Comparing Samples 1 to 4, it can be observed that the CH content gradually decreases by approximately half as the SP content increases from 0 to 20%, while the tobermorite content increases by five to seven times. When the content of SP increases from 15 to 20%, the aforementioned change trend changes—that is, the CH content increases slightly and the tobermorite content decreases slightly, which completely corresponds to the change rule of flexural and compressive strengths of Samples 1 to 4 in Fig. 4.

TG-DTG analysis

Figure 6 illustrates the thermogravimetric analysis (TG-DTG) curves of the samples, indicating a distinct endothermic peak close to 450°C on the DTG curve. This peak is primarily attributed to the disintegration of CH, the hydration byproduct of cement. The endothermic peak near 520°C is due to the disintegration of CaCO₃. Furthermore, the prominent endothermic peak between 700 and 750°C results from the rupture of some Si-O-H bonds of tobermorite, with two hydroxyl groups being separated from the structure, as reported in the literature.⁴³⁻⁴⁵ In conjunction with the TG curve, the CH content is partially estimated by the mass loss at approximately 450°C and partially by the amount of CO₂ produced during the disintegration of calcium carbonate, as depicted in Eq. (3). Similarly, the tobermorite content can be calculated according to Eq. (4)

$$m_{\text{CH}} = 74 \left[\frac{TG_1}{18} + \frac{TG_2}{44} \right] \quad (3)$$

$$m_{\text{C}_5\text{S}_6\text{H}_5} = 730 \times \frac{TG_3}{90} \quad (4)$$

where m_{CH} is the Ca(OH)₂ content, %; $m_{\text{C}_5\text{S}_6\text{H}_5}$ is the tobermorite content, %; TG_1 is the weight loss from 400 to 500°C, %; TG_2 is the weight loss from 500 to 600°C, %; and TG_3 is

Table 3—CH and C₅S₆H₅ content under XRD algorithm, wt %

Code	m_{CH}	$m_{\text{C}_5\text{S}_6\text{H}_5}$
1	45.2	9.7
2	26.4	50.1
3	19.9	71.0
4	22.0	60.4
5	19.6	64.5
6	14.4	48.1

Table 4—CH and C₅S₆H₅ content, wt %

Code	m_{CH}	$m_{\text{C}_5\text{S}_6\text{H}_5}$
1	12.97	2.51
2	9.53	39.50
3	9.10	46.23
4	10.00	58.64
5	8.01	45.58
6	5.78	35.77

the weight loss from 650 to 750°C, %. The results are shown in Table 4.

Upon comparing the data in Table 4 with that in Table 3, notable discrepancies between the calculated CH and tobermorite contents by TG and XRD methods are observed, yet the variations in the calculated results by the two methods follow similar trends. The correlation between the CH and tobermorite contents as determined by the TG and XRD approaches is illustrated in Fig. 7.

A high linear positive correlation is observed between the CH and tobermorite content determined by both TG and XRD algorithms, signifying the precision of these two methodologies. The TG method is commonly considered to provide more precise quantitative analysis results. Based on the chemical composition of the raw materials provided in Table 1 and the mixture ratios in Table 2, the calcium ion-silicon ion ratios (*C/S*) of Samples 1 to 4 can be calculated. The tobermorite content of each sample, calculated using the TG method, is then compared to its *C/S*. The outcomes are presented in Fig. 8.

Figure 8 shows a high linear positive correlation between the content of tobermorite and *C/S*, and the R^2 is close to 1, which means the content of tobermorite is mainly affected by *C/S*. As the *C/S* increases, the content of tobermorite exhibits an upward trend. Further analysis demonstrates that the incorporation of SP leads to a significant decrease in the content of CH featuring an unstable structure. Consequently, the consumption capacity of CH is used as an indicator for assessing the activity of admixtures.⁴⁶

The foregoing analysis indicates that the replacement of cement by SP alters the *C/S* in the sample, thereby favoring the formation of tobermorite and leading to an enhancement in the sample's flexural and compressive strengths.

For Sample 5, which was mixed with SP+GGBS, or Sample 6, which was mixed with SP+SF, the hydrothermal synthesis products differ from those of Samples 2 to 4 due to

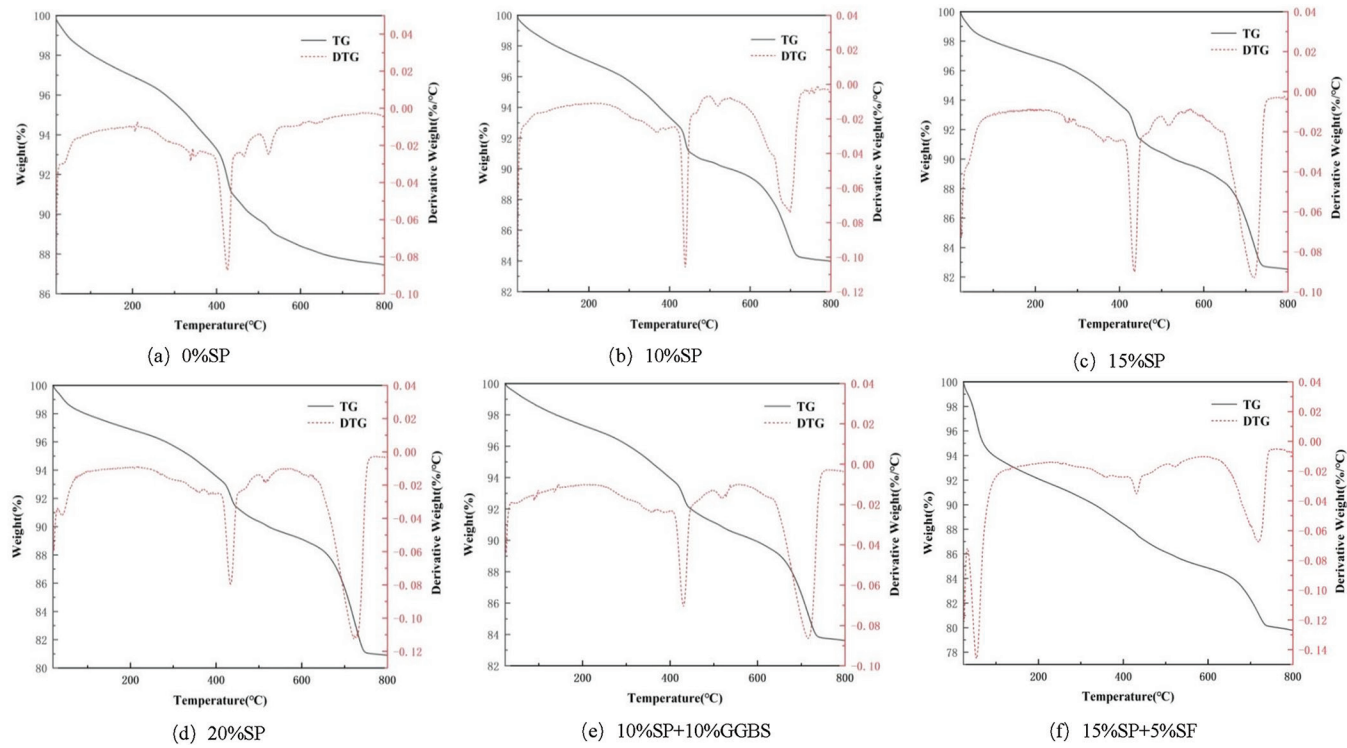


Fig. 6—TG-DTG curve of samples.

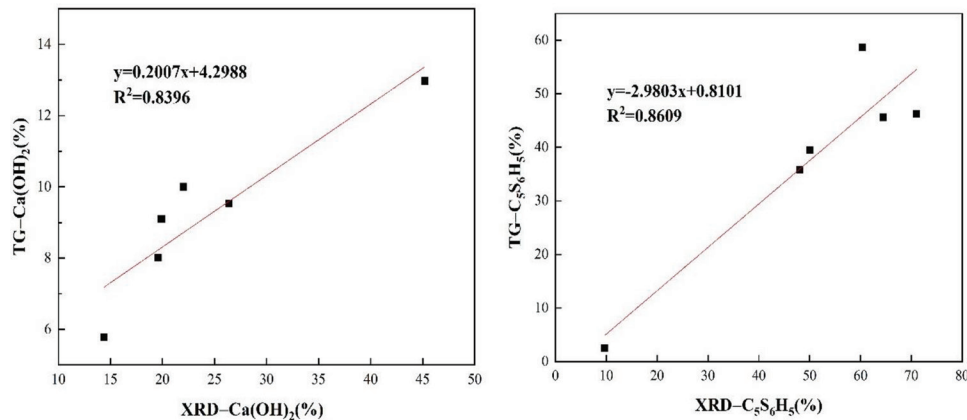


Fig. 7—Relationship between CH and tobermorite content under TG and XRD.

GGBS and SF having high hydration activity under natural conditions and undergoing pozzolanic reaction with cement prior to autoclaved curing. Therefore, despite the tobermorite content of Samples 5 and 6 not being higher than that of Samples 2 to 4, their compressive and flexural strengths are significantly improved. This is attributed to the combined effect of SP addition resulting in higher tobermorite production and GGBS or SF addition leading to pozzolanic reaction.

Pore size distribution

The test results of mercury injection test of each sample are shown in Fig. 9. The data in Fig. 9 are segmented and the results are shown in Table 5.

Wu⁴⁷ presented a classification of concrete pores into four categories: harmless pores (<20 nm), harmful pores (20 to 50 nm), less-harmful pores (50 to 200 nm), and more-harmful pores (>200 nm). Harmless and harmful pores refer

to the small pores in concrete that are too small to have any significant negative impact on the strength of the hydrated cement paste. Conversely, less-harmful and more-harmful pores in concrete represent larger pores that are significant enough to have severe negative impacts on the strength of the hydrated cement paste.

Figure 9 displays the pore distribution curve of the control sample, where three peaks can be observed. The highest peak appears at approximately 10 nm, while the other two peaks are positioned between 100 and 150 nm. Conversely, the peak positions of other samples that include SP fall between 10 and 20 nm. Table 3 illustrates that the addition of SP leads to a significant reduction in the porosity of each cement mortar specimen, with an increased proportion of harmless pores less than 20 nm. The proportion of harmless pores is the highest when SP is mixed with GGBS and SF, and when SP alone is used, a proportion of harmless pores

Table 5—Pore parameter statistics of samples

Code	Porosity, %	Average pore diameter, nm	Pore diameter distribution, %			
			<20	20 to 50	50 to 200	>200
1	21.09	23.71	36.34	19.74	27.93	15.99
2	17.48	15.61	62.29	19.44	10.16	8.11
3	18	15.47	62.84	21.46	9.53	6.18
4	19.18	18.15	51.24	22.35	18.88	7.53
5	14.77	12.3	79.75	10.95	2.79	6.51
6	16.07	10.06	88.65	4.40	1.08	5.87

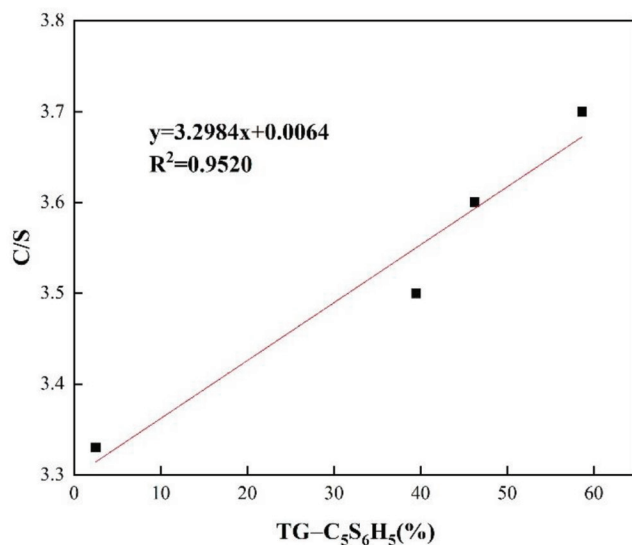


Fig. 8—Relationship between tobermorite content and C/S of Samples 1 to 4.

higher than 10 and 20% can be achieved with an SP content of only 15%. Moreover, the proportion of less-harmful and more-harmful pores is also reduced by adding SP. The results suggest that the addition of an appropriate amount of SP can significantly improve the pore structure of cement paste, and the optimal effect is obtained when SP is mixed with GGBS and SF. The analysis reveals that SP functions as a pore-filling and nucleation agent when its content is below 15%, which optimizes the pores of cement-based materials. Nevertheless, an excessive amount of SP could have a negative impact on the development of cement hydration products morphology. This is due to the presence of “free” SP, which increases the specific surface area and results in higher water demand. As a result, the workability of cement mortar decreases, hindering vibration and compaction, ultimately leading to increased porosity of mortar and reduced flexural and compressive strengths.⁴⁸

SEM analysis

Figure 10 shows SEM analysis of each sample. The microstructural evolution of the samples can be observed from Fig. 10(a) to (d), where the grain size of tobermorite gradually decreases with the increasing SP content, while the number of grains increases. This trend contributes to enhancing the compactness of the sample’s microstructure. In addition, the microstructural analysis of the samples

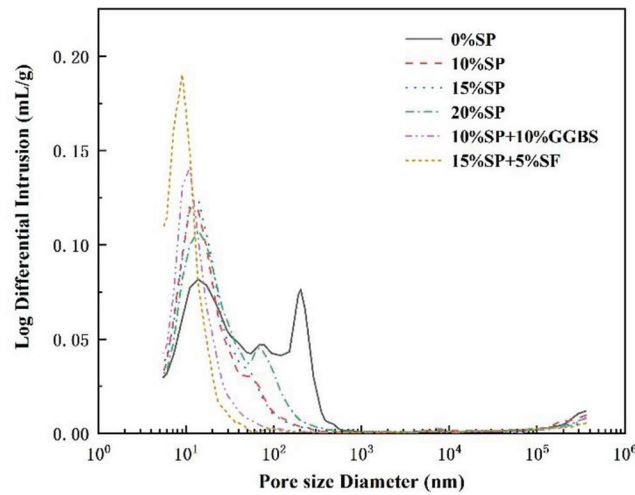


Fig. 9—Pore size distribution curve of samples.

doped with SP+GGBS (Fig. 10(e)) and SP+SF (Fig. 10(f)) demonstrates a gradual reduction in the crystal size of tobermorite, accompanied by an increase in its quantity with the increase in SP content. This signifies that the introduction of SP elevates the crystallization point of tobermorite, leading to a more compact microstructure. Furthermore, the presence of GGBS or SF, with their higher hydration activity, strengthens the aforementioned effects, ultimately resulting in a significant enhancement of the compressive and flexural strengths of the samples.

CONCLUSIONS

1. Stone powder (SP) can effectively improve the mechanical strength of high-strength autoclaved products. The compressive and flexural strengths of autoclaved cement mortar increase initially and then decrease with increased SP content, in which the optimal SP content is 15%. The addition of SP + ground-granulated blast-furnace slag (GGBS) or SP + silica fume (SF) further enhances the mechanical strength.

2. The strengthening mechanism of SP has been elucidated, providing a theoretical foundation for its use in high-strength autoclaved products made from cement:

- SP substitution for cement improves mechanical strength of the cement stone by altering the calcium ion-silicon ion ratio (*C/S*) and promoting tobermorite formation.
- Increasing the SP proportion decreases CH content and markedly increases tobermorite content, resulting in strength improvement.

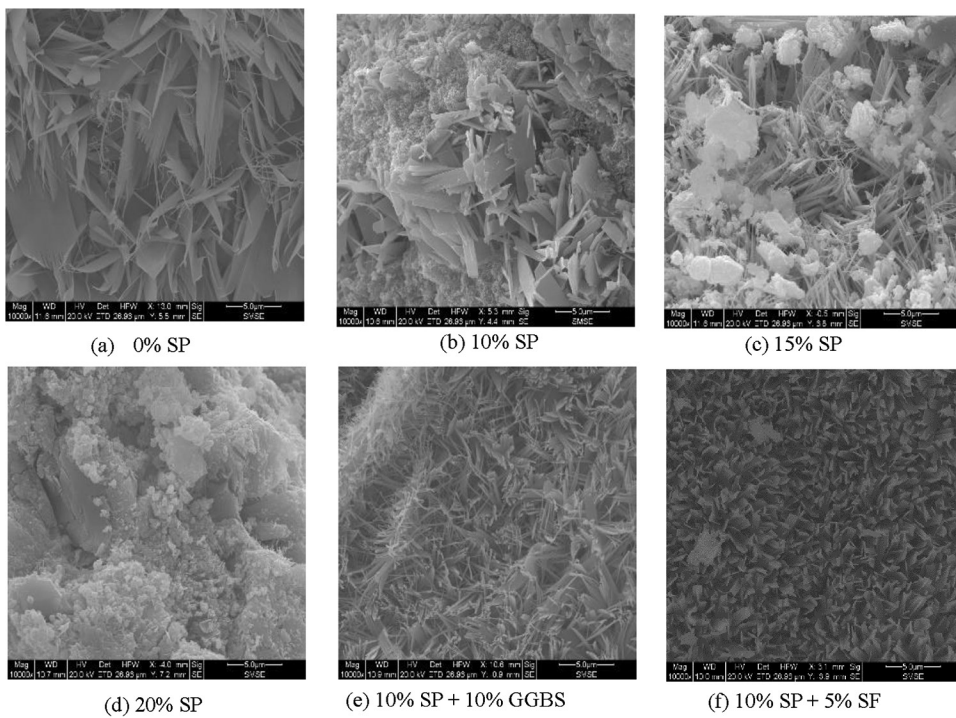


Fig. 10—SEM images of samples.

- The increased tobermorite crystallization points with the addition of SP reduces grain size and increases grain quantity, therefore improving the microstructure compactness.
- The mechanical strength of cement composites doping SP+GGBS or SP+SF was further improved through superposition effects of SP and GGBS or SF with high activity.

AUTHOR BIOS

Hongbo Zhu is an Associate Professor at Tongji University, Shanghai, China. He received his MS and PhD from Wuhan University of Technology, Wuhan, China, in 2003 and 2005, respectively. His research interests include the durability of concrete and the comprehensive use of industrial waste slag in concrete.

Yilu Zhang is a Postgraduate in the School of Materials Science and Engineering at Tongji University. She received her BS from Nanjing Tech University, Nanjing, China, in 2020. Her research interests include the mechanism of the effect of stone powder on the properties of concrete admixtures and soil stabilizers.

Hongxiang Gou is a PhD Candidate in the Department of Infrastructure engineering at the University of Melbourne, Melbourne, Australia. He received his BS from Southwest University, Chongqing, China, in 2017, and his MS from Tongji University in 2020. His research interests include low-carbon concrete, solid waste use, and high-performance concrete.

Liang Ren is a Postgraduate of School of Materials Science and Engineering, Tongji University. In 2020, he received his BS from Nanjing University of Science and Technology, Nanjing, China. His research interests include the application of the electrochemical deposition method to repair concrete cracks.

Qing Chen is a Professor at Tongji University. He received his BS in civil engineering from Xiamen University, Xiamen, China, in 2004, and his MS in structural engineering and PhD in civil engineering from Tongji University in 2008 and 2014, respectively. His research interests include micro-damage control of underground structures and the functionalization of concrete.

ACKNOWLEDGMENTS

This study was funded by the National Natural Science Foundation of China (52122808, 52078381, and 51878496) and the National Key R&D Program of China (2022YFC3803104).

REFERENCES

- Choi, S. J.; Jun, S. S.; Oh, J. E.; and Monteiro, P. J. M., "Properties of Alkali-Activated Systems with Stone Powder Sludge," *Journal of Material Cycles and Waste Management*, V. 12, No. 4, 2010, pp. 275-282. doi: 10.1007/s10163-010-0297-6
- Marchetti, G.; Rahhal, V. F.; and Irassar, E. F., "Influence of Packing Density and Water Film Thickness on Early-Age Properties of Cement Pastes with Limestone Filler and Metakaolin," *Materials and Structures*, V. 50, No. 2, 2017, p. 111. doi: 10.1617/s11527-016-0979-1
- Wang, H.; Han, F. H.; Pu, S. C.; and Zhang, H., "Properties of Blended Cement Containing Iron Tailing Powder at Different Curing Temperatures," *Materials (Basel)*, V. 15, No. 2, 2022, p. 693. doi: 10.3390/ma15020693
- Han, F. H.; Song, S. M.; Liu, J. H.; and Huang, S., "Properties of Steam-Cured Precast Concrete Containing Iron Tailing Powder," *Powder Technology*, V. 345, 2019, pp. 292-299. doi: 10.1016/j.powtec.2019.01.007
- Han, X.; Fu, H.; Li, G.; Tian, L.; Pan, C.; Chen, C.; and Wang, P., "Volume Deformation of Steam-Cured Concrete with Slag during and after Steam Curing," *Materials (Basel)*, V. 14, No. 7, 2021, pp. 1647-1668. doi: 10.3390/ma14071647
- Wongkeo, W.; Thongsanitgarn, P.; and Chaipanich, A., "Compressive Strength and Drying Shrinkage of Fly Ash-Bottom Ash-Silica Fume Multi-Blended Cement Mortars," *Materials & Design*, V. 36, No. 4, 2012, pp. 655-662. doi: 10.1016/j.matdes.2011.11.043
- Li, P. P.; Cao, Y.; Brouwers, H.; Chen, W.; and Yu, Q. L., "Development and Properties Evaluation of Sustainable Ultra-High-Performance Pastes with Quaternary Blends," *Journal of Cleaner Production*, V. 240, 2019, p. 118124. doi: 10.1016/j.jclepro.2019.118124
- Bonavetti, V.; Donza, H.; Rahhal, V.; and Irassar, E., "Influence of Initial Curing on the Properties of Concrete Containing Limestone Blended Cement," *Cement and Concrete Research*, V. 30, No. 5, 2000, pp. 703-708. doi: 10.1016/S0008-8846(00)00217-9
- Zanni, H.; Cheyrezy, M.; Maret, V.; Philippot, S.; and Nieto, P., "Investigation of Hydration and Pozzolanic Reaction in Reactive Powder Concrete (RPC) Using 29 Si NMR," *Cement and Concrete Research*, V. 26, No. 1, 1996, pp. 93-100. doi: 10.1016/0008-8846(95)00197-2
- Richard, P., and Cheyrezy, M., "Composition of reactive powder concretes," *Cement and Concrete Research*, V. 25, No. 7, 1995, pp. 1501-1511. doi: 10.1016/0008-8846(95)00144-2
- Karimipour, A.; Jahangir, H.; and Rezazadeh Eidgahee, D., "A Thorough Study on the Effect of Red Mud, Granite, Limestone and Marble Slurry

- Powder on the Strengths of Steel Fibres-Reinforced Self-Consolidation Concrete: Experimental and Numerical Prediction," *Journal of Building Engineering*, V. 44, 2021, p. 103398. doi: 10.1016/j.jobe.2021.103398
12. Mikhilif, A. G. H.; Jumaily, I. A.; and Al-Numan, B. S., "Mechanical Properties of Sustainable Concrete Using Local Limestone Powder as Partial Replacement of Cement," *Proceedings, 12th International Conference on Developments in eSystems Engineering (DeSE)*, 2019, pp. 105-108.
 13. Wang, D.; Shi, C.; Farzadnia, N.; Shi, Z.; and Jia, H., "A Review on Effects of Limestone Powder on the Properties of Concrete," *Construction and Building Materials*, V. 192, 2018, pp. 153-166. doi: 10.1016/j.conbuildmat.2018.10.119
 14. Aliabdo, A. A.; Abd Elmoaty, A. E. M.; and Auda, E. M., "Re-Use of Waste Marble Dust in the Production of Cement and Concrete," *Construction and Building Materials*, V. 50, 2014, pp. 28-41. doi: 10.1016/j.conbuildmat.2013.09.005
 15. Rodrigues, R.; de Brito, J.; and Sardinha, M., "Mechanical Properties of Structural Concrete Containing Very Fine Aggregates from Marble Cutting Sludge," *Construction and Building Materials*, V. 77, 2015, pp. 349-356. doi: 10.1016/j.conbuildmat.2014.12.104
 16. Hyun, J.; Lee, B.; and Kim, Y., "Composite Properties and Micro-mechanical Analysis of Highly Ductile Cement Composite Incorporating Limestone Powder," *Applied Sciences (Basel, Switzerland)*, V. 8, No. 2, 2018, pp. 151-161. doi: 10.3390/app8020151
 17. Bentz, D. P.; Ferraris, C. F.; Jones, S. Z.; Lootens, D.; and Zunino, F., "Limestone and Silica Powder Replacements for Cement: Early-Age Performance," *Cement and Concrete Composites*, V. 78, 2017, pp. 43-56. doi: 10.1016/j.cemconcomp.2017.01.001
 18. Zhang, Z.; Wang, Q.; and Chen, H., "Properties of High-Volume Limestone Powder Concrete under Standard Curing and Steam-Curing Conditions," *Powder Technology*, V. 301, 2016, pp. 16-25. doi: 10.1016/j.powtec.2016.05.054
 19. De Weerdt, K.; Ben Haha, M.; Le Saout, G.; Kjellsen, K. O.; Justnes, H.; and Lothenbach, B., "Hydration Mechanisms of Ternary Portland Cements Containing Limestone Powder and Fly Ash," *Cement and Concrete Research*, V. 41, No. 3, 2011, pp. 279-291. doi: 10.1016/j.cemconres.2010.11.014
 20. Pliya, P., and Cree, D., "Limestone Derived Eggshell Powder as a Replacement in Portland Cement Mortar," *Construction and Building Materials*, V. 95, 2015, pp. 1-9. doi: 10.1016/j.conbuildmat.2015.07.103
 21. Schöler, A.; Lothenbach, B.; Winnefeld, F.; and Zajac, M., "Hydration of Quaternary Portland Cement Blends Containing Blast-Furnace Slag, Siliceous Fly Ash and Limestone Powder," *Cement and Concrete Composites*, V. 55, 2015, pp. 374-382. doi: 10.1016/j.cemconcomp.2014.10.001
 22. Wu, H.; Shen, B.; Ma, K.; and Xuan, D., "Assessment of Mechanical Properties of C80 Concrete Prepared with Different Stone Powder Contents by a Statistical Analysis," *Journal of Building Engineering*, V. 56, 2022, p. 104754. doi: 10.1016/j.jobe.2022.104754
 23. Çelik, T., and Marar, K., "Effects of Crushed Stone Dust on Some Properties of Concrete," *Cement and Concrete Research*, V. 26, No. 7, 1996, pp. 1121-1130. doi: 10.1016/0008-8846(96)00078-6
 24. Li, B. X.; Ke, G. J.; and Zhou, M. K., "Influence of Manufactured Sand Characteristics on Strength and Abrasion Resistance of Pavement Cement Concrete," *Construction and Building Materials*, V. 25, No. 10, 2011, pp. 3849-3853. doi: 10.1016/j.conbuildmat.2011.04.004
 25. Arunataş, H. Y.; Gürü, M.; Dayı, M.; and Tekin, İ., "Utilization of Waste Marble Dust as an Additive in Cement Production," *Materials & Design*, V. 31, No. 8, 2010, pp. 4039-4042. doi: 10.1016/j.matdes.2010.03.036
 26. Binici, H.; Shah, T.; Aksogan, O.; and Kaplan, H., "Durability of Concrete Made with Granite and Marble as Recycle Aggregates," *Journal of Materials Processing Technology*, V. 208, No. 1-3, 2008, pp. 299-308. doi: 10.1016/j.jmatprotec.2007.12.120
 27. Knop, Y.; Peled, A.; and Cohen, R., "Influences of Limestone Particle Size Distributions and Contents on Blended Cement Properties," *Construction and Building Materials*, V. 71, 2014, pp. 26-34. doi: 10.1016/j.conbuildmat.2014.08.004
 28. Nanthagopalan, P., and Santhanam, M., "Fresh and Hardened Properties of Self-Compacting Concrete Produced with Manufactured Sand," *Cement and Concrete Composites*, V. 33, No. 3, 2011, pp. 353-358. doi: 10.1016/j.cemconcomp.2010.11.005
 29. Alyousef, R.; Benjeddou, O.; Soussi, C.; Khadimallah, M. A.; and Mustafa Mohamed, A., "Effects of Incorporation of Marble Powder Obtained by Recycling Waste Sludge and Limestone Powder on Rheology, Compressive Strength, and Durability of Self-Compacting Concrete," *Advances in Materials Science and Engineering*, V. 2019, 2019, p. 4609353. doi: 10.1155/2019/4609353
 30. Abbasi, S.; Jannaty, M. H.; Faraj, R. H.; Shahbazpanahi, S.; and Mosavi, A., "The Effect of Incorporating Silica Stone Waste on the Mechanical Properties of Sustainable Concretes," *Materials (Basel)*, V. 13, No. 17, 2020, p. 3832. doi: 10.3390/ma13173832
 31. Ghannam, S.; Najm, H.; and Vascone, R., "Experimental Study of Concrete Made with Granite and Iron Powders as Partial Replacement of Sand," *Sustainable Materials and Technologies*, V. 9, 2016, pp. 1-9. doi: 10.1016/j.susmat.2016.06.001
 32. Matos, A. M.; Ramos, T.; and Sousa-Coutinho, J., "Strength, ASR and Chloride Penetration of Mortar with Granite Waste Powder," *Key Engineering Materials*, V. 634, 2014, pp. 139-150. doi: 10.4028/www.scientific.net/KEM.634.139
 33. Li, P.; Brouwers, H. J. H.; Chen, W.; and Yu, Q., "Optimization and Characterization of High-Volume Limestone Powder in Sustainable Ultra-High Performance Concrete," *Construction and Building Materials*, V. 242, 2020, p. 118112 doi: 10.1016/j.conbuildmat.2020.118112
 34. Das, S.; Aguayo, M.; Dey, V.; Kachala, R.; Mobasher, B.; Sant, G.; and Neithalath, N., "The Fracture Response of Blended Formulations Containing Limestone Powder: Evaluations Using Two-Parameter Fracture Model and Digital Image Correlation," *Cement and Concrete Composites*, V. 53, 2014, pp. 316-326. doi: 10.1016/j.cemconcomp.2014.07.018
 35. Ramezanianpour, A. A.; Ghasavand, E.; Nickseresht, I.; Mahdikhani, M.; and Moodi, F., "Influence of Various Amounts of Limestone Powder on Performance of Portland Limestone Cement Concretes," *Cement and Concrete Composites*, V. 31, No. 10, 2009, pp. 715-720. doi: 10.1016/j.cemconcomp.2009.08.003
 36. Sato, T., and Diallo, F., "Seeding Effect of Nano-CaCO₃ on the Hydration of Tricalcium Silicate," *Transportation Research Record: Journal of the Transportation Research Board*, V. 2141, No. 1, 2010, pp. 61-67. doi: 10.3141/2141-11
 37. Bentz, D. P., "Activation Energies of High-Volume Fly Ash Ternary Blends: Hydration and Setting," *Cement and Concrete Composites*, V. 53, 2014, pp. 214-223. doi: 10.1016/j.cemconcomp.2014.06.018
 38. Bentz, D. P.; Ardani, A.; Barrett, T.; Jones, S. Z.; Lootens, D.; Peltz, M. A.; Sato, T.; Stutzman, P. E.; Tanesi, J.; and Weiss, W. J., "Multi-Scale Investigation of the Performance of Limestone in Concrete," *Construction and Building Materials*, V. 75, No. 30, 2015, pp. 1-10. doi: 10.1016/j.conbuildmat.2014.10.042
 39. Chen, Q.; Wang, H.; Jiang, Z.; Zhu, H.; Ju, J.-W.; and Yan, Z., "Reaction Degree Based Multi-Scale Predictions for the UHPC's Effective Properties," *Magazine of Concrete Research*, V. 3, 2020, pp. 1-35.
 40. Zhang, Y.; Man, G. P.; and Li, J. C., "Influence of Admixtures and their Compound Use on Strength of Steam Cured Concrete Products," *Concrete and Cement Products*, V. 10, 2019, pp. 31-36.
 41. Hu, B.; Cui, C.; Cui, X.; Qin, J.; and Ma, H., "Structure and Morphology Transition of Tobermorite after Calcined at 725°C," *Journal of the Chinese Ceramic Society*, V. 43, No. 2, 2015, pp. 237-240.
 42. Xia, X. W.; Zhang, X. Q.; and Cao, C. Y., "Calibrate the Metallographic Phase of Magnetic Samples by Semi-Quantitative Phase Analysis of Reference Strength Method," *Journal of Jinggangshan University: Natural Science Edition*, V. 31, No. 5, 2010, pp. 35-37.
 43. Alhozaimy, A.; Fares, G.; Al-Negheimish, A.; and Jaafar, M. S., "The Autoclaved Concrete Industry: An Easy-to-Follow Method for Optimization and Testing," *Construction and Building Materials*, V. 49, 2013, pp. 184-193. doi: 10.1016/j.conbuildmat.2013.08.024
 44. Alawad, O. A.; Alhozaimy, A.; Jaafar, M. S.; Aziz, F. N. A.; and Al-Negheimish, A., "Effect of Autoclave Curing on the Microstructure of Blended Cement Mixture Incorporating Ground Dune Sand and Ground Granulated Blast Furnace Slag," *International Journal of Concrete Structures and Materials*, V. 9, No. 3, 2015, pp. 381-390. doi: 10.1007/s40069-015-0104-9
 45. Yang, X.-L.; Cui, X.-Y.; Cui, C.; Ma, H.-L.; and Yang, Q., "Study on High-Temperature Phase Change of Tobermorite," *Guangpuxue Yu Guangpu Fenxi*, V. 33, No. 8, 2013, pp. 2227-2230.
 46. Zhu, H.; Li, C.; Cheng, Y.; Jiang, Z.; and Wu, K., "Pozzolanicity of Fly Ash Modified by Fluidized Bed Reactor-Vapor Deposition," *Construction and Building Materials*, V. 156, 2017, pp. 719-727. doi: 10.1016/j.conbuildmat.2017.09.034
 47. Wu, Z. W., "An Approach to the Recent Trends of Concrete Science and Technology," *Journal of The Chinese Ceramic Society*, V. 7, No. 3, 1979, pp. 262-270.
 48. Liu, T.; Yu, B. T.; Wang, H.; Xie, C.; and Li, S., "Influence of High Adsorbent Stone Powder Content on Mechanical Properties and Microstructure of Cement Mortar," *Journal of Highway and Transportation Research and Development*, V. 38, No. 8, 2021, pp. 16-22.

Title No. 120-M69

Alkali-Silica Reaction Evaluation of Coarse Aggregates from Massachusetts Using Accelerated Tests

by J. F. Muñoz, C. Balachandran, A. Shastry, R. Mulcahy, J. M. Robertson, and T. S. Arnold

The periodic evaluation of the alkali-silica reaction (ASR) susceptibility of aggregates is a key strategy to eliminate the risk of ASR development in transportation infrastructure. A reliable and practical accelerated ASR test is paramount to improve the frequency and efficiency of the aggregate evaluation campaign. This paper assesses the suitability of the new Turner-Fairbank Highway Research Center ASR susceptibility test (T-FAST) as a cost-effective tool to evaluate aggregates. Thirty-eight aggregates of varying mineralogies, including carbonates, were characterized using the T-FAST and AASHTO T 380. The results were compared with historic AASHTO T 303 data. The T-FAST accurately classified the reactivity of the aggregates and was identified as the most sensitive among the three accelerated tests. Additionally, the combination of the T-FAST results with the possibility of accurately determining the alkali thresholds of the aggregates provided a broader understanding of the conditions conducive to triggering ASR in the field.

Keywords: alkali-carbonate reaction (ACR); alkali-silica reaction (ASR); alkali threshold (AT); coarse aggregates; miniature concrete prism test (MCPT); Turner-Fairbank Highway Research Center ASR susceptibility test (T-FAST).

INTRODUCTION

The identification of alkali-silica reaction (ASR) distress in the Springfield Memorial Bridge during the 1990s is one of the earliest examples of transportation infrastructures in Massachusetts affected by this common concrete degradation mechanism.¹ The ASR symptoms manifested in the concrete deck and some decorative elements of the bridge. By 1996, the severity of the damages caused by ASR forced the replacement of the full concrete deck. In the following decade, the Massachusetts Department of Transportation (MassDOT) identified 40 different transportation infrastructure elements—including bridges, highway sign foundations, strain pole foundations, and highway sound barrier foundations—affected by ASR.²

In 1998, MassDOT began requesting the producers for an annual ASR evaluation of the aggregates in response to the discovery of the first ASR cases. Since then, the annual testing campaign of the aggregates used in the construction of transportation infrastructure has become an important part of the MassDOT ASR prevention strategy. The American Association of State Highway and Transportation Officials (AASHTO) T 303 accelerated mortar bar test (AMBT) was the reference accelerated test used to evaluate the aggregates.³ In certain cases, the information provided by the AMBT was further supported by petrographic information gathered according to ASTM C295-08.^{1,4} In 2003, MassDOT

launched an in-house ASR testing campaign in parallel with the evaluation performed by the producers. Five years later, in 2008, MassDOT created a list of approved independent testing laboratories for performing the ASR evaluation of the aggregates. The combined efforts between the state agency and the industry to standardize the ASR scrutiny of the aggregates helped in identifying the highly reactive (HR) aggregate source behind the majority of the 40 cases of transportation infrastructure elements affected by ASR.^{1,2} In an effort to better understand the long-term behavior of the local aggregates, in 2012, MassDOT partnered with the Federal Highway Administration (FHWA) to construct an outdoor concrete exposure site in Lawrence, MA.^{1,5} This facility contains 73 concrete blocks produced with 11 local coarse and fine aggregates and is instrumental in understanding the efficacy of different mitigation strategies.

Since its implementation in 2003, MassDOT has been looking into the possibility of improving the accuracy and efficiency of the in-house ASR testing campaign of the aggregates. In 2009, MassDOT started exploring the possibility of using the ASTM C1293 concrete prism test (CPT) as an alternative to the AMBT.^{1,6} The lack of accuracy of the AMBT, reflected by the high frequency of false positives and negatives in its results, motivated the interest in the CPT, a test with a better correlation with the field performance of the aggregates.⁷⁻⁹ In 2017, MassDOT evaluated all the approved aggregate sources in the state using the CPT. However, the excessive length of the CPT compared with the AMBT (1 year versus 16 days) complicated the possibility of maintaining the annual frequency of the in-house aggregate evaluation campaign. Therefore, 1 year later, MassDOT used the newly approved AASHTO T 380 instead.^{1,10} The mortar concrete prism test (MCPT) only requires between 56 and 84 days to reproduce the CPT results, which significantly improved the efficiency of the testing campaign.^{11,12} More recently, in 2019, MassDOT, in cooperation with the FHWA, launched a research project to evaluate a new chemical ASR test, known as the Turner-Fairbank Highway Research Center ASR susceptibility test (T-FAST), as a faster and easier alternative to the MCPT. The T-FAST relies on a novel chemical index to predict the alkali-silica reactivity of an aggregate instead of the classic evaluation of the

physical expansion of concrete specimens such as that used in the CPT and MCPT.¹³ This feature provided important advantages over the two physical tests. The T-FAST offers the possibility of generating accurate results within 21 days using merely 60 g of aggregate without the need to mix the concrete.¹⁴ These attributes make the T-FAST an interesting candidate to improve the accuracy and reduce the cost of the annual aggregate evaluation campaign. AASHTO included the T-FAST as a new provisional test (TP 144-21) in its latest publication, "Standard Specifications for Transportation Materials and Methods of Sampling and Testing and AASHTO Provisional Standards."^{15,16} Besides the possibility of having results within 21 days, the new T-FAST provides additional advantages, such as the possibility of accurately determining the alkali threshold (AT) of any aggregate, because the test takes place in a closed system with no alkali leaching.^{14,17} The AT information in combination with the ASR classification provided by the T-FAST is instrumental in better gauging the ASR risk posed in the field by certain types of slowly (SR) and moderately reactive (MR) aggregates.

This paper documents the results of characterizing 38 different MassDOT-approved aggregates under the new T-FAST and AT tests. The aggregates selected for this comparative study are representative of the diverse mineralogical compositions of the 113 aggregates approved by MassDOT to be used in the construction of transportation infrastructure. The information obtained with these new tests was compared with previous classifications based on recent MCPT measurements and historic AMBT results.

RESEARCH SIGNIFICANCE

Traditional concrete and mortar accelerated ASR methods like the CPT and AMBT can accurately detect the presence of alkali-silica reactive phases in most aggregates. However, for certain SR or MR aggregates, this information is insufficient to assess their field performance.^{14,17-20} The new T-FAST standard is a sensitive method capable of accurately detecting the presence of alkali-silica reactive phases in any type of aggregate, including SR and MR.²¹ The high sensitivity of the method, coupled with the possibility of accurately determining the AT, provides a broader understanding of the conditions susceptible to triggering the alkali-silica reactivity of these aggregates in the field. This paper provides examples of how T-FAST and AT results can be used to predict the field performance of SR and MR aggregates. Additionally, the paper proposes a new set of criteria that opens the possibility of using the T-FAST to identify and accurately classify the reactivity in a series of carbonate aggregates.

EXPERIMENTAL PROCEDURE

Materials

Sixty-two samples of aggregates were analyzed in this study. The samples came from a total of 38 coarse aggregates with representative mineralogies of the 113 aggregates approved by MassDOT. Twenty-four of them were collected in two consecutive sampling campaigns to evaluate the repeatability of the T-FAST. The classification rendered by

the T-FAST was compared against recent MCPT and historic AMBT expansion data. Tables 1 and 2 provide the general petrographic descriptions of the noncarbonate and carbonate aggregates used in the study.

The MCPT specimens were prepared using a Type I/II ordinary portland cement and a nonreactive (NR) sand. The cement had a total sodium equivalent content ($\text{Na}_2\text{O}_{\text{eq}}$) of 1.1%. The NR fine aggregate used was a manufactured limestone sand from San Antonio, TX.^{22,23} Three different reagent-grade chemicals—calcium oxide (CaO), sodium hydroxide, and deionized water (16 MΩ·cm)—were used in the T-FAST. The CaO had an average particle size of 4.6 μm.

Methods

Concrete specimens of 50 x 50 x 285 mm were prepared to evaluate the aggregates under the MCPT. The proportioning and mixing of the concrete were done according to the specifications in AASHTO T 380.¹⁰ Three specimens were cast per aggregate, each one containing a maximum alkali content of 1.25% of $\text{Na}_2\text{O}_{\text{eq}}$. After 24 hours, the specimens were demolded and stored in water at 60°C for 24 hours. Following this 24-hour conditioning, the specimens were immersed in a 1 N NaOH solution at 60°C for testing. The length of the prisms was measured at regular intervals for 56 or a maximum of 84 days, depending on the reactivity of the aggregate. The aggregate reactivity was determined based on the classification criteria proposed by the standard.¹⁰

The T-FAST was also used to determine the alkali-silica reactivity of the aggregates.^{14,15} This chemical test did not require the mixing of concrete or mortar. Instead, a representative 600 g sample of the aggregate, obtained in accordance with AASHTO R 90-18 and AASHTO R 76-16, was crushed down to two fractions: a finer fraction passing a No. 50 (297 μm) and retained on a No. 100 (149 μm) sieve (referred to as No. 100); and a coarser fraction passing a No. 30 (595 μm) and retained on a No. 50 (297 μm) sieve (referred to as No. 50).^{24,25} The test only required 5 g of the crushed aggregate divided into two portions of 3.125 ± 0.005 g retained on No. 50 and 1.875 ± 0.002 g retained on No. 100. The 5 g, with both fractions thoroughly combined, and 25 mL of 1 N NaOH solution were introduced in a 50 mL polytetrafluoroethylene (PTFE) test tube for 21 days under four different conditions, as shown in Table 3. Three replicates were prepared for each condition.

All the PTFE tubes were assembled in the same way, independent of the condition, by placing the corresponding amount of CaO at the bottom, followed by the 5 g of aggregate sample on top and the 25 mL of 1 N NaOH solution covering both solids. The PTFE test tubes, properly sealed with caps, were stored for 21 days at $55.0 \pm 2^\circ\text{C}$ for conditions 1, 2, and 3, or $80.0 \pm 2^\circ\text{C}$ for condition 4. Immediately after the 21-day incubation, the liquid fraction inside the PTFE tubes was filtered using a glass microfiber filter of <0.7 μm pore size. The elemental concentrations, in millimoles per liter (mM), of silicon ([Si]), calcium ([Ca]), and aluminum ([Al]) were measured in the filtered liquid fraction using inductively coupled plasma spectroscopy. Lastly, the reactivity index (RI) of each PTFE test tube was calculated according to Eq. (1) to assess the alkali-silica reactivity of

Table 1—General mineralogy, AMBT, MCPT, and T-FAST results and AT of noncarbonate aggregates used in study

ID	Description	AMBT	MCPT	T-FAST	AT, kg Na ₂ O _{eq} /m ³
M-1	Mixed gneiss/schist/quartzite	HR	MR	HR	nm
M-2	Granite gneiss	MR	MR	HR	nm
M-3	Mixed quartzite/quartz-mica schist/metasandstone	MR	MR	MR	3
M-4	Mixed gneiss/granitic	MR	HR	MR	3.2
M-5	Quartz diorite/leucogranite	na	MR	MR	3.2
M-6	Basalt/diabase	na	NR	MR	3.6
M-7	Basalt	na	NR	MR	3.6
M-8	Mica (muscovite) schist	NR	MR	MR	3.6
M-9	Mixed granite/granite gneiss/quartzite/metasandstone	MR	MR	MR	3.8
M-10	Diorite/granitic/volcanic (traces)	NR	MR	MR	3.8
M-11	Basalt	NR	MR	MR	4
M-12	Quartz diorite	HR	MR	MR	4.1
M-13	Granite/pegmatite	MR	na	MR	4.1
M-14	Quartz-feldspathic/pegmatite vein	MR	MR	MR	4.2
M-15	Granitic gneiss/quartzite/schist/basalt	MR	NR	MR	4.4
M-16	Granite (dominant biotite)	NR	MR	MR	4.5
M-17	Quartz diorite	na	na	MR	4.5
M-18	Quartz mica schists/metasandstone/quartzite/metavolcanics	NR	NR	MR	4.6
M-19	Basalt/diabase	MR	na	MR	4.6
M-20	Basalt/diabase	NR	NR	MR	4.8
M-21	Pinkish metagranite	MR	MR	MR	4.9
M-22	Granite	MR	MR	MR	5
M-23	Mixed granite /granite gneiss/biotite-amphibole gneiss/schist	na	MR	MR	5.2
M-24	Mixed diorite/gneiss/granite/schist	NR	MR	SR	5.2
M-25	Diabase/granite/diorite/sandstone/granite gneiss/schist	MR	MR	MR	5.4
M-26	Mixed quartzite/granitic gneiss/granite/basic volcanic rocks	NR	NR	MR	5.7
M-27	Mixed quartzite/schist/granite gneiss/metavolcanics	na	MR	MR	6.1
M-28	Schists/granite/granitic gneiss/quartzite	na	NR	SR	6
M-29	Granite/quartz diorite	NR	MR	SR	6.4
M-30	Granite/gneisses/schists	na	MR	SR	6.5
M-31	Granite	na	MR	SR	6.5
M-32	Mica (biotite) schist	na	na	SR	6.5
M-33	Gabbro	NR	NR	NR/SR	6.4
M-34	Granodiorite/tonalite	NR	MR	NR/SR	nm

Note: nm is not measured; na is not available; NR is nonreactive; SR is slow reactive; MR is moderately reactive; R is reactive; HR is highly reactive.

the aggregates based on the classification criteria proposed by the T-FAST.¹⁵ The results of both accelerated tests, MCPT and T-FAST, were compared against historic AASHTO T 303 results.

$$RI = \frac{[Si]}{[Ca] + [Al]} \quad (1)$$

The ATs of all the aggregates from Tables 1 and 2 classified as SR or MR by the T-FAST were determined using a modified T-FAST protocol.¹⁷ The aim of measuring the ATs

of these aggregates, traditionally referred to as marginal, had a twofold purpose: first, to help understand why these aggregates, despite being labeled as reactive, do not show reactivity in the field; and second, knowing the AT of these aggregates allows stakeholders the opportunity to prescribe alternative mitigation strategies beyond the common prescription of fly ash or slag. The ATs were measured by exposing the aggregates to a range of alkali contents, from 0.25 to 1.55% Na₂O_{eq} (1.05 to 6.51 kg/m³ Na₂O_{eq}). All experiments were conducted under condition 2 (0.25 g CaO in the test tube and 55°C). This amount of CaO was selected to simulate

Table 2—General mineralogy, AMBT, MCPT, and T-FAST results, and AT of carbonate aggregates used in study

ID	Description	AMBT	MCPT	T-FAST	AT, kg Na ₂ O _{eq} /m ³
M-35	Dolomitic limestone	na	MR	SR	3
M-36	Dolomitic marble (quartz and tremolite)	NR	NR	SR	2.9
M-37	Metacarbonate	NR	na	SR	1.4
M-38	Limestone	na	NR	SR	2

Table 3—Summary of T-FAST conditions

Condition	CaO, g	Temperature, °C
1	0.13	55
2	0.25	
3	0.34	
4	0.25	80

the mixture design proportions of ASTM C1293, that is, concrete prisms made with 420 kg/m³ of a standard Type I/II cement and containing an average portlandite content of 0.16 g Ca(OH)₂/g dry paste.^{14,26} The different alkali loadings in the tube were achieved by changing the NaOH concentration of the solution using the following set of equations.¹⁷

$$M_{Cement} = \frac{V_{Sol}}{w/c} \quad (2)$$

$$Na_2O_{eq,Tube} = M_{Cement} \frac{Na_2O_{eq}\%}{100} \quad (3)$$

$$M_{NaOH} = Na_2O_{eq,Tube} \frac{2000}{MW_{Na_2O} V_{Sol}} \quad (4)$$

The mass of cement (M_{Cement}) in grams was calculated for a total solution of 100 mL (volume of solution [V_{Sol}]) using an average water-cement ratio (w/c) of 0.435 (Eq. (2)). V_{Sol} was assumed to be 100 mL to ensure an adequate volume of solution to prepare three replicate test tubes. The Na₂O_{eq} content of the solution in grams in the tube (Na₂O_{eq,Tube}) was calculated based on the alkali content (Na₂O_{eq} percentage) that wants to be simulated (Eq. (3)). Lastly, the molarity of sodium hydroxide (M_{NaOH}) was obtained through Eq. (4), where MW_{Na_2O} is the molecular weight of Na₂O, and V_{Sol} is in milliliters (100 mL). Figure 1 shows the ATs of three aggregates from Table 1. The ATs were calculated at the exact point at which each of the aggregate curves crosses the 0.45 RI threshold line (horizontal dotted line in Fig. 1).¹⁴

RESULTS AND DISCUSSION

Classification of aggregates based on T-FAST

The bar graph in Fig. 2 provides the distribution of the T-FAST classification for all the coarse aggregates in Tables 1 and 2. The T-FAST considered the majority of the analyzed aggregates as MR, 63%, followed by SR with 23%, and HR and borderline NR/SR, both with 5.3%. None of the

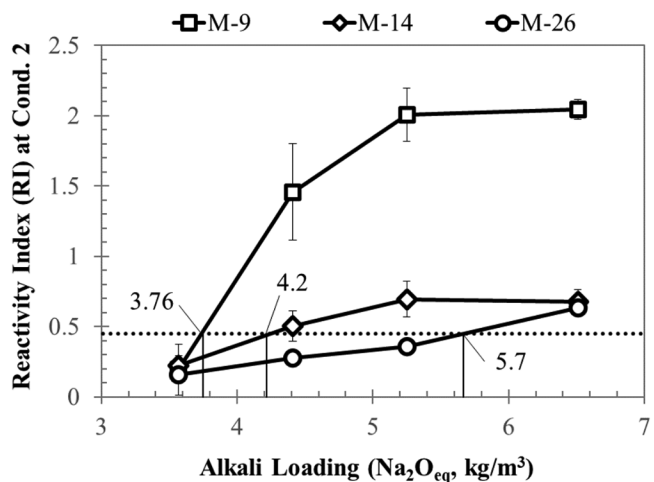


Fig. 1—Effect of alkali loading on RI of coarse aggregate samples. (Source: FHWA.)

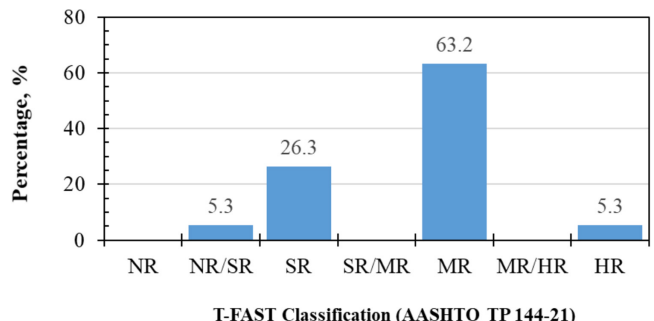


Fig. 2—Distribution of T-FAST classification of 38 coarse aggregates rendered by AASHTO TP 144-21. (Source: FHWA.)

38 aggregates was identified as pure NR, meaning that all of them contained alkali-silica reactive phases. The distribution of the bar graph in Fig. 2 depicts a majority of the aggregates as MR or SR (86% of the total), which aligns with the prototypic concrete aggregate used in Massachusetts. Silicon is one of the most abundant constituents of the earth's crust, making the presence of silica-based minerals common among the different types of rocks used in construction.^{27,28} This condition implies that several of the minerals found in aggregate used in construction are silica-bearing and potentially susceptible to developing ASR.²⁹⁻³³ Therefore, a majority of aggregates can logically be categorized as MR or SR. However, despite the abundance of MR and SR aggregates, the presence of alkali-silica reactive phases in an aggregate does not necessarily imply that it will exhibit ASR in the field. The latter will occur only if the mixture design and field exposure conditions of the concrete in which the aggregate is used are conducive to developing ASR. The relation between the presence of alkali-silica phases in aggregate and its likelihood of developing ASR in the field will be discussed in greater depth in subsequent sections of this paper.

Carbonate aggregates

The aggregates listed in Table 2 posed an interesting case. They were initially classified as MR/HR based on the

Table 4—Concentrations of silicon and aluminum, and RI values of carbonate aggregates for all four conditions tested with T-FAST

Sample ID	Average concentration in conditions 1, 2, and 3			Condition 4		
	Si, mM	Al, mM	RI	Si, mM	Al, mM	RI
M-35	7.57	0.07	66.7	33.39	0.82	41.78
M-36	1.42	0.06	9.92	4.32	0.07	40.17
M-37	4.61	0.13	20.92	30.76	1.46	20.28
M-38	4.75	0.12	20.82	12.83	1.19	9.95
Typical MR/HR values	3.05 to 11.7	1.1 to 9.65	1.1 to 1.85	104.45 to 363.35	1.08 to 1.95	66.8 to 232.81

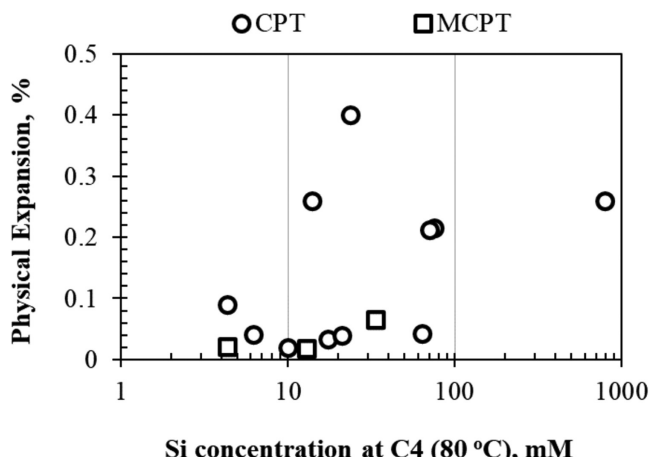


Fig. 3—Correlation between physical expansion and concentration of silicon in condition 4 of T-FAST for group of dolomites, dolomitic limestones, and dolostone. (Source: FHWA.)

T-FAST protocol. However, all these samples were characterized by low concentrations of aluminum in conditions 1, 2, and 3, and silicon in condition 4. The data in Table 4 show that the concentration of aluminum in the first three conditions was less than 0.2 mM, 10 times smaller than that observed in traditional MR/HR aggregates.^{13,14,17,21} These two circumstances caused an overestimation of the RI values, thereby resulting in an incorrect T-FAST classification of these aggregates.

Interestingly, all these aggregates were carbonate aggregates with dolomite as part of their mineral composition. Further, the concentrations of silicon in condition 4 revealed the presence of alkali-silica-reactive minerals, as has been observed in other carbonate aggregates.³⁴⁻³⁷ In such aggregates, the physical expansion correlated with the amount of alkali-silica-reactive minerals.^{36,38} The relationship between the CPT and MCPT physical expansion of different carbonate aggregates from Pennsylvania and New York—mainly dolomites, dolomitic limestones, and dolostones—and the silicon concentrations measured at condition 4 while testing these aggregates in the T-FAST is illustrated in Fig. 3. A direct correlation between physical expansion and silicon concentration in condition 4 was not expected for several reasons. First, the physical expansion data used in this comparison was not obtained from one accelerated test method but a combination of both CPT and MCPT expansion results. Second, the NR aggregate used in conjunction

Table 5—New T-FAST criteria for classification of carbonate aggregates with silicon concentration in condition 4 > 1 mM and aluminum concentration in condition 2 < 0.2 mM

[Si], mM, at condition 4	Description of aggregate reactivity
$1 < [\text{Si}] \leq 50$	SR
$50 < [\text{Si}] \leq 100$	MR
$100 < [\text{Si}] \leq 1000$	HR
$[\text{Si}] > 1000$	VHR

Note: VHR is very highly reactive.

with the reactive aggregates in the physical expansion tests was not the same for all aggregates as the data were compiled from physical expansion tests carried out by several laboratories. Despite these uncontrolled variables in the physical expansion data, Fig. 3 revealed a distinct trend of increasing physical expansion with increasing silicon concentration. This relationship between physical expansion and silicon concentration in condition 4 observed for carbonate aggregates suggested that the concentration of silicon in condition 4 could be used to rank the ASR reactivity of these aggregates, as proposed in Table 5. This table only applies when the aggregate has a silicon concentration greater than 1 mM in condition 4 and an aluminum concentration less than 0.2 mM in condition 2. Using these new criteria, the classification of the four carbonate aggregates in Table 2 changed from the initial MR/HR to SR in all four cases. The latter one agreed better with the low concentration values of silicon measured in all conditions (refer to Table 4) and the AMBT and MCPT values reported in Table 2.

Evaluation of samples from consecutive testing campaigns

The T-FAST results of a total of 24 samples of aggregates collected during two different testing campaigns in 2018 and 2019 are compared in Table 6. The small amount of aggregates used in the T-FAST, only 5 g per tube, highlights the importance of a sturdy and rigorous sampling process to properly capture the heterogeneous mineralogical composition of some of the aggregates. As mentioned in the “Methods” section of this paper, AASHTO R 90 and R 76 were followed to ensure adequate sampling when characterizing aggregates using the T-FAST. The data in Table 6 show that the T-FAST rendered coherent results for those aggregates sampled during different campaigns. In more than 70% of the cases, the 2019 T-FAST classification remained the

Table 6—RI values under four T-FAST conditions (conditions 1 through 4) for aggregate samples collected during two consecutive testing campaigns

ID	2018					2019				
	C-1	C-2	C-3	C-4	Class.	C-1	C-2	C-3	C-4	Class.
M-3	1.7	1.38	1.3	61.82	MR	1.43	1.22	1.17	103.03	MR/HR
M-5	0.32	0.37	0.74	29.52	SR	1.43	0.7	0.63	66.33	MR
M-6	0.93	0.75	0.7	12.69	MR	1	0.77	0.6	16.78	MR
M-8	0.66	0.44	0.28	4.45	SR	1.8	1.14	1.06	36.48	MR
M-9	1.12	0.89	0.8	38.77	MR	1.33	1.15	1	232.81	MR/HR
M-10	0.73	0.53	0.48	2.8	MR	0.63	0.43	0.32	2.99	SR
M-11	1.19	0.81	0.71	34.3	MR	1.43	1.17	0.91	29.78	MR
M-14	1.25	1.32	1.29	56.64	MR	1.08	1.19	1.19	5.5	MR
M-15	0.85	0.64	0.62	17.21	MR	0.81	0.59	0.53	35.98	MR
M-16	0.44	0.32	0.26	2.69	NR/SR	0.26	0.53	0.8	4.03	MR
M-18	0.88	0.59	0.27	6.42	MR	0.57	0.37	0.26	1.61	NR/SR
M-19	0.75	0.91	0.48	15.77	MR	1.61	1.19	1.19	40.81	MR
M-22	1.01	0.49	0.34	5.93	MR	1.16	0.59	0.34	27.38	MR
M-23	0.64	0.34	0.26	4.62	SR	0.54	0.47	0.29	5.09	MR
M-24	0.44	0.38	0.23	4.36	NR/SR	0.61	0.32	0.34	8.09	SR
M-27	1.27	0.65	0.42	8.8	MR	1.26	0.85	0.63	24.29	MR
M-28	0.46	0.34	0.25	4.08	SR	0.43	0.41	0.3	9.76	NR/SR
M-29	0.79	0.31	0.25	3.12	SR	0.35	0.5	0.76	2.16	MR
M-30	0.3	0.31	0.45	10.58	SR	0.4	0.27	0.35	6.79	NR/SR
M-31	0.52	0.35	0.26	12.34	SR	0.34	0.25	0.23	3.37	SR
M-32	0.45	0.29	0.27	3.78	SR	0.34	0.39	0.53	8.29	SR
M-33	0.62	0.44	0.58	1.57	NR/SR	0.8	0.57	0.49	1.18	NR/SR
M-35	na	na	na	41.77	SR	na	na	na	15.17	SR
M-38	na	na	na	9.95	SR	na	na	na	14.67	SR

Note: C-1 through C-4 are conditions 1 through 4; Class. is classification.

same or slightly changed to a borderline category compared with the 2018 one (for example, M-3, M-9, M-24, M-28, or M-30). The 2019 classification changed with respect to the previous one in only 30% of the cases, as shown in Table 6. However, in none of these cases was the difference between both years' classifications significant enough to cause a fundamental change between NR and reactive categories. In fact, the discrepancies in the reactivity categories were not concerning from a practical point of view because the variations were not large enough to trigger a difference in how the aggregates are treated while incorporating them into a concrete mixture. These observed discrepancies in the classification were expected due to the intrinsic variation in the aggregates' mineralogy.^{21,39} Intrinsic mineralogical variations often manifest in ASR accelerated mortar and concrete tests as variations in the final physical expansion values.^{18,40-42}

Comparison of ASR classification

The classification of all the aggregates obtained by the T-FAST was compared against results rendered by the

AMBT and MCPT, as illustrated in Fig. 4 and 5, respectively. In both cases, the T-FAST showed higher sensitivity in detecting the presence of alkali-silica reactive phases in the aggregate compared to the AMBT or MCPT. As shown in Fig. 4, the AMBT classified 50% of the aggregates as NR, while the T-FAST classified 8.3% as NR/SR, 16.7% as SR, and 25% as MR. The T-FAST also displayed higher sensitivity than the MCPT, as depicted by the two graphs in Fig. 5. The 30% of aggregates identified as NR by the MCPT were further subdivided into NR/SR and SR by the T-FAST. Specific petrographic examinations were performed in those aggregate samples showing alkali-silica reactivity in the T-FAST but not in the MCPT to verify the presence of reactive mineral phases. This analysis could not be performed on aggregates M-33 and M-36 due to a lack of sufficient material. The analysis detected the presence of alkali-silica reactive mineral phases in all the samples classified as NR by the MCPT.⁴³ Microcrystalline quartz and strained quartz were the common mineral phases observed within those aggregate samples. Interestingly, the T-FAST was able to detect all the aggregates in which any reactive phase was present.

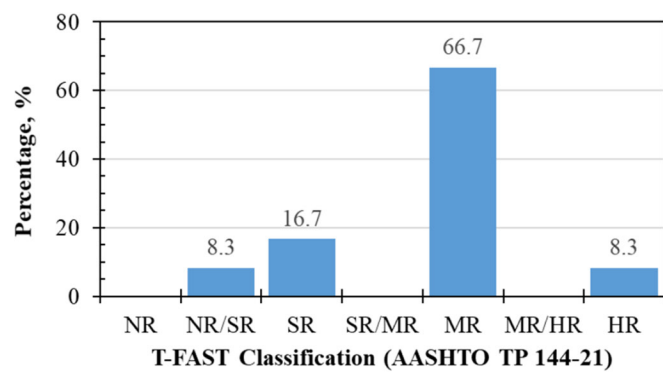
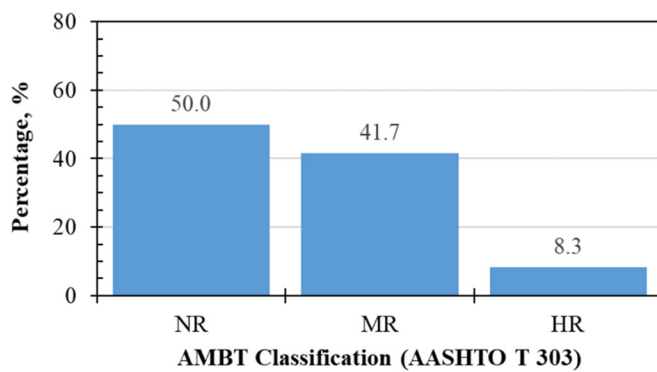


Fig. 4—Comparison of ASR classification reported by AMBT and AASHTO TP 144-21. (Source: FHWA.)

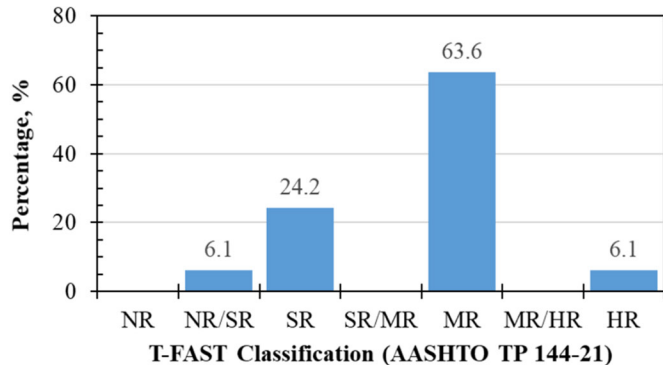
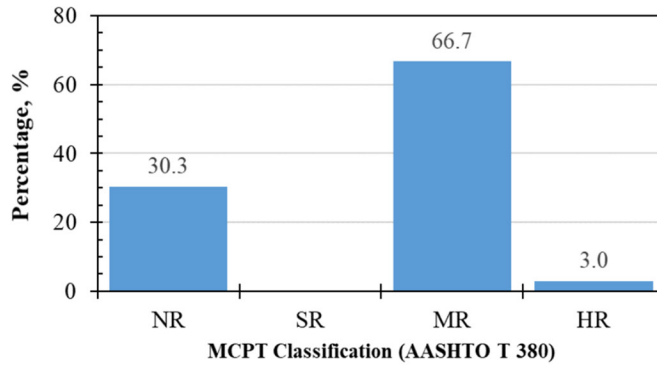


Fig. 5—Comparison of ASR classification reported by MCPT and AASHTO TP 144-21. (Source: FHWA.)

Prediction of field performance based on AT data of aggregates

The data in Fig. 4 and 5 confirm the higher sensitivity of the T-FAST compared to the AMBT and MCPT in detecting the presence of alkali-silica reactive phases in the aggregates. However, despite its high sensitivity, the T-FAST, or any other ASR accelerated test, cannot accurately predict the reactivity of an aggregate under the alkali loading conditions of a specific concrete.^{30,44} For this reason, knowing the AT of aggregates is important. The AT is defined as the specific alkali level at which the ASR reaction is triggered in an aggregate. Knowing the AT of an aggregate is an important piece of information that provides insight into the field behavior of a concrete when combined with the alkali loading of the concrete. For example, an aggregate will develop ASR inside of a specific concrete only when the alkali loading of the concrete, expressed as kilograms of Na₂O_{eq} per cubic meter, is higher than the AT of the aggregate. By contrast, a concrete will remain risk-free from developing ASR if its alkali loading is maintained below the AT of the aggregates. Figure 6 shows the correlation between the T-FAST classification and the corresponding AT value for all the NR/SR, SR, and MR aggregates in Tables 1 and 2. The carbonate aggregates listed in Table 2 were included in Fig. 6 as a different series. The carbonate aggregates analyzed in this study were observed to have lower ATs in comparison with noncarbonate aggregates.⁴⁵ The analysis and discussion of the AT for these aggregates have been presented separately. In this case, because the expansion of these aggregates correlated with the concentration of silicon (refer to Fig. 3), the AT was calculated by tracking the changes in silicon concentration

as a function of alkali content in the test tubes instead of the RI. The concentration value of 1 mM of silicon was set as the threshold to calculate the AT, instead of the 0.45 value of the RI used for noncarbonate aggregates (refer to Fig. 1).

The AT data of noncarbonate aggregates in Fig. 6 displayed a strong correlation with the T-FAST classification because the former predictably decreased when moving toward more reactive T-FAST classifications. Additionally, the analysis of the AT values provided a better understanding of the potential field performance of these aggregates. For example, all the NR/SR and SR aggregates had AT values greater than 5 kg Na₂O_{eq}/m³. This result implies that, despite the presence of reactive phases in such aggregates, they would not develop ASR in concrete with alkali loading less than 3 kg Na₂O_{eq}/m³ regardless of the type and dosage of supplementary cementitious materials (SCMs) used. The AT values of the MR aggregates ranged from 2.7 up to 6.1 kg Na₂O_{eq}/m³, suggesting that not all MR aggregates would necessarily develop ASR in the field. For instance, 25% of the MR aggregates had an AT between 4.8 and 6.1 kg Na₂O_{eq}/m³, similar to the NR/SR and SR ones. The AT of half of the MR aggregates ranged from 3.6 to 4.8 kg Na₂O_{eq}/m³, meaning that other factors, such as the nature of the fine aggregate along with the type and dosage of the SCMs, should be taken into consideration when the concrete is designed to avoid future ASR development. Lastly, 25% of the MR aggregates had AT values ranging from 2.7 to 3.6 kg Na₂O_{eq}/m³. For ASR mitigation, this group of MR aggregates should be treated as HR aggregates despite their MR classification. Therefore, the highest degree of precaution should be applied to this type of MR aggregate when the mitigation strategies are

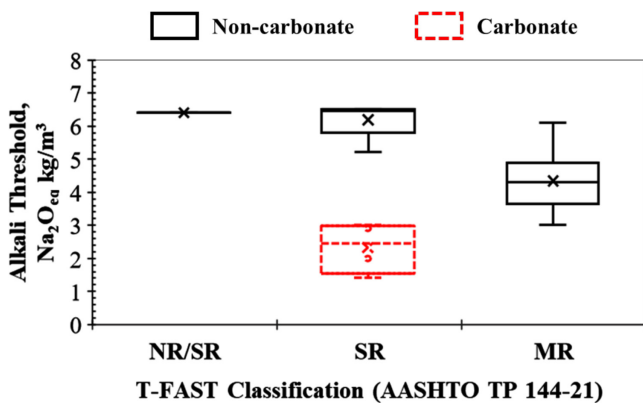


Fig. 6—Correlation between T-FAST classification and AT of noncarbonate and carbonate aggregates. (Source: FHWA.)

planned. Interestingly, approximately 75% of the MR aggregates in Fig. 6 had AT values ranging between 3 and 5 kg $\text{Na}_2\text{O}_{\text{eq}}/\text{m}^3$, as previously reported by other researchers.^{46,47}

Figure 6 also illustrates that all the aggregates in Table 1 identified by the T-FAST as SR had AT values ranging between 5 and 6.6 kg $\text{Na}_2\text{O}_{\text{eq}}/\text{m}^3$. By contrast, carbonate aggregates with the same SR classification had AT values ranging between 1.3 and 3 kg $\text{Na}_2\text{O}_{\text{eq}}/\text{m}^3$, as shown in Fig. 6. It is interesting to note that certain carbonate aggregates that are potentially prone to alkali–carbonate reaction (ACR) have been known to trigger expansion in the field when used in concrete mixtures of low alkali loading.^{45,48} While the carbonate aggregates used in this study are not believed to be susceptible to ACR, the possibility of these aggregates undergoing ASR reaction in the field at unexpectedly low levels of alkali loading cannot be ruled out. A thorough comparison of the T-FAST classification and AT values of a wide range of carbonate aggregates with varying mineralogies and reactivities has to be completed to understand how prevalent this phenomenon is within these types of aggregates.

Benefits of combination of T-FAST and AT measurements

As discussed in the section “Comparison of ASR classification,” the T-FAST, being more sensitive than other tests such as the AMBT and MCPT, can detect the presence of alkali–silica reactive phases in aggregates where other tests failed. The lack of sensitivity of the commonly used mortar- or concrete-based accelerated ASR tests has practical implications. The data in Fig. 4 and 5 clearly indicated that the AMBT and MCPT systematically mislabeled certain aggregates with reactive phases as NR. The main risk of mislabeling these aggregate types is that inadequate ASR preventive measures may be applied when these aggregates are used in a concrete mixture design. As an example, if both the aggregates used in a mixture are believed to be NR, the overall alkali loading of the concrete may not necessarily be limited to 3 kg $\text{Na}_2\text{O}_{\text{eq}}/\text{m}^3$ by the corresponding prescription of a low-alkali cement, or an adequate dosage of SCMs may not be applied in the concrete mixture design. The occurrence of such cases in the field is low due to the widespread

practice of using SCMs in most concrete mixtures to address sustainability concerns. However, several documented cases exist in which aggregates believed to be NR “unexpectedly” developed ASR in the field.^{1,14,17,20} The presumed NR character of these aggregates was, in many cases, corroborated by historic field performance and innocuous expansion records in mortar- or concrete-based accelerated ASR tests. The systematic characterization of aggregates under the T-FAST will eliminate the risk of having reactive aggregate mislabeled as “NR” and being used in mixture designs without the proper precautions, resulting in the potential occurrence of ASR.

The aforementioned field cases reveal the importance of having an accurate and sensitive accelerated ASR test, such as the T-FAST, as the first step to understanding how aggregates behave in the field.³⁰ However, as mentioned before, the T-FAST alone does not provide enough information to determine the ASR risk of an aggregate under specific concrete conditions. The information provided by the T-FAST should be combined with the AT of the aggregates and alkali loading of the concrete to accurately predict the ASR risk of a particular concrete mixture. Knowing the AT of an aggregate allows the establishment of a limit in the alkali loading of the concrete in which the aggregate is intended to be used to eliminate the risk of ASR. As a rule of thumb, the alkali loading of the concrete should always be smaller than the AT of the aggregate combination. As illustrated in Fig. 6, the method used in this study to measure the AT of aggregates made it possible to rank the aggregates based on their AT values. Knowing the AT of any aggregate combination opens the door to prescribing specific alkali loading limits for each concrete mixture design. This knowledge, in turn, would allow a move from the current approach of limiting the alkali content of cement to 0.6% of $\text{Na}_2\text{O}_{\text{eq}}$ when reactive aggregates are used regardless of their reactivity to a new scenario where the limit of the alkali content of the cement can vary as a function of the alkali loading limit of a particular mixture design.

The combination of the T-FAST and AT measurements has another important benefit: their implementation could be used to ameliorate the progressive decrease in the availability of Class F fly ash. ASR mitigation strategies currently in use across most state highway agencies in the United States heavily rely on the use of Class F fly ash. Unfortunately, the availability of this SCM has decreased over the years due to the continuing closure of coal-fired power plants.^{49–51} The implementation of AT measurements would help relieve the high demand for Class F fly ash by allowing the possibility of using SCMs other than Class F fly ash for specific cases. For example, the data in Fig. 6 indicate that alternative SCMs other than Class F fly ash could be used in mixtures containing those SR and MR aggregates with AT values greater than 4 kg $\text{Na}_2\text{O}_{\text{eq}}/\text{m}^3$, provided the SCMs do not cause the alkali loading of the mixture to increase above 3 kg $\text{Na}_2\text{O}_{\text{eq}}/\text{m}^3$. Furthermore, the Class F fly ash could be reserved to exclusively mitigate those MR aggregates in Fig. 6 with AT values ranging from 2.7 to 3.6 kg $\text{Na}_2\text{O}_{\text{eq}}/\text{m}^3$.

CONCLUSIONS

The classification of the sample population in this study using the new Turner-Fairbank Highway Research Center alkali-silica reaction (ASR) susceptibility test (T-FAST) along with the measurements of alkali threshold (AT) provided several conclusions regarding the capacity of this new test to separate the aggregates based on their alkali-silica reactivity, its sensitivity compared to other accelerated ASR tests, and its potential to predict field performance of the aggregates in combination with AT measurements.

The T-FAST classified 86% of the aggregates as moderately reactive (MR) or slow reactive (SR), indicating the presence of alkali-silica-reactive minerals in them. This classification reflects the widespread prevalence of these types of minerals as components of the rocks commonly used as aggregate for concrete production. The test also displayed high sensitivity toward those aggregates with low aluminum-leaching capacities, such as carbonate aggregates containing dolomite. The results presented in this paper confirmed that the physical expansion of these carbonate aggregates correlated with the amount of alkali-silica reactive minerals in them, as reported in previous studies. Thus, this paper proposed a new set of criteria to allow the T-FAST to detect and classify carbonate aggregates more reliably. The AT of these aggregates was, on average, 56% lower than noncarbonate aggregates with the same T-FAST classification, confirming the propensity of the former to expand, even when low-alkali cement was used, as reported in previous studies.

Despite the relatively small sample size used in the T-FAST to analyze an aggregate (a total of 60 g equally divided into 12 tubes), the systematic analysis of the aggregates sampled in consecutive sampling campaigns rendered meaningful results. The experiment confirmed that the T-FAST is an efficient alternative method that can potentially be used in the annual Massachusetts Department of Transportation (MassDOT) in-house ASR testing campaign.

The sensitivity to detect the presence of alkali-silica-reactive phases within an aggregate was different among the three tests evaluated. The T-FAST had the highest sensitivity, followed by the mortar concrete prism test (MCPT) and accelerated mortar bar test (AMBT). Even with this high sensitivity, the information supplied by any of these tests was not sufficient to accurately predict the field behavior on an aggregate with respect to the development of ASR. The measurement of the AT of the aggregate provided the missing piece of information required to evaluate field performance. As discussed in this paper, the combination of the T-FAST and AT measurements put forth two important benefits. First, the use of this combination of tools eliminates the risk of having reactive aggregate mislabeled as “nonreactive” (NR), which in turn may result in them being used in mixture designs without the proper precautions. The second benefit is that the combination of these two measurements allows stakeholders to be more selective in prescribing the most effective supplementary cementitious materials (SCMs)—for example, Class F fly ash—only for the more reactive aggregates that really require it. In fact, the effective use of the T-FAST and AT measurements offers the possibility of prescribing less-effective SCMs to certain aggregate

combinations with AT values greater than 4 kg Na₂O_{eq}/m³, provided the SCM does not cause alkali loading of the mixture to increase above 3 kg Na₂O_{eq}/m³.

AUTHOR BIOS

Jose F. Muñoz is a Researcher with SES Group and Associates, LLC, at Turner-Fairbank Highway Research Center (TFHRC) in McLean, VA. His research interests include the application of nano-additives to engineer the structure of cementitious materials and the development of new and rapid test methods to identify aggregates that cause alkali-silica reaction (ASR) in concrete.

Chandni Balachandran is a Research Chemist with SES Group and Associates, LLC, at TFHRC. Her research interests include concrete degradation mechanisms such as ASR, the application of spectroscopic techniques and microscopy to investigate the same, and the development of a new accelerated test method to detect alkali-silica reactivity in aggregates.

Anant Shastry is a Researcher with SES Group and Associates, LLC, at TFHRC. His research interests include developing test methods to identify ASR in concrete; characterizing additives used in asphalt binder; contents of heavy metals in glass beads; and the characterization of diverse inorganic materials such as cement, supplementary cementitious materials, clay minerals, and aggregates using different analytical techniques.

Richard Mulcahy is the Materials Field Control Engineer for the Massachusetts Department of Transportation (MassDOT) Research and Materials Section, where he manages the sampling, testing, and inspection programs for MassDOT's precast/prestressed concrete fabrication and highway construction materials source verification; develops MassDOT materials and construction specifications; and leads cement concrete research. His research interests include ASR, alternative cementitious materials solutions, fiber-reinforced concrete, ultra-high-performance concrete, and cement concrete mixture design optimization.

Jason M. Robertson is the Chief of Labs for the MassDOT Research and Materials Section, where he manages the laboratory testing for MassDOT's highway projects. He has more than 16 years of experience in material sampling and testing. His research interests include ASR, ultra-high-performance concrete, and cement concrete mixture design optimization.

Terence S. Arnold is a Senior Research Chemist with the Federal Highway Administration (FHWA) TFHRC. He has more than 20 years of experience working with the chemistry of pavement materials. His research interests include concrete and asphalt materials in highways and transportation structures.

ACKNOWLEDGMENTS

The authors would like to thank F. Zerai, T. Mirach, and J. R. R. Aguayo of SES Group & Associates, LLC; and C. Rotaru, J. Sanchez, L. Figueiredo, and N. M. Sosa of the MassDOT Research and Materials Laboratory for their technical assistance. This support is gratefully acknowledged. The review by M. Prael is also greatly appreciated. Certain commercial products may be identified in this paper to specify the material used and procedures employed. In no case does such an identification imply endorsement or recommendation by the Federal Highway Administration (FHWA), nor does it indicate that the products are necessarily the best available for the purpose. This material is based on work supported by the FHWA under Contract No. DTFH61-17-D-00017. Any opinions, findings, conclusions, or recommendations expressed in this publication are those of the author(s) and do not necessarily reflect the views of the FHWA.

REFERENCES

1. Grieco, J., and Mulcahy, R., “The Identification and Prevention of Alkali Silica Reactive (ASR) Aggregates,” 2017 Northeastern States’ Engineers Association (NESMEA) Annual Conference, Hartford, CT, Oct. 17-18, 2017, <https://nesmea.engr.uconn.edu/wp-content/uploads/sites/2933/2020/01/Mulcahy-Grieco-Akali-Silica-Reaction-in-Mass.pdf>. (last accessed Sept. 26, 2023)
2. Jiang, L.; Sherman, M. R.; and Grieco, J., “Inspection, Risk Assessment, and Management Planning of MassDOT Transportation Structures Affected by Alkali-Silica Reaction,” Transportation Research Board 94th Annual Meeting, Paper No. 15-4927, 2015, 17 pp.
3. AASHTO T 303-00 (2021), “Standard Method of Test for Accelerated Detection of Potentially Deleterious Expansion of Mortar Bars Due

- to Alkali–Silica Reaction,” American Association of State Highway and Transportation Officials, Washington, DC, 2000, 7 pp.
4. ASTM C295-08, “Standard Guide for Petrographic Examination of Aggregates for Concrete,” ASTM International, West Conshohocken, PA, 2008, 9 pp.
 5. Thomas, M. D. A.; Folliard, K. J.; Fournier, B.; Drimalas, T.; and Garber, S. I., “Methods for Preventing ASR in New Construction: Results of Field Exposure Sites,” Report No. FHWA-HIF-14-004, Federal Highway Administration, Washington, DC, 2013, 36 pp.
 6. ASTM C1293-20a, “Standard Test Method for Determination of Length Change of Concrete Due to Alkali–Silica Reaction,” ASTM International, West Conshohocken, PA, 2020, 6 pp.
 7. Bérubé, M.-A., and Fournier, B., “Canadian Experience with Testing for Alkali–Aggregate Reactivity in Concrete,” *Cement and Concrete Composites*, V. 15, No. 1-2, 1993, pp. 27-47. doi: 10.1016/0958-9465(93)90037-A
 8. Sims, I., and Nixon, P., “RILEM Recommended Test Method AAR-0: Detection of Alkali-Reactivity Potential in Concrete—Outline Guide to the Use of RILEM Methods in Assessments of Aggregates for Potential Alkali-Reactivity,” *Materials and Structures*, V. 36, No. 7, Aug. 2003, pp. 472-479. doi: 10.1007/BF02481527
 9. Thomas, M.; Fournier, B.; Folliard, K.; Ideker, J.; and Shehata, M., “Test Methods for Evaluating Preventive Measures for Controlling Expansion Due to Alkali–Silica Reaction in Concrete,” *Cement and Concrete Research*, V. 36, No. 10, Oct. 2006, pp. 1842-1856. doi: 10.1016/j.cemconres.2006.01.014
 10. AASHTO T 380-19, “Standard Method of Test for Potential Alkali Reactivity of Aggregates and Effectiveness of ASR Mitigation Measures (Miniature Concrete Prism Test, MCPT),” American Association of State Highway and Transportation Officials, Washington, DC, 2019, 10 pp.
 11. Latifee, E. R., and Rangaraju, P. R., “Miniature Concrete Prism Test: Rapid Test Method for Evaluating Alkali–Silica Reactivity of Aggregates,” *Journal of Materials in Civil Engineering*, ASCE, V. 27, No. 7, July 2015, p. 04014215. doi: 10.1061/(ASCE)MT.1943-5533.0001183
 12. Konduru, H.; Rangaraju, P.; and Amer, O., “Reliability of Miniature Concrete Prism Test in Assessing Alkali–Silica Reactivity of Moderately Reactive Aggregates,” *Transportation Research Record: Journal of the Transportation Research Board*, V. 2674, No. 4, Apr. 2020, pp. 23-29. doi: 10.1177/0361198120912247
 13. Muñoz, J. F.; Balachandran, C.; and Arnold, T. S., “New Chemical Reactivity Index to Assess Alkali–Silica Reactivity,” *Journal of Materials in Civil Engineering*, ASCE, V. 33, No. 4, Apr. 2021, p. 04021037. doi: 10.1061/(ASCE)MT.1943-5533.0003640
 14. Muñoz, J. F.; Balachandran, C.; and Arnold, T. S., “New Turner-Fairbank Alkali–Silica Reaction Susceptibility Test for Aggregate Evaluation,” *Transportation Research Record: Journal of the Transportation Research Board*, V. 2675, No. 9, Sept. 2021, pp. 798-808. doi: 10.1177/03611981211004584
 15. AASHTO TP 144-21, “Standard Method of Test for Determining the Potential Alkali–Silica Reactivity of Coarse Aggregates (TFHRC-TFAST),” American Association of State Highway and Transportation Officials, Washington, DC, 2021, 10 pp.
 16. AASHTO, “Standard Specifications for Transportation Materials and Methods of Sampling and Testing and AASHTO Provisional Standards,” 41st edition, American Association of State Highway and Transportation Officials, Washington, DC, 2021.
 17. Muñoz, J. F.; Balachandran, C.; Beyene, M.; and Arnold, T. S., “A Novel Approach for the Assessment of ASR Susceptibility of Concrete Mixtures in Airfield Pavements and Infrastructure,” Report No. FHWA-HRT-21-103, Federal Highway Administration, Washington, DC, 2021, 90 pp.
 18. Lindgård, J.; Nixon, P. J.; Borchers, I.; Schouenborg, B.; Wigum, B. J.; Haugen, M.; and Åkesson, U., “The EU ‘PARTNER’ Project—European Standard Tests to Prevent Alkali Reactions in Aggregates: Final Results and Recommendations,” *Cement and Concrete Research*, V. 40, No. 4, Apr. 2010, pp. 611-635. doi: 10.1016/j.cemconres.2009.09.004
 19. Nixon, P., and Fournier, B., “Assessment, Testing and Specification,” *Alkali–Aggregate Reaction in Concrete: A World Review*, I. Sims and A. Poole, eds., CRC Press, London, UK, 2017, pp. 33-61.
 20. Deschenes, R. A. Jr., and Hale, W. M., “Alkali–Silica Reaction in Concrete with Previously Inert Aggregates,” *Journal of Performance of Constructed Facilities*, ASCE, V. 31, No. 2, Apr. 2017, p. 04016084. doi: 10.1061/(ASCE)CF.1943-5509.0000946
 21. Muñoz, J. F.; Balachandran, C.; Lichtenwalner, R. L.; Li, Z.; and Arnold, T. S., “Optimization of Parameters of the New Tuner-Fairbank Alkali–Silica Reactivity Susceptibility Test (T-Fast),” *Journal of Testing and Evaluation*, V. 51, No. 2, Mar. 2023, 16 pp. doi: 10.1520/JTE20220033
 22. Folliard, K. J.; Barborak, R.; Drimalas, T.; Du, L.; Garber, S.; Ideker, J.; Ley, T.; Williams, S.; Juenger, M. C.; Fournier, B.; and Thomas, M. D. A., “Preventing ASR/DEF in New Concrete: Final Report,” Report No. FHWA/TX-06/0-4085-5, Center for Transportation Research, The University of Texas at Austin, Austin, TX, 2006, 266 pp.
 23. Ideker, J. H.; Bentivegna, A. F.; Folliard, K. J.; and Juenger, M. C. G., “Do Current Laboratory Test Methods Accurately Predict Alkali–Silica Reactivity?” *ACI Materials Journal*, V. 109, No. 4, July-Aug. 2012, pp. 395-402.
 24. AASHTO R 90-18 (2022), “Standard Practice for Sampling Aggregate Products,” American Association of State Highway and Transportation Officials, Washington, DC, 2018, 6 pp.
 25. AASHTO R 76-16 (2020), “Standard Practice for Reducing Samples of Aggregate to Testing Size,” American Association of State Highway and Transportation Officials, Washington, DC, 2016, 8 pp.
 26. Kim, T., and Olek, J., “Effects of Sample Preparation and Interpretation of Thermogravimetric Curves on Calcium Hydroxide in Hydrated Pastes and Mortars,” *Transportation Research Record: Journal of the Transportation Research Board*, V. 2290, No. 1, Jan. 2012, pp. 10-18. doi: 10.3141/2290-02
 27. Haxel, G. B.; Hedrick, J. B.; and Orris, G. J., “Rare Earth Elements—Critical Resources for High Technology,” Fact Sheet 087-02, U.S. Geological Survey, Reston, VA, 2002, <https://pubs.usgs.gov/fs/2002/fs087-02/>. (last accessed Sept. 26, 2023)
 28. Kaladharan, G.; Szeles, T.; Stoffels, S. M.; and Rajabipour, F., “Novel Admixtures for Mitigation of Alkali–Silica Reaction in Concrete,” *Cement and Concrete Composites*, V. 120, July 2021, Article No. 104028. doi: 10.1016/j.cemconcomp.2021.104028
 29. Broekmans, M. A. T. M., “Structural Properties of Quartz and Their Potential Role for ASR,” *Materials Characterization*, V. 53, No. 2-4, Nov. 2004, pp. 129-140. doi: 10.1016/j.matchar.2004.08.010
 30. Fernandes, I.; Broekmans, M. A. T. M.; Nixon, P.; Sims, I.; dos Anjos Ribeiro, M.; Noronha, F.; and Wigum, B., “Alkali–Silica Reactivity of Some Common Rock Types. A Global Petrographic Atlas,” *Quarterly Journal of Engineering Geology and Hydrogeology*, V. 46, No. 2, May 2013, pp. 215-220. doi: 10.1144/qjegh2012-065
 31. Rajabipour, F.; Giannini, E.; Dunant, C.; Ideker, J. H.; and Thomas, M. D. A., “Alkali–Silica Reaction: Current Understanding of the Reaction Mechanisms and the Knowledge Gaps,” *Cement and Concrete Research*, V. 76, Oct. 2015, pp. 130-146. doi: 10.1016/j.cemconres.2015.05.024
 32. Tiecher, F.; Florindo, R. N.; Vieira, G. L.; Gomes, M. E. B.; Dal Molin, D. C. C.; and Lermen, R. T., “Influence of the Quartz Deformation Structures for the Occurrence of the Alkali–Silica Reaction,” *Materials (Basel)*, V. 11, No. 9, Sept. 2018, Article No. 1692. doi: 10.3390/ma11091692
 33. Fanijo, E. O.; Kolawole, J. T.; and Almakrab, A., “Alkali–Silica Reaction (ASR) in Concrete Structures: Mechanisms, Effects and Evaluation Test Methods Adopted in the United States,” *Case Studies in Construction Materials*, V. 15, Dec. 2021, Article No. e00563. doi: 10.1016/j.cscm.2021.e00563
 34. Katayama, T., “A Critical Review of Carbonate Rock Reactions—Is Their Reactivity Useful or Harmful?” *Proceedings of the 9th International Conference on Alkali–Aggregate Reaction*, A. B. Poole, ed., London, UK, July 1992, pp. 508-518.
 35. Katayama, T., “Modern Petrography of Carbonate Aggregates in Concrete—Diagnosis of So-Called Alkali–Carbonate Reaction and Alkali–Silica Reaction,” *Proceedings, Marc-André Bérbé Symposium on Alkali–Aggregate Reactivity in Concrete*, Montreal, QC, Canada, May 2006, pp. 423-444.
 36. Grattan-Bellew, P. E.; Mitchell, L. D.; Margeson, J.; and Min, D., “Is Alkali–Carbonate Reaction Just a Variant of Alkali–Silica Reaction ACR = ASR?” *Cement and Concrete Research*, V. 40, No. 4, Apr. 2010, pp. 556-562. doi: 10.1016/j.cemconres.2009.09.002
 37. Katayama, T., “The So-Called Alkali–Carbonate Reaction (ACR)—Its Mineralogical and Geochemical Details, with Special Reference to ASR,” *Cement and Concrete Research*, V. 40, No. 4, Apr. 2010, pp. 643-675. doi: 10.1016/j.cemconres.2009.09.020
 38. Gillott, J. E., “Petrology of Dolomitic Limestones, Kingston, Ontario, Canada,” *Geological Society of America Bulletin*, V. 74, No. 6, 1963, pp. 759-778. doi: 10.1130/0016-7606(1963)74[759:PODLKO]2.0.CO;2
 39. Marinoni, N., and Broekmans, M. A. T. M., “Microstructure of Selected Aggregate Quartz by XRD, and a Critical Review of the Crystallinity Index,” *Cement and Concrete Research*, V. 54, Dec. 2013, pp. 215-225. doi: 10.1016/j.cemconres.2013.08.007
 40. Rogers, C. A., “Multi-Laboratory Study of the Accelerated Mortar Bar Test for Alkali–Silica Reaction,” *Proceedings of the 10th International Conference on Alkali–Aggregate Reaction*, A. Shayan, ed., Melbourne, VIC, Australia, 1996, pp. 362-369.
 41. Fournier, B.; Chevrier, R.; DeGrosbois, M.; Lisella, R.; Folliard, K.; Ideker, J. H.; Shehata, M.; Thomas, M.; and Baxter, S., “The Accelerated Concrete Prism Test (60°C): Variability of the Test Method and Proposed

- Expansion Limits,” *Proceedings of the 12th International Conference on Alkali-Aggregate Reaction in Concrete*, Beijing, China, Oct. 15-19, 2004.
42. Sims, I., and Nixon, P. J., “Assessment of Aggregates for Alkali-Aggregate Reactivity Potential: RILEM International Recommendations,” *Proceedings*, 8th CANMET/ACI International Conference on Recent Advances in Concrete Technology, Montreal, QC, Canada, May-June 2006.
 43. FHWA-TFHRC Aggregate and Petrography Laboratory, “Petrographic Analyses Report of MassDOT ASR Study Aggregates,” Turner-Fairbank Highway Research Center, Federal Highway Administration, McLean, VA, 2022.
 44. Broekmans, M. A. T. M.; Fernandes, I.; and Nixon, P., “A Global Petrographic Atlas of Alkali-Silica Reactive Rock Types: A Brief Review,” *Proceedings of the 12th Euroseminar on Microscopy Applied to Building Materials*, B. Middendorf, A. Just, D. Klein, A. Glaubitt, and J. Simon, eds., Dortmund, Germany, Sept. 2009, pp. 39-50.
 45. CSA A23.1:19/CSA A23.2:19, “Concrete Materials and Methods of Concrete Construction/Test Methods and Standard Practices for Concrete,” CSA Group, Toronto, ON, Canada, 2019.
 46. Sibbick, R. G., and Page, C. L., “Threshold Alkali Contents for Expansion of Concretes Containing British Aggregates,” *Cement and Concrete Research*, V. 22, No. 5, Sept. 1992, pp. 990-994. doi: 10.1016/0008-8846(92)90123-D
 47. Lindgård, J.; Andic-Çakir, Ö.; Fernandes, I.; Rønning, T. F.; and Thomas, M. D. A., “Alkali-Silica Reactions (ASR): Literature Review on Parameters Influencing Laboratory Performance Testing,” *Cement and Concrete Research*, V. 42, No. 2, Feb. 2012, pp. 223-243. doi: 10.1016/j.cemconres.2011.10.004
 48. Thomas, M. D. A.; Fournier, B.; and Folliard, K. J., “Alkali-Aggregate Reactivity (AAR) Facts Book,” Report No. FHWA-HIF-13-019, Office of Pavement Technology, Federal Highway Administration, Washington, DC, 2013, 224 pp.
 49. Johnson, S., and Chau, K., “More U.S. Coal-Fired Power Plants are Decommissioning as Retirements Continue,” *Today in Energy*, U.S. Energy Information Administration, Washington, DC, July 26, 2019, <https://www.eia.gov/todayinenergy/detail.php?id=40212>. (last accessed Sept. 26, 2023)
 50. Kaladharan, G.; Gholizadeh-Vayghan, A.; and Rajabipour, F., “Review, Sampling, and Evaluation of Landfilled Fly Ash.” *ACI Materials Journal*, V. 116, No. 4, July 2019, pp. 113-122. doi: 10.14359/51716750
 51. Al-Shmaisani, S.; Kalina, R.; O’Quinn, K.; Jang, J. K.; Rung, M.; Ferron, R.; and Juenger, M., “Supplementary Cementitious Materials: Assessment of Test Methods for New and Blended Materials,” Report No. FHWA/TX-21/0-6966-1, Center for Transportation Research, The University of Texas at Austin, Austin, TX, 2021, 108 pp.

CALL FOR ACTION

ACI Invites You To...

**Share your
expertise**

Do you have EXPERTISE in any of these areas?

- BIM
- Chimneys
- Circular Concrete Structures Prestressed by Wrapping with Wire and Strand
- Circular Concrete Structures Prestressed with Circumferential Tendons
- Concrete Properties
- Demolition
- Deterioration of Concrete in Hydraulic Structures
- Electronic Data Exchange
- Insulating Concrete Forms, Design, and Construction
- Nuclear Reactors, Concrete Components
- Pedestal Water Towers
- Pipe, Cast-in-Place
- Strengthening of Concrete Members
- Sustainability

**Then become a REVIEWER for the
ACI Structural Journal or the *ACI Materials Journal*.**

**Become a
Reviewer for the
ACI Journals**

How to become a Reviewer:

1. Go to: <http://mc.manuscriptcentral.com/aci>;
2. Click on “Create Account” in the upper right-hand corner; and
3. Enter your E-mail/Name, Address, User ID and Password, and Area(s) of Expertise.

**Update your
Manuscript
Central user
account
information**

Did you know that the database for MANUSCRIPT CENTRAL, our manuscript submission program, is separate from the ACI membership database?

How to update your user account:

1. Go to <http://mc.manuscriptcentral.com/aci>;
2. Log in with your current User ID & Password; and
3. Update your E-mail/Name, Address, User ID and Password, and Area(s) of Expertise.

QUESTIONS?

E-mail any questions to Journals.Manuscripts@concrete.org.

American Concrete Institute

Always advancing



Title No. 120-M70

Corrosion Behavior of Conventional and Corrosion-Resistant Steel Reinforcements in High-Performance and Ultra-High-Performance Concrete

by Ben Wang, Abdeldjelil Belarbi, Mina Dawood, and Bora Gencturk

This paper presents the findings of an experimental study on the corrosion performance of both conventional and corrosion-resistant steel reinforcements in normal-strength concrete (NC), high-performance concrete (HPC), and ultra-high-performance concrete (UHPC) columns in an accelerated corrosion-inducing environment for up to 24 months. Half-cell potential (HCP), linear polarization resistance (LPR), and electrochemical impedance spectroscopy (EIS) methods were used to assess the corrosion activities and corrosion rates. The reinforcement mass losses were directly measured from the specimens and compared to the results from electrochemical corrosion rate measurements. It was concluded that UHPC completely prevents corrosion of reinforcement embedded inside, while HPC offers higher protection than NC in the experimental period. Based on electrochemical measurements, the average corrosion rate of mild steel and high-chromium steel reinforcement in NC in 24 months were, respectively, 6.6 and 2.8 times that of the same reinforcements in HPC. In addition, corrosion-resistant steel reinforcements including epoxy-coated reinforcing bar, high-chromium steel reinforcing bar, and stainless-steel reinforcing bar showed excellent resistance to corrosion compared to conventional mild steel reinforcement. There was no active corrosion observed for epoxy-coated and stainless steel reinforcements during the 24 months of the accelerated aging; the average corrosion rateS of high-chromium steel was 50% of that of mild steel in NC based on the electrochemical corrosion measurements; and the average mass loss of high-chromium steel was 47% and 75% of that of mild steel in NC and HPC, respectively. The results also showed that the LPR method might slightly overestimate the corrosion rate. Finally, pitting corrosion was found to be the dominant type of corrosion in both mild and high-chromium steel reinforcements in NC and HPC columns.

Keywords: corrosion; high-performance concrete (HPC); mass loss; steel reinforcement; ultra-high-performance concrete (UHPC).

INTRODUCTION

The corrosion of reinforcing bars is a major problem for reinforced concrete (RC) structures globally, particularly for structures in marine environments and bridges exposed to deicing chemicals. Studies have revealed that chloride attack is the most common cause of the initiation of reinforcement corrosion (ACI Committee 222 2001). Concrete is alkaline in nature with a pore solution pH of 12 to 13, which creates a passive film and protects the reinforcing bars from corrosion. Once chloride penetrates the concrete cover and reaches a specific concentration (chloride threshold), the passive film on the reinforcement surface is damaged locally. Once the passive film breaks down, reinforcement

corrosion initiates in the presence of oxygen and water, followed by the consumption of virgin steel and the production of less-dense corrosion products. The corrosion products—such as ferrous hydride, ferric hydroxide, and ferric oxide—have volumes that are two to 10 times that of virgin steel. The volume expansion creates pressure within the concrete, causing concrete cracking, and eventually leading to concrete spalling around the reinforcing bars.

One way to enhance the durability of RC structures in corrosive environments is through the use of corrosion-resistant reinforcing steels and high-performance concretes (HPCs). These corrosion-resistant steel reinforcements include various types of epoxy-coated (EC), high-chromium (HC), and stainless (SS) steel reinforcements. These corrosion-resistant reinforcements either use physical coatings to limit the access of moisture and oxygen or alter the chemical compositions of steel to improve the corrosion resistance. Several studies examined the performance of these corrosion-resistant reinforcements in conventional normal-strength concrete (NC). Results indicated that EC, HC, and SS steel reinforcement exhibit high corrosion resistance (Cui 2003; Darwin et al. 2013; Hansson et al. 2007; Ji 2005; Rizkalla et al. 2005; Wang et al. 2022).

HPCs show improved durability and mechanical properties compared to NC. In recent years, HPC and ultra-high-performance concrete (UHPC) have been developed and used in infrastructure projects. HPC is defined by ACI Committee 363 (2010) as "...a concrete meeting special combinations of performance and uniformity requirements that cannot always be achieved routinely using conventional constituents and normal mixing, placing, and curing practice...," while UHPC is generally considered to have a compressive strength greater than 150 MPa (Graybeal 2006).

Studies have shown that HPC has better durability and corrosion resistance compared to NC. HPC is achieved through a low water-binder ratio (w/b) and the use of supplementary cementitious materials. The reduced water content and the pozzolanic reactions from the supplementary materials result in a denser matrix with low permeability, which significantly delays chloride penetration and reinforcement

corrosion rates. Researchers have conducted several studies to investigate the durability and corrosion resistance of HPC and compared the reinforcement corrosion characteristics of steel reinforcing bars in NC and HPC (Aïtcin 2003; El-Gelany 2001; Gowripalan and Mohamed 1998; Hansson et al. 2006; Ismail and Ohtsu 2006; Ismail and Soleymani 2002; Jaffer 2007; Lopez-Calvo et al. 2017, 2018; Nazim 2017; Presuel-Moreno et al. 2018; Soleymani and Ismail 2004; Tan 2015; Wang 2019). Gowripalan and Mohamed (1998) investigated the effectiveness of HPC in reducing the corrosion of conventional mild steel (MS) and galvanized steel. Silica fume was used to replace 10% of cement in HPC mixtures with water-cement ratios (w/c) of 0.25 and 0.35. The authors performed the rapid chloride-ion penetration test (RCPT) (ASTM C1202 2012), half-cell potential (HCP) test, and pH tests to evaluate the corrosion performance. RCPT test results showed that the charge passed through HPC at different ages (7, 28, 56, and 90 days) were much lower (0.05 to 0.5 times) than that in NC ($w/c = 0.45$ and 0.55), indicating that HPC reduces chloride-ion penetration significantly. HCP results showed that corrosion of both mild and galvanized steel reinforcements in NC started earlier than that in HPC. Cracking was observed in both NC and HPC after the HCP was lower than the assumed threshold of -350 mV. The findings also indicated that sufficient cover thickness was necessary for HPC, especially for structures in aggressive environments. Galvanized steel also delays the initiation of chloride-induced corrosion. Hansson et al. (2006) investigated the influence of concrete types and properties on microcell and macrocell corrosion rates. Three concrete mixtures were tested: NC ($w/c = 0.43$, 28-day concrete compressive strength $f'_c = 41.1$ MPa), HPC with 25% slag ($w/b = 0.35, f'_c = 59.5$ MPa), and HPC with 25% fly ash ($w/b = 0.35, f'_c = 59.3$ MPa). The specimens were made according to ASTM G109 (2013) and they were exposed to 2 weeks of ponding with 3% NaCl solution followed by 2 weeks of drying for 180 weeks. The linear polarization resistance (LPR) method was used to measure corrosion rates over time. It was found that the electrical resistivity of HPC was more than 5.5 times that of NC. In addition, the electrical charge passed through HPC in 6 hours per ASTM C1202 was less than 0.17 of that of NC at both 28 and 56 days. These results proved that HPC has significantly better corrosion resistance than NC. Moreover, the results of the experimental program indicated that microcell corrosion is the major mechanism of reinforcement corrosion in concrete, and that microcell corrosion is more dominant in HPC than NC due to the high resistance of HPC to ionic flow. Corrosion rate measurements showed that the macrocell corrosion rate of steel in HPC was three to four orders of magnitude lower than that in NC, while the microcell corrosion rate in HPC was just one order of magnitude lower than that in NC.

Apart from its exceptional mechanical strength, UHPC exhibits remarkable durability characteristics due to its unique composition of materials and carefully crafted mixture proportions. The dense cementitious matrix of UHPC results in low permeability, offering high resistance against moisture penetration, chloride ingress, acid exposure,

carbonation, and freezing-and-thawing cycles. This has been verified through many studies that have tested the durability of UHPC made using various ingredients in various environments over the past two decades (Abbas et al. 2016; Alkaysi et al. 2016; Batoz and Behloul 2009; Ferdosian and Camões 2016; Ghafari et al. 2015; Graybeal 2005; Graybeal and Hartman 2003; Graybeal and Tanesi 2007; Pernicová 2014; Piérard et al. 2009, 2013; Shareef 2013; Sharma et al. 2018; Sritharan 2015). Graybeal and Hartman (2003), Graybeal (2005), and Graybeal and Tanesi (2007) investigated the strength and durability of UHPC mixtures ($w/b = 0.15, f'_c > 186$ MPa) that were cured in steam or ambient environments. The UHPC mixtures in these references were made of portland cement, silica fume, fine sand, ground quartz, high-range water-reducing admixture, and 2% (by volume) steel fibers with 0.2 mm diameter and 13 mm length. The durability investigations included chloride-ion penetration, abrasion, alkali-silica reaction (ASR), freezing-and-thawing, and scaling tests. Results of the RCPT per ASTM C1202 showed that the rapid chloride-ion permeability of all UHPC mixtures was very low or negligible and the total Coulombs passed in the tests (recorded at 1-minute intervals over the 6-hour time frame) were as low as 18 for UHPC under steam curing. Results of the chloride penetration test per AASHTO T 259 (2002) showed that the average chloride content for all mixtures was less than 0.05 kg/m³ of concrete, which was below the minimum accuracy threshold of this test method, indicating that UHPC shows excellent resistance to chloride penetration. Results of the abrasion resistance test per ASTM C944/C944M (2012) showed that the air-cured UHPC had a higher weight loss of 1.18 to 2.1 g per abrading, while steam-cured UHPC mixtures only had 0.08 to 0.34 g per abrading. Results of the ASR test per ASTM C1260 (2014) showed that the ASR expansions of all mixtures were in the range from 0.004 to 0.023% (14 to 28 days), which was approximately an order of magnitude below the innocuous alkali-silica resistance defined by the specifications. In addition, the results of the freezing-and-thawing resistance tests per ASTM C666/C666M (2015) and scaling resistance tests per ASTM C672/C672M (2012) indicated that all UHPC mixtures had great resistance to both freezing and thawing and scaling. Based on these test results, it was concluded that UHPC mixtures exhibit superior durability, and steam-cured UHPC sections are immune to chloride-ion penetration, scaling, and freezing-and-thawing damage. Piérard et al. (2009) studied the durability and cracking of UHPC ($w/b = 0.18, f'_c = 148$ MPa) without fibers. The UHPC mixture was made of CEM I 42.5R cement (BS EN 197-1 2011), silica fume, quartz sand (up to 1 mm), porphyry aggregate (1 to 3 mm), and high-range water-reducing admixture. NC ($w/b = 0.5, f'_c = 51$ MPa) and HPC ($w/b = 0.33, f'_c = 101$ MPa) were also included for comparison. Two curing methods were considered: moist curing and air curing. Resistance to carbonation and chloride ingress were investigated. Accelerated carbonation test results showed that the carbonation rate of moist-cured NC, HPC, and UHPC was 0.95, 0.2, and 0.03 mm/ $\sqrt{\text{day}}$ respectively, while the carbonation rate of air-cured NC, HPC, and UHPC was 1.42, 0.55, and 0.06 mm/ $\sqrt{\text{day}}$ respectively, indicating

Table 1—Mixture proportions of concrete by weight

Concrete	Cement, Type I/II	Fly ash, Type F	Silica fume	Gravel	Fine sand	Silica sand 1	Silica sand 2	Silica powder	High-range water- reducing admixture	Water	CaCl ₂ flakes (85%)
NC	1	—	—	2.04	2.49	—	—	—	0.0075	0.5	0.04
HPC	1	0.25	—	2.88	2.88	—	—	—	0.0125	0.56	0.04
UHPC	1	0.3	0.31	—	—	0.79	0.46	0.31	0.1	0.31	0.02

that the carbonation rate of UHPC was one order of magnitude lower than that of NC and HPC. Results of the 56-day accelerated chloride diffusion test per NT Build 443 (1995) showed that the effective chloride diffusion coefficient of moist-cured NC, HPC, and UHPC was 15.0×10^{-12} , 1.0×10^{-12} , and $0.4 \times 10^{-12} \text{ m}^2/\text{s}$, respectively, while the effective chloride diffusion coefficient of air-cured NC, HPC, and UHPC was 22.2×10^{-12} , 2.1×10^{-12} , and $0.4 \times 10^{-12} \text{ m}^2/\text{s}$, respectively, indicating that UHPC has considerably better chloride diffusion resistance than NC and HPC. In addition, the authors investigated the cracking tendency of UHPC under restrained conditions by performing shrinkage measurements and ring tests. The results of these tests showed that UHPC has higher autogenous shrinkage, which potentially could lead to cracking. The authors also indicated that by adding steel fibers to UHPC mixtures, resistance of UHPC to microcracks caused by restricted shrinkage can be improved.

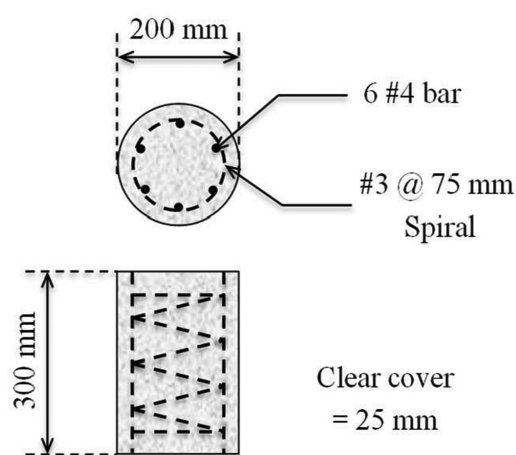
Despite previous studies having demonstrated the improved durability and corrosion resistance of HPC and UHPC, as well as that of corrosion-resistant reinforcing steels, there remains a lack of a systematic study of the corrosion behavior of different types of reinforcements in different types of concrete. This study aims to directly compare the corrosion performance of various reinforcements, including conventional MS, EC, HC, and SS steel, when embedded in different types of concretes, including NC, HPC, and UHPC.

RESEARCH SIGNIFICANCE

The corrosion of steel reinforcement in RC structures has been a major issue globally. To address this, two practical solutions are the use of more durable concretes and corrosion-resistant reinforcements. This study directly compares the corrosion resistance of various reinforcements, including conventional MS, EC, HC, and SS steel, in different types of concretes (NC, HPC, and UHPC) for large-scale specimens in circular column configuration. The results from this research are expected to promote the wider use of corrosion-resistant reinforcements and more durable concretes, leading to the creation of more sustainable and long-lasting civil infrastructure.

EXPERIMENTAL INVESTIGATION

The corrosion resistance of four commonly used reinforcements—MS, EC, HC, and SS steel—were investigated in three different types of concrete with varying levels of strength and durability—that is, NC, HPC, and UHPC. MS reinforcement in NC was used as a reference for comparison. Circular columns with both longitudinal and transverse

**Fig. 1—Schematic of column specimens.**

reinforcements were used to simulate real RC structures. The HCP, LPR, and electrochemical impedance spectroscopy (EIS) were used to assess the corrosion activity and corrosion rate, along with direct reinforcement mass loss measurements of the corroded reinforcements after accelerated aging exposure.

Materials

The proportions of the concrete mixtures are presented in Table 1. The compressive strengths at 28 days for NC, HPC, and UHPC were 42.7, 69.6, and 150 MPa, respectively. In this study, CaCl₂ flakes were added to the concrete mixtures directly during mixing to accelerate the corrosion process. The four types of reinforcement studied were ASTM A615/A615M Grade 60 conventional MS reinforcement, ASTM A775/A775M Grade 60 EC reinforcement, ASTM A1035/A1035M Grade 100 HC steel reinforcement, and ASTM A995/A995M Grade 75 SS reinforcement (Type 2304 SS). The chemical compositions of these reinforcements are given in Tables 2 and 3.

Specimens

Column specimens, as shown in Fig. 1, were selected in this experimental program to imitate real-life RC structures. Different combinations of three different types of concrete and four types of reinforcements were investigated in the experimental program, as shown in Table 4. A volumetric transverse reinforcement ratio of 2.45% and six longitudinal bars were used to ensure the column specimen with traditional materials (NC+MS) complies with ACI 318-19 recommendations (ACI Committee 318 2019). The reinforcement arrangement in all column specimens was identical to eliminate any impact on corrosion behavior. A total

Table 2—Chemical composition of transverse steel reinforcing bars

Element, wt. %	C	Mn	P	S	Si	Cu	Ni	Cr
MS	0.410	0.800	0.012	0.029	0.210	0.290	0.200	0.170
EC	0.440	0.630	0.009	0.050	0.180	0.360	0.140	0.140
HC	0.100	0.670	0.008	0.010	0.390	0.110	0.080	9.81
SS	0.016	1.500	0.031	0.0003	0.570	0.270	4.230	22.58
Element, wt. %	V	Mo	Sn	N	Cb	Co	Al	CE
MS	0.002	0.041	0.008	—	—	—	0.002	—
EC	—	0.034	0.011	—	0.001	—	0.001	—
HC	0.020	0.020	0.008	0.012	—	—	—	1.200
SS	—	0.180	—	0.128	—	0.080	—	—

Table 3—Chemical composition of longitudinal steel reinforcing bars

Element, wt. %	C	Mn	P	S	Si	Cu	Ni	Cr
MS	0.370	0.970	0.014	0.019	0.210	0.320	0.180	0.220
EC	0.430	0.790	0.014	0.037	0.180	0.360	0.130	0.170
HC	0.110	0.640	0.007	0.009	0.300	0.150	0.100	9.71
SS	0.017	1.800	0.030	0.0009	0.470	0.240	3.740	22.58
Element, wt. %	V	Mo	Sn	N	Cb	Co	Al	CE
MS	0.004	0.039	—	—	—	—	—	—
EC	0.001	0.046	0.010	—	0.002	—	0.002	—
HC	0.020	0.020	0.011	0.013	—	—	—	1.190
SS	—	0.270	—	0.166	—	0.100	—	—

Table 4—Test matrix

Conc.\Reinf.	MS	EC	HC	SS
NC	Two specimens—exposure of 12 and 24 months, respectively, for each concrete and reinforcement combination			
HPC				
UHPC				

of 24 specimens were made and subjected to aggressive environmental exposure for up to 24 months to evaluate the corrosion performance of the reinforcements and measure the mass loss due to corrosion. The initial weight of each longitudinal and transverse reinforcing bar was recorded and then secured in a cage for concrete casting. Plastic ties, rather than steel wires, were used to tie the longitudinal and transverse bars, avoiding any influence on reinforcement corrosion. Copper wires were connected to both the longitudinal and transverse reinforcements for electrochemical corrosion rate measurements, and the connection areas were sealed with electrical tape.

Test procedures

First, column specimens were fabricated at a concrete plant. After a 28-day curing period in ambient environment, all specimens were put into an aggressive environment (refer to the next section) for 12 months. Once the first 12 months of exposure were completed, the reinforcing bars were carefully extracted from the columns to avoid damaging the bars. These reinforcing bars were then cleaned according to ASTM G1 (2003), and the mass loss was measured. The

remaining 12 specimens were kept in the accelerated environment for an additional 12 months. After 24 months of exposure, the reinforcing bars were extracted in a similar way, and the mass loss was measured and recorded.

Environmental conditions

In this study, the process of corrosion was accelerated by immersing the concrete columns in a heated 5% (wt. %) chloride solution for 9 months. The temperature was maintained at 40°C. The solution was drained and the specimens were allowed to dry for 2 days in every 4-day cycle. Starting from the tenth month, the wetting-and-drying cycle was increased to every 4 hours (2 hours wet, 2 hours dry) to further increase the rate of corrosion.

Electrochemical corrosion measurements

The corrosion of reinforcement in the columns was monitored using a potentiostat. Three corrosion evaluation techniques were used: HCP, LPR, and EIS. HCP tests were used to assess the initiation of corrosion, while the LPR tests were used to measure corrosion rates of MS, HC, and SS reinforcements. EIS tests were used to measure the corrosion rate of EC due to the limitation of LPR. Figure 2 illustrates the three electrodes necessary for LPR and EIS tests. In the test setup, reinforcing bars within the column served as the working electrodes (WE), with a copper/copper sulfate reference electrode (RE) probe acting as the RE and placed on top of the concrete through a wet sponge to maintain an electrical connection. A titanium mesh surrounding the surface of the columns was used as the counter electrode

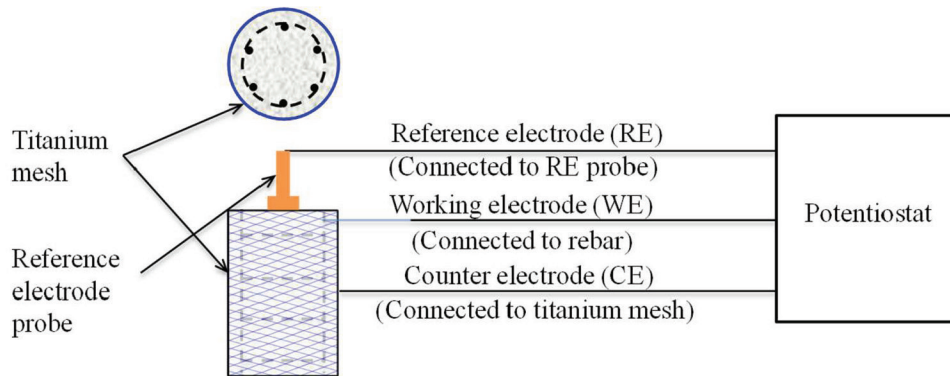


Fig. 2—Schematic of LPR/EIS test setups.

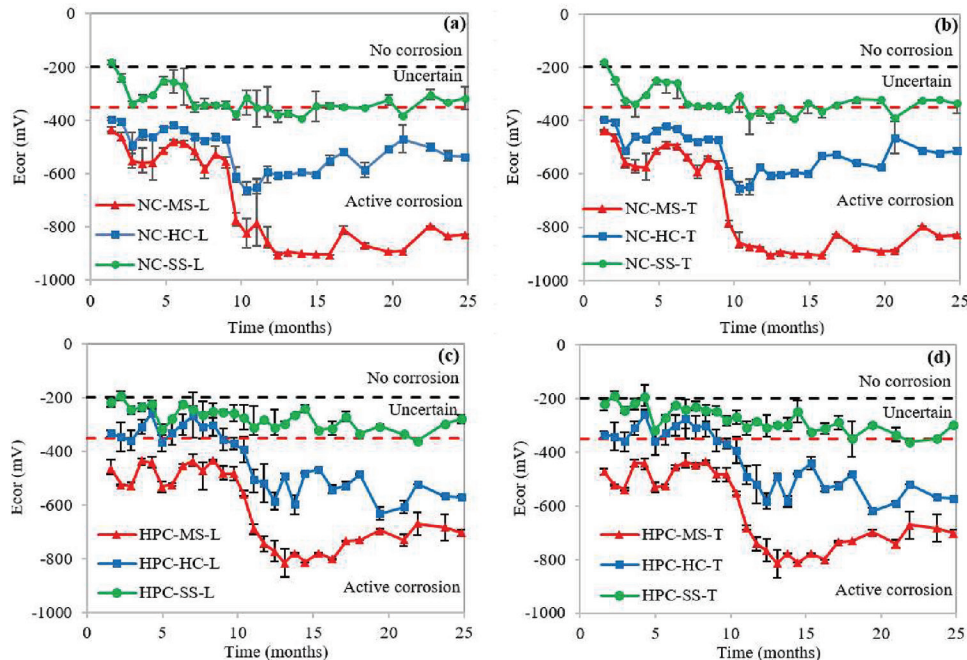


Fig. 3—HCP measurements of reinforcements in columns: (a) NC longitudinal; (b) NC transverse; (c) HPC longitudinal; and (d) HPC transverse reinforcement.

(CE), with an electrical connection maintained by a damp cloth between the titanium mesh and the column surface.

EXPERIMENTAL RESULTS AND DISCUSSION

Half-cell potential

The HCP results of MS, HC, and SS in the NC, HPC, and UHPC columns are presented in Fig 3. The data shown in the figure are the average of four readings taken from two columns and two readings from different locations of one column during 2 to 13 months and 14 to 25 months, respectively. The vertical error bars in the figure indicate the range of the minimum and maximum values among all the readings at a given time. The x-axis represents the time in months and the y-axis represents the HCP relative to the reference electrode. The dashed lines in the figure divide the “no corrosion,” “uncertain,” and “active corrosion” zones according to ASTM C876 (2015), with values of –200 and –350 mV, respectively.

It is seen in Fig. 3 that in both NC and HPC columns, the HCP values from high to low follow the order of SS, HC,

and MS, indicating the order of corrosion activity from low to high. The HCP values of MS and HC were always below –350 mV and in the “active corrosion” region, indicating that NC and even HPC were not able to provide adequate protection to the reinforcement under the aggressive environmental conditions of this study. Furthermore, the HCP values of MS and HC decreased significantly in the ninth month and remained relatively stable thereafter, indicating significant corrosion activity between 10 and 25 months. Additionally, no significant differences in HCP values were observed between the longitudinal and transverse reinforcements in both NC and HPC columns. For SS, the HCP values were always close to or higher than –350 mV, indicating a very minor possibility of active corrosion.

The HCP values for MS, HC, and SS in the UHPC columns were consistently above –350 mV, indicating a low likelihood of active corrosion. This demonstrates that UHPC provides exceptional durability and effectively protects the reinforcement from corrosion.

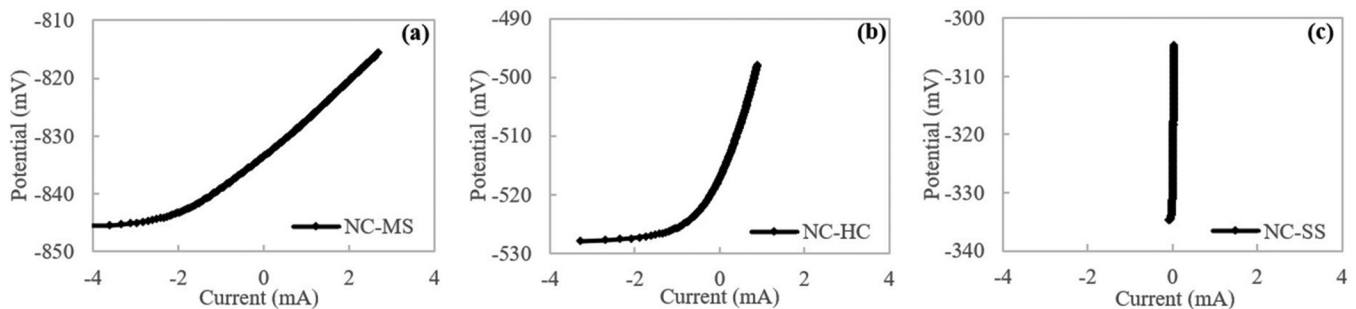


Fig. 4—LPR plot examples of reinforcement in NC at 24 months of exposure: (a) MS; (b) HC; and (c) SS.

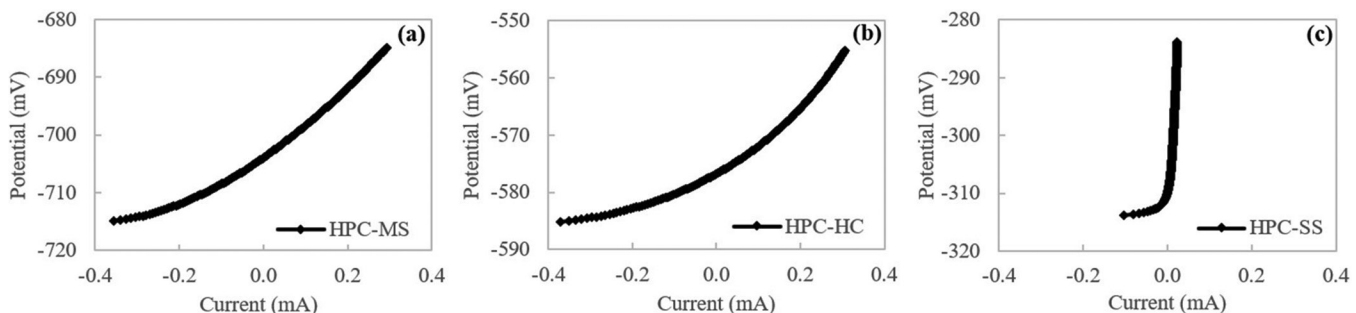


Fig. 5—LPR plot examples of reinforcement in HPC at 24 months of exposure: (a) MS; (b) HC; and (c) SS.

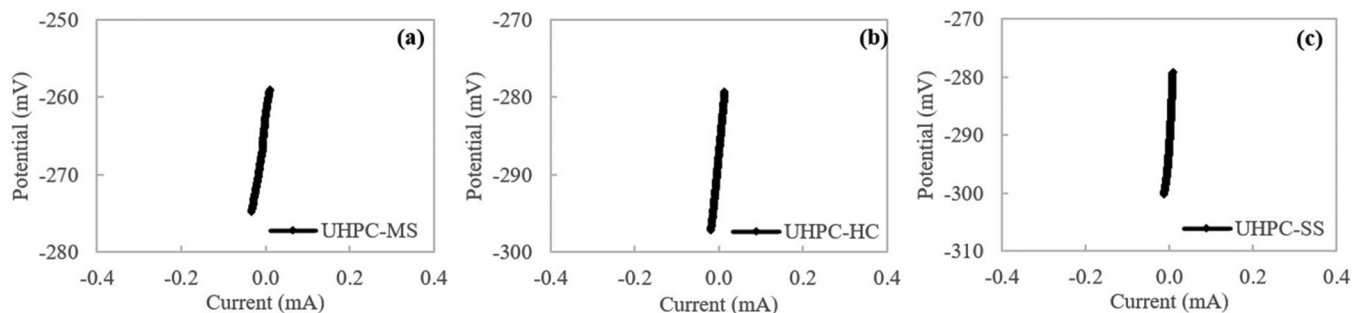


Fig. 6—LPR plot examples of reinforcement in UHPC at 24 months of exposure: (a) MS; (b) HC; and (c) SS.

Corrosion rate

The corrosion rates of bare reinforcement were determined using LPR tests. Figures 4, 5, and 6 show the representative LPR plots of MS, HC, and SS in NC, HPC, and UHPC columns, respectively, after 24 months of accelerated aging exposure. In the plots, the x-axis represents the corrosion current and the y-axis represents the corrosion potential relative to the copper/copper sulfate RE. The slope of the LPR curves near the corrosion potential (where the corrosion current is zero) indicates the polarization resistance. Figure 4 demonstrates that in NC columns, the MS curve has the smallest slope, while the SS curve has the largest slope among the three curves, indicating that the polarization resistance from large to small follows the order of SS, HC, and MS. In HPC columns, as shown in Fig. 5, the slopes of the MS and HC LPR plots are similar, while the slope of the SS curve is much larger, meaning that SS has a much higher polarization resistance than MS and HC, and MS and HC have close polarization resistances. In the UHPC columns, as shown in Fig. 6, all slopes were very large and the polarization resistances were very high, indicating negligible corrosion rates.

The corrosion rate of the EC reinforcement was determined using the EIS tests. Figure 7 presents an example of the EIS plot of EC in both NC and HPC. The Nyquist plot, as depicted in Fig. 7(a), has the real part of the impedance (Z_{real}) on the x-axis and the imaginary part of the impedance (Z_{img}) on the y-axis. The magnitude of the impedance ($|Z|$) is represented by the distance between the plotted point and the origin, and the slope of the line connecting the plotted point to the origin represents the phase shift (Φ). In the Bode plot, shown in Fig. 7(b), the x-axis is the applied alternating current (AC) frequency (w), the magnitude of the impedance ($|Z|$) is on the left y-axis, and the phase shift (Φ) is on the right y-axis. The electrical equivalent circuit (EEC) shown in Fig. 8 was used to fit the EIS data in this study. The EEC includes the resistance of the concrete (R_s), the resistance and capacitance of the epoxy-coating pores (R_c and CPE_c), the resistance and capacitance of the film on the reinforcement surface (R_{layer} and CPE_{layer}), the capacitance of the double layer (CPE_{dl}), and the polarization resistance (R_{ct}). It should be noted that in the concrete-reinforcement system, the coating capacitance, film capacitance, and electric double-layer capacitance often deviate from pure capacitance due to

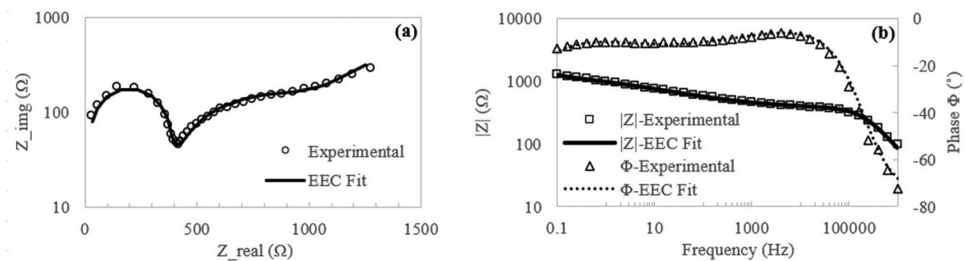


Fig. 7—EIS data fitting example of EC in: (a) Nyquist plot; and (b) Bode plot.

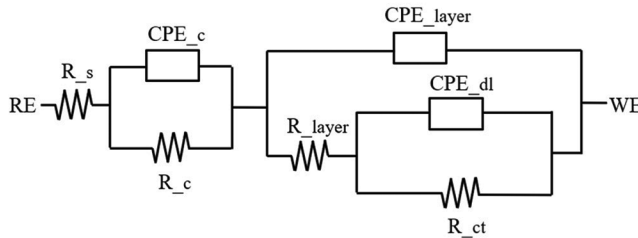


Fig. 8—Electrical equivalent circuit used in EIS fitting.

the dispersion effect. As a result, the constant phase element (CPE) was used in the EEC model instead of pure capacitance. The results of the fitting showed that the proposed EEC fits the experimental data well, as illustrated in Fig. 7.

Once the polarization resistances were obtained, the corrosion rate of the reinforcement was determined according to ASTM G102 (1989). The results are shown in Fig. 9, which summarizes the corrosion rates obtained from LPR tests on MS, HC, and SS in NC and HPC columns. The average corrosion rate values displayed in the figure are based on the average of four measurements on two columns and two measurements on one column during 2 to 13 months and 14 to 25 months, respectively. The error bars in the figure indicate the range between the minimum and maximum values among all the measurements taken at a certain time. On the x-axis, the time is measured in months, while the y-axis represents the corrosion rate in mils per year (mpy). The dashed lines in the figure correspond to the dividing values for low, moderate, and high corrosion rates according to Cady and Gannon (1993) and Ji (2005) with values of 0.046, 0.228, and 0.456 mpy, respectively.

As seen in Fig. 9, MS in NC columns underwent severe corrosion in the accelerated aging environment. The first measurement of the corrosion rate at the end of the first month was approximately 0.5 mpy, and by the end of the 24-month exposure, the rate had increased fourfold to over 2 mpy. The maximum corrosion rate recorded during the entire period was 2.9 mpy. Meanwhile, HC reinforcements showed similar corrosion rates before the seventh month but then significantly decreased. After the 12th month, the corrosion rates of HC were less than half those of MS. On the other hand, the corrosion rates of SS reinforcements were negligible throughout the entire exposure period. Additionally, it was discovered that the transverse reinforcements of MS and HC experienced slightly higher corrosion rates than the longitudinal reinforcements. This is because the transverse reinforcements were closer to the concrete cover and

had better access to moisture, oxygen, and the accelerated corrosion environment. Furthermore, as shown in Fig. 10, more corrosion was observed on the outer surface of the transverse reinforcements for the same reason.

In HPC columns, both MS and HC reinforcements showed low to moderate corrosion rates, with values less than 0.5 mpy at all times. These rates were significantly lower than those of MS and HC in NC columns, indicating the better protection provided by HPC. There was no significant difference between the corrosion rates of MS and HC throughout the entire accelerated aging exposure, which may be due to the protection of HPC making the controlling factor for corrosion the access to moisture and oxygen, rather than the reinforcement's corrosion resistance. Additionally, longitudinal and transverse reinforcements showed similar corrosion rates in HPC due to the overall low corrosion rates of the reinforcements well-protected by HPC cover. The corrosion rates of SS reinforcements remained negligible throughout the entire period, as they did in NC.

In NC and HPC columns, the EIS tests revealed that the EC reinforcements had negligible corrosion rates, owing to the effective protection provided by the epoxy coating that prevented the steel reinforcements from being exposed to moisture and oxygen, which are the essential elements for corrosion. Additionally, throughout the entire exposure period, the corrosion rates of all four types of reinforcements in UHPC columns were always negligible, as the high packing density of the UHPC effectively inhibited the diffusion of oxygen and moisture, which are crucial factors for corrosion.

In summary, the results of the electrochemical corrosion rate measurements demonstrated that none of the EC and SS reinforcements in NC and HPC, and all the reinforcements in UHPC showed signs of corrosion during the 24-month accelerated corrosion exposure. The corrosion rates of MS and HC in NC were much higher compared to the same reinforcement types in HPC during the same measurement periods. On average, the corrosion rate of MS and HC in NC was 6.6 and 2.8 times, respectively, that of the same reinforcement types in HPC over the 24-month exposure period. UHPC showed the best corrosion resistance, followed by HPC, while NC exhibited the weakest performance. Additionally, the results showed that MS had a higher corrosion rate than HC in NC, with the average corrosion rate of MS being twice that of HC. However, in HPC, the average corrosion rates of MS and HC were almost the same, likely due to limited access to oxygen and moisture.

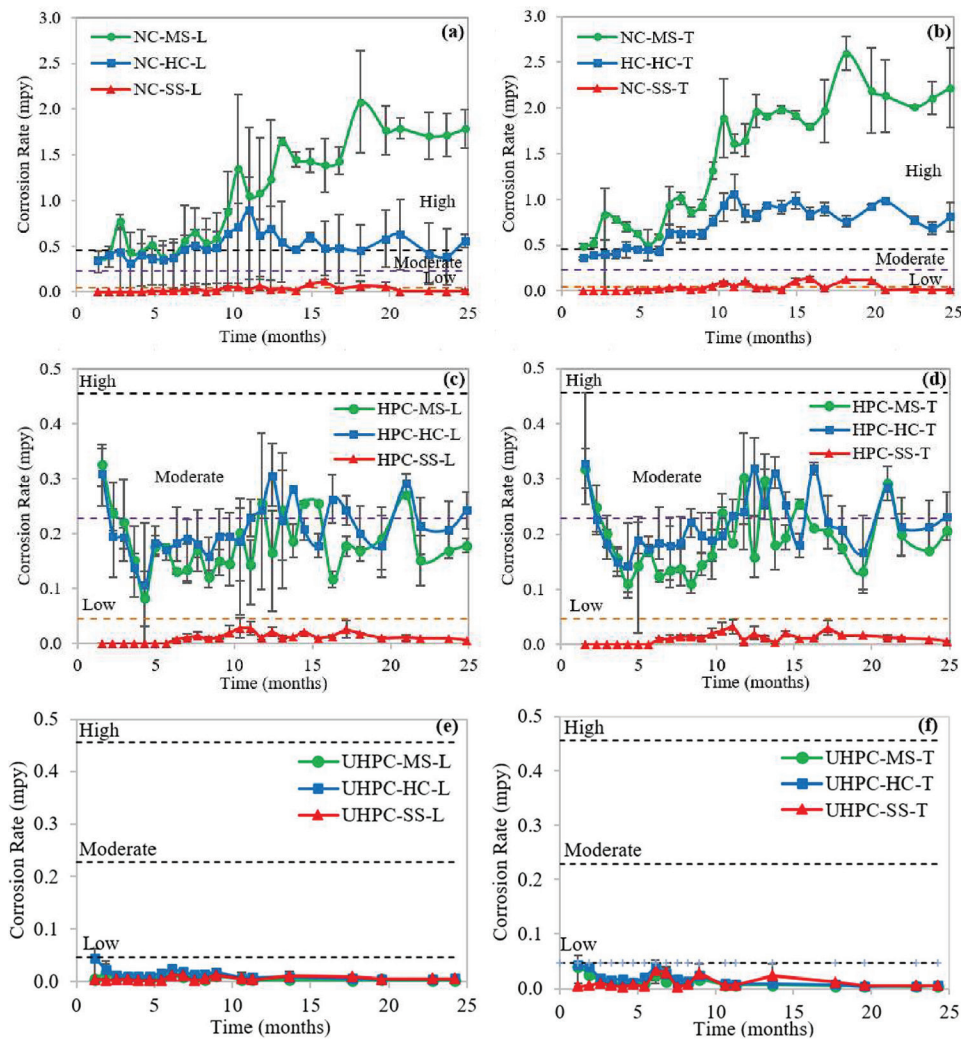


Fig. 9—LPR corrosion rates of reinforcement in columns: (a) NC longitudinal; (b) NC transverse; (c) HPC longitudinal; (d) HPC transverse; (e) UHPC longitudinal; and (f) UHPC transverse reinforcement.

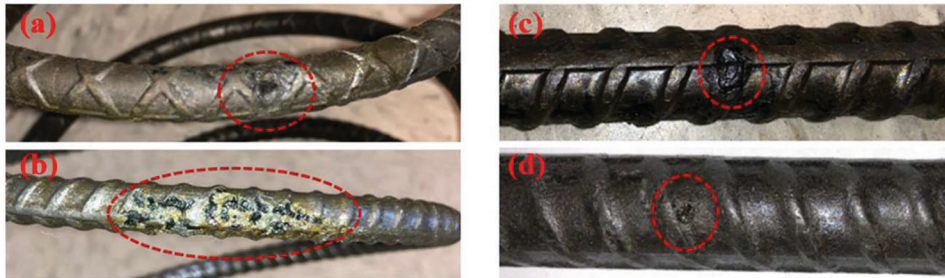


Fig. 10—Examples of pitting corrosion of reinforcement in HPC: (a) MS transverse; (b) HC transverse; (c) MS longitudinal; and (d) HC longitudinal reinforcement.

Reinforcement mass loss

At the end of 12 and 24 months of exposure, the reinforcing bars were carefully removed from the column specimens to prevent damage. These reinforcing bars were then cleaned according to ASTM G1, and the mass loss was measured. As depicted in Fig. 10, MS and HC in HPC columns also exhibited signs of pitting corrosion. Moreover, corrosion was evident only on one side of the reinforcing bars, the side facing the cover concrete, which was closer to the aggressive environment.

The results of the mass loss measurements of the column specimens after 12 and 24 months of accelerated corrosion exposure are presented in Fig. 11. The results showed negligible mass loss for EC and SS reinforcements, indicating that they remained free of corrosion even after 24 months of exposure to the aggressive environment. On the other hand, loss of mass was observed in MS and HC reinforcements. The mass losses of MS, both longitudinal and transverse reinforcements, were found to be higher than those of HC: the mass losses of HC were 44 to 54% (with an average of 47%) and 64 to 82% (with an average of 75%) of that

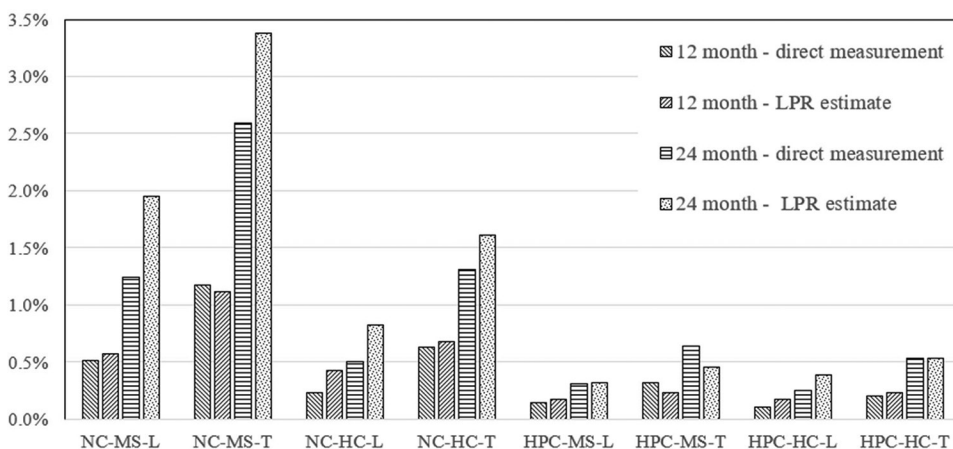


Fig. 11—Reinforcement mass loss in NC and HPC columns. (Note: L and T, respectively, indicate longitudinal and transverse reinforcement.)

of MS in NC and HPC columns, respectively. The results also indicated that the mass losses of MS and HC in NC after 24 months of exposure were 4.0 and 2.3 times, respectively, that of MS and HC in HPC. This can be attributed to the protection offered by HPC against the penetration of oxygen and moisture. The results also showed that the mass loss of transverse reinforcements were higher than those of longitudinal reinforcements, with the average mass loss of transverse reinforcements being 2.3 and 2.1 times that of longitudinal reinforcements in NC and HPC, respectively, due to the easier access of moisture and oxygen to transverse reinforcement. Finally, the findings indicated that the mass losses in the second 12 months (months 13 to 25) were slightly higher than twice those of the first 12 months (months 1 to 13), suggesting that corrosion in the second 12 months was more active than in the first 12 months. For UHPC specimens, no mass loss was observed in any of the four types of reinforcements, owing to the excellent protection offered by the UHPC cover, which has been demonstrated to have the highest durability.

The results from the mass loss measurements were compared with the mass loss estimations obtained from the electrochemical corrosion rate measurements using Faraday's law, which is expressed as

$$m = \frac{M \cdot I \cdot t}{n \cdot F} \quad (1)$$

where m is the mass loss of steel in grams; M is the atomic weight, which is 55.85 g/mol for iron; I is the current in amperes; t is the time in seconds; n is the number of valence electrons, which is 2 for iron; and F is Faraday's constant, which is 96,487 coulombs/mol.

Figure 11 presents the calculated mass loss from electrochemical corrosion rate measurements for the NC and HPC columns. There are differences between the mass loss directly measured from columns and the ones estimated from electrochemical measurements; the directly measured mass loss was 54 to 106% (with an average of 78%) and 60 to 142% (with an average of 97%) of the estimated mass loss in NC and HPC columns, respectively. The differences are attributed to three reasons. First, the directly measured

mass loss reflected the total impact of corrosion activities over the entire exposure period, while the estimated mass loss only represented the corrosion activities at the moment the corrosion rate measurements were taken. Second, it was noted that electrochemical methods may overestimate the corrosion rate (Alghamdi and Ahmad 2014; Zou et al. 2011). Alghamdi and Ahmad (2014) reported that the gravimetrically measured corrosion rate was on average 86% of the electrochemically measured rate, which agrees with the findings here. Lastly, corrosion activity may vary greatly in different parts of the same column and in different reinforcements in different columns.

CONCLUSIONS

An experimental study that directly compares the corrosion behavior of mild steel (MS), epoxy-coated steel (EC), high-chromium steel (HC), and stainless steel (SS) in normal-strength concrete (NC), high-performance concrete (HPC), and ultra-high-performance concrete (UHPC) in a chloride environment was performed. The research findings led to the following main conclusions:

1. UHPC proved to be highly durable, protecting the embedded reinforcements from any corrosion activity even after 24 months of accelerated corrosion exposure. HPC was also found to be more durable than NC, with the mass loss of MS and HC in HPC being 25 to 49% of that in NC.
2. EC and SS showed negligible mass loss even after 24 months in an aggressive environment.
3. HC was found to have better corrosion resistance than MS in NC. Based on the measurements after 24 months of exposure, the average corrosion rates of HC were 50% and 75% of that of MS in NC and HPC, respectively.
4. Transverse reinforcing bars were more susceptible to corrosion than longitudinal reinforcing bars, due to their higher exposure to chloride, moisture, and oxygen. Mass loss measurements revealed that the corrosion rates of longitudinal reinforcements were 48%, 39%, 49%, and 47% of those of transverse reinforcements for MS in NC, HC in NC, MS in HPC, and HC in HPC, respectively, after 24 months of accelerated aging exposure.
5. Pitting corrosion was found to dominate MS and HC in NC and HPC under a chloride attack environment.

6. Half-cell potential (HCP) was found to be a reliable indicator of corrosion activity, with results for MS, HC, SS reinforcements in all three types of concrete agreeing with the mass loss measurements.

7. Linear polarization resistance (LPR) tests were found to potentially overestimate corrosion activity. Results showed that the mass losses directly measured from columns were 78% and 97% of that estimated from the electrochemical corrosion rate measurements in NC and HPC, respectively. It is noted that the mass loss measured directly from the reinforcements in columns represents the cumulative mass loss over 24 months of exposure, while the mass loss estimated from electrochemical corrosion rate measurements only represent the instantaneous corrosion status at the time when these measurements were taken.

AUTHOR BIOS

Ben Wang is a Researcher at the University of Houston, Houston, TX, where he received his PhD in civil engineering. He received his BS and MS from Tongji University, Shanghai, China. His research interests include high-performance concrete (HPC), ultra-high-performance concrete (UHPC), corrosion-resistant reinforcement, durability of reinforced concrete, service life prediction, and life-cycle cost analysis of reinforced concrete structures.

Abdeldjalil Belarbi, FAccI, is a Hugh Roy and Lillie Cranz Cullen Distinguished Professor at the University of Houston. He is the current Chair of the ACI Technical Activities Committee's Subcommittee on ACI/ASCE-SEI Joint Committees; past Chair of Joint ACI-ASCE Committee 445, Shear and Torsion, and ACI Subcommittee 440-E, FRP-Prof Education; and a member of ACI Committees 341, Performance-Based Seismic Design of Concrete Bridges, and 440, Fiber-Reinforced Polymer Reinforcement; and ACI Subcommittee 318-E, Section and Member Strength. His research interests include constitutive modeling, analytical and experimental investigations of reinforced and prestressed concrete structures, as well as the use of advanced materials for new construction and rehabilitation of existing infrastructure.

Mina Dawood is an Associate Professor at the University of Houston and an Associate Editor of the ASCE Journal of Composites for Construction. His research interests include the development and implementation of new materials, systems, and techniques in structural applications for both repair/rehabilitation and new construction.

Bora Gencturk is an Associate Professor in the Sonny Astani Department of Civil and Environmental Engineering and the Director of the Structures and Materials Research Laboratory at the University of Southern California, Los Angeles, CA. Gencturk is a member of ACI Committees 341, Performance-Based Seismic Design of Concrete Bridges, and 440, Fiber-Reinforced Polymer Reinforcement. His research interests include the durability and extreme event resilience of reinforced concrete structures with an emphasis on application of high-performance materials.

ACKNOWLEDGMENTS

The funding for this research was provided by the National Priorities Research Program of the Qatar National Research Fund (a member of the Qatar Foundation) under award No. NPRP 7-410-2-169. The statements made herein are solely the responsibility of the authors and do not necessarily reflect the opinions of the sponsor.

REFERENCES

AASHTO T 259, 2002, "Standard Method of Test for Resistance of Concrete to Chloride Ion Penetration," American Association of State Highway and Transportation Officials, Washington, DC.

Abbas, S.; Nehdi, M. L.; and Saleem, M. A., 2016, "Ultra-High Performance Concrete: Mechanical Performance, Durability, Sustainability and Implementation Challenges," *International Journal of Concrete Structures and Materials*, V. 10, No. 3, pp. 271-295. doi: 10.1007/s40069-016-0157-4

ACI Committee 222, 2001, "Protection of Metals in Concrete Against Corrosion (ACI 222R-01)," American Concrete Institute, Farmington Hills, MI, 41 pp.

ACI Committee 318, 2019, "Building Code Requirements for Structural Concrete (ACI 318-19) and Commentary (ACI 318R-19) (Reapproved 2022)," American Concrete Institute, Farmington Hills, MI, 625 pp.

ACI Committee 363, 2010, "Report on High-Strength Concrete (ACI 363R-10)," American Concrete Institute, Farmington Hills, MI, 65 pp.

Aitcin, P. C., 2003, "The Durability Characteristics of High-Performance Concrete: A Review," *Cement and Concrete Composites*, V. 25, No. 4-5, pp. 409-420. doi: 10.1016/S0958-9465(02)00081-1

Alghamdi, S. A., and Ahmad, S., 2014, "Service Life Prediction of RC Structures Based On Correlation Between Electrochemical and Gravimetric Reinforcement Corrosion Rates," *Cement and Concrete Composites*, V. 47, pp. 64-68. doi: 10.1016/j.cemconcomp.2013.06.003

Alkaysi, M.; El-Tawil, S.; Liu, Z.; and Hansen, W., 2016, "Effects of Silica Powder and Cement Type On Durability of Ultra High Performance Concrete (UHPC)," *Cement and Concrete Composites*, V. 66, pp. 47-56. doi: 10.1016/j.cemconcomp.2015.11.005

ASTM C666/C666M-15, 2015, "Standard Test Method for Resistance of Concrete to Rapid Freezing and Thawing," ASTM International, West Conshohocken, PA.

ASTM C672/C672M-12, 2012, "Standard Test Method for Scaling Resistance of Concrete Surfaces Exposed to Deicing Chemicals," ASTM International, West Conshohocken, PA.

ASTM C876-15, 2015, "Standard Test Method for Corrosion Potentials of Uncoated Reinforcing Steel in Concrete," ASTM International, West Conshohocken, PA.

ASTM C944/C944M-12, 2012, "Standard Test Method for Abrasion Resistance of Concrete or Mortar Surfaces by the Rotating-Cutter Method," ASTM International, West Conshohocken, PA.

ASTM C1202-12, 2012, "Standard Test Method for Electrical Indication of Concrete's Ability to Resist Chloride Ion Penetration," ASTM International, West Conshohocken, PA.

ASTM C1260-14, 2014, "Standard Test Method for Potential Alkali Reactivity of Aggregates," ASTM International, West Conshohocken, PA.

ASTM G1-03(2011), 2003, "Standard Practice for Preparing, Cleaning, and Evaluating Corrosion Test," ASTM International, West Conshohocken, PA.

ASTM G102-89(2010), 1989, "Standard Practice for Calculation of Corrosion Rates and Related Information from Electrochemical Measurements," ASTM International, West Conshohocken, PA.

ASTM G109-13, 2013, "Standard Test Method for Determining the Effects of Chemical Admixtures on the Corrosion of Embedded Steel Reinforcement in Concrete Exposed to Chloride Environments," ASTM International, West Conshohocken, PA.

Batoz, J., and Behloul, M., 2009, "UHPFRC Development on the Last Two Decades: An Overview," *UHPFRC Conference*, Marseille, France, pp. 1-13.

BS EN 197-1:2011, 2011, "Cement - Composition, Specifications and Conformity Criteria for Common Cements," British Standards Institution, London, UK.

Cady, P. D., and Gannon, E. J., 1993, "Condition Evaluation of Concrete Bridges Relative to Reinforcement Corrosion, Volume 8: Procedure Manual," *SHRP-S-330*, Strategic Highway Research Program, Washington, DC.

Cui, F., 2003, "Corrosion Behavior of Stainless Steel Clad Rebar," PhD dissertation, University of South Florida, Tampa, FL.

Darwin, D.; O'Reilly, M.; Somogie, I.; Sperry, J.; Lafikes, J.; Storm, S.; and Browning, J., 2013, "Stainless Steel Reinforcement as a Replacement for Epoxy Coated Steel in Bridge Decks," Report FHWA-OK-13-08, University of Kansas Center for Research, Inc., Lawrence, KS.

El-Gelany, M., 2001, "Short-Term Corrosion Rate Measurement of NC and HPC Reinforced Concrete Specimens by Electrochemical Techniques," *Materials and Structures*, V. 34, No. 7, pp. 426-432. doi: 10.1007/BF02482289

Ferdosian, I., and Camões, A., 2016, "Ultra-High Durable Concrete: A Way Towards Safe and Durable Structures," *7th International Conference on Safety and Durability of Structures (ICOSADOS 2016)*, Vila Real, Portugal.

Ghafari, E.; Arezoumandi, M.; Costa, H.; and Júlio, E., 2015, "Influence of Nano-Silica Addition in the Durability of UHPC," *Construction and Building Materials*, V. 94, pp. 181-188. doi: 10.1016/j.conbuildmat.2015.07.009

Gowripalan, N., and Mohamed, H. M., 1998, "Chloride-Ion Induced Corrosion of Galvanized and Ordinary Steel Reinforcement in High-Performance Concrete," *Cement and Concrete Research*, V. 28, No. 8, pp. 1119-1131. doi: 10.1016/S0008-8846(98)00090-8

Graybeal, B., 2005, "Characterization of the Behavior of Ultra-High-Performance Concrete," PhD dissertation, University of Maryland, College Park, MD.

- Graybeal, B., 2006, "Material Property Characterization of Ultra-High Performance Concrete," Report No. FHWA-HRT-06-103, Federal Highway Administration, McLean, VA.
- Graybeal, B., and Hartman, J., 2003, "Strength and Durability of Ultra-High Performance Concrete," *Concrete Bridge Conference*, pp. 1-20
- Graybeal, B., and Tanesi, J., 2007, "Durability of an Ultrahigh-Performance Concrete," *Journal of Materials in Civil Engineering*, ASCE, V.19, No. 10, pp.848-854. doi:10.1061/(ASCE)0899-1561(2007)19:10(848)
- Hansson, C. M.; Poursaei, A.; and Jaffer, S. J., 2007, "Corrosion of Reinforcing Bars in Concrete," *R&D Serial No. 3013*, Portland Cement Association, Skokie, IL.
- Hansson, C. M.; Poursaei, A.; and Laurent, A., 2006, "Macrocell and Microcell Corrosion of Steel in Ordinary Portland Cement and High Performance Concretes," *Cement and Concrete Research*, V. 36, No. 11, pp. 2098-2102. doi: 10.1016/j.cemconres.2006.07.005
- Ismail, M., and Ohtsu, M., 2006, "Corrosion Rate of Ordinary and High-Performance Concrete Subjected to Chloride Attack by AC Impedance Spectroscopy," *Construction and Building Materials*, V. 20, No. 7, pp. 458-469. doi: 10.1016/j.conbuildmat.2005.01.062
- Ismail, M., and Soleymani, H. R., 2002, "Monitoring Corrosion Rate for Ordinary Portland Concrete (NC) And High-Performance Concrete (HPC) Specimens Subjected to Chloride Attack," *Canadian Journal of Civil Engineering*, V. 29, No. 6, pp. 863-874. doi: 10.1139/I02-091
- Jaffer, S. J., 2007, "The Influence of Loading on the Corrosion of Steel in Cracked Ordinary Portland Cement and High Performance Concretes," PhD thesis, University of Waterloo, Waterloo, ON, Canada.
- Ji, J., 2005, "Corrosion Resistance of Microcomposite and Duplex Stainless Steels for Reinforced Concrete Bridge Decks," PhD dissertation, University of Kansas, Lawrence, KS.
- Lopez-Calvo, H. Z.; Montes-Garcia, P.; Alonso-Guzmán, E. M.; Martinez-Molina, W.; Bremner, T. W.; and Thomas, M. D. A., 2017, "Effects of Corrosion Inhibiting Admixtures and Supplementary Cementitious Materials Combinations On the Strength and Certain Durability Properties of HPC," *Canadian Journal of Civil Engineering*, V. 44, No. 11, pp. 918-926. doi: 10.1139/cjce-2016-0237
- Lopez-Calvo, H. Z.; Montes-Garcia, P.; Jiménez-Quero, V. G.; Gómez-Barranco, H.; Bremmer, T. W.; and Thomas, M. D. A., 2018, "Influence of Crack Width, Cover Depth and Concrete Quality On Corrosion of Steel in HPC Containing Corrosion Inhibiting Admixtures and Fly Ash," *Cement and Concrete Composites*, V. 88, pp. 200-210. doi: 10.1016/j.cemconcomp.2018.01.016
- Nazim, M., 2017, "Corrosion Propagation of Rebar Embedded in High Performance Concrete," master's thesis, Florida Atlantic University, Boca Raton, FL.
- NT Build 443, 1995, "Concrete, Hardened: Accelerated Chloride Penetration," NORDTEST, Oslo, Norway.
- Pernicová, R., 2014, "Chloride Transport in Ultra High Performance Concrete," *International Journal of Materials and Metallurgical Engineering*, V. 8, No. 11, pp. 1060-1063.
- Piérard, J.; Cauberg, N.; and Remy, O., 2009, "Evaluation of Durability and Cracking Tendency of Ultra High-Performance Concrete," *Proceedings, 8th International Conference on Creep, Shrinkage and Durability Mechanics of Concrete and Concrete Structures (CONCREP 8)*, Ise-Shima, Japan, pp. 695-700.
- Piérard, J.; Dooms, B.; and Cauberg, N., 2013, "Durability Evaluation of Different Types of UHPC," *RILEM-fib-AFGC International Symposium on Ultra-High Performance Fibre-Reinforced Concrete (UHPFRC 2013)*, F. Toutlemonde and J. Resplendino, eds., Marseille, France pp. 275-284.
- Presuel-Moreno, F. J.; Bencosme, R.; Hoque, K.; Nazim, M.; Kazemi, A.; and Tang, F., 2018, "Corrosion Propagation of Carbon Steel Rebars in High Performance Concrete," *BDV27-977-08 Final Report*, Florida Department of Transportation, Tallahassee, FL.
- Rizkalla, S.; Zia, P.; Seliem, H.; and Lucier, G., 2005, "Evaluation of MMFX Steel for NCDOT Concrete Bridges," Report No. FHWA/NC/2006-31, North Carolina Department of Transportation, Raleigh, NC, 128 pp.
- Shareef, A. Y., 2013, "A Study On Durability Properties of Ultra-High Performance Concrete (UHPC) Utilizing Local Fine Quartz Sand," master's thesis, King Fahd University of Petroleum & Minerals, Dhahran, Saudi Arabia.
- Sharma, S.; Arora, V. V.; Kumar, S.; Daniel, Y. N.; and Sharma, A., 2018, "Durability Study of High-Strength Steel Fiber-Reinforced Concrete," *ACI Materials Journal*, V. 115, No. 2, Mar., pp. 219-225. doi: 10.14359/51701122
- Soleymani, H. R., and Ismail, M. E., 2004, "Comparing Corrosion Measurement Methods to Assess the Corrosion Activity of Laboratory NC and HPC Concrete Specimens," *Cement and Concrete Research*, V. 34, No. 11, pp. 2037-2044. doi: 10.1016/j.cemconres.2004.03.008
- Sriharan, S., 2015, "Design of UHPC Structural Members: Lessons Learned and ASTM Test Requirements," *Advances in Civil Engineering Materials*, V. 4, No. 2, pp. 113-131. doi: 10.1520/ACEM20140042
- Tan, Q., 2015, "Investigation of Durability and Compressive Strength of HPC Mixtures and Modeling the Corrosion Initiation Time Through the Electrical Resistivity," master's thesis, California State University, Fullerton, Fullerton, CA.
- Wang, B., 2019, "Corrosion Behavior of Corrosion-Resistant Steel Reinforcements in High and Ultra-High-Performance Concrete in Chloride Attack Environments," PhD dissertation, University of Houston, Houston, TX.
- Wang, B.; Belarbi, A.; Dawood, M.; and Kahraman, R., 2022, "Corrosion Behavior of Corrosion-Resistant Steel Reinforcements in Normal-Strength and High-Performance Concrete: Large-Scale Column Tests and Analysis," *ACI Materials Journal*, V. 119, No. 5, Sept., pp. 89-102.
- Zou, Y.; Wang, J.; and Zheng, Y. Y., 2011, "Electrochemical Techniques for Determining Corrosion Rate of Rusted Steel in Seawater," *Corrosion Science*, V. 53, No. 1, pp. 208-216. doi: 10.1016/j.corsci.2010.09.011

ACI Honors and Awards Program Nominations



The American Concrete Institute is seeking your nominations for our Honors and Awards Program. Nominations are now being accepted for ACI's Honorary Member as well as for ACI's personal awards for individual or organizational merit, the ACI Young Member Award for Professional Achievement, the ACI Education Award, the ACI Certification Award, the ACI Concrete Sustainability Award, and more.

ACI selects the winners of its annual awards through an open nomination process.

You can participate in the Honors and Awards Program by nominating worthy candidates for award consideration.

Nomination forms can be found on the ACI website, www.concrete.org.



American Concrete Institute
+1.248.848.3188 • www.concrete.org



ACI

MATERIALS

JOURNAL

The American Concrete Institute (ACI) is a leading authority and resource worldwide for the development and distribution of consensus-based standards and technical resources, educational programs, and certifications for individuals and organizations involved in concrete design, construction, and materials, who share a commitment to pursuing the best use of concrete.

Individuals interested in the activities of ACI are encouraged to explore the ACI website for membership opportunities, committee activities, and a wide variety of concrete resources. As a volunteer member-driven organization, ACI invites partnerships and welcomes all concrete professionals who wish to be part of a respected, connected, social group that provides an opportunity for professional growth, networking, and enjoyment.



American Concrete Institute